

# Colloid-like Ionic Clusters

Structure Formation with Small Molecules through  
Weak Interactions in Solution

Dissertation

zur Erlangung des Doktorgrades der Naturwissenschaften  
(Dr. rer. nat.)

der

Naturwissenschaftlichen Fakultät II  
Chemie, Physik und Mathematik

der Martin-Luther-Universität  
Halle-Wittenberg

vorgelegt von

Frau Jana Eisermann  
geb. am 25. März 1993 in Plauen

Gutachter: Prof. Dr. Dariush Hinderberger  
Prof. Dr. Christopher Kay

Verteidigungsdatum: 10.12.2019





# Contents

<b>1. Introduction</b>	<b>1</b>
<b>2. Intermolecular Interactions</b>	<b>7</b>
2.1. Lennard-Jones potential	7
2.2. Coulomb Interaction	8
2.3. Van der Waals Interactions	9
2.3.1. <i>Keesom</i> Interaction	10
2.3.2. <i>Debye</i> Interaction	11
2.3.3. <i>London</i> Interaction	12
2.4. Repulsive Interaction	14
2.5. Additional Interactions	15
2.5.1. Hydrogen Bonds	15
2.5.2. Hydrophobic Interaction	15
2.5.3. Depletion Forces	16
2.5.4. Electrostatic Forces between Surfaces in Liquids	17
<b>3. Methods</b>	<b>19</b>
3.1. Dynamic Light Scattering	19
3.1.1. Scattering behavior for one single molecule	19
3.1.2. Basic concept of dynamic light scattering	21
3.2. Electron Paramagnetic Resonance Spectroscopy	25
3.2.1. Electron spin and resonance condition	25
3.2.2. Bloch equations and continuous microwave irradiation	27
3.2.3. Spin Hamiltonian and types of interactions	30
3.2.4. Nitroxide radicals as paramagnetic species	34
3.2.5. Pulsed EPR spectroscopy	39
<b>4. Solvation and Concentration effects</b>	<b>45</b>
4.1. Introduction	46
4.2. Experimental	47
4.2.1. Materials	47

---

4.2.2.	Solvent mixtures . . . . .	48
4.2.3.	Concentration . . . . .	48
4.2.4.	Methods . . . . .	49
4.3.	Results and Discussion . . . . .	50
4.3.1.	General remarks . . . . .	50
4.3.2.	Modifying solvent volume stoichiometry . . . . .	51
4.3.3.	Modifying glycerol:water volume ratio . . . . .	55
4.3.4.	Importance of bulk concentration . . . . .	57
4.4.	Conclusions . . . . .	60
<b>5.</b>	<b>Tuning shape anisotropy of ionoids</b>	<b>63</b>
5.1.	Introduction . . . . .	64
5.2.	Experimental . . . . .	65
5.2.1.	Materials . . . . .	65
5.2.2.	Ionic ratio . . . . .	65
5.2.3.	Methods . . . . .	66
5.3.	Results and Discussion . . . . .	66
5.3.1.	General remarks . . . . .	66
5.3.2.	Analyzing ionic ratio dependence with DLS . . . . .	67
5.3.3.	Analyzing ionic ratio dependence with CW EPR . . . . .	69
5.3.4.	Ionoid Evolution Diagram (IED) . . . . .	71
5.4.	Conclusions . . . . .	74
<b>6.</b>	<b>Self-Assembly of Ions with Variable Size and Charge</b>	<b>77</b>
6.1.	Introduction . . . . .	78
6.2.	Experimental . . . . .	81
6.2.1.	Materials . . . . .	81
6.2.2.	Size ratio . . . . .	81
6.2.3.	Methods . . . . .	82
6.3.	Results and Discussion . . . . .	83
6.3.1.	General Remarks . . . . .	83
6.3.2.	Substitution of $2^{2-}$ ( $3^{2-}$ ) . . . . .	84
6.3.3.	Substitution of $1^{4+}$ . . . . .	89
6.4.	Conclusions . . . . .	96
<b>7.</b>	<b>Shape, Size and Internal Dynamics in Ternary Solvent Systems</b>	<b>99</b>
7.1.	Introduction . . . . .	100

---

7.2. Experimental . . . . .	102
7.2.1. Materials . . . . .	102
7.2.2. Ionic ratio . . . . .	102
7.2.3. Methods . . . . .	103
7.3. Results and discussion . . . . .	104
7.3.1. General Remarks . . . . .	104
7.3.2. Solvent Characterization . . . . .	104
7.3.3. Analyzing Preferential Solvation with DLS . . . . .	106
7.3.4. Analyzing Preferential Solvation with CW EPR Spectroscopy . . . . .	110
7.4. Conclusion . . . . .	115
<b>8. Insight into the Local Solvation Shell</b>	<b>119</b>
8.1. Introduction . . . . .	119
8.2. Experimental . . . . .	121
8.2.1. Materials . . . . .	121
8.2.2. Methods . . . . .	121
8.3. Results and Discussion . . . . .	122
8.3.1. General Remarks . . . . .	122
8.3.2. Analyzing the selective substitution of solvent compounds . . . . .	122
8.3.3. Analyzing the incorporation of (partially) deuterated solvent compounds	126
8.4. Conclusion . . . . .	132
<b>9. Survival and Induced Formation of Ionoids</b>	<b>135</b>
9.1. Induced Ionoid Formation . . . . .	135
9.2. Thermal stability of globular ionoids . . . . .	144
9.3. Analyze globular ionoids with EPR spectroscopy . . . . .	146
9.4. Conclusion . . . . .	150
9.5. Overall conclusion and Outlook . . . . .	150
<b>A. Appendix - Methods</b>	<b>155</b>
A.1. DLS . . . . .	155
A.2. cmPALS . . . . .	158
A.3. EPR spectroscopy . . . . .	161
A.3.1. CW EPR spectroscopy . . . . .	161
A.3.2. Pulsed EPR spectroscopy . . . . .	165
A.4. IEDs . . . . .	169
<b>B. Appendix - Chapter 4</b>	<b>173</b>

C. Appendix - Chapter 5	194
D. Appendix - Chapter 6	198
E. Appendix - Chapter 7	224
F. Appendix - Chapter 8	248
G. Appendix - Chapter 9	260
References	273
List of Abbreviations and Symbols	287
Acknowledgements	293
Scientific Contributions	295
Publishing Permission	297
Curriculum Vitae	299
Eigenständigkeitserklärung	301

# 1 | Introduction

## Soft Matter and Nanoscience

*"What do we mean by soft matter? Americans prefer to call it "complex fluids". This is a rather ugly name, which tends to discourage the young students. But it does indeed bring in two of the major features:*

*1) Complexity. [...] 2) Flexibility."*<sup>1</sup>

**Pierre-Gilles de Gennes, 1991**

The cited sentences mark the beginning of the Noble lecture of Pierre-Gilles de Gennes from 1991, one of the most prominent pioneers in the field of soft matter science. His bold visions in this subarea of condensed matter established guidelines of how to treat problems in such a multifaceted field, which comprises a variety of independent classes, most of them exemplary embedded in his Noble lecture. The referred groups of rather independent systems include polymers, colloids, amphiphiles, membrane micelles, emulsions, dendrimers, liquid crystals, polyelectrolytes, and their mixtures.<sup>2</sup> All of them usually possess structural length scales in the region of one to several hundred nanometers and thus are categorized in the domain of 'nanotechnology'.<sup>3,4</sup> A characteristic feature of soft matter materials is that they are deformed or structurally altered by thermal or mechanical stress, which is located near the magnitude of thermal energy. Therefore, relatively small perturbations or very mild chemical actions can cause drastic structural changes.<sup>1,2</sup> Soft matter in general gained tremendous attention in the last decades, especially in the industrial (paints, porous media, plastics, ceramic precursors, textiles etc.)<sup>2</sup> and biological (proteins, polysaccharides, blood etc.)<sup>2,5</sup> field.

Returning to the domain of nanotechnology and nanoscience, their focus is gradually shifting from the synthesis of individual components to the assembly of larger systems and nanostructured materials. Nowadays, hundreds (or even thousands) of procedures are available allowing tailor-made sizes, shapes, material properties or surface chemistry of nanoscopic particles, like e. g. nanoscopic spheres, rods, ellipsoids, plates, (voided) core/shell particles, and nanocages.<sup>3</sup> Besides manufacturing large quantities of these structures with a variety of 'educts' (like

metals, oxides or inorganic salts) and gradually improving monodispersity, flexible functionalization using organic ligands is also possible. Therefore, nanoscience is already proclaimed as the 'next technological revolution'<sup>3,6</sup> (after the steam engine, electricity, and information technology), which generates high expectations and demands revolutionary solutions from this research field. Note that many of the schemed applications (like e. g. in medical diagnostics or drug delivery) do not base on individual nano-objects, but rather on their respective assembled setups (as mentioned earlier), in which interactions and purposefully organization of the basic units dominate. These conditions lead to the development of efficient and robust ways of assembling nanocomponents.

## Supramolecular Chemistry

*"Supramolecular chemistry is the chemistry of the intermolecular bond, covering the structure and functions of the entities formed by association of two or more chemical species."*<sup>7</sup>

**Jean-Marie Lehn, 1987**

While talking about the broad and interdisciplinary field of soft (condensed) matter, it is mandatory to also highlight the research area of supramolecular chemistry. Here, the introductory words come from the in 1987 written Noble lecture of Jean-Marie Lehn, one of the early innovators in this field. Beyond molecular chemistry based on the covalent bond, supramolecular chemistry aims at developing highly complex chemical systems from components interacting through noncovalent intermolecular forces.<sup>8,9</sup> The goal is to gain progressive control over the complex spatial (structural) and temporal (dynamic) features of matter through the process of self-organization. Three main themes can be associated with the development of supramolecular chemistry,<sup>8,9</sup> which will be briefly outlined.

The first theme contains the molecular recognition between artificial receptors with tailor-made design and their substrates. Beyond preorganization lies as second theme the design of programmed systems that self-organize through explicit manipulation of molecular recognition features. The applied interactions to achieve architectural complexity reach from hydrogen bonding over donor-acceptor to metal coordination interactions. One example for building units, which enable the formation of supramolecular structures through self-organization are so-called mechanically interlocked molecules.<sup>10</sup> The third theme introduces adaption and evolution, relying on self-organization through selection. This feature operates on dynamic constitutional diversity in response to either internal or external factors (due to the lability of the interactions that connect the molecular components) to achieve adaptations as well as

---

continuous change in constitutions. Therefore, supramolecular chemistry is a constitutional dynamic chemistry with a specific expression to dynamic combinatorial chemistry.<sup>11,12</sup> The latter one implements the reversible connection of pools of basic components to give access to virtual combinatorial libraries, whereas the actually expressed constituents are expected to be the ones presenting the strongest interaction with a given target.

## Ionic Self-Assembly

One of the most promising candidates for solving the challenge of constructing larger systems based on nanostructured materials, following the rules of supramolecular chemistry,<sup>13</sup> can be found in the principle of self-assembly.<sup>3,4</sup> Self-assembly is the spontaneous formation of ordered structures via noncovalent (or reversible) interaction between two objects, here e. g. nanoparticles, and can lead to well-defined entities. This energetically favorable procedure, which is used by chemists as a tool to mimic biological processes, ends principally with perfect structures, if allowed to reach its lowest energy level.<sup>4</sup> The information required to achieve the well-defined superstructure are embedded inside the starting building blocks, so no nanoassemblers or nanorobots for physical manipulation are required. Note that practical implementations to craft defect-free structures are difficult to obtain and reaching the equilibrium state can take a very long time. Additionally, the dynamic formation of these structures implements a time-dependent alteration, creating the need to design device layouts with build-in defect tolerance.<sup>4</sup>

If the coupling of structurally different building blocks is mainly dominated by electrostatic interactions, then the self-organization process is often described as ionic self-assembly (ISA).<sup>13</sup> In contrast to simple coulombic binding of salts is ionic self-assembly usually accompanied by a cooperative binding mechanism, meaning that the first bonds stimulate further binding propagating towards the final self-assembled structures. Furthermore, ISA has to make use of distinct geometric shapes, functionality patterns, and distributions of cohesion objects due to the non-selectivity and long-range character of the Coulomb interaction. The secondary structural elements, which contain weaker noncovalent interaction patterns, support the alignment driven by the charge-charge coupling.<sup>13</sup> With this it is principally possible to mutually bound and arrange a broad variety of building blocks, like e. g. geometric multivalent counterions, charged surfactants or polyelectrolytes.

Recently, the formation of highly defined, colloid-like ionic clusters in solution was described based on the process of ionic self-assembly.<sup>14</sup> The next section will focus on these soft and size monodisperse structures, the associated and most important results as well as prospective studies for this specific topic, which strongly influenced my own research.

## Colloid-like Ionic Cluster in Solution

### Status Quo

The building units, which were used to craft the colloid-like ionic cluster in solution, are the recently highlighted multicationic molecular box ( $\mathbf{1}^{4+}$ ) from Sessler and coworkers<sup>15</sup> and small dianionic salts  $(\text{KSO}_3)_2\text{CH}_2$  ( $\mathbf{2}^{2-}$ ) as well as  $(\text{KSO}_3)_2\text{NO}^-$  ( $\mathbf{3}^{2-}$ )<sup>a</sup>. Note that the multicationic box was already applied in the field of supramolecular chemistry as mechanically interlocked molecule to craft metal-organic rotaxane frameworks<sup>16</sup> and supramolecular necklaces.<sup>17</sup> By preparing a system of  $\mathbf{1}^{4+}:\mathbf{2}^{2-}$  ( $\mathbf{1}^{4+}:\mathbf{3}^{2-}$ , respectively) with a concentration ratio of 1 mM:3 mM, a defined assembly of the ionic compounds could be detected. Therefore, a rather complex solvent mixture of DMSO and 88% aqueous glycerol with a 1:1 volume ratio was needed.<sup>14</sup>

Dynamic light scattering (DLS) measurements revealed spherical, monodisperse structures with a hydrodynamic radius of 6.2 nm. Important here are the relatively low scattering intensity of the self-assembled entities and the detection after an incubation period of ten days. Reference measurements with purely the solvent mixture and solely  $\mathbf{1}^{4+}$  revealed no autocorrelation function. The detected loosely bound ion-based colloids, further named as ionoids, show an impressive long-term stability in solution (over the course of 140 days), whereas their size was slightly increasing.<sup>14</sup> In combination with the performed molecular dynamic and Monte Carlo simulations as well as electron paramagnetic resonance (EPR) spectroscopy measurements it could be demonstrated that long-range electrostatic correlations through the multicationic boxes mainly stabilize the well-ordered ionoids. The anionic compound  $\mathbf{2}^{2-}$  ( $\mathbf{3}^{2-}$ , respectively) seems to act as 'ionic glue' between  $\mathbf{1}^{4+}$  macrocycles, forcing them into a short-distance arrangement.<sup>14</sup>

### Motivation

The observed ionoid formation is obviously based on noncovalent interactions among the constituents, whereas electrostatic interactions play a major role for the detected durability of the final structure. Note that at this point it is difficult to quantify the influence of each noncovalent interaction for the complete formation process. However, the self-assembled entities are, due to the ISA process itself, probably sensitive towards even minor changes in solvent properties, ionic strength of the solution and/or concentration of the constituents. These considerations mark the starting point for my own research and the prepared PhD thesis. One major goal of my studies was (and still is) to analyze the ionic self-assembly of

---

<sup>a</sup> The structure of the applied ionic building units will be presented in later chapters and can be read up in Ref. 14.



ionoids and to assign specific parameters, later named 'design elements', characterizing the self-assembled entities. Fig. 1.1 shows 'design elements', which possess the potential to influence the formation of ionoids in solution. Similar to the presented results in Ref. 14, I used DLS and EPR spectroscopy as main methods to determine the importance of the mentioned 'design elements'. Therefore, I focused on the already established system containing the multicationic box  $1^{4+}$  in combination with the small dianionic salts contributing  $2^{2-}$  ( $3^{2-}$ , respectively) in the rather specific ternary solvent mixture of DMSO, glycerol and water.

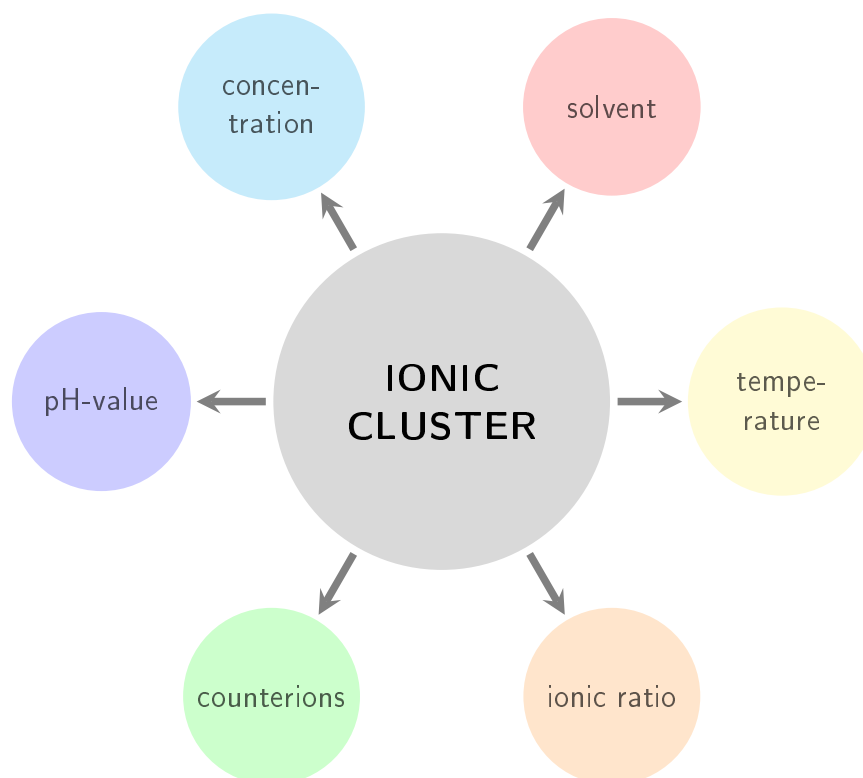


Fig. 1.1.: Potential 'design elements' affecting the formation of loosely bound ion-based colloids, named ionoids.

Another major goal of my PhD studies was to expand the formation of ionoids to other ionic building units to liberate this process from its 'special case' status. By establishing more systems capable of building such soft, yet well-defined structures with the same ionic self-assembly process, ionoids could be introduced to the field of supramolecular chemistry as new responsive material class or as subclass of "ultra divided matter"<sup>1</sup>, better known as colloids.

## Thesis structure

The overall structure of my PhD thesis represents the chronological development of analyzing the formation of colloid-like ionic clusters in solution. Before presenting my research results in detail, I highlight in Chapter 2 the molecular and particle interactions which define soft (con-

densed) matter. Note that I focus on *intermolecular* forces that are the basis of self-assembly and therefore the build up of ionoids. The two main methods, dynamic light scattering and electron paramagnetic resonance spectroscopy, are introduced in Chapter 3.

Chapter 4 presents my first study analyzing solvent and concentration effects on the self-assembly process of loosely bound colloid-like ionic cluster in solution. Here, variations in the volume ratio of DMSO, glycerol and water led to the formation of different self-assembled entities (in respect to size, shape and stability) compared to the small and spherical ionoids. As result, a new terminology was introduced to describe the ISA process of multicationic box  $\mathbf{1}^{4+}$  with small dianionic salts in a holistic manner. Afterwards, I analyzed, as described in Chapter 5, the influence of the ionic ratio as potential 'design element'. To adjust this parameter between the established ionic building units, I systematically changed the molar ratio of  $\mathbf{1}^{4+}:\mathbf{2}^{2-}$  ( $\mathbf{1}^{4+}:\mathbf{3}^{2-}$ , respectively) starting from the already published 1:3 system. Here, adjusting the ionic ratio in a defined manner enabled tuning the shape anisotropy of the self-assembled entities. Moreover, so-called ionoid evolution diagrams (IEDs) were introduced as a versatile tool to summarize the complex data sets for describing the temporal development of ionic clusters in solution.

At this point, the research topic splits up into two rather independent sections. On the one side, I studied the formation of loosely bound colloid-like ionic cluster based on new cationic and anionic building units. These new systems, as highlighted in Chapter 6, can be categorized based on the size of the applied building units, whereas each category demands a specific ionic ratio to build up stable self-assembled entities. On the other side, I expanded my studies to the solvation effect on the ISA process in respect to the model system of  $\mathbf{1}^{4+}:\mathbf{2}^{2-}$  ( $\mathbf{1}^{4+}:\mathbf{3}^{2-}$ , respectively). Chapter 7 shows the importance of DMSO, glycerol and water inside the ternary solvent mixture by systematically exchanging each component with another solvent, altering physical properties such as viscosity, dielectric constant and hydrogen bonding capability. Preferential solvation is further analyzed in Chapter 8, whereas the focus lies on results gathered with pulsed EPR spectroscopy. Besides the new solvent mixtures, which were already introduced in the previous chapter, I studied partially deuterated solvent mixtures of the established ternary combination of DMSO, glycerol and water. The last chapter summarizes measurement series that present interesting features regarding the stability and 'survival' of ionoids, but need further examination to gain conclusive insight into the complete self-assembly process.

## 2 | Intermolecular Interactions

This chapter focuses on the basic forces which keep soft matter in the condensed state. It refers to interactions among objects such as atoms, molecules, mesoscopic particles, surfaces and interfaces. Note that I do not intend to elaborately describe each possible interaction, but rather give an overview over the important forces regarding the ISA process of colloid-like ionic cluster in solution. For a more detailed depiction of this complex subject, Ref. 18 and 19 can be used as reading matter. Furthermore, a variety of reviews exist highlighting nanoscale forces and/or electrostatics and their application in self-assembly.<sup>3,20–23</sup>

### 2.1. Lennard-Jones potential

Interactions in general can be attractive or repulsive, meaning the respective interaction potential energy decreases or increases by approaching interaction partners. The stable 'equilibrium' distance of the interacting particles is reached, when the superposition of attractive and repulsive interaction potentials leads to a minimum. Systems in principle tend to the 'energetically more favorable' state (with minimum potential energy) by adopting their structural parameters.<sup>18,19</sup>

In terms of nonmetallic, nonionic, and non-electrolytic substances, *intramolecular* interactions are dominated by covalent bonding in contrast to *intermolecular* van der Waals forces and hydrogen bonds. This is clearly visible in the binding energies of the mentioned interactions: covalent bonds typically possess a (i) one or (ii) two order of magnitude higher binding energy compared to (i) hydrogen bonds or (ii) van der Waals forces. As parameter to characterize the strength of a bond (or interaction), the binding energy  $\varepsilon$  is used. Its order of magnitude per particle for covalent bonds amounts to  $10^{-19}$  J.<sup>18</sup>

To describe the interplay of attractive and repulsive forces among atoms and molecules depending on the separation distance  $r$  of the interaction partners, the *Lennard-Jones potential* is a standard starting point for the interaction potential energy. It can be formally represented as

$$W(r) = 4\varepsilon \left\{ \left( \frac{r_0}{r} \right)^{12} - \left( \frac{r_0}{r} \right)^6 \right\} \quad (2.1)$$

with  $\varepsilon$  as binding energy or depth of the potential well and  $r_0$  as finite distance at which the potential is zero ( $W(r = r_0) = 0$ ).<sup>18,24</sup> A graphical representation of equation 2.1 can be found in Fig. 2.1.

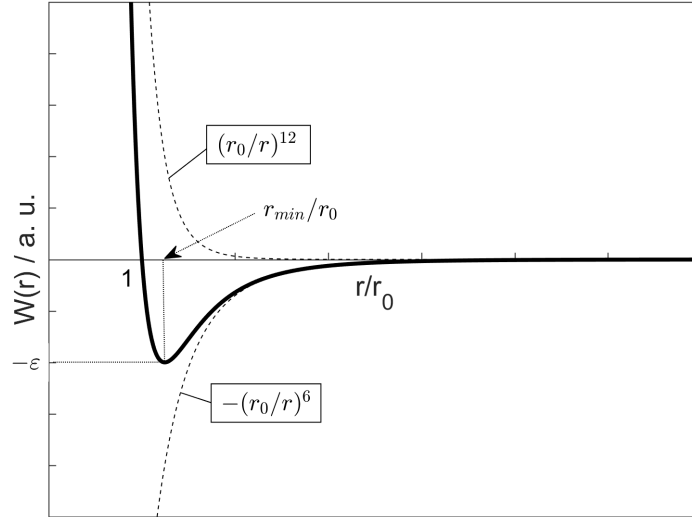


Fig. 2.1.: Lennard-Jones potential  $W(r)$  as function of the distance  $r$  of the interacting particles in units  $r_0$  (adapted from Ref. 18).

The repulsive part in the Lennard-Jones potential (also known as 12-6 potential) is positive and scales proportional to  $r^{-12}$ , whereas the attractive contribution with a negative sign has a  $r^{-6}$  dependence. For  $r = r_{min}$  the resulting superimposed potential contains a minimum, indicating the equilibrium distance of the interacting particles. The interaction force between the respective particles can be calculated as  $\vec{F}(r)d\vec{r} = -dW$  and vanishes for the equilibrium distance ( $F(r_{min}) = 0$ ). The general stabilization principle tends to minimize the total potential energy by adapting the microstructure of a system.<sup>18</sup>

The binding energy  $\varepsilon$  itself as depth of the potential well has a positive quantity, but the equilibrium potential  $W(r_{min}) = -\varepsilon$  is negative. If the system contains many degrees of freedom, then entropic contributions must be taken into account and the term 'potential' is interpreted in a thermodynamic sense<sup>b</sup>. The following sections highlight the different couplings, which can contribute to the superimposed potential  $W(r)$ .<sup>18</sup>

## 2.2. Coulomb Interaction

The electric field of a point charge  $q_2$  can be expressed as

<sup>b</sup> Distinct thermodynamic values, which reach a minimal value at equilibrium, are the Helmholtz free energy and the Gibbs free energy.

$$\vec{E}_{q_2} = \frac{1}{4\pi\epsilon_0\epsilon_r} \frac{q_2}{r^2} \vec{r} \quad (2.2)$$

with  $\epsilon_0$  as the electric field constant and  $\epsilon_r$  as relative permittivity of the medium. The respective Coulomb force acting on another point charge  $q_1$  with the distance  $r$  to  $q_2$  and the unit vector  $\vec{r}$  pointing between these two charges is

$$\vec{F}_{Coul,q_1} = q_1\vec{E}_{q_2} = \frac{1}{4\pi\epsilon_0\epsilon_r} \frac{q_1q_2}{r^2} \vec{r} . \quad (2.3)$$

Note that the Coulomb force on point charge  $q_2$  amounts to  $\vec{F}_{Coul,q_2} = -\vec{F}_{Coul,q_1}$ . Based on the general context of  $W$  and  $F$  (see previous section), the potential energy is

$$W_{Coul} = \frac{1}{4\pi\epsilon_0\epsilon_r} \frac{q_1q_2}{r} . \quad (2.4)$$

Depending on the sign of both point charges, they will attract (opposite signs,  $W_{Coul} < 0$ ) or repel (same signs,  $W_{Coul} > 0$ ) each other. The weak distance dependence of Coulomb force/potential further indicates the long-range interaction of ionized groups compared to interactions substantiated by dipoles (see next section).<sup>18,25</sup> Note that the binding energy per molecule amounts to roughly  $10^{-19}$  J, meaning that the strength of an ionic bond is similar to a covalent bond. Therefore, ionic compounds are mostly crystalline solids at room temperature, which can melt and become liquids at usually high temperatures.<sup>19</sup>

## 2.3. Van der Waals Interactions

For nonmetallic and non-electrolytic soft matter, van der Waals interaction represents the most important *intermolecular* force. It is based on Coulomb couplings of permanent or induced electric dipoles and can therefore be subdivided into three special cases<sup>26,27</sup>:

1. *Keesom* interaction: interactions of permanent molecular dipoles
2. *Debye* interaction: interactions of a permanent dipole and an induced dipole
3. *London* interaction: interactions of induced dipoles.

Before describing these three cases separately, the term dipole must be further defined. An electric dipole (with its respective dipole moment  $\vec{\mu}$ ) forms inside a molecule if the center of positive charge (i. e. of the nuclei) and the center of negative charge (i. e. of the electron clouds) do not coincide permanently or temporarily.<sup>18</sup> The respective formula

$$\vec{\mu} = q\vec{l} \quad (2.5)$$

contains the magnitude of the net charge  $q$  as well as the distance vector  $\vec{l}$  connecting the center of positive and negative charge. To analyze the different types of van der Waals interactions, the potential energy of an electric dipole inside the electrostatic field of another electric dipole must be determined<sup>c</sup>.

### 2.3.1. Keesom Interaction

To represent two dipoles, a total of four point charges can be used, leading to the formation of six pairs of interacting point charges. The *intra*-dipole couplings are not of interest in this case, leaving four *inter*-dipole interaction pairs. For the case of arbitrary (long-distance) arrangements and orientations of the dipole moment vectors  $\vec{\mu}_1$  and  $\vec{\mu}_2$ , the dipole-dipole interaction energy can be described as

$$W_{12} = \frac{1}{4\pi\epsilon_0\epsilon_r} \left( \frac{\vec{\mu}_1 \cdot \vec{\mu}_2}{r^3} - \frac{3(\vec{r} \cdot \vec{\mu}_1)(\vec{r} \cdot \vec{\mu}_2)}{r^5} \right) \quad (2.6)$$

with  $\vec{\mu}_1 = q_1\vec{l}$  and  $\vec{\mu}_2 = q_2\vec{l}$ .<sup>18</sup> Fig. 2.2 represents a possible arrangement for the electric dipole moments  $\vec{\mu}_1$  and  $\vec{\mu}_2$  utilizing the angles  $\vartheta_1$ ,  $\vartheta_2$  and  $\varphi$ .

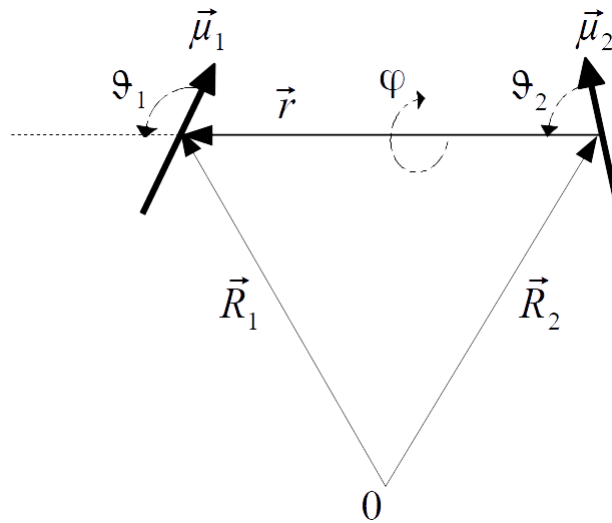


**Fig. 2.2.:** Electric dipole-dipole interaction: The inter-dipole vector is defined as  $\vec{r} = \vec{R}_1 - \vec{R}_2$ . The orientation of the dipole moments  $\vec{\mu}_1$  and  $\vec{\mu}_2$  relative to  $\vec{r}$  is characterized by the angles  $\vartheta_1$  and  $\vartheta_2$ , respectively.  $\varphi$  describes the angle between the planes spanned by the vector pairs  $\vec{\mu}_1, \vec{r}$  and  $\vec{\mu}_2, \vec{r}$  (adapted from Ref. 18).

Applying the angles defined by Fig. 2.2, equation 2.6 can be rewritten as<sup>18,28</sup>

<sup>c</sup> Further descriptions are restricted to the treatment of two-particle interactions. More-particle contributions can be estimated by the so-called *pairwise additivity approximation*, which will not be further discussed.

$$W_{12}(r, \varphi, \vartheta_1, \vartheta_2) = -\frac{1}{4\pi\epsilon_0\epsilon_r} \frac{\mu_1\mu_2}{r^3} (2\cos\vartheta_1\cos\vartheta_2 - \sin\vartheta_1\sin\vartheta_2\cos\varphi). \quad (2.7)$$

For the special case that two electric dipoles are aligned along a straight line, resulting in  $\vec{\mu}_1 \parallel \vec{r}$ ,  $\vec{\mu}_2 \parallel \vec{r}$  and  $\vec{\mu}_1 \parallel \vec{\mu}_2$ , expression 2.7 can be simplified to

$$W_{12} = -\frac{1}{4\pi\epsilon_0\epsilon_r} \frac{2\mu_1\mu_2}{r^3} \quad (\text{with } \vartheta_1 = \vartheta_2 = 0). \quad (2.8)$$

The thermal motion of molecules in liquid materials enables rotational diffusion, leading to orientational fluctuations of the dipoles relative to each other. Therefore, the interaction energy (equation 2.6) must be averaged over all possible dipole alignments. For example, the parallel alignment (equation 2.8) leads to a negative, energetically favorable interaction potential, whereas the orientation with  $\vartheta_1 = \pi$  and  $\vartheta_2 = 0$  contains a positive, energetically unfavorable potential. To describe the average value for  $W_{12}$ , the weighted form must be calculated with the aid of the orientation distribution function utilizing the Boltzmann factor<sup>d, 18</sup>

The resulting weighted average of the dipole-dipole interaction potential over the whole range of the angles  $\varphi$ ,  $\vartheta_1$  and  $\vartheta_2$  results in

$$\langle W_{12}(r, \varphi, \vartheta_1, \vartheta_2) \rangle = -\frac{1}{3(4\pi\epsilon_0\epsilon_r)^2} \frac{1}{k_B T} \frac{\mu_1^2 \mu_2^2}{r^6}, \quad (2.9)$$

containing the Boltzmann constant  $k_B$  as well as the absolute temperature  $T$ . Equation 2.9 is also known as *Keesom interaction energy* of a single pair of permanent molecular dipoles, valid for the high-temperature limit  $k_B T \gg W_{12}$ . The respective interaction energy per mol (multiplied with Avogadro's number) contains the order of  $-10 \frac{\text{kJ}}{\text{mol}}$ , indicating an attractive interaction potential. Furthermore, the Keesom interaction possesses a much faster decay ( $r^{-6}$ ) compared to the pure ionic interaction potential from equation 2.4 ( $r^{-1}$ ).<sup>18,19</sup>

### 2.3.2. Debye Interaction

For this type of van der Waals interaction the interplay between a polar molecule (containing a permanent dipole  $\vec{\mu}_{perm}$ ) and a nonpolar molecule is of interest. The electric field with the respective field strength  $\vec{E}_{perm}$  of the permanent dipole induces a dipole moment  $\vec{\mu}_{ind}$  inside the unpolar molecule, which can be calculated based on

$$\vec{\mu}_{ind} = \alpha \vec{E}_{perm}, \quad (2.10)$$

where  $\alpha$  describes the polarizability of the nonpolar molecule.<sup>25</sup> In the long-distance case, meaning the length of the permanent dipole  $l_{perm}$  is significantly smaller than the distance  $r$

<sup>d</sup> The Boltzmann factor can be written as  $p(r, \varphi, \vartheta_1, \vartheta_2) = \exp\{-W_{12}(r, \varphi, \vartheta_1, \vartheta_2)/k_B T\}$ .

to the induced dipole, the magnitude of the electric field strength is given based on Fig. 2.3 as

$$E_{perm}(r, \vartheta) \approx \frac{1}{4\pi\epsilon_0\epsilon_r} \frac{\mu_{perm}}{r^3} \sqrt{1 + 3\cos^2\theta} \quad \text{for } r \gg l_{perm}. \quad (2.11)$$

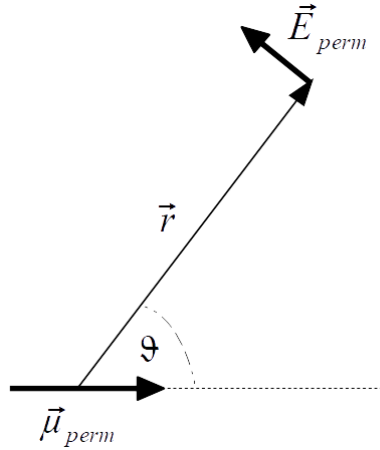


Fig. 2.3.: Electric field strength of a permanent dipole  $\vec{\mu}_{perm}$  in a distance  $\vec{r}$  (adapted from Ref. 18).

Note that the local vector directions inside the nonpolar molecule are parallel to each other,  $\vec{\mu}_{ind} \parallel \vec{E}_{perm}$ . The respective potential energy of the induced dipole in the electric field can be obtained with

$$W(r, \vartheta) = -\frac{1}{2} \alpha E_{perm}^2, \quad (2.12)$$

and describes the energy gained from moving the induced dipole from the infinite to the position  $r$ . After inserting equation 2.11 into  $W(r, \vartheta)$  and averaging this expression over all angles  $\vartheta$ , the *Debye interaction potential* is derived

$$\langle W(r, \vartheta) \rangle = -\frac{\alpha \mu_{perm}^2}{(4\pi\epsilon_0\epsilon_r)^2} \frac{1}{r^6}. \quad (2.13)$$

$\langle W(r, \vartheta) \rangle$  shows, similar to the Keesom interaction potential, a attractive nature as well as a  $r^{-6}$  distance correlation. The order of magnitude for the Debye interaction potential, which is in addition to the Keesom interaction, amounts to  $-1 \frac{\text{kJ}}{\text{mol}}$ .<sup>18,19</sup>

### 2.3.3. London Interaction

The most general variant of the van der Waals interactions acts in addition to the couplings mentioned before, but is particularly important for phenomena such as e. g. adhesion, surface tension, physical adsorption, or the flocculation of particles in liquids. It is most widely known



as *depletion force*, whereas this name is interlinked with the dispersion of light in the visible (vis) and ultraviolet (UV) regions of the spectrum.<sup>19,29</sup>

The main features of depletion forces are summarized in the following list<sup>19</sup>:

1. They are long-range forces and can be effective from greater than 10 nm down to inter-atomic spacing (0.2 nm).
2. They may be repulsive or attractive and the dispersion force between two molecules does not follow a simple power law.
3. Dispersion forces tend to mutually align or orient molecules (weaker than dipolar interactions).
4. They are not additive, so the force between two bodies is affected by the presence of other bodies nearby.

The origin of dispersion forces is of quantum mechanical nature, but an intuitive description can be given: For a nonpolar atom, the time average of its dipole moment is zero. However, at any instant there exists a finite dipole moment given by the instantaneous positions of the electrons about the nuclear protons, which generates an electric field. This field can polarize any nearby neutral atom, inducing a dipole moment in it. The resulting interaction between the two dipoles give rise to an attractive force, whereas the time average of the force/potential is finite.<sup>18,19</sup>

For a semiquantitative understanding of the arising force, the interaction of two Bohr atoms is analyzed. The smallest distance between the electron orbiting around a proton is known as the first Bohr radius  $a_0$

$$a_0 = \frac{e^2}{8\pi\epsilon_0 h\nu} = 0.053 \text{ nm} , \quad (2.14)$$

with  $h$  as Planck constant and  $\nu$  as orbiting frequency of the electron. The instantaneous dipole moment  $\mu = a_0 e$  (containing the elementary charge  $e$ ) of a Bohr atom will polarize a nearby neutral atom with its respective electric field. The rising attractive interaction is analogous to the dipole-induced dipole interaction described previously and the energy of this interaction in a vacuum ( $\epsilon_r = 1$ ) amounts to

$$W(r) = -\frac{1}{(4\pi\epsilon_0\epsilon_r)^2} \frac{\mu^2\alpha}{r^6} = -\frac{1}{(4\pi\epsilon_0)^2} \frac{(a_0 e)^2\alpha}{r^6} , \quad (2.15)$$

where  $\alpha$  describes the electronic polarizability of the second Bohr atom. Inserting  $a_0$  (equation 2.14) and applying  $\alpha = 4\pi\epsilon_0 a_0^3$ ,<sup>e</sup> the above interaction energy approximately transforms to

---

<sup>e</sup> The polarizability can be estimated based on the equilibrium between the magnitude of the internal force

$$W(r) \approx -\frac{h\nu}{(4\pi\epsilon_0)^2} \frac{\alpha^2}{r^6}. \quad (2.16)$$

Expect the numerical factor, equation 2.16 represents the expression for the *London interaction potential* using quantum mechanical perturbation theory. The 'exact' dispersion interaction energy between two identical atoms or molecules can be written as

$$W(r) = -\frac{3}{4} \frac{h\nu}{(4\pi\epsilon_0)^2} \frac{\alpha^2}{r^6}. \quad (2.17)$$

Note that the  $r^{-6}$  distance dependence for the applied model is the same as for the two other polarization interactions, the Keesom and Debye interaction. Together they contribute to the net van der Waals force.<sup>19</sup>

## 2.4. Repulsive Interaction

For approaching interacting molecules their electron orbitals start to overlap more and more, resulting in rising repulsive interactions, which will dominate at the end. Besides the Coulomb repulsion due to the electron clouds, the Pauli exclusion principle also contributes to this behavior. Note that electron orbital states are characterized by sets of certain quantum numbers specifying atomic shell, orbital angular momentum, and spin states. The overlap of electron clouds leads to electrons located in identical states in the same space region, which is quantum mechanically not permitted. Therefore, at least one electron is forced to adopt to a non-occupied higher-energy state, increasing the potential energy of the molecules.<sup>18,19</sup>

Orbital wave functions tend to decay exponentially at long distances, allowing the *Born repulsive interaction* as approach for the repulsive interaction energy

$$W_{rep}(r) = C \exp\left\{-\frac{r}{a}\right\}, \quad (2.18)$$

where  $C$  is a (positive) constant and  $a$  characterizes the extension of the orbital. Normally, the power law

$$W_{rep}(r) = 4\epsilon \left(\frac{r_0}{r}\right)^{12} \quad (2.19)$$

is applied with  $\epsilon$  as binding energy. Combining the repulsive interaction from equation 2.19 with the respective van der Waals attractive potentials, leads to the Lennard-Jones potential given in equation 2.1.<sup>18</sup>

---

due to Coulomb interaction between the respective charges and the external force (caused by an external electric field) the particle is subjected to.

The next section provides a short summary about other attractive and/or repulsive interactions, which can also play an important role for the behavior of soft (condensed) matter, whereas their respective role depends on the specific class of soft matter.

## 2.5. Additional Interactions

### 2.5.1. Hydrogen Bonds

This sort of interaction refers to pairs of electronegative atoms and is therefore predominantly electrostatic in nature but remains some elements of covalent bonding. The addressed pairs consists of the donor  $X$  and acceptor  $Y$ , enclosing the hydrogen atom in between. Note that the distance of the hydrogen atom is shorter to the donor (about 0.1 nm for O—H) than to the acceptor (about 0.176 nm for O...H),<sup>19</sup> as represented by the scheme  $XH\cdots Y$ . The fairly directional interaction can be of an *intra-* or *intermolecular* nature. Typical binding energies range from  $40 \frac{\text{kJ}}{\text{mol}}$  to  $< 4 \frac{\text{kJ}}{\text{mol}}$ ,<sup>30</sup> which corresponds to a region between ordinary covalent bonds and van der Waals interactions.<sup>18</sup>

The origin of hydrogen bonds cannot be traced back to a single principle and analytical treatments are hardly feasible. Empirically, the attractive part of its interaction potential scales with the donor-acceptor distance as  $\propto r^{-2}$ . Concerning the binding energy of hydrogen bonds in soft matter applications, it has to be comment that the mentioned order of magnitude refers to the gaseous state. Regarding (biological) systems and dealing with condensed phases in aqueous environments, the dissociation of a hydrogen bond between *intra-* and *intermolecular* solute groups is accompanied by instantaneous formation of a follow-up hydrogen bond to an adjacent water molecule. The resulting effective dissociation energy, describing the difference between the respective binding energies, is lower than the nominal binding energy of a solute acceptor-donor pair.<sup>18</sup> However, the biological importance of hydrogen bonds (especially in relation to e. g. protein structures) cannot be overemphasized.<sup>31</sup> Further information concerning the vast field of hydrogen bonding can be found in Ref. 32.

### 2.5.2. Hydrophobic Interaction

Hydrophobic interaction is actually not a self-contained coupling mechanism, but rather the negation of hydrogen bonding between solute and solvent molecules (e. g. for nonpolar solutes in water). Hydrophobic species are not able to form hydrogen bonds and the thermodynamically more favorable state refers to the association with equal molecules.<sup>18</sup>

Even though the segregation process seems to be a direct consequence of the reduction of the number of hydrogen bonds among water molecules due to the presence of the nonpolar solute molecules, the effect is primarily not of an enthalpic nature. The fluctuating hydrogen bond

network surrounding the solute molecules is rearranged, engaging them with solvation shells in which hydrogen bonds tend to be directed tangentially to the solvation molecules. The number of hydrogen bonds in water stays more or less constant. Note that the formation of such solvation shells is accompanied with a mobility loss for the water molecules, which is thermodynamically unfavorable due to a reduced entropy. To maximize the entropy, the hydrophobic species starts to aggregate to minimize the aqueous solvation shell formation. Therefore, the hydrophobic effect is predominantly of an entropic nature<sup>18,19</sup> and it is responsible for the assembly of cell membranes and intracellular compartments.<sup>33</sup>

### 2.5.3. Depletion Forces

Emulsified droplets and colloids suspensions are typical systems where depletion forces can arise. Here, the systems consist of a dispersion of particles of substantially deviating size, e. g. a few large particles (in the mesoscopic length scale) are dispersed in a medium containing relatively small molecules.<sup>34</sup> As a matter of statistical physics, the mere presence of small particles effectively produces an attractive force between these large particles, even when they do not interact directly with other particles.<sup>18</sup>

The concept of depletion forces is derived from the dependence of the Helmholtz free energy for the small particles on the mutual distance  $h'$  of the large particles  $A_H = A_H(h')$ , as shown in Fig. 2.4. The provided force among the large particles is expected as

$$F = - \left( \frac{\partial A_H}{\partial h'} \right)_T . \quad (2.20)$$

The subscript on the right-hand side indicates that isothermal conditions are anticipated and  $A_H = A_H(h')$  depends on the separation  $h'$  between the large particles.

For a general understanding of the concept of depletion forces and  $A_H(h')$ , it is important to analyze the respective volume for the small particles in the presence of the larger particles. The volume available ( $V_{avail}$ ) for the centers of the small particles is reduced by the excluded volume  $V_{ex}$ . Furthermore, the larger particles are surrounded by so-called *depletion zones*, spherical shells of thickness  $r_s$ . Depletion zones are defined by the nearest distance the centers of the small particle can approach the surface of the larger particles. At this point, two 'simple' scenarios (with respective values for  $V_{ex}$ ) can be distinguished:

1. the depletion zones do not overlap and
2. the depletion zones overlap.

The second case has an increased  $V_{avail}$  (reduced  $V_{ex}$ ) for the small molecules due to the volume formed by the overlap 'lens' with a width of  $w$ , leading to an increase in entropy, which is thermodynamically more favorable. As consequence, an attractive force between the large

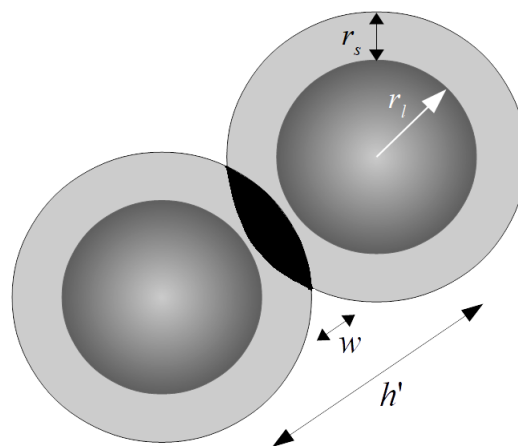


**Fig. 2.4.:** A shell of thickness  $r_s$  around the large particles is inaccessible to the centers of the small particles and forms a volume excluded for the small particles. If two such *depletion zones* overlap, the excluded volume will be reduced by a lens-shaped volume of width  $w$ . The distance of the centers of the large particles is denoted by  $h'$  (adapted from Ref. 18).

particles occurs. The attractive character of this force can lead to flocculation of emulsions (due to a higher aggregation tendency for the larger particles)<sup>18</sup> and to phase separation in colloidal suspensions.<sup>35</sup>

#### 2.5.4. Electrostatic Forces between Surfaces in Liquids

As soon as phases of different polar media form an interface, charge separation will partially take place. This especially refers to solid-like surfaces of polar materials exposed to water or aqueous electrolyte solutions. The polarity of the surface charge depends on the nature of the constituents of the system. Two main reasons responsible for this phenomenon are:

1. preferential adsorption of one ion species due to different chemical affinity and
2. the dissociative ionization of surface groups.

Both mechanism, which apply to isolated surfaces exposed to a liquid medium, are effective in electrolyte solutions, providing strong surface charges. These are balanced out by counterions attracted (with their respective solvation shell) by the charged surface.<sup>18</sup> A different type of charge exchange mechanism occurs between two closely packed dissimilar surfaces, where charges hop across from one surface to the other.<sup>19</sup>

Charged colloid particles are subject to van der Waals attraction and, additionally, to Coulomb interactions due to their net charges. Moreover, the Coulomb coupling is more complicated compared to the previously described systems with two-point charges due to the screening of the charged colloid particle with the sufficient counterions. Some of the counterions are bound,

usually transiently, to the surface within the so-called *Stern* or *Helmholtz* layer, while others form an atmosphere of ions in rapid thermal motion close to the surface, known as the diffuse *electric double-layer*.<sup>18,19</sup> In later studies (see e. g. Chapter 6), this electric double-layer will play a rather important role for characterizing the colloidal stability of self-assembled ionoids by determine the electrokinetic potential, also known as zeta potential (see Chapter A for further information).

## 3 | Methods

The following chapter offers a basic introduction into the two important methods, which I applied throughout all of my studies: dynamic light scattering and electron paramagnetic resonance spectroscopy. Note that Appendix A contains the information regarding the used instrumentation, performed sample preparations as well as chosen steps to analyze the recorded data sets. However, Chapter 3 serves as introduction to the fundamental principles of these rather complementary techniques.

### 3.1. Dynamic Light Scattering

In general, light scattering techniques provide a well-established foundation for the characterization of protein, polymer and colloidal structures along with nanostructured materials.<sup>36–39</sup> Dynamic light scattering (DLS, also known as photon correlation spectroscopy or quasi-elastic light scattering) is a versatile and useful method to determine size, size distributions and in some cases the shape of nanoparticles.<sup>40</sup> Actually, one determines the hydrodynamic radius  $R_H$ , which is the radius of the hypothetical hard sphere that diffuses with the same speed as the particles studied with DLS.<sup>41</sup>

The following section serves as short introduction into this technique, where one starts describing the scattering of polarized, monochromatic light at one single molecule. After that, one focuses on the transition from the recorded intensity fluctuations of the analysed sample to the final autocorrelation function, which can be fitted with different algorithms to gain the desired size distribution. A more detailed view regarding the method of dynamic light scattering can be found in Ref. 36 and 42, which served as foundation for the upcoming section.

#### 3.1.1. Scattering behavior for one single molecule

Electromagnetic waves consist generically of an oscillating electric and magnetic field. In the case of monochromatic, linearly polarized light, both field vectors  $\vec{E}$  and  $\vec{H}$  (respectively) are aligned perpendicular to each other, as shown in Fig. 3.1. Note that for the scattering process, the magnetic field can be neglected.

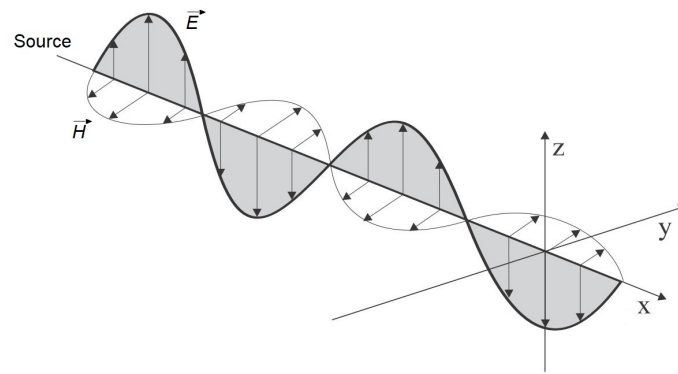


Fig. 3.1.: Electric and magnetic field (with their respective field vectors) of an electromagnetic wave (adapted from Ref. 43).

Based on a harmonic electromagnetic wave propagating in  $x$ -direction, the electric field vector can be expressed over<sup>36</sup>

$$E(x,t) = E_0 \left( \sin \left( \frac{2\pi x}{\lambda} \right) + \sin \left( \frac{2\pi c}{\lambda} t \right) \right), \quad (3.1)$$

with  $E_0$  as amplitude,  $\lambda$  as wavelength and  $c$  as the speed of light. A molecule, which is positioned at  $x=0$ , builds up a dipole moment  $\vec{\mu}$  due to the oscillating electric field

$$\vec{\mu} = \alpha \vec{E}, \quad |\vec{E}| = E_0 \exp \{i(2\pi\nu t - kx)\}. \quad (3.2)$$

Note that the induced dipole contains the same frequency as the external field and vibrates parallel to  $\vec{E}$ . The parameter  $\alpha$  describes the polarizability of the molecule,  $\nu = c/\lambda$  the frequency of the light and  $k = 2\pi/\lambda$  the length of the wave vector. To keep a constant amplitude, the oscillation dipole emits an alternating electromagnetic field, the so-called scattered light field. If the induced dipole is aligned along the  $z$ -axis, then the scattered light is isotrop in  $xy$ -plane and independent from the azimuth angle  $\theta$  (see Fig. 3.2).

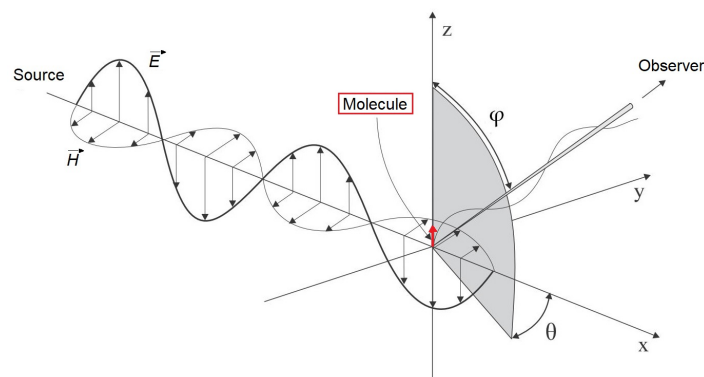


Fig. 3.2.: Oscillation dipole induced by an incident light wave and accordingly emitted light in respect to the angles  $\theta$  and  $\phi$  (adapted from Ref. 43).



Considering the distance vector  $\vec{r}$  from the dipole to the detector as well as the polar angle  $\varphi$ , one receives for the scattered electric field<sup>36,43</sup>

$$E_s = \frac{4\pi^2\alpha E_0 \sin\varphi}{r\lambda^2} \exp\{i(2\pi\nu t - \vec{k}\vec{r})\} . \quad (3.3)$$

In a light scattering experiment, one does not detect the amplitude of the electric wave vector, but the scattered intensity  $I_s = E_s E_s^* = |E_s|^2$ . Comparing the intensity ratios of the initial electromagnetic wave and the scattered light leads to the Rayleigh scattering term

$$\frac{I_s}{I_0} = \frac{16\pi^4\alpha^2}{r^2\lambda^4} \sin^2\varphi . \quad (3.4)$$

Note that due to the dependency of the intensity term from  $\varphi$  in equation 3.4, no radiation is visible in the vibration direction of the dipole ( $\varphi = 0$ ). When using unpolarized light, which can be described as superposition of many independent polarized waves with arbitrary alignment in the  $yz$ -plane, to perform light scattering experiments, equation 3.4 has to be adapted by substituting  $(1 + \cos^2\theta)/2$  for  $\sin^2\varphi$ <sup>44</sup>

$$\frac{I_s}{I_0} = \frac{8\pi^4\alpha^2}{r^2\lambda^4} (1 + \cos^2\theta) . \quad (3.5)$$

In respect to particles instead of single molecules, one has to mention that Rayleigh scattering is only valid for particles with much smaller size compared to the wavelength of the applied light ( $< \lambda/10$ ). For particles exceeding this threshold, the scattered light is (i) unequal in energy to the incident light and (ii) angle-dependent, whereas the scattered light is most intense towards the direction of the incident light. Here, one has to switch to the more complex model of Mie scattering to mathematically describe the light scattering pattern.<sup>41</sup>

### 3.1.2. Basic concept of dynamic light scattering

Particles in their dispersion medium follow the brownian motion, which causes fluctuations in the scattered light intensity  $I(t)$  with time. Theoretically, one could directly measure the existing intensity fluctuations with an interferometer, but the velocity of the molecular motion is by far smaller than the speed of light. The resulting frequency shifts due to the Doppler effect are marginal. Therefore, one does not analyze the frequency shift directly, but its fourier-transformed version known as autocorrelation function, which will be explained in the next paragraphs.

#### Fluctuations and autocorrelation function

Fig. 3.3 presents the time-dependent behavior of the scattering intensity  $I(t)$  for continuously mobile particles within dispersion. The detected intensity fluctuates, due to constructive and

destructive interference of the scattered light, around a mean value of  $\langle I \rangle$ .

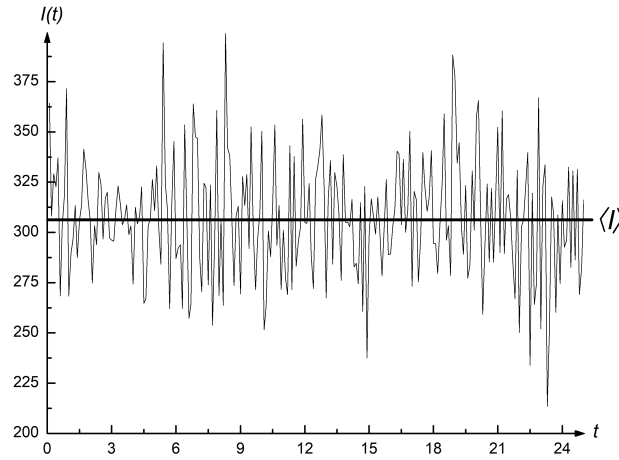


**Fig. 3.3.:** Time-dependent fluctuation of the detected scattering intensity  $I(t)$  around a mean value  $\langle I \rangle$ .

Based on the recorded fluctuations like shown in Fig. 3.3, one determines the scattering intensity for the time  $t$  and compares it with the value at moment  $t + \tau$ , whereas  $\tau$  describes the correlation time. For small  $\tau$ -values, the similarities for particles regarding position, velocity and movement direction are large, leading to a strong correlation between  $I(t)$  and  $I(t + \tau)$ . Increasing the correlation time causes a loss in both similarity and correlation. To formally introduce the correlation time  $\tau$ , the time axis (here named  $t_M$ ) gets divided into a total of  $N$  discrete measuring intervals with the size of  $\Delta t$

$$t_M = N \cdot \Delta t \quad (3.6)$$

$$\tau = n \cdot \Delta t \quad \text{with} \quad 0 \leq n \leq N . \quad (3.7)$$

The correlation between the mentioned scattering intensities is defined as

$$\langle I(t) \cdot I(t + \tau) \rangle = \frac{1}{t_M} \sum_{t=0}^{t_M} I(t) \cdot I(t + \tau) \Delta t . \quad (3.8)$$

Equation 3.8 describes the formation of all products with one correlation time  $\tau$  throughout the total time scale, which are then summed up and averaged by the division with  $t_M$ . In the case of  $\Delta t \rightarrow 0$ , the sum can be transferred into an integral

$$\langle I(t) \cdot I(t + \tau) \rangle = \lim_{t_M \rightarrow \infty} \frac{1}{t_M} \int_{t=0}^{t_M} I(t) \cdot I(t + \tau) dt . \quad (3.9)$$

Fig. 3.4 pictures the temporal development of equation 3.9, whereas two special cases can be highlighted:

1.  $\tau = 0$ : the correlation function reaches the mean squared intensity  $\langle I(t)^2 \rangle$  and
2.  $\tau \rightarrow \infty$ : the correlation function approaches the squared value of the mean intensity  $\langle I(t) \rangle^2$ .

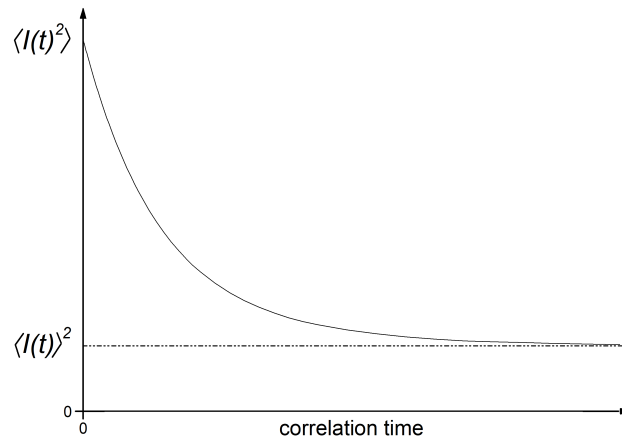


Fig. 3.4.: Graphical representation of the autocorrelation function  $\langle I(t) \cdot I(t + \tau) \rangle$ .

By dividing equation 3.9 with the mean squared intensity, one gains the normalized (scattered) intensity autocorrelation function  $g_2(\tau)$

$$g_2(\tau) = \frac{\langle I(t) \cdot I(t + \tau) \rangle}{\langle I(t)^2 \rangle}, \quad (3.10)$$

which theoretically should follow a single-exponential decay function from 2 to 1. Note that the applied DLS devices in the following studies (see Appendix A for further information) deliver  $g_2$  as measurement result. To simplify the data analysis, especially for polydisperse samples (see next section), it is common to plot the autocorrelation function in a semilogarithmic scale, as shown throughout all the following studies.

Besides formulating a normalized autocorrelation function for the scattering intensity, one can also utilize the amplitude of the electric field vector  $\vec{E}$ . The corresponding electric field autocorrelation function  $g_1(\tau)$  possesses a rather straightforward connection to  $g_2(\tau)$  known as the Siegert relation<sup>39,45</sup>

$$g_2(\tau) = B + \beta |g_1(\tau)|^2 \quad (3.11)$$

with  $B$  as baseline ( $\approx 1$ ) and  $\beta$  as coherence factor depending on detector area, optical alignment and scattering properties of the particles. The Siegert relation is founded on the approximations that (i) one detects a homodyne scattering and (ii) the photon counting is a random Gaussian process.

### Dispersity of the system

In an ideal case, the studied system consists of particles with a uniform size (monodisperse), therefore presenting an autocorrelation function with a single-exponential decay, expressed for  $g_1(\tau)$  as

$$g_1(\tau) = e^{-\Gamma\tau} . \quad (3.12)$$

The  $\Gamma$  in equation 3.12 describes the decay constant of the exponential function, which can be rewritten with  $g_2(\tau)$  as

$$g_2(\tau) = 1 + \beta e^{-2\Gamma\tau} . \quad (3.13)$$

However, a studied system mostly consists of particles with different dimensions/polydisperse sizes, so  $g_1(\tau)$  cannot be represented by a single exponential decay, but as an intensity-weighted integral over a distribution of decay rates  $G(\Gamma)$

$$g_1(\tau) = \int_0^{\infty} G(\Gamma) e^{-\Gamma\tau} d\Gamma . \quad (3.14)$$

The decay constant directly correlates with the diffusion behavior of the studied particles over

$$\Gamma = Dq^2 , \quad (3.15)$$

where  $q$  describes the scattering vector with  $q = \frac{4\pi n}{\lambda} \sin \frac{\theta}{2}$ , containing the refractive index of the solvent ( $n$ ), the laser wavelength ( $\lambda$ ) and the scattering angle  $\theta$ . In the case for spherical particles in a dilute solution, one can directly calculate the hydrodynamic radius  $R_H$  with the Stokes-Einstein equation

$$D = \frac{k_B T}{6\pi\eta R_H} , \quad (3.16)$$

utilizing the Boltzmann constant  $k_B$ , the absolute temperature  $T$  and the solvent viscosity  $\eta$ . Note that the translational diffusion coefficient is concentration-dependent and equation 3.16 refers to the self-diffusion coefficient of the studied particles.

### Data analysis

Modern DLS devices are supplied with packages that perform the data analysis, whereas different approaches are available to evaluate the size and homogeneity of the studied system. In general, one can distinguish between two options to fit the autocorrelation function: monomodal distribution and non-monomodal distribution methods.<sup>39</sup>

The cumulant analysis method, a rather common way to analyse DLS data introduced by Koppel,<sup>46</sup> can be categorized into the section of monomodal distribution methods. It provides mean values of the diffusion coefficient, but no distributions for this parameter, limiting its application for monodisperse systems with a Gaussian-like distribution around the mean value of  $D$ . Despite these limitations, the cumulant analysis method became widely popular due to its ease and reliability (in respect to the before mentioned limitations).

In contrary, non-monomodal methods do not assume a certain type of distribution of diffusion properties and can be better applied for polydisperse systems. Here, several algorithms are known, which are listed below:

- the non-negative least squares (NNLS) method,
- the maximum-entropy method,
- the exponential sampling method and
- the constrained regularization method for inverting data (CONTIN).

The DLS data presented in the following chapters were analyzed with the CONTIN algorithm (see Appendix A), developed by Provencher.<sup>47,48</sup> Here, the NNLS equation is modified to minimize regularized residuals and includes an appropriate weighing function.<sup>39</sup> Further information to the CONTIN algorithm can be found e. g. in Ref. 49.

## 3.2. Electron Paramagnetic Resonance Spectroscopy

Electron paramagnetic resonance (EPR) spectroscopy comprises in a narrow sense measuring the resonance frequency of unpaired electrons inside an external electric field. In a broader sense, one can summarize with EPR spectroscopy methods, which determine (i) transition frequencies of nuclear spins or (ii) couplings between electron spins based on the resonance excitation of electron spins.<sup>50</sup> In all cases, one is able to gain information about the structure, dynamics as well as spatial distribution of paramagnetic centers, which have to be incorporated into the respective system of interest. The respective parameters, which encode these information from the studied systems, will be emphasized throughout the next pages. A more refined description can be found in Ref. 51–53.

### 3.2.1. Electron spin and resonance condition

Starting in 1920, Otto Stern and Walther Gerlach observed that a beam of silver atoms splits into two separate lines when passing an inhomogeneous magnetic field.<sup>54,55</sup> The quantum mechanical explanation for this experimental phenomenon, nowadays known as Stern-Gerlach

experiment, followed in 1925 by George E. Uhlenbeck and Samuel A. Goudsmit.<sup>56,57</sup> They postulated an intrinsic property of the electron, the quantized angular momentum also known as 'spin'.<sup>50</sup> The 'spin' angular momentum  $\vec{S}$  gives, similar to the orbital angular momentum, rise to a magnetic momentum  $\vec{\mu}_{Spin}$  with

$$\vec{\mu}_{Spin} = \hbar\gamma\vec{S} = -g_e\mu_B\vec{S}, \quad (3.17)$$

whereas  $\gamma$  describes the magnetogyric ratio of the electron,  $\mu_B$  the Bohr magneton and  $g_e$  the  $g$ -factor for a free electron.  $\vec{S}$  itself can be defined with the magnetic quantum number  $m_s = \pm\frac{1}{2}$ , leading to two individual spin states. In order to separate the energy levels of the initial degenerated spin states, the electron has to be subjected to an external magnetic field  $\vec{B}$ . Based on  $\vec{B} = (0, 0, B_0)$ , one can calculate these energy levels with<sup>50</sup>

$$E = m_s g_e \mu_B B_0. \quad (3.18)$$

The energy difference between the two respective spin states with  $m_s = +\frac{1}{2}$  and  $m_s = -\frac{1}{2}$  can be assigned to an electromagnetic wave with larmor frequency  $\omega_s$ , leading to the following resonance condition

$$\Delta E = \hbar\omega_s = g_e\mu_B B_0. \quad (3.19)$$

A schematic representation of this phenomenon can be found in Fig. 3.5. The resonance frequencies corresponding to an external magnetic field are, from a historical viewpoint, divided into separate bands. Most commercially available spectrometers operate at X-band (9.4 GHz), Q-band (34 GHz) and W-band (94 GHz).

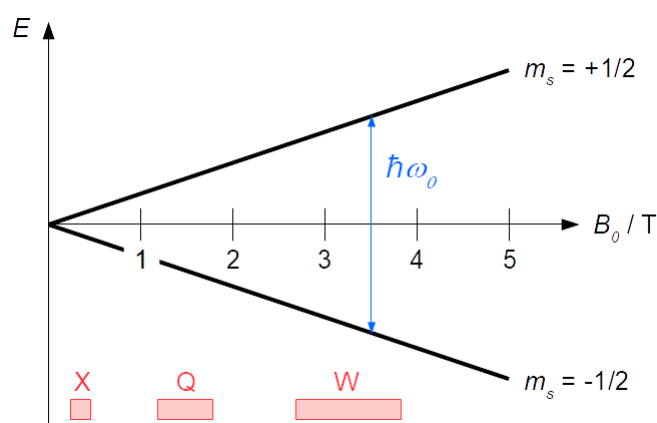


Fig. 3.5.: Splitting of the energy levels of an electron ( $g = g_e$ ) subjected to a magnetic field. Typical EPR microwave bands are also highlighted (adapted from Ref. 58).

Note that in EPR spectroscopy one does not detect single electron spins, but rather an ensemble of magnetic moments due to several electron spins. The measured parameter is the

macroscopic magnetization  $\mathbf{M}$ , which describes the net magnetic moment per volume  $V$

$$\mathbf{M} = \frac{1}{V} \sum_{i=1}^N \boldsymbol{\mu}_i . \quad (3.20)$$

Due to interactions of the electron spin (or rather magnetization) with e. g. magnetic nuclei in its vicinity, the resonance condition is altered. To describe the different energetic contributions to the system of interest, one has to look at its spin Hamiltonian, which will be discussed later in this section.<sup>50</sup>

### 3.2.2. Bloch equations and continuous microwave irradiation

The motion of a magnetic moment in a magnetic field gives, following the Larmor theorem, rise to a torque. This can be expressed for a single spin by

$$\hbar \frac{d\mathbf{S}}{dt} = \boldsymbol{\mu} \times \mathbf{B} . \quad (3.21)$$

By applying the net magnetization  $\mathbf{M}$  introduced in equation 3.20 and dividing by  $V$ , one gets

$$\hbar \frac{d\mathbf{M}}{dt} = \mathbf{M} \times \gamma \mathbf{B} . \quad (3.22)$$

In case (i) the magnetization is in equilibrium and (ii) a static magnetic field is applied along the z-axis, the magnetization vector cannot be detected because it is time-invariant. A displacement from the z-axis, resulting in a precessing motion around this axis with Larmor frequency  $\omega_0$ , induces a detectable alternating magnetic field. Therefore, defining a coordinate system that rotates counterclockwise with the microwave frequency  $\omega_{mw}$  is convenient. The precessing movement of the magnetization vector (visualized in Fig. 3.6 a)) can now be described with its respective frequency  $\Omega_s = \omega_0 - \omega_{mw}$ , which encompasses the resonance offset between Larmor and microwave frequency.

At this point, an additional oscillating microwave field  $\mathbf{B}_1^T = (B_1 \cos(\omega_{mw}t), B_1 \sin(\omega_{mw}t), 0)$  has to be applied along the x-axis to detect an EPR signal. As shown in Fig. 3.6 b), the magnetization vector moves away from its equilibrium position. For on-resonant mw irradiation ( $\Omega_s = 0$ ), the magnetization vector precesses around the x-axis and the effective nutation frequency  $\omega_{eff}$  equals  $\omega_1 = g\mu_B B_1 / \hbar$ . If the mw frequency is far off-resonant ( $\Omega_s > \omega_1$ ), then the magnetization vector is hardly affected.

Besides the already mentioned mechanisms, one also has to consider relaxation effects to fully describe the motion of the magnetization vector. The two types of relaxation effects, which influence the behavior of  $\mathbf{M}$ , are:

- the longitudinal relaxation time  $T_1$  characterizing the process(es) that recover the thermal equilibrium state of the magnetization vector and

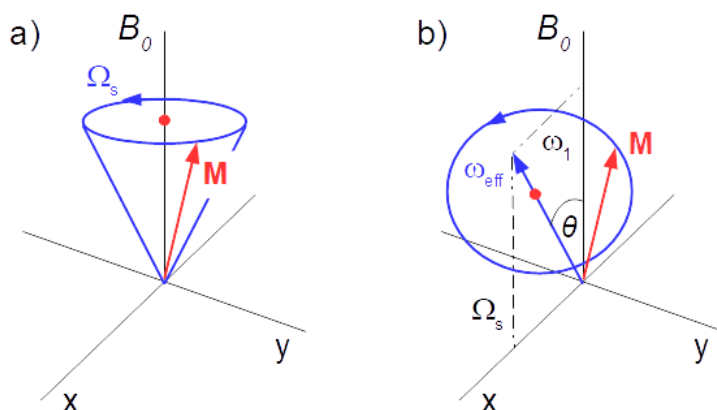


Fig. 3.6.: a) Free precession of the magnetization vector  $\mathbf{M}$  in the rotation frame with precession frequency  $\Omega_s$  (see main text). b) Nutation of the magnetization vector during off-resonant mw irradiation with a circularly polarized mw field along the  $x$ -axis with amplitude  $\omega_1$  (adapted from Ref. 53).

- the transverse relaxation time  $T_2$  describing the loss of coherence in the transverse plane due to spin-spin interactions.

Regarding the precession and the relaxation processes, one can formulate the equations of motion (Bloch equations) for the evolution of the magnetization<sup>50</sup>

$$\frac{dM_x}{dt} = -\Omega_s M_y - \frac{M_x}{T_2}, \quad (3.23)$$

$$\frac{dM_y}{dt} = \Omega_s M_x - \omega_1 M_z - \frac{M_y}{T_2}, \quad (3.24)$$

$$\frac{dM_z}{dt} = -\omega_1 M_y - \frac{M_z - M_0}{T_1}. \quad (3.25)$$

Note that  $M_z$  is called the longitudinal magnetization, whereas compounds  $M_x$  and  $M_y$  are named transverse magnetization, based on the particular relaxation processes.

### Continuous microwave irradiation

The most basic EPR experiment can be realized by continuously irradiating a sample placed in a magnetic field and detect the microwave absorption. Due to the difficulties to produce microwave sources that cover a broad and variable frequency range with sufficient quality (like amplitude and frequency stability), one keeps the mw frequency constant while changing or sweeping the magnetic field. Another feature, which has to be considered, originates from the used detectors inside the respective instrumentation. These microwave diodes are sensitive to a broad frequency range, so the EPR signal is modulated by a sinusoidal modulation of the magnetic field to reduce the detected noise. Note that only the modulated part of the



diode output voltage is detected. Moreover, this method (also known as CW EPR) implies recording the first derivative of the absorption spectrum and not the 'initial' absorption line. To avoid disturbed line shapes, the applied modulation amplitude (which affects the detected signal intensity) should not exceed one third of the peak-to-peak line width  $B_{pp}$ .<sup>58</sup>

The magnetization will reach a stationary state after a long enough continuous microwave irradiation, so that the time derivatives of the respective vector vanish. Therefore, the Bloch equations from 3.23 to 3.25 can be further analyzed as a linear system of equations. A detailed description can be found in Ref. 50 and 58.  $M_z$  cannot be detected with conventional experimental setups, whereas the transverse magnetization compounds can be measured simultaneously with the phase of the signal shifted by  $90^\circ$  in respect to each other. Based on that, one obtains a complex signal expressed as

$$V = -M_y + iM_x . \quad (3.26)$$

The real part of this complex signal ( $M_y$ ) corresponds to a Lorentzian absorption line containing a line width  $T_2^{-1}$  and the imaginary part to the respective Lorentzian dispersion line, as shown in Fig. 3.7.

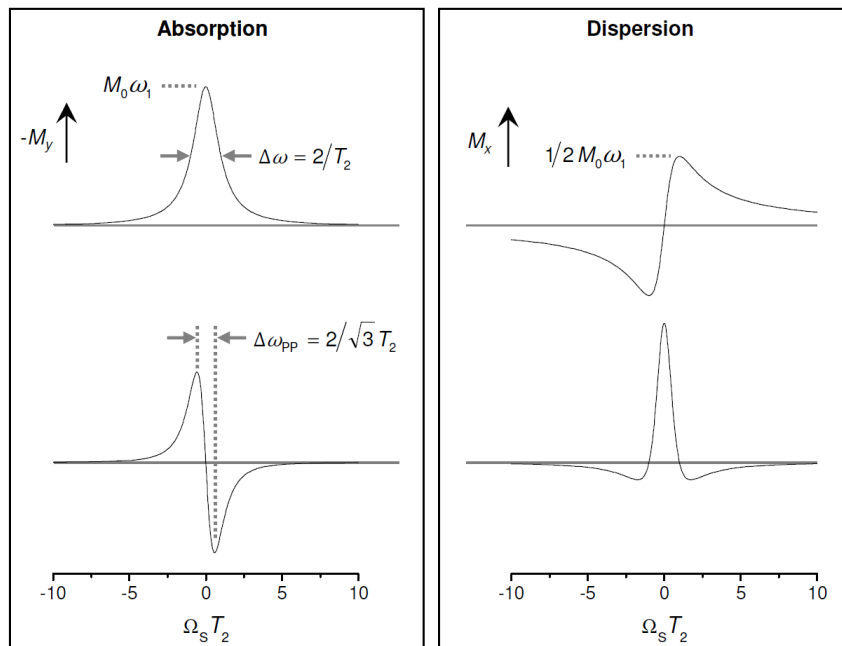


Fig. 3.7.: Lorentzian absorption and dispersion line shapes (top) compared to the respective first derivative ones (bottom); adapted from Ref. 58.

For analyzing the recorded first derivative spectra, the usage of the already mentioned peak-to-peak line width  $B_{pp}$  is favoured. It relates to the full width at half maximum (FWHM) of the Lorentzian absorption line with  $B_{pp} = \text{FWHM}/\sqrt{3}$ .<sup>53</sup> If the spectrum is not homogeneously broadened due to e. g. unresolved hyperfine couplings, the signal consists of Gauss or Voigt

lines rather than pure Lorentzian lines.

### 3.2.3. Spin Hamiltonian and types of interactions

The static, meaning time-independent Hamiltonian of an effective electron spin  $S$  coupled to  $m$  nuclei with spin  $I$  is given by<sup>53</sup>

$$H_0 = H_{EZ} + H_{ZFS} + H_{HF} + H_{NZ} + H_{NQ} + H_{e-e} . \quad (3.27)$$

The following sections serve to explain each term in equation 3.27 more in detail.

#### Electron Zeeman interaction $H_{EZ}$

For systems with  $S = \frac{1}{2}$  and usually applied magnetic fields (high field approximation), the electron Zeeman interaction displays the dominant term inside the spin Hamiltonian. It contains the interaction between the electron spin and the respective external magnetic field

$$H_{EZ} = \frac{\mu_B}{\hbar} \mathbf{B}_0^T \mathbf{g} \mathbf{S} , \quad (3.28)$$

leading to the splitting shown in Fig. 3.5. Due to the orientation-dependency of both spin operator  $\mathbf{S}$  and external magnetic field  $\mathbf{B}_0$ ,  $\mathbf{g}$  assumes the general form of a 3x3 matrix. Via Euler angle transformation of the magnetic field vector to the molecular coordinate system of the radical, the initial matrix can be diagonalized to<sup>50,58</sup>

$$\mathbf{g} = \begin{pmatrix} g_{xx} & g_{xy} & g_{xz} \\ g_{yx} & g_{yy} & g_{yz} \\ g_{zx} & g_{zy} & g_{zz} \end{pmatrix} = \begin{pmatrix} g_{xx} & 0 & 0 \\ 0 & g_{yy} & 0 \\ 0 & 0 & g_{zz} \end{pmatrix} . \quad (3.29)$$

Deviations of  $\mathbf{g}$  from the  $g_e$  value of the free electron spin as well as its orientation-dependent character rise from the spin-orbit coupling, therefore larger variations are observed for transition metal complexes. In solution, when molecular rotation is fast about all axes, the  $\mathbf{g}$ -matrix can be averaged to an isotropic  $g_{iso}$ -factor

$$g_{iso} = \frac{1}{3}(g_{xx} + g_{yy} + g_{zz}) , \quad (3.30)$$

determining the center of the CW EPR spectrum.

#### Zero-field splitting $H_{ZFS}$

Spin systems with a group spin of  $\mathbf{S} = \sum_k \mathbf{S}_k$  ( $S > \frac{1}{2}$ ), like transition metal ions or lanthanoid ions, are able to remove the energetic  $(2S+1)$ -fold degeneracy of the ground state by dipole-dipole couplings between individual electron spins. Therefore, an energy splitting is present

even in the absence of an external magnetic field, justifying the name 'zero-field splitting', expressed as

$$H_{ZFS} = \mathbf{S}^T \mathbf{D} \mathbf{S} . \quad (3.31)$$

$\mathbf{D}$  describes the symmetric and traceless zero-field interaction tensor. Note that for spin systems with a cubic symmetry the fine structure term completely vanishes. All studied systems in this thesis contain a paramagnetic species with  $S = \frac{1}{2}$ , whereas the  $H_{ZFS}$  term of the spin Hamiltonian can be neglected.

### Hyperfine interaction $H_{HF}$

One of the most important sources of information in EPR spectroscopy can be found in the hyperfine interaction term. It characterizes the interaction between the electron spin and surrounding nuclear spins as well as describes the direct magnetic environment of the electron spin. Its contribution to the Hamiltonian is given by

$$H_{HF} = \sum_k \mathbf{S}^T \mathbf{A}_k \mathbf{I}_k = H_F + H_{DD} \quad (3.32)$$

with  $\mathbf{A}$  as the hyperfine coupling tensor and  $\mathbf{I}_k$  the spin operator of the  $k$ th coupled nucleus. Note that the sum runs over all pairwise interactions of the electron with respective nuclear spins, leading to an additional splitting of the energy levels into  $2I + 1$  sublevels. Furthermore, this Hamiltonian can be subdivided in an isotropic part  $H_F$  (Fermi contact) and a dipolar part  $H_{DD}$ .

Assuming a liquid solution and fast tumbling of the spin probe, solely the Fermi contact interaction  $H_F$  contributes to the hyperfine interaction with

$$H_F = \sum_k a_{iso,k} \mathbf{S}^T \mathbf{I}_k . \quad (3.33)$$

Parameter  $a_{iso,k}$  describes the isotropic hyperfine coupling constant for the respective nucleus  $k$  with

$$a_{iso} = \frac{2}{3} \frac{\mu_0}{\hbar} g_e \mu_B g_n \mu_n |\psi_0(0)|^2 , \quad (3.34)$$

whereas  $\mu_0$  is the vacuum permeability,  $g_n$  and  $\mu_n$  are the nuclear  $g$ -factor and nuclear magneton (respectively), and  $|\psi_0(0)|^2$  is the electron spin density at the nucleus. The origin of the isotropic hyperfine interaction lies in non-vanishing electron spin density at the s-orbitals<sup>51</sup> of the atom<sup>a</sup>. Its mechanism works through direct contact between the unpaired electron and

---

<sup>a</sup> Higher orbitals (like p, d or f) do not have a spherical symmetry and so a lower spin density at the nucleus.

the nucleus, which is already implemented in the name Fermi contact interaction. In contrast, the dipole-dipole interaction  $H_{DD}$  expressed as

$$H_{DD} = \sum_k \mathbf{S}^T \mathbf{T}_k \mathbf{I}_k \quad (3.35)$$

contains the dipolar coupling tensor  $\mathbf{T}$  and acts through space. This term averages to zero by fast and isotropic rotation of the radical, leaving solely  $H_F$ .

### Nuclear Zeeman interaction $H_{NZ}$

Analogous to the electron spins couple nuclear spins with the external magnetic field, whereas this contribution known as nuclear Zeeman interaction  $H_{NZ}$  is described over

$$H_{NZ} = -\frac{\mu_n}{\hbar} \sum_k g_{n,k} \mathbf{B}_0^T \mathbf{I}_k . \quad (3.36)$$

The notation in equation 3.36 assumes an isotropic influence of the nuclear Zeeman interaction, which is a good approximation for most experiments.<sup>58</sup>

### Nuclear quadrupole interaction $H_{NQ}$

Nuclei, which possess  $I \geq 1$ , are characterized by a non-spherical charge distribution, leading to a nuclear quadrupole moment  $Q$ . This moment interacts with the electric field gradient at the nucleus, its contribution to the overall Hamiltonian can be described with the nuclear quadrupole tensor  $\mathbf{P}$  as

$$H_{NQ} = \sum_k \mathbf{I}_k^T \mathbf{P}_k \mathbf{I}_k . \quad (3.37)$$

Quadrupole couplings appear in CW EPR spectra only as second order effects. However, in experiments that probe the nuclear environment of the electron spin (like ESEEM) they (i) can be observed as first order splittings or (ii) may broaden observed nuclear peaks.

### Weak coupling between electron spins $H_{e-e}$

Until now, one characterized strongly interacting electron spins (e. g. due to spatial proximity) with an overall spin  $S > \frac{1}{2}$ . If the coupling is relatively weak, the electron spins are rather treated individually and their interaction with each other is introduced as perturbation  $H_{e-e}$  of the two isolated electron spin states. Here, one can distinguish two types of interactions: (i)

---

Therefore, their influence in this interaction is subordinated.

Heisenberg spin exchange coupling  $H_{exch}$  and (ii) dipolar coupling  $H_{DD,e}$ , so that the respective Hamiltonian for a coupled system of two electron spins becomes

$$H(S_1, S_2) = H(S_1) + H(S_2) + H_{e-e} \quad (3.38)$$

$$= H(S_1) + H(S_2) + H_{exch} + H_{DD,e} . \quad (3.39)$$

The Heisenberg spin exchange interaction,<sup>59</sup> shortly named exchange interaction, contains the coupling term

$$H_{exch} = \mathbf{S}_1^T \mathbf{J} \mathbf{S}_2 , \quad (3.40)$$

where  $\mathbf{J}$  describes the exchange-coupling tensor<sup>b</sup>. In liquid solution, direct overlap of the electron-bearing orbitals causes the spin exchange. Therefore, it is correlated to the frequency of intermolecular collisions and can be used as measure of the local concentration of radicals.<sup>59</sup> For an empirical description, kinetics of a bimolecular chemical reaction behave rather similar. The orbital overlap, which allows exchanging the electrons of the two species, can influence CW EPR spectra by broadening, narrowing or shifting of lines, as shown in Fig. 3.8. Here, the simulated CW EPR spectra only differ in the assumed exchange rates and display the main regimes of exchange interaction on the CW EPR spectra (from bottom to top):

1. no exchange,
2. slight broadening of spectra,
3. strong exchange broadening shortly before all three lines merge into one broad line ('exchange collapse') and
4. exchange narrowing.

Variations from the broadening shown in Fig. 3.8 are possible if e. g. a distribution of exchange frequencies dominates the spectra. In the case of frozen solution (solid) samples, spin exchange can take place through bond or through solvent. Such interactions are significant up to an electron-electron distance of roughly 1.5 nm, whereas above this value dipolar interactions dominate.<sup>60</sup>

---

<sup>b</sup> Note that exchange coupling can be differentiated into an isotropic and anisotropic contribution, which will be not further discussed in this paragraph.

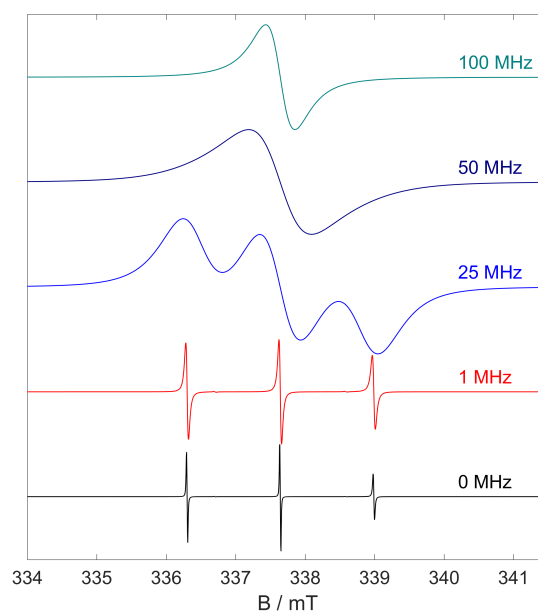


**Fig. 3.8.:** Influence of increased Heisenberg spin exchange interaction on simulated CW EPR spectra at room temperature; All parameters are equal except for the spin exchange frequency that is varied from bottom to top: 0 MHz, 1 MHz, 25 MHz, 50 MHz and 100 MHz. Simulations were performed with Matlab exploiting the EasySpin package (see Appendix A).

The dipole-dipole interaction term  $H_{DD,e}$  between electrons acts, in analogy to the magnetic dipolar coupling term  $H_{DD}$ , through space and is therefore given by

$$H_{DD,e} = \mathbf{S}_1^T \mathbf{D} \mathbf{S}_2 \quad (3.41)$$

with  $\mathbf{D}$  as dipolar coupling tensor between the two spins  $\mathbf{S}_1$  and  $\mathbf{S}_2$ . Note that in the fast motion limit, the dipolar coupling between electron spins is (again) averaged to zero and  $H_{exch}$  represents the dominant electron-electron interaction mechanism. However, measuring the dipolar coupling between electron has become powerful tool, especially in frozen solutions or in solids, to extract information on distance distributions of paramagnetic centers in the studied systems.<sup>61</sup>

### 3.2.4. Nitroxide radicals as paramagnetic species

As mentioned at the beginning of the section, a paramagnetic species is needed inside the sample to perform EPR spectroscopy. However, structural determination of systems without an initial paramagnetic center can nonetheless be achieved by incorporating such tracer molecules. Nitroxides with the structural unit  $R_2NO\cdot$  represent as stable free radicals an important class of these paramagnetic molecules. Fig. 3.9 summarizes the chemical structure of common

nitroxide derivative. In the following studies, the dianion of Fremy's salt (molecule **E**) was used as a spin probe<sup>c</sup>, meaning that the structure and dynamics of the compounds of interest are observed by non-covalent interactions.

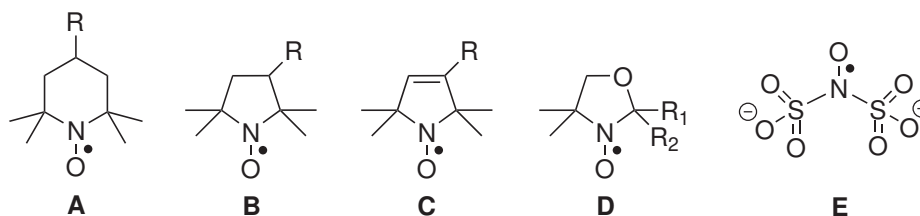


**Fig. 3.9.:** Chemical structures of common nitroxide spin probes. Depicted are derivatives of **A**: 2,2,6,6-tetramethylpiperidine-1-oxyl (TEMPO), **B**: 2,2,5,5-tetramethylpyrrolidine-1-oxyl (PROXYL), **C**: 2,2,5,5-tetramethylpyrroline-1-oxyl (dehydro-PROXYL), **D**: 4,4-dimethyl-oxazolidine-1-oxyl (DOXYL) and **E**: potassium nitrosodisulfonate (Fremy's salt). Adapted from Ref. 58

Note that the reasons for the stability of nitroxide radicals, especially for molecules **A** to **D** in Fig. 3.9, are based on the delocalized spin density as well as the full methyl substitution in  $\beta$ -position.

### Quantum mechanical description

Many terms of the static spin Hamiltonian (see equation 3.27) can be neglected for nitroxides in dilute liquid solution. Therefore, the interactions of the unpaired electron and the magnetic <sup>14</sup>N nucleus ( $I = 1$ ) can be characterized by the electron and nuclear Zeeman interaction as well as the hyperfine coupling term, leading to the adapted spin Hamiltonian  $H_{NO}$  with

$$H_{NO} = \mu_B \mathbf{B}_0^T \mathbf{g} \mathbf{S} - \frac{\mu_n g_n}{\hbar} \mathbf{B}_0^T \mathbf{I} + \mathbf{S}^T \mathbf{A} \mathbf{I} . \quad (3.42)$$

Note that possible quadrupolar contribution from the <sup>14</sup>N nucleus are neglected in equation 3.42. By solving the Schrödinger equation, the energy eigenvalues can be determined, whereas a fast, isotropic rotation displays six eigenstates with energies

$$E_{NO} = g_{iso} \mu_B B_0 m_s - g_n \mu_n B_0 m_I + a_{iso} m_s m_I . \quad (3.43)$$

In the case of anisotropic motion,  $g_{iso}$  and  $a_{iso}$  in equation 3.43 have to be substituted by the effective values with their respective orientation. Fig. 3.10 pictures the energy level diagram with the three allowed EPR transitions

<sup>c</sup> Another option to incorporate a paramagnetic species is by chemically attaching it as a so-called spin label to the material of interest.

$$\Delta E_{NO} = \hbar\omega_I = g_{iso}\mu_B B_0 + a_{iso}m_I \quad (3.44)$$

based on the selection rules  $\Delta m_s = \pm 1$  and  $\Delta m_I = 0$ .

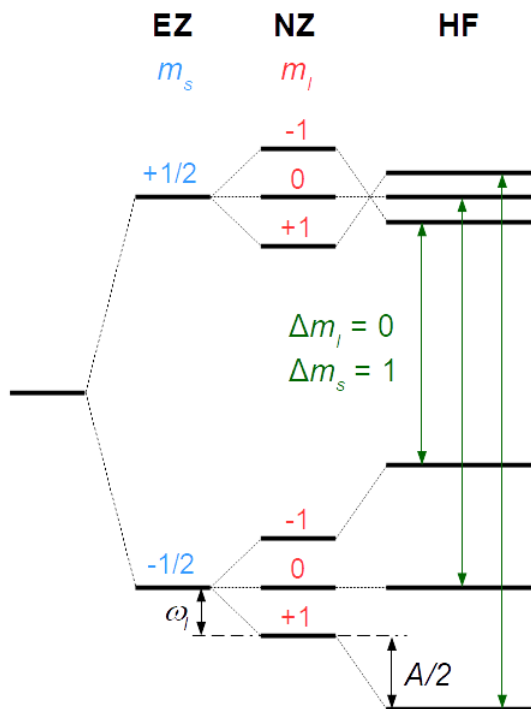


Fig. 3.10.: Energy level diagram for spin system with  $S = 1/2$ ,  $I = 1$  in the strong coupling case  $|A/2| > |\omega_I|$ . The allowed EPR transitions are highlighted in green (adapted from Ref. 58). **EZ**: electron Zeeman, **NZ**: nuclear Zeeman, **HF**: hyperfine coupling.

The molecular coordinate system for nitroxides, as shown in Fig. 3.11, defines the z-axis along the  $2p_z$  orbital of the nitrogen atom. Along the N–O bond, the x-axis is directed and the y-axis proceeds perpendicular to the xz-plane. For the hypothetical case that one only detects orientations along the principal axes, the recorded spectra would present the form illustrated in Fig. 3.11. Note that the position of the center line marks the principal  $g$  tensor element, whereas the spacing is defined by the corresponding hyperfine tensor element.



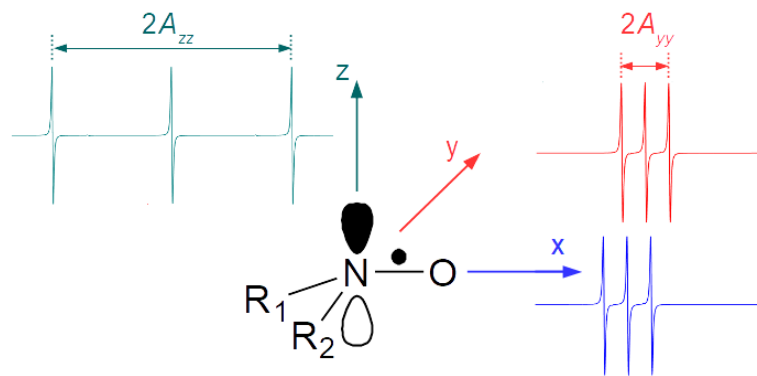


Fig. 3.11.: Definition of the molecular coordinate system of nitroxides (adapted from Ref. 58). Hypothetical spectra are included based on the following collinear  $\mathbf{g}$  and  $\mathbf{A}$  tensor values:  $g_{xx} = 2.0086$ ,  $g_{yy} = 2.0064$ ,  $g_{zz} = 2.0029$  and  $A_{xx} = A_{yy} = 5.2\text{ G}$ ,  $A_{zz} = 28.5\text{ G}$ .

### Nitroxide dynamics

To describe the rotational diffusion of a spin probe or a spin label molecule, one can determine the rotational correlation time  $\tau_c$ , which can be roughly categorized into the following regimes: (i) isotropic limit ( $\tau_c \leq 1\text{ ps}$ ), (ii) fast motion ( $\tau_c \approx 0.1\text{ ns}$ ), (iii) slow motion ( $\tau \approx 1\text{ ns}$ ) and (iv) rigid limit ( $\tau_c \geq 1\text{ }\mu\text{s}$ ). As long as the spins remain in the observed sample volume and the static field is homogeneous, translational motion does not infect the spectral shape, because only the angular motion relative to the applied  $B_0$  affects magnetic interactions. The effect of the rotational diffusion on EPR spectra is exemplarily shown in Fig. 3.12.

The two 'extreme' states for the rotational mobility of the spin probe and therefore the observed EPR spectra (as shown in Fig. 3.12) can be summarized as:

1. a very fast rotation of the paramagnetic center, whereas the hyperfine couplings in different directions average to an isotropic value  $a_{iso}$  and three equal lines are obtained for the spectrum and
2. a prohibited rotational motion of the nitroxide, leading to an anisotropic powder spectrum.

In between, the spectral shape strongly correlates with the time frame of the rotational diffusion, which can be characterized with the already mentioned rotational correlation time  $\tau_c$ . This parameter is formally calculated by the summation of all autocorrelation functions of the Wigner rotation matrices  $\mathbf{D}(\Omega(t))$  with<sup>62,63</sup>

$$\tau_c = \int_{t_0}^{\infty} \langle D_{l,m,n}(\Omega(t)) | D_{l,m,n}(\Omega(t_0)) \rangle dt . \quad (3.45)$$

Assuming the model of isotropic Brownian motion, meaning that the tip of an orientation

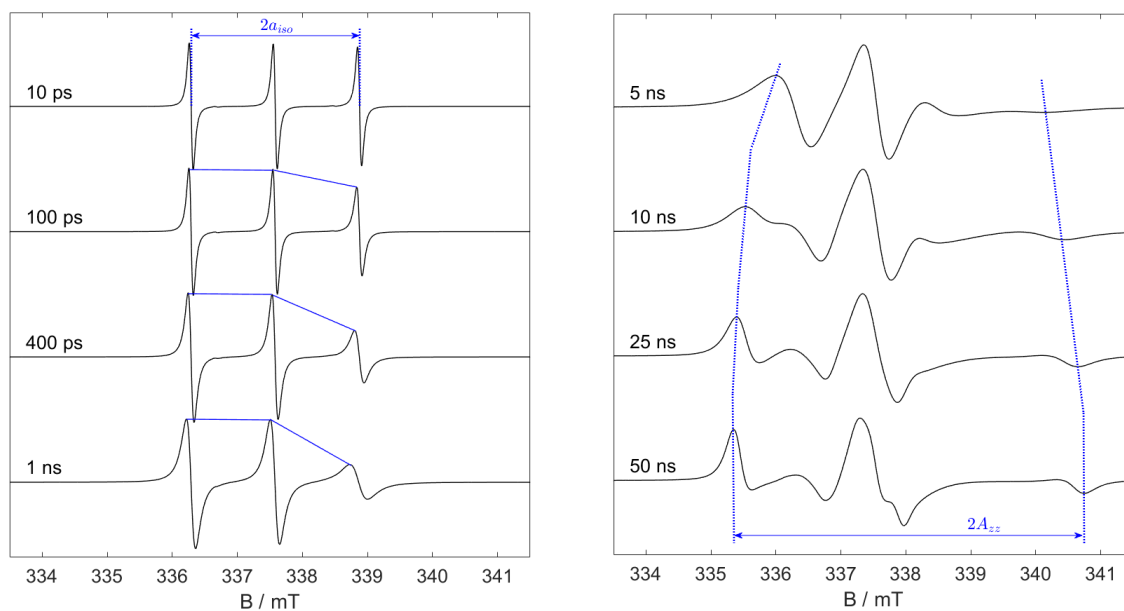


Fig. 3.12.: EPR spectral dependence on rotational dynamics for rotational diffusion in the liquid isotropic and slow motion regime (see main text). The spectra were obtained by simulation applying the  $\mathbf{g}$  and  $\mathbf{A}$  tensor from Fig. 3.11 (adapted from Ref. 58).

vector of the radical performs a random walk over the surface of a sphere, the connection between rotational correlation time and rotational diffusion simplifies to

$$\tau_c = \frac{1}{6D_r} . \quad (3.46)$$

In this case,  $D_r$  represents the Stokes-Einstein coefficient of rotational diffusion of a sphere. By applying the Stokes-Einstein relationship (see equation 3.16), one could calculate the effective radius of the paramagnetic species based on  $\tau_c$ , which is a good approximation for small nitroxide radicals in isotropic solvents.

For nitroxide radicals, where the rotation is hindered in several directions (e. g. due to chemical attachment), an anisotropy is introduced to the model of Brownian motion. Given a fast rotation around one axis and a slowed-down motion about directions perpendicular to that, the principal axes frame of the rotational coefficient can be expressed as<sup>62</sup>

$$\mathbf{D}_r = \begin{pmatrix} D_{\perp} & 0 & 0 \\ 0 & D_{\perp} & 0 \\ 0 & 0 & D_{\parallel} \end{pmatrix} . \quad (3.47)$$

The respective rotational correlation time  $\tau_c$  can thus be calculated with

$$\tau_c = \frac{1}{6\sqrt[3]{D_{\perp}^2 D_{\parallel}}} . \quad (3.48)$$

### Environmental influences

Spin probes contain in the recorded EPR spectra besides information about their dynamics also statements about their local environment. Depending on the interactions between molecules and their surrounding, the electronic structure of a nitroxide slightly alters, which mainly affects the hyperfine splitting initiated by  $^{14}\text{N}$ . The same kind of spin probe can therefore display deviations in the isotropic hyperfine coupling constant  $a_{iso}$  (liquid state) or for the  $A_{zz}$  tensor element (rigid limit) in solvents with different polarity, proticity or hydrophobicity. Note that also the  $g_{xx}$  value is affected by the already mentioned parameters, but in a reduced degree. To observe the correlation of  $g_{xx}$  and  $A_{zz}$ , one has to utilize high-field/high frequency EPR spectroscopy (e. g. W-band).<sup>64</sup>

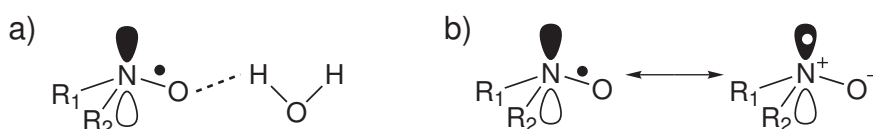


**Fig. 3.13.:** Origin of the polarity and proticity dependence of nitroxide spectra (adapted from Ref. 58). a) Decrease of the spin-orbit coupling due to hydrogen bonding. b) Increased spin density at the nitrogen atom through stabilization of the zwitterionic resonance structure.

Polar solvents stabilize the zwitterionic resonance structure presented in Fig. 3.13 b), which relocates spin density to the nitrogen nucleus. As a result,  $A_{zz}$  increases and  $g_{xx}$  decreases, whereas the latter one correlates with the weakend spin-orbit coupling in the oxygen orbitals. At a given polarity, this spin-orbit coupling can also be decreased if the oxygen atom acts as hydrogen acceptor (see Fig. 3.13 a)). Again, the  $g_{xx}$  value gets smaller as well as its deviation from the  $g_e$  value from the free electron. Note that at X-band frequencies with spin probes in the fast motion regime, the above mentioned effects are represented in the respective isotropic values of  $a_{iso}$  and  $g_{iso}$ .

### 3.2.5. Pulsed EPR spectroscopy

Until now, one focused on recording a EPR spectrum by applying a continuous microwave irradiation to the respective sample. The drawback of this efficient way is that the complete spin Hamiltonian is observed. Therefore, the provided spectra contain information, which cannot be completely separated into the different terms of the initial spin Hamiltonian. By using pulsed EPR spectroscopy, one can purposefully manipulate the spin system by the applied microwave pulses to produce signals 'just' containing the desired information. Therefore, different techniques are available to analyze the 'interaction of interest'.

In the following section, only the pulsed EPR methods are summarized, which were actually

utilized to study colloid-like ionic clusters in solution. Moreover, to maintain the character of a short summary, one does not present a quantum mechanical description of the spin evolution of the magnetization vector under the influence of an applied microwave pulse. This aspect can be checked in detail in Ref. 53.

### Methods based on the primary echo

Most EPR experiments are founded on the detection of electron spin echoes (ESE)<sup>d</sup>. The spin echo, introduced by E. L. Hahn,<sup>65</sup> describes the recovery of magnetization as an echo of the initial magnetization. The simplest representation of a spin echo is known as primary echo (or Hahn echo) and can be observed after the pulse sequence  $\pi/2 - \tau - \pi - \tau$ , as shown in Fig. 3.14.

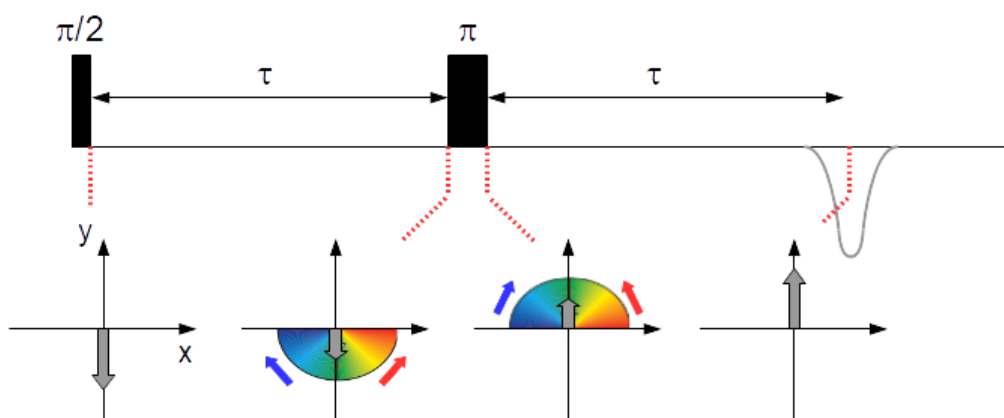


Fig. 3.14.: Formation of the primary echo after the pulse sequence  $\pi/2 - \tau - \pi - \tau$  in combination with the position of the magnetization vector at different moments of the detection sequence (adapted from Ref. 50).

The first  $\pi/2$ -pulse across the  $x$ -axis of the rotating coordinate system flips the magnetization vector in the  $-y$ -direction. During  $\tau$ , the time of free evolution, spin packets with different Larmor frequencies gain a phase shift in respect to their variant angular precession. As a result, they fan out according to their resonance offset, decreasing the magnitude of the initial magnetization vector. The second  $\pi$ -pulse inverts the sign of the  $y$ -component and after another evolution period (with the length of  $\tau$ ) the spin packets are refocused, leading to a maximized magnetization vector.

Note that the pulse sequence only refocuses inhomogeneous spin packets. 'Lost' magnetization because of relaxation processes cannot be regained. Therefore, the echo intensity shows an

<sup>d</sup> Fourier Transform EPR, where just a single  $\pi/2$  pulse is applied to detect the free induction decay (FID) as a transient signal, is rarely used. The major issue here is the so-called deadtime, which prevents recording a signal after the used excitation pulse ( $\approx 100$  ns for X-band)

exponential decay with increasing evolution time, whereas its characteristic time is the phase memory time  $T_m$ .  $T_m$  itself holds a close relation to the transverse relaxation time  $T_2$ .

For recording the primary echo signal, one has to sweep the magnetic field (analogous to the continuous wave technique) to overcome the insufficient excitation bandwidth. While recording the echo intensity as a function of the magnetic field, the microwave frequency as well as pulse sequence are kept constant. As a result, one receives EPR absorption spectra. At ambient temperatures, most of the paramagnetic species contain a short phase memory time, which prevents the detection of the respective echo. To provide sufficiently long  $T_m$  values, the samples are measured at lower temperature e. g. at 50 K for nitroxide radicals.

Since the primary echo sequence delivers a decay of the echo signal with increasing the second free evolution time  $\tau$ , one could directly measure the phase memory time  $T_m$  by analyzing the echo intensity with gradually ( $\Delta\tau$  steps) larger evolution periods. Ideally, the normalized echo intensity  $V(2\tau)/V(0)$ , as a function of  $\tau + \Delta\tau$ , can be expressed with

$$\frac{V(2\tau)}{V(0)} = \exp\left\{\frac{-2\tau}{T_m}\right\}. \quad (3.49)$$

In the case that the spin system is not determined by a single phase memory time, one can analyze the decay applying a biexponential or a stretched exponential decay. Note that there are several physical processes that lead to spin-spin relaxation, like instantaneous diffusion or methyl group rotation. Based on the EPR-active substance, the used temperature and the chemical environment of these processes might dominate the decay of the magnetization. However,  $T_m$  is often not determined by one single process, which leads to a non-single exponential behavior.

While recording the decay of the primary echo, one can detect a superimposed, repeated oscillation or modulation with a specific frequency. This modulation of the echo decay is called (two-pulse) electron spin echo envelope modulation (ESEEM). It (i) originates from the fact that the second  $\pi$ -pulse does not only invert the phase of the electron coherence, but also redistributes the electron coherence during the experiment and (ii) stems from weak hyperfine coupling of the detected electron spin to magnetic nuclei. The modulation of the ESE decay can be expressed for a model system with  $S = 1/2$  and  $I = 1/2$  over (not accounting relaxation processes)<sup>53</sup>

$$V_{2p-ESEEM}(2\tau) = 1 - \frac{k}{4} [2 - 2\cos(\omega_\alpha \tau) - 2\cos(\omega_\beta \tau) + \cos(\omega_- \tau) + \cos(\omega_+ \tau)]. \quad (3.50)$$

In equation 3.50,  $k$  describes the modulation depth of the superimposed oscillations. Moreover, it contains modulations from both nuclear spin manifolds ( $\omega_\alpha$  and  $\omega_\beta$ ) as well as from the sum ( $\omega_+$ ) and difference ( $\omega_-$ ) frequencies. Combining equations 3.49 and 3.50 delivers the

time domain signal including both electron spin relaxation and nuclear modulation

$$\frac{V'(2\tau)}{V'(0)} = \exp\left\{\frac{-2\tau}{T_m}\right\} \cdot V_{2p-ESEEM}(2\tau). \quad (3.51)$$

When the electron spin couples with  $p$  different nuclei, the modulations are multiplicative and  $V_{2p-ESEEM}(2\tau)$  transforms into  $\prod V_{2p-ESEEM}(2\tau, p)$ , leading to a more complex time-domain trace. To analyze these data sets, one divides out the electron spin relaxation (encoded in the exponential decay) and subsequently performs a fourier transformation of the signal. The calculated frequency domain spectra still can be hard to interpret because of the occurring peaks from the  $\omega_+$  and  $\omega_-$  frequencies.

### Methods based on the stimulated echo

The pulse sequence for recording a stimulated echo (see Fig. 3.15) can be viewed as a modified primary echo detection sequence, whereas the second  $\pi$ -pulse is separated into two  $\pi/2$ -pulses and the respective time  $T$ .

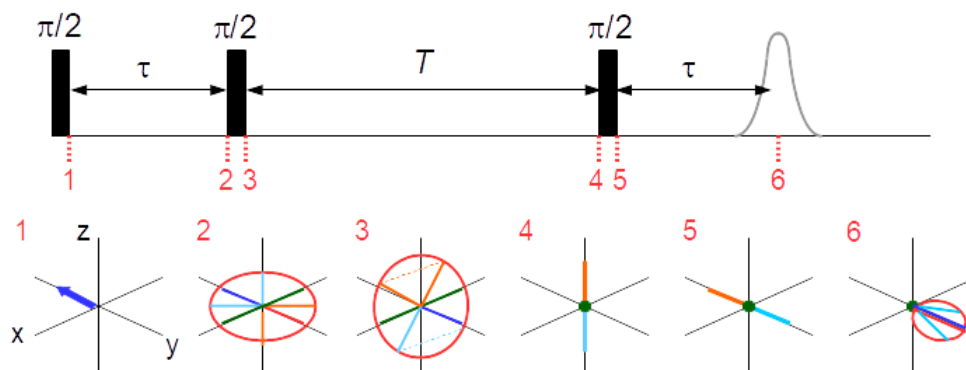


Fig. 3.15.: Formation of the stimulated echo after the pulse sequence  $\pi/2 - \tau - \pi/2 - T - \pi/2 - \tau$  in combination with the position of the magnetization vector at different moments of the detection sequence (adapted from Ref. 50).

Similar to the primary echo detection sequence, the magnetization vector flips after the first  $\pi/2$ -pulse in the  $-y$ -direction and the different spin packets fan out throughout the evolution period  $\tau$ . The second pulse rotates the 'unfolded' magnetization about the  $x$ -axis. In the case of  $T \gg T_m$ , the  $x$ -component of the magnetization has vanished due to transverse relaxation. The third pulse flips the remaining  $z$ -components of the magnetization vectors in the  $y$ -component. After the second evolution period  $\tau$ , an echo is formed with the respective vectors aligned on a circle centered along the  $y$ -axis. In a different description, the first sequence  $\pi/2 - \tau - \pi/2$  forms a polarization grating, which is stored throughout the time  $T$ . The last  $\pi/2$ -pulse induces a free induction decay of this grating, presenting the incidental shape of an echo.

In analogy to the previously introduced 2p-ESEEM technique, one can observe an envelope modulation of the stimulated echo by gradually increasing the time delay  $T$ . Looking at a two-spin system, the modulation part of the echo signal for the respective three pulse (3p) ESEEM method is given by

$$V_{3p-ESEEM} = 1 - \frac{k}{4} \{ [1 - \cos(\omega_\beta \tau)] [1 - \cos(\omega_\alpha (\tau + T))] \} - \frac{k}{4} \{ [1 - \cos(\omega_\alpha \tau)] [1 - \cos(\omega_\beta (\tau + T))] \} \quad (3.52)$$

In contrary to the two pulse technique, no nuclear combination frequencies are observed, which significantly simplifies the analysis of the frequency domain data. Also the spectral resolution is improved, because the echo decay is related to the phase memory time of the nuclear spins  $T_m^{(n)}$ , which is much longer than  $T_m$ . However, the factors in equation 3.52 containing the term  $1 - \cos(\omega_{\alpha,\beta} \tau)$  can vanish for certain values  $\omega_{\alpha,\beta}$  with

$$\omega_{\alpha,\beta} = \frac{2\pi n}{\tau} \quad \text{with } n = 0, 1, 2, \dots \quad (3.53)$$

In 3p-ESEEM measurements, modulation for a given nuclear frequency may vanish for evolution times  $\tau$  that fulfill equation 3.53, creating so-called blind spots in the respective spectra. Therefore, one has to perform this technique at several values of  $\tau$  to ensure all modulations of the studied system are recorded<sup>e</sup>. The overall 3p-ESEEM signal consists of a total of three contributions: the electron spin-spin relaxation ( $T_m$ ) during interval  $\tau$ , nuclear spin-spin relaxation ( $T_m^{(n)}$ ) during interval  $T$  and the ESEEM signal from equation 3.52

$$V'_{3p-ESEEM}(\tau, T) = \exp \left\{ \frac{-T}{T_m^{(n)}} \right\} \exp \left\{ \frac{-2\tau}{T_m} \right\} V_{3p-ESEEM}(\tau, T) . \quad (3.54)$$

The analysis of the recorded 3p-ESEEM time domain data can be performed analogous to the already mentioned two pulse technique. More advanced methods, which are based on the three pulse ESEEM technique (like the two-dimensional HYSORE) will not be presented in the following studies and are therefore not focused in this summary.

---

<sup>e</sup> Note that such blind spots can be considered as an advantage if one wants to suppress a strong modulation to a certain nuclear spin to highlight the rather shallow modulation depths from other nuclear spins.





## 4 | Solvent and Concentration effects on highly defined, colloid-like ionic clusters in solution

This chapter highlights the first studies regarding the process of ionic self-assembly involving a macrocyclic tetraimidazolium molecular box and small dianionic salts into highly defined, colloid-like ionic clusters called ionoids. Here, the influence of solvent composition and bulk concentration on the size, shape and durability of the ionoids was determined. Finally, it could be the solvent and concentration range defined, in which these soft, yet durable and long lived colloid-like ionic clusters form. The complete chapter is reproduced by permission of 'The Royal Society of Chemistry'<sup>a</sup> and can be found as:

J. Eisermann, L. Prager and D. Hinderberger, *Phys. Chem. Chem. Phys.*, 2018, **20**, 1421-1430

DOI: 10.1039/c7cp06501a

<https://pubs.rsc.org/en/content/articlelanding/2018/cp/c7cp06501a>

Note that the 'Methods' part (4.2.4.) inside the 'Experimental' section was amended compared to the mentioned publication, because this dissertation owns a separate section to summarize the applied devices and techniques (see Appendix A). The remaining sections 4.1. to 4.4. can be considered as citation from Ref. 66.

My school student to this time, Lukas Prager, performed measurements regarding the solvent influence, more accurately for the series varying the glycerol:water ratio and keeping the DMSO content constant. His studies played an important role in analyzing the ternary solvent mixture and determine the optimal composition for the formation of colloid-like ionic clusters. My contribution to this publication comprises the DLS and EPR measurements regarding the solvent mixtures with adjusted volume stoichiometries of DMSO, glycerol and water as well as analyzing the bulk concentration effect on the self-assembly process of colloid-like ionic

---

<sup>a</sup> The permission from 'The Royal Society of Chemistry' is present in written form.

clusters. Furthermore, I wrote the manuscript, which was fine-tuned by my supervisor Prof. Dariush Hinderberger.

## 4.1. Introduction

Nanotechnology is a broad field of research and technology that has gained tremendous attention over the last two decades, not only from the scientific community but also from the general public and from business perspectives. Generally, 'nanostructured materials'<sup>4</sup> have properties that are based on significant features smaller than 100nm. This class of materials encompasses a diverse range of scientific and technological aspects and the approach to 'materials by design' implies a wide range of scientific and technological applications.<sup>4,67</sup>

In principle, nanomaterials can be constructed using both top-down and bottom-up techniques with self-assembly connecting these two approaches. Especially ionic self-assembly is exploited as one important approach for the fabrication<sup>68</sup> of materials including soft materials, surface morphologies and organic-inorganic hybrid materials<sup>69</sup> or polyelectrolytes.<sup>70</sup> Commonly, electrostatic interactions<sup>13</sup> form the primary driving force of ISA while weaker noncovalent interactions (hydrogen bonding, van der Waals etc.) often constitute a secondary driving force<sup>69</sup> to achieve the noncovalent coupling of structurally different building blocks. Such noncovalent systems are adaptive as well as stimuli-responsive and allow facile processing, recycling, self-healing and multifunctionality.<sup>22</sup>

Besides the applications in nanotechnology, like e. g. polysaccharides for drug delivery,<sup>71,72</sup> responsive photonic crystals,<sup>73</sup> 'nanoions',<sup>74</sup> or short peptides as modern nanodevices,<sup>75</sup> ISA is generally used for building supramolecular materials.<sup>22</sup> Here the ability to understand and 'engineer' the noncovalent interactions is crucial to develop nanoscopic particles into the desired supramolecular structures.<sup>3</sup> Promising directions for crafting such arrangements comprise e. g. polyelectrolytes,<sup>76</sup> polymers,<sup>77,78</sup> aromatic molecules,<sup>69,79</sup> sol-gel chemistry,<sup>80</sup> ionic crystals,<sup>68,81,82</sup> ionic liquids,<sup>83,84</sup> and metal-organic frameworks.<sup>85</sup>

Recently, the formation of loosely bound ion-based colloid-like globular clusters of several nanometer size, termed ionoids, as electrostatically self-assembled supramolecular structures, was described.<sup>14</sup> For the generation of ionoids, we made use of a multicationic molecular box (**1**<sup>4+</sup>; Fig. 4.1) developed by Sessler and co-workers. This compound was already used for self-assembly applications like synthesizing three-dimensional extended, metal-organic rotaxane frameworks<sup>86</sup> or stabilizing threaded molecular structures.<sup>15,17</sup> In the context of ionoids combining **1**<sup>4+</sup> and small dianionic salts,  $\text{K}(\text{SO}_3)_2\text{CH}_2$  (**2**<sup>2-</sup>) and  $(\text{KSO}_3)_2\text{NO}^-$  (**3**<sup>2-</sup>), led to highly defined, size monodisperse ionic clusters due to long-range electrostatic correlations<sup>14</sup>. However, self-assembly initiated by electrostatic attraction also requires the right interplay of van der Waals forces, entropy effects, solvation of ions, etc., to generate well-ordered and

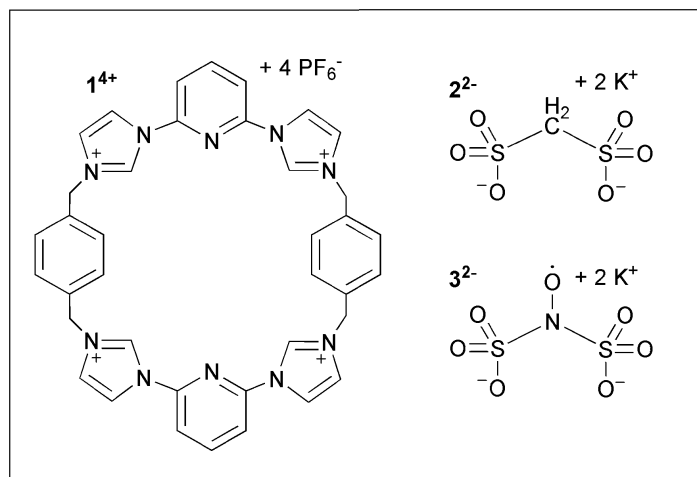


Fig. 4.1.: Molecular structure of  $1^{4+}$  (left),  $2^{2-}$  (top right) and  $3^{2-}$  (down right).

stabilized structures.<sup>3</sup> The formation of ionoids needed a mixture of  $1^{4+}$ : $2^{2-}$  ( $1^{4+}$ : $3^{2-}$ , respectively) at an approximate ratio of 1 mM:3 mM in DMSO:glycerol:water 50:43:7 (v/v/v)<sup>b</sup>.<sup>14</sup> Starting from this previously established system for ionoid formation, we hereby systematically change the solvent mixture and the bulk concentration to study their influence on the composition and size of colloid-like ionic clusters. As a result, we can define the optimal conditions for these small monodisperse objects from specific molecular building blocks and can derive information on the underlying design principles.

## 4.2. Experimental

### 4.2.1. Materials

The 'Texas-sized molecular box' ( $1^{4+}$ ) used in this study was synthesized according to Ref. 15,86 as described in Ref. 14. As small dianionic salts, we chose methanedisulfonic acid dipotassium salt ( $2^{2-}$ ; Sigma-Aldrich, Munich, Germany) with a purity  $\geq 99\%$  and Fremy's salt (potassium nitrosodisulfonate,  $3^{2-}$ ; Sigma-Aldrich) of technical grade. All of the chemicals were used as received. For producing different solvent mixtures we used deionized Milli-Q-water, DMSO with  $\leq 0.02\%$  water (Sigma-Aldrich), 86-88 wt% glycerol (Acros Organics, Nidderau, Germany) and  $\geq 98$  wt% glycerol (Fluka Analytical, Munich, Germany). Concentration of  $1^{4+}$ : $2^{2-}$  ( $1^{4+}$ : $3^{2-}$ , respectively) were varied between 1.5 mM:4.5 mM and 0.01 mM:0.03 mM.

<sup>b</sup> Additional Note: For a better comparison between all prepared solvent mixtures, the previous nomenclature of DMSO with 88% aqueous glycerol with a 1:1 volume ratio was changed. Further information can be found in Appendix B.

### 4.2.2. Solvent mixtures

Using our established solvent composition of DMSO:glycerol:water 50:43:7 (v/v/v) as a starting point, many solvent variations are possible. In this study, we focus on the following two dependencies:

1. Altering the volume stoichiometry between DMSO, glycerol and water
2. Changing the weight percentage of glycerol while keeping the volume ratio between DMSO and total glycerol:water phase, i. e. changing the relative ratio and absolute volume of water and glycerol.

Table 4.1 summarizes all solvent mixture, which were tested for the creation of colloid-like ionic clusters based on  $\mathbf{1}^{4+}:\mathbf{2}^{2-}$  ( $\mathbf{1}^{4+}:\mathbf{3}^{2-}$ , respectively) at an approximate ratio of 1 mM:3 mM.

### 4.2.3. Concentration

The influence of the  $\mathbf{1}^{4+}$  and  $\mathbf{2}^{2-}$  ( $\mathbf{3}^{2-}$ , respectively) concentration on cluster formation was determined separately from any solvent changes. Therefore, we maintained the established solvent mixture DMSO:glycerol:water 50:43:7 (v/v/v). Additionally, we kept the ratio of three anions per cation. Other ratios, like one anion per cation, lead to stronger electrostatic interactions between individual ions and thus hinder the global formation of ionoids.<sup>14</sup> We prepared seven different bulk concentrations (see Table 4.2) of  $\mathbf{1}^{4+}$  with  $\mathbf{2}^{2-}$  ( $\mathbf{3}^{2-}$ , respectively) for characterizing the effect of the total ion content on the self-assembly process.

**Table 4.1.:** Summary of all tested solvent compositions for building colloid-like ionic clusters out of  $1^{4+} \cdot 2^{2-}$  ( $3^{2-}$ ) at a ratio of 1 mM:3 mM

	volume percentage		
	DMSO	glycerol	water
start	50	43	7
volume stoichiometry	33	57	10
	25	64	11
	20	68	12
	10	77	13
	67	28	5
	75	21	4
	80	17	3
	90	9	1
	100	0	0
	0	85	15
glycerol:water volume ratio	50	5	45
	50	10	40
	50	15	35
	50	20	30
	50	25	25
	50	30	20
	50	35	15
	50	40	10
	50	45	5
	50	49	1

#### 4.2.4. Methods

The two main methods, which were used in this study are dynamic light scattering (DLS) and continuous wave (CW) electron paramagnetic (EPR) spectroscopy. Appendix A contains the most important information for both information as well as descriptions for preparation, measuring and analyzing of the respective samples. Here, the instrumentation is pointed out, which was used to perform the mentioned techniques:

1) DLS:

- ALV-NIBS high performance particle sizer (HPPS) with an ALV-5000/EPP Multiple Tau Digital Correlator (ALV-Laser Vertriebsgesellschaft m.b.H., Langen, Germany)

**Table 4.2.:** Summary of all tested bulk concentrations for building colloid-like ionic clusters out of  $\mathbf{1^{4+}}:\mathbf{2^{2-}}$  ( $\mathbf{3^{2-}}$ ) in DMSO:glycerol:water 50:43:7 (v/v/v)

concentration $\mathbf{1^{4+}}$ / mM	concentration $\mathbf{2^{2-}}$ ( $\mathbf{3^{2-}}$ ) / mM
1.5	4.5 <sup>a</sup>
0.5	1.5
0.2	0.6
0.1	0.3
0.05	0.15
0.02	0.06
0.01	0.03

<sup>a</sup> Higher concentrations are precluded due to the limited solubility of  $\mathbf{2^{2-}}$

– Litesizer 500 (Anton Paar GmbH, Graz, Austria)

2) CW EPR:

– X-band: Miniscope MS400 (magnettech, Berlin, Germany) benchtop spectrometer

– Q-band: Bruker EMX-plus spectrometer (Bruker Biospin GmbH, Rheinstetten, Germany) with ER5106QT resonator.

## 4.3. Results and Discussion

### 4.3.1. General remarks

Based on the measurements one recognized that beyond ionoids, as defined in Ref. 14 the self-assembly process can only be analyzed in a holistic manner, when other states of self-assembly are taken into account. Therefore, we create a specific terminology, which helps in separating the highly defined ionoid structures from other self-assembled entities encountered in this work. Throughout the entire study, we utilize the following terms (see Fig. 4.2).

1. (Globular) ionoids: these spherical structures with a hydrodynamic radius of between 6 nm and 8 nm show high durability in solution. Their special features lie in the incubation period of around ten days,<sup>14</sup> the monodisperse particle size distribution in DLS and the globular structure as found in Ref. 14 and confirmed here.
2. Anisotropic ionic clusters: here we include self-assembled structures with deviations from the spherical shape and/or a slightly enlarged hydrodynamic radius. Furthermore, DLS data often reveal polydisperse particle size distributions with two different entities,

indicating the transition from ion clouds to globular ionoids. In addition to that, their stability in solution is significantly reduced.

3. Ion clouds: Ion clouds with an enlarged hydrodynamic radius of  $\geq 100$  nm do not contain a highly-defined globular structure. It was assumed that these self-assembled ion clouds are starting structures for the formation of anisotropic ionic clusters as well as globular ionoids, as they can be detected immediately after the preparation of the solutions.

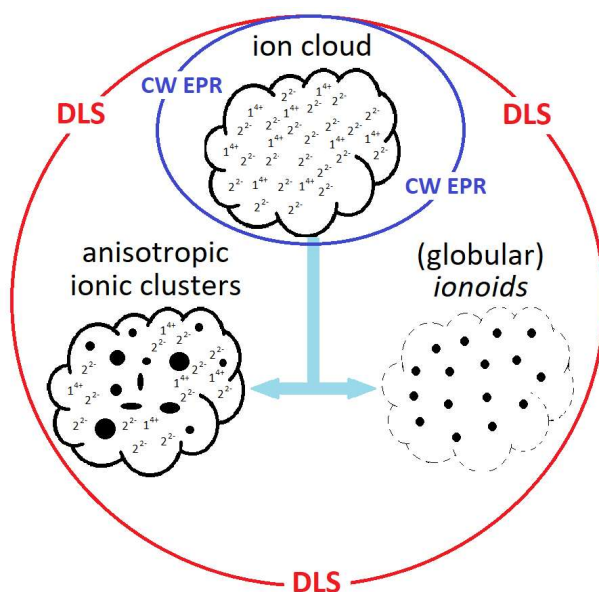


Fig. 4.2.: Illustration of the specific terminology to analyze the self-assembly process of  $1^{4+}$  and  $2^{2-}$  ( $3^{2-}$ , respectively) with DLS and CW EPR spectroscopy.

Note that we could not use CW EPR spectroscopy neither for measurements of globular ionoids nor for anisotropic ionic clusters because of Fremy's salt disproportionation in solution, which proceeds faster than the ten-day incubation period of ionoids. However, we could analyze the ion cloud-state for each  $1^{4+}$ : $3^{2-}$  sample and assign variations in the rotational mobility and anisotropy of Fremy's salt at day 0 to their future structures, which were characterized from DLS data.

#### 4.3.2. Modifying solvent volume stoichiometry

Using DLS, we can directly observe the development of ionic clusters; not only based on the hydrodynamic radius but also through the measured count rate. As dianionic component we solely use  $2^{2-}$  since it is chemically inert and stable over the course of several months at 20 °C. Fig. 4.3 summarizes the trend for the hydrodynamic radius for the tested volume stoichiometries with decreasing DMSO amount, the other solvent mixture are pointed out in Appendix

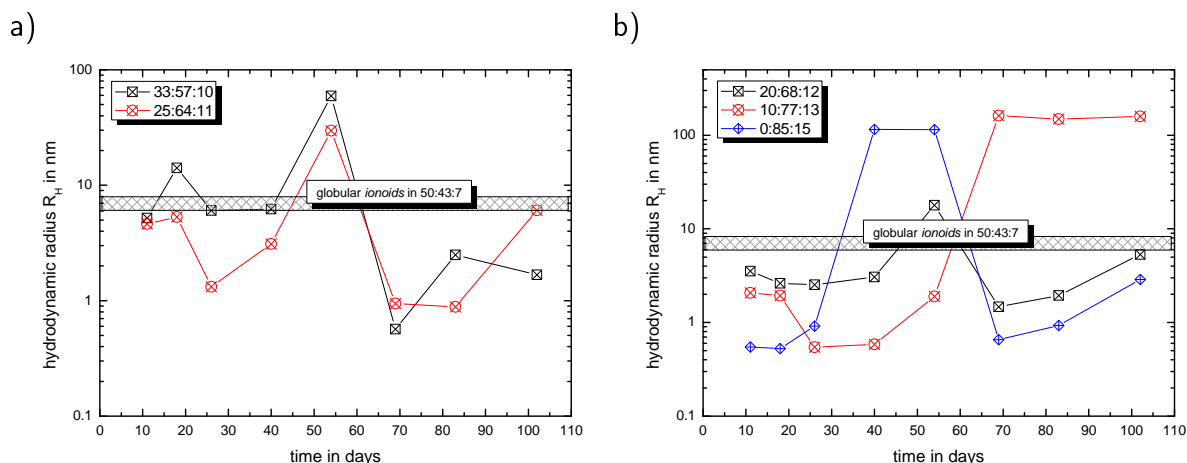


Fig. 4.3.: Development of the hydrodynamic radius for the cluster system  $1^{4+}:2^{2-}$  at a ratio of 1 mM:3 mM. We divided the results of the volume stoichiometries with decreasing DMSO amount into two graphs for clarity: a) stoichiometries 33:57:10 and 25:64:11 and b) 20:68:12 to 0:85:15. The other solvent mixtures can be found in Appendix B (Fig. B.1). Both graphs contain a patterned box that highlights the region of the hydrodynamic radius for the established solvent mixture.

B (Fig. B.1). Furthermore, we highlight the region for the ionoid size of  $1^{4+}:2^{2-}$  in the established solvent mixture, which is located between 6 nm and 8 nm.<sup>14</sup> One can clearly state that there is not a single volume stoichiometry yielding hydrodynamic radii similar to that of the original 50:43:7 (v/v/v) combination. Especially, the mixtures with a higher amount of DMSO lack the ability to build globular ionoids and remain as ion cloud formations (see Fig. B.1). The stoichiometries with a decreased amount of DMSO also do not lead to globular ionoids, but the measurements between day 11 and day 26 demonstrate a correlation between the hydrodynamic radius and the solvent mixture. The particle size decreases with the reduced DMSO content, which implies an influence of the aprotic-polar solvent on the dimension of the anisotropic ionic clusters. Note that the size distributions of all these solvent mixtures display a second entity in the first measurement days with expanded hydrodynamic radii of around 150 nm (Fig. B.2), which is omitted for clarity in Fig. 4.3. Therefore, changing the volume stoichiometry also increases the size dispersity of the system  $1^{4+}:2^{2-}$ .

After characterizing the  $1^{4+}:2^{2-}$ -system by DLS, we continued with CW EPR spectroscopy and  $1^{4+}:3^{2-}$ . A change to paramagnetic Frey's salt is required in order to apply EPR spectroscopy, but this can also influence interactions within the ion cloud. Nevertheless, the electrostatic interactions especially to  $1^{4+}$  remain unchanged, as shown in Ref. 14. Based on the reduction in hydrodynamic radius of the system with a decrease in the amount of DMSO, we only utilize CW EPR spectroscopy for the volume stoichiometries 33:57:10 to 10:77:13. In order to distinguish between the change of the rotational mobility due to (i) solvent viscosity and (ii) electrostatic interactions with  $1^{4+}$ , we measured pure Frey's salt solutions in the



respective solvent mixtures as an internal reference.

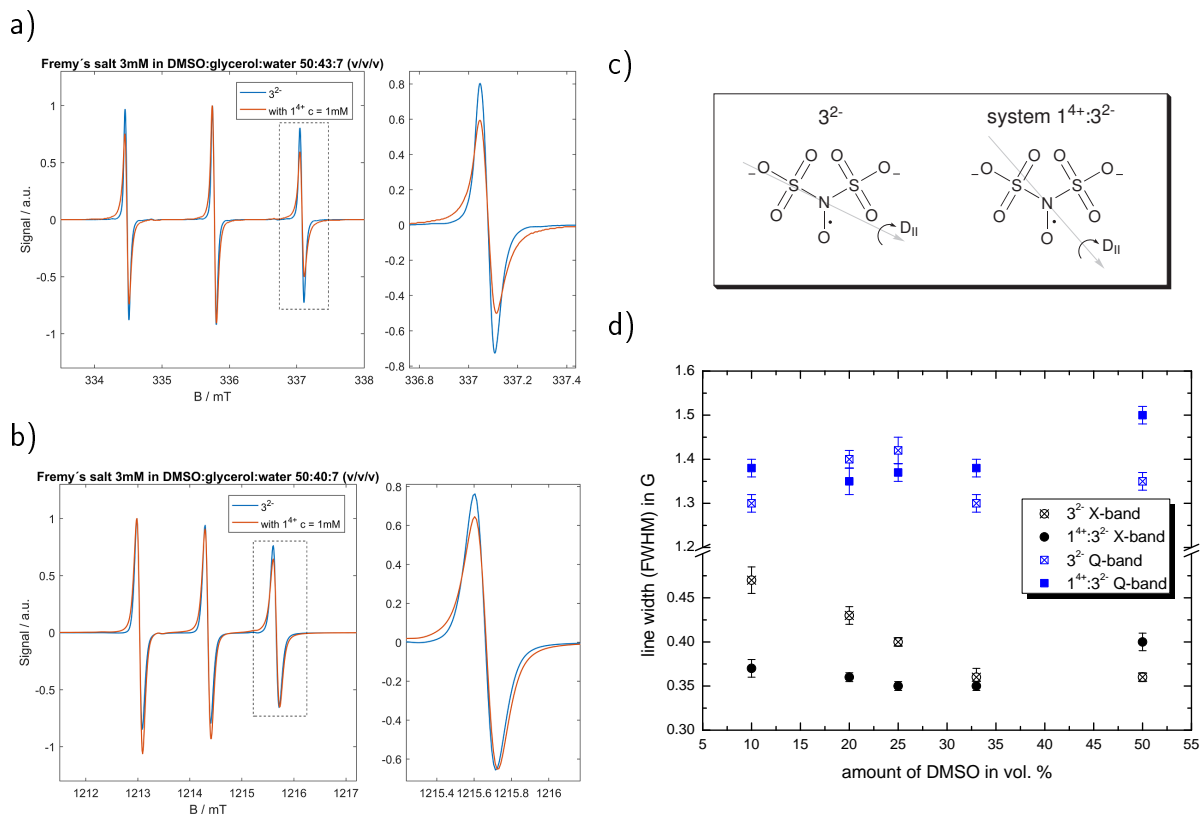


**Fig. 4.4.:** a) X-band CW EPR spectra of pure  $3^{2-}$  3 mM and  $1^{4+}:3^{2-}$  in established solvent mixture DMSO:glycerol:water 50:43:7 (v/v/v). b) Q-band CW EPR spectra of pure  $3^{2-}$  3 mM and  $1^{4+}:3^{2-}$  in established solvent mixture DMSO:glycerol:water 50:43:7 (v/v/v). The dashed box in a) and b) highlights the highfield peak, which is shown separately right next to the full spectra. c) Visualization of the rotational diffusion tensor for  $3^{2-}$ ; the gray arrow illustrates the principal axis of fast rotation ( $65^\circ$  for pure Fremy's salt and  $85^\circ$  for  $1^{4+}:3^{2-}$  from the NO-bond). d) Plot of the isotropic broadening as full width at half maximum (FWHM) of pure Fremy's salt and system  $1^{4+}:3^{2-}$  in DMSO:glycerol:water 50:43:7 (v/v/v) for X- and Q-band frequencies against the amount of DMSO in the solvent.

The CW EPR spectra of the pure nitroxide radical in the respective solvent mixture (see Fig. 4.4 a and b) display a rotational diffusion, which can be described by an axial tensor with a unique axis along the N-S bond of Fremy's salt (see Fig. 4.4 c).<sup>87,88</sup> Rotation about this preferred axis ( $D_{||}$ ) is for X-band frequencies approximately 35-fold and for Q-band frequencies approximately 22-fold faster than about the axes perpendicular ( $D_{\perp}$ ) to it. The lower value at Q-band frequencies reflects the difference in frequency/field dependence of the rotational time-frame with higher frequencies/magnetic fields.<sup>88</sup>

The X- and Q-band CW EPR spectra from  $1^{4+}:3^{2-}$  1 mM:3 mM (Fig. 4.4 a and b) show a significant line broadening, which is in line with a slowed-down rotation around the Fremy's

salt molecular z-axis. This effect leads to a decreased rotational correlation time  $\tau_c$ , but the nitroxide probe still can rotate relatively freely. At the same time, Fremy's salt still favors certain coordinations due to electrostatic attraction to  $\mathbf{1}^{4+}$  and repulsion among other  $\mathbf{3}^{2-}$  ions. In addition to that, the unique axis of the Fremy's salt axial tensor is slightly shifted from the N-S-bond towards the dissecting angle of both sulfonate groups (see Fig. 4.4 c). Furthermore, we do not find major differences for the isotropic hyperfine coupling constant<sup>c</sup>; for this reason we refrain from the discussion of this parameter and the environmental polarity at this point.

After characterizing the established solvent mixture DMSO:glycerol:water 50:43:7 (v/v/v), we then tested for changes when altering the volume stoichiometries in a range from 33:57:10 to 10:77:13. The pure Fremy's salt spectra at X- and Q-band display a slowed-down rotational mobility with a decrease in the amount of DMSO (Fig. B.4 and B.6) due to the increase in solvent viscosity. This effect is also visible for the  $\mathbf{1}^{4+}:\mathbf{3}^{2-}$  samples, but is combined with further anisotropy during the slow-down of rotational mobility through intermolecular interactions. To solely examine the latter effect on the CW EPR spectra, we combine two different evaluation systems:

1. Analyzing the line width of the CW EPR spectra through simulating isotropic broadening, which is implemented in the EasySpin program package (see Appendix A). Note that this method does not assume any physical model causing the broadening. We compare the full width at half maximum (FWHM) values for each  $\mathbf{1}^{4+}:\mathbf{3}^{2-}$  system with its respective Fremy's salt reference.
2. Calculating the anisotropy  $T$  of the rotational diffusion tensor as described in equation A.7 (see Appendix A). This parameter, which is discussed mainly in Appendix B, allows us to emphasize the distinction between  $D_{\parallel}$  and  $D_{\perp}$  (Table B.4 and B.5) as well as characterize the magnitude of electrostatic interactions in the direct vicinity of Fremy's salt.

The FWHM values for  $\mathbf{1}^{4+}:\mathbf{3}^{2-}$  (Fig. 4.4 d) show the same tendencies at X- and Q-band frequencies. Despite the slowed-down rotational mobility with a decrease amount of DMSO, we observe a drop in the line width between the established solvent mixture 50:43:7 (v/v/v) and the other tested compositions, which show nearly the same line broadening as one another. We can exclude solvent viscosity as cause for this behavior, as we would then also have to observe this trend with pure Fremy's salt, leaving electrostatic interactions as reason. Reducing the amount of DMSO in the solvent mixture decreases the electrostatic interactions between  $\mathbf{1}^{4+}:\mathbf{3}^{2-}$ . Furthermore, the increasing water content inside the solvent mixtures can induce

---

<sup>c</sup> Small variations here can be explained through inevitable temperature fluctuations in combination with Fremy's salt sensitivity for such environmental changes.<sup>89</sup>

partially solvated Fremy's salt molecules in this region. Both the effects create a more isotropic environment for Fremy's salt, which results in narrow CW EPR lines. In addition, the anisotropy  $T$  of the rotational diffusion tensor displays the same correlation, which is shown in Fig. B.5.

### 4.3.3. Modifying glycerol:water volume ratio

The measured changes in hydrodynamic radius and EPR line width with varied volume stoichiometry indicate that DMSO as an aprotic-polar solvent is the major factor leading to the divergence between anisotropic ionic clusters and globular ionoids. Nevertheless, because of these ratio modifications between DMSO, glycerol and water, it is difficult to separate the influence of each solvent component. To further resolve this, we systematically altered the glycerol:water-ratio while keeping the amount of DMSO constant. With this setup we could investigate the importance of glycerol and water on the nature of the cluster, its size as well as cluster stability.

Similar to the initial solvent mixtures we started characterizing  $\mathbf{1}^{4+}:\mathbf{2}^{2-}$  at a ratio of 1 mM:3 mM through DLS. Fig. 4.5 displays the development of the hydrodynamic radius by side and back scattering for all the ten glycerol:water-ratios. Again, there is no other solvent mixture that leads to the values obtained by our established solvent DMSO:glycerol:water 50:43:7 (v/v/v). Furthermore, we see a large variation span in the size of the self-assembled structures, which means that DMSO alone does not determine the dimension of the  $\mathbf{1}^{4+}:\mathbf{2}^{2-}$ -system (Fig. B.7). In summary, we can distinguish four different regions in the DLS data in Fig. 4.5:

1. 50:5:15 to 50:15:35: here, the initial formation of ion clouds stays throughout the entire measurement period. At least one scattering angle shows a hydrodynamic radius below 1 nm, which indicates the absence of a globular structure. The dissolved ions are (for most of the time) homogeneously distributed.
2. Between 50:15:35 and 50:40:10: we measured anisotropic ionic cluster with a hydrodynamic radius of around 100 nm. The similar results for side and back scattering refer to spheroidal structures, such as the established solvent mixture present. However, the dimensions we found in these glycerol:water-ratios are more than tenfold larger than the globular ionoids.
3. Between 50:40:10 and 50:45:5: this region contains the potential to self-assemble globular ionoids, but even small deviations from 50:43:7 lead to anisotropic ionic clusters.
4. Above 50:45:5: the behavior of the detectable structures corresponds to those in solvent mixtures of 50:15:35 to 50:40:10.

Note that the defined regions are based on the first three weeks for the system  $\mathbf{1}^{4+}:\mathbf{2}^{2-}$  1 mM:3 mM in each solvent mixture. The self-assembly into globular ionoids in the established

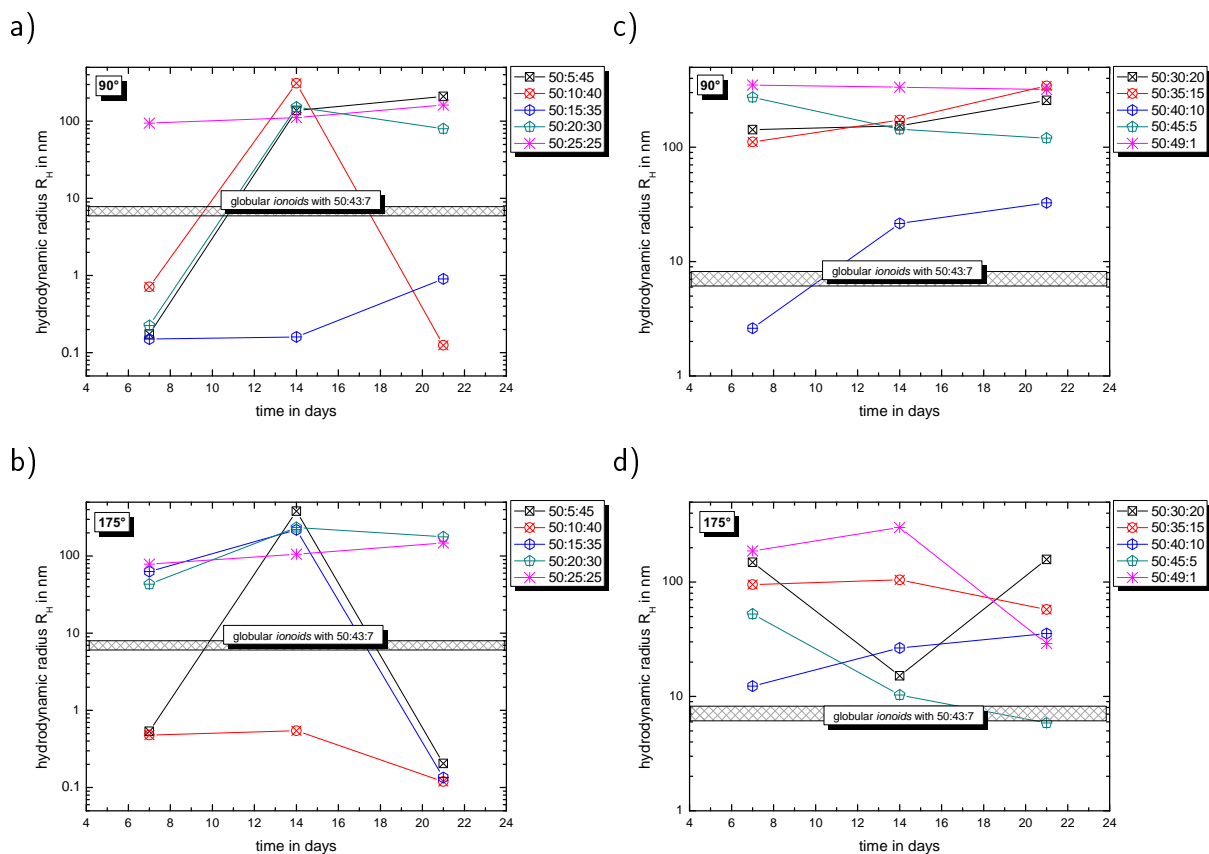


Fig. 4.5.: Development of the hydrodynamic radius for the cluster system  $1^{4+}:2^{2-}$  at an approximate ratio of 1 mM:3 mM in dependence of glycerol and water volume percentage. The results are divided into: 50:5:45 to 50:25:25 at a) side and b) back scattering and 50:30:20 to 50:49:1 at c) side and d) back scattering. All graphs contain a patterned box that highlights the region of the hydrodynamic radius for the established solvent mixture.

solvent mixture takes 10 days, permitting the preliminary performed classification. However, deriving their long-term stability cannot be fulfilled and is also not the main emphasis of these measurements. We focus on the beginning of the self-assembly process, which is crucial for the formation of well-defined structures.

To further substantiate our DLS data, we make use of CW EPR spectroscopy at X- and Q-band frequencies. In analogy to the changes involving the DMSO content, we measured pure Frey's salt and the system  $1^{4+}:3^{2-}$  in all of the solvent mixtures and determined the rotational correlation times (Table B.6 and B.6) and the isotropic broadening (see Fig. 4.6). The development of the FWHM values of pure Frey's salt, and especially  $1^{4+}:3^{2-}$  at X- and Q-band frequencies, do provide similar regions as we observed in DLS. However, we did not characterize the final, self-assembled structures using CW EPR, but the initial ion cloud state. Pure Frey's salt at X-band frequencies clearly displays a constant line width when increasing the glycerol and decreasing the water content in the solvent mixture. For this CW EPR

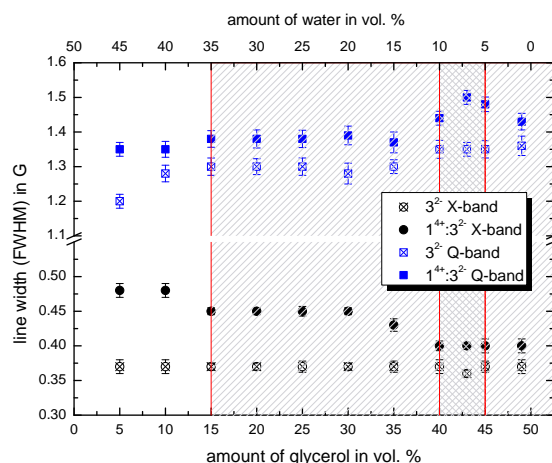


Fig. 4.6.: Plot of the isotropic broadening as full width at half maximum (FWHM) of pure Frey's salt and system  $1^{4+}:3^{2-}$  for X- and Q-band frequencies against the amount of glycerol and water in volume percentage. The regions marked in different shadings are based on the DLS as described in the text.

frequency, the effect of higher solvent viscosity is already entirely considered in the slowed-down axially symmetric rotational motion of the nitroxide. The difference in frequency/field dependence of the rotational time-frame becomes apparent when looking at the Q-band data. Here, we detect a nearly steady increase in the FWHM value with rising glycerol content.

With the addition of  $1^{4+}$ , we detect a significant increase in the line width throughout all of the solvent mixtures and at both CW EPR frequencies. Furthermore, the FWHM values do not contain the correlation with solvent viscosity as seen for pure Frey's salt. In detail, the X-band data display the change from the globular ion pair electrostatic interactions to the desired noncovalent forces between several anions and cations, while Q-band spectra show a larger line width for solvent mixtures, which are capable of forming globular ionoids due to stronger emphasis, at this frequency, on the local electrostatic interactions between  $1^{4+}$  and  $3^{2-}$ . Finally, the rotational dynamics anisotropy values (see Fig. B.9) also show a significant increase for all of the consulted solvent mixtures.

#### 4.3.4. Importance of bulk concentration

Besides testing the solvent composition for globular ionoids, we also investigated the influence of  $1^{4+}:2^{2-}$  ( $3^{2-}$ , respectively) bulk concentration on the final structure and ionic self-assembly. First, we decreased the total amount of the compounds, while keeping the ratio of three anions per cation.

The examination of the DLS data in Fig. 4.7 reveals that the ratio 0.5 mM:1.5 mM also leads to the detection of globular ionoids, but a further decrease in the total amount of  $1^{4+}$  and  $2^{2-}$

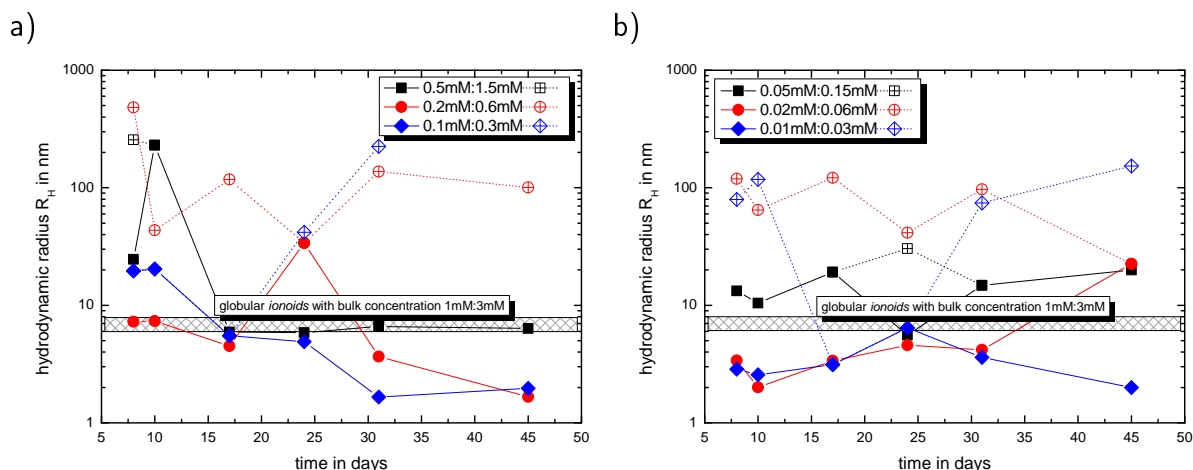


Fig. 4.7.: Development of the hydrodynamic radius for the system  $1^{4+}:2^{2-}$  in DMSO:glycerol:water 50:43:7 (v/v/v) with decreased bulk concentration. We divided the results into two graphs for clarity: a) bulk concentrations 0.5 mM:1.5 mM to 0.1 mM:0.3 mM and b) the remaining ratios. Both graphs contain a patterned box that highlights the region of the hydrodynamic radius for the established composition 1 mM:3 mM. Note that all bulk concentrations are represented with two different symbols, because the particle size distribution yields two separate species.

(0.2 mM:0.6 mM) reduces the total lifespan of these structures. They segregate into smaller and bigger assemblies, which can be described as independent entities. This trend is even more pronounced at lower bulk concentrations. Beginning at 0.1 mM:0.3 mM we do not detect no globular ionoids with a hydrodynamic radius of between 6 nm and 8 nm anymore, but mostly a mixture of anisotropic ionic clusters and ion clouds.

As a result, we can estimate from the data in Fig. 4.7 that a 5-fold diluted 1 mM:3 mM system of  $1^{4+}:2^{2-}$  still encompasses enough ions to form at least anisotropic ionic clusters primarily through electrostatic interactions. Similar to the critical micelle concentration of surfactants, we can define a 'critical ionoid concentration' for our measured system between 0.1 mM:0.3 mM and 0.2 mM:0.6 mM was possible. Note that the total scattering intensity gets weaker with decreasing bulk concentration (Fig. B.11), which influences the resolution of intensity time correlation function and particle size distribution in the DLS. This fact implies that a bulk concentration below this 'critical ionoid concentration' can still contain anisotropic ionic clusters, but their quantity is too low for light scattering.

In a second experiment, we tried to increase the bulk concentration of  $1^{4+}$  and  $2^{2-}$ . The limited solubility of  $2^{2-}$  leads to just one possible ratio of 1.5 mM:4.5 mM, which was again characterized using DLS (see Fig. 4.8). Over the whole measurement period we detect anisotropic ionic clusters, which are approximately 5-fold bigger than the globular ionoids. Furthermore, we detected significant variations in the hydrodynamic radii for all three scattering angles ( $15^\circ$ ,  $90^\circ$  and  $175^\circ$ ), implying deviations from a spherical structure. The higher local

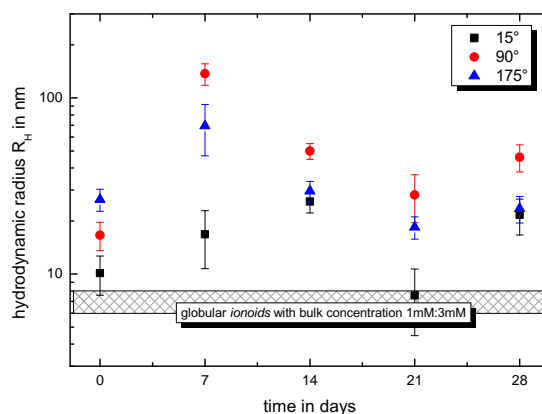


Fig. 4.8.: Development of the hydrodynamic radius for the cluster system  $\mathbf{1}^{4+}:\mathbf{2}^{2-}$  1.5 mM:4.5 mM in DMSO:glycerol:water 50:43:7 (v/v/v).

concentration seems to cause stronger electrostatic forces between  $\mathbf{1}^{4+}$  and  $\mathbf{2}^{2-}$ , disturbing the balance of weak noncovalent interactions and therefore the potential to build globular ionoids.

All seven bulk concentrations were subsequently characterized using CW EPR spectroscopy at X- and Q-band frequencies. Initially, we characterized only Fremy's salt, whose rotational mobility shows no significant changes between 4.5 mM and 0.03 mM and allows us to define a constant rotational correlation time  $\tau_c$ . Fig. 4.9 contains these pure Fremy's salt values for X- and Q-Band as a grey patterned box, which acts as a reference for the  $\mathbf{1}^{4+}:\mathbf{3}^{2-}$ -system. In addition, we focused on the development of the rotational correlation time  $\tau_c$  of  $\mathbf{1}^{4+}:\mathbf{3}^{2-}$ , both line width analysis (Fig. B.13) and rotational anisotropy  $T$  (Fig. B.14) can be found in Appendix B.

At X-band frequencies we determined a significant change in the rotational correlation time  $\tau_c$  between 0.1 mM:0.3 mM and 0.2 mM:0.6 mM (Fig. 4.9 red patterned box), which matches the 'critical ionoid concentration' based on the DLS data (Table B.8). Higher bulk concentrations on the one hand tend to a more slowed-down rotational mobility of Fremy's salt, accompanied with stronger electrostatic interactions between  $\mathbf{1}^{4+}$  and  $\mathbf{3}^{2-}$ , as well as the potential to form ionoids. Note that the CW EPR data cannot distinguish between anisotropic ionic clusters and globular ionoids, because we only measure directly on preparation day due to the limited stability of Fremy's salt in solution. Lower bulk concentrations on the other hand show just minor increases in the rotational correlation time  $\tau_c$  for  $\mathbf{3}^{2-}$ , similar to the solvent mixtures between 50:15:35 and 50:40:10 (v/v/v). These patterns indicate the formation of structures between ion clouds and anisotropic ionic clusters, which is also observed in the DLS data.

The Q-band CW EPR spectra were not as straightforward as the X-band data reflecting the transformation in the rotational correlation time  $\tau_c$  at the 'critical ionoid concentration' for

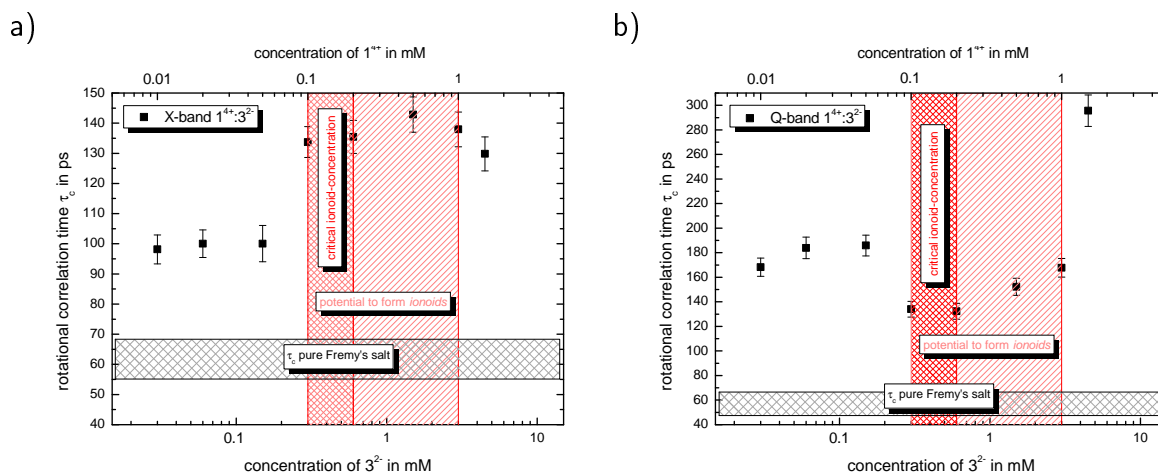


Fig. 4.9.: Rotational correlation times  $\tau_c$  at a) X-band and b) Q-band frequencies for  $1^{4+}:3^{2-}$  with all tested bulk concentrations. The grey patterned box highlights the rotational mobility of pure Frey's salt, while the red patterned box represents the critical ionoid concentration and the light red patterned box the region for building anisotropic ionic clusters and globular ionoids based on the DLS data.

$1^{4+}:3^{2-}$  (Table B.9). In general, the rotational mobility of  $3^{2-}$  is hindered compared to that of pure Frey's salt, but stays relatively constant at bulk concentrations 1 mM:3 mM and lower. Q-band frequencies are able to resolve local interactions between  $1^{4+}$  and  $3^{2-}$ , which do not change significantly with a decrease in the bulk concentration. Based on these similar local interactions we assume the later formation of small entities, which were characterized with DLS measurements. However, the bulk concentration 1.5 mM:4.5 mM contains a special feature: the  $\tau_c$  value is approximately 2-fold bigger than for the other ratios. This increase implies stronger electrostatic forces between individual  $1^{4+}$ - and  $3^{2-}$ -ions, which lead to ion clouds with the tendency to form anisotropic ionic clusters, confirming the discussed DLS data.

## 4.4. Conclusions

The structure and stability of colloid-like clusters depends heavily on the balance between the electrostatic forces of  $1^{4+}:2^{2-}$  ( $1^{4+}:3^{2-}$ , respectively) and other noncovalent interactions, and as such present the main aspect of a polyphilic system.<sup>90,91</sup> Through changes in the solvent mixture, we can manipulate the influence of ISAs primary and secondary driving forces, while each component of the solvent (DMSO, glycerol, water) implements different aspects in building globular ionoids. The amount of DMSO on the one hand determines the long-term stability of the self-assembled structures, whereas on the other hand the combined glycerol:water phase characterizes their size and shape. Overall, the established solvent mixture of DMSO:glycerol:water 50:43:7 (v/v/v) turns out to be the best choice for globular



ionoids with a hydrodynamic radius of 6 nm to 8 nm and high durability and longevity.

Next to the effects of solvent composition on ISA, which are pronounced even at small deviations from the optimal mixture, we focused on the bulk concentration of  $\mathbf{1}^{4+}:\mathbf{2}^{2-}$  ( $\mathbf{1}^{4+}:\mathbf{3}^{2-}$ , respectively). Between the ratios 1 mM:3 mM and 0.1 mM:0.3 mM the potential to form ionoids is present, but the decreasing amount of cations and anions results in anisotropic ionic clusters with lower long-term stability. Below the 'critical ionoid concentration', we find mostly ion clouds and isolated anisotropic ionic clusters, whereas at higher ratios (like 1.5 mM:4.5 mM) the yield of anisotropic ionic clusters slightly increased.

All of the measurements combined indicate that globular ionoids represent a special class of highly defined, ionically self-assembled soft particles, as they need highly specific environmental conditions to gain their small spherical structure homogeneously throughout the entire solution. In fact, ion clouds seem to be the initial state for globular ionoids, which is especially visible in the CW EPR data. Combining the X- and Q-band data allows us to picture global as well as local interactions of  $\mathbf{1}^{4+}:\mathbf{3}^{2-}$  and to evaluate these compared to effects like solvent viscosity due to the behavior of the line broadening as well as the rotational dynamics anisotropy  $T$ .

Although investigating two important parameters with an influence on the ionic self-assembly of  $\mathbf{1}^{4+}:\mathbf{2}^{2-}$  ( $\mathbf{1}^{4+}:\mathbf{3}^{2-}$ , respectively), there are still other contributing factors such as temperature, pH-value and dissolved counterions ( $\text{K}^+$ ,  $\text{PF}_6^-$ ), which still have to be examined. In the end, all these parameters act as cooperative 'design elements' for globular ionoids. Furthermore, we are currently testing alternate molecules to expand the number of systems that can form such highly defined structures. In the long run, we want to understand the delicate physical-chemical processes leading to the formation of robust yet extremely 'soft' structures, and apply the method for the formation of globular ionoids to crafting supramolecular structures with a certain functionality.



## 5 | Tuning the shape anisotropy of loosely bound colloid-like ionic clusters in solution

The following chapter continues the studies regarding the dynamic self-assembly process involving a macrocyclic tetraimidazolium molecular box and small dianionic salts into highly defined, colloid-like ionic clusters in solution, called ionoids. Here, one determined a region of privileged ionic ratios, which allow the formation of monodisperse, spheroidal structures of loosely bound ions in solution with adjustable (i) hydrodynamic radii between 6 nm and 12 nm as well as (ii) shape anisotropy. Inspired by Hertzsprung-Russell diagrams (HRDs) used in astrophysics to describe the fate of stars, ionoid evolution diagrams (IEDs) were constructed. IEDs are essential for grasping and describing the highly complex temporal development of these dynamically self-assembled structures in solution from the level of the individual ionic building blocks to stable clusters with minimum lifetime of months and such aid in crafting future globular ionoids and anisotropic ionic clusters. The results shown in Chapter 5 were already published and are reproduced by permission of 'The Royal Society of Chemistry'<sup>a</sup> from:

J. Eisermann and D. Hinderberger, *Phys. Chem. Chem. Phys.*, 2019, **21**, 1152-1159

DOI: 10.1039/c8cp06558f

<https://pubs.rsc.org/en/content/articlelanding/2019/CP/c8cp06558f>

Similar to the previous chapter, the 'Methods' subsection (5.2.3.) was changed compared to the mentioned publication. Again, the description in Appendix A was cited to highlight the applied devices and methods in a concise manner. The remaining sections 5.1. to 5.4. can be considered as citation from Ref. 92. At this point, I want to highlight the contribution of my supervisor Prof. Dariush Hinderberger. His fondness and passion to the broad field of astrophysics were the starting point of crafting the here introduced IEDs, which turned out as an important tool in future studies. Due to the high status of IEDs in analyzing ionoids, their construction is also described in a separate section in Appendix A.

---

<sup>a</sup> The permission from 'The Royal Society of Chemistry' is present in written form.

## 5.1. Introduction

Soft condensed matter comprises classes of materials like colloids, polymers, liquid crystals, amphiphiles, micelles and polyelectrolytes,<sup>2,18</sup> not to mention the whole field of biological soft matter.<sup>5,6</sup> These systems usually have structural length scales from one to several hundred nanometers and thus fall within the domain of 'nanostructured materials'.<sup>2,4</sup>

In recent publications,<sup>14,66</sup> we characterized the formation of loosely bound ion-based colloid-like globular cluster of several nanometer size, termed globular ionoids. These structures, whose fabrication is based on the process of ionic self-assembly (ISA),<sup>68</sup> represent a novel subclass inside the major field of supramolecular chemistry.<sup>8,9,22</sup> Supramolecular chemistry in general aspires to the development of highly complex chemical systems from components interacting through noncovalent intermolecular forces. The ISA process in fact involves (i) electrostatic interactions as primary driving force<sup>13</sup> and (ii) weaker noncovalent interactions (such as solvation, hydrogen bonding, van der Waals etc.) as secondary driving force.<sup>69</sup>

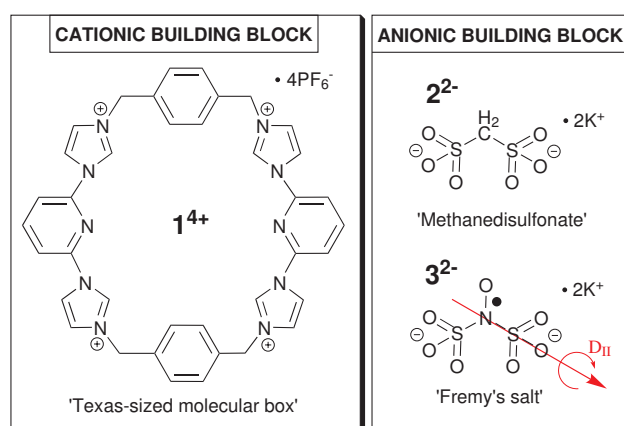


Fig. 5.1.: Molecular structure of cationic building block **1<sup>4+</sup>** (left) and anionic building blocks **2<sup>2-</sup>** (top right) and **3<sup>2-</sup>** (bottom right).

For the formation of colloid-like ionic cluster, we combine the 'Texas-sized molecular box' (**1<sup>4+</sup>**, 5.1), developed by Sessler and coworkers,<sup>15-17</sup> with small dianionic salts ('methanedisulfonate', **2<sup>2-</sup>** or Fremy's salt dianion, **3<sup>2-</sup>**, see 5.1) in our established solvent mixture of DMSO:glycerol:water 50:43:7 (v/v/v). To obtain size monodisperse supramolecular structures due to long-range electrostatic correlation, a molar ratio of **1<sup>4+</sup>:2<sup>2-</sup>** (**1<sup>4+</sup>:3<sup>2-</sup>**, respectively) 1 mM:3 mM is needed.<sup>14</sup> Changes in solvent composition or ion concentration (while keeping the molar ratio of all ions constant), as highlighted in previously performed studies, significantly affect size, shape and stability of the self-assembled entities.<sup>66</sup>

In this study, we investigate the influence of the ionic ratio of cationic and anionic building blocks (Fig. 5.1) on the self-assembly process in the optimal solvent mixture. We intend to point out the importance of cation-anion proportion as well as to define the optimal ionic

ratio for the formation of globular ionoids. Furthermore, one can now extend our approach and create a variety of different self-assembled entities with anisotropic shape, anisotropic ionoids, containing  $\mathbf{1}^{4+}:\mathbf{2}^{2-}$  ( $\mathbf{1}^{4+}:\mathbf{3}^{2-}$ , respectively), which possess the same durability as the archetypical globular ionoids introduced previously.

## 5.2. Experimental

### 5.2.1. Materials

The 'Texas-sized molecular box' ( $\mathbf{1}^{4+}$ ) used in this study was synthesized according to the work of Sessler and coworkers<sup>15,16</sup> as described in the previous studies.<sup>14,66</sup> As small dianionic salts, we chose methanedisulfonic acid dipotassium salt ( $\mathbf{2}^{2-}$ ; Sigma-Aldrich, Munich, Germany) with purity  $\geq 99\%$  and Fremy's salt (potassium nitrosodisulfonate,  $\mathbf{3}^{2-}$ ; Sigma-Aldrich) of technical grade. All chemicals were applied as received. For producing our established solvent mixture, we combined DMSO with  $\leq 0.02\%$  water (Sigma-Aldrich) in a 1:1 (v/v) ratio with 86-88 wt% glycerol (Acros Organics, Nidderau, Germany). The concentration of  $\mathbf{1}^{4+}$  was varied between 0 mM and 3 mM, while the amount of  $\mathbf{2}^{2-}$  ( $\mathbf{3}^{2-}$ , respectively) was constant at 3 mM.

### 5.2.2. Ionic ratio

We compared the studied systems with our reference system containing  $\mathbf{1}^{4+}:\mathbf{2}^{2-}$  ( $\mathbf{1}^{4+}:\mathbf{3}^{2-}$ , respectively) in a concentration ratio of 1 mM:3 mM. To study the influence of the ionic ratio on the dynamic self-assembly of ionoids, we systematically adjusted the concentration of the cationic building block, while keeping a constant concentration of the anionic component in each sample (see Table 5.1). This has the EPR spectroscopic advantage that all samples are directly comparable in EPR spectroscopy, as they have the same amount of radical  $\mathbf{3}^{2-}$  (see Fig. 5.1).

Calculating the ionic ratio inside each  $\mathbf{1}^{4+}:\mathbf{2}^{2-}$  ( $\mathbf{1}^{4+}:\mathbf{3}^{2-}$ , respectively) system is based on equation (5.1)

$$\text{ionic ratio} = \left| \frac{z^+ \cdot c(\mathbf{1}^{4+})}{z^- \cdot c(\mathbf{2}^{2-}/\mathbf{3}^{2-})} \right|, \quad (5.1)$$

where  $c(\mathbf{1}^{4+})$  and  $c(\mathbf{2}^{2-}/\mathbf{3}^{2-})$  represent the corresponding concentrations from Table 5.1. Note that we assume a constant charge  $z^\pm$  for the cationic ( $z^+ = +4$ ) and anionic ( $z^- = -2$ ) building block in all tested molar ratios.

**Table 5.1.:** Summary of all tested molar ratios for the system  $1^{4+}:2^{2-}$  ( $1^{4+}:3^{2-}$ , respectively) in DMSO:glycerol:water 50:43:7 (v/v/v) combined with their calculated ionic ratio

molar ratio	$c(1^{4+})$ / mM	$c(2^{2-}/3^{2-})$ / mM	ionic ratio <sup>a</sup>
0:1	0.0	3.0	-
1:6	0.5	3.0	1/3
1:3	1.0	3.0	2/3
1:2	1.5	3.0	1
2:3	2.0	3.0	4/3
5:6	2.5	3.0	5/3
1:1	3.0	3.0	2

<sup>a</sup> calculating ionic ratio using equation (5.1)

### 5.2.3. Methods

The two main methods, which were used in this study are dynamic light scattering (DLS) and continuous wave (CW) electron paramagnetic (EPR) spectroscopy (see Appendix A for further information). Here, the instrumentation is pointed out, which was used to perform the mentioned techniques:

1) DLS:

- Litesizer 500 (Anton Paar GmbH, Graz, Austria)

2) CW EPR:

- X-band: Miniscope MS400 (magnettech, Berlin, Germany) benchtop spectrometer
- Q-band: Bruker EMX-plus spectrometer (Bruker Biospin GmbH, Rheinstetten, Germany) with ER5106QT resonator.

## 5.3. Results and Discussion

### 5.3.1. General remarks

As introduced in our previous study,<sup>66</sup> we applied the following terms to describe the ionic self-assembly process for all measured systems:

- (i) Globular ionoids: spherical, highly stable structures with a hydrodynamic radius between 6 nm and 8 nm

- (ii) Anisotropic ionic clusters: structures with deviations from a spherical structure and/or slightly extended dimensions
- (iii) Ion cloud: initial state after sample preparation with no globular structure and  $R_H > 100$  nm.

Note that we can employ CW EPR spectroscopy only for measuring the ion cloud state that forms in the initial hours after system preparation. This is due to the disproportionation of the EPR-active Fremy's salt dianion ( $3^{2-}$ ) in solution proceeding faster than the ten-day incubation period of colloid-like ionic structures.

### 5.3.2. Analyzing ionic ratio dependence with DLS

As previously established<sup>14,66</sup>, we used DLS to directly observe the development of ionic clusters, mainly through their scattering profiles and the thus derived hydrodynamic radius. As the dianionic compound, we used  $2^{2-}$  due to its stability over the course of several months at 20 °C.

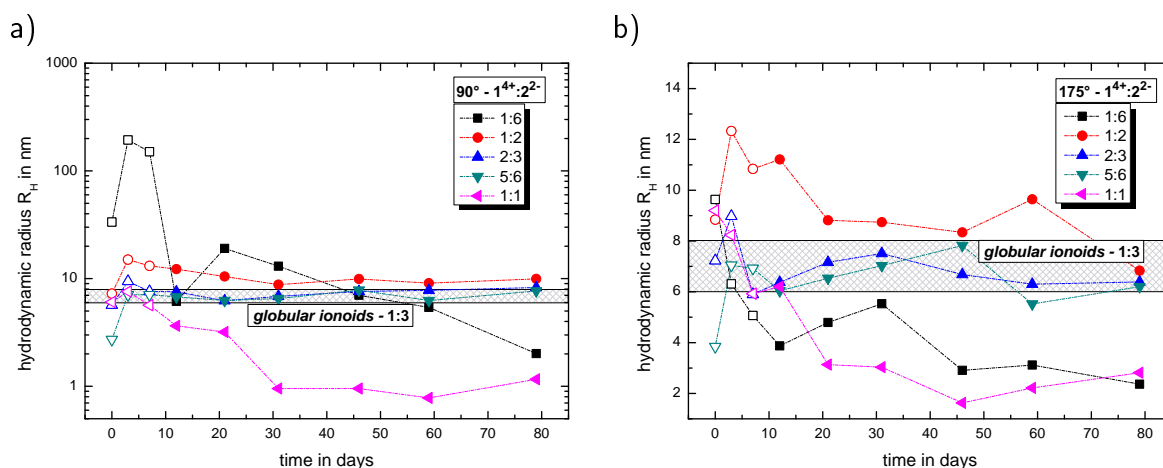


Fig. 5.2.: Development of the hydrodynamic radius with a) side ( $90^\circ$ ) and b) back ( $175^\circ$ ) scattering for the cluster system  $1^{4+}:2^{2-}$  in DMSO:glycerol:water 50:43:7 (v/v/v) depending on the molar ratio of cationic and anionic component. The first three data points of each system, which are located inside the ten-day incubation time possess open symbols. Both graphs also show a patterned box that highlights the region of the hydrodynamic radius for the established molar ratio of 1:3.

Fig. 5.2 summarizes the trend of the hydrodynamic radii with side and back scattering for all newly introduced molar ratios of  $1^{4+}:2^{2-}$  in DMSO:glycerol:water 50:43:7 (v/v/v). Furthermore, we highlight the region for the globular ionoid size in the established 1:3-system, which is located between 6 nm and 8 nm.<sup>14,66</sup> Note that we included the development of the hydrodynamic radius within the ten-day incubation period (open symbols in Fig. 5.2). During the incubation period, we can record autocorrelation functions with DLS, but the (i)

mean scattering intensities are not significantly higher compared to the pure solvent mixture DMSO:glycerol:water and (ii) the y-intercept values differ significantly between side and back scattering. After the incubation period, we obtained strongly pronounced intensity time correlation functions at  $90^\circ$  and  $175^\circ$  combined with stable count rate traces. This ten day incubation time is still enigmatic and will be discussed in a later publication.

Based on Fig. 5.2, the molar ratios 1:2, 2:3 and 5:6 are able to build up at least anisotropic ionic clusters with similar dimensions as seen for the 1:3 ratio. The present deviations between side and back scattering indicate a more spheroidal shape compared to almost perfectly spherical globular ionoids. In addition, these self-assembled structures have an inherent long-term stability, which is also visible in the intensity time correlation functions at measurement day 79 (see Fig. C.1). To further highlight the durability of our soft nanoscale structures in general, we filtered each sample again after a measuring period of 79 days and recorded DLS scattering traces. Fig. 5.3 displays exemplary the autocorrelation functions for the molar ratio  $1^{4+}:2^{2-}$  1:2 at both scattering angles. There is no significant difference visible between the DLS traces before and after filtration, indicating the unaltered size, shape and amount of ionic clusters inside the tested sample even after applying mechanical stress on to the self-assembled entities. The autocorrelation functions for all molar ratios are summarized in Appendix C (see Fig. C.2).

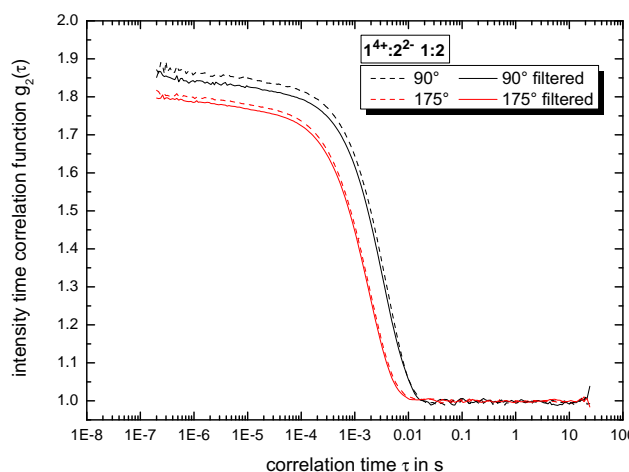


Fig. 5.3.: Intensity time correlation functions of molar ratio  $1^{4+}:2^{2-}$  1:2 in DMSO:glycerol:water 50:43:7 (v/v/v) at side (black) and back (red) scattering before (dashed lines) and after (solid lines) filtration.

The other two tested molar ratios  $1^{4+}:2^{2-}$  1:6 and 1:1 do not show pronounced autocorrelation functions after 79 days and therefore no self-assembled structures with long-term stability. Note that in Fig. 5.2, these ratios display a similar time-dependent development of the hydrodynamic radius for the back scattering angle. Both mixtures are able to build up ion cloud structures (1:6) or even smaller entities (1:1) directly after sample preparation, but



seem unable to transform this initial state into globular ionoids or anisotropic ionic clusters. A shortage or excess in  $\mathbf{1}^{4+}$  fundamentally changes the ionic self-assembly process due to the disturbed interplay between long-range electrostatic correlations and weaker noncovalent interactions.

Based on the DLS data, only ionic ratios in the region of  $2/3$  to  $5/3$  (molar ratios 1:3 to 5:6) are able to generate long-lived monodisperse, spheroidal colloid-like structures for the  $\mathbf{1}^{4+}:\mathbf{2}^{2-}$  system in DMSO:glycerol:water 50:43:7 (v/v/v).

### 5.3.3. Analyzing ionic ratio dependence with CW EPR

After characterizing the  $\mathbf{1}^{4+}:\mathbf{2}^{2-}$  system by DLS, we continued with CW EPR spectroscopy, which requires exchanging the anion  $\mathbf{2}^{2-}$  with paramagnetic Fremy's salt dianion ( $\mathbf{3}^{2-}$ ). This can influence interactions inside the ion cloud, but electrostatic correlations especially to  $\mathbf{1}^{4+}$  remain highly similar, as previously shown.<sup>14</sup> To distinguish between the influence of solely (i) solvent viscosity and (ii) electrostatic interaction with increasing  $\mathbf{1}^{4+}$  concentration on the rotational mobility of our spin probe, we measured 3 mM pure Fremy's salt in DMSO:glycerol:water 50:43:7 (v/v/v) as an internal reference (molar ratio 0:1 in Table 5.1). Additional line broadening based on dipolar interactions between multiple radicals can be neglected due to the still pronounced and fast rotational motion of the radicals, which averages out the dipolar coupling.

CW EPR spectra of the pure nitroxide radical (see Fig. C.3) in our established solvent mixture show rotational diffusion, which can be described by an axial tensor with the unique axis along the N-S-bond of Fremy's salt (see red arrow in Fig. 5.1).<sup>87,88</sup> Rotation about this unique axis ( $D_{\parallel}$ ) is at least 35-fold faster than about the axes perpendicular ( $D_{\perp}$ ) to it, in which deviations between X- and Q-band frequencies reflect the difference in frequency/field dependence of the rotational time-frame with higher frequencies/magnetic fields.<sup>88</sup> Adding  $\mathbf{1}^{4+}$  to the pure nitroxide radical (see Fig. 5.4) leads to (i) significant line broadening, mainly reflecting the slowed-down rotation around the molecular z-axis, and (ii) a shift of the unique  $D_{\parallel}$ -axis from the N-S-bond towards the dissecting angle of both sulfonate groups. The strength of the first effect depends on the concentration of the cationic building block: For the molar ratio  $\mathbf{1}^{4+}:\mathbf{3}^{2-}$  1:6 Fremy's salt still rotates relatively freely, but also starts to favor certain coordinations due to the electrostatic attraction to  $\mathbf{1}^{4+}$  and repulsion among the other  $\mathbf{3}^{2-}$  ions. At higher molar ratios, like 1:1, Fremy's salt shows slowed-down rotation around the molecular z- and x-axis, indicating a more fixed coordination to  $\mathbf{1}^{4+}$ .

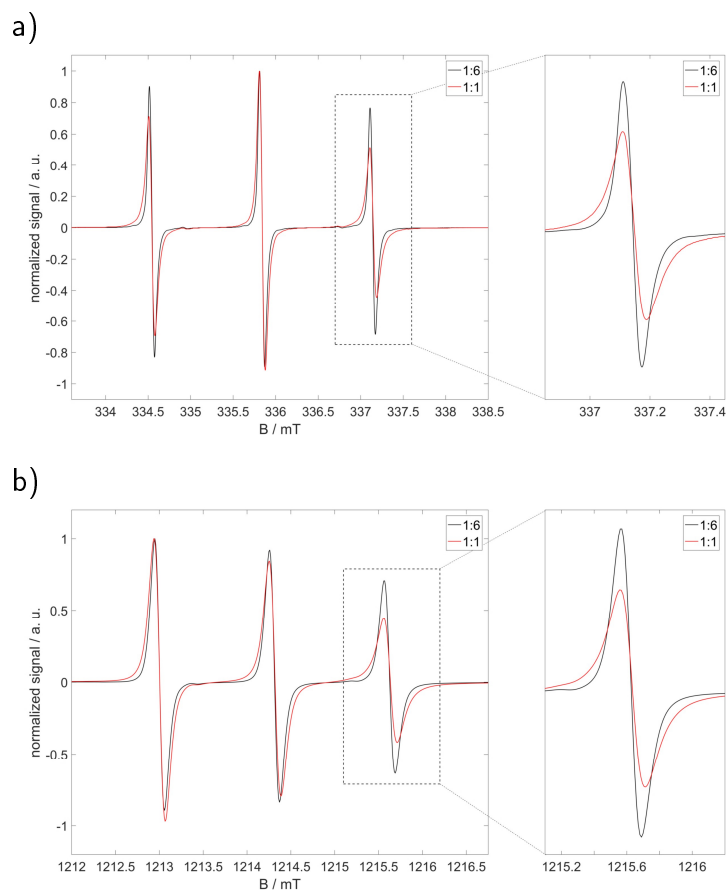


Fig. 5.4.: a) X-band and b) Q-band CW EPR spectra of  $\mathbf{1}^{4+}:\mathbf{3}^{2-}$  with molar ratios 1:6 (black) and 1:1 (red) in DMSO:glycerol:water 50:43:7 (v/v/v). The insets mark the highfield peak, which is shown separately right next to the full spectra.

To quantify the effect of increasing  $\mathbf{1}^{4+}$  concentration on the rotational mobility of Frey's salt, we combine different evaluation systems<sup>66</sup>:

- (1) Analyzing the line width, where we use the full width at half maximum (FWHM) values of the CW EPR spectra by simulating isotropic broadening, which is implemented in the EasySpin program package (see Fig. 5.5). Note that this method does not assume that any physical model is causing the broadening (see Fig. 5.5).
- (2) Calculating the anisotropy  $T$  of the rotational diffusion tensor based on equation A.7. We mainly discuss this parameter that emphasizes the distinction between  $D_{\parallel}$  and  $D_{\perp}$  and characterizes the magnitude of electrostatic interactions in the direct vicinity of Frey's salt in Appendix C.
- (3) As a very simple measure, the isotropic rotational correlation time  $\tau_c$  can be calculated even in the case of (slight) anisotropy of rotational motion (see Appendix A and C).

The FWHM values of each tested molar ratio of  $\mathbf{1}^{4+}:\mathbf{3}^{2-}$  in DMSO:glycerol:water 50:43:7

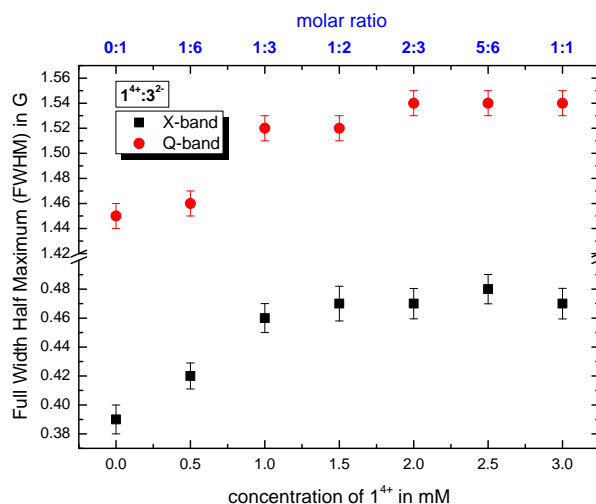


Fig. 5.5.: Plot of the isotropic broadening as full width at half maximum (FWHM) of pure Frey's salt 3 mM (molar ratio 0:1) and the system  $1^{4+}:3^{2-}$  with increasing cation concentration in DMSO:glycerol:water 50:43:7 (v/v/v).

(v/v/v), as shown in Fig. 5.5, show the same tendencies at X- and Q-band frequencies. The steady increase in the line width correlates with higher amounts of  $1^{4+}$  and stronger electrostatic interactions with and subsequent slow-down of Frey's salt. In addition, the coordination of both components shifts from a weak bond between  $1^{4+}$  and  $3^{2-}$  at a molar ratio of 1:6 to a more direct ion pair coordination at 1:1. At a ratio of 1:3 and higher, the FWHM values reach a plateau (within the margin of error), indicating that the local dynamic electrostatic attachment at day 0 of the ion mixtures (that are still in the ion cloud state, not the ionoid state) are similar above this ratio in the initial ion cloud state. Similar effects can be derived from the calculated rotational correlation time  $\tau_c$  and the anisotropy  $T$  (see Fig. C.4). Note that through the frequency-dependent differences in time-frame sensitivity/averaging X-band spectra rather mirror the globally averaged interactions and dynamics, while Q-band spectra highlight the interactions in the local environment of Frey's salt.<sup>66</sup>

#### 5.3.4. Ionoid Evolution Diagram (IED)

Inspired by so called Hertzsprung-Russell diagrams (HRDs)<sup>b</sup>, which are used in astrophysics to summarize and display the complex relationships of the properties of stars and stellar evolution during their complete lifetime of billions of years,<sup>93</sup> we propose the construction of ionoid evolution diagrams (IEDs) for summarizing the fate (here up to 79 days) of the dynamic ionic self-assembly processes that range from large ion cloud states of several hundreds of nanometers, all the way down (in size) to ion pairs and globular or anisotropic ionic clusters as

<sup>b</sup> Hertzsprung-Russell diagrams are textbook knowledge in astrophysics, see e. g. Adalbert W. A. Pauldrach 'Das dunkle Universum',<sup>93</sup> which in fact inspired this study.

remarkably stable yet flexible entities in between. More specifically, we can even illustrate the ionic ratio influence on the formation of the highly defined structures, as shown in Fig. 5.6. Hertzsprung-Russell diagrams display the distribution of stars, sorted by their luminosity on the y-axis and their surface temperature on the x-axis. Mass and time development are thus implicitly part of HRDs. Hence, these diagrams allow summarizing and displaying all stages of stellar development which is a remarkably large and complex set of data and we developed our IEDs to adapt this kind of data analysis as well as describe the dynamic ionic self-assembly process inside our solutions, which also comprises a wealth of complex data and long temporal evolution.

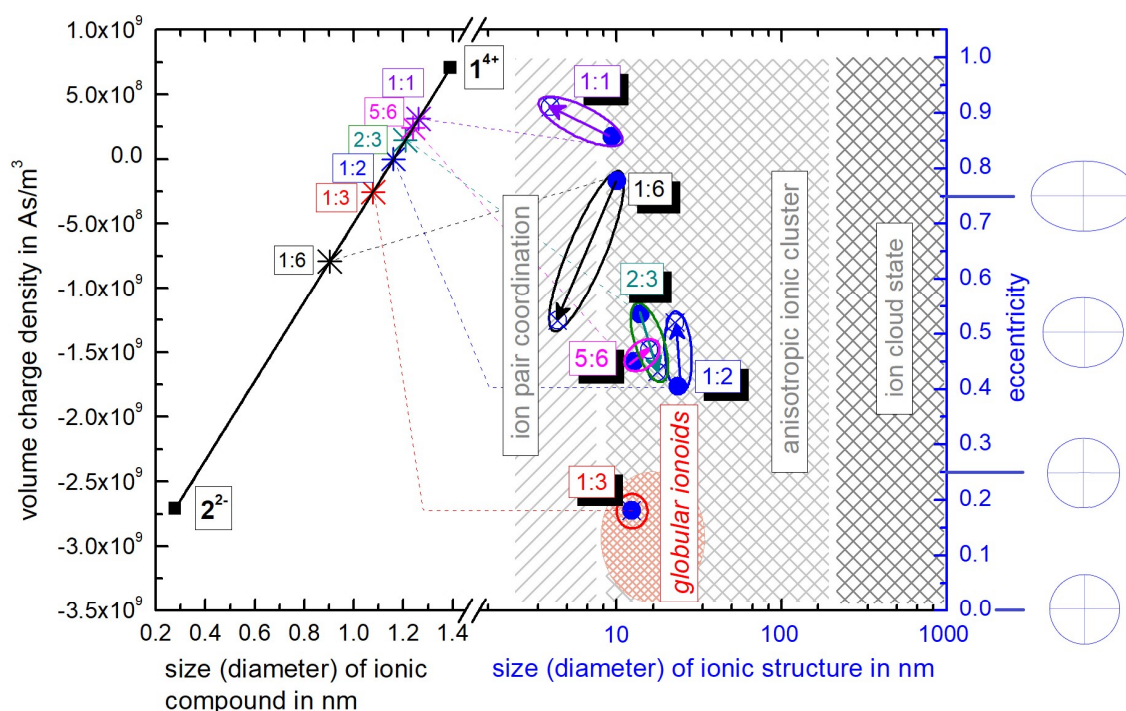


Fig. 5.6.: Ionoid evolution diagram for modifying the molar ratio between the ionic building blocks  $1^{4+}$  and  $2^{2-}$ , highlighting the three states of the ionic self-assembly process: globular ionoids, anisotropic ionic clusters and ion cloud. A detailed explanation is given in the text and Appendix A.

The left y-axis displays the volume charge density of the two building units, which could be calculated by dividing the charges  $z^{\pm}$  (multiplied with the elementary charge  $e$ ) of the cationic and anionic component by their respective volumes (see Appendix A for details). As the x-axis, we use the diameter of  $1^{4+}$  and  $2^{2-}$  (without solvation shell) due to the importance of the size and size ratio of the anionic and cationic components for the self-assembly process. By simply changing the molar ratio of  $1^{4+}$  and  $2^{2-}$ , we are able to adjust the resulting volume charge density as well as the acting electrostatic correlations<sup>25</sup> along the black connecting line of both ions (this resembles the main sequence line in Hertzsprung-Russell diagrams, see Appendix A

or Ref. 93). Starting from these intersections, we plot on the right y-axis the eccentricity  $e_{IED} = \sqrt{1 - \frac{b^2}{a^2}}$  to define deviations from a perfect sphere (with a value of  $e_{IED} = 0$ ) versus the final size of the ionic cluster based on the utilized molar ratios of  $\mathbf{1}^{4+}:\mathbf{2}^{2-}$ , illustrating the durability of more or less spherical self-assembled entities. In Fig. 5.6, we also plot the two-dimensional forms representing the eccentricities  $e_{IED} = 0$ ,  $e_{IED} = 0.25$ ,  $e_{IED} = 0.50$  and  $e_{IED} = 0.75$  to demonstrate the transition from a circular to an elliptical shape. A representation with three-dimensional structures can be found in Appendix A (see Fig. A.5). We further include the time beginning from the complete incubation period of ten days (blue full dots) until the last measurement day (arrow to blue crossed dots).

In Hertzsprung-Russell diagrams, the temporal evolution of billions of years is implicitly shown by deviations from the main sequence. Evolution with time is emphasized in IEDs by the oval (or for globular ionoids more circular) frame. Note that for our systems, we obviously does not observe the same time frame of billions of years. However, if we normalize the ionic self-assembly process to a crucial time step, which e. g. could be the translational and rotational diffusion of the ionic building blocks in solution, we can recalculate the required time steps in unit time needed to form stable ionic clusters. As a fast limit for the unit time step for the following estimations, we chose 1 ns for the diffusion itself. Hence the experimentally found incubation time of ten days for globular ionoids in unit time steps can be estimated, too. One day amounts to 86000 s or  $8.64 \times 10^{13}$  ns, leading to a total number of  $8.64 \times 10^{14}$  ns for ten days, in which the self-assembled entities form. Thereby, the building units have to experience billions of diffusion steps to gain a stable yet flexible structure.

As visualized in the IED (Fig. 5.6, we deduce the following for the  $\mathbf{1}^{4+}:\mathbf{2}^{2-}$  system:

- (1) Molar ratio 1:6 builds up initial ionic structures with significant deviations from a spherical shape, which, over time, decompose into smaller ion pair coordinations. Note that the setup of this mixture with a high amount of small anions compared to the large 'Texas-sized molecular box' is similar to polyelectrolytes e. g. PDADMAC.<sup>70,87,89</sup>
- (2) Molar ratio 1:3 delivers globular ionoids with almost perfect spherical shape. Based on the circular frame inside the IED (no change in time), we can conclude that these self-assembled entities exhibit high stability over the represented time-frame. Furthermore, we somewhat arbitrarily set the border globular ionoids to anisotropic ionic clusters at eccentricity 0.25 and a diameter of 25 nm or higher.
- (3) Molar ratios 1:2, 2:3 and 5:6 form long-lived anisotropic ionic clusters. These systems with higher amount of  $\mathbf{1}^{4+}$  compared to the established 1:3-mixture<sup>14,66</sup> do not reach

---

<sup>c</sup> Parameters  $a$  and  $b$  are the length of the semi-major and semi-minor axis of the ellipses. The exact adaptation of the eccentricity for the IEDs utilizing our DLS data can be found in AppendixA.

their low eccentricity values, indicating adjustable shapes for our self-assembled entities due to tuning the ionic ratio of  $\mathbf{1}^{4+}$  and  $\mathbf{2}^{2-}$ .

- (4) Molar ratios 1:1 and 1:6 show larger (weakly scattering) initial ionic structures that decompose into more trivial ion pair coordinations between  $\mathbf{1}^{4+}$  and  $\mathbf{2}^{2-}$ , with the system at a 1:1 ratio having an inherently more anisotropic shape.

## 5.4. Conclusions

The ionic self-assembly process of the 'Texas-sized molecular box' ( $\mathbf{1}^{4+}$ ) with the small dianionic salts  $\mathbf{2}^{2-}$  and  $\mathbf{3}^{2-}$  into globular ionoids depends significantly on the molar ratio of the respective components. For the system  $\mathbf{1}^{4+}:\mathbf{2}^{2-}$  ( $\mathbf{1}^{4+}:\mathbf{3}^{2-}$ , respectively), we detect highly defined, colloid-like structures with long-term stability<sup>14,66</sup> at molar ratios from 1:3 to 5:6, which lead to ionic ratios between  $2/3$  and  $5/3$ . Note that with changing the molar ratio of these intrinsically polyphilic molecules between 1:3 and 5:6, (i) the hydrodynamic radius of the ionic structures slightly shifts from 6 nm to 12 nm and (ii) the value of the eccentricity-parameter is rising. The modified interplay between long-range electrostatic correlations and weaker noncovalent interactions indicates the possibility of adjusting the size and shape of the colloid-like structures by tuning the molar ratio of  $\mathbf{1}^{4+}$  and  $\mathbf{2}^{2-}$  ( $\mathbf{3}^{2-}$ , respectively).

The CW EPR spectra demonstrate with increasing concentration of  $\mathbf{1}^{4+}$ , while keeping the amount of the  $\mathbf{3}^{2-}$  ion constant, a slowed-down rotational mobility of Fremy's salt as well as an increasing line width due to stronger electrostatic interactions occurs. These effects could be measured in the initial ion cloud state at X- and Q-band frequencies, indicating their appearance both globally and in the local environment. In general, this can be interpreted as Fremy's salt being trapped in the charge sphere of one  $\mathbf{1}^{4+}$ , leading to stoichiometric ion pairs and thus the formation of loosely bound ion paired structures, as shown in the DLS data. However, at this point, it is not possible to quantify the contribution of electrostatic interactions to the total self-assembly process compared to weaker noncovalent forces.

Based on the introduced ionoid evolution diagram (IED), we are able to illustrate the ionic ratio influence on the formation of the highly defined structures (i) directly after the incubation time of ten days and (ii) throughout the entire measurement period. Furthermore, we can analyze the durability of the self-assembled ionic clusters as well as characterize their deviations from a spherical shape with the calculated eccentricity. Due to the studied molar ratios, we are able to define requirements for globular ionoids in the  $\mathbf{1}^{4+}:\mathbf{2}^{2-}$  ( $\mathbf{1}^{4+}:\mathbf{3}^{2-}$ , respectively) system, which comprise a diameter between 10 nm and 25 nm and an eccentricity lower than 0.25. Note that the constructed IED is only valid for the applied solvent mixture DMSO:glycerol:water 50:43:7 (v/v/v). In the long run, we want to compare the formation of the highly defined structures in various solvent mixtures using IEDs to understand the influence of e. g. the dielectric constant

---

or viscosity on the ionic self-assembly process and to simplify the required solvent mixture regarding possible applications in soft matter and supramolecular chemistry.





## 6 | Dynamic Self-Assembly of Ions with Variable Size and Charge in Solution

Chapter 6 presents that the solution-based ionic self-assembly process leading to ionoids is a general phenomenon by characterizing new ionic building blocks which are capable of generating loosely bound globular and anisotropic structures similar to those in the established system. Using new cationic and anionic molecules, we show that variations in the size ratio between cationic and anionic component mainly affect size, shape and durability of the ionic clusters. Thus, generalized ionic ratios could be defined, in which specific combinations of ionic compounds with certain size and charge densities are able to form these soft yet durable and long-lived ionic clusters. Furthermore, the temporal development of the dynamically self-assembled structures in solution was characterized from the level of the individual ionic building blocks to stable clusters with minimum lifetimes of months through previously established ionoid evolution diagrams. The direct comparison of various cluster systems with respect to their shape, size and charges allows correlations of structural changes of the individual building blocks with the fate of self-assembled entities inside the crafted IEDs. This study generalizes the concept of ionoid formation to ions of specific sizes and charge densities. The respective results are already published and are reproduced by permission of 'The Royal Society of Chemistry'<sup>a</sup> from:

J. Eisermann, A. Kerth and D. Hinderberger, *RSC Advances*, 2019, **9**, 18627-18640

**DOI:** 10.1039/c9ra02019e

<https://pubs.rsc.org/en/content/articlelanding/2019/ra/c9ra02019e>

Note the changes inside the 'Methods' subsection (6.2.3.) in respect to the cited publication to integrate the summarized information from Appendix A. The remaining sections 6.1. to 6.4. can be considered as citation from Ref. 94. The contribution of Dr. Andreas Kerth started by picking the potential cationic and anionic building units for the formation of new

---

<sup>a</sup> The permission from 'The Royal Society of Chemistry' is present in written form.

ionoid systems based on the process of ISA. He also helped in performing the preliminary tests to define the matching molar/ionic ratios for the different size combinations of ionic building units and in planning the presented measurement series. My contribution includes carrying out and evaluating the later published measurements, ranging from scattering methods over UV-vis and fluorescence spectroscopy to EPR spectroscopy as well as writing the respective manuscript.

## 6.1. Introduction

The structure and dynamics of matter at the nanometer scale form the basis for both natural processes and technological applications reaching far beyond the pertinent nanoscale lengths, so tuning their (sub-)nanometer architecture and (sub-)microsecond dynamics can be seen as key to tuning macroscopic properties on much larger length scales and times as well.<sup>95</sup> Molecular design approaches have proven to be most beneficial in the development of next-generation materials with tailor-made properties.<sup>96</sup> Assembling various molecular building units enables the construction of numerous chemical architectures with discrete (zero-dimensional, 0D) to extended (1D, 2D and 3D) structures, ranging from inorganic to pure organic components, from disordered to regular arrangements and from non-porous to porous nature.<sup>97</sup> The interactions which are exploited to link these monomeric precursors reach from strong covalent bonds in polymers over dynamic linkages to weak supramolecular forces e. g.  $\pi$ - $\pi$  interactions, halogen bonding or hydrogen bonding.<sup>96,98</sup>

Over the course of the last three decades, numerous examples of materials with precisely controlled nano-environments could be achieved, primarily in the field of porous materials, in which one of the most fundamental principles of living systems is mimicked through offering confined spaces for molecular purposes.<sup>96</sup> Furthermore, establishing e. g. metal-organic frameworks<sup>99–107</sup> (MOFs, also known as porous coordination polymers<sup>108,109</sup>), covalent organic frameworks<sup>110–116</sup> (COFs) and hydrogen-bonding organic frameworks<sup>117–124</sup> (HOFs) inside application fields like gas separation and storage, catalysis, sensing, optoelectronics, electronic devices, proton conduction, drug delivery and imaging significantly advances the development of these tailor-made materials.<sup>96</sup> At about the same time, the synthesis and development of entangled molecular components through mechanical bonds<sup>10,125–127</sup> was introduced, starting the templating of mechanically interlocked molecules (MIMs)<sup>10,125–129</sup>. MIMs encompass besides the two archetypal examples catenanes and rotaxanes<sup>126,127,130–133</sup> also molecular shuttles and bistable molecular switches<sup>10,130,134,135</sup> as well as framework structures due to the process of molecular weaving.<sup>125</sup> Thus, the potential applications of mechanically interlocked materials include various fields, reaching from e. g. nanoelectromechanical systems<sup>135,136</sup> over artificial molecular machines<sup>128,137</sup> to drug delivery systems.<sup>138</sup>

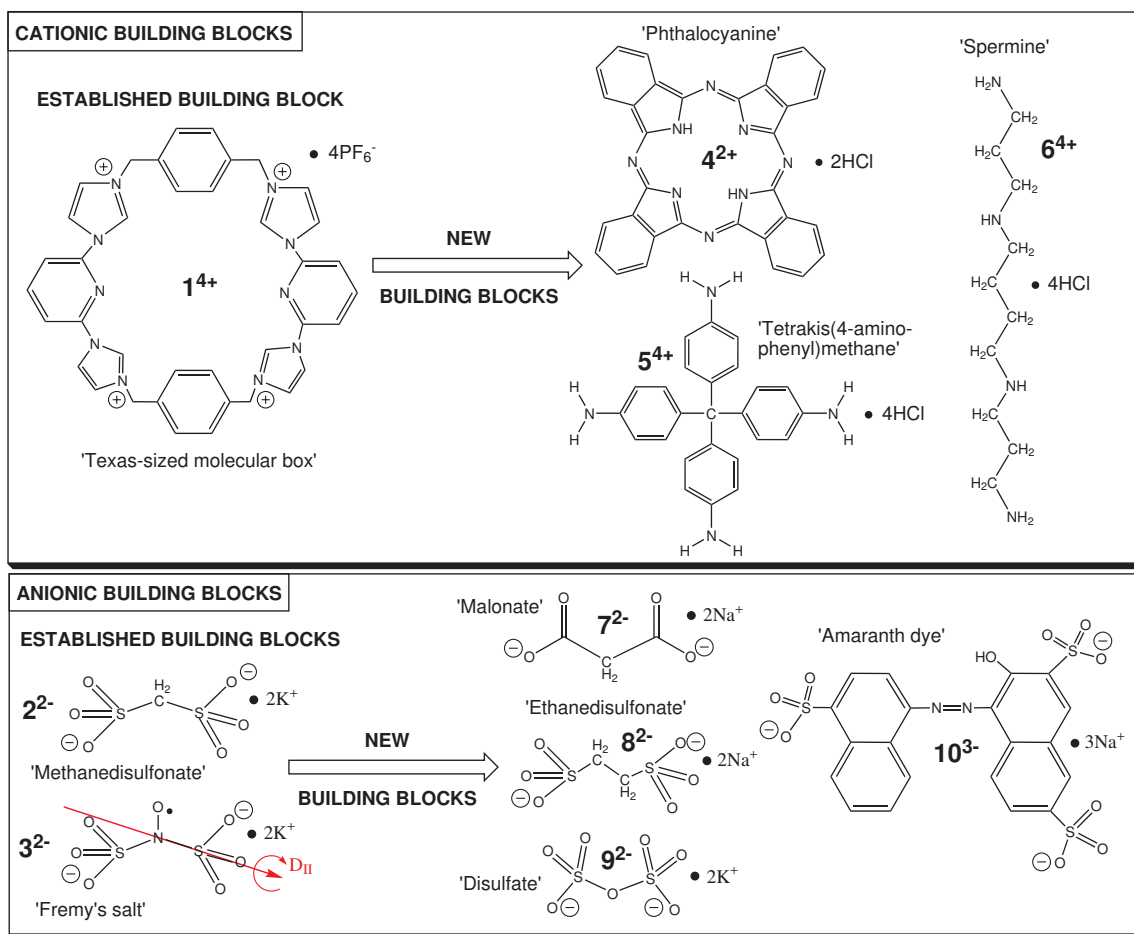


Fig. 6.1.: Summary of the utilized ionic building blocks to form *ionoids* based on the model system  $1^{4+} : 2^{2-}$  ( $1^{4+} : 3^{2-}$ , respectively).

The 'Texas-sized molecular box' ( $1^{4+}$ , Fig. 6.1), developed by Sessler and coworkers, acts as MIM and forms pseudorotaxane structures in combination with bis-carboxylate anions<sup>15–17</sup>. Going beyond solid-state structures, we discovered that in solution this compound electrostatically self-assembles in the presence of small dianionic salts ('methanedisulfonate',  $2^{2-}$  or Fremy's salt dianion,  $3^{2-}$ , see Fig. 6.1) into loosely bound, yet remarkably durable, ion-based colloid-like globular cluster of several nanometer size,<sup>14</sup> termed globular ionoids (see Ref. 66). The formation of such size-monodisperse supramolecular structures due to long-range electrostatic correlations also required the right interplay of weaker noncovalent interactions (solvation, hydrogen bonding, van der Waals interactions)<sup>3</sup>. Therefore, the composition of e. g. the solvent, in our case the established mixture DMSO:glycerol:water 50:43:7 (v/v/v), plays an important role in the ionic self-assembly process.<sup>66</sup> Based on previous studies, we postulate an initial ion cloud state after mixing cationic and anionic building units, where no globular structures are yet formed and the system has not reached its thermodynamic balance. As we have described it previously (see Ref. 66), this ion cloud state persists over an extremely

long incubation time of ten days and is defined by the existence of large structures (larger than 100 nm). We currently assume (experiments are ongoing) that the internal ion distribution obeys a Poisson-Boltzmann-type or similar mean-field interaction pattern, which characterize the phase after sample preparation. However, due to already carried out Monte Carlo simulations (see Ref. 14), which revealed a surprising long-range correlation of  $\mathbf{1}^{4+}$  at about 15 nm, we presume electrostatic and excluded volume effects as essential for the formation of ionic clusters. Reliably after the incubation period of ten days, we detect globular ionoids that are now able to withstand e. g. mechanical stress.<sup>92</sup> As depicted above, the transition from ion cloud to globular ionoids is not fully understood yet and is out of the scope in this specific study, which is solely concerned with formation of ionoid structures built from new chemical units.

To this end, we here focus on extending the concept of ionoid formation by substituting the 'Texas-sized molecular box' as well as the dianionic salts with other polyphilic ionic building blocks (see Fig. 6.1) that are capable of forming multiple partially orthogonal noncovalent interactions (like those mentioned before). This expands the mainly ionically driven self-assembly of ionoids with respect to the sizes, topologies and ionic ratios of the directly involved ionic compounds. We replace the large cation  $\mathbf{1}^{4+}$  with molecular structures that were also used in the creation of tailor-made materials like  $\mathbf{4}^{2+}$ <sup>139-141</sup> and  $\mathbf{5}^{4+}$ <sup>112,142-145</sup>, and the biological oligoamine spermine  $\mathbf{6}^{4+}$ <sup>146</sup> and/or substitute the small dianionic salts  $\mathbf{2}^{2-}$  and  $\mathbf{3}^{2-}$  with dianions of similar structure ( $\mathbf{7}^{2-}$ ,  $\mathbf{8}^{2-}$ ,  $\mathbf{9}^{2-}$ ) and with a larger trianionic chromophore ( $\mathbf{10}^{3-}$ ). Based on these modifications we use dynamic light scattering (DLS), continuous wave (CW) electron paramagnetic resonance (EPR) spectroscopy, aided by UV-vis and fluorescence spectroscopy, to investigate the interplay between chemical nature, size and ionic ratio for developing dynamically formed, persistent structures like highly defined, colloid-like ionic clusters in solution. Additionally, we study the stability of selected self-assembled, colloid-like structures in solution through characterizing their zeta potential with continuously monitored phase-analysis light scattering (cmPALS). On a more general note, we expand the structural universe of ionoids and can show that this type of very soft structure formation is not limited to the initially studied 'model' system of  $\mathbf{1}^{4+}$  and  $\mathbf{2}^{2-}$ , but rather seems to constitute a general state and process for ions that fulfill certain prerequisites in size and charge in specific solution. Finally, we rationalize our findings by describing the different ionoid systems in evolution diagrams ('ionoid evolution diagrams', IEDs). We previously developed IEDs<sup>92</sup> to be able to characterize the complex underlying molecular features, like ionic sizes and ionic ratios, and describe the long term evolution (over the course of months) of the loosely bound ionic clusters in solution.

## 6.2. Experimental

### 6.2.1. Materials

The model system for creating ionoids contains the 'Texas-sized molecular box' ( $\mathbf{1}^{4+}$ ), which was synthesized according to Ref. 15,16 as described in Ref. 14,66 and the small dianionic salts methanedisulfonic acid dipotassium salt ( $\mathbf{2}^{2-}$ , Sigma-Aldrich, Munich, Germany) with purity  $\geq 99\%$  as well as Fremy's salt (potassium nitrosodisulfonate,  $\mathbf{3}^{2-}$ , Sigma-Aldrich) of technical grade. These chemicals as well as malonic acid disodium salt ( $\mathbf{7}^{2-}$ , 99%, abcr GmbH, Karlsruhe, Germany), 1,2-ethanedisulfonic acid disodium salt ( $\mathbf{8}^{2-}$ , 99%, abcr GmbH) and potassium disulfate ( $\mathbf{9}^{2-}$ , 99%, Sigma-Aldrich) were applied as received.

The ionic building blocks phthalocyaninedihydrochloride ( $\mathbf{4}^{2+}$ ), tetrakis(4-aminophenyl)-methanetetrahydrochloride ( $\mathbf{5}^{4+}$ ), sperminetetrahydrochloride ( $\mathbf{6}^{4+}$ ) and Amaranth ( $\mathbf{10}^{3-}$ ) had to be modified or purified to be used for the study. These specific adjustments are summarized in Appendix D. All tested systems were measured in the established solvent mixture DMSO:glycerol:water 50:43:7 (v/v/v), produced with DMSO containing  $\leq 0.02\%$  water (Sigma-Aldrich) in a 1:1 (v/v) ratio with 86-88 wt% glycerol (Acros Organics, Nidderau, Germany).<sup>14,66</sup>

### 6.2.2. Size ratio

Considering the ten chosen ionic building blocks (see Fig. 6.1), there exist countless ways in combining comparatively small and large cationic and anionic components. In this study, we highlight a small selection of these possible assemblies. However, most of the studied compositions consist of rather large cations and small anions, just like the established model system  $\mathbf{1}^{4+}:\mathbf{2}^{2-}$  ( $\mathbf{1}^{4+}:\mathbf{3}^{2-}$ , respectively). Table 6.1 summarizes all tested mixtures categorized based on their underlying size ratio.

The exact concentration for each component in its associated constellation varies depending on the applied methods and is summarized in Table 6.2. Calculations of the ionic ratio for all mixtures are based on equation 6.1 for the reference system  $\mathbf{1}^{4+}:\mathbf{2}^{2-}$  ( $\mathbf{1}^{4+}:\mathbf{3}^{2-}$ , respectively) 1 mM:3 mM

$$\text{ionic ratio} = \left| \frac{z^+ \cdot c(\mathbf{1}^{4+})}{z^- \cdot c(\mathbf{2}^{2-}(\mathbf{3}^{2-}))} \right| = \left| \frac{4 \cdot 1 \text{ mM}}{-2 \cdot 3 \text{ mM}} \right| = \frac{2}{3}, \quad (6.1)$$

where  $c(\mathbf{1}^{4+})$  and  $c(\mathbf{2}^{2-}(\mathbf{3}^{2-}))$  represent the corresponding concentrations. Note that we assume a constant charge  $z^\pm$  for the cationic ( $z^+ = +4$ ) and anionic ( $z^- = -2$ ) component. Furthermore, we utilize equation 6.1 also for systems containing other ionic building blocks with their respective concentration and charge.

**Table 6.1.:** Summary of all tested mixtures in DMSO:glycerol:water 50:43:7 (v/v/v), categorized based on the size ratio between cationic and anionic component

combine	large cation	small cation
small anion	$1^{4+}:2^{2-}(3^{2-})$	$6^{4+}:2^{2-}(3^{2-})$
	$4^{2+}:2^{2-}(3^{2-})$	
	$5^{4+}:2^{2-}(3^{2-})$	
	$1^{4+}:7^{2-}$	
	$1^{4+}:8^{2-}$	
	$1^{4+}:9^{2-}$	
large anion	$1^{4+}:10^{3-}$	$6^{4+}:10^{3-}$

### 6.2.3. Methods

The main methods that were applied in this study are dynamic light scattering (DLS), continuous wave (CW) electron paramagnetic resonance (EPR) spectroscopy and continuously monitored phase-analysis light scattering (cmPALS). Appendix A covers the description of these methods. The respective instrumentation used to perform the mentioned techniques are:

- 1) DLS and cmPALS:
  - Litesizer 500 (Anton Paar GmbH, Graz, Austria)
- 2) CW EPR:
  - X-band: Miniscope MS400 (magnettech, Berlin, Germany) benchtop spectrometer
  - Q-band: Bruker EMX-plus spectrometer (Bruker Biospin GmbH, Rheinstetten, Germany) with ER5106QT resonator.

Besides using ionic building units, which have an observer electron spin, we chose other compounds possessing remarkable color properties like  $4^{2+}$ <sup>139,140,147</sup> and  $10^{3-}$ <sup>148–151</sup>. Therefore, we applied UV-vis and fluorescence spectroscopy to characterize the formation of self-assembled structures through changes in their absorption and emission spectra<sup>b</sup>.

We used the Hewlett-Packard spectrophotometer HP 8453 (Agilent Technologies, Santa Clara, United States) for UV-vis spectroscopy and the FluoroMax-2 fluorescence spectrometer (Instruments S. A. GmbH, Grasbrunn, Germany) to measure the corresponding emission spectra.

<sup>b</sup> Additional Note: UV-vis and fluorescence spectroscopy were not included in Appendix A due to their unique usage in this study. Therefore, further information are summarized in Appendix D.

**Table 6.2.:** Summary of all tested mixtures in DMSO:glycerol:water 50:43:7 (v/v/v) with their respective molar ratio and ionic ratio

system	concentration ratio	molar ratio	ionic ratio <sup>a</sup>
<b>1<sup>4+</sup>:2<sup>2-</sup> (3<sup>2-</sup>)</b>	1 mM:3 mM	1:3	2/3
<b>1<sup>4+</sup>:7<sup>2-</sup></b>	1 mM:3 mM	1:3	2/3
<b>1<sup>4+</sup>:8<sup>2-</sup></b>	1 mM:3 mM	1:3	2/3
<b>1<sup>4+</sup>:9<sup>2-</sup></b>	1 mM:3 mM	1:3	2/3
<b>1<sup>4+</sup>:10<sup>3-</sup></b>	10 μM:30 μM	1:3	4/9
<b>4<sup>2+</sup>:2<sup>2-</sup> (3<sup>2-</sup>)</b>	13.3 μM:20 μM	2:3	2/3
<b>5<sup>4+</sup>:2<sup>2-</sup> (3<sup>2-</sup>)</b>	1 mM:3 mM	1:3	2/3
<b>6<sup>4+</sup>:2<sup>2-</sup> (3<sup>2-</sup>)</b>	1.6 mM:1.2 mM	4:3	8/3
<b>6<sup>4+</sup>:10<sup>3-</sup></b>	10 μM:30 μM	1:3	4/9

<sup>a</sup> calculating ionic ratio using equation 6.1

Here, we did not prepare samples exclusively for these spectroscopic methods, but measured the already existing mixtures from dynamic light scattering at 20 °C. Reusing the DLS samples allowed us to directly comparison with the determined size as well as size distribution of the self-assembled structures with the recorded absorption and emission spectra. Additionally, we performed DLS, UV-vis and fluorescence spectroscopy in the same regular, frequent intervals to receive the optimal requirements for analyzing the potential ionic self-assembly process of **1<sup>4+</sup>:10<sup>3-</sup>** and **6<sup>4+</sup>:10<sup>3-</sup>**. We also tried to measure systems containing **4<sup>2+</sup>** ions, but the compound did not show (i) significant absorption peaks and (ii) emission spectra, probably due to the solvent mixture of DMSO:glycerol:water 50:43:7 (v/v/v).

## 6.3. Results and Discussion

### 6.3.1. General Remarks

As introduced in Ref. 66, we applied the established terms (i) globular ionoids, (ii) anisotropic ionic cluster and (iii) ion cloud to describe the ionic self-assembly process for all of the following systems. To validate the formation of such nanoscopic entities due to the complex interactions between the ionic building units, we measured the pure solvent mixture DMSO:glycerol:water 50:43:7 (v/v/v), which was treated exactly like every other sample, with DLS as shown in Fig. D.1. The solvent itself does not present pronounced autocorrelation functions and therefore no tendencies in independently establishing defined structures. Moreover, the surface tension of the mixture DMSO:glycerol:water 50:43:7 (v/v/v) (see Fig. D.2), which is significantly

lower compared to water, indicates that the building units tend to stay inside the bulk and do not move to the air-solvent interface. At last, DLS data of each building unit separately dissolved in our solvent mixture (see Fig. D.3 and D.4) were recorded to ensure that (i) these compounds alone do not present high scattering intensities and (ii) the combination of matching cationic and anionic unit is the important condition for well-defined ionic cluster.

The construction principle of our ionoid evolution diagrams, elaborately introduced in Ref. 92, can be found in Appendix A. CW EPR studies are limited in measuring the ion cloud state that forms in the initial hours after preparation of the system due to the disproportionation of the EPR-active Fremy's salt dianion ( $3^{2-}$ ) in solution proceeding faster than the ten-day incubation period of globular, colloid-like ionic structures. Finally, we mainly focus on new systems which combine (i) large cation with small anion and (ii) small cation with small anion to exemplarily discuss the size ratio influence on the dynamically driven self-assembly process of ionoids.

### 6.3.2. Substitution of $2^{2-}$ ( $3^{2-}$ )

We have substituted the anionic component in our model system  $1^{4+}:2^{2-}$  ( $1^{4+}:3^{2-}$ , respectively) to create new mixtures with the rather large multicationic molecular box  $1^{4+}$  as cationic component and the following anionic building units:

- (1) Small dianions  $7^{2-}$ ,  $8^{2-}$  and  $9^{2-}$  with the concentration ratio 1 mM:3 mM and
- (2) Large trianionic chromophore  $10^{3-}$  with the concentration ratio 10  $\mu$ M:30  $\mu$ M.

The applied concentrations for these new systems are derived from several preliminary tests, yield pronounced scattering intensities compared to the used solvent and represent ionic ratios that in the established system lead to globular, least anisotropic ionoids. Note that one reduced the concentration ratio for the Amaranth dye ( $10^{3-}$ ) to directly compare DLS with UV-vis and fluorescence spectroscopy data.

Fig. 6.2 a) and b) summarizes the intensity time correlation functions with side and back scattering for the systems with malonate ( $1^{4+}:7^{2-}$ ) and ethanedisulfonate ( $1^{4+}:8^{2-}$ ) as well as for the model system ( $1^{4+}:2^{2-}$ ) in DMSO:glycerol:water 50:43:7 (v/v/v) at measurement day ten. Both new systems, which combine a large cationic component with small dianions, display a (i) delayed decay in their autocorrelation functions and (ii) reduced y-intercept-values compared to  $1^{4+}:2^{2-}$ , indicating a preferred formation of larger entities and/or rather polydisperse particle size distributions. This fact is further highlighted in Fig. 6.2 c) and d), which shows the development of the hydrodynamic radii for the present colloid-like structures over time.  $1^{4+}:7^{2-}$  and  $1^{4+}:8^{2-}$  are able to partially build up anisotropic ionic clusters after an incubation time of ten days, but we still detect the large (> 100 nm) initial ion cloud state



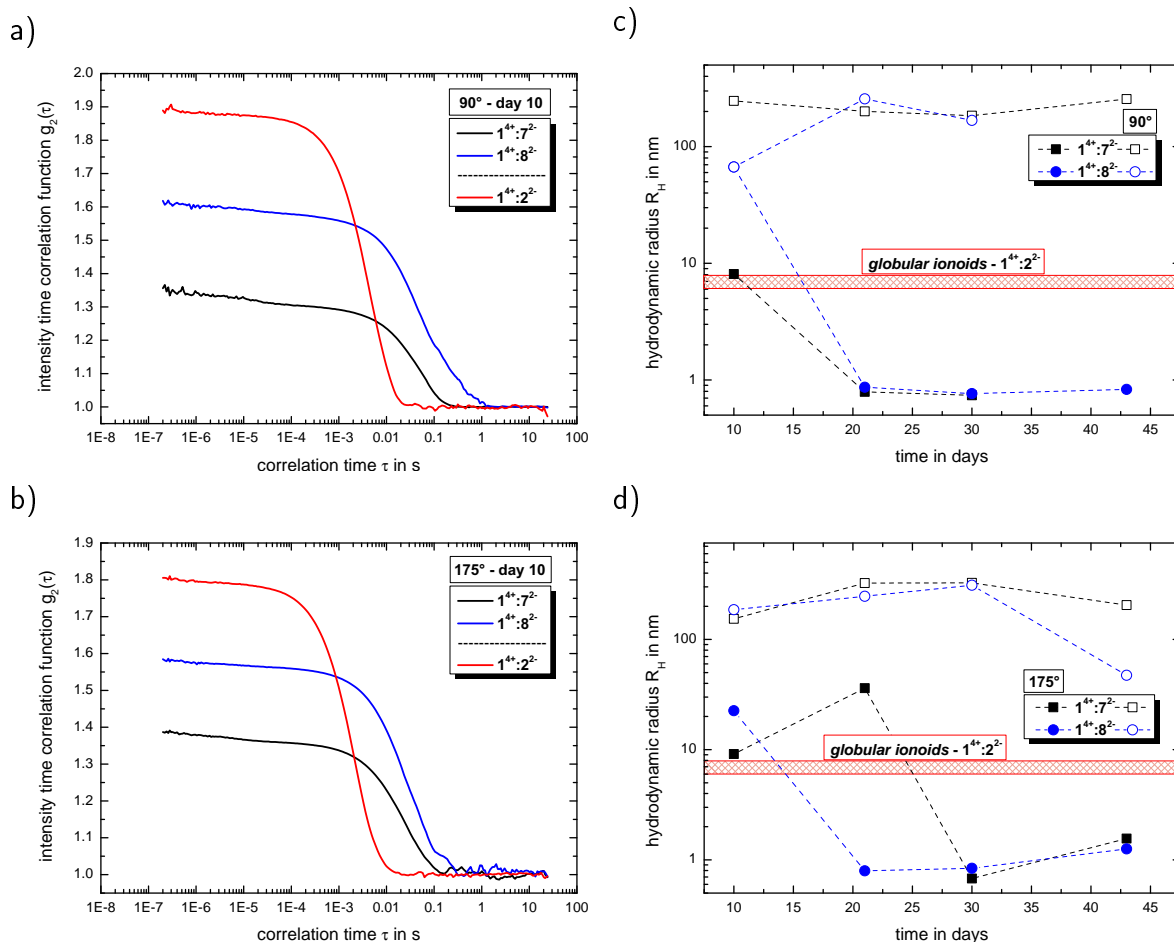


Fig. 6.2.: Comparison of the intensity time correlation functions at day ten for a) side and b) back scattering and development of the hydrodynamic radius with c) side and d) back scattering for the systems  $1^{4+}:7^{2-}$  and  $1^{4+}:8^{2-}$  in DMSO:glycerol:water 50:43:7 (v/v/v). For the model system  $1^{4+}:2^{2-}$  (same conditions) a) and b) also show the autocorrelation function, while c) and d) show a patterned box that highlights the region of its hydrodynamic radius.

(open symbols in Fig. 6.2 c) and d)) as second scattering component. Furthermore, the self-assembled entities for both systems fall apart over the course of several days, possessing reduced durability compared to the long-lived globular ionoids of  $1^{4+}:2^{2-}$ .<sup>66</sup> Note that we applied the same concentration ratio of 1 mM:3 mM as well as ionic ratio of 2/3 for the malonate- and ethanedisulfonate-system, leaving their chemical nature (see Fig. 6.4) as reason for the changed dynamically driven self-assembly process. DLS data for system  $1^{4+}:9^{2-}$  show a similar behavior compared to mixtures containing compound  $8^{2-}$  (see Fig. D.11), while the combination of both large cation and large anion ( $1^{4+}:10^{3-}$ ) builds up rather extended structures near the transition from anisotropic ionic clusters to the initial ion cloud state with a certain durability (see Fig. D.12).

Based on the performed DLS measurements, we studied the colloidal stability of systems

$\mathbf{1}^{4+}:\mathbf{7}^{2-}$  and  $\mathbf{1}^{4+}:\mathbf{8}^{2-}$  after the incubation period of ten days through the cmPALS method. Again, we used the combination of 'Texas-sized molecular box' and methanedisulfonate as reference point. Here, the self-assembled globular ionoids present a well-defined phase plot (as shown in Fig. D.6) and the calculated zeta potential of  $\zeta = 66.5\text{mV} \pm 1.2\text{mV}$ , which is in absolute numbers similar to the electrokinetic potential for nanosphere size standards made out of polystyrene (see Table D.2), supports the well-known high stability of  $\mathbf{1}^{4+}:\mathbf{2}^{2-}$  ionic clusters in solution.<sup>92</sup> Note that based on the measurements for pure  $\mathbf{1}^{4+}$  and  $\mathbf{2}^{2-}$  solutions the 'Texas-sized molecular box' is, under the influence of an external electric field and despite its larger diameter, the more mobile compound inside the DMSO:glycerol:water solvent mixture. To verify that the globular ionoids survived the treatment with the cmPALS method, we repeated the DLS measurements and compared the autocorrelation functions for both scattering angles, as shown in Fig. 6.3. The intensity time correlation functions as well as the monodisperse particle size distributions show almost no change, which again demonstrates the colloidal stability of our self-assembled entities.

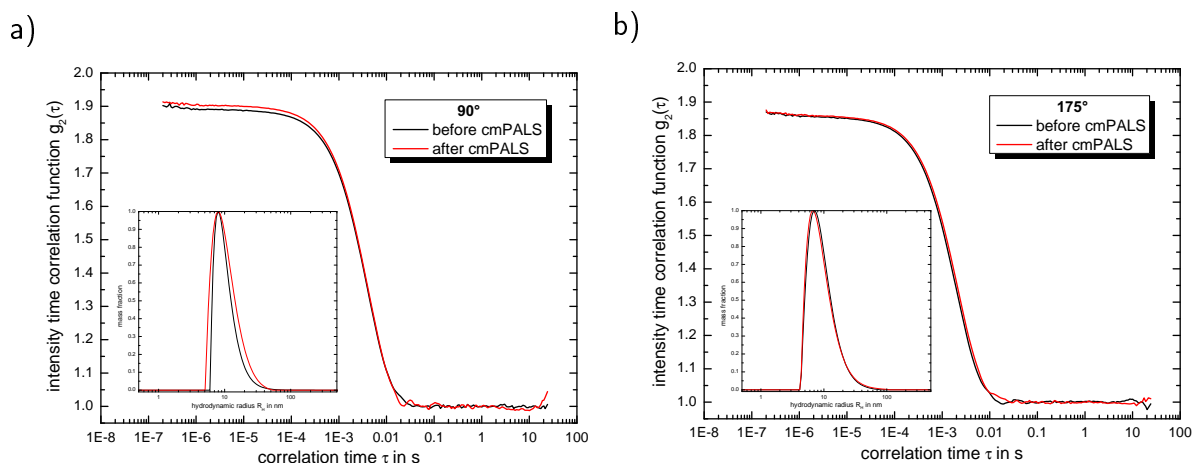


Fig. 6.3.: Comparison of the intensity time correlation functions at day ten for a) side and b) back scattering for system  $\mathbf{1}^{4+}:\mathbf{2}^{2-}$  in DMSO:glycerol:water 50:43:7 (v/v/v) before and after the cmPALS measurement. The inlays highlight the particle size distributions for the respective autocorrelation functions.

The systems containing malonate and ethanedisulfonate instead of methanedisulfonate just partially build up anisotropic ionic clusters, therefore we assume a reduced zeta potential, but  $\mathbf{1}^{4+}:\mathbf{7}^{2-}$  and  $\mathbf{1}^{4+}:\mathbf{8}^{2-}$  should still reach a value of  $\pm 30\text{mV}$  to label these self-assembled entities as highly stable. Table 6.3 summarizes the recorded electrophoretic mobilities as well as determined zeta potentials for both systems and their respective ionic building units. Note that each ionic building unit contributes their associated counterions (see Fig. 6.1) into the solution, which will be affected by the external electric field. Similar to the model system we see that the 'Texas-sized molecular box' represents the more mobile ionic building unit and mainly determines the recorded electrokinetic potential for the new systems  $\mathbf{1}^{4+}:\mathbf{7}^{2-}$  and

$1^{4+}:8^{2-}$ . Adding the anionic compounds to  $1^{4+}$  significantly reduces its margin of error for both electrophoretic mobility and zeta potential. Anisotropic ionic cluster containing malonate can be considered as highly stable, whereas the entities with ethanedisulfonate lie between highly stable and moderately stable.

**Table 6.3.:** Summary of the cmPALS results for the systems  $1^{4+}:7^{2-}$  and  $1^{4+}:8^{2-}$  1 mM:3 mM in DMSO:glycerol:water 50:43:7 (v/v/v)

compound	$\mu_e / \frac{\mu\text{mcm}}{\text{Vs}}$	$\zeta / \text{mV}$
$1^{4+I}$	$0.045 \pm 0.008$	$31.1 \pm 5.2$
$7^{2-II}$	$-0.002 \pm 0.001$	$-1.7 \pm 1.0$
$8^{2-II}$	$-0.001 \pm 0.001$	$-0.7 \pm 0.7$
$1^{4+}:7^{2-}$	$0.062 \pm 0.003$	$37.4 \pm 2.0$
$1^{4+}:8^{2-}$	$0.056 \pm 0.003$	$28.7 \pm 1.5$
$1^{4+}:2^{2-}$	$0.111 \pm 0.002$	$66.5 \pm 1.2$
polystyrene <sup>III</sup>	$-3.695 \pm 0.0210$	$-64.6 \pm 1.0$

<sup>I</sup>counterion:  $\text{PF}_6^-$ , <sup>II</sup>counterion:  $\text{Na}^+$ , <sup>III</sup>nanosphere size standards in deionized Milli-Q-water

After the cmPALS studies we repeated, similar to the model system  $1^{4+}:2^{2-}$ , DLS measurements with both systems (see Fig. D.8 and D.10). Here, the partially build up anisotropic ionic cluster do not withstand the influence of the electric field as good as well-defined globular ionoids, which is visible in the less pronounced autocorrelation functions. Note that the mixture containing malonate gets more affected by the electrophoresis process, even though the determined zeta potential is larger than for system  $1^{4+}:8^{2-}$ . The applied electric field seems to induce a rearrangement between cationic and anionic building units, which alters the scattering intensity.

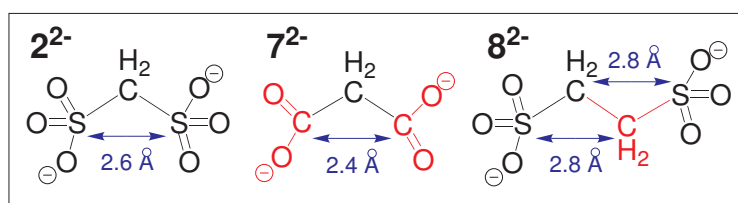


**Fig. 6.4.:** Direct comparison of the chemical structure for methanedisulfonate ( $2^{2-}$ ), malonate ( $7^{2-}$ ) and ethanedisulfonate ( $8^{2-}$ ). Significant changes in the chemical nature for the new anionic building blocks are highlighted in red.

Replacing both sulfonate-groups in compound  $2^{2-}$  with carboxylate-groups ( $7^{2-}$ ), as shown

in Fig. 6.4, significantly reduces the electrostatic interactions between the anionic building block and the 'Texas-sized molecular box', which results in the formation of ionic clusters with anisotropic shape and less durability<sup>c</sup>. A similar effect is observable when keeping the sulfonate-groups, but exchanging the methylene-group of methanedisulfonate with an ethylene-group ( $8^{2-}$ ). Here, the increased distance between both negative charges and potentially the change in charge density precludes the dynamic self-assembly into long-lived ionic clusters. At this point, however, it is not possible to quantify the changes in electrostatic interactions as well as weaker noncovalent forces.

To further (i) visualize the development of the self-assembled entities for the systems  $1^{4+}:7^{2-}$  and  $1^{4+}:8^{2-}$  over time and (ii) compare these with  $1^{4+}:2^{2-}$ , we use the ionoid evolution diagram (IED) in Fig. 6.5. The left y-axis displays the volume charge density of the applied building units, which could be calculated by dividing the charges  $z^{\pm}$  (multiplied with the elementary charge  $e$ ) of the cationic and anionic components by their respective volumes (see Appendix D). As x-axis we use the diameter of all four ions (without solvation shell) due to the importance of the size and size ratio of the anionic and cationic component for the self-assembly process. Through combining the multicationic box  $1^{4+}$  with one of the small anionic building blocks, we can profess the molar ratio of 1:3 and are able to adjust the resulting volume charge density as well as acting electrostatic correlations<sup>25</sup> along the connecting line of both ions. Each system constitutes its own main sequence with one specific intersection highlighting the utilized molar/ionic ratio for DLS measurements, allowing us to directly compare the ionic self-assembly process for different systems with e. g. similar size ratio. Starting from these intersections, we plot at the right y-axis the eccentricity  $e_{IED} = \sqrt{1 - \frac{b^2}{a^2}}$ <sup>d</sup> to define deviations from a perfect sphere (with a value of  $e_{IED} = 0$ ) versus the final size of the ionic cluster<sup>e</sup>, illustrating the shape and its deviation from a perfect, isotropic sphere of the self-assembled entities. Additionally, we include the time beginning from the complete incubation period of ten days (blue full dots) until the last measurement day (arrow to blue crossed dots). Evolution with time is emphasized in IEDs by the oval (for globular ionoids more circular) frame.

As visualized in the IED (Fig. 6.5), we deduce for the new mixtures:

- (1)  $1^{4+}:7^{2-}$  builds up initial ionic structures with anisotropic shape, which, over the course of 43 days, revert to the ion cloud state.

---

<sup>c</sup> Studying the effects of sulfonate- and carboxylate-groups are already well-known for so called 'ionomers' (polymers, which comprise fraction of ionized units), see e. g. Ref. 152,153.

<sup>d</sup> Parameters  $a$  and  $b$  are the length of the semi-major and semi-minor axis from ellipses. The exact adaptation of the eccentricity for the IEDs utilizing the DLS data can be found in Appendix A.

<sup>e</sup> For creating the IEDs, we applied the values of the hydrodynamic radius correlating to the smaller entity of the polydisperse particle size distribution. If we did not record values in the region of (at least) anisotropic ionic cluster inside the sample, we took the results indicating the ion cloud state to complete the IED.

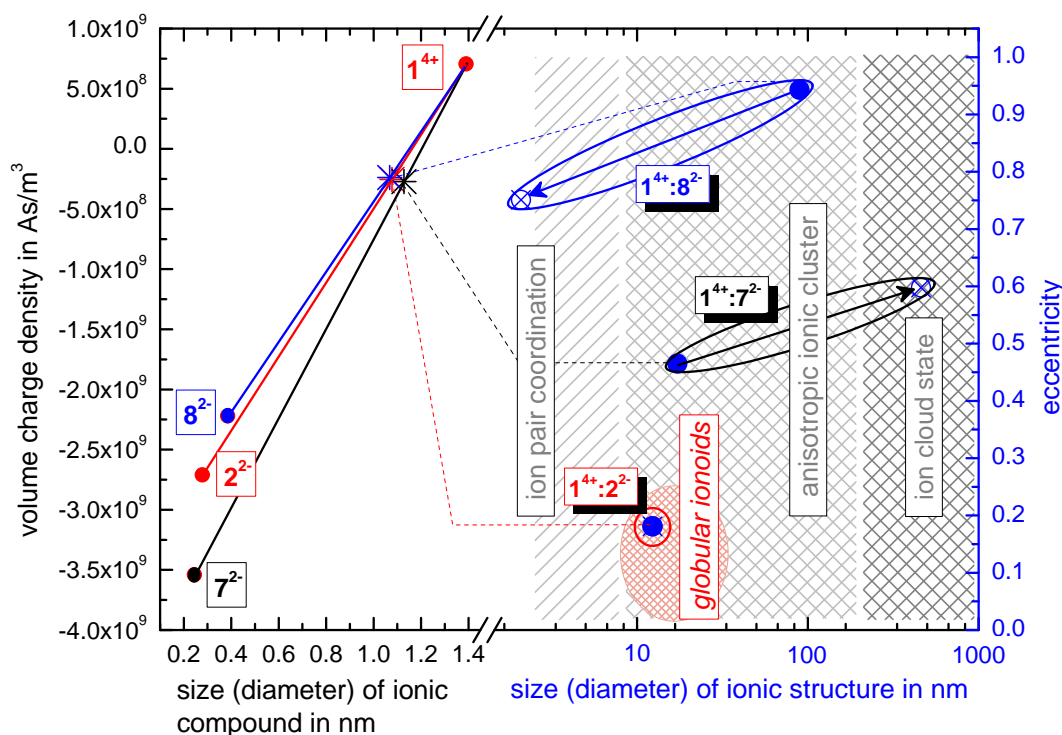


Fig. 6.5.: Ionoid evolution diagram (IED) for systems  $1^{4+}:7^{2-}$  and  $1^{4+}:8^{2-}$  with a molar ratio of 1:3 in DMSO:glycerol:water 50:43:7 (v/v/v). The model system  $1^{4+}:2^{2-}$  1:3 is incorporated as well as the three states of the ionic self-assembly process.

- (2)  $1^{4+}:8^{2-}$  shows larger initial ionic cluster with an inherently more anisotropic shape that decompose into trivial ion pair coordinations between 'Texas-sized molecular box' and ethanedisulfonate.
- (3) The size combination of large cation and small anionic component is in general capable of building anisotropic ionic cluster. However, by (i) substituting the functional sulfonate-groups ( $7^{2-}$ ) and (ii) increasing their respective distance ( $8^{2-}$ ) in methanedisulfonate, the durability as well as monodispersity of the self-assembled entities is significantly reduced.

### 6.3.3. Substitution of $1^{4+}$

Replacing the 'Texas-sized molecular box' in the model system  $1^{4+}:2^{2-}$  can be used to create new mixtures with the small dianion  $2^{2-}$  ( $3^{2-}$ , respectively) and:

- (1) Cations of similar size as  $1^{4+}$  like  $4^{2+}$  (13.3  $\mu$ M:20  $\mu$ M) and  $5^{2+}$  (1 mM:3 mM) and
- (2) The more flexible and slightly smaller  $6^{4+}$  (1.6 mM:1.2 mM).

Again the molar ratios are highlighted, which (based on preliminary investigations) currently present the most promising cation-anion-compositions. Note that we had to reduce the con-

centration for the  $4^{2+}$ -system to record DLS with sufficient transmission. At last, we prepared a mixture containing  $6^{4+}$  together with the large trianionic chromophore  $10^{3-}$  ( $10\ \mu\text{M}:30\ \mu\text{M}$ ). Here, we (i) substituted both established building blocks at the same time and (ii) created a system with the inverse size ratio (small cation with large anion) compared to  $1^{4+}:\text{2}^{2-}$ . Further information about this mixture can be found in Appendix D.

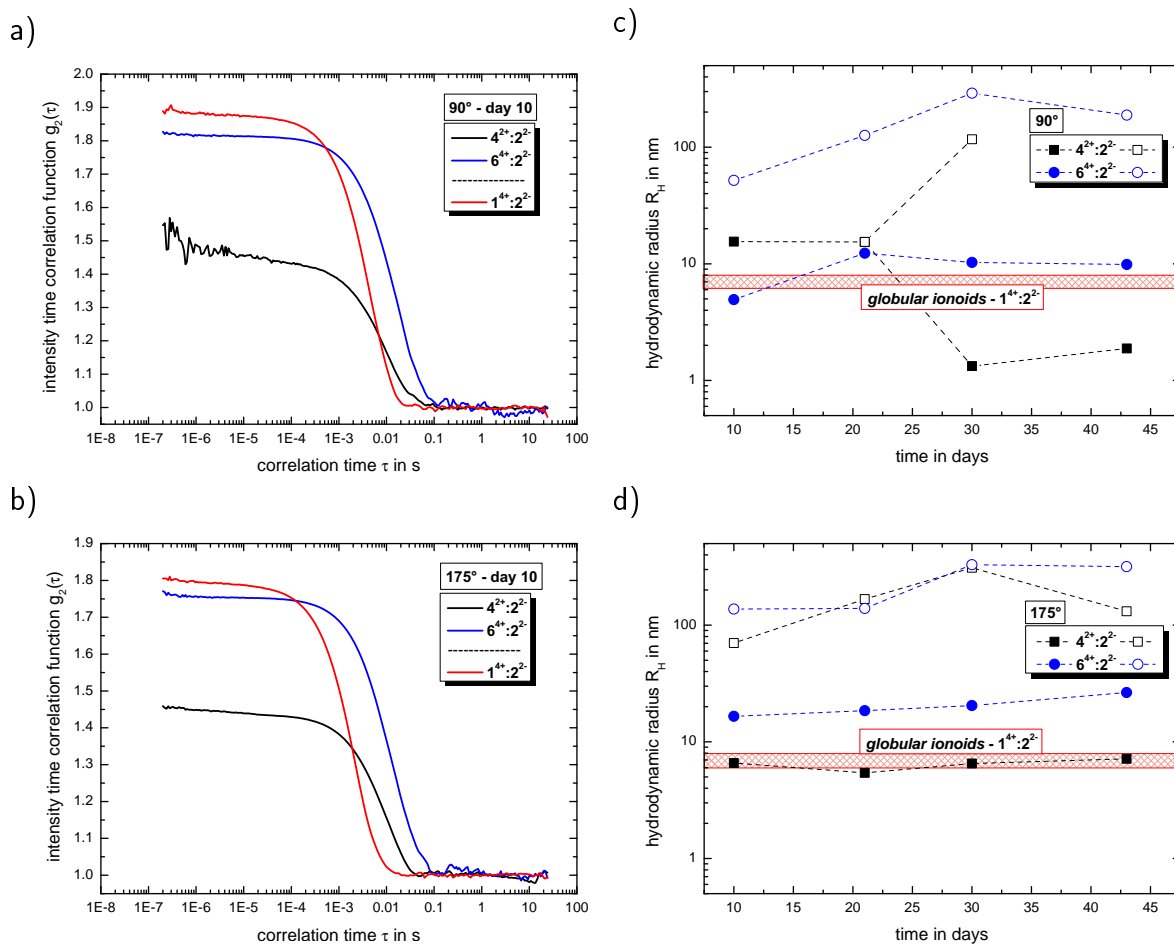


**Fig. 6.6.:** Comparison of the intensity time correlation functions at day ten for a) side and b) back scattering and development of the hydrodynamic radius with c) side and d) back scattering for the systems  $4^{2+}:\text{2}^{2-}$  and  $6^{4+}:\text{2}^{2-}$  in DMSO:glycerol:water 50:43:7 (v/v/v). For the model system  $1^{4+}:\text{2}^{2-}$  (same conditions) a) and b) also show the autocorrelation function, while c) and d) show a patterned box that highlights the region of its hydrodynamic radius.

Fig. 6.6 a) and b) summarize the intensity time correlation functions with side and back scattering for the systems with phthalocyanine ( $4^{2+}:\text{2}^{2-}$ ) and spermine ( $6^{4+}:\text{2}^{2-}$ ) as well as for the model system ( $1^{4+}:\text{2}^{2-}$ ) in DMSO:glycerol:water 50:43:7 (v/v/v) at measurement day ten. The autocorrelation functions for the system  $4^{2+}:\text{2}^{2-}$  possess reduced y-intercept-values, but just minor delays in their incipient decays compared to the established system. For the  $6^{4+}:\text{2}^{2-}$  mixture, we record autocorrelation functions with similar shaping in relation to

$1^{4+}:2^{2-}$ , which present their decays at higher correlation times  $\tau$ . Both new systems show the potential to at least partially build up anisotropic ionic cluster, which is further highlighted in Fig. 6.6 c) and d). Here, we display the time-dependent evolution of the hydrodynamic radii for the present colloid-like structures. Besides the formation of relatively stable self-assembled anisotropic clusters for  $4^{2+}:2^{2-}$  and  $6^{4+}:2^{2-}$  over the course of 43 days, we also detect larger entities (open symbols in Fig. 6.6 c) and d)) throughout the total measurement period, representing the initial ion cloud state. Note that for the combination of large cation and small anion ( $4^{2+}:2^{2-}$ ) the same ionic ratio of  $2/3$  as for the systems containing the 'Texas-sized molecular box' was used, while for the system of small cation and small anion ( $6^{4+}:2^{2-}$ ) the ionic ratio is  $8/3$ . This shows that based on the dimensions, conformational flexibilities and charge densities of the utilized ionic building units we have to adjust the ionic ratio to build up colloid-like ionic cluster. Compound  $5^{4+}$  in combination with methanedisulfonate does not build up ionoids or anisotropic ionic cluster after the ten-day incubation period, even if we apply the ionic ratio of  $2/3$  (see Fig. D.17).

To study the colloidal stability of the promising new system  $6^{4+}:2^{2-}$ , we again used the cmPALS method followed by renewed DLS measurements. Table 6.4 summarizes the recorded electrophoretic mobility as well as determined zeta potential for this system and its respective ionic building units. The electrokinetic potential for the anisotropic ionic clusters surpass the value of  $\pm 30$  mV, which verifies the existence of highly stable self-assembled entities. Note that the mixture with spermine did not reach the zeta potential value from the globular ionoids with  $1^{4+}$ , because of (i) just partially build up self-assembled entities and (ii) the significantly lower electrophoretic mobility of spermine in the solvent mixture DMSO:glycerol:water 50:43:7 (v/v/v).

**Table 6.4.:** Summary of the cmPALS results for the system  $6^{4+}:2^{2-}$  1.6 mM:1.2 mM in DMSO:glycerol:water 50:43:7 (v/v/v)

compound	$\mu_e / \frac{\mu\text{mcm}}{\text{Vs}}$	$\zeta / \text{mV}$
$6^{4+I}$	$0.005 \pm 0.008$	$3.6 \pm 5.4$
$2^{2-II}$	$-0.001 \pm 0.003$	$-0.3 \pm 1.0$
$6^{4+}:2^{2-}$	$0.067 \pm 0.003$	$39.8 \pm 1.8$
$1^{4+}:2^{2-}$	$0.111 \pm 0.002$	$66.5 \pm 1.2$

<sup>I</sup>counterion:  $\text{Cl}^-$ , <sup>II</sup> counterion:  $\text{K}^+$

The repetitive DLS measurement of  $6^{4+}:2^{2-}$  after the electrophoresis displays, analogous to the model system, an unaltered autocorrelation function and particle size distribution for side

scattering, as shown in Fig. 6.7. For back scattering (see Fig. D.21) a less pronounced autocorrelation function was recorded, which indicates a prorated decay or changed shape of the anisotropic ionic clusters. However, compared to the new system with substituted methanedisulfonate, the mixture  $6^{4+}:2^{2-}$  builds up the most stable self-assembled entities.

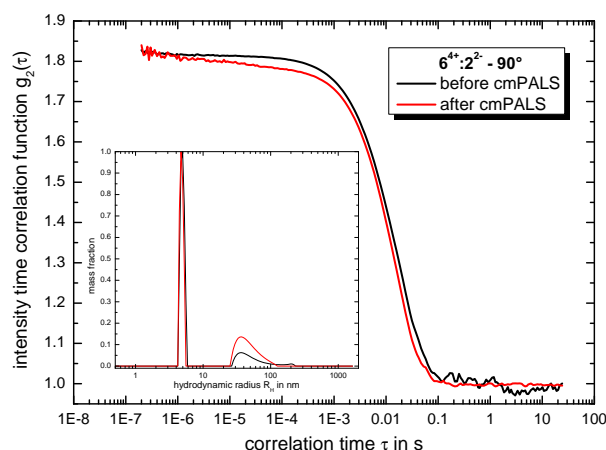


Fig. 6.7.: Comparison of the intensity time correlation functions at day ten for side scattering for system  $6^{4+}:2^{2-}$  in DMSO:glycerol:water 50:43:7 (v/v/v) before and after the cmPALS measurement. The inlays highlight the particle size distributions for the respective autocorrelation functions.

In contrast to the substitution of  $2^{2-}$ , we could apply CW EPR spectroscopy by using Frey's salt dianion, leading to the adjusted mixtures  $4^{2+}:3^{2-}$  and  $6^{4+}:3^{2-}$  in DMSO:glycerol:water 50:43:7 (v/v/v). Replacing  $2^{2-}$  with  $3^{2-}$  can influence interactions inside the ion cloud, but electrostatic correlations especially to the cation remain unchanged, as shown in Ref. 14. To assess the electrostatic interactions between our 'new' cationic component and the nitroxide radical, we measured different molar ratios for the tested systems and analyzed the resulting spectra. Note that we had to increase the concentration of Frey's salt in the system  $4^{2+}:3^{2-}$  to  $200 \mu\text{M}$  to obtain spectra with sufficient signal-to-noise ratio due to the fast decomposition of the nitroxide. Higher concentrations could not be used, because of the low solubility of  $4^{2+}$  in the solvent mixture DMSO:glycerol:water 50:43:7 (v/v/v). Furthermore, we measured pure Frey's salt with its respective concentrations in the established solvent to distinguish between the influence of solely (i) solvent viscosity and (ii) electrostatic interaction with increasing cationic concentration on the rotational mobility of our spin probe. To quantify the latter effect of increasing  $4^{2+}$  or  $6^{4+}$  concentration on the rotational mobility of Frey's salt, we applied the evaluation systems<sup>66</sup> already established for the model system  $1^{4+}:3^{2-}$ :

- (1) Analyzing the line width (as full width at half maximum (FWHM) values) of the CW EPR spectra by simulating isotropic broadening, which is implemented in the EasySpin program package (see Fig. 6.8 c) and d)) Note that this method does not assume any



physical model causing the broadening.

- (2) Calculating the anisotropy  $T$  of the rotational diffusion tensor as based on equation A.3. We mainly discuss this parameter that emphasizes the distinction between  $D_{\parallel}$  and  $D_{\perp}$  and characterizes the magnitude of electrostatic interactions in the direct vicinity of Fremy's salt in Appendix D.
- (3) As a very simple measurement, the isotropic rotational correlation time  $\tau_c$  can be calculated even in the case of (slight) anisotropy of rotational motion (see Appendix A and D).

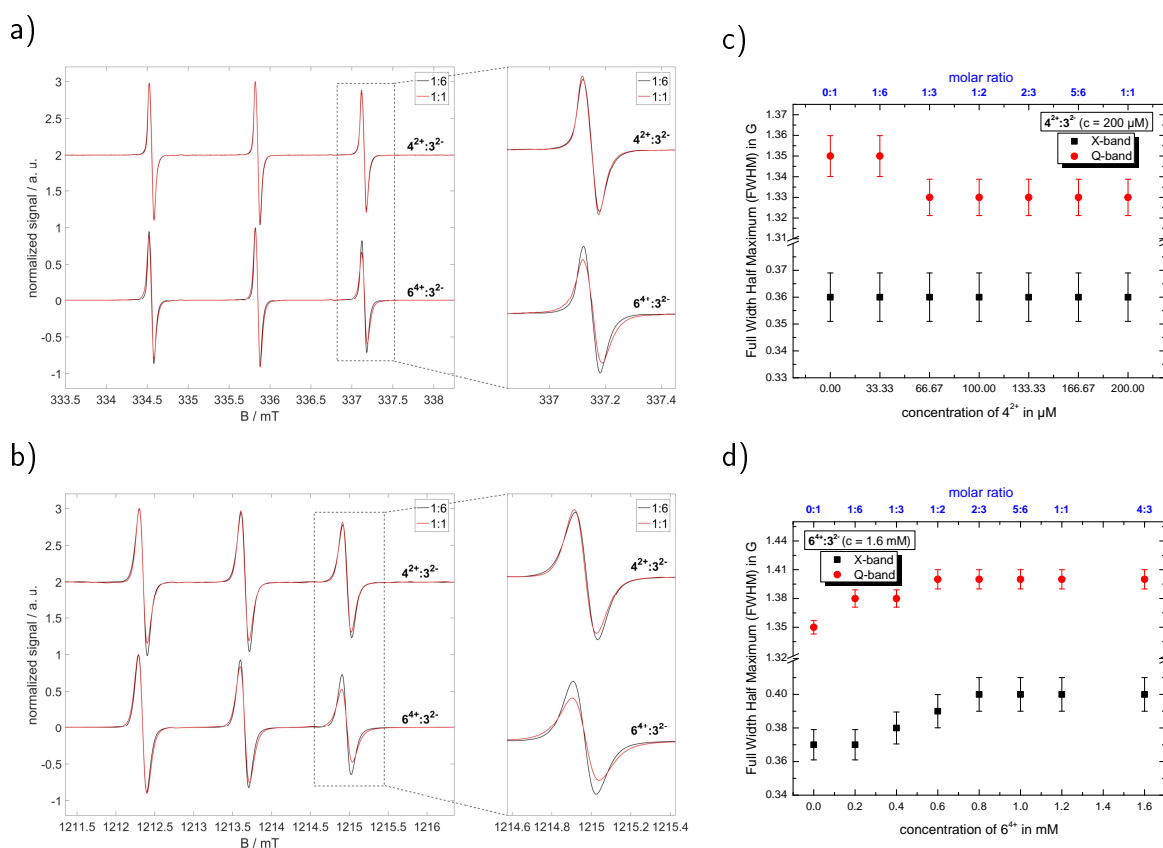


Fig. 6.8.: a) X-band and b) Q-band CW EPR spectra of  $4^{2+} : 3^{2-}$  and  $6^{4+} : 3^{2-}$  with molar ratios 1:6 (black) and 1:1 (red) in DMSO:glycerol:water 50:43:7 (v/v/v). The insets mark the highfield peak, which is shown separately right next to the full spectra. c) and d) Plots of the isotropic broadening as full width at half maximum (FWHM) of pure Fremy's salt ( $4^{2+}$  and  $6^{4+}$  at molar ratio 0:1) for the systems c)  $4^{2+} : 3^{2-}$  and d)  $6^{4+} : 3^{2-}$  with increasing cation concentration.

Fig. 6.8 a) and b) show the effect of adding one of the cationic components,  $4^{2+}$  or  $6^{4+}$ , to the pure radical at X- and Q-band frequencies for the molar ratios 1:6 and 1:1, the complete development of the line width with their increasing concentration is plotted in Fig. 6.8 c) and

d). For the model system  $\mathbf{1}^{4+}:\mathbf{3}^{2-}$  in the established solvent mixture we know<sup>66</sup> that the pure nitroxide shows rotational diffusion based on an axial tensor with the unique axis ( $D_{\parallel}$ ) along the N-S-bond of Fremy's salt (see red arrow in Fig. 6.1). Adding  $\mathbf{1}^{4+}$  leads to significant line broadening due to slowed-down rotation of Fremy's salt dianion mainly around its molecular z-axis. One can further follow the transition from weak electrostatic correlations between  $\mathbf{1}^{4+}$  and  $\mathbf{3}^{2-}$  to a more direct ion pair coordination with increasing cation concentration.<sup>92</sup> The frequency-dependent differences in time-frame sensitivity/averaging lead to a stronger pronounced coordination transition inside the Q-band spectra due to a better resolution at the limit of fast rotation.

For the system  $\mathbf{4}^{2+}:\mathbf{3}^{2-}$  we record no significant changes in the rotational mobility of the nitroxide at both frequencies as well as no line broadening effects (Fig. 6.8 c)) due to electrostatic interactions between the phthalocyanine and Fremy's salt dianion. One reason could be the reduced concentration of  $\mathbf{3}^{2-}$  with 200  $\mu\text{M}$  compared to the studies with the model system (3 mM), which drastically hinders the formation of e. g. ion pair coordinations at larger molar ratios directly after sample preparation (day 0). Another cause could be that phthalocyanines in general are fairly rigid molecules with limited options for conformational flexibility<sup>154</sup> compared to the 'Texas-sized molecular box' with its conformational flexibility and adjustable shape to accommodate guest molecules.<sup>15,17</sup> However, analyzing the anisotropy  $T$  (see Fig. D.16) reveals changes for the distinction between the unique axis  $D_{\parallel}$  and the axes perpendicular to it ( $D_{\perp}$ ), which indicates the initial self-assembly process of the later detected anisotropic ionic cluster.

The system  $\mathbf{6}^{4+}:\mathbf{3}^{2-}$  shows effects in the CW EPR spectra at X- and Q-band frequencies that are similar to those in the model system with the multicationic box  $\mathbf{1}^{4+}$ <sup>92</sup>:

- (1) Steady increase in the line width correlating with higher amounts of  $\mathbf{6}^{4+}$  and stronger electrostatic interactions with and subsequent slow-down of Fremy's salt and
- (2) Reaching a plateau value for the FWHM at a molar ratio of 1:2 (within the margin of error), indicating similar local dynamic electrostatic attachment inside the ion cloud state at day 0 for mixtures above this ratio.

It seems that the flexibility of the ionic building block  $\mathbf{6}^{4+}$  allows,<sup>155</sup> just like for  $\mathbf{1}^{4+}$ , the formation of strong enough electrostatic interactions with the dianion of Fremy's salt to significantly influence its rotational mobility. Note that the absolute effect for line broadening as well as rising rotational correlation time  $\tau_c$  (see Fig. D.23) due to spermine do not reach the extent observed with the 'Texas-sized molecular box', which can explain the formation of just partially anisotropic clusters instead of monodisperse globular ionoids based on the DLS data. One reason could be again the slightly reduced concentration of 1.6 mM or the general alteration from a multicationic box to a more linear structure (see Fig. 6.1).

Similar to the section describing the exchange of methanedisulfonate  $2^{2-}$ , we summarize the ionic self-assembly process for  $4^{2+}:2^{2-}$  and  $6^{4+}:2^{2-}$  in an ionoid evolution diagram (see Fig. 6.9). To compare the discussed systems, we include their respective main sequence lines with their specific intersection for the applied molar/ionic ratios. Note that the main sequence lines show a more prominent separation compared to Fig. 6.5, especially between the two larger cations and the rather small  $6^{4+}$ , due to the stronger deviations in their volume charge densities.

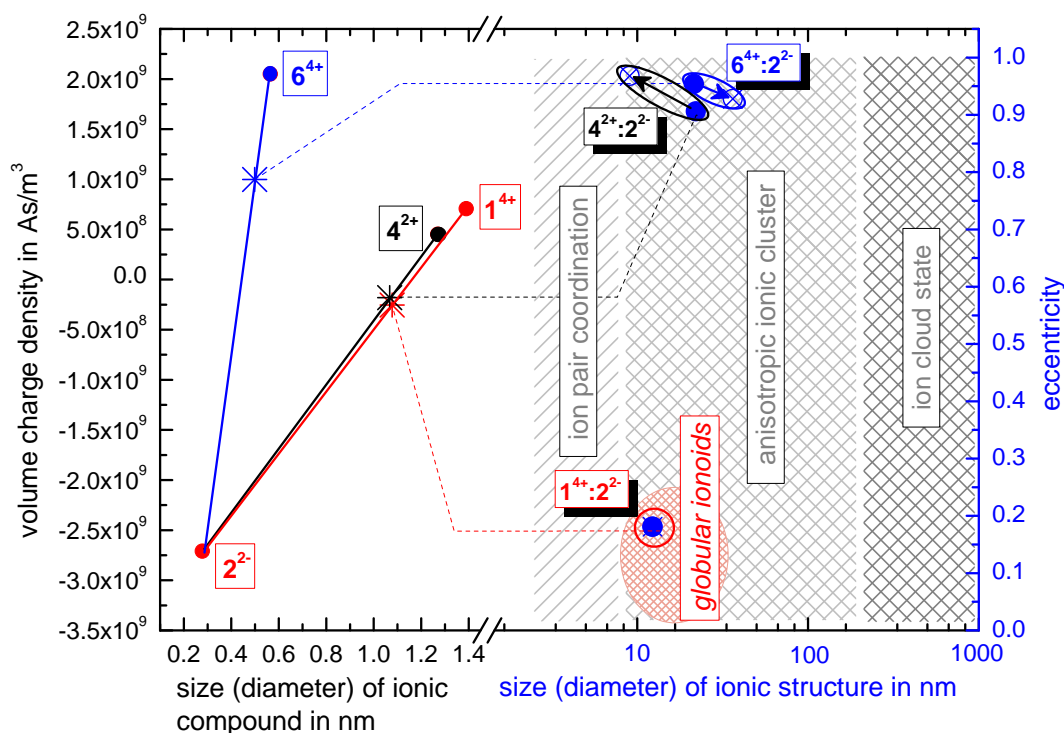


Fig. 6.9.: Ionoid evolution diagram (IED) for systems  $4^{2+}:2^{2-}$  (molar ratio 2:3) and  $6^{4+}:2^{2-}$  (molar ratio 4:3) in DMSO:glycerol:water 50:43:7 (v/v/v). The model system  $1^{4+}:2^{2-}$  1:3 is incorporated as well as the three states of the ionic self-assembly process.

Based on the IED in Fig. 6.9 we can deduce:

- (1)  $4^{2+}:2^{2-}$  builds up ionic cluster in the size range of globular ionoids, but with highly increased shape anisotropy. Over the total measurement time of 43 days we recognize a slight decrease in the diameter of the self-assembled entities, which indicates a slow decomposition into rather trivial ion pair coordinations. Similar to the new systems, which also combine large cations with small anions ( $1^{4+}:7^{2-}$  and  $1^{4+}:8^{2-}$ ), we obtain anisotropic ionic cluster at an ionic ratio of 2/3. Note that for these introduced systems the self-assembled entities inside the phthalocyanine ( $4^{2+}$ ) mixture possess the highest durability, which is visible in the IED with the small elongation of its oval frame.

- (2)  $6^{4+}:2^{2-}$  shows small and durable anisotropic ionic cluster, which display just minor increase in their diameter over the course of the total measurement time. The IED again highlights the stability of the self-assembled entities through the small elongation of the oval frame. Replacing  $1^{4+}$  and changing the size ratio to small cation and small anion can lead to long-lived ionic clusters, when the ionic ratio is correctly adapted. For the system  $6^{4+}:2^{2-}$  we used the ionic ratio  $8/3$ , which has to be further verified with other ionic building blocks.

## 6.4. Conclusions

We set out to explore the previously described ionic self-assembly process towards ionoids in systems containing 'new' polyphilic ionic building units. In the main text we highlighted mixtures, which can be categorized due to their size ratio of cationic and anionic component into systems with (i) large cation and small anion and (ii) small cation and small anion. Based on the DLS data, we assigned a specific ionic ratio for both variations, which lead to the partial build up of anisotropic ionic clusters in solution after the incubation period of ten days. For the size combination mentioned first, we applied the ionic ratio of  $2/3$ , while for the second one we had to adapt the ionic ratio to  $8/3$ . Note that these values can only serve as an indication for the formation of highly defined structures, because other parameters like the ion concentration also affect the self-assembly process.<sup>66</sup>

This aspect can be further analyzed for systems falling into the first size ratio category. Even under constant measurement conditions (temperature, solvent mixture, concentration and ionic ratio), we arrive at long-lived globular ionoids for the system  $1^{4+}:2^{2-}$ , but solely obtain anisotropic ionic clusters with reduced long-term stability when replacing one of the model components. The lowered zeta potential for our new systems, which still own electrokinetic potentials between 29 mV and 40 mV, confirms their weakened colloidal stability. The chemical nature of the 'Texas-sized molecular box' and the methanedisulfonate apparently represent an optimal combination to build up highly defined structures in solution. The multicationic box with conformational flexibility acts as structuring unit, while the small dianionic methanedisulfonate contains two sulfonate-groups with the right distance to each other for the formation of long-range electrostatic interactions as well as well-balanced weaker noncovalent forces. Note that at this point it is not possible to quantify the contribution of electrostatic interactions and noncovalent forces let alone their modifications by the substitution of one of the model compounds. This is ongoing work.

The previously introduced ionoid evolution diagrams (IED) are able to illustrate the influence of various parameters (like e. g. molar ratio or size ratio) on the formation of our highly defined structures (i) directly after the incubation time of ten days and (ii) throughout the

entire measurement period. Furthermore, we can analyze the durability of the self-assembled ionic clusters as well as characterize their deviations from a spherical shape with the calculated eccentricity. The respective IEDs in Fig. 6.5 and 6.9 allow the direct comparison between the new systems (and the model system  $1^{4+}:2^{2-}$ ) with respect to size/ionic ratio and are thus valuable tools for optimizing the ionic self-assembly process for a variety of ionic building units. We further try to expand (i) different combinations between the introduced ionic building units and (ii) the measured molar/ionic ratios for already established systems to refine the design parameters for the formation of ionic clusters.

Going beyond the solution-based self-assembly processes in ionoids one may speculate whether the here described processes may be relevant for other structure formation processes, e. g. for the above mentioned mechanically interlocked molecules or even crystallization of ionic substances from solution. Currently, this type of questions connecting solid state structures formed from solution with our dynamically self-assembled clusters cannot be conclusively answered and is a central question in current work. Another future aim will be to achieve anisotropic clusters (or even globular ionoids) in simpler solvent mixtures and the general aim remains to understand the delicate physical-chemical processes leading to the formation of these remarkably robust yet extremely 'soft', solution-based structures.



# 7 | Shape, Size and Internal Dynamics of Loosely Bound Colloid-Like Ionic Clusters in Ternary Solvent Systems

Chapter 7 picks up the first studies regarding the influence of the solvent composition as important 'design element' for the ionic self-assembly process of colloid-like ionic clusters in solution. Again, we focus on the model system containing the macrocyclic tetraimidazolium molecular box in combination with small dianionic salts. Here, individual solvents in the established optimal ternary solvent mixture DMSO:glycerol:water 50:43:7 (v/v/v) are substituted, namely DMSO through DMF, glycerol through ethylene glycol and water through *N*-methylpropionamide, and such can characterize the changes in shape and size of the structures of loosely bound ionic clusters induced by the substitution of a specific solvent component. In this study, DLS is used to associate size, shape and initial durability of ionic clusters with solvent parameters like dynamic viscosity and relative permittivity to highlight the importance of solvent composition for the build up of globular ionoids as well as anisotropic ionic clusters. To further analyze the solvation state of the dianionic building unit inside the initial ion cloud state, which later affects the self-assembly process to ionic cluster, we perform CW EPR spectroscopy measurements at X-band ( $\sim 9.4$  GHz) and Q-band ( $\sim 34$  GHz) frequencies. The following results are also published and are 'Reprinted with permission from

J. Eisermann, A. F. Roth and D. Hinderberger, *J. Phys. Chem. B*, 2019, **123**, 8154-8165

DOI: 10.1021/acs.jpcc.9b07343

<https://pubs.acs.org/doi/10.1021/acs.jpcc.9b07343>

Copyright (2019) American Chemical Society<sup>a</sup>. Analogous to the previous chapters, the 'Methods' subsection (7.2.3.) was changed compared to the original publication to use the summarized information in Appendix A. The remaining sections 7.1. to 7.4. can be considered

---

<sup>a</sup>The permission from the 'American Chemical Society' is present in written form.

as citation from Ref. 156.

At this point I want to highlight the contribution of my former bachelor student Anna Franziska Roth to this specific study. Her bachelor thesis focused on analyzing the influence of the respective ternary solvent mixtures for the shape, size and internal dynamics of loosely bound colloid-like ionic clusters. She performed most of the initial DLS and CW EPR spectroscopy measurements, which will be presented in the upcoming sections. For the final publication, I remeasured the CW EPR spectroscopy spectra at room temperature as well as carried out the additional low temperature spectra at Q-band frequencies. Similar to the previous chapters, I also wrote the manuscript containing all results.

## 7.1. Introduction

Solvation, defined as stabilizing interaction of a solute (a solute moiety, respectively) and the solvent or as similar interaction of a solvent with moieties of a chiefly insoluble material,<sup>157</sup> is a switchable dynamic and reversible process and plays an important role in chemistry,<sup>158–162</sup> natural biosystems,<sup>5,163–165</sup> biomimetic systems<sup>166,167</sup> and other related fields. Host-guest assemblies, which represent one prominent class of supramolecular structures,<sup>8,9,21,168,169</sup> possess altered association behavior based on the solvent system and its properties. In these systems, the driving forces for self-assembly include electrostatic interactions (ion-ion, ion-dipole, dipole-dipole and dipole-induced dipole) as well as van der Waals,  $\pi$ - $\pi$  stacking, hydrogen bonding and other weak interactions.<sup>13,69,170</sup> To explain the interplay between the mentioned driving forces, solvation effects are crucial and strongly affect the strength of host-guest complexation. Solvents can coarsely be divided into two categories: (i) nonstructured or nonself-organized solvents (like hydrocarbons) and (ii) structured or self-organized solvents (like water<sup>170,171</sup> or ionic liquids<sup>172–174</sup>).

In dilute polymer solutions, the conformation of a polymer chain is similarly influenced by the interaction between chain segments and between chain segments and solvents. The interaction between chain and solvents leads to a solvent categorization into three types: (1) good, (2) poor and (3) theta solvent.<sup>6,175</sup> These three categories concisely summarize the chain dimension of the polymer in solution as well as the thermodynamics of the dilute solution.<sup>176</sup> Polyelectrolytes, that is, polymers that dissociate into a charged polymer chain and oppositely charged counterions,<sup>177,178</sup> show an even more complicated behavior because of intra- as well as intermolecular electrostatic interactions defining the resulting solution properties.<sup>179</sup>

In the former studies (see Ref. 66,92) we have described the formation of loosely bound ion-based colloid-like globular clusters of several nanometers in size, termed globular ionoids.<sup>66,92</sup> Formation of these structures is the result of an ionic self-assembly (ISA)<sup>68</sup> process and as such based on the already mentioned driving forces for supramolecular systems. For size-



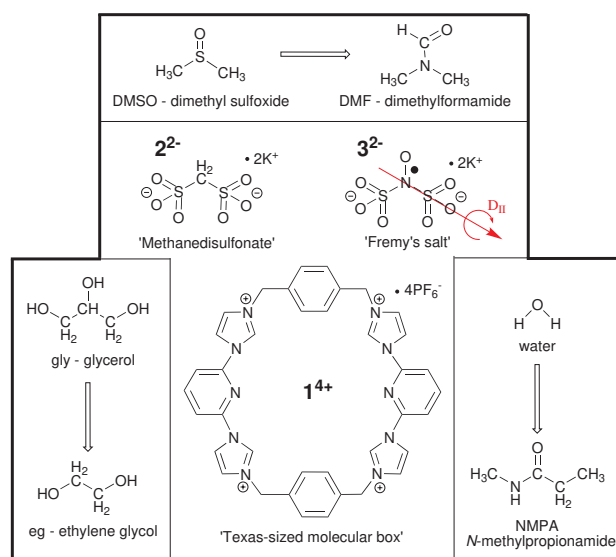


Fig. 7.1.: Molecular structure of cationic building block  $1^{4+}$  as well as anionic building blocks  $2^{2-}$  and  $3^{2-}$  in the center, surrounded by the systematic exchange of the established solvent components DMSO, glycerol (gly) and water with DMF, ethylene glycol (eg) and *N*-methylpropionamide (NMPA).

monodisperse colloid-like ionic cluster, we combine the 'Texas-sized molecular box' ( $1^{4+}$ , Fig. 7.1), introduced by Sessler and coworkers<sup>15–17</sup>, with small dianionic salts (methanedisulfonate,  $2^{2-}$  or Fremy's salt dianion,  $3^{2-}$ , see Fig. 7.1) in a ternary solvent mixture of dimethyl sulfoxide (DMSO):glycerol:water 50:43:7 (v/v/v).<sup>14,66</sup> Furthermore, we can tune the size and shape anisotropy of the self-assembled entities depending on the ionic ratio between cationic and anionic building block as well as analyze and visualize their development in the course of months with the recently introduced ionoid evolution diagrams (IEDs).<sup>92</sup>

It is quite remarkable that the ternary mixture of the above mentioned composition is needed for the fuzzy self-assembly process into ionoids and anisotropic ionic clusters. As we have shown earlier,<sup>66</sup> the composition of the ternary mixture has a slight robustness against changes in relative content of individual solvent constituents, but even moderate changes of the relative contributions or simplifying the ternary mixture into at least a binary mixture by selectively removing one component yields rather trivial solutions of ions. In this report, we focus on a better understanding of the physical role of each solvent component in the ionoid formation process by selectively replacing each of the three solvents with another solvent that is chosen to change only (or at least mainly) one of the physical solvent properties such as viscosity, relative permittivity, and hydrogen bonding capability. Thus, from the established DMSO:glycerol:water we create three new solvent mixtures by selectively replacing DMSO by dimethyl formamide (DMF), glycerol by ethylene glycol (eg) and water by *N*-methylpropionamide (NMPA) as one of the components, as shown in Fig. 7.1 and discussed in the following.

## 7.2. Experimental

### 7.2.1. Materials

Based on our previous studies,<sup>66,92</sup> we applied the 'Texas-sized molecular box' ( $\mathbf{1}^{4+}$ ) as a cationic building unit, which was synthesized as described in the publications of Sessler and co-workers.<sup>15,16</sup> The rather smaller anionic building units were provided by methanedisulfonic acid dipotassium salt ( $\mathbf{2}^{2-}$ ; Sigma-Aldrich, Munich, Germany) with purity  $\geq 99\%$  and Fremy's salt (potassium nitrosodisulfonate,  $\mathbf{3}^{2-}$ ; Sigma-Aldrich) of technical grade. We used those chemicals without further purification. The adjusted concentrations for  $\mathbf{1}^{4+}$  reached from 0 mM and 3 mM, whereas  $\mathbf{2}^{2-}$  ( $\mathbf{3}^{2-}$ , respectively) stayed at a value of 3 mM (see Ref. 92).

For producing all solvent mixtures, we used DMSO containing  $\leq 0.02\%$  of water (Sigma-Aldrich), 86-88 wt% glycerol (Acros Organics, Nidderau, Germany), 99.5 wt% glycerol (Acros), DMF (Sigma-Aldrich) with  $\geq 99\%$  purity, ethylene glycol (Sigma-Aldrich) with  $\geq 99\%$  purity, NMPA (Sigma-Aldrich) with 98% purity and deionized Milli-Q-water. These components were combined to form the following solvent mixtures with a respective volume stoichiometrie of 50:43:7 (see Appendix E for further information): (1) DMSO:glycerol:water, (2) DMF:glycerol:water, (3) DMSO:ethylene glycol:water and (4) DMSO:glycerol:NMPA.

### 7.2.2. Ionic ratio

Analogous to our previous study analyzing the ionic ratio and its influence on the rather dynamic formation process of ionoids,<sup>92</sup> we gradually varied the concentration of the 'Texas-sized molecular box', but kept the concentration of compounds  $\mathbf{2}^{2-}$  ( $\mathbf{3}^{2-}$ , respectively) constant (see Table 7.1). For our electron paramagnetic resonance (EPR) spectroscopy studies the latter point is rather important because all samples contain the same amount of nitroxide radical and are therefore directly comparable (see Fig. 7.1).

Calculating the ionic ratio inside each  $\mathbf{1}^{4+}:\mathbf{2}^{2-}$  ( $\mathbf{1}^{4+}:\mathbf{3}^{2-}$ , respectively) system is based on equation (7.1)

$$\text{Ionic ratio} = \left| \frac{z^+ \cdot c(\mathbf{1}^{4+})}{z^- \cdot c(\mathbf{2}^{2-}/\mathbf{3}^{2-})} \right|, \quad (7.1)$$

where  $c(\mathbf{1}^{4+})$  and  $c(\mathbf{2}^{2-}/\mathbf{3}^{2-})$  represent the corresponding concentrations from Table 7.1. Note that we assume a constant charge  $z^\pm$  for both ionic building units with  $z^+ = +4$  and  $z^- = -2$  in the respective molar ratios as well as solvent mixtures.

**Table 7.1.:** Summary of all Tested Molar Ratios for the System  $\mathbf{1}^{4+}:\mathbf{2}^{2-}$  ( $\mathbf{1}^{4+}:\mathbf{3}^{2-}$ , Respectively) Combined with Their Calculated Ionic Ratio

molar ratio	$c(\mathbf{1}^{4+})/\text{mM}$	$c(\mathbf{2}^{2-}/\mathbf{3}^{2-})/\text{mM}$	ionic ratio <sup>a</sup>
0:1	0.0	3.0	-
1:6	0.5	3.0	1/3
1:3	1.0	3.0	2/3
1:2	1.5	3.0	1
2:3	2.0	3.0	4/3
5:6	2.5	3.0	5/3
1:1	3.0	3.0	2

<sup>a</sup> Calculating ionic ratio using equation (7.1)

### 7.2.3. Methods

The main methods, which were used for this study are again dynamic light scattering (DLS) in combination with continuous wave (CW) electron paramagnetic resonance (EPR) spectroscopy at X- and Q-band frequencies. At higher microwave frequencies one performed measurements at 20 °C as well as at low temperatures (150 K). Appendix A covers the description of these methods. The respective instrumentation used to perform the mentioned techniques are:

1) DLS:

- Litesizer 500 (Anton Paar GmbH, Graz, Austria)

2) CW EPR:

- X-band: Miniscope MS5000 (magnettech, Berlin, Germany) benchtop spectrometer
- Q-band: Bruker EMX-plus spectrometer (Bruker Biospin GmbH, Rheinstetten, Germany) with ER5106QT resonator

Additionally, one applied specific techniques to determine the solvent properties, which are not explicitly described in Appendix A. To analyze the solvent influence on the dynamic self-assembly process of ionoids, we initially determined the dynamic viscosity  $\eta$  and relative permittivity  $\epsilon_r$  to characterize the pure solvents. The first parameter indicates that for a laminar flow of a fluid, the shear stress to the velocity gradient is perpendicular to the plane of shear<sup>180</sup> and was determined by recording flow curves at 20 °C, which demonstrate a Newtonian correlation<sup>181</sup> for all solvent mixtures (see Fig. E.1). As a rheometer we used the Physica MCR301 (Anton Paar GmbH, Graz, Austria) with a cone-plate (CP50-2/TG) measuring system.

The second parameter describes the ratio of the electric field strength in vacuum to that in a given medium<sup>180</sup> and significantly influences the electrostatic interactions inside the solution.<sup>19</sup> Here, we used the Keysight 16452A Liquid Test Fixture (Keysight Technologies, Santa Rosa, United States) in combination with the automatic RLC Meter RLC 300 (Grundig AG, Fürth, Germany) operating at a frequency of 10 kHz. The exact routine for transforming the recorded capacities into the desired relative permittivities can be found in Appendix E.

## 7.3. Results and discussion

### 7.3.1. General Remarks

As introduced in our previous studies<sup>66,92,94</sup>, the following terms (adapted from Ref. 92) are used to describe the ISA process for all measured systems in solution:

- (i) globular ionoids: spherical, highly stable structures with a hydrodynamic diameter between 10 nm and 25 nm as well as an eccentricity lower than  $e_{IED} < 0.25$ <sup>92</sup>
- (ii) anisotropic ionic cluster: structures with deviations from a spherical structure and/or slightly extended dimensions
- (iii) ion cloud: initial state after sample preparation with larger entities of  $R_H > 100$  nm.

CW EPR spectroscopy can only aid in characterizing the ion cloud state forming in the initial hours after the sample preparation. The used EPR-active Frey's salt dianion ( $3^{2-}$ ) disproportionates in solution within a few hours, hence the sample cannot be measured after the ten-day incubation period of colloid-like ionic clusters. We have shown earlier that  $3^{2-}$  and  $2^{2-}$  are interchangeable so that insights from long-term studies with  $2^{2-}$  and from initial studies with  $3^{2-}$  can be combined.

### 7.3.2. Solvent Characterization

Before highlighting the dynamic self-assembly process of colloid-like ionic clusters inside the new solvent mixtures, we analyze the properties of the new pure solvent mixtures to subsequently compare them with the particularities of the established mixture DMSO:glycerol:water 50:43:7 (v/v/v).<sup>66,92</sup> Table 7.2 summarizes the determined values of dynamic viscosities  $\eta$  as well as relative permittivities  $\epsilon_r$  for all four solvent mixtures. The respective values for each solvent component alone can also be found in Table 7.2. Substituting glycerol with ethylene glycol shows the expected drop in dynamic viscosity based on the respective value for both alcohols.<sup>182-184</sup> The solvent mixture with NMPA presents an unexpected lower  $\epsilon_r$  compared to the established one, although pure NMPA has a much higher relative permittivity (more than

twofold) than water.<sup>185,186</sup> The large permittivities in pure *N*-methyl amides result from chain-wise and parallel association through hydrogen bonding with the single amino hydrogen.<sup>185</sup> The combination of small amounts of NMPA with DMSO and glycerol seems to suppress this association or at least lead to solvent associates with much smaller numbers, resulting in a reduced  $\epsilon_r$ -value.

**Table 7.2.:** Summary of Measured Dynamic Viscosities  $\eta$  and Relative Permittivities  $\epsilon_r$  as well as Calculated Bjerrum Lengths  $\lambda_B$  for All Tested Solvent Mixtures as well as for Each Solvent Component

solvent mixture	$\eta$ / mPas	$\epsilon_r$	$\lambda_B$ / nm <sup>a</sup>
DMSO	2.20 <sup>187</sup>	46.60 <sup>187</sup>	1.22
DMF	0.85 <sup>188</sup>	38.93 <sup>189</sup>	1.46
gly	1499 <sup>182b</sup>	43.52 <sup>190</sup>	1.31
eg	18.8 <sup>191</sup>	40.80 <sup>192</sup>	1.40
water	1.00 <sup>193</sup>	80.09 <sup>194</sup>	0.71
NMPA	6.02 <sup>195</sup>	185.23 <sup>194</sup>	0.31
DMSO:gly:water	22.64±0.12	54.83±1.42	1.04
DMF:gly:water	12.86±0.10	47.81±1.25	1.19
DMSO:eg:water	5.70±0.06	52.36±1.37	1.08
DMSO:gly:NMPA	22.79±0.05	53.11±1.38	1.07

<sup>a</sup> Calculating  $\lambda_B$  using equation (7.2), <sup>b</sup> Interpolated value for pure glycerol (see Ref. 182)

Furthermore, we calculated the Bjerrum length  $\lambda_B$ , which specifies the distance between the centers of two unit charges when their Coulomb energy equals the thermal energy  $k_B T$ , based on equation (7.2)

$$\lambda_B = \frac{e^2}{4\pi\epsilon_0\epsilon_r k_B T} \quad (7.2)$$

with  $e$  = elementary charge,  $\epsilon_0$  = vacuum permittivity,  $k_B$  = Boltzmann constant and  $T$  = temperature. The Bjerrum length often appears in equations associated with electrostatic interactions in electrolyte solutions (e. g. ion-condensation and ion-correlation interactions),<sup>19</sup> in which these interactions are important below  $\lambda_B$ , whereas at longer distances, thermal fluctuations prevail.<sup>196</sup> Note that only the combination DMF:gly:water has significant reductions in  $\epsilon_r$  and  $\eta$  and presents a significantly higher Bjerrum length than the established solvent mixture, indicating the possibility of substantial changes in the electrostatic interactions between  $1^{4+}$  and  $2^{2-}$  ( $3^{2-}$ , respectively) by substituting DMSO with DMF.

### 7.3.3. Analyzing Preferential Solvation with DLS

As we have previously shown,<sup>14,66,92</sup> DLS is a simple and well-suited tool to characterize the development of ionic clusters, mainly through their scattering profiles and the derived hydrodynamic radius. As dianionic compound one applied  $2^{2-}$  due to its stability at 20 °C over the course of several months. Moreover, we focus our discussions on the molar ratios 1:3 and 5:6 for the system  $1^{4+}:2^{2-}$ , which we have found as the limiting values of ionic ratios capable of building up durable ionic cluster.<sup>92</sup> The results for the ratio combinations outside this viable range can be found in Appendix E (see Fig. E.4 and E.5).

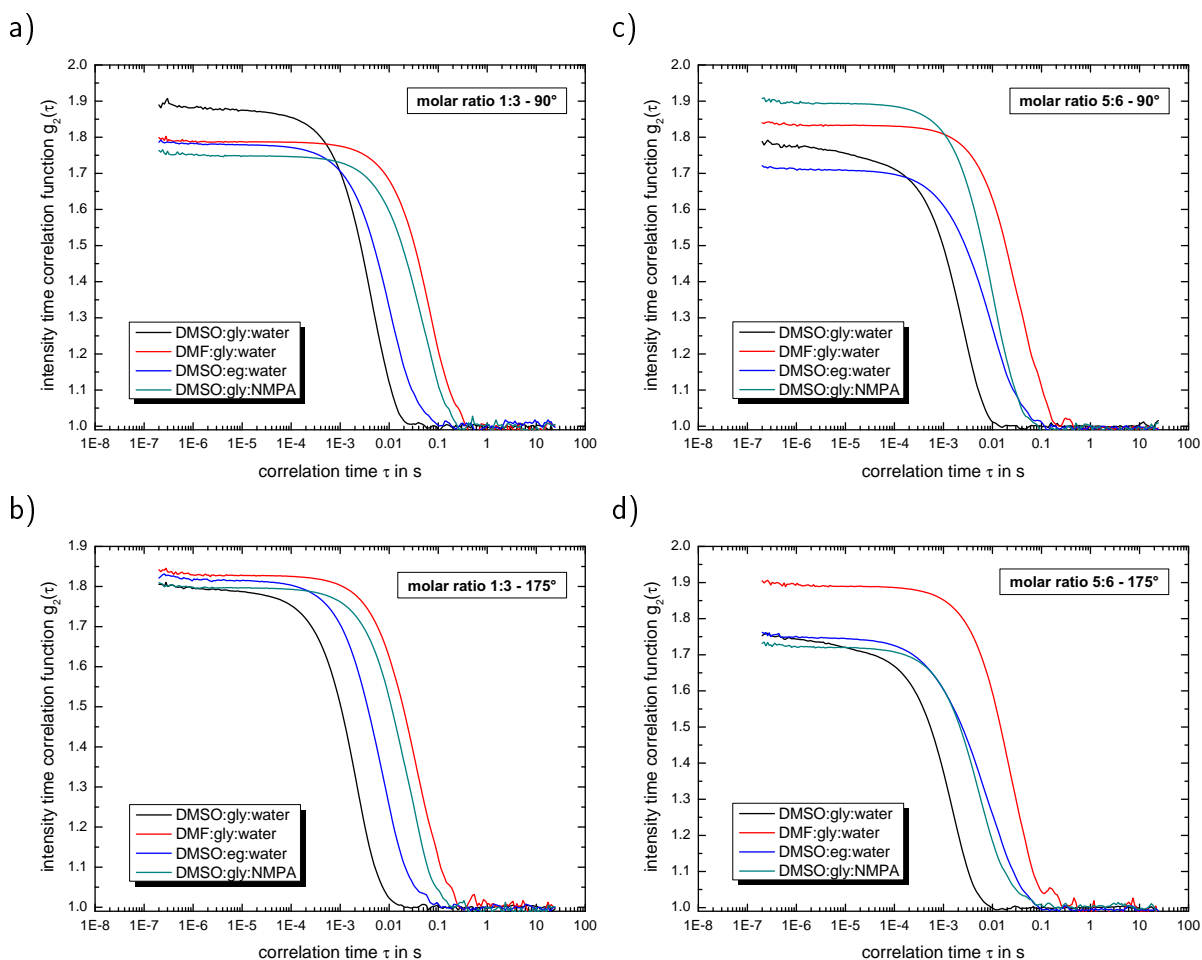


Fig. 7.2.: Intensity time correlation functions at measurement day ten for all four solvent mixtures at side (a) and c)) and back (b) and d)) scattering. a), b) graphs for  $1^{4+}:2^{2-}$  1:3 and c), d) graphs for  $1^{4+}:2^{2-}$  5:6.

Fig. 7.2 shows the intensity time correlation functions of  $1^{4+}:2^{2-}$  at the molar ratios 1:3 and 5:6 from measurement day 10 for all four solvent mixtures at side and back scattering. The established solvent mixture DMSO:gly:water in all cases displays the earliest decay, even though it possesses a relatively large dynamic viscosity. If in a lower-viscosity solvent, for example, the solvent containing ethylene glycol, ionic clusters built up with sizes similar to the established

one, the autocorrelation function would decay at shorter correlation times. Based on the delayed decay for all new solvent mixtures, we can deduce that these mixtures form (i) enlarged ionic cluster or (ii) self-assembled entities with a polydisperse size distribution directly after the incubation period of 10 days. Note that DMF:gly:water for molar ratios 1:3 and 5:6 shows strongly pronounced graphs with long-lasting intensity correlation, indicating the formation of unstructured aggregates rather than well-defined ionic clusters with a hydrodynamic radius  $R_H > 100\text{nm}$ .

In the following, we (i) visualize the development of the self-assembled entities for the systems  $\mathbf{1}^{4+}:\mathbf{2}^{2-}$  1:3 and 5:6 over time and (ii) compare the applied solvent mixtures by using the IEDs in Fig. 7.3. On the left y-axis the volume charge density of the applied building units is shown, which we calculated by dividing the charges  $z^\pm$  (multiplied with the elementary charge  $e$ ) of the cationic and anionic component by their respective volumes (see Appendix A for details). The leftmost part of the x-axis below 1.5 nm denotes the diameter of the individual ions (without solvation shell) and together, this part of the IED summarizes the size and size ratio of the anionic and cationic components that makes the self-assembly process possible. Through combining the multicationic box  $\mathbf{1}^{4+}$  with the dianion of methanedisulfonic acid  $\mathbf{2}^{2-}$ , at molar ratios of 1:3 as well as 5:6, one adjusts the resulting volume charge density, which determines the electrostatic correlations<sup>25</sup> along the connecting line of both ions. The molar ratios set the starting points along the connecting line of the temporal development in solution (essentially following a lever-type rule, see Appendix A and Ref. 92 for details) for all new solvent mixtures and are directly comparable to the IEDs in the established solvent.<sup>92</sup> As we have stated in Ref. 94: "starting from these points, we plot at the right y-axis the eccentricity  $e_{IED} = \sqrt{1 - \frac{b^2}{a^2}}$  to define deviations from a perfect sphere (with a value of  $e_{IED} = 0$ ) versus the final size of the ionic cluster<sup>c</sup>, illustrating the shape and its deviation from a perfect, isotropic sphere of the self-assembled entities. Additionally, we include the time beginning from the complete incubation period of ten days (blue full dots) until the last measurement day (arrow to blue crossed dots). Evolution with time is emphasized in IEDs by the oval (for globular ionoids more circular) frame around the arrows.

The IED for four solvent mixtures at molar ratio 1:3 (see Fig. 7.3 a)) displays that only in DMSO:gly:water, well-defined globular ionoids with long-term stability are formed. For all new solvent mixtures the IED highlights the formation of self-assembled structures with significant fluctuation in size as well as shape already at first sight when following the arrows

<sup>b</sup> Parameters  $a$  and  $b$  are the length of the semi-major and semi-minor axis from ellipses. We have adapted this definition of eccentricity in IEDs to our DLS data, which can be found in A.

<sup>c</sup> In the IEDs, we use the smaller hydrodynamic radius values of the polydisperse particle size distribution. If no sizes of (at least) anisotropic ionic clusters were detected in the sample, we present the data on the ion cloud state to complete the IED.

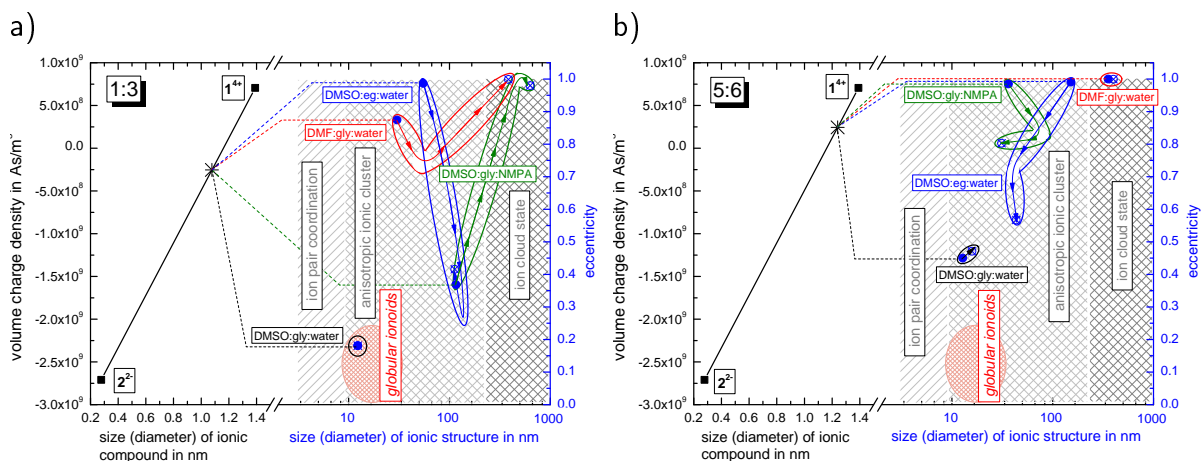


Fig. 7.3.: Ionoid evolution diagram (IED) for system  $1^{4+}:2^{2-}$  with molar ratio a) 1:3 and b) 5:6 for all new solvent mixtures. The optimal solvent mixture DMSO:gly:water is incorporated as well as the three states of the ionic self-assembly process. The total time of observation reflected in the IEDs amounts to 30 days.

of the temporal evolution. As already qualitatively observable in the intensity time correlation functions in Fig. 7.2, the substitution of DMSO with DMF leads to initial anisotropic ionic clusters which rapidly assemble into larger aggregates. Similar tendencies are visible for the solvent containing NMPA, even though it shows almost the same dynamic viscosity and relative permittivity as the established one with water. Note that DMSO:gly:NMPA initially builds up anisotropic ionic clusters with less deviations from a spherical shape compared to DMF:gly:water. DMSO:eg:water shows highly anisotropic ionic clusters at measurement day 10, which obtains a more spheroidal shape throughout the total measurement time. The significant increase in diameter may well be connected with the considerably reduced dynamic viscosity going along with the substitution of glycerol with ethylene glycol.

When increasing the amount of the cationic building unit, for example, to molar ratio 5:6, the temporal development of ionic clusters in all four solvent mixtures (see Fig. 7.3 b)) is altered. The established solvent mixture DMSO:gly:water still builds up small anisotropic ionic clusters, but with a higher eccentricity-value compared to the almost spherical structures found at a molar ratio of 1:3. The substitution of DMSO with DMF shows an immediate formation of large aggregates with high eccentricity. The solvent mixture containing NMPA initially builds up highly anisotropic ionic cluster, which reduce their eccentricity in the course of the total measurement time. A similar behavior can be found for DMSO:eg:water, but here we detect anisotropic ionic clusters with (i) almost the same spheroidal shape and (ii) a quadrupled diameter as compared to the established solvent mixture. Note that the fourfold rise in size is accompanied by a dynamic viscosity of ethylene glycol that is only a quarter of that of glycerol. We can further validate the stability of the anisotropic ionic clusters in DMSO:eg:water by



filtering the solution after a measurement period of one month (see Fig. E.7).<sup>92</sup> The recorded intensity time correlation functions still present a well pronounced y-intercept value for the 5:6 ratio sample of system  $1^{4+}:2^{2-}$  at both scattering angles, indicating the general survival of the self-assembled entities after filtration. Note that due to the mechanical stress of filtering the sample, we record an earlier decay for the autocorrelation function, which correlates with a reduced amount of larger self-assembled entities inside the solution with initial polydisperse size distribution.

Based on the large sets of results summarized in the IEDs of the different samples with selective replacement of individual solvent components, one can derive first attributes, which qualify a solvent mixture to build up durable ionic clusters of this combination of ions in solution:

- (1) DMSO holds an important role inside the solvent mixture. Besides adjusting the relative permittivity, which directly has influence on the Bjerrum length  $\lambda_B$ , it functions as hydrogen bonding acceptor.<sup>197,198</sup> Therefore it adjusts the electrostatic and dipolar interactions as well as the weaker noncovalent forces mainly through the formation of an extensive dipole network and the ability to accept hydrogen bonds and in addition specifically solvate organic molecules through the methyl groups (potentially London forces or simple 'hydrophobic effect'). Apparently, the substitution of DMSO with DMF largely disturbs this favorable combination of dipole-dipole orientation and alkyl solvation, leading to the formation of larger aggregates.
- (2) Glycerol stands out with a high dynamic viscosity due to its ability and tendency to form a hydrogen bonding network covering the entire sample,<sup>199–201</sup> which is still partially present in the optimal solvent mixture. When comparing the glycerol-containing and the ethylene glycol-containing samples, it seems that glycerol mainly determines the diameter as well as the shape of the self-assembled entities. Reducing the dynamic viscosity with ethylene glycol (i) limits the region for molar ratios capable of building up ionic cluster between 2:3 to 5:6 and (ii) enlarges the size of the self-assembled entities. However, the ionic self-assembly process apparently still operates in a comparable manner because of the similar hydrogen bonding network in ethylene glycol and glycerol.<sup>202,203</sup>
- (3) Water, even though it only makes up a small fraction inside the solvent mixture (7 vol.%), seems to link the dipolar/hydrogen bonding networks of DMSO and glycerol. Replacing water with NMPA, which presents a different network formation,<sup>185,186</sup> yields sample that are not able to replicate this joint network structure and therefore present modified ionic clusters for the system  $1^{4+}:2^{2-}$ .

### 7.3.4. Analyzing Preferential Solvation with CW EPR Spectroscopy

Going beyond the characterization of the long-term characterizing of the structure formation of the  $\mathbf{1}^{4+}:\mathbf{2}^{2-}$  system in the selective solvent mixtures, we study the initial solvation environment of the ions in the ion cloud state in all solvents with CW EPR spectroscopy. This requires exchanging the anion  $\mathbf{2}^{2-}$  with paramagnetic, EPR-active Fremy's salt dianion ( $\mathbf{3}^{2-}$ ). This substitution can influence interactions inside the ion cloud, but electrostatic correlations especially to  $\mathbf{1}^{4+}$  remain highly similar, as shown previously.<sup>14,92</sup> It is of great importance to be able to discriminate effects of (i) solvent viscosity and (ii) electrostatic interaction with increasing  $\mathbf{1}^{4+}$  concentration on the rotational mobility of our spin probe. To this end, we measured pure Fremy's salt 3 mM in all four solvent mixtures as an internal reference (molar ratio 0:1 in Table 7.1).

The respective CW EPR spectra of the pure nitroxide radical (see Fig. E.8 in Appendix E) show rotational diffusion which can be described by an axial tensor with the unique axis along the N-S-bond of Fremy's salt (see red arrow in Fig. 7.1).<sup>87,88</sup> Rotation about this unique axis ( $D_{\parallel}$ ) is significantly faster than about the axes perpendicular ( $D_{\perp}$ ) to it. Moreover, measurements at two microwave frequency/magnetic field bands (X- and Q-band, microwave frequencies around 9.4 GHz and 34 GHz, respectively) can reveal differences in the rotational time-frame through their frequency/field dependence. This is in particular true when the rotational diffusion is a superposition of slower and faster or different anisotropic motions.<sup>88</sup> Fremy's salt dianion shows the highest rotational mobility as well as lowest difference between  $D_{\parallel}$  and  $D_{\perp}$  in DMSO:eg:water, indicating a rather isotropic environment around the nitroxide. When using the solvent mixtures DMF:gly:water and DMSO:gly:NMPA, we gradually increase the dynamic viscosity inside the solution, which leads to a decrease in rotational mobility and a more anisotropic environment for  $\mathbf{3}^{2-}$ . Note that the nitroxide radical presents a slightly higher mobility inside the solvent mixture DMSO:gly:water compared to the one containing NMPA, even though the  $\eta$ -values are similar. However, the anisotropy of rotation as reflected in the difference between  $D_{\parallel}$  and  $D_{\perp}$  is higher for the established solvent, which can again be reconciled with the idea of a modified dipolar/hydrogen bonding network by the substitution of water with NMPA.

Adding  $\mathbf{1}^{4+}$  to the pure nitroxide radical in the established solvent mixture leads, as previously described,<sup>92</sup> to (i) significant line broadening, mainly reflecting the slowed-down rotation around the molecular z-axis, and (ii) a shift of the unique  $D_{\parallel}$ -axis from the N-S-bond towards the dissecting angle of both sulfonate groups. By correlating the strength of the line broadening with the concentration of the multicationic box, one can observe the transition in Fremy's salt mobility, which at low concentrations rotates relatively freely but with higher concentrations of the multication Fremy's salt rotational motion becomes substantially more

restricted. Starting from this complex set of information of dianion mobility, it is tested, how changes in the solvent mixture affect this coordination behavior inside the initial ion cloud state and therefore influence the self-assembly process for ionic clusters, as already described by DLS with the system  $1^{4+}:2^{2-}$ .

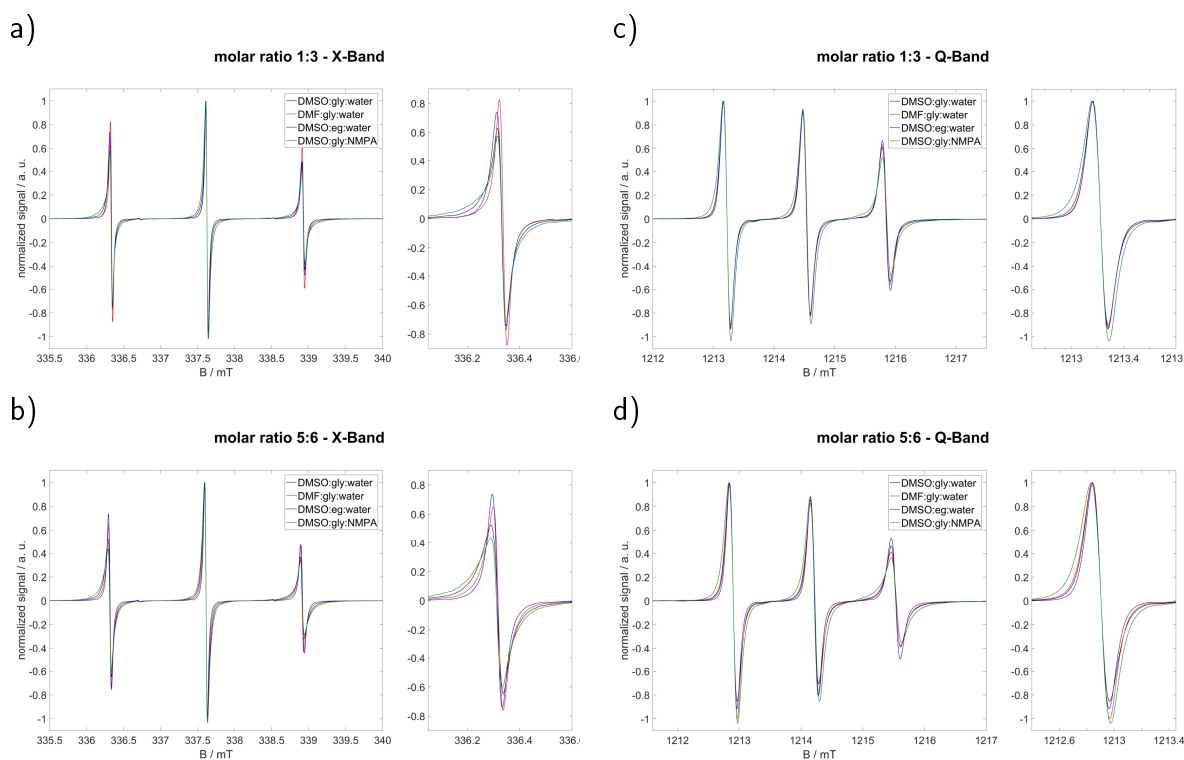


**Fig. 7.4.:** a), b) X-band and c), d) Q-band CW EPR spectra of  $1^{4+}:3^{2-}$  with molar ratios 1:3 (a) and c)) and 5:6 (b) and d)) in all four solvent mixtures. The lowfield peak of the spectra is shown separately right next to the full spectra.

Fig. 7.4 shows the CW EPR X-band and Q-band spectra of  $1^{4+}:3^{2-}$  with molar ratios 1:3 and 5:6 for all four solvent mixtures. In DMSO:eg:water at both frequencies the line broadening due to electrostatic interactions between cationic and EPR-active anionic building unit is less dominant compared to the established solvent mixture containing glycerol instead of ethylene glycol. The reduced dynamic viscosity allows for higher rotational and coupled to it translational mobility in the solution and such hinders the formation of more ordered, relative coordinations and orientations, even at higher concentrations of  $1^{4+}$  like, for example, molar ratio 5:6. This drives the self-assembly process towards the formation of larger ionic clusters. The solvent DMF:gly:water presents an interesting frequency-dependent picture of Frey's salt rotational mobility: At X-band frequencies we record a significant line broadening only when the cationic component reaches high concentrations like for molar ratio 2:3 (see Fig. 7.4 b)), but Q-band spectra show broadenings already at lower molar ratios like 1:3. Note that through the frequency (and such time-frame)-dependent differences in rotational motion

sensitivity/averaging, X-band spectra reflect the globally averaged interactions and dynamics, while Q-band spectra highlight the interactions in the local environment of Frey's salt.<sup>66,92</sup> The reduced relative permittivity upon the substitution of DMSO with DMF, which enhances the long-range electrostatic interactions between  $\mathbf{1}^{4+}$  and  $\mathbf{3}^{2-}$ , also alters the influence of weaker noncovalent interactions and such predominantly affects the direct vicinity of the nitroxide. The solvent mixture containing NMPA instead of water displays prominent line broadening for all molar ratios at both measured frequencies, surpassing the effects with DMSO:gly:water. The respective spectra indicate a stronger coordination of the Frey's salt dianion to the multicationic box.

To quantify the effect of solvent composition on the rotational mobility of our spin probe inside  $\mathbf{1}^{4+}:\mathbf{3}^{2-}$ , we combine different parameters of evaluation, as we have in detail explained in detail in Ref. 66,92 and also in Appendix A. These are: (1) the full width at half maximum (FWHM) of the CW EPR lines (simulated with isotropic broadening) as well as (2) the anisotropy  $T$  of the rotational tensor based on equation A.7 into electrostatic interactions of Frey's salt (see Appendix E). (3) The much simpler isotropic rotational correlation time  $\tau_c$  can give information on the rotational motion changes for (slightly) anisotropic rotational motion (see Appendix E).

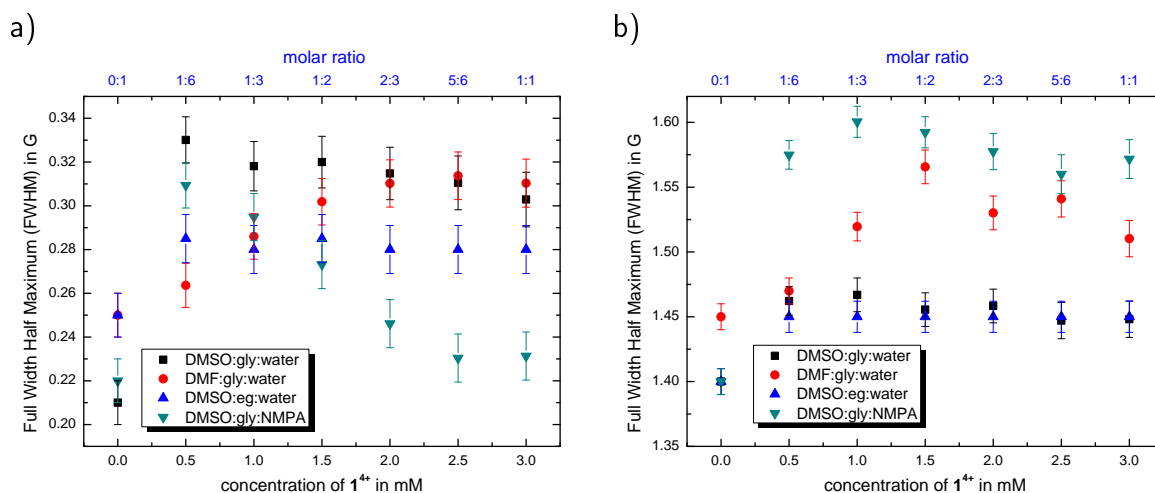


**Fig. 7.5.:** Plot of the isotropic broadening (full width at half maximum, FWHM) of the high-field line of pure Frey's salt at 3 mM (molar ratio 0:1, leftmost data point) and Frey's salt in the system  $\mathbf{1}^{4+}:\mathbf{3}^{2-}$  with increasing cation concentration in all four solvent mixtures at a) X-band and b) Q-band frequencies.

As presented in Fig. 7.5, Frey's salt FWHM values of the tested molar ratio samples in the DMSO:gly:water and DMSO:eg:water mixtures have a comparable trend at both frequencies: Above a ratio of 1:6 the FWHM values reach a plateau (within the margin of error), indicating similar local dynamic electrostatic attachment at day 0 inside the initial ion cloud state. However, in the established solvent mixture with its relatively large dynamic viscosity less

mobile Fremy's salt dianions ensue with a more restrained/fixed coordination with  $\mathbf{1}^{4+}$ , which is (i) visible through the broader flanks in the CW EPR spectra and (ii) exposed by the rotational correlation time  $\tau_c$  (see Fig. E.11). The solvent mixture containing DMF also reaches a plateau for the FWHM values at both frequencies, but at a higher concentration of the cationic component. Note that for the Q-band spectra, the full width at half maximum results exceeds those from the established solvent mixture. The substitution of DMSO with DMF provides stronger correlations between  $\mathbf{1}^{4+}$  and  $\mathbf{3}^{2-}$  in the local environment of Fremy's salt, which is visible in the Q-band spectra, whereas X-band spectra present a less fixed coordination for molar ratios below 2:3. The solvent mixture DMSO:gly:NMPA shows an opposing development of its FWHM values, in which the molar ratio 1:2 serves as the turning point: The line width (i) decreases at X-band and (ii) increases at Q-band frequencies for higher molar ratios. The significantly broadened flanks in the CW EPR spectra with NMPA are mainly based on the slowed-down rotational mobility of Fremy's salt (see Fig. E.19), whereas the coordination with the multicationic box gets locally stronger at molar ratio 1:2 and higher. This change in the vicinity of  $\mathbf{3}^{2-}$  is well pronounced in our Q-band spectra and provides the increased line width. The drastic adjustments inside the ion cloud state can also be connected with the DLS data (see Fig. 7.3), which show a completely different self-assembly behavior for the molar ratios 1:3 and 5:6 in DMSO:gly:NMPA.

To further characterize the solvation of Fremy's salt in all four solvent mixtures, we performed low temperature CW EPR measurements at Q-band frequencies with samples containing a molar ratio of  $\mathbf{1}^{4+}:\mathbf{3}^{2-}$  1:3. Here, we are able to receive a better resolution for the EPR parameters  $g_{xx}$  and  $A_{zz}$  (tensor elements of the  $\mathbf{g}$  and hyperfine tensor), which are mainly sensitive to the proticity and polarity, respectively, of the local environment.<sup>172,204</sup> Note that here one analyzes a 'snapshot' (shock frozen, glassy solution) of our samples. Fig. 7.6 highlights the CW EPR spectra at 150 K of solely  $\mathbf{3}^{2-}$  (molar ratio 0:1) in all tested solvent mixtures, serving as reference for the solutions containing the cationic building unit.

By exchanging glycerol with ethylene glycol, we neither change the polarity nor the hydrogen bonding network in the direct vicinity of our spin probe, which matches with the comparable behavior from the FWHM values. The solvent mixture DMF:gly:water presents a visible shift to higher  $g_{xx}$  as well as a smaller  $A_{zz}$  value. Both trends indicate a more apolar environment and a weakened hydrogen bonding network around Fremy's salt. Note that the increase in  $g_{xx}$  is around  $1 \times 10^{-4}$ , whereas the hydrogen bonding with a single water molecule was estimated to give a shift for  $\Delta g_{xx}$  of  $\approx 4 \times 10^{-4}$ .<sup>205</sup> The substitution of DMSO with DMF does not fully remove one complete hydrogen bond out of the system, but rather seems to reduce the strength of the existing hydrogen bonds. The solvent mixture DMSO:gly:NMPA shifts the complete spectra to slightly lower  $g$ -values ( $\Delta g_{xx} = 5 \times 10^{-5}$ ), indicating a stronger hydrogen bonding network around  $\mathbf{3}^{2-}$ . This fact reinforces our hypothesis that the 7 vol.% water link

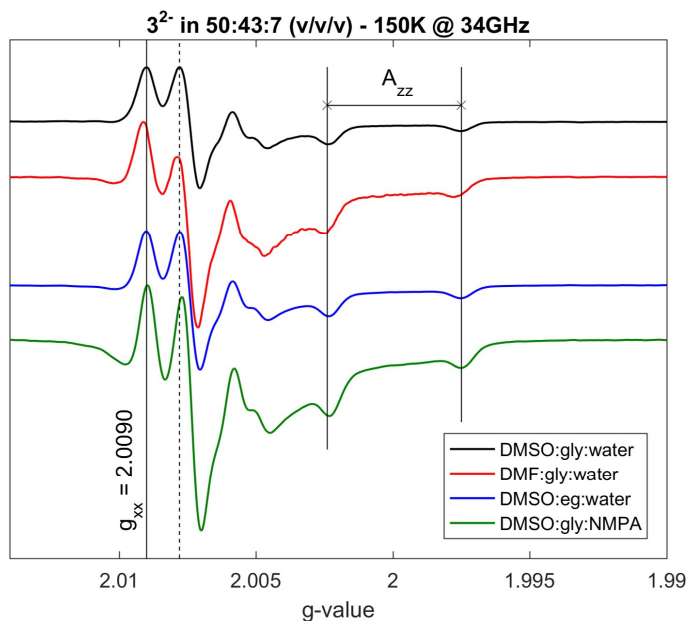


Fig. 7.6.: CW Q-band spectra at 150 K for  $3^{2-}$  3 mM in all four solvent mixtures. The inserted black lines highlight the position of  $g_{xx}$  as well as  $A_{zz}$  in relation to the established solvent DMSO:glycerol:water 50:43:7 (v/v/v).

the dipolar/hydrogen bonding networks of DMSO and glycerol, whereas NMPA alters this 'connection' process. Additionally, we can conclude a rather close proximity between Fremy's salt and water (NMPA, respectively), otherwise we would not detect this change. When one now adds  $1^{4+}$  to the nitroxide radicals, the CW EPR spectra all display an additional broad 'feature', as shown in Fig. 7.7 (see blue asterisk) for the established solvent mixture.

Strong dipolar interactions between our cationic and anionic building unit induce the formation of the additional signal, which is also visible as a superimposed effect between  $g$ -values 2.006 and 2.002 as a slightly wider distance between the spectra and the dotted baseline in Fig. 7.7. Based on the chosen solvent mixture, the intensity of the peak varies as shown in Fig. E.20. Looking at the EPR parameters  $g_{xx}$  and  $A_{zz}$ , we do not detect changes inside the established solvent mixture by adding  $1^{4+}$ , indicating no changes in the solvation shell directly surrounding Fremy's salt. To analyze changes in the outer solvation shell of Fremy's salt, we performed detailed pulsed EPR measurements with all new solvent mixtures as well as with partially deuterated systems of DMSO:gly:water. Because these large sets of data of the immediate solvation shell around  $3^{2-}$  are beyond the scope of this study on general solvation in ionoids, they will be discussed in a separate study. Similarly, for DMF:gly:water (see Fig. E.20 a)), the initial shift of  $g_{xx}$  of  $1 \times 10^{-4}$  is also found after addition of  $1^{4+}$ . DMSO:eg:water as well as DMSO:gly:NMPA (Fig. E.20 b) and c)) present a shift of  $1 \times 10^{-4}$  to higher  $g_{xx}$  values after adding the multicationic box to Fremy's salt. The weakened hydrogen bonding networks in both systems inside the initial ion cloud state could be the reason for the enlarged anisotropic

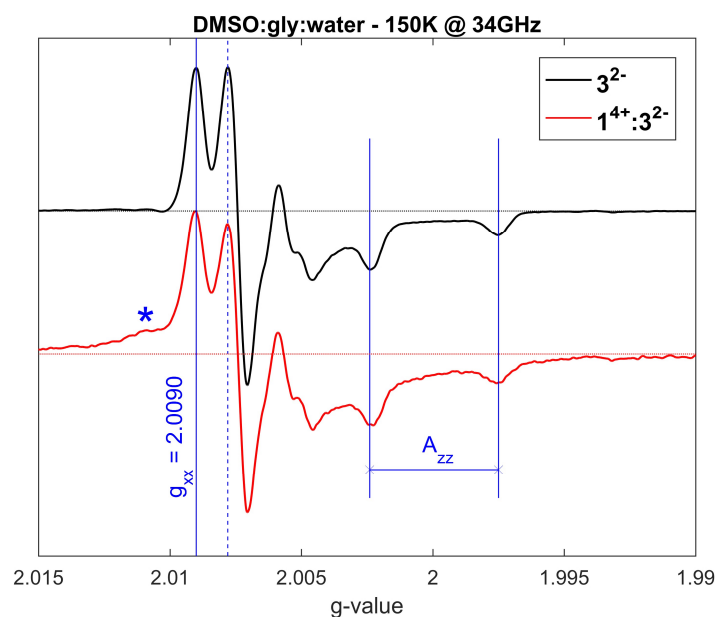


Fig. 7.7.: CW Q-band spectra at 150 K for  $1^{4+}:3^{2-}$  molar ratio 1:3 in DMSO:gly:water 50:43:7 (v/v/v). The inserted blue lines highlight the position of  $g_{xx}$  as well as  $A_{zz}$  in relation to the  $3^{2-}$  reference. The blue asterisk highlights an additional 'feature' due to the interaction of both ionic building units.

ionic clusters observed with DLS.

## 7.4. Conclusion

The ISA process of the 'Texas-sized molecular box' ( $1^{4+}$ ) with the small dianionic salts  $2^{2-}$  and  $3^{2-}$  into globular ionoids depends significantly on the solvent composition in combination with the molar ratio of the respective components. Based on the optimal solvent mixture DMSO:gly:water 50:43:7 (v/v/v), we substituted each component with a similar solvent to specify the boundary conditions for the formation of durable ionic cluster in solution. Therefore, we determined the dynamic viscosity  $\eta$  and relative permittivity  $\epsilon_r$  for each solvent mixture as well as analyzed their templated nanostructure to examine the interplay of electrostatic interactions with weaker noncovalent forces. Fig. 7.8 graphically summarizes the results for the discussed molar ratios 1:3 and 5:6.

Decreasing the relative permittivity inside the solvent mixture by exchanging DMSO with DMF leads to the formation of enlarged, highly shape-anisotropic aggregates for all tested molar ratios. The reduced screening of cationic and anionic building units disturbs the balance between long-range electrostatic interactions to dipolar interactions and weaker noncovalent forces (e. g. London forces), which negatively affects the dynamic self-assembly process of the ionic clusters. Especially the strength of the hydrogen bonding network is reduced, which is

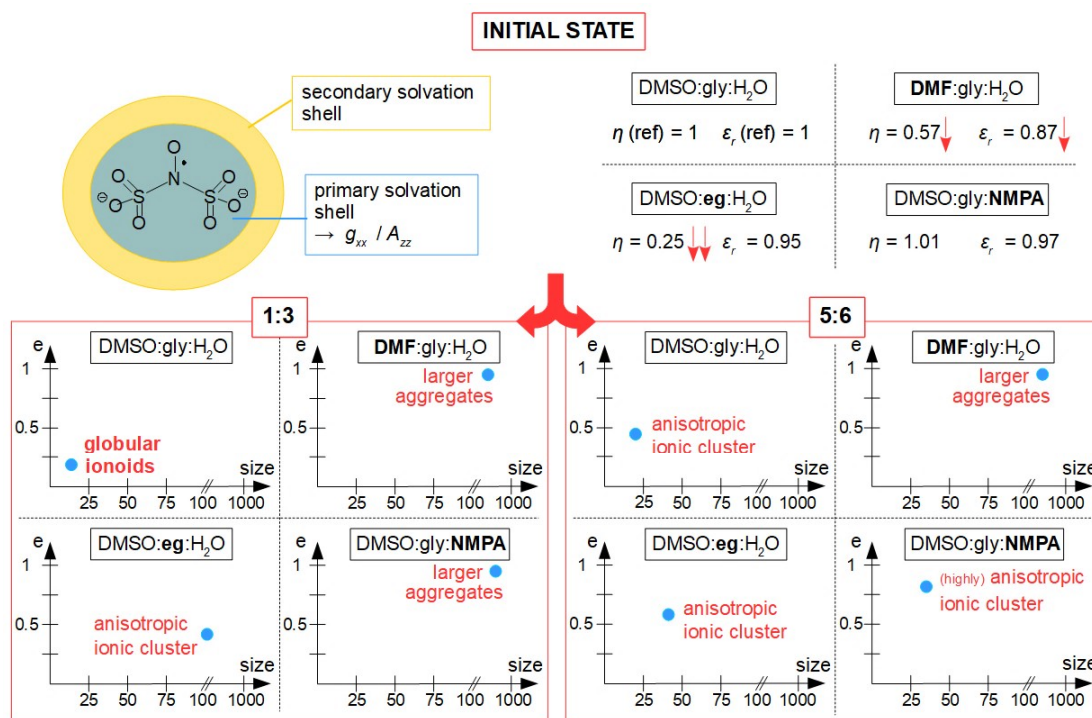


Fig. 7.8.: Schematic representation of the determined self-assembled entities for the molar ratios  $1^{4+}:2^{2-}$  1:3 and 5:6 based on all four tested solvent mixtures, whereas their dynamic viscosity  $\eta$  and relative permittivity  $\epsilon_r$  are highlighted (with DMSO:gly:water as internal reference). Additionally, the solvation shell of Frey's salt is shown and its respective size composition is further discussed in the main text.

evident in the shift of  $g_{xx}$  to higher values. The substitution of glycerol with ethylene glycol mainly affects the dynamic viscosity and therefore the size and shape of the resulting ionic cluster. Frey's salt in the initial ion cloud state has a more dynamic, less restricted local electrostatic attachment to  $1^{4+}$  compared to the established solvent mixture. To compensate the higher mobility of our anionic component, we can increase the cation concentration to receive anisotropic ionic clusters with remarkable stability, as shown for the molar ratio  $1^{4+}:2^{2-}$  ( $1^{4+}:3^{2-}$ , respectively) 5:6. By exchanging the small amount of water inside the established mixture with *N*-methylpropionamide, we did not transform the macroscopic properties of the solvent, but rather its hydrogen bonding network. Our low temperature CW Q-band spectra indicate a stronger hydrogen bonding network for solely Frey's salt with NMPA (compared to the solvent mixture with water), which partially disrupted after adding the multicationic box with a molar ratio of 1:3. Exact transformations cannot be determined based on our data. Nevertheless, these adjustments drastically affect the initial ion cloud state because of the formation of strong coordinations between Frey's salt and  $1^{4+}$ , especially at molar ratio 1:2 and higher. Above this ratio, we detect anisotropic ionic clusters in solution, which possess enlarged diameters as well as higher shape eccentricities.



---

The formation of globular ionoids seems firmly rooted in the specific solvent composition of DMSO:gly:water 50:43:7 (v/v/v) and the solvation of the different ionic components (see Ref. 94 for the different sets of cations and anions that form ionoids or anisotropic ionic clusters in solution). In order to simplify the required solvent mixture regarding possible applications in soft matter and supramolecular chemistry, adaptation of the macroscopic and microscopic parameters of the solvent as well as the templated nanostructure is one of the key goals. Here, we have shown how delicately physical properties of the solvent mixture govern the fuzzy self-assembly in solution, further studies will aim e. g. at simplifying the solvent mixture from a ternary to a binary solvent and specifying the preferential direct solvation shells of the individual ionic components.



# 8 | Further Insight into the Local Solvation Shell of the Initial Ion Cloud State

This chapter continues studying the preferential solvation of the model compounds 'Texas-sized molecular box'  $\mathbf{1}^{4+}$  and 'methanedisulfonate'  $\mathbf{2}^{2-}$  (Fremy's salt  $\mathbf{3}^{2-}$ , respectively) inside the initial ion cloud state. In Chapter 7 we showed that replacing one component inside the optimal solvent mixture DMSO:glycerol:water 50:43:7 (v/v/v) can drastically change the ISA process and prevents the formation of globular ionoids. Additionally, it was possible to assess the main contribution or respective role of DMSO, glycerol and water for (partially) monitoring the build up of soft, yet well-defined self-assembled entities:

- (1) DMSO seems to form an extensive dipole network, which adjusts the electrostatic interactions and van der Waals forces,
- (2) Glycerol provides a wide hydrogen bonding network and predetermines the final size and shape of the colloid-like ionic cluster due to its high dynamic viscosity and
- (3) Water links the dipolar and hydrogen bonding networks together.

Based on these findings, we focus in Chapter 8 (which contains unpublished results) mainly on the solvation behavior of the anionic component and how its solvation shell is adjusted after adding the multicationic box into the observed system. The goal is to quantify the (relative) amount of DMSO, glycerol and water in the direct vicinity of  $\mathbf{2}^{2-}$  ( $\mathbf{3}^{2-}$ , respectively).

## 8.1. Introduction

The role of solvation in a variety of research fields, especially for the formation of colloid-like ionic clusters, was already highlighted in the previous chapter. Based on the presented findings, we focus in this study more on the solvation process inside the initial ion cloud state for the model system containing the 'Texas-sized molecular box' ( $\mathbf{1}^{4+}$ ) in combination with the small dianionic salts ('methanedisulfonate',  $\mathbf{2}^{2-}$  or Fremy's salt dianion,  $\mathbf{3}^{2-}$ ). Therefore,

we combined two complementary advances (see Fig. 8.1) in analyzing the optimal solvent mixture of DMSO:glycerol:water 50:43:7 (v/v/v):

1. Selectively replacing one of the components with dimethyl formamide (DMF), ethylene glycol (eg) and *N*-methylpropionamide (NMPA), as introduced in Chapter 7 and
2. Partially incorporate deuterated solvent compounds inside the optimal mixture.

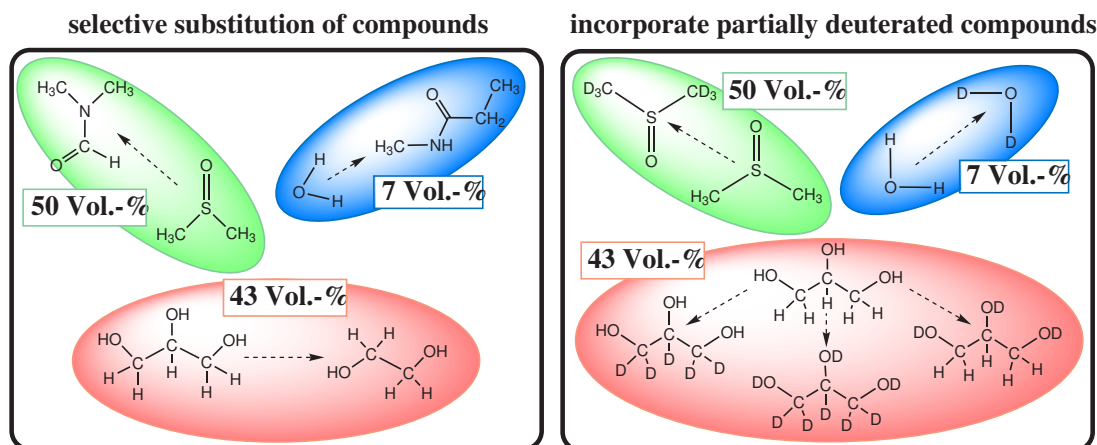


Fig. 8.1.: Schematic representation for the two advances of analyzing the solvation behavior inside the initial ion cloud state.

The second approach, which incorporates partially deuterated solvent components, is designed to individually mark DMSO, glycerol and water and to determine their contribution to the solvation shell of methanedisulfonate or Frey's salt dianion. Moreover, potential changes for the so-called preferential solvation (excess of one solvent component in respect to the composition inside the bulk solvent mixture)<sup>206</sup> of  $\mathbf{2}^{2-}$  ( $\mathbf{3}^{2-}$ , respectively) after adding  $\mathbf{1}^{4+}$  are of interest. Note that due to H/D isotope effects (like e. g. the Ubbelohde effect)<sup>207,208</sup> the interplay between electrostatic interactions and weaker noncovalent forces is altered. Therefore, the direct comparison regarding the solvation shell of the anionic building unit with and without interaction partner ( $\mathbf{1}^{4+}$ ) gains in importance.

To analyze the solvation behavior in the initial ion cloud state, we predominantly studied the  $\mathbf{1}^{4+}:\mathbf{3}^{2-}$  system and used a combination of continuous wave EPR spectroscopy, as already established in Chapter 7, and pulsed EPR spectroscopy. In general, utilizing methods based on EPR spectroscopy to study the solvation of paramagnetic ions, especially of transition metal ions,<sup>209–211</sup> was established more than 20 years ago.<sup>212</sup> In the following case, electron-spin-echo envelope modulation (ESEEM) spectroscopy<sup>213,214</sup> is proposed as main technique, which is capable of estimating the distance and number of nuclear spins (donated from proton and deuterium nuclei of the respective solvent components) in the proximity of an electron spin.<sup>215</sup>

## 8.2. Experimental

### 8.2.1. Materials

The 'Texas-sized molecular box' ( $\mathbf{1}^{4+}$ ) used in this study was synthesized analogous to the previous chapters. As small dianionic salts, we chose methanedisulfonic acid dipotassium salt ( $\mathbf{2}^{2-}$ ; Sigma-Aldrich, Munich, Germany) with purity  $\geq 99\%$  and Fremy's salt (potassium nitrosodisulfonate,  $\mathbf{3}^{2-}$ ; Sigma-Aldrich) of technical grade. All chemicals were applied as received. The concentration ratio for the  $\mathbf{1}^{4+}:\mathbf{2}^{2-}$  ( $\mathbf{1}^{4+}:\mathbf{3}^{2-}$ , respectively) was constant at 1 mM:3 mM (molar ratio 1:3).

The optimal solvent mixture, which serves as reference point, contains DMSO with  $\leq 0.02\%$  water (Sigma-Aldrich) and 86-88 wt% aqueous glycerol (Acros Organics, Nidderau, Germany) in a 1:1 volume ratio. For producing the solvent mixtures for the selective substitution of compounds, we used 99.5 wt% glycerol (Acros), DMF (Sigma-Aldrich) with  $\geq 99\%$  purity, ethylene glycol (Sigma-Aldrich) with  $\geq 99\%$  purity, NMPA (Sigma-Aldrich) with 98% purity and deionized Milli-Q-water. These components were combined to form the following solvent mixtures with a respective volume stoichiometrie of 50:43:7: (1) DMSO:gly:H<sub>2</sub>O, (2) DMF:gly:H<sub>2</sub>O, (3) DMSO:eg:H<sub>2</sub>O and (4) DMSO:gly:NMPA.

To craft solvent mixtures, which incorporate deuterated solvent compounds (see Fig. 8.1), we additionally applied d<sub>6</sub>-DMSO (Sigma-Aldrich) with 99.9% purity, D<sub>2</sub>O (Sigma-Aldrich) with 99.9% purity, d<sub>5</sub>-glycerol (d<sub>5</sub>-gly; Sigma-Aldrich) with 98% purity and glycer-d<sub>3</sub>-ol (d<sub>3</sub>-gly; Sigma-Aldrich) with 99%. These new components were combined to form the following solvent mixtures with a respective volume stoichiometrie of 50:43:7: (1) d<sub>6</sub>-DMSO:gly:H<sub>2</sub>O, (2) DMSO:gly:D<sub>2</sub>O, (3) DMSO:d<sub>5</sub>-gly:H<sub>2</sub>O and (4) DMSO:d<sub>3</sub>-gly:D<sub>2</sub>O. Note that the last two solvent mixtures are prepared in this way so that all protons capable in forming hydrogen bonds are either (3) <sup>1</sup>H or (4) D (<sup>2</sup>H) nuclei.

### 8.2.2. Methods

The main methods that are applied in this study are continuous wave (CW) and pulsed electron paramagnetic resonance (EPR) spectroscopy. DLS measurements were performed complementary, but do not directly aid in analyzing the solvation behavior inside the ion cloud state. Appendix A covers the description of these methods, whereas following instrumentation was used to perform the mentioned techniques:

- 1) DLS:
  - Litesizer 500 (Anton Paar GmbH, Austria)
- 2) CW EPR:

- X-band: Miniscope MS5000 (magnettech, Berlin, Germany) benchtop spectrometer
- Q-band: Bruker EMX-plus spectrometer (Bruker Biospin GmbH, Rheinstetten, Germany) with ER5106QT resonator

3) Pulsed EPR:

- Elexsys E580 EPR spectrometer (Bruker Biospin GmbH) at frequencies of  $\approx 9.4$  GHz with a Flexline split-ring resonator ER4118X-MS3.

## 8.3. Results and Discussion

### 8.3.1. General Remarks

As established in Chapters 4 and 5 as well as utilized in Chapters 6 and 7, we used the following terms to describe for all measured systems in solution the ionic self-assembly process:

- Globular ionoids,
- Anisotropic ionic clusters and
- Ion cloud state.

EPR spectroscopy again can just be applied for the ion cloud state that forms in the initial hours after sample preparation due to the fast disproportionation of Fremy's salt dianion ( $\mathbf{3}^{2-}$ ) compared to the ten-day incubation period of the self-assembled entities. However, we want to exactly focus on the solvation behavior in this suspected crucial time-frame, exploiting its contribution to the complete ionic self-assembly process.

### 8.3.2. Analyzing the selective substitution of solvent compounds

Chapter 7 already highlighted DLS and CW EPR spectroscopy data for the solvent mixtures, which selectively substitute DMSO with DMF, glycerol (gly) with ethylene glycol (eg) and water with *N*-methylpropionamide (NMPA). To further characterize these systems in the initial ion cloud, we applied pulsed EPR spectroscopy. At first, we performed echo-detected field sweep measurements, which can be regarded as analogous to CW field-swept spectra, except that the spectra here are recorded and shown as absorption spectra rather than derivatives.<sup>216</sup> Fig. 8.2 shows the echo-detected field sweep spectra from pure Fremy's salt and system  $\mathbf{1}^{4+}:\mathbf{3}^{2-}$  with molar ratio 1:3 in DMSO:gly:H<sub>2</sub>O 50:43:7 (v/v/v). By adding the 'Texas-sized molecular box' to the nitroxide radical, we detect a broadening as well as an additional 'feature' at the flank of the spectra (see blue asterisk in Fig. 8.2). These phenomena, which

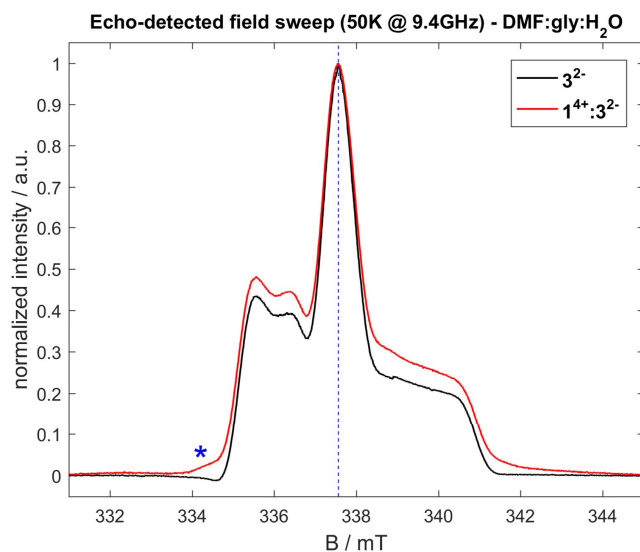


Fig. 8.2.: Echo-detected field sweep spectra measured at 50K of Fremy's salt and system  $1^{4+}:3^{2-}$  in established solvent mixture DMSO:gly:H<sub>2</sub>O 50:43:7 (v/v/v). The latter applied B-field position for ESEEM measurements is also highlighted.

are based on strong dipolar interactions between the cationic and anionic building unit, could also be recorded with CW Q-band spectra at low temperatures (see Fig. 7.7). The respective graphs for DMF:gly:H<sub>2</sub>O, DMSO:eg:H<sub>2</sub>O and DMSO:gly:NMPA are summarized in Fig. F.1 of Appendix F. For the subsequently performed ESEEM measurements, we used the B-field position that contains the maximal intensity of the echo-detected field sweep spectra, as shown in Fig. 8.2.

Regarding the performed electron-spin-echo envelope modulation spectroscopy, we started with the respective two pulse measurements with an initial interpulse delay  $\tau$  of 176 ns. The primary 2p-ESEEM data for pure Fremy's salt present a similar stretched-exponential decay for the solvent mixtures DMSO:gly:H<sub>2</sub>O, DMSO:eg:H<sub>2</sub>O and DMSO:gly:NMPA, as shown in Fig. 8.3 a). The only exception represents the system, which selectively substituted DMSO with DMF. Here, the determined phase memory time  $T_m$  is roughly two times smaller with DMF compared to the established solvent mixture. In the low-temperature limit, transverse relaxation is mainly based on fluctuations of the hyperfine field at the electron spin. These mentioned fluctuations are dominated by proton spin diffusion, which is strongly pronounced in e. g. solvents containing methyl groups. Methyl group rotation can persist down to very low temperatures and cause a strong modulation of the hyperfine field.<sup>217</sup> DMSO as well as DMF contain two methyl groups in their molecule structure (see Fig. 8.1), indicating that the structure alone cannot explain the drastic change in the phase memory time. As indicated in Chapter 7 DMF forms, compared to DMSO, a different dipole network with glycerol and water, which could explain the drop in the phase memory time.

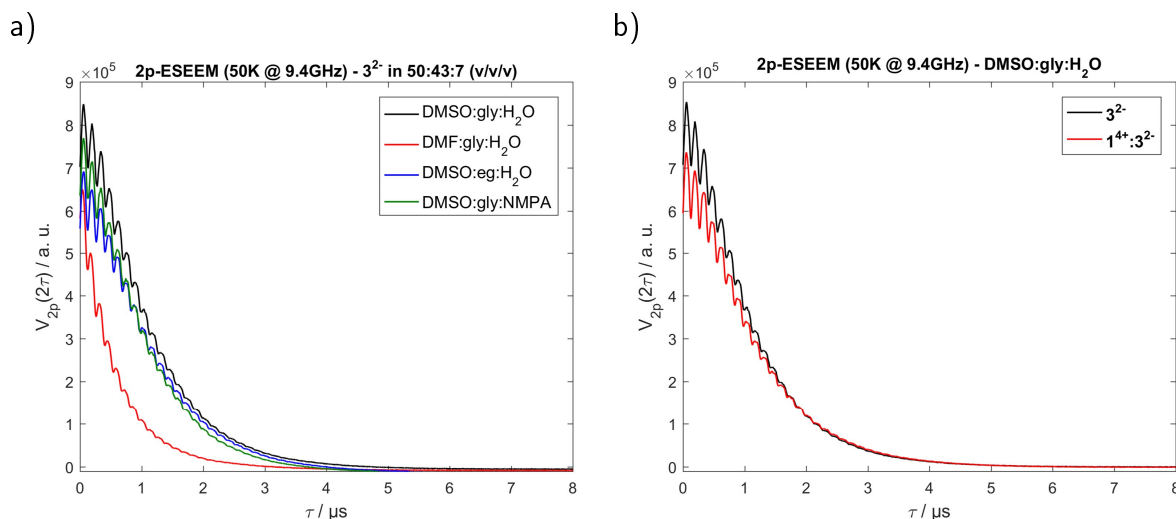


Fig. 8.3.: a) Comparison of the primary 2p-ESEEM data of pure Fremy's salt in all four high-lighted solvent mixtures. b) Comparison of the primary 2p-ESEEM data of  $3^{2-}$  and system  $1^{4+}:3^{2-}$  in established solvent mixture DMSO:gly:H<sub>2</sub>O 50:43:7 (v/v/v).

Adding  $1^{4+}$  to the nitroxide spin probe, as visualized in Fig. 8.3 b) for DMSO:gly:H<sub>2</sub>O, does not change the phase memory time in a significant manner, which also holds true for the other three solvent mixtures (see Fig. F.2 in Appendix F). The visible modulations overlaying the decay of the primary 2p-ESEEM data are contributed by the proton nuclei from the respective solvent components. To analyze changes in e. g. their modulation depths  $k$  and therefore the number of nuclei coupled to the electron spin,<sup>215</sup> we additionally performed 3p-ESEEM measurements.

Fig. 8.4 shows the three-pulse ESEEM results for all four solvent mixtures, highlighting the frequency domain data. We further display the respective time domain data, presented as normalized nuclear modulation functions, as inlay. Note that the modulation depth  $k$  contains only minor changes between all measured samples. Therefore, we focus on the frequency domain to compare the behavior of solely Fremy's salt with the  $1^{4+}:3^{2-}$  system containing the molar ratio of 1:3. All recorded spectra show one specific matrix peak at roughly 14 MHz, which represents the nuclear frequency from the surrounding protons donated by the respective solvation shell of Fremy's salt. Measuring  $3^{2-}$  3 mM provides similar intensity values for all solvent mixtures excluding DMSO:eg:H<sub>2</sub>O. Here, the proton signal is, based on the maximum of the recorded matrix peak,  $\approx 72.5\%$  stronger compared to the established system DMSO:gly:H<sub>2</sub>O. Our previously discussed CW Q-band spectra (see Chapter 7) do not show changes in the  $g_{xx}$ -value and the inner solvation shell of Fremy's salt, so exchanging glycerol with ethylene glycol mainly affects the outer coordination sphere. Note that at this point the specific influence of each solvent component on the increased electron nuclear hyperfine interaction cannot be certainly defined.



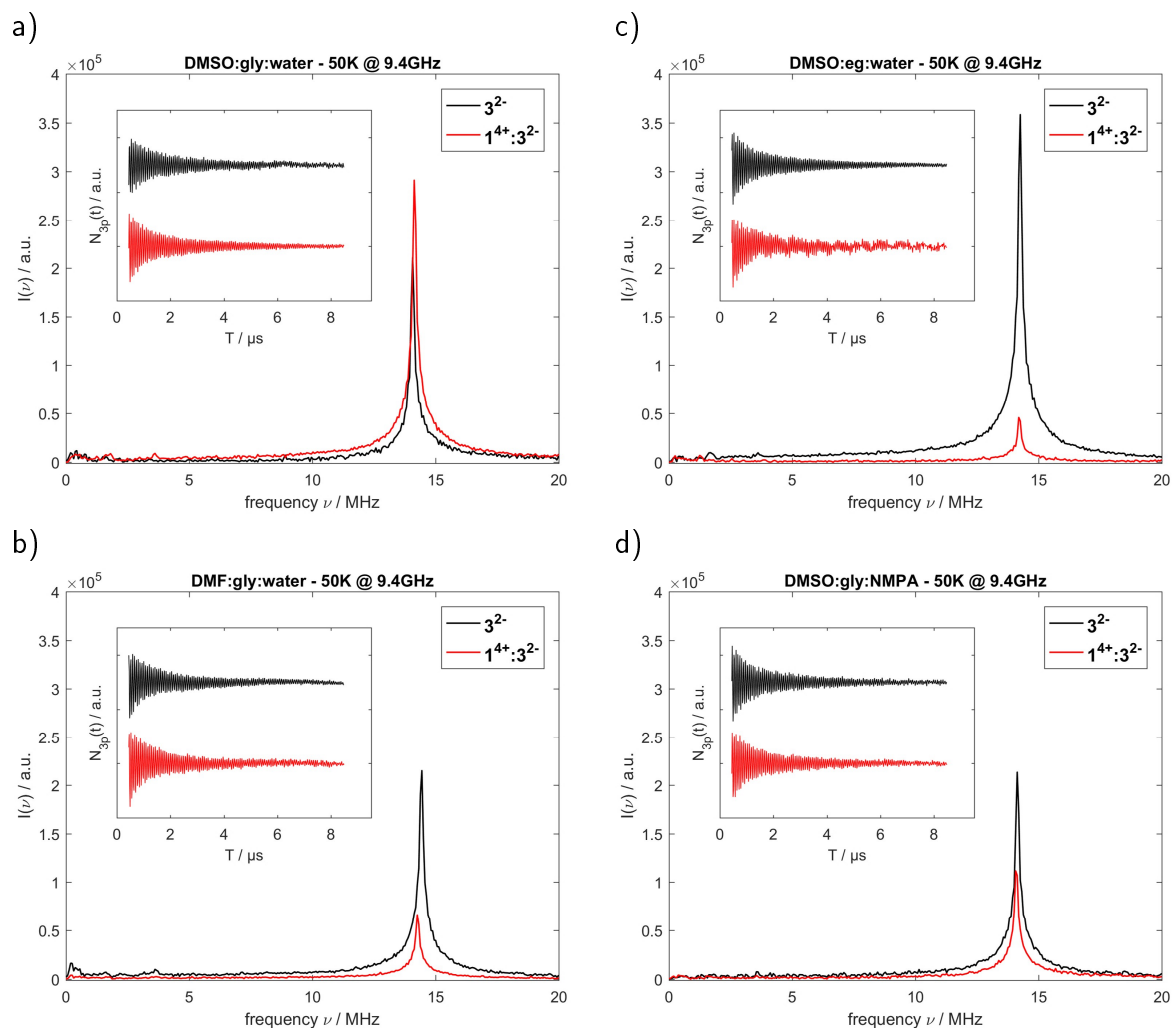


Fig. 8.4.: 3p-ESEEM frequency domain data  $I(\nu)$  at 50K for  $3^{2-}$  3 mM and  $1^{4+}:3^{2-}$  molar ratio 1:3 in a) DMSO:gly:water, b) DMF:gly:water, c) DMSO:eg:water and d) DMSO:gly:NMPA. All graphs contain the respective normalized time domain data as inlay.

Adding  $1^{4+}$  to the nitroxide radical leads to an increase of the proton signal for DMSO:gly:H<sub>2</sub>O, but a strong decrease for all other solvent mixtures. The multicationic box itself prefers DMSO inside the optimal solvent mixture, whereas Frey's salt is better soluble in the glycerol:water phase. By combining the cationic and anionic building unit, we can assume that in the initial phase of the ionic self-assembly process  $1^{4+}$  claims the available DMSO for itself. Therefore, the aprotic polar solvent partially moves away from the outer solvation shell of Frey's salt and the nitroxide radical is preferentially surrounded by the glycerol:water mixture. These changes in the solvation shell, which are determined based on a 'snapshot' of the rather dynamic composition, could explain the increase for the detected proton signal. Note that the described rearrangements of DMSO, glycerol and water must occur almost immediately after combining both ionic building units, because the ESEEM samples were directly shock

frozen after preparing the  $\mathbf{1}^{4+}:\mathbf{3}^{2-}$  system. To verify our hypothesis, we performed 3p-ESEEM measurements with the established DMSO:gly:H<sub>2</sub>O mixture, where each component is replaced with its deuterated analogue, which will be discussed in the next section. By comparing the behavior of proton and deuterium signal (occurring by 2 MHz) for a various set a deuterated solvent mixtures, we aim to individually track the behavior of each component.

The intensity of the proton signal for all 'new' solvent mixtures can be organized starting from lowest to highest in the following order: DMSO:eg:H<sub>2</sub>O < DMF:gly:H<sub>2</sub>O < DMSO:gly:NMPA. Note that the described sequence matches the behavior for the determined dynamic viscosity  $\eta$  (see Table 7.2). This verifies our assumption that the rearrangement of the solvent compounds occurs immediately after combining  $\mathbf{1}^{4+}$  and  $\mathbf{3}^{2-}$  because a reduced  $\eta$  (compared to the optimal solvent mixture) simplifies the reordering of all components. However, the decrease in proton signal intensity of  $\approx 61\%$  for DMSO:gly:NMPA, which possesses a similar dynamic viscosity as DMSO:gly:H<sub>2</sub>O, cannot be explained by this macroscopic parameter. The altered dipolar/hydrogen bonding network with NMPA, which affects the solvation shell in the direct vicinity of Fremy's salt, seems to improve the preferential DMSO solvation of the multicationic box.

### 8.3.3. Analyzing the incorporation of (partially) deuterated solvent compounds

#### Review formation of globular ionoids with DLS

Before we discuss the initial state for the formation of globular ionoids in model system  $\mathbf{1}^{4+}:\mathbf{2}^{2-}$  ( $\mathbf{1}^{4+}:\mathbf{3}^{2-}$ , respectively) with molar ratio 1:3, we have to check if the self-assembled entities are still present after the ten-day incubation period when using deuterated solvent mixtures. Therefore, we performed DLS measurements, whereas Fig. 8.5 summarizes the recorded intensity time correlation functions at day ten for both side and back scattering.

The solvent mixtures DMSO:gly:D<sub>2</sub>O as well as d6-DMSO:gly:H<sub>2</sub>O present similar autocorrelation functions compared to the reference setup with just proton nuclei. The respective particle size distributions (see Fig. F.4 in Appendix F) indicate the build up of monodisperse, spherical structures that fall under the category of globular ionoids. This is not the case for the solvent mixtures DMSO:d5-gly:H<sub>2</sub>O and DMSO:d3-gly:D<sub>2</sub>O. Here, the established combination of cationic and anionic building unit does not present well-defined autocorrelation functions after the incubation period of ten days, indicating the absence of colloid-like ionic clusters. Note that both exchanging the protons in the carbon backbone of glycerol (d5-gly) and modifying all hydrogen-bonds to deuterium-bonds (d3-gly:D<sub>2</sub>O) prevent the formation of the self-assembled entities. Macroscopic parameters, like the dynamic viscosity  $\eta$  are just minorly different (as shown in Table F.3) and cannot explain the drastic change for the io-

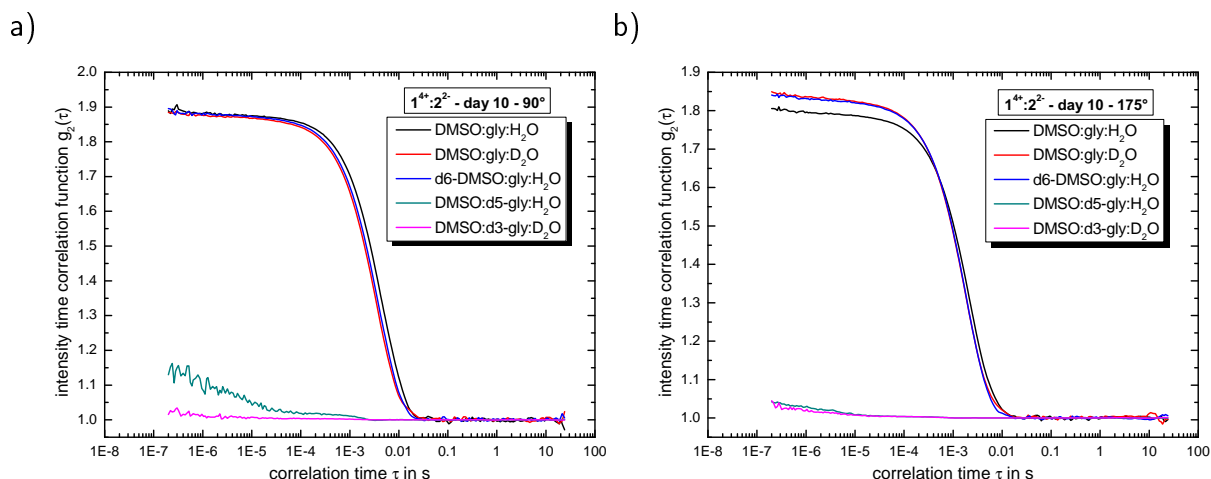


Fig. 8.5.: Comparison of intensity time correlation functions of system  $1^{4+}:2^{2-}$  molar ratio 1:3 in all tested deuterated solvent mixtures at a) side and b) back scattering.

nic self-assembly process inside the solvent mixtures incorporating deuterated glycerol. One possible explanation is based on an altered dipole network for DMSO:d5-gly:H<sub>2</sub>O or rather an altered hydrogen bonding network for DMSO:d3-gly:D<sub>2</sub>O. To further examine the interaction behavior of cationic and anionic component, especially in the crucial initial phase of the self-assembly process, we performed CW EPR experiments at 20 °C.

### Summary of the CW EPR spectroscopy measurements

Fig. 8.6 provides CW EPR spectra at X- and Q-band frequencies for pure Fremy's salt and with the 'Texas-sized molecular box' (molar ratio 1:3) in d6-DMSO:gly:H<sub>2</sub>O and DMSO:d5-gly:H<sub>2</sub>O. We summarized the respective spectra for the remaining solvent mixtures in Appendix F (see Fig. F.5). A rather drastic difference can be detected in the presented Q-band spectra for system  $1^{4+}:3^{2-}$ , which highlight the interactions in the local environment of Fremy's salt.<sup>66</sup> In d6-DMSO:gly:H<sub>2</sub>O, we recognize a strongly reduced rotational correlation time  $\tau_c$  and a pronounced line broadening due to electrostatic interactions between cationic and EPR-active anionic building unit. Both phenomena are less pronounced in the solvent mixture DMSO:d5-gly:H<sub>2</sub>O, indicating a reduced interaction force for both ionic compounds that could alter the ensuing ionic self-assembly process. Because of the initial focus of this chapter to study the solvation behavior in the ion cloud state, the measurements at 20 °C will not be discussed in detail. However, we want to shortly point out the low temperature CW Q-band measurements (similar to Chapter 7), which are used to read out the EPR parameters  $g_{xx}$  and  $A_{zz}$  that can characterize the proticity and polarity, respectively, of the local environment of the nitroxide radical.<sup>172,204</sup>

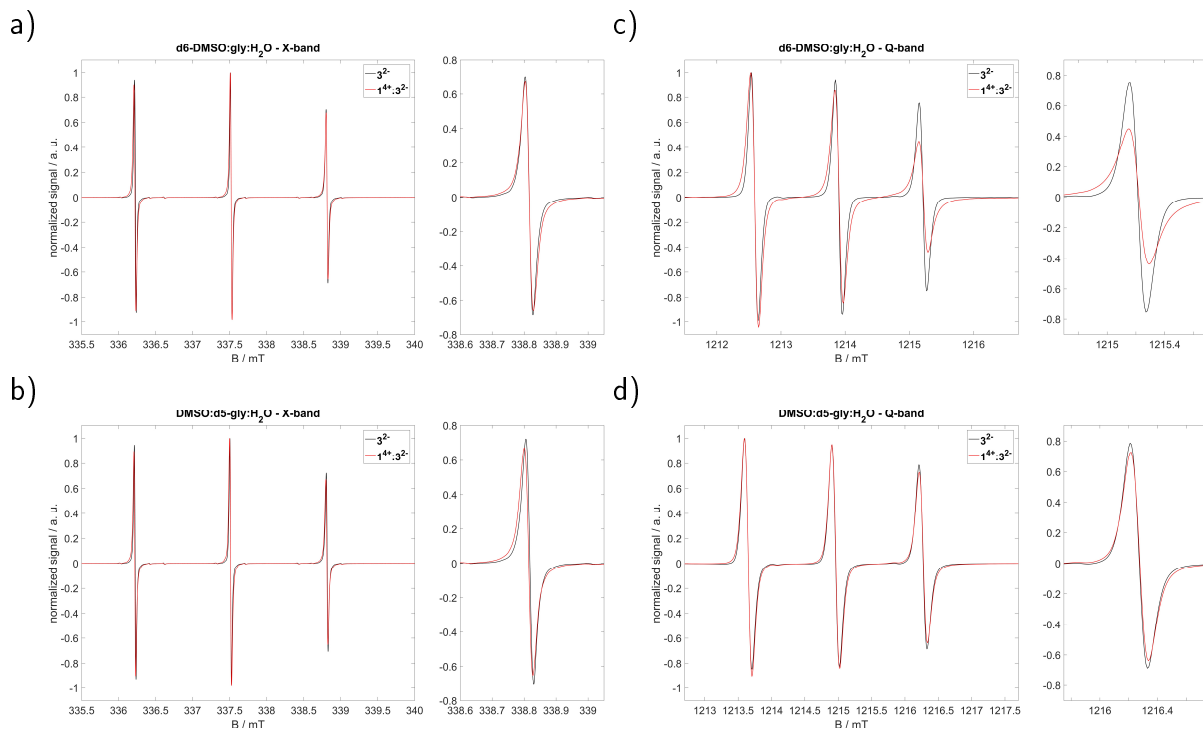


Fig. 8.6.: a), b) X-band and c), d) Q-band CW EPR spectra of pure Frey's salt and  $14^+ : 32^-$  with molar ratios 1:3 in d6-DMSO:gly:H<sub>2</sub>O (a) and c)) and DMSO:d5-gly:H<sub>2</sub>O (b) and d)). The highfield peak of the spectra is shown separately right next to the full spectra.

Fig. 8.7 highlights the respective CW Q-band spectra at 150 K for pure Frey's salt in all tested deuterated solvent mixtures. In general, we detect a shift to higher  $g_{xx}$  compared to the fully protonated solvent mixture of roughly  $\approx 1 \times 10^{-4}$ , which indicates a weakened hydrogen bonding network. The only exception for this effect applies to the system containing d6-DMSO, where the shift is slightly less pronounced ( $\approx 5 \times 10^{-5}$ ) due to the fact that DMSO itself 'just' operates as hydrogen bonding acceptor. Note that the substitution of 7 vol% water shows a similar (or slightly more pronounced) change in the hydrogen bonding network compared to the substitution of 50 vol% DMSO, again highlighting the importance of water inside the solvent mixture. However, we have to keep in mind that H/D exchange between glycerol and D<sub>2</sub>O is possible, so it is more accurate to assume a rather homogeneous distribution of deuterium nuclei inside the glycerol:water region for the solvent mixture DMSO:gly:D<sub>2</sub>O.

By adding the  $14^+$  (as shown in Fig. F.7 in Appendix F), we do not detect significant changes for the EPR parameters  $g_{xx}$  and  $A_{zz}$ , presenting a similar behavior compared to the fully protonated solvent mixture. Therefore, we can conclude that no drastic changes in the direct solvation shell of Frey's salt are visible, even when deuterated solvent components are incorporated. To study the outer solvation shell, we perform pulsed EPR spectroscopy as introduced for the solvent mixtures, which selectively substitute DMSO, glycerol and water.

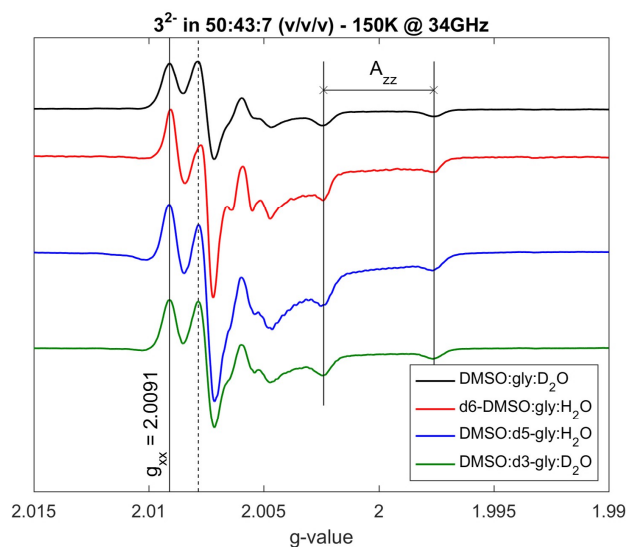


Fig. 8.7.: CW Q-band spectra at 150K for  $3^{2-}$  3mM in all tested deuterated solvent mixtures. The inserted black lines highlight the position of  $g_{xx}$  as well as  $A_{zz}$  in relation to DMSO:gly:D<sub>2</sub>O 50:43:7 (v/v/v).

### Summary of the pulsed EPR spectroscopy measurements

As starting point, we measured the echo-detected field sweep spectra at 50 K for pure Fremy's salt and system  $1^{4+}:3^{2-}$  with molar ratios 1:3 in all tested deuterated solvent mixtures (see Fig. F.8 in Appendix F). Similar to the fully protonated solvent mixture DMSO:gly:H<sub>2</sub>O, we can detect strong dipolar couplings between the cationic and anionic building unit in all setups, which is contrary to the low temperature CW EPR Q-band spectra (see asterisks in Fig. F.8). Note that the advantage of the echo-detected field sweep is the direct recording of the absorption spectrum, which improves detecting very flat sections in CW EPR measurements. These sections are often hard to analyze against an existing baseline drift.<sup>53</sup> The following ESEEM measurements are again performed with the B-field positions that represent the maximum of the respective echo-detected field sweep spectra.

Fig. 8.8 a) contains the primary 2p-ESEEM time traces for pure Fremy's salt in all four tested deuterated solvent mixtures. Besides the solvent mixture d6-DMSO:gly:H<sub>2</sub>O, which presents a delayed stretched-exponential decay (corresponding to a much larger phase memory time<sup>a</sup>), show all samples the same progress. Based on the solvent compounds containing deuterium nuclei and their amount in the final mixture, we detect more or less strongly pronounced deuterium modulations overlaying the stretched-exponential decay. For the solvent mixture containing d6-DMSO to provide the displayed pronounced modulations, the former methyl groups of the organic solvent have to dominate the fluctuations of the hyperfine field at

<sup>a</sup> This behavior could be expected due to the decreased line width for the echo-detected field sweep spectrum.

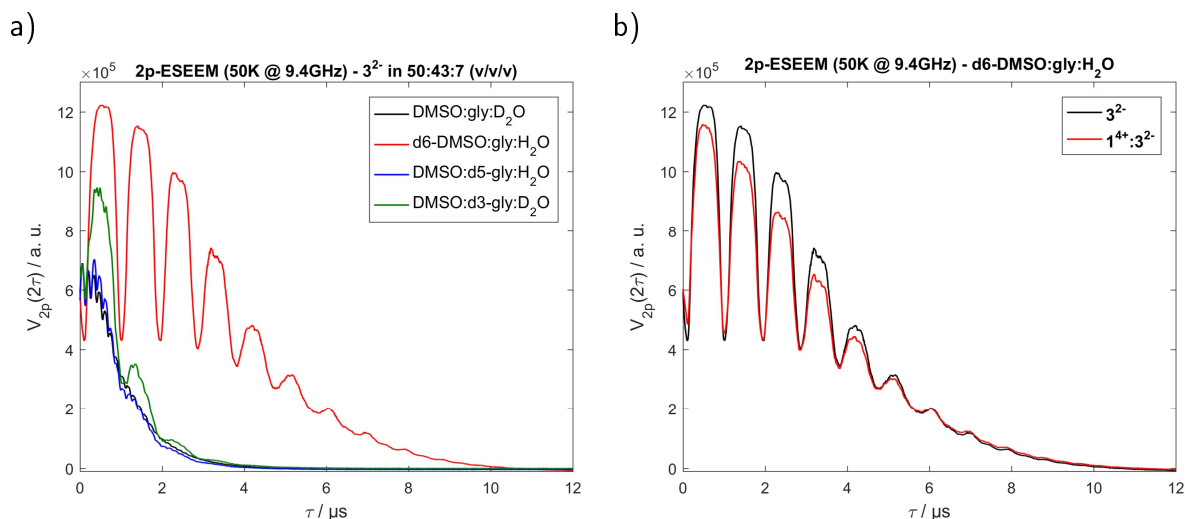


Fig. 8.8.: a) Comparison of the primary 2p-ESEEM data of pure Fremy's salt in all four highlighted deuterated solvent mixtures. b) Comparison of the primary 2p-ESEEM data of  $3^{2-}$  and system  $1^{4+}:3^{2-}$  in solvent mixture d6-DMSO:gly:H<sub>2</sub>O 50:43:7 (v/v/v).

the electron spin. The strength of the modulation patterns will be further analyzed by the 3p-ESEEM measurements.

By adding the  $1^{4+}$  to the nitroxide radical, as exemplarily shown for solvent mixture d6-DMSO:gly:H<sub>2</sub>O (see Fig. 8.8), we do not observe significant changes for the recorded decay itself. This was also found for the solvent mixtures introduced in Chapter 7. Note that variations in the (deuterium) modulation depth are clearly visible, therefore a more refined analysis with the 3p-ESEEM measurements seems reasonable.

Fig. 8.9 combines the already mentioned 3p-ESEEM results for all four deuterated solvent mixtures with  $\tau = 176$  ns, again highlighting the frequency domain data, whereas the normalized nuclear modulation functions are displayed as inlay. At first, we want to focus on the intensity of the matrix peaks inside the magnitude spectra, which are dominated by the signals correlating to the proton nuclear frequency (14 MHz) and the deuterium nuclear frequency (2 MHz). By adding the 'Texas-sized molecular box', variations in the signal intensities for both matrix peaks are visible, whereas the solvent mixtures can be divided into three different categories:

1. General increase in signal intensity - DMSO:gly:D<sub>2</sub>O and DMSO:d5-gly:H<sub>2</sub>O
2. General decrease in signal intensity - d6-DMSO:gly:H<sub>2</sub>O
3. Mixed behavior - DMSO:d3-gly:D<sub>2</sub>O.

For solvent mixture DMSO:d3-gly:D<sub>2</sub>O the intensity by the proton nuclear frequency rises by  $\approx 25\%$ , whereas the respective deuterium signal decreases by the same percentage value. This behavior fits nicely with the results for system DMSO:d5-gly:H<sub>2</sub>O, which contains glycerol

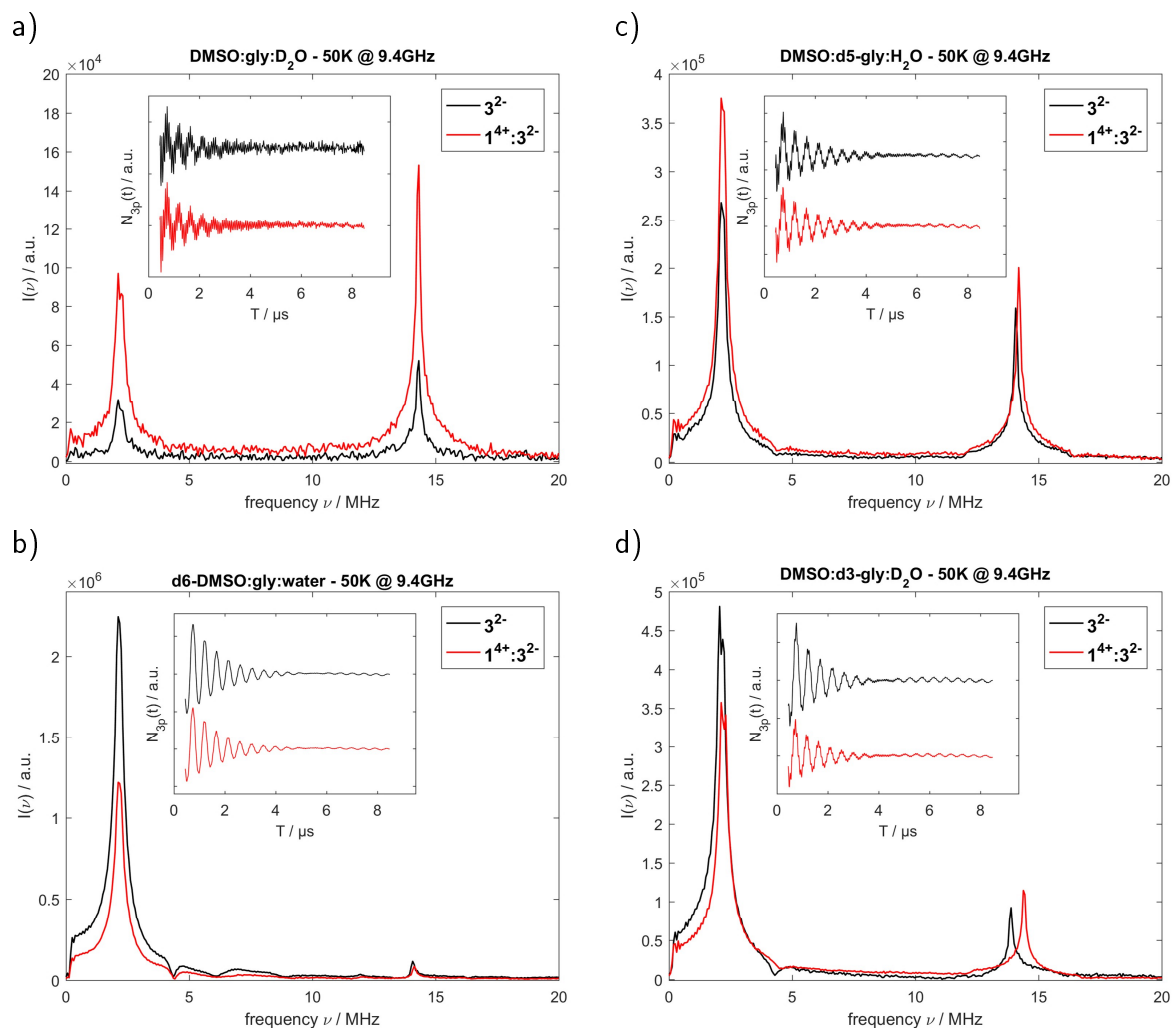


Fig. 8.9.: 3p-ESEEM frequency domain data  $I(\nu)$  at 50 K for  $3^{2-}$  3 mM and  $1^{4+}:3^{2-}$  molar ratio 1:3 in a) DMSO:gly:D<sub>2</sub>O, b) d6-DMSO:gly:H<sub>2</sub>O, c) DMSO:d5-gly:H<sub>2</sub>O and d) DMSO:d3-gly:D<sub>2</sub>O. All graphs contain the respective normalized time domain data as inlay.

that is only deuterated at the carbon backbone. Here, the deuterium matrix peak increases by roughly 35% and the proton signal again by  $\approx 25\%$ .

By combining the trends for the matrix peaks in all deuterated solvent mixtures, we can conclude that Frey's salt is initially surrounded by all solvent compounds, whereas DMSO seems to dominate the outer solvation sphere. Inserting  $1^{4+}$  ions into the setup ensures that DMSO gets partially pulled out of the solvation shell. Therefore, more glycerol and water molecules tend to surround the nitroxide radical inside the initial ion cloud state. To back up the results based on the magnitude spectra, we compare the modulation depths  $k_D^b$  from the deuterium modulations for pure Frey's salt and the  $1^{4+}:3^{2-}$  system, which were calculated

<sup>b</sup> The introduced index for  $k$  ( $k_D$ ) helps clarifying that we analyze deuterium modulations.

based on the descriptions in Appendix A. The results are summarized in Table 8.1.

**Table 8.1.:** Summary of the determined modulation depths  $k_D$  for pure Fremy's salt and system  $\mathbf{1}^{4+}:\mathbf{3}^{2-}$  (molar ratio 1:3) based on the 3p-ESEEM measurements at 50 K for all deuterated solvent mixtures

solvent	$k_D (\mathbf{3}^{2-})$	$k_D (\mathbf{1}^{4+}:\mathbf{3}^{2-})$
DMSO:gly:D <sub>2</sub> O	0.031	0.039
d6-DMSO:gly:H <sub>2</sub> O	0.612	0.500
DMSO:d5-gly:H <sub>2</sub> O	0.088	0.089
DMSO:g3-gly:D <sub>2</sub> O	0.244	0.150

The performed 3p-ESEEM measurements with an interpulse delay of 136 ns show a similar behavior for the stretched-exponential decay as well as the determined magnitude spectra and modulation depths. Note that this  $\tau$ -value represents a blind spot for the proton nuclear frequency, meaning that the recorded primary data is only influenced by the surrounded deuterium nuclei.

## 8.4. Conclusion

Our performed pulsed EPR studies regarding the solvation behavior of the anionic compound (the dianion of Fremy's salt) in the initial ion cloud state for well-defined, self-assembled entities support and extend the previous studies. Especially 3p-ESEEM emphasized itself as useful technique to analyze the outer solvation shell of compound  $\mathbf{3}^{2-}$ . Further studies are planned, which contain an even more quantitative approach for analyzing the primary 3p-ESEEM data sets as well as refining them with other pulsed techniques. For the first aspect, we attempt to perform the so-called *ratio analysis* method developed by Ichikawa and coworkers<sup>218</sup> to determine the number and distance of nuclear spins in the direct vicinity of the observed electron spin. The second point can be achieved by using the electron nuclear double resonance (ENDOR) technique, which is often described as counterpart to ESEEM. Here, useful information on strongly coupled nuclei (like those in the inner coordination sphere of the electron spin)<sup>216</sup> can be derived through the excitation of EPR and NMR transitions by microwave and radiofrequency irradiation, respectively.<sup>219</sup>

One major finding based on the applied pulsed EPR spectroscopy is the almost instant adaption of the outer solvation shell of Fremy's salt after adding the  $\mathbf{1}^{4+}$ . This could be detected for the solvent mixture with selective substituted and included deuterated solvent compounds. Note that macroscopic parameters such as the dynamic viscosity  $\eta$  as well as altered nanoscopic



features (like the present dipolar/hydrogen bonding network) can affect the change of Frey's salt's solvation shell. For pure  $3^{2-}$  in solution, its solvation shell contains all constituents of the established mixture with DMSO, glycerol and water, presumably in their respective bulk ratios. The aprotic polar component with its volume ratio of 50% dominates the fluctuations of the hyperfine field at the electron spin, which could be visualized by the solvent mixtures DMF:gly:H<sub>2</sub>O and d6-DMSO:gly:H<sub>2</sub>O. After adding the multicationic box, DMSO preferential dissolves this ionic building unit and partially 'disappears' from the outer solvation shell of Frey's salt. In return, the nitroxide radical gets surrounded by a more glycerol:water-rich phase. Note that based on the results of DMSO:d5-gly:H<sub>2</sub>O and DMSO:d3-gly:D<sub>2</sub>O the glycerol seems to prefer a specific orientation towards  $3^{2-}$ : the hydroxyl-groups tend to turn away from the location of the observable electron spin, whereas the protons from the carbon backbone phase this direction. The 7 vol% water inside the total solvent mixture appear to help with the selective orientation of glycerol.

The described solvation behavior for system  $1^{4+}:3^{2-}$  ( $1^{4+}:2^{2-}$ , respectively) with a molar ratio of 1:3 represents the first study focusing on the initial ion cloud state and its role in the complete ionic self-assembly process for colloid-like ionic clusters in solution. Following experiments should analyze the effect of changing the molar ratio in the range of 1:3 to 5:6, which allows the formation of at least anisotropic ionic cluster. Furthermore, studies examine the solvation behavior throughout the entire incubation period of ten days are needed to unravel the reason for this extended formation process. At last, directly applying EPR spectroscopy for globular ionoids as well as anisotropic ionic clusters would definitely help in characterizing these soft, yet well-defined structures in solution.



# 9 | Survival and Induced Formation of colloid-like ionic clusters in solution

Chapter 9, which represents the final chapter of this thesis, possesses a different structure compared to the previous ones. Here, a variety of commenced and unpublished investigations with noteworthy results will be highlighted, which still need additional data to verify their meaningfulness. One can interpret this chapter as 'Outlook' for the research of colloid-like ionic clusters in solution and its potential for further studies.

The main theme of Chapter 9 is based on the idea to induce the formation of globular ionoids, meaning that one can skip the ten-day incubation period and still receive well-defined and stable self-assembled entities. The two tested methods are thermally-induced and electrophoretic-induced globular ionoids. Regarding the temperature tests we also checked the resistance of already developed colloid-like ionic clusters against this external parameter.

Another aspect, which will be addressed in Chapter 9, refers to the usage of EPR spectroscopy after the ten-day incubation period. The starting point constitutes the system of 'Texas-sized molecular box' and methanedisulfonate, where one purposefully adjusted the concentration ratio for the  $1^{4+}:2^{2-}$  system. Here, the now partially 'missing' anionic compound (compared to the established molar ratio 1:3) gets replaced with the EPR-active Fremy's salt after the incubation period of ten days. We hope that the  $3^{2-}$  ions migrate into the already formed self-assembled entities and allow measurements of globular ionoids. Note that reference measurements with DLS are needed to determine the size and shape of the 'incomplete'  $1^{4+}:2^{2-}$  system. If this approach can be carried out reliably, then we are able to compare the local structure inside the ion cloud state and the self-assembled globular ionoids.

## 9.1. Induced Ionoid Formation

As already mentioned, we tested two different methods to induce the formation of well-defined colloid-like ionic clusters: thermally-induced and electrophoretic-induced. For both methods the goal is to reduce or even skip the ten-day incubation period without altering the charac-

teristic features of globular ionoids.

## Thermally-induced Ionoid Formation

We performed the first test to thermally-induce the formation of globular ionoids for the system  $1^{4+}:2^{2-}$  ( $1^{4+}:3^{2-}$ , respectively) with molar ratio 1:3 in the optimal solvent mixture with the temperature ramp highlighted in Fig. 9.1 a). We went from 20 °C to 60 °C in 5 K steps, where a waiting period of 30 min at each temperature was introduced. Afterwards, a direct cool-down to 20 °C occurred<sup>a</sup>. DLS measurements after this cool-down present well-defined autocorrelation functions, as shown for the side scattering angle in Fig. 9.1 b).

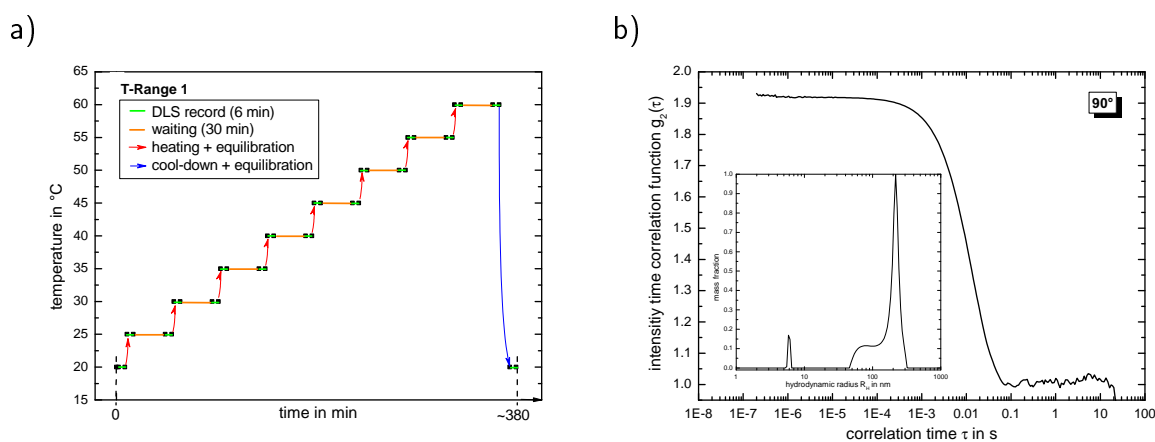


Fig. 9.1.: a) Schematic representation of the temperature ramp for thermally-induce ionoids.

b) Intensity time correlation function at side scattering for system  $1^{4+}:2^{2-}$  molar ratio 1:3 in DMSO:gly:H<sub>2</sub>O 50:43:7 (v/v/v) after cool-down. The respective particle size distribution is shown as inlay.

The particle size distribution displays a peak for smaller sized, self-assembled entities with a hydrodynamic radius of roughly 6 nm, which is in the range for globular ionoids. Note that the majority of the distribution correlates to a larger, more aggregated species. It seems that applying thermal energy to the system helps building up a pronounced autocorrelation function, but its amount was too high for solely crafting small self-assembled entities. The development of the mean scattering intensity over the complete temperature range (see Fig. 9.2) also visualizes the formation of rather aggregated species. For comparing the scattering intensities throughout the total temperature range, one used the reference measurement shown in Fig. G.1 of Appendix G to adjust the recorded values based on a fixed laser attenuation. With this we can determine an almost five times higher scattering intensity for system  $1^{4+}:2^{2-}$  after passing the temperature ramp.

<sup>a</sup> The heating and cooling of the sample was performed inside the quartz cell for the DLS measurements. The Litesizer 500 features a precise temperature control setup, which was used to adjust the respective temperature ramp.

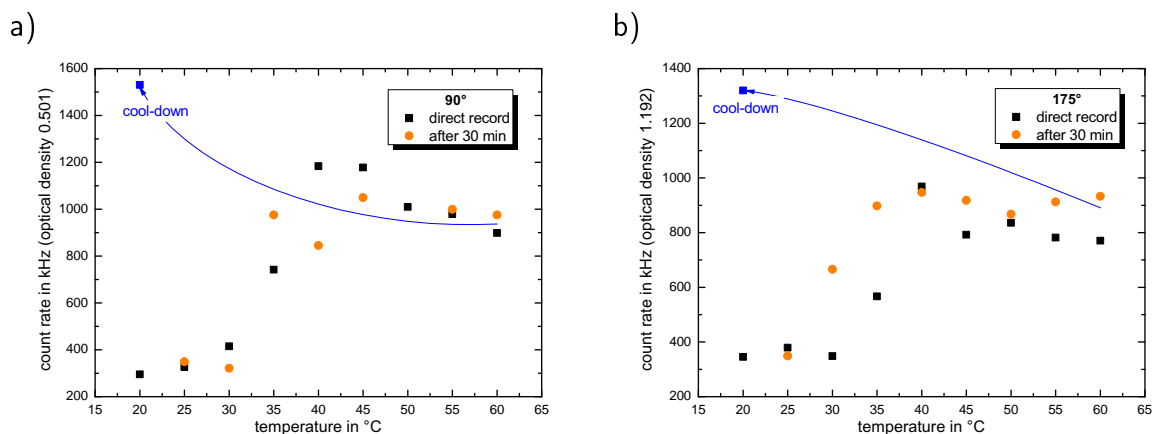


Fig. 9.2.: Development of the mean scattering intensities at a) side and b) back scattering for  $1^{4+}:2^{2-}$  molar ratio 1:3 in DMSO:gly:H<sub>2</sub>O 50:43:7 (v/v/v) at day 0.

In addition to the DLS measurements, we performed CW EPR spectroscopy studies utilizing a slightly adjusted temperature ramp for the system  $1^{4+}:3^{2-}$  molar ratio 1:3 in the established solvent mixture. Note that here we only could use the Miniscope MS5000 to measure at X-band frequencies, because the Q-band instrument is not capable of recording CW EPR spectra above room temperature. Based on the thermal stability of Frey's salt (see Fig. G.2 in Appendix G) inside the solvent mixture DMSO:gly:H<sub>2</sub>O, we removed the 30 min waiting period at each temperature step. Fig. 9.3 a) presents the CW EPR spectra for pure  $3^{2-}$  in the temperature range of 20 °C to 60 °C.

Pure Frey's salt displays a faster and more isotropic rotational mobility in DMSO:gly:H<sub>2</sub>O with increasing temperature. Note that the macroscopic dynamic viscosity  $\eta$  decreases with rising temperature, which favors this rotational behavior of  $3^{2-}$  ions. Another striking feature is the linear increase in the isotropic hyperfine coupling constant  $a_{iso}$  from 20 °C to 60 °C. This rather pronounced temperature dependency of  $a_{iso}$  was already discussed in other publications (see e. g. Ref. 220) and enables the use of Frey's salt as internal thermometer for EPR spectroscopy. After the sample was cooled down to 20 °C, we could still detect a pronounced CW EPR spectra with just minor deviations from the initially recorded spectra, as shown in Fig. 9.3 b). The overall signal intensity dropped by roughly 37%, which could be expected based on the performed stability tests with solely nitroxide radical in DMSO:gly:H<sub>2</sub>O 50:43:7 (v/v/v). Appendix G summarizes the simulation results for these measurements.

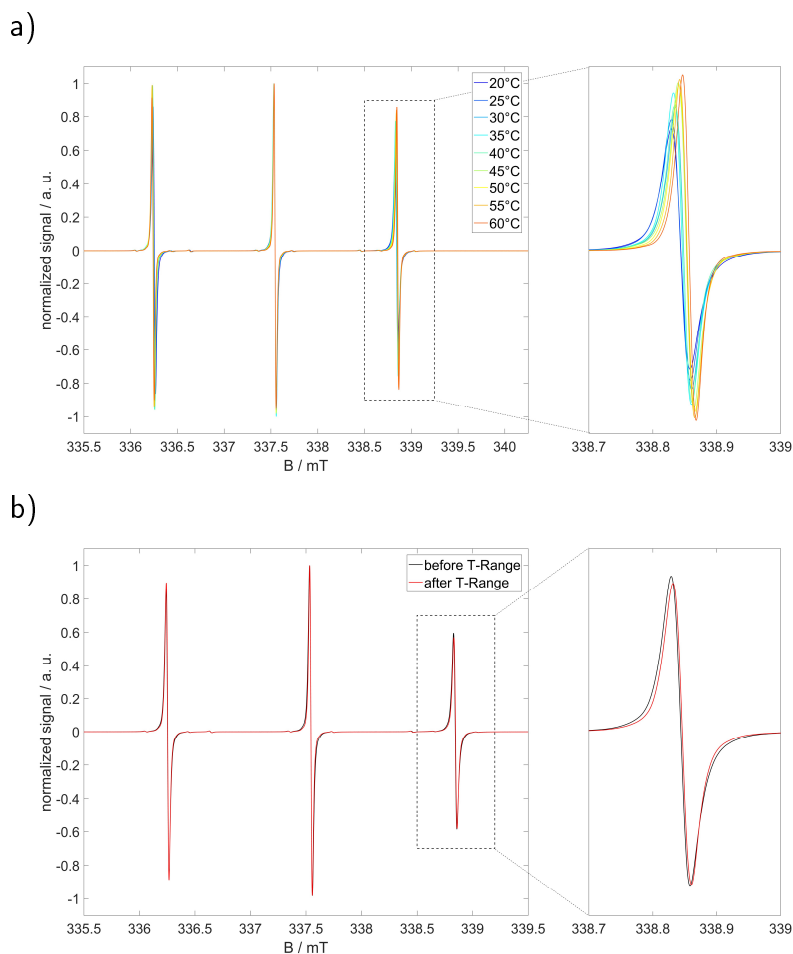


Fig. 9.3.: a) X-band CW EPR spectra of Frey's salt 3 mM for the temperature range of 20 °C to 60 °C. b) Comparison of Frey's salt 3mM at 20 °C before and after the temperature ramp.

Adding  $\mathbf{1}^{4+}$  to the Frey's salt for the final molar ratio of 1:3 and performing the same temperature dependent measurement as discussed for the pure nitroxide radical, we could record CW EPR spectra till 55 °C (see Fig. 9.4). At 60 °C the  $\mathbf{3}^{2-}$  was fully decomposed and not EPR-active anymore, leading to a not evaluable signal and we also could not record a spectrum after cooling down to 20 °C. The strong interactions between the cationic and anionic building unit seem to promote collisions between the Frey's salt dianions, which accelerate its decomposition inside the solution. Similar to the reference measurement with pure nitroxide radical, we can see an increase in the isotropic hyperfine coupling constant  $a_{iso}$ . The intensity of the highfield peak slightly increases till 40 °C, but starts to drop at higher temperatures. At the same temperature value, the line width of the recorded spectra decreases, indicating reduced electrostatic interactions between both building units.

Increasing the temperature inside the  $\mathbf{1}^{4+}:\mathbf{3}^{2-}$  system controls two mechanisms, which influence the recorded CW EPR spectra:

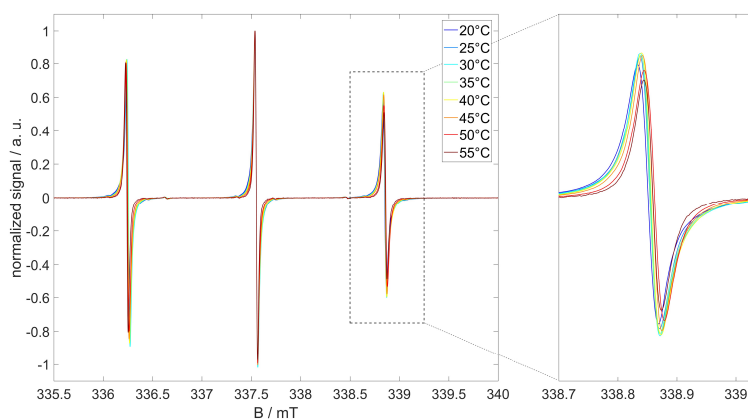


Fig. 9.4.: X-band CW EPR spectra of system  $1^{4+}:3^{2-}$  molar ratio 1:3 for the temperature range of 20 °C to 55 °C.

1. The decomposition of the radical species, which is accompanied with reducing the concentration of Fremy's salt as well as adjusting the molar ratio of 1:3. As described in Chapter 5, changing the molar ratio from 1:6 to 1:1 leads to a more 'fixed' coordination of  $3^{2-}$  and a reduced rotational mobility for the nitroxide radical.
2. The decrease of the dynamic viscosity  $\eta$  increases the rotational mobility of the anionic building unit as well as the translational diffusion coefficient of the ionic building units. The latter point also promotes collisions of nitroxide radicals and therefore their disproportionation.

At the beginning of the temperature ramp, both mechanisms compensate each other, which results in a rather stable line width for the CW EPR spectra. Above 40 °C, the thermal diffusion seems to dominate: the ionic building units move too fast inside the solution to reach a 'fixed' coordination, leading to a decreased line width. The simulation results for these measurements are again summarized in Appendix G. Besides applying a temperature ramp to thermally-induce the formation of globular ionoids, we tried to directly 'jump' to a fixed temperature, then perform a DLS measurement at side and back scattering and directly cool-down to 20 °C. For this method, three different temperatures were chosen: 1) 40 °C, 2) 60 °C and 3) 90 °C. Here, we just want to highlight the development of the intensity time correlation functions for system  $1^{4+}:2^{2-}$  molar ratio 1:3 after a temperature jump to 60 °C (see Fig. 9.5).

The autocorrelation functions do not show significant changes over the course of the first 14 days after performing the temperature jump. Note that we again receive a well-pronounced autocorrelation function at day 0, similar to the test with the respective temperature ramp. The hydrodynamic radius of the self-assembled entities is roughly 70 nm, which is smaller than the rather aggregated species from the first test, but they are still too big to classify

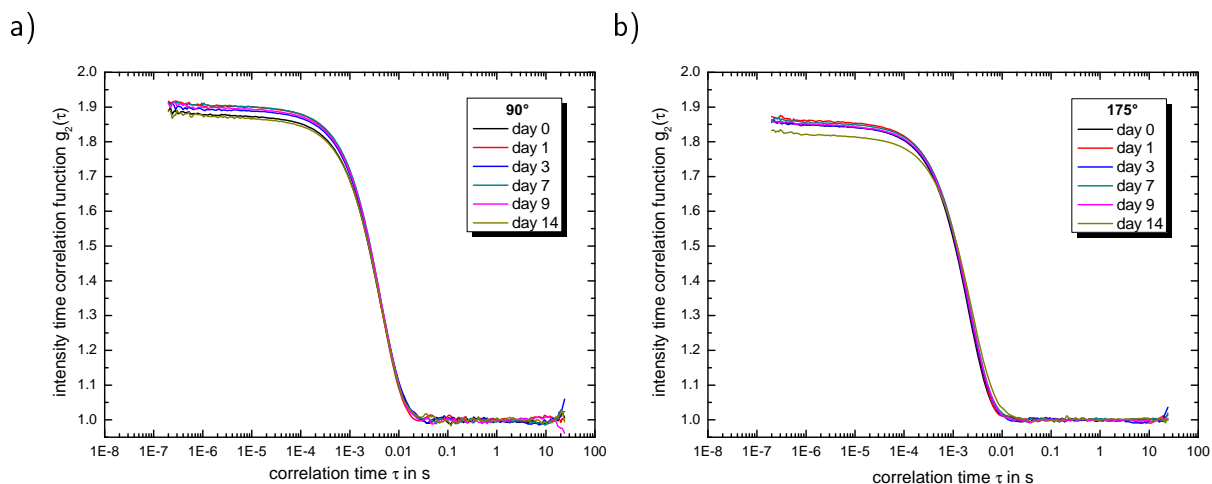


Fig. 9.5.: Development of the intensity time correlation functions at a) side and b) back scattering for the model system  $1^{4+}:2^{2-}$  after the temperature jump to  $60^\circ\text{C}$ .

them as globular ionoids. However, we can conclude that the thermal energy, which was incorporated into the system  $1^{4+}:2^{2-}$  through a temperature jump to  $60^\circ\text{C}$ , induced the formation of anisotropic ionic clusters in solution. The long-term stability of such thermally-induced structures as well as their resistance against mechanical stress (like filtration) was not tested yet. Furthermore, we have to clarify if the supply of thermal energy promotes a chemical reaction or altering of the ionic building units or not. Therefore, additional measurements like e. g. NMR or IR spectroscopy are needed to demonstrate that the present structures are formed based purely on a self-assembly process.

## Electrophoretic-induced Ionoid Formation

The stability of the self-assembled globular ionoids after the ten-day incubation period was already tested (see Chapter 6) by determine their zeta potential with cmPALS.<sup>94</sup> The system  $1^{4+}:2^{2-}$  with molar ratio 1:3 delivered a electrokinetic potential of  $66.5\text{ mV}$ , which is noticeably above the reference value of  $\pm 30\text{ mV}$  for highly stable nanoparticles. Now, we want to use the alternating electric field, which is applied for a cmPALS measurement, to induce the formation of small, yet defined structures in solution.

Therefore, we first systematically changed the strength of the applied electric field by adjusting the respective voltage value, whereas the measuring time was kept constant. The exact settings are listed below:

- Sample: system  $1^{4+}:2^{2-}$  molar ratio 1:3 in DMSO:gly:H<sub>2</sub>O 50:43:7 (v/v/v) at day 0
- Voltage: between  $40\text{ V}$  and  $15\text{ V}$ , varied in  $5\text{ V}$  steps
- Recording: three separate measurements with each one lasting for 200 runs.



To analyze a potential formation of self-assembled entities in solution, we performed DLS measurements directly after the cmPALS treatment. Table 9.1 summarizes the recorded electrophoretic mobility values  $\mu_e$  as well as calculated zeta potentials  $\zeta$  depending on the electric field strength/voltage value.

**Table 9.1.:** Summary of the electrophoretic mobility  $\mu_e$  and zeta potential  $\zeta$  based on the applied voltage value for system  $\mathbf{1}^{4+}:\mathbf{2}^{2-}$  molar ratio 1:3

voltage / V	$\mu_e / \frac{\mu\text{mcm}}{\text{Vs}}$	$\zeta^a / \text{mV}$
40	$0.0290 \pm 0.004$	$16.4 \pm 2.0$
35	$0.0408 \pm 0.002$	$22.4 \pm 1.2$
30	$0.0359 \pm 0.006$	$19.7 \pm 3.2$
25	$0.0417 \pm 0.003$	$22.9 \pm 1.5$
20	$0.0358 \pm 0.008$	$19.7 \pm 4.4$
15	$0.0385 \pm 0.005$	$20.4 \pm 2.3$

<sup>a</sup> calculating zeta potential using equation (A.3) with  $F(\kappa a) = 1.27$

We can recognize small fluctuations for  $\mu_e$  and  $\zeta$  probably due to the disordered nature of the initial ion cloud state, whereas no correlation between these slight variations and both mentioned parameters is visible. It seems that the chosen electric field strengths did not affect the directed movement of the ionic building units. Note that the determined zeta potential for system  $\mathbf{1}^{4+}:\mathbf{2}^{2-}$  is smaller than for the reference solution with pure  $\mathbf{1}^{4+}$  (see Table 6.3). The recorded intensity time correlation functions (see Fig. G.4) contain a large y-intercept value indicating the formation of self-assembled entities, but do not present drastical differences based on the applied voltage value. Therefore, we focus on the mean scattering intensities and the calculated hydrodynamic radii, which are both plotted in Fig. 9.6.

All tests to induce the formation of globular ionoids with cmPALS measurements led to an increase in the recorded scattering intensity, indicating the formation of partially defined nanostructures. The increase of the scattering intensity with a reduced electric field strength/voltage value indicates a more efficient transformation from the disordered ion cloud state to defined ionic clusters. The particle size distributions demonstrate for almost every test measurement two distinct peaks, one matching the size range of globular ionoids and one appearing at larger hydrodynamic radii. The latter one tends to shift to slightly higher values with decreasing electric field strength, which validates the progress of the mean scattering intensity. The applied voltages of 30 V and 35 V seem very promising to induce the self-assembly of globular ionoids because of the similar  $R_H$ -values at side and back scattering for the 'first'

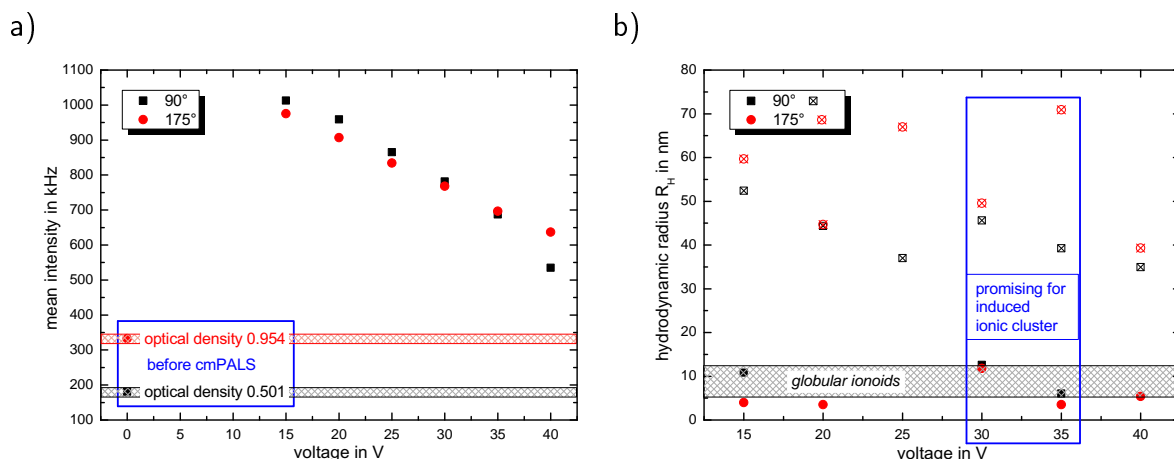


Fig. 9.6.: Comparison of the a) mean scattering intensity and b) hydrodynamic radius  $R_H$  for system  $1^{4+}:2^{2-}$  molar ratio 1:3 after cmPALS measurements depending on the applied electric field/voltage value.

peak of the particle size distribution, indicating a rather spherical shape for the self-assembled entities. The long-term stability of these partially formed colloid-like ionic clusters, which represents an important characteristic of these structures, is still under investigation. Preliminary tests with one sample treated with 30 V for the cmPALS measurement showed the build up of aggregated species over the course of two weeks (see Fig. G.5 in Appendix G). To prevent the formation of larger, less defined structures, we started to change the settings for the cmPALS method (regarding number of runs and number of repetitive measurements) to improve the number and stability of globular ionoids through the electrophoretic-induced technique. Besides analyzing the changes inside the initial ion cloud state after applying an alternating electric field with DLS, we performed CW EPR spectroscopy at X- and Q-band frequencies with system  $1^{4+}:3^{2-}$  molar ratio 1:3. Here, we limit the used electric field strengths to the voltage values of 40 V, 30 V and 20 V, whereas a reference sample of pure Fremy's salt 3 mM was also analyzed with the highest voltage value of 40 V.  $3^{2-}$  alone does not present drastical changes in its rotational mobility, as shown in Fig. G.6. Note that for X-band frequencies we measured in 10 min steps over the course of 50 min to estimate an accelerated decomposition of the nitroxide radical, especially in the  $1^{4+}:3^{2-}$  system. Table 9.2 summarizes the measured electrophoretic mobilities  $\mu_e$  as well as calculated zeta potentials for the system containing both ionic building units depending on the applied electric field strength. Compared to the established DLS system with  $2^{2-}$  as anionic building unit, we determine for  $1^{4+}:3^{2-}$  slightly lower values for both  $\mu_e$  and  $\zeta$ . One reason could be the higher electrophoretic mobility of Fremy's salt in respect to methanedisulfonate, which affects the movement of the 'Texas-sized molecular box' in the alternating electric field. Note that again we do not determine a change in the zeta potential by decreasing the voltage value for the electric field.

**Table 9.2.:** Summary of the electrophoretic mobility  $\mu_e$  and zeta potential  $\zeta$  based on the applied voltage value for pure  $\mathbf{3}^{2-}$  as well as for system  $\mathbf{1}^{4+}:\mathbf{3}^{2-}$  molar ratio 1:3

voltage / V	$\mu_e / \frac{\mu\text{mcm}}{\text{Vs}}$	$\zeta^a / \text{mV}$
$\mathbf{3}^{2-}$ - 40	$0.0138 \pm 0.0003$	$9.7 \pm 1.5$
40	$0.0335 \pm 0.002$	$18.4 \pm 1.3$
30	$0.0303 \pm 0.002$	$16.7 \pm 1.2$
20	$0.0305 \pm 0.001$	$16.8 \pm 1.0$

<sup>a</sup> calculating zeta potential using equation (A.3) with  $F(\kappa a) = 1.27$  for  $\mathbf{1}^{4+}:\mathbf{3}^{2-}$  and with  $F(\kappa a) = 1.00$  for  $\mathbf{3}^{2-}$

<sup>l</sup> counterion:  $\text{K}^+$

The recorded X- and Q-band CW EPR spectra after cmPALS treatment can be found in Fig. 9.7. Applying an alternating electric field in system  $\mathbf{1}^{4+}:\mathbf{3}^{2-}$  led to a decreased line width at X-band frequencies, indicating weakened electrostatic interactions between both ionic building units. Furthermore, we could detect a slightly higher rotational mobility for Fremy's salt based on the increase of the signal intensity for the highfield peak. This tendency is visible at both frequencies and gets more pronounced with decreased voltage value. Another feature that gets more pronounced with decreasing electric field strength is the decomposition of the nitroxide radical, as shown in Fig. G.7 in Appendix G. The alternating electric field seems to induce a rather persistent separation of cationic and anionic building unit, which could explain the less 'fixed' coordination/higher mobility of Fremy's salt as well as its faster disproportionation. It is also possible that the solvation shell in the direct vicinity of Fremy's salt and the 'Texas-sized molecular box' changes and affects the balance between electrostatic interactions and weaker noncovalent forces. To analyze a perchance altered solvation shell around Fremy's salt, one could perform CW Q-band measurements at low temperatures in combination with pulsed EPR spectroscopy, as carried out in Chapter 8.

In general, the electrophoretic-induced formation of globular ionoids could be a promising technique to shorten the incubation period for the respective self-assembled entities. However, we must improve the stability of such crafted colloid-like clusters, before applying the technique for over systems capable of building up well-defined structures in solution.

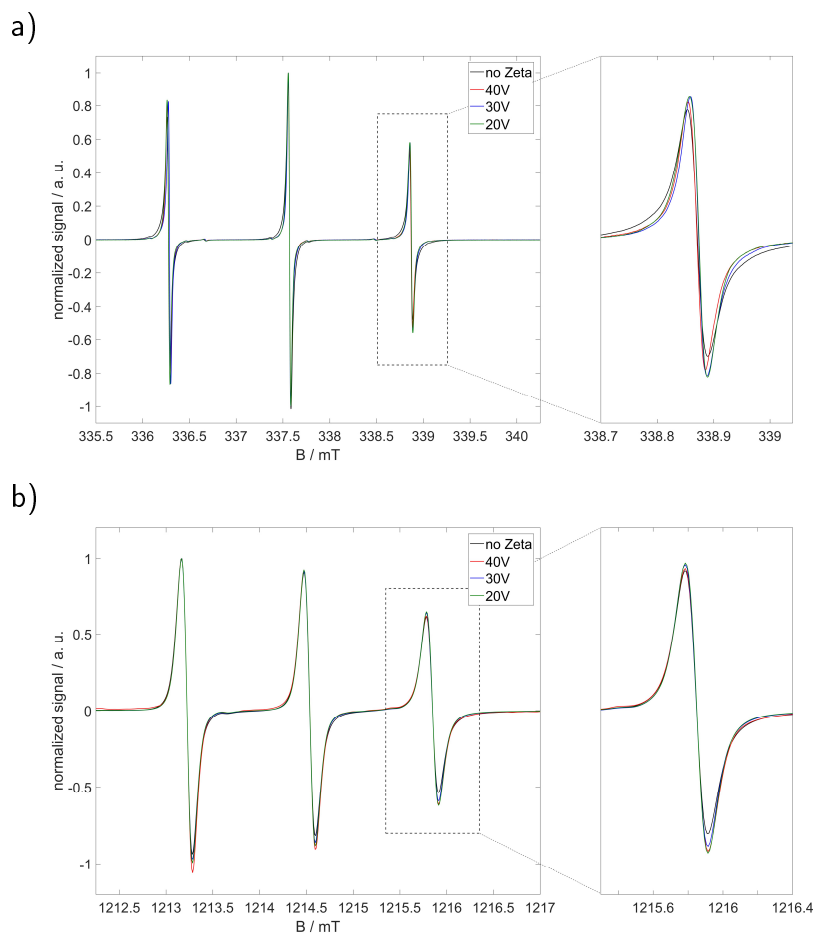


Fig. 9.7.: Comparison of a) X-band and b) Q-band CW EPR spectra of system  $1^{4+}:3^{2-}$  molar ratio 1:3 after cmPALS treatment in respect to the applied voltage value. The spectra without cmPALS treatment (black lines) are shown as reference.

## 9.2. Thermal stability of globular ionoids

Inside the previous chapters, one already highlighted the stability of globular ionoids containing the ionic building units  $1^{4+}$  and  $2^{2-}$  against mechanical stress (see Chapter 5) and while applying an alternating electric field (see Chapter 6). In this section, we want to focus on the behavior of colloid-like ionic clusters while carrying out the temperature ramp from Fig. 9.1 a). The development of the intensity time correlation functions for both scattering angles throughout the temperatures of 20 °C to 60 °C is summarized as Fig. G.9 in Appendix G.

Throughout the temperature range, we recognize a constant shift for the autocorrelation functions to smaller correlation times. This shift coheres with the reducing dynamic viscosity  $\eta$  of the solvent mixture DMSO:gly:H<sub>2</sub>O 50:43:7 (v/v/v). Another feature starts occurring at temperatures surpassing 40 °C. Here, the before pronounced autocorrelation functions start to

decompose, which leads to reduced y-intercept values<sup>b</sup>. A similar behavior can be recognized for the mean scattering intensities, as shown in Fig. 9.8. Note that the mean scattering intensity already decreased at 35 °C, indicating the first changes in the structural arrangement for both ionic building units.

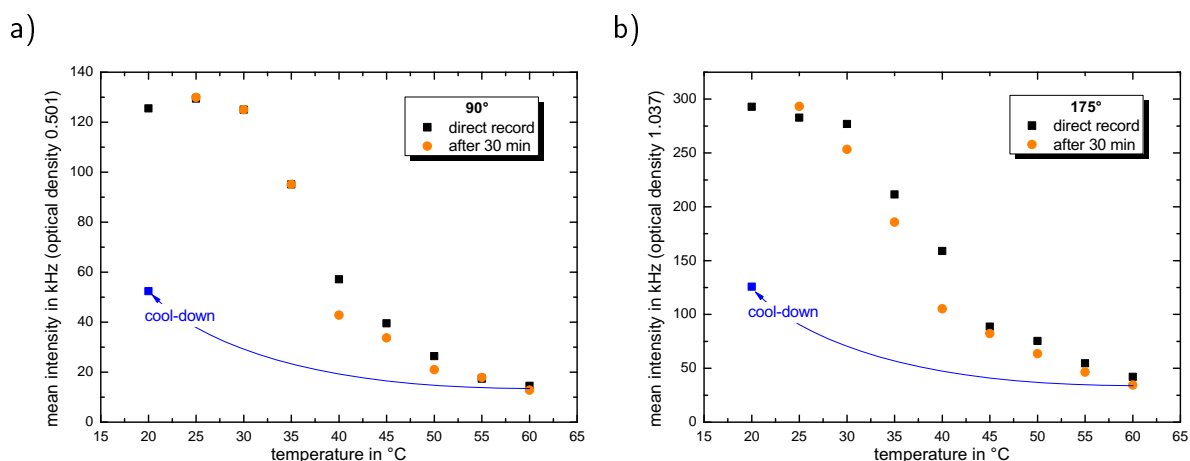


Fig. 9.8.: Development of the mean scattering intensities at a) side and b) back scattering for the model system  $1^{4+}:2^{2-}$  molar ratio 1:3 throughout the complete temperature ramp.

Both the decreased y-intercept value as well as the reduced mean scattering intensity indicate a partial decomposition or shrinking of the initial spherical globular ionoids. The cool-down to the starting temperature of 20 °C indicates, based on the data of the mean scattering intensity, a prorated recovery of the initial system. Fig. 9.9 presents the intensity time correlation functions as well as particle size distributions at 20 °C for system  $1^{4+}:2^{2-}$  molar ratio 1:3 before and after the respective temperature ramp.

The autocorrelation functions representing the model system after the temperature ramp show a reduced y-intercept value, but they almost regained their pronounced shape. Note that the time between the second measurement at 60 °C and the cooled-down 20 °C amounts to roughly ten minutes<sup>c</sup>. The fast recovery of system  $1^{4+}:2^{2-}$  can also be reviewed by the calculated particle size distributions: At both scattering angles a monodisperse distribution could be determined, whereas the maxima appear at slightly lower hydrodynamic radii compared to the former globular ionoids. This could be due to changes in the thickness of the solvation shell around the self-assembled entities, which affects the hydrodynamic radius. Furthermore,

<sup>b</sup> This is contrary to the temperature ramp tests performed directly after sample preparation (see previous section). The drastic difference between these two tests further backs up the idea of a transition from a disordered initial state to globular ionoids.

<sup>c</sup> Here, we only refer to the used equilibration time of the DLS measurement. With the required time to adjust the temperature as well as the optical setup, one has to add two to three minutes.

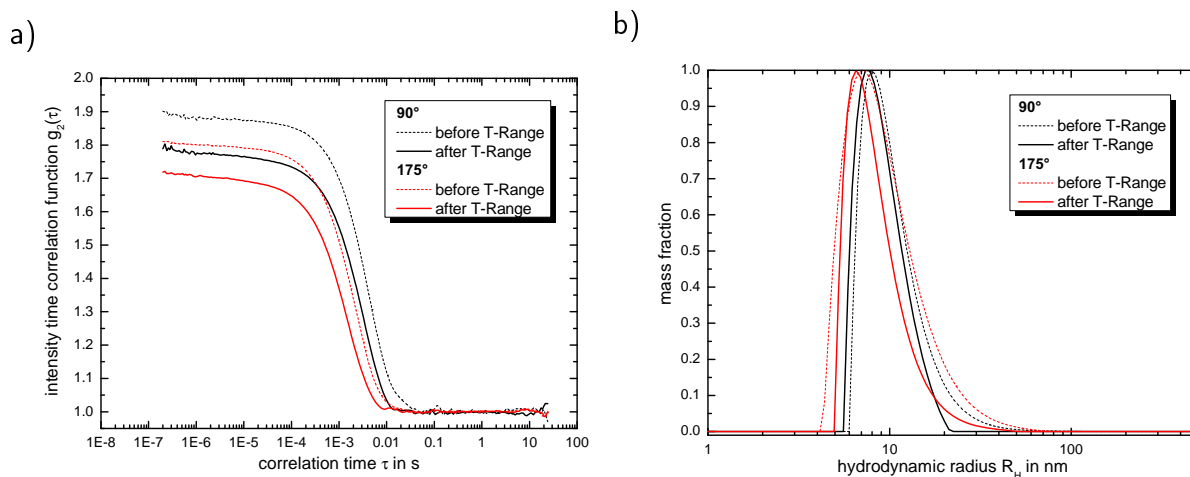


Fig. 9.9.: Comparison of the a) intensity time correlation functions and b) particle size distributions (at both scattering angles) for system  $1^{4+}:2^{2-}$  molar ratio 1:3 at  $20^\circ\text{C}$  before and after the temperature ramp.

we detect rather similar  $R_H$  values for  $90^\circ$  and  $175^\circ$ , indicating the recovery of more or less spherical structures.

At this point, the reason for the observed reversible break down and reordering of the presented soft, yet well-defined structures is not fully understood. Further investigations with other molar ratios of  $1^{4+}:2^{2-}$  and other experimental methods (like e. g. differential scanning calorimetry) are needed to unravel the presented phenomena.

### 9.3. Analyze globular ionoids with EPR spectroscopy

The previous chapters highlighted how EPR spectroscopy (as continuous wave or as pulsed technique) is capable in analyzing the disordered initial ion cloud state observed through the nitroxide radical Fremy's salt. However, studies with samples containing globular ionoids or anisotropic ionic clusters were not possible due to the fast disproportionation of  $3^{2-}$  compared to the long incubation period for colloid-like ionic clusters in solution.

To overcome this shortcoming, we thought about the following experiment: At first, a system containing  $1^{4+}$  and  $2^{2-}$  will be prepared with a concentration of 1.07 mM:2.79 mM. Compared to the model system with molar ratio 1:3, one intentionally reduces the amount of methanedisulfonate to prepare this sample<sup>d</sup>. This so called 'incomplete' mixture will run through the ten-day incubation period. At day ten, Fremy's salt will be added to create a mixture of  $1^{4+}:2^{2-}:3^{2-}$  with a final concentration ratio of 1.0 mM:2.6 mM:0.4 mM. Based on preliminary DLS measurements we can check if the Fremy's salt is migrating into the existing structures

<sup>d</sup> Instead of combining a 1:1 volume ratio of 2 mM  $1^{4+}$  and 6 mM  $2^{2-}$  solution, we reduced the volume for the anionic component.

build up with  $\mathbf{1}^{4+}$  and  $\mathbf{2}^{2-}$  and if such self-assembled entities are similar to the desired globular ionoids. As reference, the 'incomplete' mixture will be completed with methanedisulfonate to reach the respective  $\mathbf{1}^{4+}:\mathbf{2}^{2-}$  system with molar ratio 1:3. Fig. 9.10 presents the development of the intensity time correlation functions for the  $\mathbf{1}^{4+}:\mathbf{2}^{2-}:\mathbf{3}^{2-}$  mixture as well as the mentioned reference.

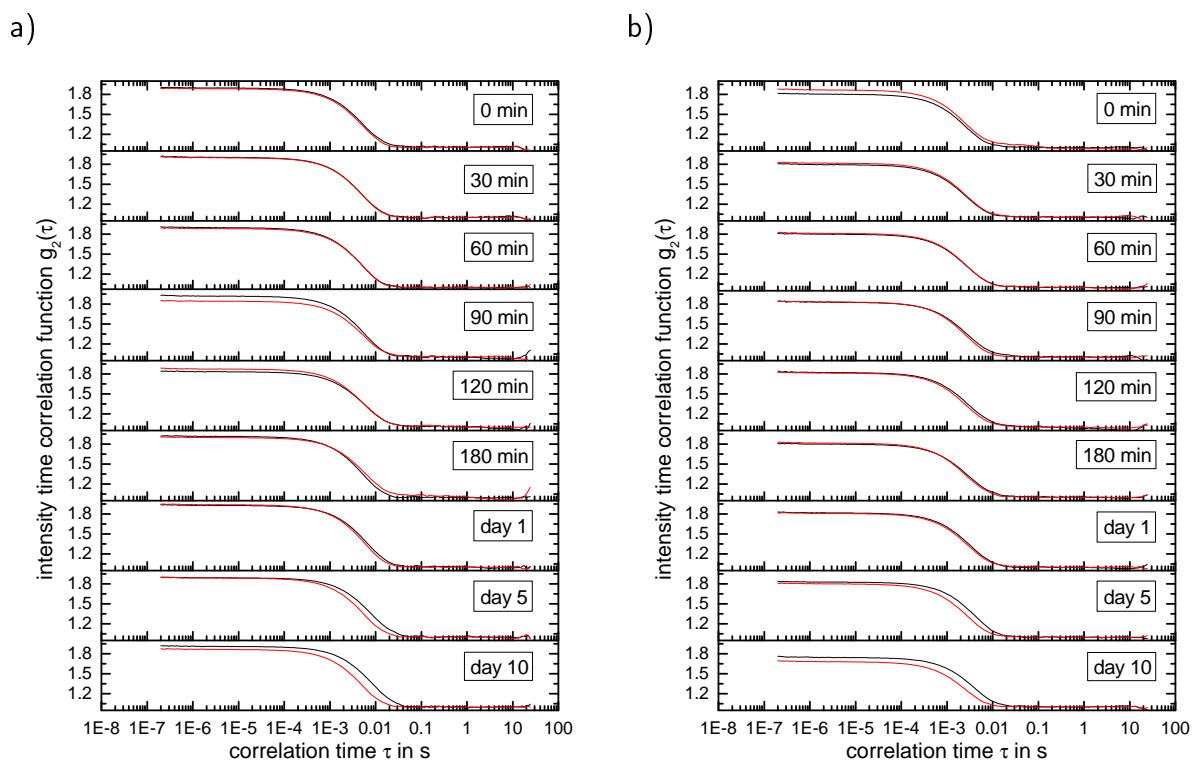


Fig. 9.10.: Development of the intensity time correlation functions at a) side and b) back scattering for the 'incomplete' system  $\mathbf{1}^{4+}:\mathbf{2}^{2-}$  after adding Frey's salt (black lines) and methanedisulfonate (red lines) after the incubation period of ten days.

Throughout the first three hours after adding the respective anionic building unit, no drastical differences could be detected between the  $\mathbf{1}^{4+}:\mathbf{2}^{2-}:\mathbf{3}^{2-}$  and the completed  $\mathbf{1}^{4+}:\mathbf{2}^{2-}$  system. Over the course of ten days, the system containing Frey's salt shows a shift for the auto-correlation functions to larger correlation times. The reason here could be the decomposition of the nitroxide radical, which induced the formation of enlarged and more shape anisotropic species. The calculated hydrodynamic radii are plotted against the measuring time in Fig. G.10 of Appendix G.

The completed  $\mathbf{1}^{4+}:\mathbf{2}^{2-}$  system presents at  $90^\circ$  directly after inserting the additional methanedisulfonate two distinct peaks in the particle size distribution, whereas one of them appears at roughly 5 nm. Note that this peak vanishes in the following measurements, indicating the absence of structures in this specific size range. However, throughout the first two hours the hydrodynamic radius for the completed  $\mathbf{1}^{4+}:\mathbf{2}^{2-}$  system jumps between 10 nm and 18 nm,

which indicates a rather dynamic structure where the position of ions seems interchangeable. After this initial phase, the size and shape of the self-assembled entities stays rather constant at roughly 14 nm. Adding Fremy's salt to the 'incomplete'  $1^{4+}:2^{2-}$  setup presents similar fluctuations of the hydrodynamic radius throughout the first two to three hours of measuring DLS. The following observations present an increase for the size of the self-assembled entities to roughly 20 nm. Note that added Fremy's salt and methanedisulfonate show in DLS the same behavior for the first two hours after inserting the respective anionic building unit, which backs up the basic idea of exchanging  $2^{2-}$  with  $3^{2-}$  for the already discussed results.

For the following CW EPR measurements, we focus on the first two hours after including the Fremy's salt into the 'incomplete'  $1^{4+}:2^{2-}$  system. As reference, the Fremy's salt was directly added after preparing the mixture of  $1^{4+}$  and  $2^{2-}$  (labeled with 'day 0'). At first the signal intensity of the X-band spectra was compared, as shown in Fig. G.11 of Appendix G. Including the nitroxide radical at 'day 0', presented a slowed-down decrease of the normalized signal intensity compared to the  $1^{4+}:3^{2-}$  system due to the reduced concentration of Fremy's salt, leading to fewer collisions which could promote the disproportionation of  $3^{2-}$ . Adding Fremy's salt after the ten-day incubation period shows an initial increase of the normalized signal intensity, which turns into a decay after 15 min. A possible reason for this trend could be the present self-assembled entities which direct the position of Fremy's salt or even its incorporation into these structures.

After focusing on the signal intensity, we analyze the X-band spectra for the prioritized 'day 10' system with  $1^{4+}:2^{2-}:3^{2-}$ . Over the course of two hours the recorded spectra did not present drastical differences. Therefore, Fig. 9.11 highlights selected CW EPR spectra for system  $1^{4+}:2^{2-}:3^{2-}$  'day 10' as well as for the internal 'day 0' reference.

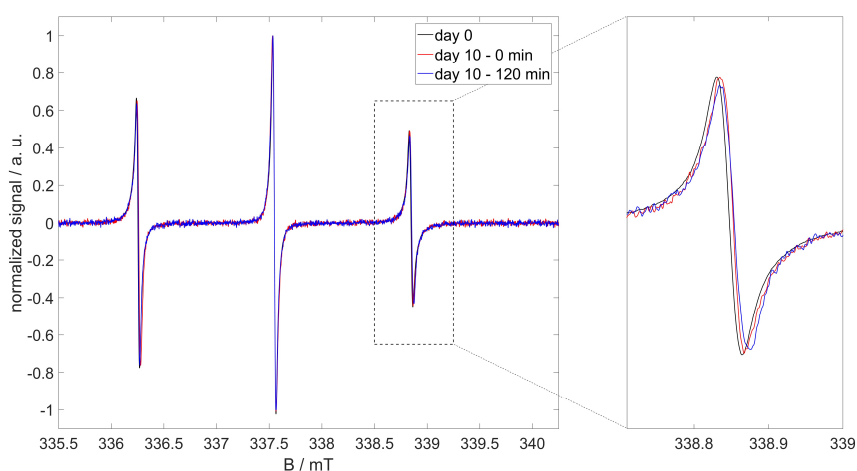


Fig. 9.11.: Comparison of the CW X-band spectra of 'incomplete'  $1^{4+}:2^{2-}$  system after the addition of Fremy's salt at 'day 0' and 'day 10'.

Due to the rather similar character of the X-band spectra, we went to Q-band frequencies



to reflect a different frequency/field dependence of the rotational time-frame. Again we have chosen selected CW EPR spectra throughout the initial two hours observation period, as shown in Fig. 9.12 a). Here, a slight increase in the intensity of the highfield peak as well as larger line widths could be detected for the  $1^{4+}:2^{2-}:3^{2-}$  setup, which introduced the Fremy's salt after the ten-day incubation period. Therefore, Fig. 9.12 b) displays the development of the rotational correlation time  $\tau_c$  for the fraction of freely rotating Fremy's salt and the line width of the CW Q-band spectra throughout the complete two hours observation period.

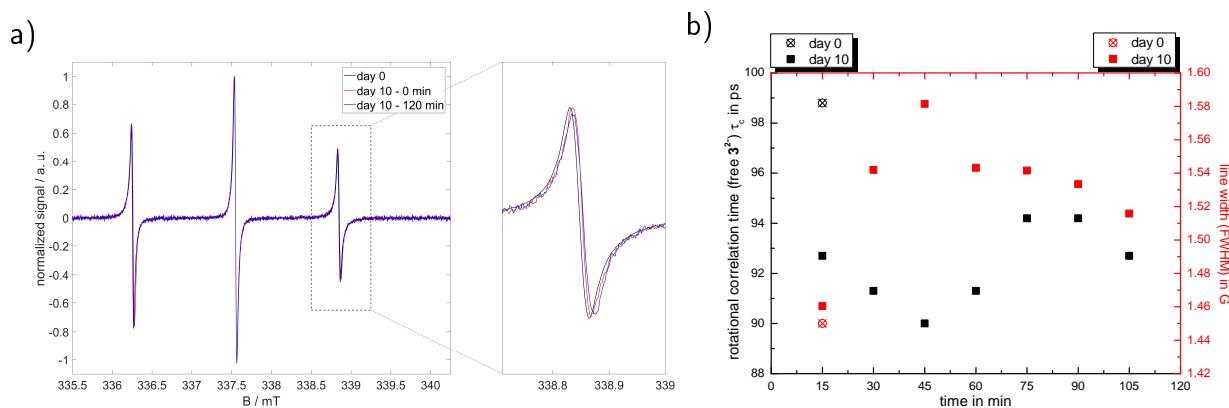


Fig. 9.12.: a) Comparison of the CW Q-band spectra of 'incomplete'  $1^{4+}:2^{2-}$  system after the addition of Fremy's salt at 'day 0' and 'day 10'. b) Development of the rotational correlation time  $\tau_c$  (for freely rotating nitroxide component) and line width of the recorded CW Q-band spectra of system  $1^{4+}:2^{2-}:3^{2-}$  'day 0' and 'day 10'.

The rotational correlation time  $\tau_c$  presents a rather fluctuating character, whereas the mean value for the mobile component of Fremy's salt is  $92 \text{ ps} \pm 2 \text{ ps}$ . Compared to the  $1^{4+}:2^{2-}:3^{2-}$  'day 0' system the  $\tau_c$ -value dropped rather drastically, indicating a different local environment for the nitroxide radical inside the 'day 10' setup. The change of the line width contains a specific time dependent behavior, which can be divided into two separate sections. Within the first 45 min, we observe an increase in the line width, implying stronger electrostatic interactions between the Fremy's salt and the 'Texas-sized molecular box'. It can be assumed that  $3^{2-}$  tries to enter the already existing self-assembled entities of  $1^{4+}:2^{2-}$  or it wants to switch positions with methanedisulfonate. After the first 45 min the line width reaches a more stable value, which is still significantly larger compared to its starting value or the result for the 'day 0' setup. It seems that the Fremy's salt found a preferable position inside the existing structures due to its endeavor to balance out electrostatic and weaker noncovalent forces. At this point, CW Q-band measurements at low temperatures as well as pulsed EPR spectroscopy studies are planned and already partially executed. Due to the time dependent variations of the line width for the Q-band spectra, we think about freeze-quenching the  $1^{4+}:2^{2-}:3^{2-}$  'day 10' setup at different times after adding the Fremy's salt. This should help in characterizing the rather dynamic construction between these ionic compounds.

## 9.4. Conclusion

The presented results in Chapter 9 display just a small portion of the performed measurements, which still need some refinement and further investigation to be fully understood. The first tests to induce the formation of globular ionoids result in either enlarged anisotropic ionic clusters (thermally-induced) or partially build up globular ionoids, which tend to aggregate to larger, less defined structures (electrophoretic-induced). Both applied techniques possess potential for improving the quality of the self-assembled entities. One way to estimate the right amount of thermal or electric energy to build up globular ionoids without the ten-day incubation period is to calculate the respective values based on the already performed measurements and use these as reference. The temperature dependent development of the small, yet well-defined structures from the discussed stability test with the model system  $\mathbf{1}^{4+}:\mathbf{2}^{2-}$  molar ratio 1:3 in DMSO:gly:H<sub>2</sub>O should also be taken into account for optimizing the process to induce the ionoid formation.

Regarding the aspect of using EPR spectroscopy to directly study the condition of globular ionoids, we established a very promising routine to include the respective nitroxide radical Fremy's salt. Note that the so called 'incomplete' setup of the  $\mathbf{1}^{4+}:\mathbf{2}^{2-}$  system has to experience the ten-day incubation period, before adding  $\mathbf{3}^{2-}$ . Because of the changed concentration ratio between the 'Texas-sized molecular box' and the methanedisulfonate, the self-assembled entities are slightly enlarged compared to the globular ionoids with a molar ratio of 1:3. However, the performed CW EPR spectroscopy measurements, especially the spectra at Q-band frequencies, present a drastical, time dependent change in their line width. These variations indicate a different local environment for the Fremy's salt compared to the normally studied  $\mathbf{1}^{4+}:\mathbf{3}^{2-}$  system with molar ratio 1:3 at 'day 0'. Based on the performed CW EPR measurements at 20 °C, we started to analyze the  $\mathbf{1}^{4+}:\mathbf{2}^{2-}:\mathbf{3}^{2-}$  system(s) at low temperatures with the Q-band spectrometer as well as with pulsed EPR spectroscopy. Additionally, one could try to change the amount of added Fremy's salt (and therefore the concentration ratio of the 'incomplete'  $\mathbf{1}^{4+}:\mathbf{2}^{2-}$  system) to receive self-assembled entities, which resemble the globular ionoids even better. The best solution would be to find a new system, which incorporates an EPR-active species that could be analyzed starting from the sample preparation day and throughout the complete incubation process.

## 9.5. Overall conclusion and Outlook

Fig. 9.13 gives a schematic summary of the performed studies for the formation of well-defined, colloid-like ionic clusters in solution, which were discussed throughout my complete PhD thesis. It highlights the tested 'design elements' for the complete ISA process, external

parameters which influence the ion cloud state as well as mentioned main themes with their respective chapter number.

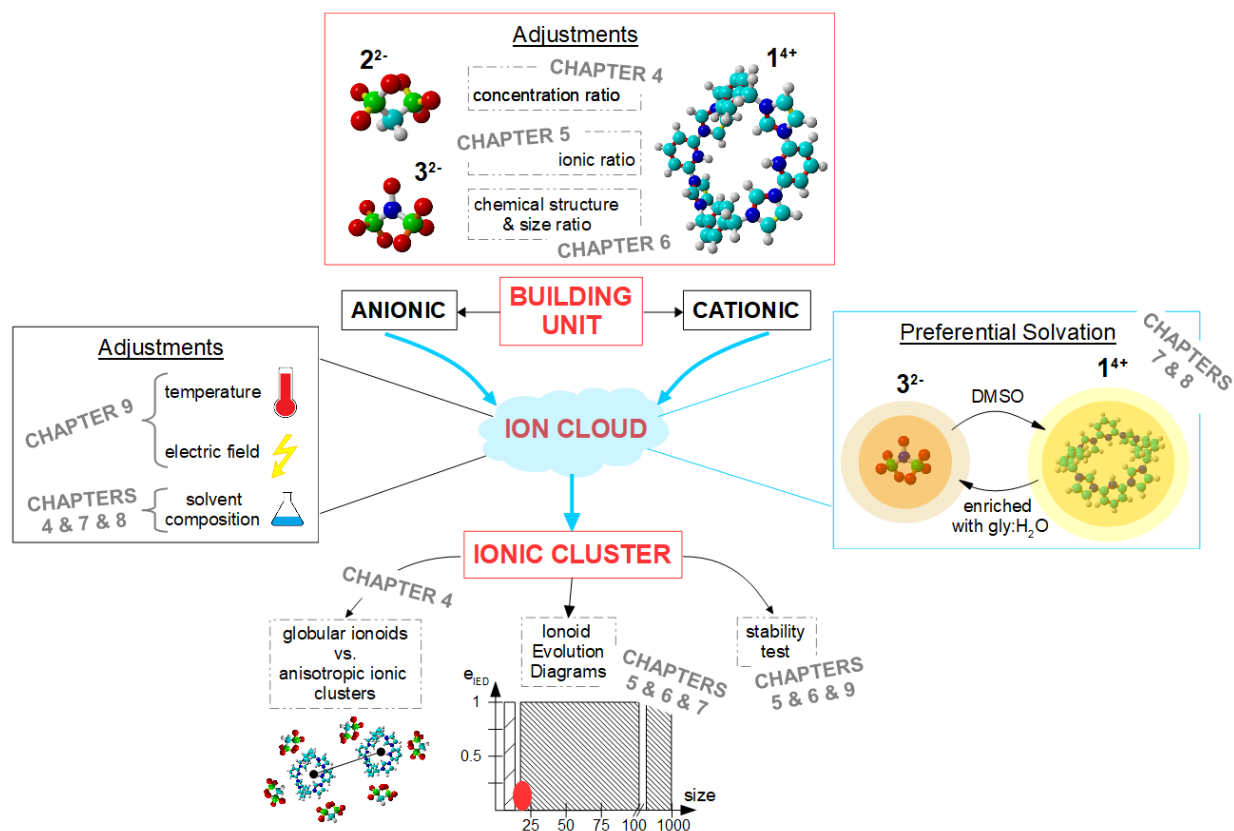


Fig. 9.13.: Schematic representation of the experimental investigations in this work. The center of the graphic highlights the transition from the initial ion cloud state to the desired ionic clusters.

At this point, I want (with the help of Fig. 9.13) to highlight the 'milestones' of my PhD thesis. The first important step in studying the formation of colloid-like ionic clusters in solution was to expand the existing terminology from the work of Kurzbach et. al.<sup>14</sup> Besides the almost perfectly spherical (globular) ionoids, we could characterize self-assembled entities with an enlarged radius and/or a more spheroidal shape after the incubation period of ten days. This 'new' class is summed up as anisotropic ionic clusters.<sup>66</sup> Moreover, we assume that cationic and anionic building units are situated in an initial ion cloud state at the beginning of the self-assembly process. Here, no globular structures can be detected and the internal ion distribution obeys a Poisson-Boltzmann-type or similar mean-field interaction pattern. As shown in Chapter 4, the composition of the solvent mixture containing DMSO, glycerol and water as well as the bulk concentration determine the fate of the ion cloud state regarding the build up of globular ionoids or anisotropic ionic clusters.

The second major achievement is based on the construction of our ionoid evolution diagrams, which were introduced in Chapter 5. IEDs have proved themselves as useful tool to summarize

the self-assembly process after the incubation period of ten days. Moreover, one can compare different ionic ratios<sup>92</sup> and the solvent influence<sup>156</sup> for one specific system as well as various combinations of ionic building units with the same construction parameters (like e. g. ionic ratio).<sup>94</sup> These graphs encode information regarding the time-dependent changes of size, shape and stability for colloid-like ionic clusters. Moreover, IEDs helped in setting boundaries between globular ionic clusters and anisotropic ionic clusters. The former self-assembled entities are formed if the hydrodynamic radius lies between 10 nm and 25 nm and the eccentricity-value stays below 0.25.<sup>92</sup>

The third 'milestone' corresponds to the system incorporating the rather large 'Texas-sized molecular box' and the small dianionic building units methanedisulfonate or Fremy's salt. This system, throughout my PhD thesis designated as model system  $\mathbf{1}^{4+}:\mathbf{2}^{2-}$  ( $\mathbf{1}^{4+}:\mathbf{3}^{2-}$ , respectively), helped in untangle characteristic features in the formation of globular ionoids in solution. The structural elements of both building units<sup>94</sup> in combination with the optimal solvent mixture of DMSO:glycerol:water 50:43:7 (v/v/v)<sup>66,156</sup> interplay perfectly for the build up of globular ionoids. Furthermore, this system shows sensitive reactions while adapting to changes in the 'design elements' solvent composition, ionic ratio and concentration ratio, allowing us to study the importance of primary and secondary driving forces for the complete ISA process. One aspect, which really stands out here is the durability or rather robustness of the model system. As soon as we could detect the small, yet soft self-assembled entities based on  $\mathbf{1}^{4+}:\mathbf{2}^{2-}$ , neither (i) mechanical stress,<sup>92</sup> (ii) applying an alternating electric field,<sup>94</sup> nor (iii) temperature changes (see Chapter 9) could destruct the globular ionoids in solution.

The last achievement, which I want to point out in this setting is the fact that we could introduce new polyphilic building blocks in order to build up colloid-like ionic clusters in solution.<sup>94</sup> Therefore, the mentioned goal in my motivation section to liberate the formation process of model system  $\mathbf{1}^{4+}:\mathbf{2}^{2-}$  ( $\mathbf{1}^{4+}:\mathbf{3}^{2-}$ , respectively) from its 'special case' could be fulfilled. However, the new systems lack in features like long-term stability or size monodispersity, leaving the aspect of crafting globular ionoids based on other polyphilic ions as a future goal.

Regarding the listed 'milestones' of my PhD thesis, the 'design elements' concentration ratio, ionic ratio or solvent composition, which were already addressed in the Introduction (see Fig. 1.1), can definitely be seen as important parameters for characterizing the self-assembly process of colloid-like ionic clusters. Moreover, we can acknowledge the importance of these 'design elements' for size, shape and durability of globular ionoids and anisotropic ionic clusters. However, there are still other parameters listed in Fig. 1.1 like the pH-value or the present counterions, which were not studied yet, but have the potential to significantly affect the self-assembly process.

The idea of introducing ionoids as new subclass for colloids and therefore in the wide field of supramolecular chemistry seems reasonable, but the present limitations for the formation

of the desired globular ionoids still marks a barrier for this intend, which has to be mastered in future works. The only system that is capable of crafting globular ionoids is still the one containing the 'Texas-sized molecular box' with methanedisulfonate or Fremy's salt dianion, respectively, in the rather special solvent mixture of DMSO:gly:H<sub>2</sub>O 50:43:7 (v/v/v). To expand the catalog of ionic building units capable of building up self-assembled entities, which contain the characteristic features of globular ionoids, one has to find or synthesize molecules with matching structural features compared to the model compounds delivering **1**<sup>4+</sup> and **2**<sup>2-</sup> (**3**<sup>2-</sup>, respectively) ions. Another major goal is to simplify the solvent composition from currently three components to just two constituents. This step would also help in analyzing the solvation behavior of the ionic building units inside the initial ion cloud state and the final self-assembled entities due to the reduced interaction partners inside the solution. The breakthrough for this project would be to introduce a system capable of crafting colloid-like ionic clusters, which also could fulfill a specific task or could be used in a specific application. Therefore, the presented work does not conclude the research of understanding the formation of colloid-like ionic clusters in solution, but rather marks its beginning.



# A | Appendix - Methods

## A.1. Dynamic Light Scattering (DLS)

As already mentioned in Chapter 3, is DLS a versatile and useful method to determine size, size distributions and in some cases the shape of nanoparticles. In the following section, one describes the used instrumentation, the preparation routine for all samples as well as the process of data analysis in detail.

### Instrumentation

Firstly, the ALV-NIBS high performance particle sizer (HPPS) equipped with an ALV-5000/EPP Multiple Tau Digital Correlator (ALV-Laser Vertriebsgesellschaft m.b.H., Langen, Germany) was used. The built-in HeNe-Laser irradiates with a typical wavelength of  $\lambda = 632.8\text{nm}$  and 3mW output power, whereby an automatic attenuator optimal adjusts the count rate traces. This setup records at a back scattering angle of  $173^\circ$  relative to the incident monochromatic light. The Peltier temperature control unit keeps the cell temperature at  $20^\circ\text{C}$ . As measurement cell the UV-cuvette micro (BRAND, Wertheim, Germany) was utilized, because of the small sample volumes ( $\approx 200\ \mu\text{l}$ ) and the durability against most polar solvents.

The second device for recording DLS was a Litesizer 500 (Anton Paar GmbH, Graz, Austria), which unites DLS and static light scattering as well as zeta potential, transmittance and refractive index measurements. It uses a correlator, which can perform up to 248 auto/cross-correlations simultaneously over a time-range of 10 ns to 85 s. Here, a 40 mW semiconductor laser with a typical wavelength of  $\lambda = 658\text{nm}$  was used to irradiate the sample and an automatic configuration of the heatable optical bench allows perfected count rate traces. Furthermore, the Litesizer 500 can measure DLS at three different detection angles: back ( $175^\circ$ ), side ( $90^\circ$ ) and forward ( $15^\circ$ ) scattering, which allow measuring a broader range of samples and obtaining information on potential geometrical anisotropy.<sup>221</sup> The samples were filled into quartz cells (Hellma Analytics, Müllheim, Germany), and mostly measured at back and side scattering at a fixed temperature of  $20^\circ\text{C}$ . Further information about utilizing the Litesizer 500 for analyzing the particle size as well as zeta potential of nanostructured materials can be found in the corresponding guideline from Anton Paar, see Ref. 222.

## Sample preparation and Measuring settings

Sample preparation for DLS were identical for measurements in both DLS devices. Before dissolving the respective compounds with different solvent mixtures, one filtered all of them using Millex filter units containing hydrophilic LCR (PTFE)-membranes pore-size 450 nm. After obtaining the final solution, a second filtration step (with the same filter-types) was added while filling the cells to remove last contaminations like dust.<sup>36</sup> All samples were measured in regular, frequent intervals to obtain insight into long-term stability. The resulting autocorrelation functions were analyzed using device specific software called ALV-5000/E/EPP (ver. 3.0.1.13) and Kalliope (ver. 2.6.0).

Independently from the DLS device one measured all samples with a quality setup of six runs, where each run took 30s and all runs were averaged into one intensity time correlation function. Next to correlation functions and particle radius distributions the behavior of the mean scattering intensity or mean count rate was also examined. The adjustments for the laser attenuation, which have a direct impact on the mean scattering intensity, were carried out automatically in order to detect optimized count rate traces. Therefore, one will always specify the current laser attenuation while presenting these values.

## Data analysis

The ALV device with a fixed back scattering angle of  $\theta = 173^\circ$  obtains the intensity time correlation function  $g_2(\tau)$  from the homodyne detected scattering intensity. Subsequently,  $g_2(\tau)$  was directly fitted using a constrained regularization method, which is included inside the ALV software. The mathematical background of regularization DLS data is precisely described in the CONTIN 2DP program by Provencher.<sup>47,48</sup> Equation A.1 shows the ALV nonlinear fit model for calculating smooth distribution functions

$$g_2(\tau) - 1 = \left( \int_{\Gamma_{min}}^{\Gamma_{max}} e^{-\Gamma\tau} G(\Gamma) d\Gamma \right)^2, \quad (\text{A.1})$$

where  $G(\Gamma)$  denotes the distribution function of the decay rate  $\Gamma$ . The decay rate itself coheres with the diffusion coefficient  $D$  through  $\Gamma = Dq^2$ , as already in Chapter 3. Under the assumption that (i) scattering particles behave as hard spheres in dilute solution and (ii) Rayleigh-Debye theory is valid, the Stokes-Einstein-equation (equation 3.16) allows calculating the distribution of the hydrodynamic radius  $R_H$ . The final 'mass weighted' particle radius distribution function results in adjusting the amplitudes of the decay rate in order to cut nonphysically large contributions at small particle radii.

The Litesizer 500 (in combination with the Kalliope software) also records the intensity time correlation function  $g_2(\tau)$ , but here one has to deal with a slightly different algorithm. The



Kalliope Software contains a 'non-negative least square' (NNLS) fitting routine with Tikhonov regularization.<sup>223,224</sup> In addition, one could decide between the options 'general' and 'narrow', which influence the regularization parameter of the Tikhonov-NNLS. The latter variation was chosen, because of the smaller peak width in the calculated particle radius distribution function. Furthermore, the 'volume weighted' particle size distribution function was used in order to report analogous results compared to the ALV measurements.

Chapter 4, containing data of the first study regarding the formation of ionoids, presents results recorded with both DLS devices. In later studies, only the Litesizer 500 was used for dynamic light scattering experiments. To compare these measurements with the previous results, the intensity time correlation functions from the Anton Paar device were analyzed with the ALV-5000/E/EPP software. Therefore, all presented hydrodynamic radii and size distributions are based on one uniform algorithm. One exception is depicted by the mean intensity or mean count rate values, which were directly adopted from the Kalliope software.

## A.2. Continuously Monitored Phase-Analysis Light Scattering (cmPALS)

Continuously monitored phase-analysis light scattering (cmPALS) is based on the method of electrophoretic light scattering (ELS) and allows evaluating the zeta potential for sensitive samples like e. g. highly conductive protein solutions.<sup>225,226</sup> The zeta potential, also known as electrokinetic potential,<sup>227</sup> describes the potential at the slipping/shear plane between the Stern layer, which consists of strongly bound ions, and the outer (diffuse) region with less firmly associated ions of a colloidal particle moving under an electric field.<sup>37,41</sup> It represents an important parameter for a number of applications including characterization of biomedical polymers,<sup>228</sup> electrokinetic transport of particles<sup>229–231</sup> and the isoelectric point of proteins.<sup>232</sup> For the self-assembled ionic cluster the zeta potential was used as indicator for colloidal stability,<sup>233,234</sup> which is already established in drug delivery research. There, nanoparticle dispersions are classified as highly unstable, relatively stable, moderately stable and highly stable based on the zeta potential values  $\pm 0$ -10 mV,  $\pm 10$ -20 mV,  $\pm 20$ -30 mV and above  $\pm 30$  mV.<sup>41,235</sup>

### Instrumentation

The cmPALS measurements were again performed with the Litesizer 500 in combination with the respective Kalliope software. As measurement cell the so-called Univette (Anton Paar GmbH) was used, which allows zeta potential measurement with organic solvents as well as reduced sample volume (70  $\mu$ l) compared to the standard Omega cuvette.<sup>236</sup> By techniques, which are based on electrophoretic light scattering (like PALS), the speed of the mobile particles is determined through the frequency shift between the scattered light and the original laser (Doppler shift). In short the laser beam splits into two, whereas the first part is directed towards the sample and the second part is combined or optically mixed with a modulated reference beam to determine the Doppler shift. The special feature of PALS exists in the fact that the rate of phase change between these two beams is analyzed. The newly patented method cmPALS from Anton Paar further compensates non-linearities of the modulator and the results are not affected by any longer-term deterioration in the performance of the modulator.<sup>226</sup> Ref. 222 can be recommended as reading matter, because it contains a detailed description about the cmPALS method in general as well as the technical implementation inside the Litesizer 500.

## Sample preparation and Measuring settings

The sample preparation itself was carried out after the described routine in the DLS section. Each probe was analyzed after the incubation period of ten days with an applied voltage of 40 V (if not directly mentioned) and a constant temperature of 20 °C. A complete data set consists of three repetitive measurements with a waiting period of 1 min between each measurement to prevent changes inside the sample due to the influence of Joule heating, a common side effect of this technique. The recorded electrophoretic mobilities  $\mu_e$ , which are the actual accessible parameter in ELS, were averaged and subsequently transferred into the desired zeta potentials. To examine the survival of the self-assembled structures inside the samples, one again performed DLS and compare the autocorrelation functions as well as size distributions before and after the cmPALS measurements.

## Data analysis

The zeta potential cannot be measured directly and is deduced from the electrophoretic mobility  $\mu_e$  of charged particles under the applied electric field.<sup>41</sup> The electrophoretic mobility itself is defined as

$$\mu_e = \frac{v}{E}, \quad (\text{A.2})$$

with  $v$  as velocity of the charged particles and  $E$  as electric field strength. The zeta potential  $\zeta$  is calculated with the measured electrophoretic mobility  $\mu_e$  by the Henry's equation (A.3)

$$\mu_e = \frac{2\varepsilon_0\varepsilon_r\zeta F(\kappa a)}{3\eta}, \quad (\text{A.3})$$

with  $\varepsilon_0$  as vacuum permittivity,  $\varepsilon_r$  as relative permittivity and  $F(\kappa a)$  as Henry's function. The Henry's function itself depends on the thickness of the electric double layer  $\kappa^{-1}$  and the particle radius  $a$ , which was replaced with the measured hydrodynamic radius  $R_H$ . To receive the actual zeta potential values, the relative permittivity of the used solvent mixture was determined with the Keysight 16452A Liquid Text Fixture (Keysight Technologies, Santa Rosa, United States) in combination with the automatic RLC Meter RLC 300 (Grundig AG, Fürth, Germany) operating at a frequency of 10 kHz<sup>e</sup>. The thickness of the electric double layer, also known as Debye length  $\lambda_D$ , can be calculated with equation A.4

$$\lambda_D = \kappa^{-1} = \sqrt{\frac{\varepsilon_0\varepsilon_r k_B T}{2e^2 I N_A}} \quad (\text{A.4})$$

applying the elementary charge  $e$ , the Avogadro's number  $N_A$  and the ionic strength  $I$ . The

---

<sup>e</sup> A more precise description for the determination of  $\varepsilon_r$  is given in the respective studies.

ionic strength inside each tested sample depends on the concentration  $c_i$  and charge  $z_i$  of the included ionic building units and can be determined with  $I = \frac{1}{2} \sum c_i z_i^2$ . For the Henry's function  $F(\kappa a)$  the approximate mathematical expression introduced by Swan and Furst<sup>237</sup> was used

$$F(\kappa a) = \frac{16 + 18\kappa a + 3(\kappa a)^2}{16 + 18\kappa a + 2(\kappa a)^2}. \quad (\text{A.5})$$

The determined values for ionic strength and Henry's function, which were used to transfer the measured electrophoretic mobility into the final zeta potential, will be mentioned in combination with the respective system.

## A.3. Electron Paramagnetic Resonance (EPR) spectroscopy

Electron paramagnetic resonance (EPR) spectroscopy was used to explore the local structure in the self-assembled systems from the perspective of an observer electron spin.<sup>60</sup> This allows a nanoscopic, local view and is complementary to the model-derived ensemble properties (such as hydrodynamic radius) gained from DLS. The observer spins are localized on compound **3**<sup>2-</sup>, the dianion of Fremy's salt, which can replace methanedisulfonate **2**<sup>2-</sup>. EPR techniques in general are highly sensitive as well as selective and can operate on structurally disordered materials.<sup>87,89</sup>

### A.3.1. Continuous Wave (CW) EPR spectroscopy

In a CW experiment the sample is irradiated continuously by low-intensity monochromatic microwave radiation. As the magnetic field is swept over a defined range, different EPR transitions are brought into resonance by the applied microwave radiation. CW field-swept spectra are typically measured and presented as derivatives because a modulation amplitude detection method is used experimentally. This method of detection leads to an increased signal-to-noise ratio.<sup>216</sup>

For the studies CW EPR measurements were performed predominantly at 20 °C at two different microwave frequencies: X-band (9.4 GHz) as well as Q-band (34 GHz) frequencies. Higher frequencies/magnetic fields were used to improve the spectral (*g*-)resolution and helped in obtaining a different view on rotational motion of the radicals.<sup>88</sup> Note that CW EPR spectra simplify considerably when recorded in fluid solution. If molecules are free to tumble and magnetic interactions are averaged so that only isotropic components survive, then all molecules are equivalent and experience the same average interaction with the applied magnetic field.<sup>216</sup>

In progressed studies (see Chapters 7 and 8) low temperature CW EPR measurements at Q-band frequencies were also executed. In the here measured frozen solution the orientation of each molecule is fixed with respect to the applied field and consequently the magnitude of the interactions is different. The respective CW spectrum is a weighted sum of all the possible molecular orientations, whereas all but the largest electron–nuclear spin interactions (hyperfine couplings) are masked by the relatively broad linewidths.<sup>216</sup> The determined EPR parameters  $g_{xx}$  and  $A_{zz}$  (tensor elements of the *g* and hyperfine tensor) serve as 'sensor' mainly for proticity and polarity, respectively, of the local environment of the nitroxide radical.<sup>172,204</sup>

## Instrumentation

The first CW EPR measurements at X-band frequencies were performed with the Miniscope MS400 (magnettech, Berlin, Germany). The connected temperature controller HO3 (magnettech) kept the sample temperature constant at 20 °C. A frequency counter (initially the Racal Dana, model 2101, Neu-Isenburg, Germany; later the FC 400, magnettech) was used to record the microwave frequency. In later studies (see Chapters 7, 8 and 9) the Miniscope MS5000 (magnettech) benchtop spectrometer was utilized. This device provides automatic frequency control and a stable temperature with the temperature controller TCH04 (magnettech).

Q-band CW EPR measurements were performed using a Bruker EMX-plus spectrometer with an ER5106QT resonator (Bruker Biospin GmbH, Rheinstetten, Germany) and a RDK-408D2 cold head (Sumitomo (SHI) Cryogenics of America Inc, Allentown, USA). To precisely control the temperature while measuring, one used a Mercury ITC cryogenic environment controller (Oxford Instruments, Abingdon, United Kingdom).

## Sample preparation and Measuring settings

Sample preparation was similar for both X-band and Q-band EPR spectroscopy. About 10  $\mu\text{l}$  to 15  $\mu\text{l}$  of the mixed solutions were filled into small capillaries (Blaubrand, Wertheim, Germany) and capped with matching tube sealant (Leica Critoseal). All samples were measured directly after preparation (day 0), since Fremy's salt in solution is not long-term stable at 20 °C.<sup>238</sup> For the low temperature Q-band measurements, the prepared capillaries were transferred into 3 mm quartz tubes and freeze-quenched with supercooled iso-pentane.

The applied measuring settings varied based on the used instrument and the applied temperature. Therefore, the parameter settings in combination with the respective device will be listed, starting with the benchtop spectrometers at X-band frequency:

- |                                 |                                 |
|---------------------------------|---------------------------------|
| 1. MS400 (magnettech):          | 2. MS5000 (magnettech):         |
| • field sweep: 100 G            | • field sweep: 100 G            |
| • sweep time: 60 s              | • sweep time: 60 s              |
| • modulation amplitude: 600 mG  | • modulation amplitude: 200 mG  |
| • microwave power: 1 mW (20 dB) | • microwave power: 1 mW (20 dB) |
| • number of scans: 3            | • number of scans: 3            |

The only difference between the parameter settings for both benchtop X-band EPR spectrometers lies in the used modulation amplitude. For the older MS400 the modulation amplitude surpassed the standard limit of  $< 0.5 B_{pp}$  ( $B_{pp}$  as peak-to-peak line width) to gain spectra

with a improved phase resolution. The new MS5000 did not present this phase problem, so a reduced modulation amplitude could be used. Fig. A.1 pictures the difference between recorded spectra with the MS400 and MS5000 for Fremy's salt  $c = 3\text{ mM}$  in DMSO:glycerol:water 50:43:7 (v/v/v). The drastical reduce of the modulation amplitude affects predominately the line width of the spectra, which also affects the relative intensity between central peak and low/high field peak.

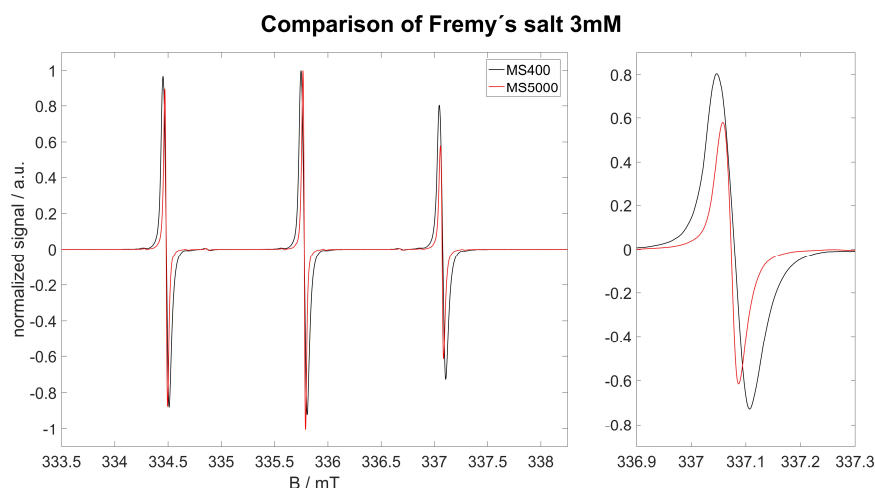


Fig. A.1.: Comparison of CW EPR spectra of Fremy's salt 3mM in DMSO:glycerol:water 50:43:7 (v/v/v) at X-band frequencies recorded with the benchtop spectrometer MS400 and MS5000 (parameter settings see text). The highfield peak of the spectra is shown separately right next to the full spectra.

The measuring settings for CW Q-band were varied based on the used temperature ( $20^\circ\text{C}$  versus low temperature), as shown below.

1.  $20^\circ\text{C}$ :

- field sweep: 130 G
- sweep time: 60 s
- modulation amplitude: 1000 mG
- microwave power: 1 mW (20 dB)
- number of scans: 10

2. 150 K:

- field sweep: 300 G
- sweep time: 90 s
- modulation amplitude: 1000 mG
- microwave power: 0.36 mW (25 dB)
- number of scans: 10

### Data analysis

All spectral analysis (like e. g. determine  $g_{xx}$ ) and simulations were performed in Matlab (R2016a, v. 9.0) exploiting the EasySpin package (v. 5.2.23).<sup>239</sup> The important step for the

simulation approach, which is based on the slow-motion theory developed by Schneider and Freed<sup>240</sup>, was to choose suitable starting parameters for Fremy's salt **g**-tensor and hyperfine coupling tensor **A**. Based on literature data<sup>241</sup> the following parameter sets were taken for the first studies, which were carried out with the MS400:

- **g**-tensor:  $g_{xx} = 2.0086$ ,  $g_{yy} = 2.0064$ ,  $g_{zz} = 2.0029$
- hyperfine-tensor (X-band):  $A_{xx} = 5.3\text{ G}$ ,  $A_{yy} = 5.5\text{ G}$ ,  $A_{zz} = 28.3\text{ G}$
- hyperfine-tensor (Q-band):  $A_{xx} = 5.5\text{ G}$ ,  $A_{yy} = 5.6\text{ G}$ ,  $A_{zz} = 28.3\text{ G}$

Other values like line broadening and rotational diffusion rates that have to be implied into the simulation routine, depend significantly on the analyzed 'design elements' and the applied cationic building unit. Therefore, one describes and characterizes these results separately inside each chapter.

Performing measurements with the MS5000 (starting from Chapter 7) revealed, for most of the spectra, line shapes with an anisotropic line broadening, which indicates the existence of two components inside the respective sample. Adding  $\mathbf{1}^{4+}$  to the Fremy's salt leads to a

- 1) 'fast' rotating component, where the unique axis  $D_{\parallel}$  is, similar to pure Fremy's salt along the N-S-bond of the nitroxide and
- 2) 'slow' rotating component with the shift of the  $D_{\parallel}$ -axis to the dissection angle of both sulfonate groups.

The amount (or fraction) of each component as well as their respective **g**-tensor and hyperfine coupling tensor values depend on the properties of the observed system (like e. g. concentration ratio or solvent mixture) and will be discussed inside the chapters. In this context, parameters like line broadening and rotational diffusion rates that have to be implied into the simulation routine will also be highlighted.

For calculating the rotational correlation time  $\tau_c$  (see equation A.6), one stucked to a simple model of Brownian diffusion with an axial rotational diffusion tensor containing the values  $D_{\parallel}$  (unique axis) and  $D_{\perp}$  (perpendicular to the unique axis)<sup>88</sup>

$$\tau_c = \frac{1}{6\sqrt[3]{D_{\perp}^2 D_{\parallel}}} \quad . \quad (\text{A.6})$$

The discussed information about the line width of all measured CW EPR spectra are based on isotropic broadening, which is implemented in the EasySpin program package. Note that this method does not assume any physical model causing the broadening. The full width at half maximum (FWHM) values of pure Fremy's salt was instead compared with  $\mathbf{1}^{4+}:\mathbf{3}^{2-}$  in every



investigated system to specify the effect of the multicationic box and also with other cationic building units.

Besides calculating the rotational correlation time  $\tau_c$  as well as determine the isotropic broadening, a routine to analyze the present anisotropy of the rotational diffusion tensor was established. Note that even paramagnetic molecules in the 'fast-motion regime' significantly reflect deviations from the isotropic case through their CW EPR spectra.<sup>88</sup> Based on the rotational diffusion tensor containing  $D_{\parallel}$  and  $D_{\perp}$ , its anisotropy  $T$  was calculated using equation A.7

$$T = \frac{D_{\parallel} - D_{\perp}}{D_{\parallel} + 2D_{\perp}} . \quad (\text{A.7})$$

A larger  $T$ -value indicates stronger separation between  $D_{\parallel}$  and  $D_{\perp}$ , while smaller  $T$ -values reflect more isotropic tumbling, which can be attributed to weaker electrostatic interactions in the direct vicinity. For ion clouds with later self-assembly into globular ionoids the right balance between attractive and repulsive electrostatic forces is important, which translates into an anisotropy  $T$  that must be situated in a specific range. Based on the established system<sup>14</sup> one knows the anisotropy preceding formation of ionoids and use it as a reference for all tested variations.

Finally, so-called Euler angles  $\alpha$ ,  $\beta$  and  $\gamma$  had to be implied to simulate CW EPR spectra at both frequencies with the EasySpin package. The principal axis of fast rotation for pure Fremy's salt and its shift after adding  $\mathbf{1}^{4+}$  were mentioned shortly, a more detailed description can be read up inside the chapters. Also, the entire set of Euler angles will also be given inside the respective chapters.

### A.3.2. Pulsed EPR spectroscopy

In a modern pulsed EPR experiment the field is kept constant and the sample is irradiated with short (nanosecond) and high-intensity microwave pulses. It enables isolation, detection and measurement of the interactions that contribute to the shape and behavior of a CW spectrum. Importantly, pulsed EPR experiments can be designed to address a specific interaction (i. e. a specific term in the spin Hamiltonian). Due to the very short relaxation times at room temperature, pulsed EPR measurements normally require cryogenic temperatures and are suitable to study powder and frozen-solution samples. Note that the requirement for solid-state samples brings the advantage of measuring dipolar magnetic interactions, which are suppressed by motional averaging in liquid solution.<sup>216</sup>

## Instrumentation

All pulsed EPR measurements were performed at X-band frequencies (9.4 GHz) with an Elexsys E580 EPR spectrometer (Bruker Biospin GmbH) using a Flexline split-ring resonator ER4118X-MS3. The resonator was overcoupled to  $Q \approx 400$ . The temperature was set to 50 K for all experiments by cooling with a closed cycle cryostat (ARS AF204, customized for pulsed EPR).

## Sample preparation and Measuring settings

Samples were loaded into 3 mm quartz tubes (50  $\mu$ l to 100  $\mu$ l) and shock-frozen with super-cooled iso-pentane, similar to the Q-band CW low temperature probes. The measuring settings are described separately for the respective pulsed EPR experiments. Note that general settings like number of scans (depending on the respective technique) and Video Gain were identical for all tested samples.

*Echo-detected field sweep:* Field-swept, echo-detected EPR was performed with a Hahn echo sequence  $\pi/2-\tau-\pi-\tau$ -echo<sup>53</sup> and a 200 G field sweep. The interpulse delay time,  $\tau$ , was 176 ns and the pulse lengths were 16 ns for the  $\pi/2$  pulse and 32 ns for the  $\pi$  pulse.

*Electron-spin-echo envelope modulation (ESEEM):* For this technique, two different setups were applied based on the total number of pulses inside the detection sequence. Two-pulse ESEEM (2p-ESEEM) experiments record the intensity of the primary echo (based on the previously described Hahn echo sequence) as a function of  $\tau$ .<sup>219</sup> The initial interpulse delay  $\tau$  of 176 ns was therefore stepwise increased with a fixed increment of 4 ns. The recorded decay of the echo characterizes the phase memory time  $T_m$ , which is in most cases of the order of a few microseconds.<sup>53</sup> The disadvantage of the fast decay in 2p-ESEEM can be circumvented with the three-pulse ESEEM (3p-ESEEM) experiment, where the decay of the here observed stimulated echo signal is determined by the electron spin lattice relaxation time and spectral diffusion of magnetization (see Ref. 53 and Ref. 219 for further information). The experiment was performed with a  $\pi/2-\tau-\pi/2-T-\pi/2-\tau$ -echo pulse sequence and a standard four-step phase cycle. The pulse length of the  $\pi/2$  pulse was still 16 ns and two different interpulse delay times  $\tau$  were chosen with (i) 176 ns and (ii) 136 ns, whereas latter one corresponds to a proton blind spot. The evolution time  $T$  had an initial value of 300 ns and was incremented in steps of 16 ns.

## Data analysis

Analyzing the recorded pulsed EPR measurements was performed with home-written MATLAB programs. The field-swept, echo-detected EPR spectra were phase-corrected and plotted against their respective magnetic field. Note that the determined magnetic field position corresponding to the maximal intensity was used for the following ESEEM experiments. To

evaluate the ESEEM measurements (especially with three-pulse detection sequence), the following methods were applied.

*Magnitude spectrum  $I(\nu)$* : The primary ESEEM data are corrected for the unmodulated part by fitting the decay with a stretched-exponential function  $B(t)$ <sup>87</sup> and subtracting  $B(t)$  from the primary data. The magnitude spectra  $I(\nu)$  (see Fig. A.2 as reference) were now computed by applying a Hamming window, zero-filling the data to four times their original length and final Fourier transformation.

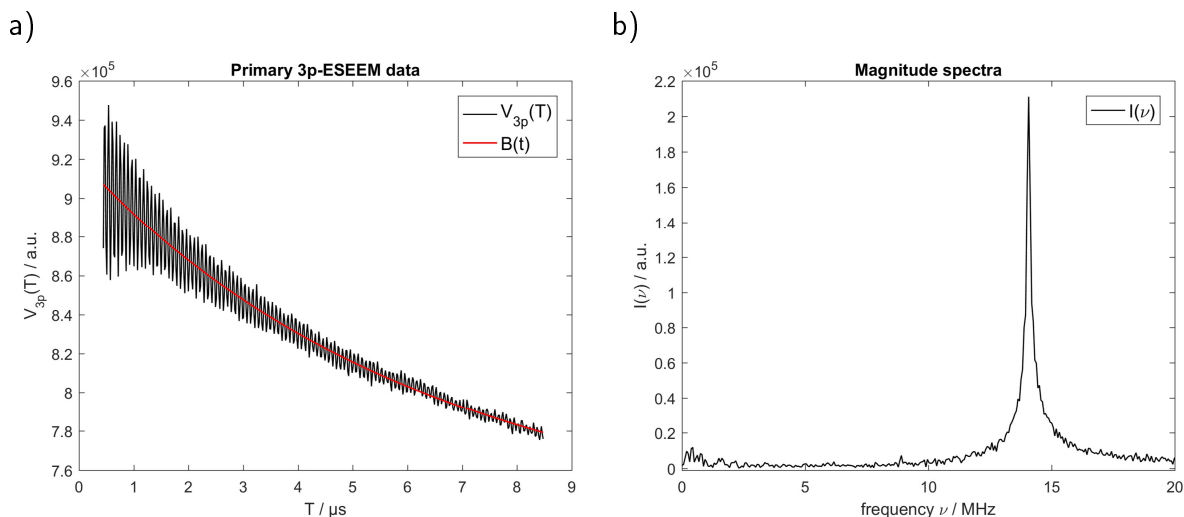


**Fig. A.2.:** a) Primary 3p-ESEEM data  $V_{3p}(T)$  with final stretched-exponential function  $B(t)$ . b) Computed magnitude spectrum  $I(\nu)$ . Both graphs highlight the 3p-ESEEM measurement with  $\tau = 176$  ns for Fremy's salt 3 mM in DMSO:glycerol:water 50:43:7 (v/v/v).

*Modulation depth  $k$* : The modulation depth  $k$  for the 3p-ESEEM measurements was determined based on the description in Ref. 215. The primary ESEEM was again fitted and subtracted with the background function  $B(t)$ . Afterwards, one divided the received difference by the background function  $B(t)$  to obtain the deconvoluted and normalized nuclear modulation function  $N(t)$ .  $N(t)$  was then least-square fitted using a damped harmonic oscillation (see equation A.8) with Gaussian decay envelope and fixed frequency as well as variable amplitude, phase and Gaussian width

$$D(t) = k \cos(2\pi\nu T + \phi) \exp\{-T^2/\tau_0^2\} . \quad (\text{A.8})$$

The parameters included in equation A.8 are the modulation depth  $k$ , the nuclei frequency  $\nu$  (in this case either proton or deuterium frequency), the step-wise increasing evolution time  $T$ , the phase  $\phi$  and the damping constant  $\tau_0$ . Fig. A.3 exemplarily shows the fitting procedure.

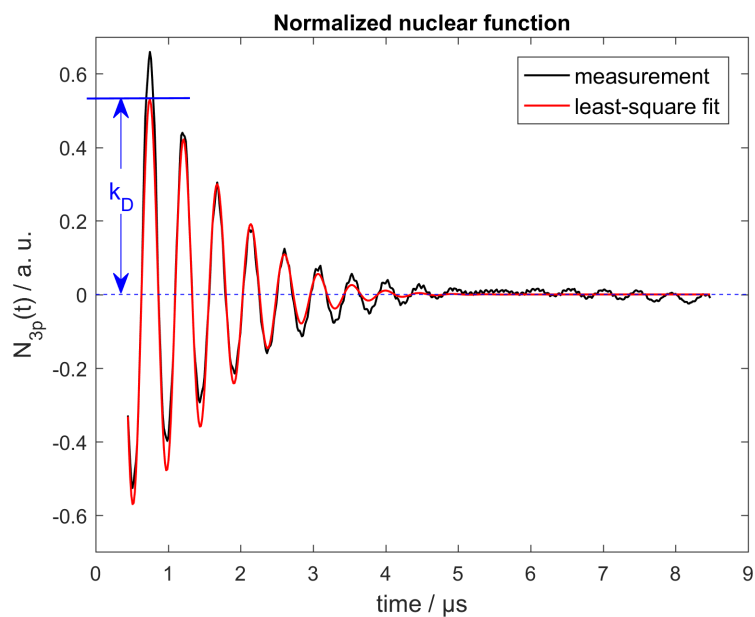


Fig. A.3.: Normalized nuclear function  $N_{3p}(t)$  for the sample Frey's salt 3 mM in d6-DMSO:glycerol:H<sub>2</sub>O measured with interpulse delay  $\tau = 176$  ns. Direct comparison of measurement (black line) and least-square fit based in equation A.8 (red line).

## A.4. Ionoid Evolution Diagrams (IEDs)

IEDs are strictly speaking not a method, but rather a tool to analyze the temporal development of systems capable of building colloid-like ionic cluster in solution. Due to their versatile usage in several studies, a separate section for the general construction principle of ionoid evolution diagrams was prepared, which were introduced in Chapter 5. Fig. A.4 displays on the one hand the IED for modifying the ionic ratio of  $1^{4+}:2^{2-}$  and on the other hand a Hertzsprung-Russell diagram (HRD) as inspirational foundation.

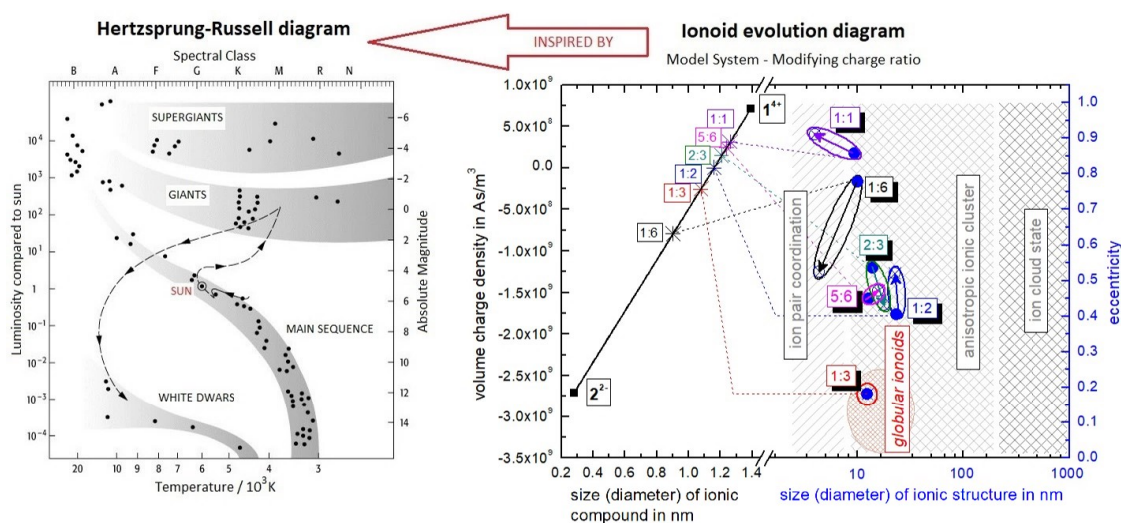


Fig. A.4.: Comparison between a Hertzsprung-Russell diagram, which summarizes complex relationships of the properties of stars and stellar evolution during their complete lifetimes (here exemplary for the sun) and the ionoid evolution diagram for describing the dynamic ionic self-assembly process of for all tested molar ratios of  $1^{4+}:2^{2-}$ .

Hertzsprung-Russell diagrams display the classification of stars as well as stellar evolution during their complete lifetime through plotting the luminosity (often as relative value compared to the sun) on the y-axis against their surface temperature on the x-axis. Mass and time development are thus implicitly part of HRDs. Hence, these diagrams allow summarizing and displaying all stages of stellar development which is a remarkably large and complex set of data and one developed IEDs to describe the dynamic ionic self-assembly process inside the solutions, which also comprises a wealth of complex data and long temporal evolution. To include important design elements like molar/ionic ratio, fitting parameters needed to be defined, which can represent the present electrostatic correlations between anionic and cationic component. Based on the fact that the source of electric fields lies in a charge or charge density,<sup>25</sup> one plots the volume charge density of the ionic building blocks versus their respective diameter (without a solvation shell around them).

Both parameters, diameter as well as volume charge density, were determined using the YASARA-structure software.<sup>242</sup> After implementing the ionic building units into the software,

the already existing experiment 'Energy minimization'<sup>f</sup> was applied to optimize their chemical structure at a temperature of  $T = 293\text{K}$ . At the end one could (i) read off the diameter and (ii) calculate the volume  $V$  (based on the molecular surface) of each ionic building unit to finally obtain the volume charge density  $\rho$  using equation (A.9):

$$\rho = \frac{z^{\pm} \cdot e}{V} \quad \text{with} \quad [\rho] = \frac{\text{As}}{\text{m}^3}, \quad (\text{A.9})$$

with  $z^{\pm}$  as charge for the cationic/anionic component and  $e$  for the elementary charge. Table A.1 summarizes for each ionic building unit the derived information from the YASARA-structure software for the established ionic building units. The respective values for the newly introduced ionic building units are presented in the respective chapter (see description in Chapter 6).

**Table A.1.:** Summary of all derived information from the YASARA-structure software to construct the ionoid evolution diagrams

ionic compound	diameter / nm	charge $z^{\pm} \cdot e$ / $10^{-19}\text{As}$	volume $V$ / $\text{\AA}^3$	volume charge density $\rho$ / $10^9 \frac{\text{As}}{\text{m}^3}$
<b>1<sup>4+</sup></b>	1.390	6.408	907.15	0.706
<b>2<sup>2-</sup></b>	0.278	-3.204	118.36	-2.710
<b>3<sup>2-</sup></b>	0.285	-3.204	106.48	-3.010

After characterizing the ionic building units based on the parameters in Table A.1, the studied system **1<sup>4+</sup>:2<sup>2-</sup>** in the IED were illustrated by simply combining the two affected ionic compounds. Note that each possible molar/ionic ratio between both components can be highlighted as an intersection point along their connection line, as shown in Fig. A.4. In the next step, one wants to analyze the dynamic ionic self-assembly process after the incubation time of ten days starting from the previously established intersection point. Therefore, one (i) extends the x-axis to incorporate the build up ionic structures and (ii) introduces a second y-axis that is able to describe the shape<sup>g</sup> of these formations. The so-called eccentricity  $e_{IED}$  (subscript serves as distinction feature to the elementary charge  $e$ ) was utilized, which is known in mathematics as a measure of how much a conic section deviates from being circular, e. g. ellipses can be calculated through equation (A.10)

<sup>f</sup> This experiment creates a simulation box with periodic cell boundaries around the ionic building unit. Furthermore, it applies the AMBER03 forcefield to run the simulation.

<sup>g</sup> Present deviations from a spherical structure are an important feature to distinguish between globular ionoids and anisotropic ionic clusters. DLS results based on different scattering angles can be used to derive these information. However, parameters like the particle form factor  $P(q)$  or the  $\rho$ -ratio, which are able to describe the morphology of the ionic structures more in detail, can be derived by measuring e. g. static light scattering.<sup>36</sup>

$$e_{IED} = \sqrt{1 - \frac{b^2}{a^2}} \quad (\text{A.10})$$

with  $a$  as length of its semi-major axis and  $b$  as length of its semi-minor axis. Circles have an eccentricity of  $e_{IED} = 0$ , while ellipses strictly stay below the value of one. One adapts equation (A.10) to characterize the three-dimensional self-assembled structures by exchanging parameter  $a$  and  $b$  with the measured hydrodynamic radii at side and back scattering. If the particle size distribution shows two separate entities, the values from the smaller ones were applied into the IED, because one wants to highlight the building process of the globular structures in the sample. Note that the following 'rule' had to be established: The higher value from DLS will be set as  $a$  (semi-major axis) independent from the scattering angle.

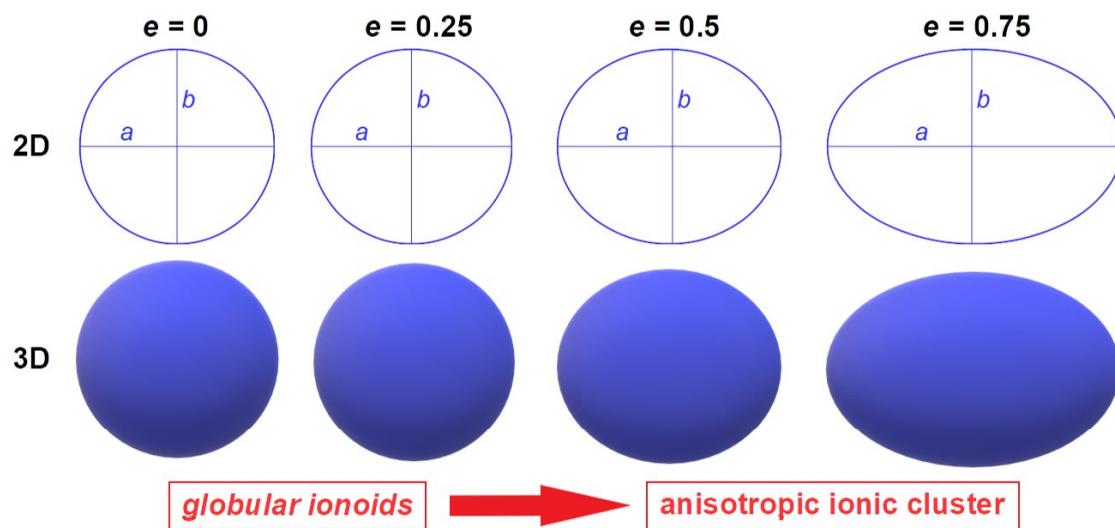


Fig. A.5.: Two- and three dimensional structures based on the eccentricity-values of  $e_{IED} = 0$ ,  $e_{IED} = 0.25$ ,  $e_{IED} = 0.5$  and  $e_{IED} = 0.75$  together with the transition from globular ionoids to anisotropic ionic clusters. The two-dimensional shapes contain the semi-major axis  $a$  and semi-minor axis  $b$ , which are directly embedded in equation (A.10).

To further highlight the advantage of using the eccentricity as parameter to analyze the shape of the highly defined ionic clusters, one exemplary displays simple two- and three-dimensional structures in Fig. A.5 with  $e_{IED} = 0$ ,  $e_{IED} = 0.25$ ,  $e_{IED} = 0.50$  and  $e_{IED} = 0.75$ . To generate these four eccentricities, the following values (without a specific length unit) for the semi-major axis  $a$  and semi-minor axis  $b$  were applied:

- (1)  $e_{IED} = 0.00$ :  $a = 6.00$  and  $b = 6.00$ ,
- (2)  $e_{IED} = 0.25$ :  $a = 6.20$  and  $b = 6.00$ ,
- (3)  $e_{IED} = 0.50$ :  $a = 6.95$  and  $b = 6.00$  and

(4)  $e_{IED} = 0.75$ :  $a = 9.07$  and  $b = 6.00$ .

The visual difference between the eccentricities  $e_{IED} = 0$  and  $e_{IED} = 0.25$  appears less significant compared to  $e = 0.25$  and  $e = 0.5$ , which leads one to set the value of  $e_{IED} = 0.25$  as border globular ionoids to anisotropic ionic clusters (see Chapter 5 for further description). Note that this value is currently just valid for the  $\mathbf{1}^{4+}:\mathbf{2}^{2-}$  system and has to be verified with other ionic building blocks. Applying equation (A.10) to the DLS results, one is also able to analyze the time-dependent behavior of the self-assembled structures, e. g. in Fig. A.4 the blue full dots show measurement day ten and the blue crossed dot day 79. The arrow between a pair of dots highlights the development over time and allows a better comparison between different molar/ionic ratios. At last, evolution with time is also emphasized in IEDs by the oval (or for globular ionoids more circular) frame.



## B | Appendix - Chapter 4

### Sample preparation

#### Preparing solvent mixtures

The preparation of all the final solvent mixtures, which were used in our study, is based on the simple procedure of combining the pure solvents in the right volume proportions. Table B.1 enumerates the composition of the solvents, which contain different volume stoichiometries of DMSO and glycerol 88 wt% aqueous solution.

**Table B.1.:** Preparation of all solvent mixtures with altering the volume stoichiometry of the 'stock solvents' DMSO and glycerol 88 wt%

volume stoichiometry DMSO:glycerol:water	volume DMSO / ml	volume glycerol 88 wt% / ml
33:57:10	1	2
25:64:11	1	3
20:68:12	0.5	2
10:77:13	0.4	3.6
67:28:5	2	1
75:21:4	3	1
80:17:3	2	0.5
90:9:1	3.6	0.4
100:0:0	1	0
0:85:15	0	1

The stated ratios of DMSO:glycerol:water (v/v/v) were calculated using the density of glycerol 88 wt% ( $\rho_{gly88} = 1.226 \frac{\text{g}}{\text{cm}^3}$ ) and pure glycerol ( $\rho_{gly} = 1.261 \frac{\text{g}}{\text{cm}^3}$ ) as well as the respective volume of glycerol 88 wt% ( $V_{gly88}$ ) from Table B.1. Equation B.1 summarizes the conversion of glycerol's weight percentage into his final volume percentage ( $v_{gly}$ ) for each solvent mixture

$$v_{gly} = \frac{w V_{gly88} \rho_{gly88}}{\rho_{gly}} \quad \text{with} \quad w = 88 \text{ wt\%} . \quad (\text{B.1})$$

Table B.2 lists the manufacturing for all solvents with a constant amount of DMSO, but gradually changing the glycerol:water ratio. Note that here we used glycerol  $\geq 98$  wt% aqueous solution to produce the different solvent compositions. Furthermore, the calculation of the final volume percentages for DMSO:glycerol:water was simplified, because we only divided the specific volume from each compound with the total volume of the solvent mixture and neglected the impurity of glycerol  $\geq 98$  wt% except for the last mixture 50:49:1 (v/v/v).

**Table B.2.:** Preparation of all solvent mixtures with altering the glycerol:water ratio

glycerol:water volume ratio DMSO:glycerol:water	volume DMSO / ml	volume glycerol / ml	volume water / ml
50:5:45	2	0.2	1.8
50:10:40	2	0.4	1.6
50:15:35	2	0.6	1.4
50:20:30	2	0.8	1.2
50:25:25	2	1.0	1.0
50:30:20	2	1.2	0.8
50:35:15	2	1.4	0.6
50:40:10	2	1.6	0.4
50:45:5	2	1.8	0.2
50:49:1	2	2.0	0.0

## Preparing bulk concentrations

Decreasing the bulk concentration of  $1^{4+}:2^{2-}$  ( $1^{4+}:3^{2-}$ , respectively) started with producing the following stock solutions in DMSO:glycerol:water 50:43:7 (v/v/v):

- 2 mM  $1^{4+}$  and
- 6 mM  $2^{2-}$  ( $3^{2-}$ , respectively).

The two stock solutions were then diluted separately into the desired concentrations in Table B.3, which we combined in a 1:1 (v/v) stoichiometry to gain the final concentration ratios.

**Table B.3.:** Concentrations of  $1^{4+}$  and  $2^{2-}$  ( $3^{2-}$ , respectively) before preparing the final ratios for DLS and CW EPR spectroscopy

concentration ratio / mM:mM	concentration $1^{4+}$ / mM	concentration $2^{2-}$ ( $3^{2-}$ ) / mM
0.5:1.5	1	3
0.2:0.6	0.4	1.2
0.1:0.3	0.2	0.6
0.05:0.15	0.1	0.3
0.02:0.06	0.04	0.12
0.01:0.03	0.02	0.06

A similar setup was used for the ratio of 1.5 mM:4.5 mM, but we increased the stock solution concentration of  $1^{4+}$  to 3 mM and for  $2^{2-}$  ( $3^{2-}$ , respectively) to 9 mM.

## Modifying solvent volume stoichiometry

### a) DLS results

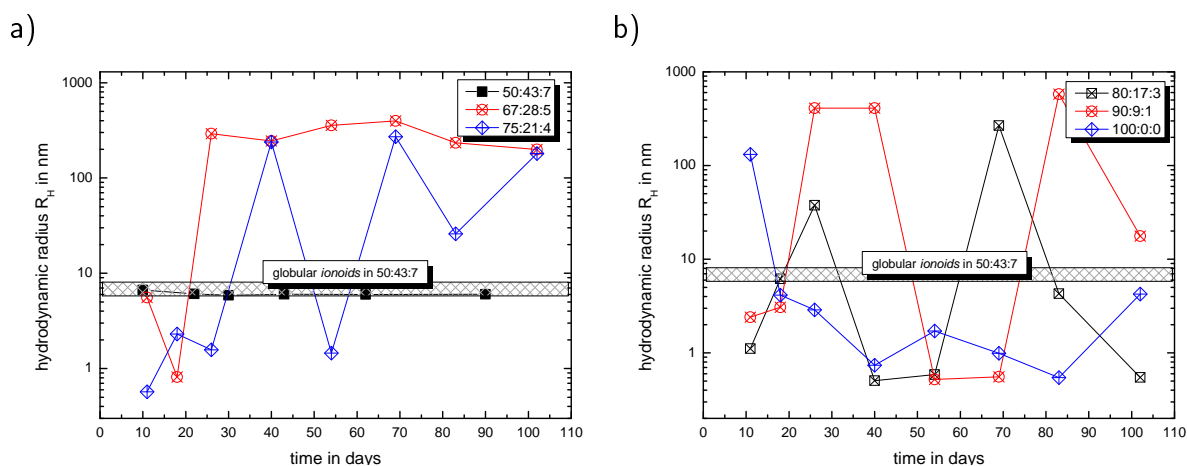


**Fig. B.1.:** Development of the hydrodynamic radius for the cluster system  $1^{4+}:2^{2-}$  at a ratio of 1 mM:3 mM. We divided the results of the volume stoichiometries with increasing DMSO amount into two graphs for clarity: a) stoichiometries 67:28:5 and 75:21:4 and b) 80:17:3 to 100:0:0. Both graphs contain a patterned box that highlights the region of the hydrodynamic radius for the established solvent mixture. Additionally, the left graph contains the DLS data for the 50:43:7 solvent mixture as reference.

Fig. B.1 contains the remaining volume stoichiometries, which were left out in Chapter 4. The solvent mixtures with increasing amount of DMSO do not show a correlation between the

solvent composition and the development of the hydrodynamic radius at any given measurement day. Furthermore, we recognize a rather large fluctuation in the  $R_H$ -values in all solvent mixtures for the system  $1^{4+}:2^{2-}$ , indicating the absence of highly-defined structures. It seems that the  $1^{4+}$ - and  $2^{2-}$ -ion are more or less settled in the initial ion cloud state.

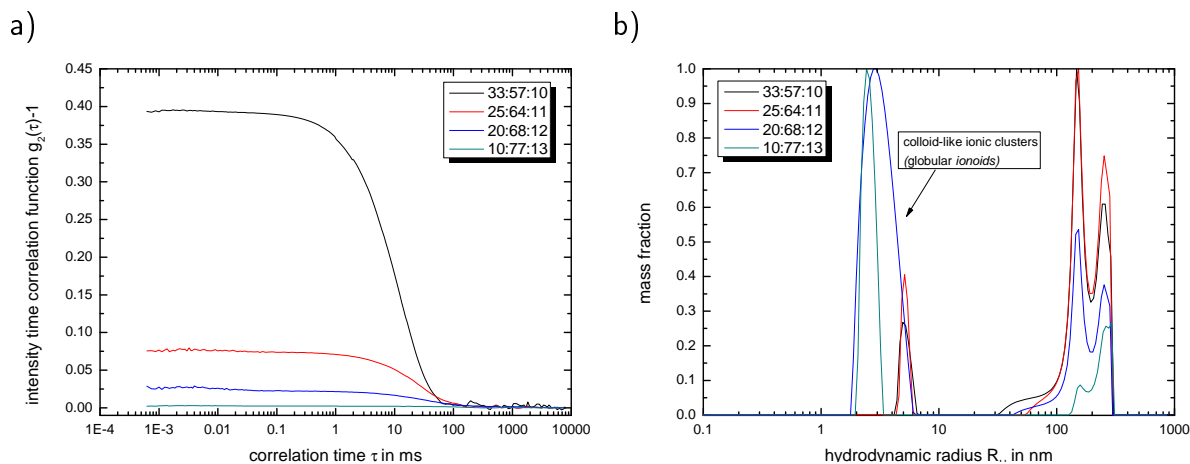
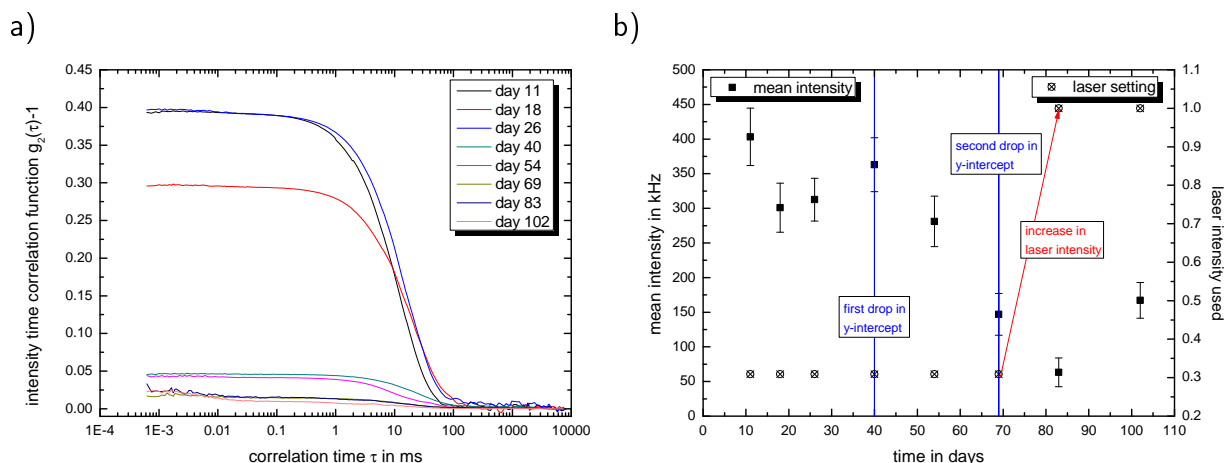


Fig. B.2.: a) Intensity time correlation function and b) particle radius distribution function for  $1^{4+}:2^{2-}$  in the solvent mixtures DMSO:glycerol:water with decreasing amount of DMSO (33 vol.-% to 10 vol.-%) at measurement day 11.

Fig. B.2 contains the intensity time correlation and particle radius distribution function for  $1^{4+}:2^{2-}$  dissolved in the volume stoichiometries with decreasing amount of DMSO (33 vol.-% to 10 vol.-%) at measurement day 11. We detect that all four intensity time correlation functions decay at almost the same correlation time, indicating the existence of at least one particle type with similar size. This trend corresponds with the particle radius distributions, implying a strong dependency of the decay rate by the second entity with  $R_H \approx 150$  nm. Furthermore, the y-intercept of the intensity time correlation function decreases with the amount of DMSO in the solvent mixture. This behavior coheres with the changing mass fraction for both sample entities. The volume stoichiometries 33 vol.-% to 10 vol.-% show that the weighting in the particle radius distribution shifts from the second to the first peak. These self-assembled structures with their small size deliver, based on the Rayleigh theory, a reduced mean scattering intensity, which significantly effects the intensity time correlation function.

Besides characterizing the four volume stoichiometries with decreasing amount of DMSO, we want to highlight the long-term stability for one solvent mixture. Fig. B.3 displays the development of the intensity time correlation function and the mean scattering intensity through the total measurement time for  $1^{4+}:2^{2-}$  in DMSO:glycerol:water 33:57:10 (v/v/v).

The intensity time correlation functions show two major drops in their y-intercepts at day 40 and day 69, which are also marked in the diagram with the mean scattering intensities. For day 40, we do not see significant changes in the mean count rate, but the particle radius distribution



**Fig. B.3.:** a) Intensity time correlation function and b) mean scattering intensity with laser settings for  $1^{4+}:2^{2-}$  in DMSO:glycerol:water 33:57:10 in dependence of the measurement time.

indicates the beginning decomposition of the present anisotropic ionic clusters. The second drop however coheres with the decreasing mean scattering intensity, which implies the absence of highly defined structures inside the solution. To support the permanent character of this radical change, we expanded the DLS measurement still day 102. Furthermore, we had to increase the laser intensity (maximum value of 1.0) for the last two measurements in order to maintain the mean count rate. In general, we can evaluate the stability of colloid-like ionic clusters through comparing the intensity time correlation function with the associated mean scattering intensity.

## b) CW EPR results

Before discussing the additional CW EPR results, the set of Euler angles for the measured samples has to be included, as mentioned in Appendix A. They are made out of:

- pure Fremy's salt:  $\alpha = 65^\circ$ ,  $\beta = 90^\circ$ ,  $\gamma = 15^\circ$  and
- $1^{4+}:3^{2-}$ :  $\alpha = 85^\circ$ ,  $\beta = 90^\circ$ ,  $\gamma = 15^\circ$ .

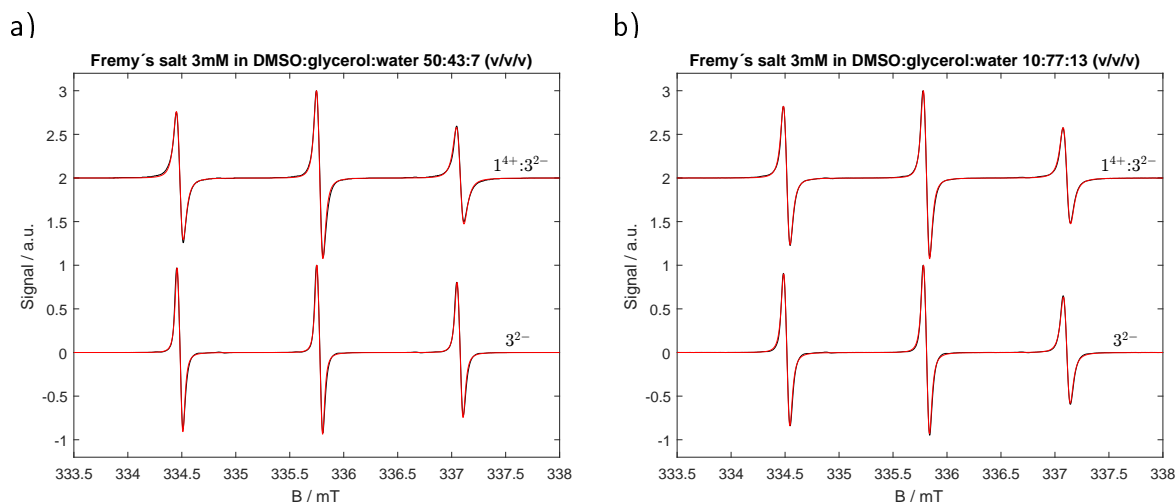


Fig. B.4.: a) X-band CW EPR spectra of Fremy's salt 3mM and  $1^{4+}:3^{2-}$  in DMSO:glycerol:water 50:43:7 (v/v/v). b) X-band CW EPR spectra for the same components in DMSO:glycerol:water 10:77:13 (v/v/v). Both graphs contain the experimental data as black lines and the simulated data as red lines.

Based on the rotational mobility of Fremy's salt in the established solvent mixture DMSO:glycerol:water 50:43:7 (v/v/v), we received a reference diffusion tensor at X-Band frequencies (see Table B.4). The increase of glycerol in the solvent mixture causes due to the higher viscosity a hindered rotational mobility of pure Fremy's salt, which leads to smaller  $D_{\perp}$  and  $D_{\parallel}$  values. In addition to that, the  $1^{4+}:3^{2-}$  system does effect the rotational mobility around the molecular z-axis. This variation is also visible in the behavior of the anisotropy  $T$ , where both X- and Q-band data show the same tendencies (see Fig. B.5).

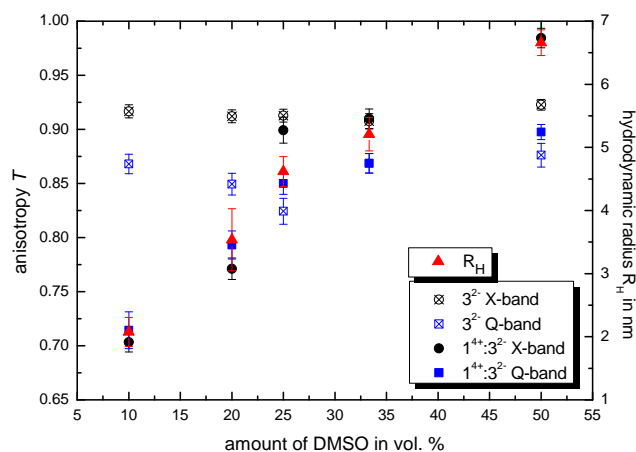


Fig. B.5.: Plot of the anisotropy  $T$  (equation A.7) of pure Fremy's salt and system  $1^{4+}:3^{2-}$  for X- and Q-band against the amount of DMSO in the solvent. The red triangles show the behavior of the hydrodynamic radius of  $1^{4+}:2^{2-}$  at day 11.

The anisotropy of the pure Fremy's salt displays only minor changes with reducing amount of

DMSO inside the solvent mixture. Note that the reduced anisotropy at Q-band frequencies correlates with the difference in frequency/field dependence of the rotational time-frame with higher frequencies/magnetic fields, just like the spectra in Chapter 4 visualize exemplary. Furthermore, we see an outstanding decay in the anisotropy for the system  $\mathbf{1}^{4+}:\mathbf{3}^{2-}$  throughout all tested volume stoichiometries. We can exclude solvent viscosity as cause for this behavior, as we then would also have to observe this trend with pure Fremy's salt, leaving electrostatic interactions as origin. Reducing the amount of DMSO in the solvent mixture decreases the electrostatic interactions between  $\mathbf{1}^{4+}:\mathbf{3}^{2-}$ , which creates a more isotropic environment for Fremy's salt and a less pronounced difference between  $D_{\perp}$  and  $D_{\parallel}$ . Besides the decrease in DMSO content, we increase the water content inside the solvent mixture, inducing partially solvated Fremy's salt molecules in this region as well as lower  $T$ -values. In general, we can correlate the trend of the anisotropy in the ion clouds and the hydrodynamic radius of the self-assembled structures.

Table B.4 combines all simulated  $D_{\perp}$  and  $D_{\parallel}$  values for pure Fremy's salt as well as the system  $\mathbf{1}^{4+}:\mathbf{3}^{2-}$  that were used to calculate the rotational correlation time  $\tau_c$  (equation A.1) as well as the rotational anisotropy  $T$ . The results for pure Fremy's salt with the tested solvent mixtures are expanded with data of  $\mathbf{3}^{2-}$  in pure water, DMSO and glycerol 88 wt%.

**Table B.4.:** Summary of the simulated axial rotational diffusion tensor  $D_{\perp}$  and  $D_{\parallel}$  as well as the calculated rotational correlation time  $\tau_c$  and anisotropy  $T$  for pure Fremy's salt and  $\mathbf{1}^{4+}:\mathbf{3}^{2-}$  at X-band frequencies while changing the volume stoichiometry of the solvent mixture DMSO:glycerol:water

solvent	$\mathbf{3}^{2-}$				$\mathbf{1}^{4+}:\mathbf{3}^{2-}$			
	$D_{\perp}/s^{-1}$	$D_{\parallel}/s^{-1}$	$\tau_c/ps$	$T$	$D_{\perp}/s^{-1}$	$D_{\parallel}/s^{-1}$	$\tau_c/ps$	$T$
50:43:7	9.5e8	3.5e10	52.72	0.923	2.1e8	4.0e10	137.94	0.984
33:57:10	4.6e8	1.4e10	116.05	0.908	3.2e8	1.0e10	165.35	0.910
25:64:11	3.4e8	1.1e10	153.84	0.913	2.7e8	7.5e9	203.82	0.899
20:68:12	2.8e8	9.0e9	187.21	0.912	3.6e8	4.0e9	207.47	0.771
10:77:13	2.5e8	8.5e9	205.79	0.917	3.7e8	3.0e9	224.22	0.703
0:0:100	3.0e10	6.0e10	4.41	0.250	-	-	-	-
100:0:0	4.0e9	4.0e10	19.34	0.750	-	-	-	-
0:85:15	2.0e8	7.0e9	254.76	0.919	-	-	-	-

At Q-band frequencies, the behavior of the rotational anisotropy  $T$  of  $\mathbf{1}^{4+}:\mathbf{3}^{2-}$  and pure Fremy's salt is analogous to the X-band data and therefore will not be explained separately. However, Fig. B.6 contains the measured Q-band CW EPR spectra with decreasing amount of DMSO

inside the solvent mixture (50 vol.-% to 10 vol.-%).

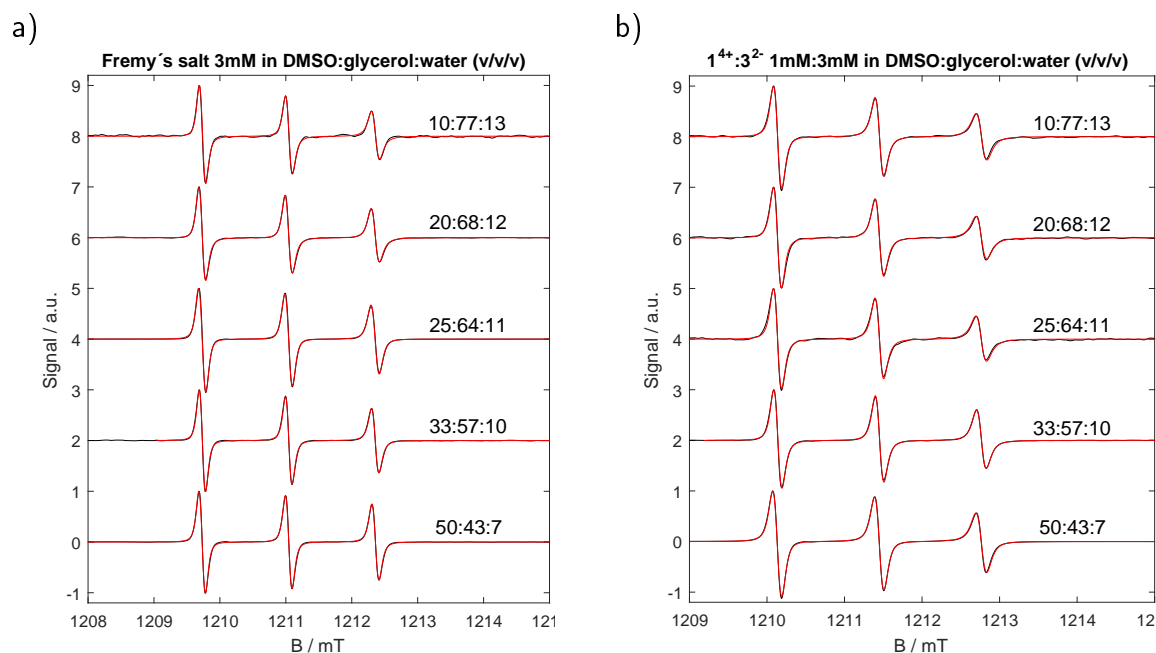


Fig. B.6.: Q-band CW EPR spectra of a) Frey's salt and b)  $1^{4+}:3^{2-}$  in DMSO:glycerol:water with decreasing amount of DMSO (50 vol.-% to 10 vol.-%). Again we illustrate the experimental data with black lines and the simulated data with red lines.

Pure Frey's salt delivers the expected trend with increasing amount of glycerol in the solvent mixture; the rotational mobility of the nitroxide declines due to the rising solvent viscosity. Adding  $1^{4+}$  results in further restriction for the rotational mobility of  $3^{2-}$  and broader line widths due to electrostatic interactions. Table B.5 combines, equivalent to the X-band results, the important values from the simulations/calculations. However, the rotational correlation times  $\tau_c$  from  $1^{4+}:3^{2-}$  in DMSO:glycerol:water 25:64:11 and 20:68:12 (v/v/v) surpass significantly the values for all the other listed solvents. In contrary, the anisotropy does not rise, because of the simultaneous drop of  $D_{\perp}$  and  $D_{\parallel}$ . One reason for this special behavior can be found in stronger local electrostatic interactions between  $1^{4+}$  and  $3^{2-}$  due to local aberrations in the solvent compositions from the macroscopic ratio inside the ion cloud.



**Table B.5.:** Summary of the simulated axial rotational diffusion tensor  $D_{\perp}$  and  $D_{\parallel}$  as well as the calculated rotational correlation time  $\tau_c$  and anisotropy  $T$  for pure Fremy's salt and  $\mathbf{1}^{4+}:\mathbf{3}^{2-}$  at Q-band frequencies while changing the volume stoichiometry of the solvent mixture DMSO:glycerol:water

solvent	$\mathbf{3}^{2-}$				$\mathbf{1}^{4+}:\mathbf{3}^{2-}$			
	$D_{\perp}/s^{-1}$	$D_{\parallel}/s^{-1}$	$\tau_c/ps$	$T$	$D_{\perp}/s^{-1}$	$D_{\parallel}/s^{-1}$	$\tau_c/ps$	$T$
50:43:7	9.0e8	2.0e10	65.87	0.876	3.3e8	9.0e9	167.79	0.898
33:57:10	7.2e8	1.5e10	84.13	0.869	3.6e8	7.5e9	168.25	0.869
25:64:11	6.5e8	9.8e9	103.79	0.824	2.5e8	4.5e9	254.38	0.850
20:68:12	5.3e8	9.5e9	120.16	0.849	2.8e8	3.5e9	256.48	0.793
10:77:13	4.1e8	8.5e9	147.97	0.868	4.0e8	3.4e9	204.17	0.714
0:0:100	3.6e10	6.2e10	3.86	0.194	-	-	-	-
100:0:0	7.0e9	3.5e10	13.92	0.571	-	-	-	-
0:85:15	3.5e8	5.0e9	196.25	0.816	-	-	-	-

## Modifying glycerol:water volume ratio

### a) DLS results

Based on the description in Chapter 4, Fig. B.7 displays the intensity time correlation functions at day 7 and day 14 for selected solvent compositions. Here, we chose at least one mixture out of each DMSO:glycerol:water (v/v/v) region:

1. 50:5:45 to 50:15:35
2. between 50:15:35 and 50:40:10
3. between 50:40:10 and 50:45:5
4. above 50:45:5.

Note that the defined regions are based on the first three weeks for the system  $\mathbf{1}^{4+}:\mathbf{2}^{2-}$  1 mM:3 mM in each solvent mixture. The self-assembly into globular ionoids in DMSO:glycerol:water 50:43:7 (v/v/v) takes 10 days, permitting the preliminary performed classification. However, it is difficult to derive their long-term stability, which is not the main emphasis of these DLS measurements. We focus on the beginning of the self-assembly process, which is crucial for the formation of well-defined structures.

The solvent mixture DMSO:glycerol:water 50:10:40 (v/v/v) does not form highly-defined self-assembled structures, which is already visible in the weakly pronounced intensity time cor-

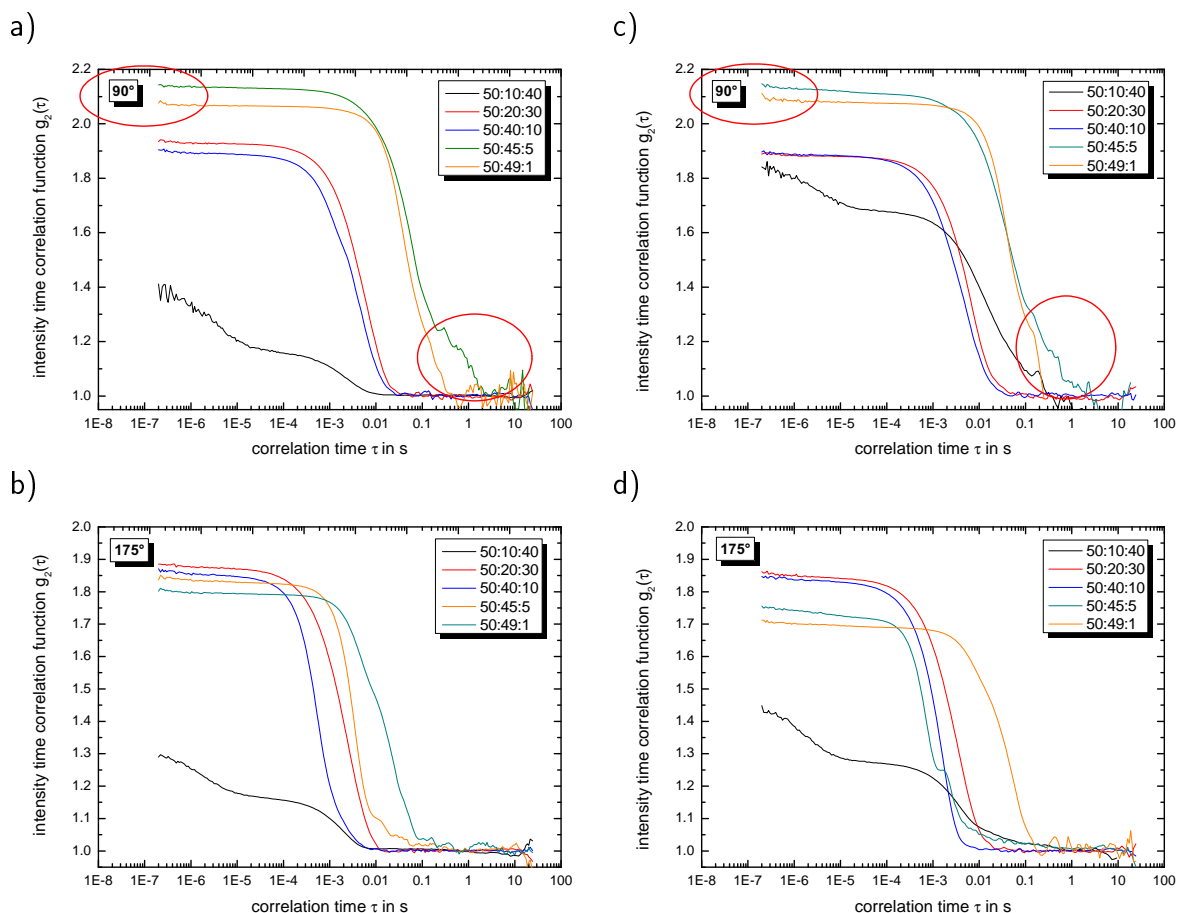


Fig. B.7.: a)-d) Intensity time correlation function of  $1^{4+}:2^{2-}$  1 mM:3 mM in solvent mixtures with various DMSO:glycerol:water (v/v/v) ratios. a)-b) Results from day 7 with side and back scattering. c)-d) Results from day 14 with side and back scattering.

relation functions. Furthermore, the trend of these graphs stays constant throughout the measuring time even at different scattering angles, implying a stagnation at the ion cloud state. Increasing the amount of glycerol in the solvent mixture helps building anisotropic ionic clusters throughout the entire solution, which results in nicely shaped intensity time correlation functions. However, at the ratio of 50:40:10 (v/v/v), we detect (for both scattering angles) a shift of these graphs to lower correlation times. This indicates the formation of smaller aggregates and leads to highly defined globular ionoids in the solvent mixture DMSO:glycerol:water 50:43:7 (v/v/v).

Further changes in the glycerol:water ratio towards higher amounts of glycerol invert the movement for the intensity time correlation function. At side scattering, we also detect intensity time correlation functions with an elevated baseline as well as larger y-intercept values than 2 (see the red circles in Fig. 2.4). These features hint out the existence of number fluctuations. Number fluctuations occur, when a small amount of larger particles pass the laser, while the remaining solution provides only minor scattering intensity. The system  $1^{4+}:2^{2-}$  initiates

from large ion cloud formations, but also keeps a minor potential to form at least anisotropic ionic clusters. Due to these variations in the hydrodynamic radius, the detection of number fluctuations seems likely possible.

## b) CW EPR results

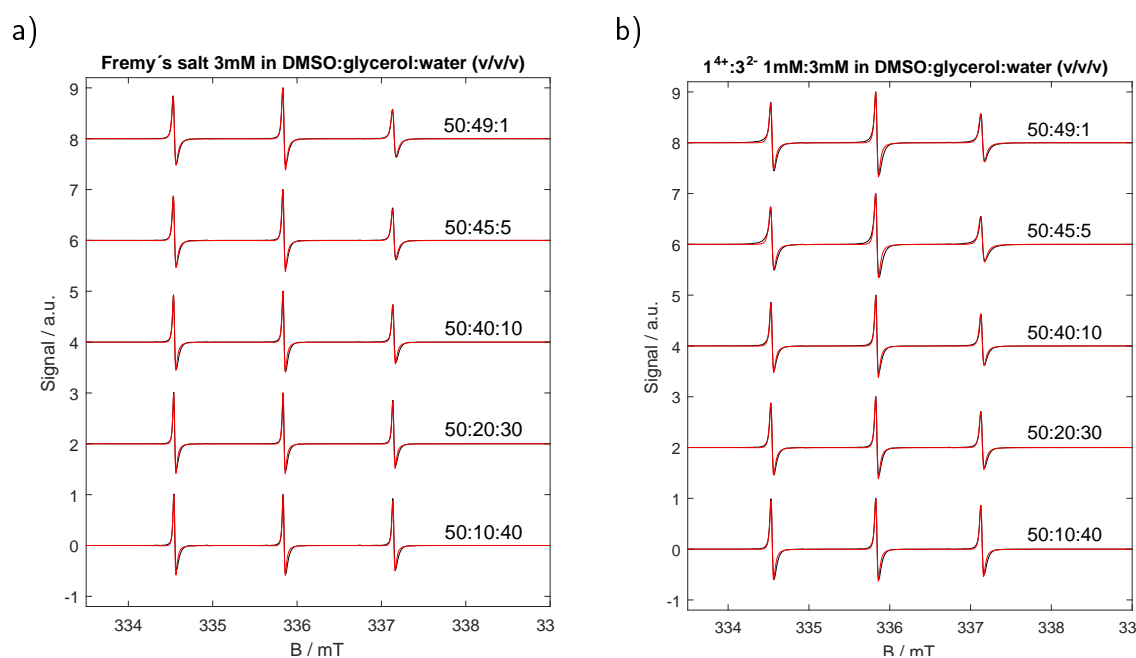


Fig. B.8.: X-band CW EPR spectra of a) Fremy's salt and b)  $1^{4+}:3^{2-}$  in various DMSO:glycerol:water (v/v/v) ratios containing both experimental (black lines) as well as simulated data (red lines).

Similar to the first solvent mixtures, we measure a correlation between the hindered rotational mobility for pure Fremy's salt with increasing viscosity or amount of glycerol. Through adding  $1^{4+}$ , we determine an additional slow-down for  $3^{2-}$  (see Fig. B.8 and B.10), which results in a reduced  $D_{\perp}$  tensor.

The development of the rotational dynamics anisotropy-values of pure Fremy's salt and especially  $1^{4+}:3^{2-}$  for X- and Q-band frequencies do not provide four different regions as we observed them with DLS, as Fig. B.9 demonstrates. This is different compared to the line width analysis in Chapter 4, which provides similar regions compared to the light scattering method.

Pure Fremy's salt at X-band frequencies clearly displays a steady increase in  $T$  beginning at the glycerol:water-ratio 15:35, when increasing the glycerol and decreasing the water content in the solvent mixture. As a result, we just see the expected slow-down in axially symmetric rotational motion when increasing the solvent viscosity. Again, the difference in frequency/field dependence of the rotational time-frame becomes apparent when looking at the Q-band data.

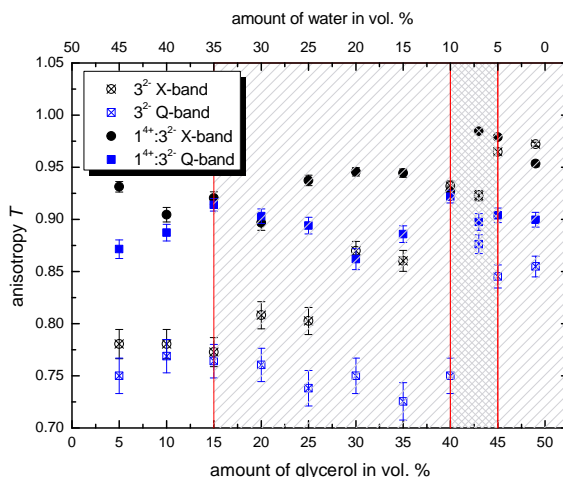


Fig. B.9.: Plot of the anisotropy  $T$  (equation A.7) of pure Frey's salt and system  $\mathbf{1}^{4+}:\mathbf{3}^{2-}$  for X- and Q-band against the amount of glycerol and water in volume percentage. The regions marked in different shadings are based on the DLS data as described in Chapter 4.

Here the increase in the  $T$ -value only starts at glycerol:water 40:10.

With adding the  $\mathbf{1}^{4+}$ , we detect a significant increase in the anisotropy throughout all solvent mixtures and at both CW EPR frequencies. Furthermore, the  $T$ -values do not contain the correlation with solvent viscosity as seen for pure Frey's salt. The effects of the (i) electrostatic interactions between  $\mathbf{1}^{4+}$  and  $\mathbf{3}^{2-}$  and the (ii) constant amount of DMSO inside the solvent mixture are strong enough, to overlay the influence of the glycerol:water-ratio. Thus the volume ratio of glycerol and water determines mainly the size and shape of the self-assembled structures, but not a specific behavior for the anisotropy  $T$ .

Table B.6 summarizes, equal to the first section, the important parameters for calculating  $\tau_c$  and  $T$ . A closer look at the rotational correlation times for  $\mathbf{1}^{4+}:\mathbf{3}^{2-}$  reveals a significant increase of  $\tau_c$  at solvent mixture DMSO:glycerol:water 50:15:35 (v/v/v). Based on the DLS data we know that this solvent marks the starting point for creating at least anisotropic ionic clusters. Thereby, we can associate the increase of  $\tau_c$  with stronger globular electrostatic interactions between  $\mathbf{1}^{4+}$  and  $\mathbf{3}^{2-}$  inside the ion cloud state, which are important to form highly defined self-assembled structures. The other regions that were characterized with DLS, can not be distinguished through CW EPR at X-band frequencies due to the restriction of analyzing the initial ion cloud.

Utilizing Q-band frequencies, the behavior of the rotational anisotropy  $T$  of  $\mathbf{1}^{4+}:\mathbf{3}^{2-}$  and pure Frey's salt is in most parts analogous with the X-band results and was already discussed. The Q-band CW EPR spectra (Fig. B.10) deliver for solely  $\mathbf{3}^{2-}$  the familiar correlation between rotational mobility and solvent viscosity. The same can be determined while adding the  $\mathbf{1}^{4+}$  with the exception for solvent mixtures DMSO:glycerol:water 50:45:5 and 50:49:1 (v/v/v).

**Table B.6.:** Summary of the simulated axial rotational diffusion tensor  $D_{\perp}$  and  $D_{\parallel}$  as well as the calculated rotational correlation time  $\tau_c$  and anisotropy  $T$  for pure Fremy's salt and  $\mathbf{1}^{4+}:\mathbf{3}^{2-}$  at X-band frequencies while changing the glycerol:water ratio of the solvent mixtures

solvent	$\mathbf{3}^{2-}$				$\mathbf{1}^{4+}:\mathbf{3}^{2-}$			
	$D_{\perp}/\text{s}^{-1}$	$D_{\parallel}/\text{s}^{-1}$	$\tau_c/\text{ps}$	$T$	$D_{\perp}/\text{s}^{-1}$	$D_{\parallel}/\text{s}^{-1}$	$\tau_c/\text{ps}$	$T$
50:5:45	3.0e9	3.5e10	24.50	0.780	1.2e9	5.0e10	40.06	0.931
50:10:40	3.0e9	3.5e10	24.50	0.780	1.7e9	5.0e10	31.76	0.904
50:15:35	2.5e9	2.8e10	29.80	0.773	7.0e8	2.5e10	72.30	0.920
50:20:30	2.2e9	3.0e10	31.71	0.808	7.4e8	2.0e10	75.05	0.897
50:25:25	2.5e9	3.3e10	28.21	0.803	6.1e8	2.8e10	76.31	0.937
50:30:20	1.9e9	4.0e10	31.68	0.870	4.7e8	2.5e10	94.29	0.946
50:35:15	1.9e9	3.7e10	32.60	0.860	5.0e8	2.6e10	89.31	0.944
50:40:10	9.5e8	4.0e10	50.43	0.932	4.6e8	1.8e10	106.72	0.927
50:45:5	4.8e8	4.0e10	79.49	0.965	2.5e8	3.5e10	128.39	0.979
50:49:1	3.8e8	4.0e10	92.89	0.972	3.2e8	2.0e10	131.24	0.953

The first mixture displays an additional slow-down for the rotational mobility of Fremy's salt, which is already visible in the highfield peak of the CW EPR spectra (see Fig. B.10). A further increase of glycerol inside the solvent cancels the effect and provides rotational correlation times in the region of DMSO:glycerol:water 50:40:10 (v/v/v).

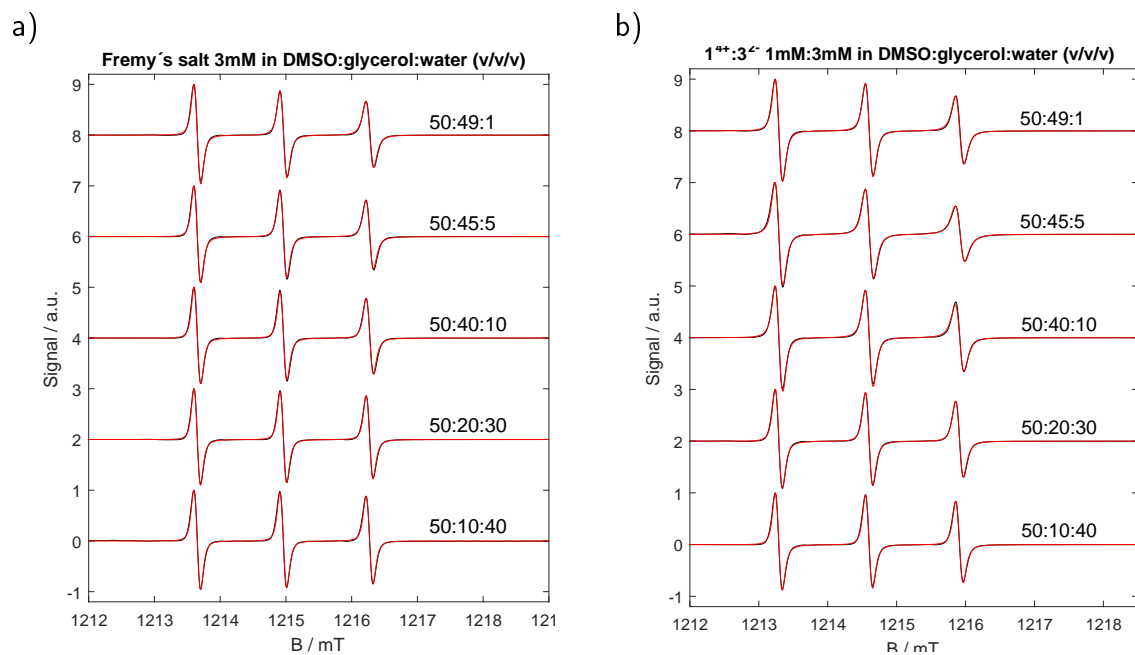


Fig. B.10.: Q-band CW EPR spectra of a) Fremy's salt and b)  $1^{4+}$  and  $3^{2-}$  in various DMSO:glycerol:water (v/v/v) ratios containing both experimental (black lines) as well as simulated data (red lines).

Note that this additional phenomena occurs with solvent mixture, where we found based on the DLS results the potential to form globular ionoids. The initial ion cloud seems to induce stronger local electrostatic interactions between  $1^{4+}$  and  $3^{2-}$ , which are on the one hand only detectable at higher frequencies/magnetic fields and on the other hand important to create either future anisotropic ionic clusters or globular ionoids. The exact values for  $D_{\perp}$ ,  $D_{\parallel}$ ,  $\tau_c$  and  $T$  are written down in Table B.7.

**Table B.7.:** Summary of the simulated axial rotational diffusion tensor  $D_{\perp}$  and  $D_{\parallel}$  as well as the calculated rotational correlation time  $\tau_c$  and anisotropy  $T$  for pure Fremy's salt and  $\mathbf{1}^{4+}:\mathbf{3}^{2-}$  at Q-band frequencies while changing the glycerol:water ratio of the solvent mixtures

solvent	$\mathbf{3}^{2-}$				$\mathbf{1}^{4+}:\mathbf{3}^{2-}$			
	$D_{\perp}/s^{-1}$	$D_{\parallel}/s^{-1}$	$\tau_c/ps$	$T$	$D_{\perp}/s^{-1}$	$D_{\parallel}/s^{-1}$	$\tau_c/ps$	$T$
50:5:45	4.5e9	4.5e10	17.19	0.750	1.5e9	3.2e10	40.06	0.871
50:10:40	4.1e9	4.5e10	18.30	0.780	1.3e9	3.2e10	44.07	0.887
50:15:35	4.2e9	4.5e10	18.00	0.764	7.6e8	2.5e10	68.44	0.914
50:20:30	3.8e9	4.0e10	20.01	0.761	7.6e8	2.2e10	71.42	0.903
50:25:25	3.7e9	3.5e10	21.30	0.738	7.6e8	2.0e10	73.73	0.894
50:30:20	3.3e9	3.3e10	23.44	0.750	7.1e8	1.4e10	86.89	0.862
50:35:15	2.8e9	2.5e10	28.69	0.725	7.0e8	1.7e10	82.22	0.886
50:40:10	2.0e9	2.0e10	38.68	0.750	3.3e8	1.2e10	152.45	0.922
50:45:5	9.2e8	1.6e10	69.93	0.845	2.5e8	7.3e9	216.50	0.904
50:49:1	7.5e8	1.4e10	83.77	0.854	4.3e8	1.2e10	127.78	0.900

## Importance of bulk concentration

### a) DLS results

Based on the declarations in Chapter 4, we divide Fig. B.11 into bulk concentrations, which are able to build at least anisotropic ionic clusters with the system  $\mathbf{1}^{4+}:\mathbf{2}^{2-}$  in DMSO:glycerol:water 50:43:7 (v/v/v) and compositions that remain mainly in the ion cloud state. The important transition point is the 'critical ionoid concentration' between 0.1 mM:0.3 mM and 0.2 mM:0.6 mM. Higher bulk concentrations contain enough  $\mathbf{1}^{4+}$ - and  $\mathbf{2}^{2-}$ -ions to induce the formation of highly defined self-assembled structures.

$\mathbf{1}^{4+}:\mathbf{2}^{2-}$  with bulk concentration 1 mM:3 mM and lower were observed for 45 days (i) to highlight the crucial initial state for the formation of globular ionoids and (ii) to check the stability of the structures through the mean scattering intensity. The second fact delivered stable values after the formation of the two separated entities at lower bulk concentrations was fulfilled. Furthermore, we can describe the change of globular ionoids to anisotropic ionic clusters using the mean scattering intensity (see Fig. B.11). Based on the results on day 10 we recognize two facts:

1. a drop in the mean scattering intensity and

2. an increase in the used laser power at bulk concentration 0.2 mM:0.6 mM.

Both aspects imply a significant loss in the overall arrangement of  $\mathbf{1}^{4+}$  and  $\mathbf{2}^{2-}$ , which is equated with the transformation from monodisperse globular ionoids to anisotropic ionic clusters.

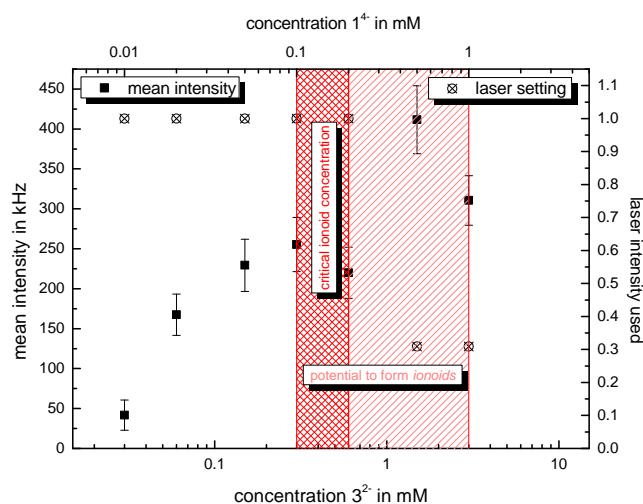


Fig. B.11.: Mean scattering intensity with laser settings at day 10 for the system  $\mathbf{1}^{4+}:\mathbf{2}^{2-}$  in DMSO:glycerol:water 50:43:7 (v/v/v) dependent on the bulk concentration. The light red patterned box highlights the concentration region with the potential to form anisotropic ionic clusters as well as globular ionoids, while the red patterned box displays the 'critical ionoid concentration'.

Bulk concentrations below the 'critical ionoid concentration' can not self-assemble into well-defined structures throughout the entire solution due to weaker electrostatic interactions between  $\mathbf{1}^{4+}$  and  $\mathbf{2}^{2-}$ . Therefore, we detect mainly ion clouds, which deliver lower mean scattering intensities. Note that here the mean scattering intensity decreases almost linear with reducing bulk concentration, which indicates a steady modification from a defined  $\mathbf{1}^{4+}:\mathbf{2}^{2-}$ -structure to homogeneously distributed ions. In general, using mean scattering values allows one to track the smooth transition from globular ionoids over anisotropic ionic clusters to ion clouds.

The second experiment, which includes the highest tested bulk concentration of 1.5 mM:4.5 mM was left out in Fig. B.11, because it was not recorded with the same DLS device. In addition, we measured this sample for 28 days due to its reliable mean scattering intensity and absent formation of two separated entities.



## b) CW EPR results

Table B.8 summarizes the simulated values of  $D_{\perp}$  and  $D_{\parallel}$  as well as the calculated rotational correlation times  $\tau_c$  and rotational anisotropy  $T$  for all tested bulk concentrations at X-band frequencies.

**Table B.8.:** Summary of the simulated axial rotational diffusion tensor  $D_{\perp}$  and  $D_{\parallel}$  as well as the calculated rotational correlation time  $\tau_c$  and anisotropy  $T$  for pure Fremy's salt and  $\mathbf{1}^{4+}:\mathbf{3}^{2-}$  in DMSO:glycerol:water 50:43:7 (v/v/v) at X-band frequencies while changing the bulk concentration

c-ratio mM:mM	$\mathbf{3}^{2-}$				$\mathbf{1}^{4+}:\mathbf{3}^{2-}$			
	$D_{\perp}/s^{-1}$	$D_{\parallel}/s^{-1}$	$\tau_c/ps$	$T$	$D_{\perp}/s^{-1}$	$D_{\parallel}/s^{-1}$	$\tau_c/ps$	$T$
1.5:4:5	9.0e8	3.5e10	54.66	0.927	2.3e8	4.0e10	129.82	0.983
0.5:1:5	9.5e8	3.5e10	52.72	0.923	1.8e8	5.0e10	141.91	0.989
0.2:0.6	8.0e8	3.7e10	58.04	0.938	2.1e8	4.0e10	137.94	0.984
0.1:0.3	7.2e8	4.0e10	60.65	0.948	2.2e8	4.0e10	133.73	0.975
0.05:0.15	8.5e9	3.5e10	56.78	0.934	3.4e8	4.0e10	100.04	0.975
0.02:0.06	8.0e9	4.0e10	59.12	0.934	3.4e8	4.0e10	100.04	0.975
0.01:0.03	1.1e9	4.0e10	46.52	0.942	3.5e8	4.0e10	98.13	0.974

Analogous to the X-band results, combines Table B.9 the data of  $D_{\perp}$ ,  $D_{\parallel}$ ,  $\tau_c$  and  $T$  at Q-band frequency for all tested bulk concentrations.

**Table B.9.:** Summary of the simulated axial rotational diffusion tensor  $D_{\perp}$  and  $D_{\parallel}$  as well as the calculated rotational correlation time  $\tau_c$  and anisotropy  $T$  for pure Fremy's salt and  $\mathbf{1}^{4+}:\mathbf{3}^{2-}$  in DMSO:glycerol:water 50:43:7 (v/v/v) at Q-band frequencies while changing the bulk concentration

c-ratio mM:mM	$\mathbf{3}^{2-}$				$\mathbf{1}^{4+}:\mathbf{3}^{2-}$			
	$D_{\perp}/s^{-1}$	$D_{\parallel}/s^{-1}$	$\tau_c/ps$	$T$	$D_{\perp}/s^{-1}$	$D_{\parallel}/s^{-1}$	$\tau_c/ps$	$T$
1.5:4:5	1.2e9	2.8e10	48.60	0.882	1.7e8	6.2e9	295.63	0.922
0.5:1:5	1.0e9	2.0e10	61.40	0.863	4.0e8	8.2e9	152.24	0.867
0.2:0.6	9.0e8	4.0e10	52.28	0.935	4.5e8	9.2e9	135.45	0.866
0.1:0.3	9.2e8	4.0e10	51.52	0.934	4.5e8	9.5e9	134.01	0.870
0.05:0.15	9.2e8	4.0e10	51.52	0.934	2.8e8	9.2e9	185.84	0.914
0.02:0.06	9.2e8	4.0e10	51.52	0.934	2.8e8	9.5e9	183.87	0.917
0.01:0.03	9.2e8	4.0e10	51.52	0.934	3.2e8	9.5e9	168.21	0.905

Looking at the rotational correlation time  $\tau_c$ , we can display two major differences between Q-band and X-band measurements, which are also highlighted in Chapter 4:

1. the significant increase at bulk concentration 1.5 mM:4.5 mM and
2. the higher  $\tau_c$  values by 0.05 mM:0.15 mM and 0.02 mM:0.06 mM.

The first deviation occurs, because of a simultaneous decrease in both axial rotational diffusion tensors  $D_{\perp}$  and  $D_{\parallel}$ , implying stronger electrostatic interactions throughout the entire ion cloud state and the tendency to form anisotropic ionic clusters. The second deviation is based on a minor decay in the  $D_{\perp}$  tensor, which indicates changes in the molar ratio of 1:3 between  $\mathbf{1}^{4+}$  and  $\mathbf{3}^{2-}$ . Smaller molar ratios lead to disturbances inside the ionic cloud state that hinder the formation of highly defined globular ionoids. In addition to the values in Table B.8 and B.9, we present the X- and Q-band CW EPR spectra for  $\mathbf{1}^{4+}:\mathbf{3}^{2-}$  at all seven bulk concentration in Fig. B.12 to support the discussed differences.

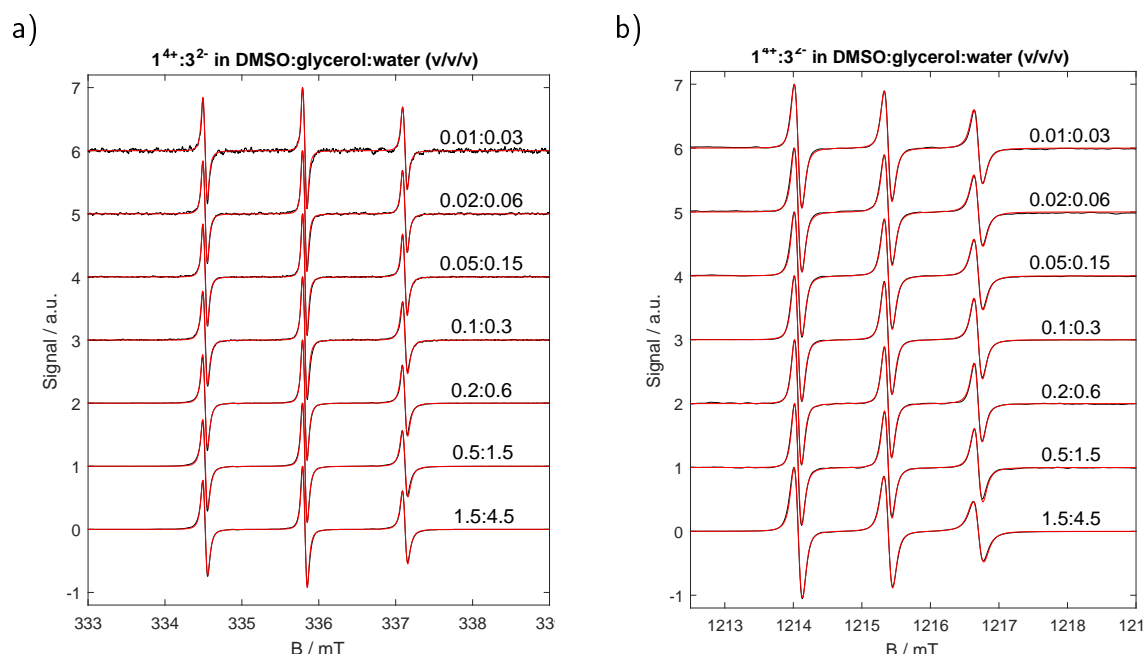


Fig. B.12.: a) X-band and b) Q-band CW EPR spectra of  $\mathbf{1}^{4+}:\mathbf{3}^{2-}$  in DMSO:glycerol:water 50:43:7 (v/v/v) with all seven bulk concentrations. The graphs again contain both the experimental data (black lines) as well as the simulated data (red lines).

Along with analyzing the rotational correlation time  $\tau_c$  for X- and Q-band frequencies, we focused on the full width at half maximum (FWHM) values of the simulated spectra, which are presented in Fig. B.13.

The X-band data represents a similar pattern like the rotational correlation time  $\tau_c$ , which was discussed in Chapter 4. Pure Fremy's salt displays no significant correlation between line width and concentration, while the system  $\mathbf{1}^{4+}:\mathbf{3}^{2-}$  contains two 'steps':

1. between the highest bulk concentration 1.5 mM:4.5 mM and the established 1 mM:3 mM ratio and
2. after the 'critical ionoid concentration'.

The first drop in the FWHM line width indicates stronger electrostatic interactions between  $\mathbf{1}^{4+}$  and  $\mathbf{3}^{2-}$  at higher concentrations consistently inside the ion cloud state. Throughout the region, which is capable of forming ionoids, we get a constant line width, implying comparable global noncovalent interactions. Again, we can not distinguish between globular ionoids and anisotropic ionic clusters like with DLS, because CW EPR just observes the initial ion cloud state. The second drop in the FWHM line width can be interpreted as a sign for reaching the 'critical ionoid concentration', but the difference compared to higher bulk concentrations is rather small.

Q-band CW EPR spectra deliver, just like the rotational correlation time  $\tau_c$ , a different connection between FWHM values and bulk concentration. Pure Fremy's salt shows a prominent

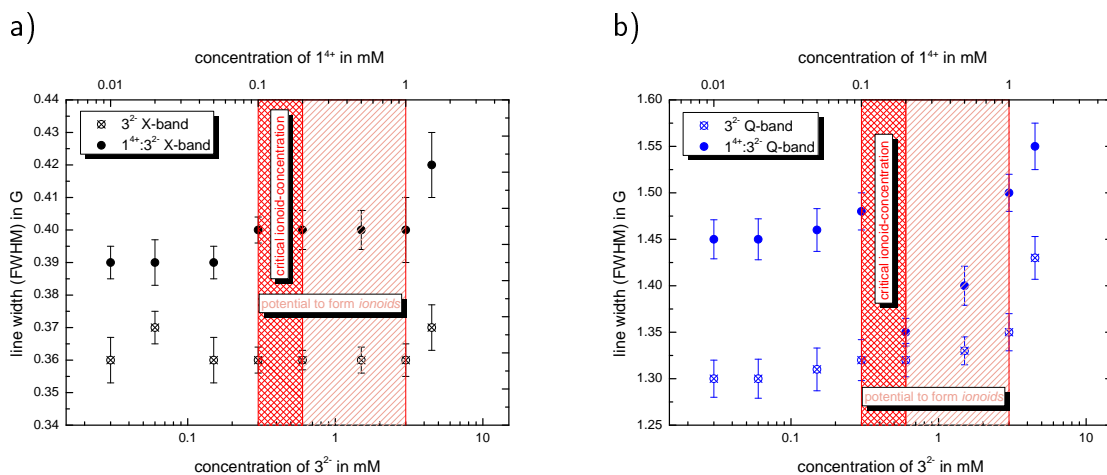


**Fig. B.13.:** Isotropic broadenings of Fremy's salt and  $1^{4+} : 3^{2-}$  in DMSO:glycerol:water 50:43:7 (v/v/v) at different bulk concentrations for a) X-band and b) Q-band frequencies. Both graphs contain separated highlighted regions, which are based on the DLS data (see Chapter 4).

decreased line width while reducing the concentration from 4.5 mM to 3 mM probably due to less collisions between the paramagnetic molecules.<sup>243</sup> Adding  $1^{4+}$  leads to (i) an almost linear decay of the FWHM value between 1.5 mM:4.5 mM and 0.2 mM:0.6 mM and (ii) a sudden increase in the line width at 0.1 mM:0.3 mM, which then stays almost constant even for lower bulk concentrations. The first phenomena correlates with weaker electrostatic interactions between  $1^{4+}$  and  $3^{2-}$  and the possibility to highlight the local environment of Fremy's salt due to higher frequencies/magnetic fields. The second effect, the sudden rise of the line width, can be interpreted with the formation of ion pairs between  $3^{2-}$  and its  $K^+$  counterions. In addition, we observe a similar 'jump' for the anisotropy  $T$  of the rotational diffusion tensor, which will be discussed in the next section.

Besides characterizing the rotational correlation time  $\tau_c$  and FWHM values for both CW EPR frequencies, we also compare the behavior of the rotational anisotropy  $T$  (see Fig. B.14). The X-band spectra for pure Fremy's salt deliver a relatively constant anisotropy, which increases significantly while adding  $1^{4+}$  due to present electrostatic interactions. Furthermore, we recognize slightly smaller  $T$ -values for bulk concentrations below the 'critical ionoid concentration', indicating weakened attractions between  $1^{4+} : 3^{2-}$  inside the ion cloud.

The anisotropy  $T$  based on the Q-band spectra display some major differences compared to the discussed X-band values. Pure Fremy's salt anisotropy decays slightly till 1.5 mM, but then rises to a constant value for all other concentrations. It seems  $3^{2-}$  prefers the water phase inside the solvent mixture. At higher concentrations, Fremy's salt dissolves mainly in this more isotropic environment and thus reduces the anisotropy. Decreasing the concentration provides two possible reasons for the sudden jump in  $T$ :

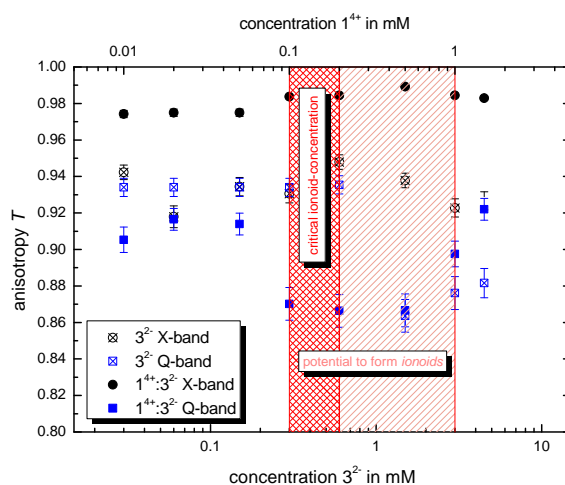


Fig. B.14.: Plot of the anisotropy  $T$  of pure Fremy's salt and system  $1^{4+}:3^{2-}$  in DMSO:glycerol:water 50:43:7 (v/v/v) for X- and Q-band against the concentration of  $1^{4+}$  and  $3^{2-}$ . The separated highlighted regions are based on the DLS results (see Chapter 4).

1. the total number of  $3^{2-}$  inside the water phase decays, which causes a reinforced signal from the nitroxide-ions in DMSO and glycerol or
2. the formation of ion pairs between  $3^{2-}$  and  $K^+$  inside the solvent.

The system  $1^{4+}:3^{2-}$  also delivers a decay in  $T$  from 1.5 mM:4.5 mM till 0.5 mM:1.5 mM, mainly due to weaker electrostatic forces between those two ions. In the region of the 'critical ionoid concentration', we do not see a change in the rotational dynamics, which indicates similar local attractions between  $1^{4+}$  and  $3^{2-}$  inside the ion cloud compared to the previous bulk concentration. Further decreases in the bulk concentration lead to higher  $T$  values, but here they do not surpass the results from pure Fremy's salt. We assume that  $1^{4+}$  prevents partially the formation of ion pairs of  $3^{2-}$  with  $K^+$ , leading to a comparatively isotropic environment.

# C | Appendix - Chapter 5

## Sample preparation

Preparing the different molar ratios for the  $\mathbf{1^{4+}:2^{2-}}$  ( $\mathbf{1^{4+}:3^{2-}}$ , respectively) system started with producing following stock solutions in DMSO:glycerol:water 50:43:7 (v/v/v):

- $c(\mathbf{1^{4+}}) = 6 \text{ mM}$  and
- $c(\mathbf{2^{2-}}) = c(\mathbf{3^{2-}}) = 6 \text{ mM}$ .

The two stock solutions were then combined based on Table C.1 to receive the desired molar ratios.

**Table C.1.:** Summary of all tested molar ratios for the system  $\mathbf{1^{4+}:2^{2-}}$  ( $\mathbf{1^{4+}:3^{2-}}$ , respectively) in DMSO:glycerol:water 50:43:7 (v/v/v) combined with their calculated ionic ratio

molar ratio	$c(\mathbf{1^{4+}})$ / mM	$c(\mathbf{2^{2-}/3^{2-}})$ / mM	$V(\mathbf{1^{4+}})$ / $\mu\text{l}$	$V(\mathbf{2^{2-}/3^{2-}})$ / $\mu\text{l}$	$V(\text{solvent})$ / $\mu\text{l}$	ionic ratio <sup>a</sup>
0:1	0.0	3.0	0	120	120	-
1:6	0.5	3.0	20	120	120	1/3
1:3	1.0	3.0	40	120	80	2/3
1:2	1.5	3.0	60	120	60	1
2:3	2.0	3.0	80	120	40	4/3
5:6	2.5	3.0	100	120	20	5/3
1:1	3.0	3.0	120	120	0	2

<sup>a</sup> calculating ionic ratio using equation (5.1)

Calculating the ionic ratio inside each  $\mathbf{1^{4+}:2^{2-}}$  ( $\mathbf{1^{4+}:3^{2-}}$ , respectively) system is based on equation (5.1). Note that we assume a constant charge  $z^{\pm}$  for the cationic ( $z^+ = +4$ ) and anionic ( $z^- = -2$ ) building block in all tested molar ratios.

## Analyzing ionic ratio dependence with DLS

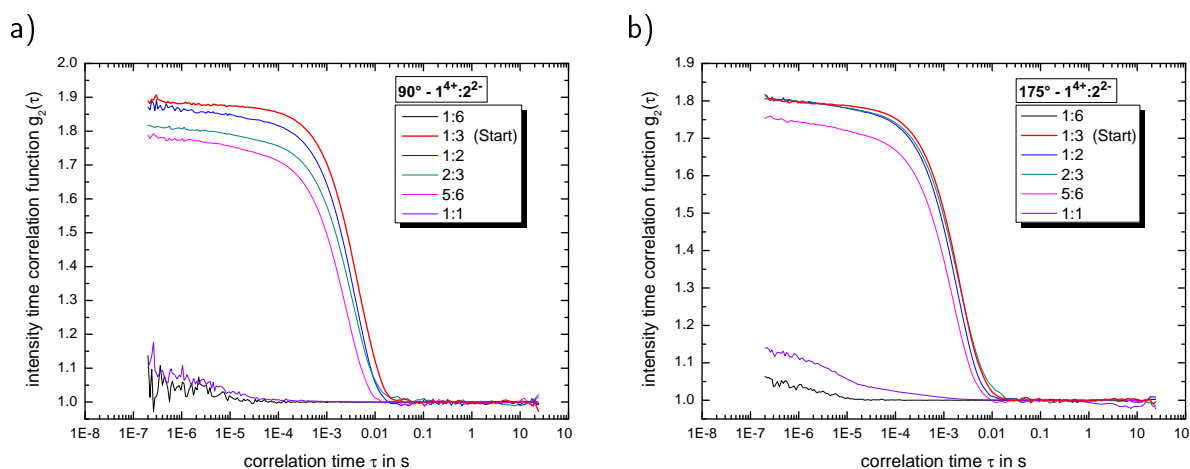


Fig. C.1.: Intensity time correlation functions at measurement day 79 with a) side and b) back scattering for the cluster system  $1^{4+}:2^{2-}$  in DMSO:glycerol:water 50:43:7 (v/v/v) depending on the molar ratio of cationic and anionic component. The well-known 1:3-ratio is highlighted with a slightly thicker red line.

Based on the intensity time correlation functions at measurement day 79 (see Fig. C.1) one can clearly state that the molar ratios  $1^{4+}:2^{2-}$  1:3 to 5:6 show almost the same decay. The small deviations, which are present, provide the shifts in the hydrodynamic radius for the self-assembled ionic structures. In contrary, the molar ratios 1:6 and 1:1 do not show a pronounced autocorrelation function, indicating the absence of highly defined structures. Fig. C.2 confirms this by displaying the autocorrelation functions for the 79 days old samples after filtering them.

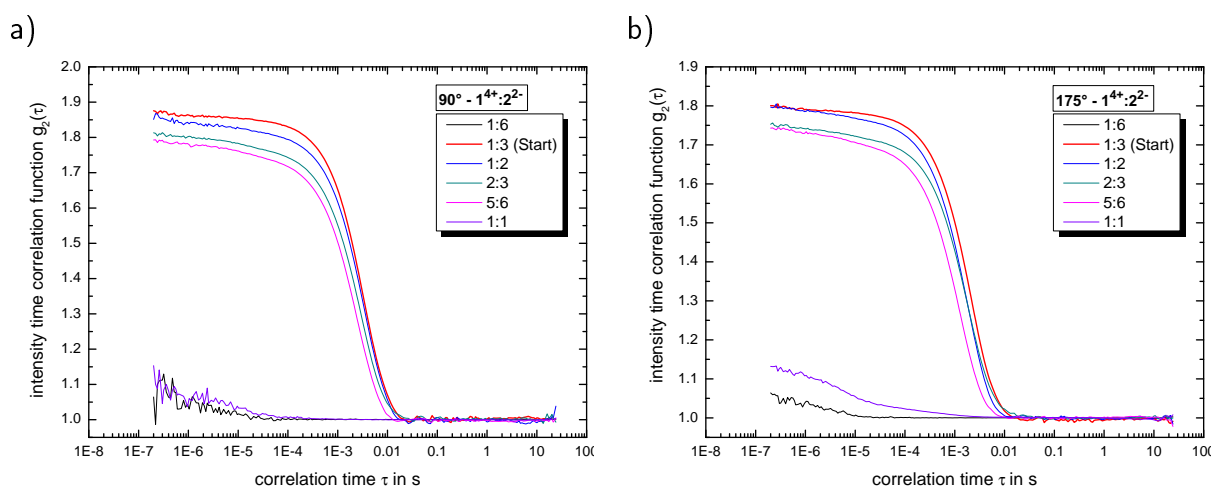


Fig. C.2.: Intensity time correlation functions after sample filtration with a) side and b) back scattering for the cluster system  $1^{4+}:2^{2-}$  in DMSO:glycerol:water 50:43:7 (v/v/v) depending on the molar ratio of cationic and anionic component. The well-known 1:3-ratio is highlighted with a slightly thicker red line.

## Analyzing ionic ratio dependence with CW EPR

Before discussing the CW EPR results, the set of Euler angles for the measured samples is included, as mentioned in Appendix A. They are made out of:

- pure Fremy's salt:  $\alpha = 65^\circ$ ,  $\beta = 90^\circ$ ,  $\gamma = 15^\circ$  and
- $\mathbf{1}^{4+}:\mathbf{3}^{2-}$ :  $\alpha = 85^\circ$ ,  $\beta = 90^\circ$ ,  $\gamma = 15^\circ$ .

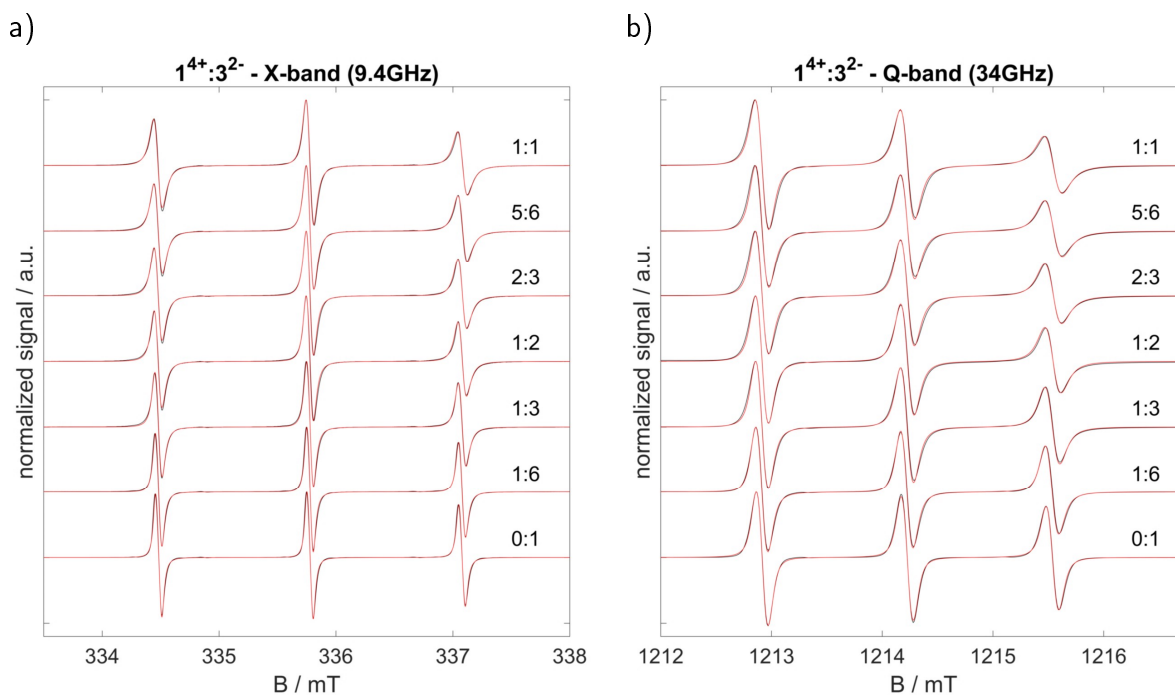


Fig. C.3.: a) X-band and b) Q-band CW EPR spectra for system  $\mathbf{1}^{4+}:\mathbf{3}^{2-}$  in DMSO:glycerol:water 50:43:7 (v/v/v) depending on the molar ratio. Both graphs show for each mixture the measured spectrum (black line) as well as the simulated spectrum (red line).

Fig. C.3 displays all measured and simulated CW EPR spectra at both X- and Q-band frequencies for the system  $\mathbf{1}^{4+}:\mathbf{3}^{2-}$  in DMSO:glycerol:water 50:43:7 (v/v/v) depending on the molar ratio. One can clearly state that with increasing concentration of the 'Texas-sized molecular box' the rotational mobility of Fremy's salt continuously decreases (see also Fig. C.4 a)). This is also visible in the rising FWHM values, which are described in Chapter 4. The coordination between both components shifts with higher ionic ratios from relatively free to a more fixed one, which disturbs the following self-assembly process into highly defined, globular structures.



While rotational correlation time  $\tau_c$  and line width show the same tendencies at X- and Q-band frequencies, we detect significant differences in their anisotropy values (see Fig. C.4 b)). At X-band frequencies, we mainly observe the drop of  $D_{\perp}$  with higher concentration, resulting in increasing  $T$ -values. However, higher frequencies display the formation of fixed coordinations between  $\mathbf{1}^{4+}$  and  $\mathbf{3}^{2-}$ , which decrease  $D_{\perp}$  as well as  $D_{\parallel}$  and keeps  $T$  at a constant lower value. It seems that X-band data show the existing electrostatic interactions in the total ion cloud state, while Q-band spectra highlight the direct coordination behavior of Fremy's salt.

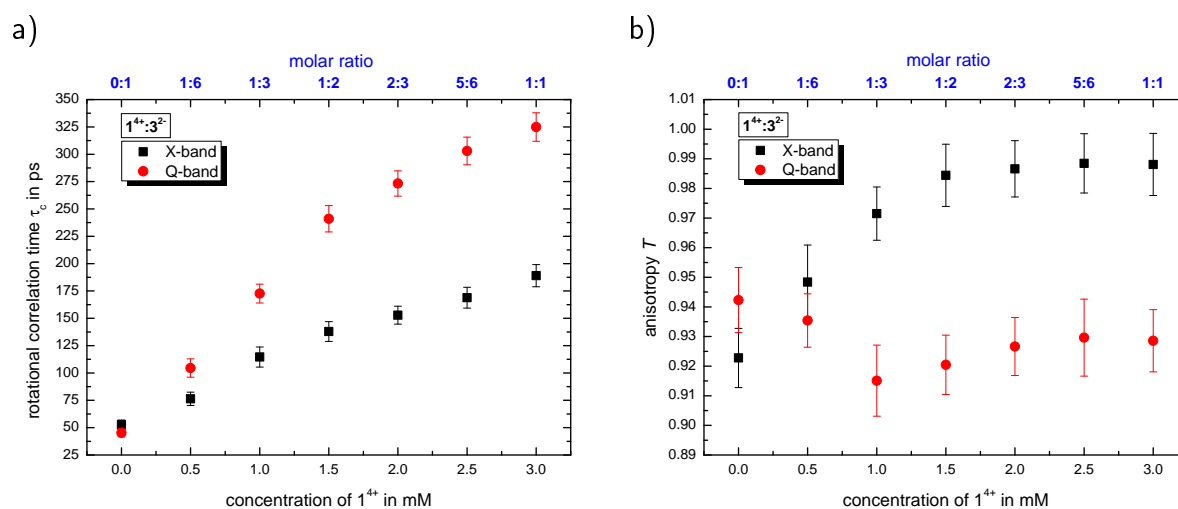


Fig. C.4.: a) Rotational correlation time  $\tau_c$  and b) anisotropy  $T$  of the system  $\mathbf{1}^{4+}:\mathbf{3}^{2-}$  versus the concentration of  $\mathbf{1}^{4+}$  in DMSO:glycerol:water 50:43:7 (v/v/v).

Table C.2 summarizes the simulation results for both frequencies.

Table C.2.: Summary of the simulated axial rotational diffusion tensor  $D_{\perp}$  and  $D_{\parallel}$  as well as the calculated rotational correlation time  $\tau_c$  and anisotropy  $T$  of system  $\mathbf{1}^{4+}:\mathbf{3}^{2-}$  in DMSO:glycerol:water 50:43:7 (v/v/v) depending on the molar ratio

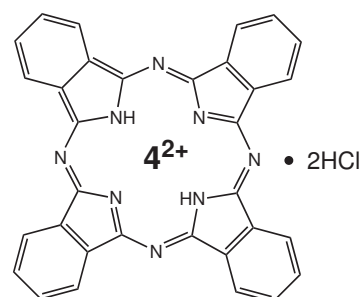
ratio	X-band				Q-band			
	$D_{\perp}/s^{-1}$	$D_{\parallel}/s^{-1}$	$\tau_c / ps$	$T$	$D_{\perp}/s^{-1}$	$D_{\parallel}/s^{-1}$	$\tau_c / ps$	$T$
0:1	9.5e8	3.5e10	52.72	0.923	1.0e9	5.0e10	45.24	0.942
1:6	5.7e8	3.2e10	76.36	0.948	4.5e8	2.0e10	104.56	0.935
1:3	3.1e8	3.2e10	114.61	0.971	3.0e8	1.0e10	172.62	0.915
1:2	2.1e8	4.0e10	137.94	0.984	2.1e8	7.5e9	241.00	0.920
2:3	1.8e8	4.0e10	152.87	0.987	1.8e8	7.0e9	273.30	0.927
5:6	1.55e8	4.0e10	168.89	0.988	1.6e8	6.5e9	303.02	0.930
1:1	1.4e8	3.5e10	188.98	0.988	1.5e8	6.0e9	324.89	0.929

## D | Appendix - Chapter 6

### Modifying the ionic building blocks

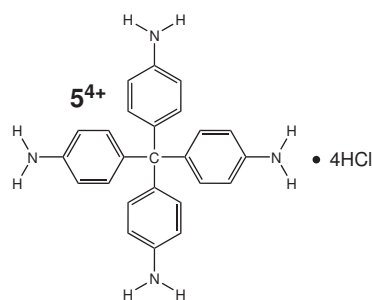
#### Phthalocyaninedihydrochloride ( $4^{2+}$ )

As starting material we used 29H,31H-Phthalocyanine (Sigma-Aldrich) with a purity of 98%. In order to transform this organic compound into its correlated dihydrochloride, we dissolved the material in a 50 ml round bottom flask with dichlormethane. After sealing the round bottom flask with a rubber septum, we added hydrochloric acid ( $c = 2 \text{ mM}$ ) dissolved in diethyl ether to the stirred suspension. After six days, the precipitate was filtered, washed with diethyl ether and dried at  $60^\circ\text{C}$  to receive the wanted Phthalocyaninedihydrochloride.

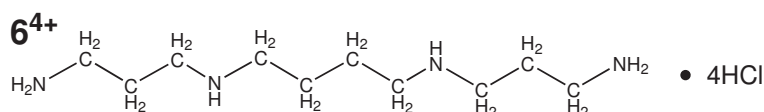


#### Tetrakis(4-aminophenyl)methanetetrahydrochloride ( $5^{4+}$ )

We used Tetrakis(4-aminophenyl)methane (Sigma-Aldrich) with a purity of  $\geq 95\%$  as starting material. The same procedure as described for compound  $4^{2+}$  was used. After adding the hydrochloric acid ( $c = 2 \text{ mM}$ ) dissolved in diethyl ether and drying the washed filter residue, we obtained the Tetrakis(4-aminophenyl)methanetetrahydrochloride.



#### Sperminetetrahydrochloride ( $6^{4+}$ )

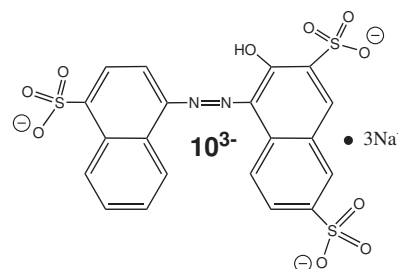


Spermine (Sigma-Aldrich) with a purity of 98% was used as starting material. Again, we added hydrochloric acid ( $c = 2 \text{ mM}$ ) dissolved in diethyl ether in order to receive the corre-

sponding hydrochloride. After washing and drying the filter residue, we received the wanted Sperminetetrahydrochloride.

## Amaranth dye ( $10^{3-}$ )

The Amaranth trisodium salt (Trisodium (4E)-3-oxo-4-[(4-sulfonato-1-naphthyl)hydrazono]naphthalene-2,7-disulfonate; Sigma-Aldrich) with a purity of 85% was recrystallized. Therefore, we dissolved the starting material with a mixture of methanol:ethanol:water 6:3:1 (v/v/v) and heat the solution for one hour under constant stirring. After storing the mixture at  $-20^{\circ}\text{C}$  for a couple of weeks, the precipitated Amaranth was filtered and washed with n-hexane. We received Amaranth with  $\geq 98\%$  purity.



## Supplement UV-vis and fluorescence spectroscopy

UV-vis spectra, especially for the systems  $1^{4+}:10^{3-}$  and  $6^{4+}:10^{3-}$ , were recorded with the diode-array spectrophotometer HP 8453 (Agilent Technologies, Santa Clara, United States). Note that we had to measure a blank spectrum from the solvent mixture DMSO:glycerol:water 50:43:7 (v/v/v) before characterizing the cluster systems in order to solely display the absorption from the chromophore. Based on the explored absorption spectra of Amaranth in the systems  $1^{4+}:10^{3-}$  and  $6^{4+}:10^{3-}$ , we could also apply fluorescence spectroscopy. Here, we utilized the Fluoromax-2 spectrometer to record the emission spectra. For each sample we took (i) three scans to improve the signal-to-noise ratio and (ii) the current lamp intensity as internal reference.

Additionally, we characterize pure  $10^{3-}$  ( $c = 30\mu\text{M}$ ) in DMSO:glycerol:water 50:43:7 (v/v/v) to gain a reference absorption and emission spectra. Note that the dye concentration corresponds to its amount in the cluster systems. By comparing the band intensities and positions of  $1^{4+}:10^{3-}$  and  $6^{4+}:10^{3-}$  with our reference, we can try to link deviations here with detected globular structures from DLS data.

## Supplement IED

Table D.1 summarizes for each ionic building unit the derived information from the YASARA-structure software, which are needed to craft the IEDs after the description from Appendix A.

**Table D.1.:** Summary of all derived information from the YASARA-structure software to construct the ionoid evolution diagrams

ionic compound	diameter / nm	charge $z^{\pm} \cdot e$ / $10^{-19} \text{As}$	volume $V$ / $\text{\AA}^3$	volume charge density $\rho$ / $10^9 \frac{\text{As}}{\text{m}^3}$
<b>1<sup>4+</sup></b>	1.390	6.408	907.15	0.706
<b>2<sup>2-</sup></b>	0.278	-3.204	118.36	-2.710
<b>3<sup>2-</sup></b>	0.285	-3.204	106.48	-3.010
<b>4<sup>2+</sup></b>	1.270	3.204	709.61	0.452
<b>5<sup>4+</sup></b>	0.991	6.408	528.49	1.210
<b>6<sup>4+</sup></b>	0.564	6.408	312.07	2.050
<b>7<sup>2-</sup></b>	0.245	-3.204	90.57	-3.540
<b>8<sup>2-</sup></b>	0.385	-3.204	144.59	-2.220
<b>9<sup>2-</sup></b>	0.251	-3.204	96.72	-3.310
<b>10<sup>3-</sup></b>	1.050	-4.806	550.85	-0.872

## Characteristics of solvent mixture and ionic building units

Before discussing the new systems, which were created through the substitution of the model compounds **1<sup>4+</sup>** and **2<sup>2-</sup>** (**3<sup>2-</sup>**, respectively), we want to point out the scattering behavior of the pure solvent mixture DMSO:glycerol:water 50:43:7 (v/v/v) as well as the respective ionic building units. The intensity time correlation functions at side and back scattering for the solvent itself can be found in Fig. D.1. After preparing the solvent mixture in the same manner like the 'real' DLS samples, we do not (i) record pronounced autocorrelation functions as well as (ii) low scattering intensities, indicating the absence of nanostructured entities inside the sample. Therefore, we can be concluded that the solvent mixture itself does not show tendencies for the formation of defined structures and the following intensity time correlation functions derive from introducing the ionic building units into DMSO:glycerol:water.

Additionally, we measured the surface tension of the solvent mixture DMSO:glycerol:water 50:43:7 (v/v/v). Based on this value we can, considering the surface tensions of pure water and DMSO, estimate the probability of the ionic building units to move to the air-solvent interface. To determine the surface tension of the solvent mixture, we used a DCAT 21 tensiometer (DataPhysics Instruments GmbH, Filderstadt, Germany) with a Du Noüy ring setup. We inserted the ring into the solvent and applied a total of 20 cycles, where the surface tension was calculated with the respective Software SCAT 31 while pulling and pushing the created lamella into the bulk, as shown in Fig. D.2. Through averaging the values for the last ten

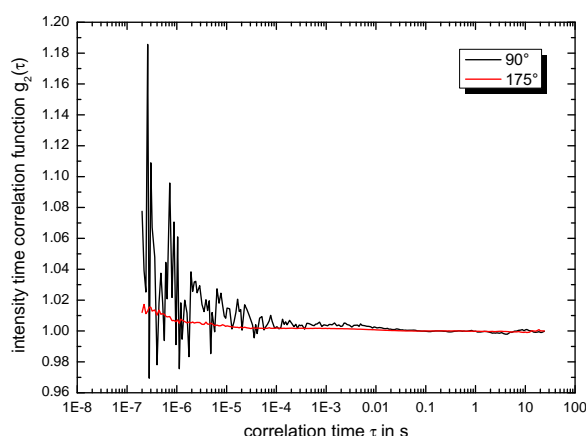


Fig. D.1.: Intensity time correlation function from the pure solvent mixture DMSO:glycerol:water 50:43:7 (v/v/v) at side and back scattering.

cicles, we obtained a surface tension for the solvent mixture of  $53.698 \text{ mN/m} \pm 0.008 \text{ mN/m}$ . This result is much closer to pure DMSO ( $43.670 \text{ mN/m} \pm 0.002 \text{ mN/m}$ ) than to pure water ( $72.287 \text{ mN/m} \pm 0.046 \text{ mN/m}$ ), which reduces the potential of the amphiphil building units to attach at the air-solvent interface, but to remain inside the bulk.

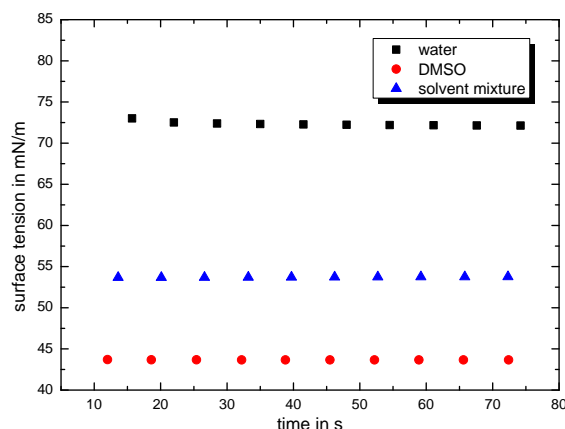


Fig. D.2.: Surface tension of water, DMSO and the solvent mixture DMSO:glycerol:water 50:43:7 (v/v/v) recorded over a course of 20 cycles. The graph contains the values while pulling the Du Noüy ring setup from the air-solvent interface.

To present the DLS data for all ionic building units (which were used for DLS measurements) at side and back scattering in a combined manner, we prepared two separate panels. The first panel (see Fig. D.3) highlights the cationic building units  $1^{4+}$ ,  $4^{2+}$ ,  $5^{4+}$  and  $6^{4+}$  with the same concentration as used inside the tested DLS samples containing methanedisulfonate ( $2^{2-}$ ). All plots of the intensity time correlation functions are intentionally reaching 1.9 at the y-axis, because (i) it helps comparing the different building units and (ii) the model system comprises, after the initial incubation period of ten days, such well pronounced graphs. Furthermore, we

wanted to highlight the y-intercept of 1.3, which marks an important indicative value for analyzing the signal-to-noise ratio of a recorded sample: If the autocorrelation functions stay below this value, then only weakly scattering particles or turbid samples are present.

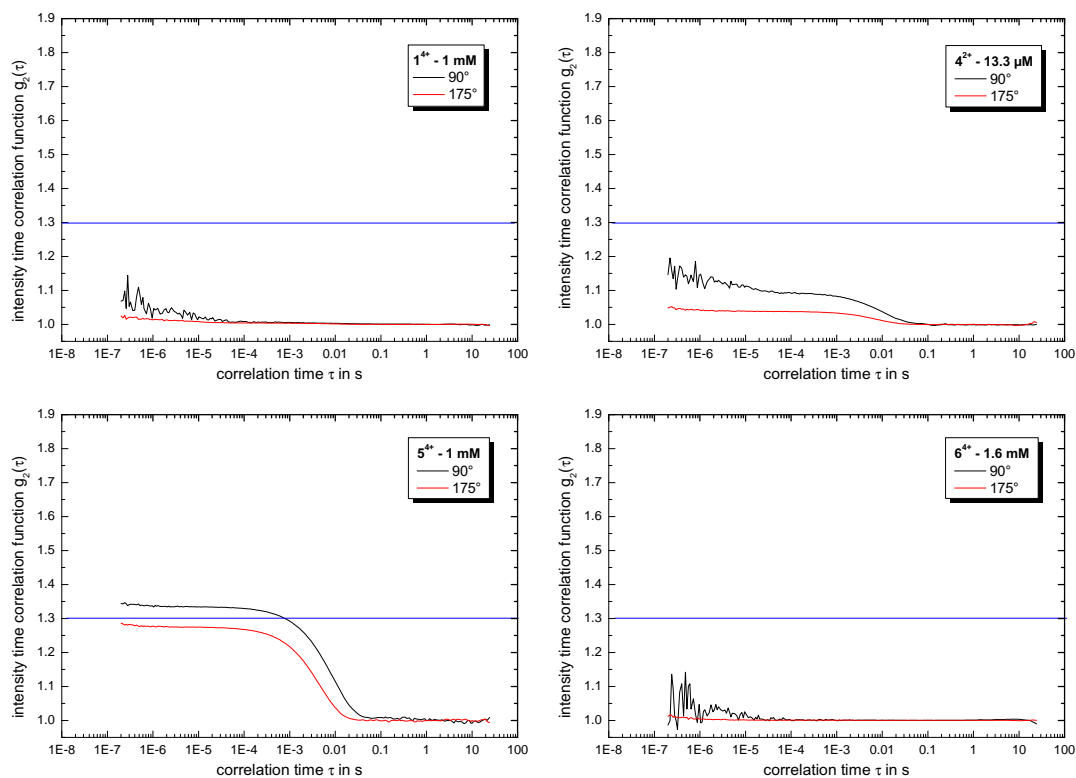


Fig. D.3.: Intensity time correlation functions from the four tested cationic building units  $1^{4+}$ ,  $4^{2+}$ ,  $5^{4+}$  and  $6^{4+}$  in DMSO:glycerol:water 50:43:7 (v/v/v) at side (black line) and back (red line) scattering. The added blue lines at y-intercept value 1.3 aid as guidance and are further described in the text.

Based on the established indicative value, we can conclude that only  $5^{4+}$ -ions with a concentration of 1 mM show a high enough scattering intensity to create autocorrelation functions with a reasonable signal-to-noise ratio. Note that this cation presents in combination with methanedisulfonate less resolved scattering profiles after the incubation period of ten days, which will be discussed separately. The other cations  $1^{4+}$ ,  $5^{4+}$  and  $6^{4+}$  do not present tendencies in forming aggregates or some kind of well-defined structure inside the ternary solvent mixture and are therefore good candidates for the build up of colloid-like ionic cluster.

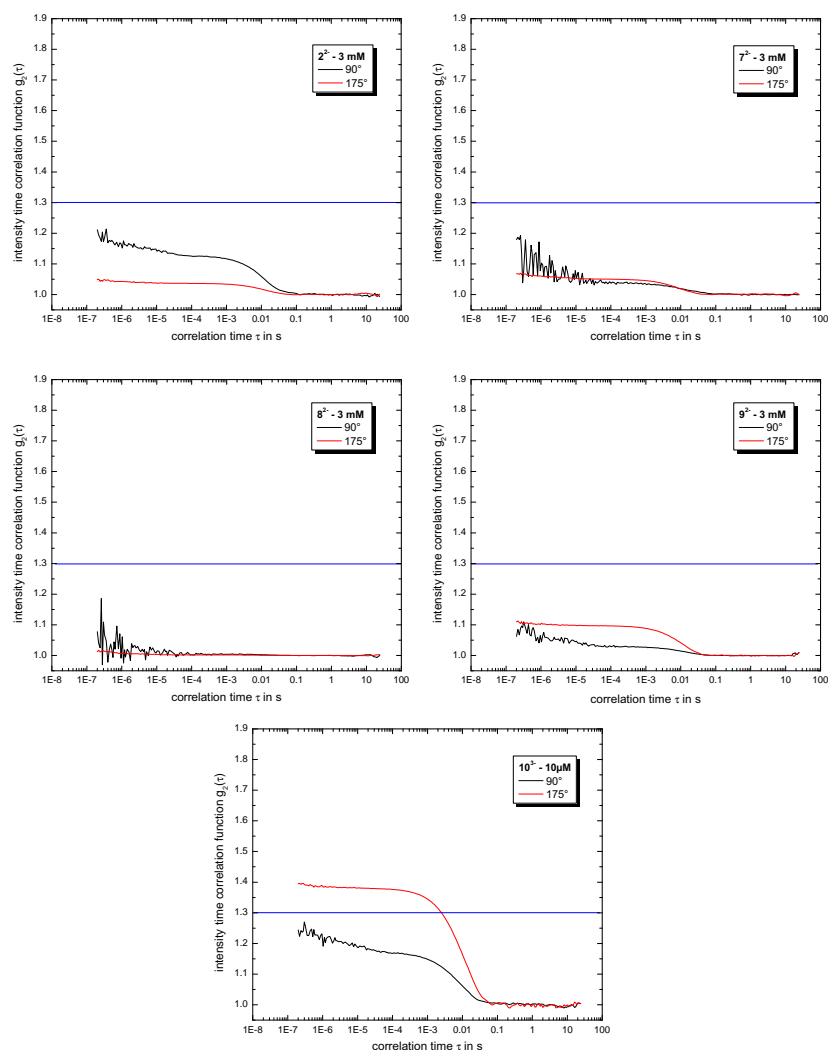


Fig. D.4.: Intensity time correlation functions from the five tested anionic building units  $2^{2-}$ ,  $7^{2-}$ ,  $8^{2-}$ ,  $9^{2-}$  and  $10^{3-}$  in DMSO:glycerol:water 50:43:7 (v/v/v) at side (black line) and back (red line) scattering. The again added blue lines at y-intercept value 1.3 aid as guidance.

The second panel in Fig. D.4 presents the anionic building units  $2^{2-}$ ,  $7^{2-}$ ,  $8^{2-}$ ,  $9^{2-}$  and  $10^{3-}$  with their respective concentration as applied in mixtures containing the 'Texas-sized molecular box'. The dianion of Fremy's salt ( $3^{2-}$ ) was not measured in this context, because we exclusively used the nitroxide radical for CW EPR spectroscopy. Based on the established 'rule' for the cationic building units, we can conclude that only the relatively large trianionic chromophore  $10^{3-}$  shows pronounced intensity time correlation functions. This will be considered when we describe the behavior of the systems  $1^{4+} : 10^{3-}$  as well as  $6^{4+} : 10^{3-}$ . The remaining small anionic building units do not possess a high enough scattering intensity to form well resolved autocorrelation functions.

## Analyze model system with cmPALS method

In this section, we want (i) to further characterize the zeta potential for the model system  $1^{4+}:2^{2-}$  after the incubation period of ten days and (ii) to compare these results with nanosphere size standards from Thermo Scientific. The used size standard containing polystyrene particles with a certified mean diameter of 51 nm and an approximate concentration of 1% solids. The stock solution of polystyrene particles was diluted with a mixture of deionized Milli-Q-water with sodium chloride to a final concentration of 0.02% solids and an ionic strength of  $I = 10\text{mM}$ . Fig. D.5 shows the DLS measurement of the final probe with back scattering. The particle size distribution delivers a mean hydrodynamic radius of  $R_H = 28.4\text{nm}$ , which is in the range of the predetermined hydrodynamic diameter (50-58 nm) for these nanosphere size standards. Note that the DLS results for the model system  $1^{4+}:2^{2-}$  are already displayed in Chapter 6.

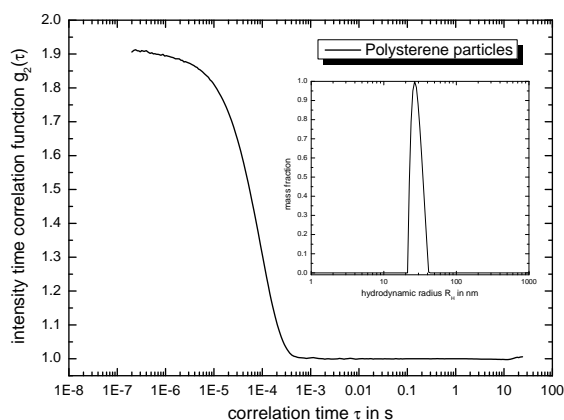


Fig. D.5.: Intensity time correlation function and particle size distribution for polystyrene particles at back scattering.

After characterizing the size of the particles, we can perform cmPALS measurements to obtain the mean zeta potential for both polystyrene particles and the globular ionoids with  $1^{4+}:2^{2-}$ . Therefore, the recorded phase plots (see Fig. D.6) are analyzed by the Kalliope software. The slopes of the straight lines in the phase plot are directly related to the Doppler shift, which is used to determine the electrophoretic mobility of our charged entities. The visible inflection points are caused by the inversion of the electric field, leading to a change in the direction of the particle movement. The comparison of both phase plots already shows that the sign of the electrokinetic potential of the polystyrene particles and the globular ionoids must be switched. Moreover, the amplitude inside the phase plot is more pronounced for the reference material due to their higher mobility inside the low-viscosity solvent water.

Table D.2 combines the calculated parameters ionic strength  $I$  and Henry's function  $F(\kappa a)$  with the measured electrophoretic mobility  $\mu_e$  to present the actual zeta potential  $\zeta$  for both



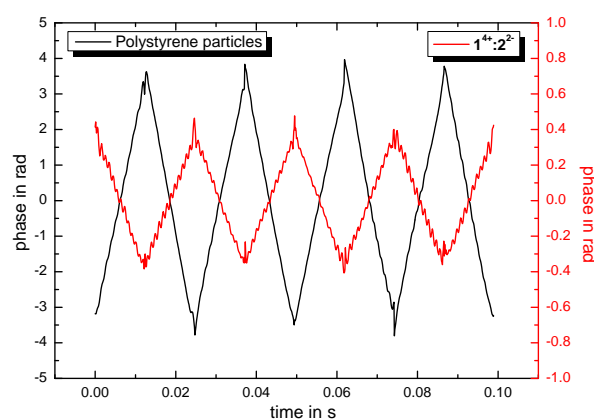


Fig. D.6.: Phase plot of polystyrene particles and globular ionoids containing the ionic building units  $\mathbf{1}^{4+}$  and  $\mathbf{2}^{2-}$ .

samples. Note that each ionic building unit contributes, besides their main compound like  $\mathbf{1}^{4+}$ , counterions like  $\text{PF}_6^-$  into the final sample. Additionally, we tested the ionic building units  $\mathbf{1}^{4+}$  and  $\mathbf{2}^{2-}$  alone with their respective concentration of 1 mM and 3 mM to examine their mobility inside the established solvent mixture.

Table D.2.: Summary of the cmPALS results with the polystyrene particles and the globular ionoids containing  $\mathbf{1}^{4+}$  and  $\mathbf{2}^{2-}$

compound	$I$ / mM	$F(\kappa a)$	$\mu_e / \frac{\mu\text{mcm}}{\text{Vs}}$	$\zeta$ / mV
polystyrene <sup>I</sup>	10	1.101	$-3.695 \pm 0.0210$	$-64.6 \pm 1.0$
$\mathbf{1}^{4+II}$	10	1.004	$0.045 \pm 0.008$	$31.1 \pm 5.2$
$\mathbf{2}^{2-III}$	9	1.000	$-0.001 \pm 0.003$	$-0.3 \pm 1.0$
$\mathbf{1}^{4+}:\mathbf{2}^{2-}$	19	1.168	$0.111 \pm 0.002$	$66.5 \pm 1.2$

<sup>I</sup>nanosphere size standards, <sup>II</sup>counterion:  $\text{PF}_6^-$ , <sup>III</sup>counterion:  $\text{K}^+$

## Substitution of $\mathbf{2}^{2-}$ ( $\mathbf{3}^{2-}$ )

This section (as well as the following ones) will be divided based on the discussed systems to present additional DLS and CW EPR data as well as the UV-vis and fluorescence spectra of Amaranth-based mixtures.

## $1^{4+}:7^{2-}$ ('Texas-sized molecular box':malonate)

Fig. D.7 summarizes all intensity time correlation functions for the system  $1^{4+}:7^{2-}$  with 1 mM:3 mM in the established solvent mixture. The initial phase of the self-assembly process clearly shows pronounced y-intercept-values for the autocorrelation functions, indicating potential for the formation of ionoid-like structures. However, their decay is also shifted to higher correlation times  $\tau$ , which correlates with the build up of larger entities. Over the total measurement time, we record a constant reduce for the autocorrelation function, implying the return to the initial ion cloud state. Note that we applied the ionic ratio of 2/3 to directly compare  $1^{4+}:7^{2-}$  to the model system  $1^{4+}:2^{2-}$ . The substitution of methanedisulfonate with malonate, which includes changing the sulfonate-groups with carboxylate-groups, mainly affects the stability and the shape of the self-assembled entities, as mentioned in Chapter 6.

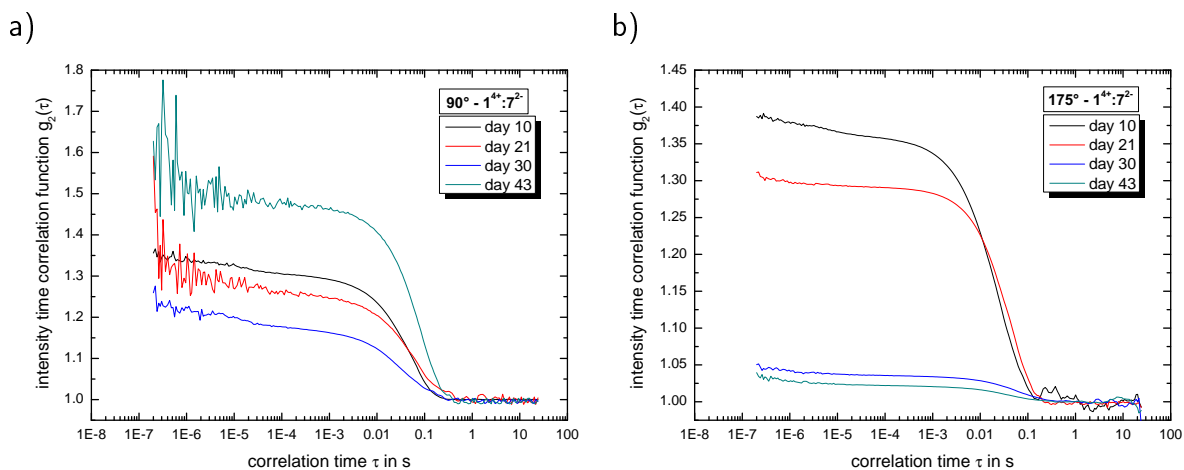


Fig. D.7.: Intensity time correlation function with a) side and b) back scattering for the cluster system  $1^{4+}:7^{2-}$  1 mM:3 mM in DMSO:glycerol:water 50:43:7 (v/v/v) for all measurement days.

In Addition to the information in Chapter 6, Table D.3 combines the important parameter for characterizing the zeta potential for the system  $1^{4+}:7^{2-}$ .

Table D.3.: Summary of the cmPALS results for system made out of 'Texas-sized molecular box' and malonate ( $7^{2-}$ )

compound	$I / \text{mM}$	$F(\kappa a)$	$\mu_e / \frac{\mu\text{mcm}}{\text{Vs}}$	$\zeta / \text{mV}$
$7^{2-}$	9	1.000	$-0.002 \pm 0.001$	$-1.7 \pm 1.0$
$1^{4+}:7^{2-}$	19	1.153	$0.062 \pm 0.003$	$37.4 \pm 2.0$

$l$ counterion:  $\text{Na}^+$

Similar to the model system with methanedisulfonate, we repeated the DLS measurements with

this system after performing the cmPALS studies (see Fig. D.8). The intensity time correlation functions show a significantly reduce for their y-intercept values, indicating a decrease in the overall scattering intensity. The partially build up anisotropic ionic cluster cannot handle the treatment with an external electric field and therefore alter their size and shape. Due to the cmPALS treatment it seems that (in some extent) the return to the initial ion cloud state is accelerated.

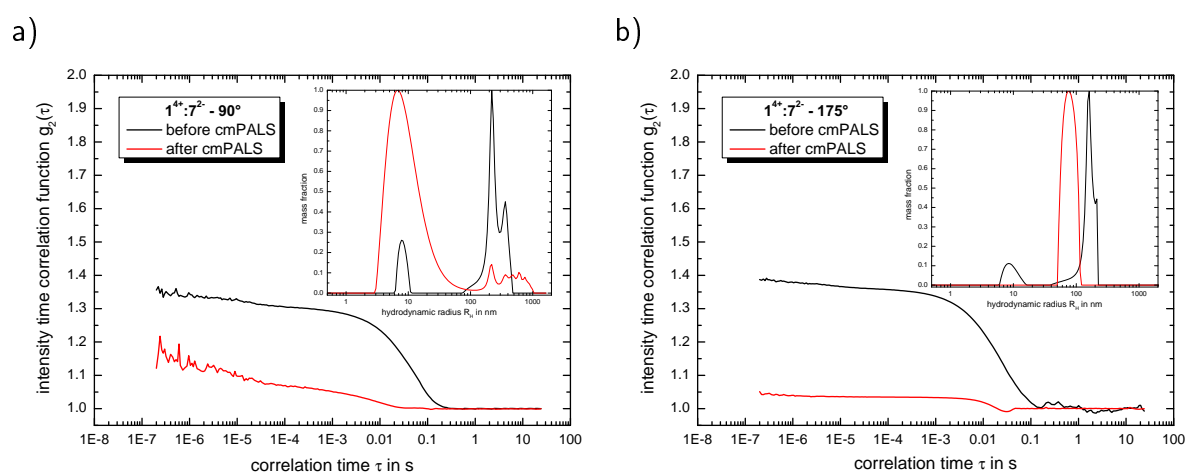


Fig. D.8.: Intensity time correlation function and particle size distribution as inlay with a) side and b) back scattering for the cluster system  $1^4+:7^2-$  1 mM:3 mM in DMSO:glycerol:water 50:43:7 (v/v/v) at day 10 before and after cmPALS measurement.

### $1^4+:8^2-$ ('Texas-sized molecular box':ethanedisulfonate)

Fig. D.9 summarizes all intensity time correlation functions for the system  $1^4+:8^2-$  with 1 mM:3 mM in the established solvent mixture. We detect strongly pronounced autocorrelation functions directly after the ten-day incubation period, which are already shifted to higher correlation times  $\tau$ . These delayed decays stay throughout the entire measurement period, while the initial y-intercept-values of the intensity time correlation functions decrease. Compared to the model system  $1^4+:2^2-$  with the same ionic ratio of  $2/3$ , we solely see tendencies to build up anisotropic ionic clusters. It seems that exchanging the methanedisulfonate with the slightly larger ethanedisulfonate prevents the formation of highly-defined structures with high durability due to changes in the electrostatic interactions with the 'Texas-sized molecular box'.

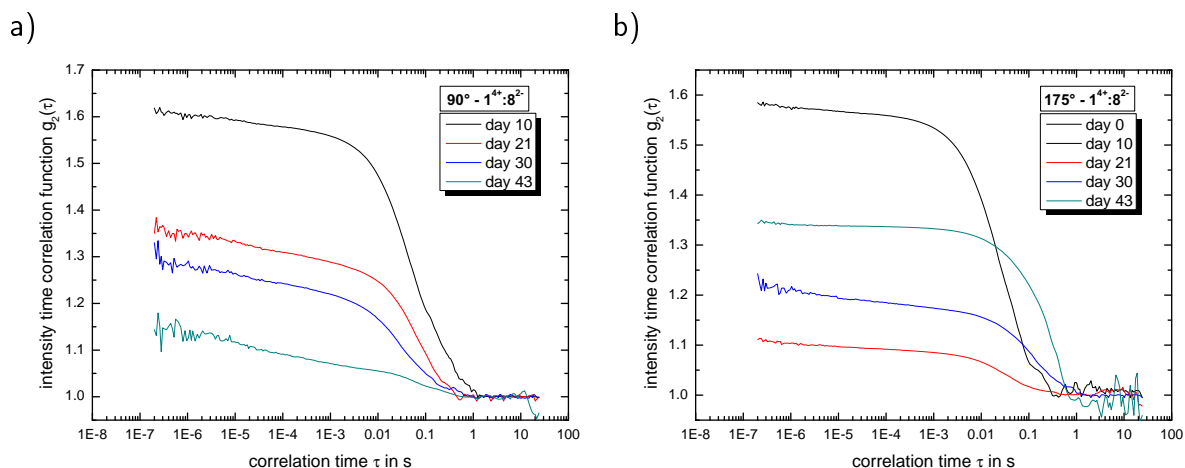


Fig. D.9.: Intensity time correlation function with a) side and b) back scattering for the cluster system  $1^{4+}:8^{2-}$  1 mM:3 mM in DMSO:glycerol:water 50:43:7 (v/v/v) for all measurement days.

Table D.4 combines the important parameter for characterizing the zeta potential for the system  $1^{4+}:8^{2-}$  in a similar way compared to the system containing malonate.

Table D.4.: Summary of the cmPALS results for system made out of 'Texas-sized molecular box' and ethanedisulfonate ( $8^{2-}$ )

compound	$I$ / mM	$F(\kappa a)$	$\mu_e / \frac{\mu\text{mcm}}{\text{Vs}}$	$\zeta$ / mV
$8^{2-}$	9	1.000	$-0.001 \pm 0.001$	$-0.7 \pm 0.7$
$1^{4+}:8^{2-}$	19	1.362	$0.056 \pm 0.003$	$28.7 \pm 1.5$

$I_{\text{counterion}}$ :  $\text{Na}^+$

The direct comparison of the recorded intensity time correlation functions in Fig. D.10 demonstrates with back scattering a significant lower y-intercept value for the measurement after the cmPALS studies. For side scattering the y-intercept stays almost constant, but the shape of the autocorrelation function changed, which leads to the detection of two distinctive peaks in the particle size distribution. Note that the pattern of the size distributions switched between both applied scattering angles, but the position of the recorded peaks remains. The system of  $1^{4+}:8^{2-}$  can better cope with the influence of the electric field compared to the mixture with malonate probably due to the stronger electrostatic interactions of  $1^{4+}$  with the sulfonate-groups in compound  $8^{2-}$ , as mentioned in Chapter 6.

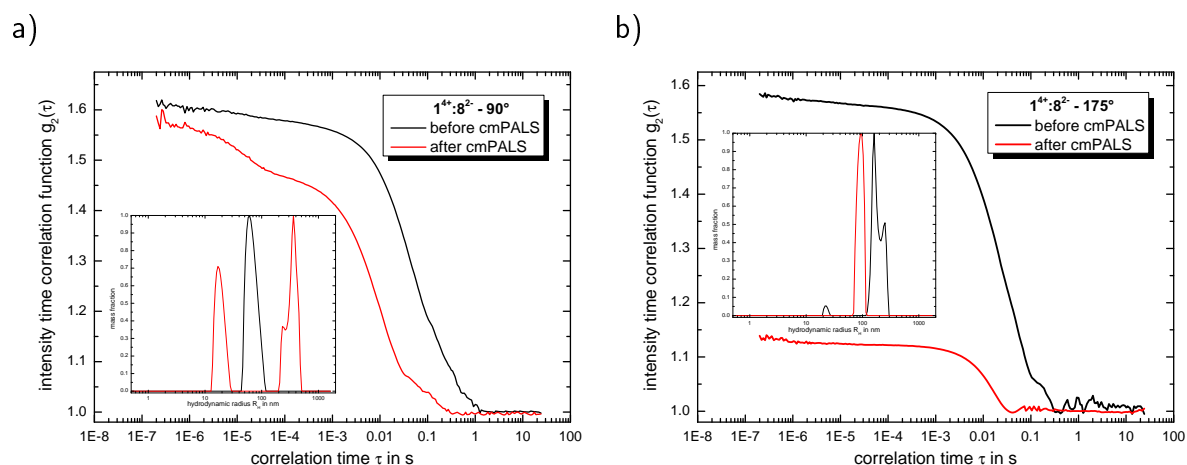


Fig. D.10.: Intensity time correlation function and particle size distribution as inlay with a) side and b) back scattering for the cluster system  $1^4+:8^2-$  1 mM:3 mM in DMSO:glycerol:water 50:43:7 (v/v/v) at day 10 before and after cmPALS measurement.

### $1^4+:9^2-$ ('Texas-sized molecular box':disulfate)

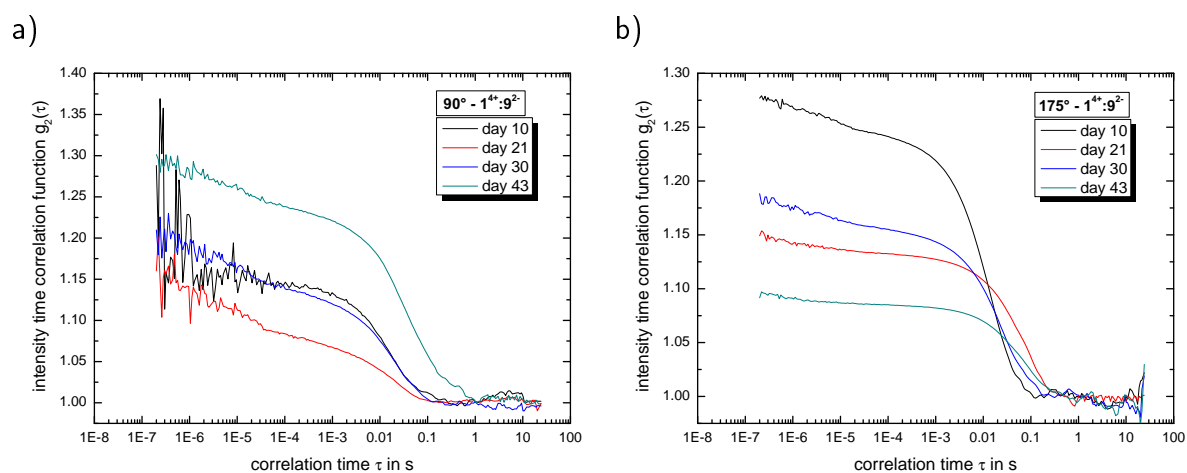


Fig. D.11.: Intensity time correlation function with a) side and b) back scattering for the cluster system  $1^4+:9^2-$  1 mM:3 mM in DMSO:glycerol:water 50:43:7 (v/v/v) for all measurement days.

Fig. D.11 summarizes all intensity time correlation functions for the system  $1^4+:9^2-$  with 1 mM:3 mM in the established solvent mixture. Here, we see a similar behavior compared to the system containing  $8^2-$ . Replacing methanedisulfonate with disulfate also prevents the formation of globular ionoids, probably due to the decomposition of the anionic component. This aspect leads to the conversion of the dianion into smaller sulfate units with just one negative charge, which can not assist the ionic self-assembly process. Note that the y-intercept value of this system is, even directly after the initial incubation period of ten days, relatively

low with values around 1.3. This feature strengthens the impression of the decomposition of the disulfate over time.

### $1^{4+}:10^{3-}$ ('Texas-sized molecular box':Amaranth dye)

Fig. D.12 summarizes all intensity time correlation functions for the system  $1^{4+}:10^{3-}$  with concentrations  $10\ \mu\text{M}:30\ \mu\text{M}$  in the established solvent mixture. The autocorrelation functions that are significantly stronger pronounced than for the pure trianionic chromophore sample (see Fig. D.4), present in the initial self-assembly process a shift to larger correlation times, which is more dominant for the side scattering angle. However, the y-intercept of these graphs stays rather constant, compared to the already discussed systems. We can conclude that system  $1^{4+}:10^{3-}$  with a ionic ratio of 4/9 tends to build up rather large anisotropic ionic cluster with a certain durability.

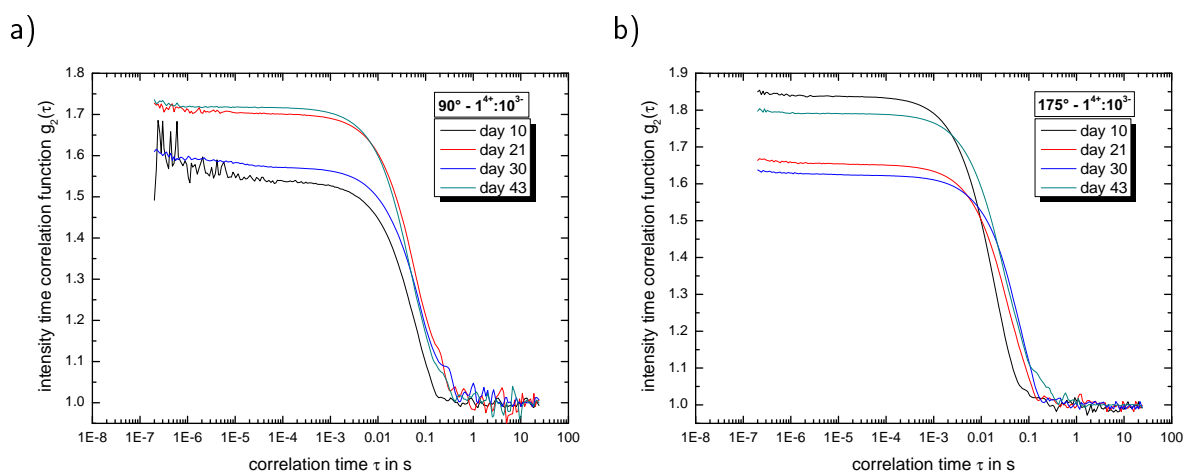


Fig. D.12.: Intensity time correlation function with a) side and b) back scattering for the cluster system  $1^{4+}:10^{3-}$   $10\ \mu\text{M}:30\ \mu\text{M}$  in DMSO:glycerol:water 50:43:7 (v/v/v) for all measurement days.

Based on the DLS data we can compare the recorded UV-vis and fluorescence spectra of system  $1^{4+}:10^{3-}$  at each measurement day with the reference of pure Amaranth dye with  $c = 30\ \mu\text{M}$ , which is shown in Fig. D.13. Both absorption and emission band from the cluster system are, respectively, shifted by roughly 5 nm to higher wavelength indicating an influence of  $1^{4+}$  on the solvation shell of Amaranth. In addition, the extinction value of the absorption band slightly decreases, whereas the fluorescence intensity fluctuates throughout the total measurement time. Note that the fluorescence intensity of Amaranth significantly changes for the pure solvents DMSO, glycerol and water, making it difficult to directly correlate the detected fluctuations with the DLS data and the build up of anisotropic ionic clusters.

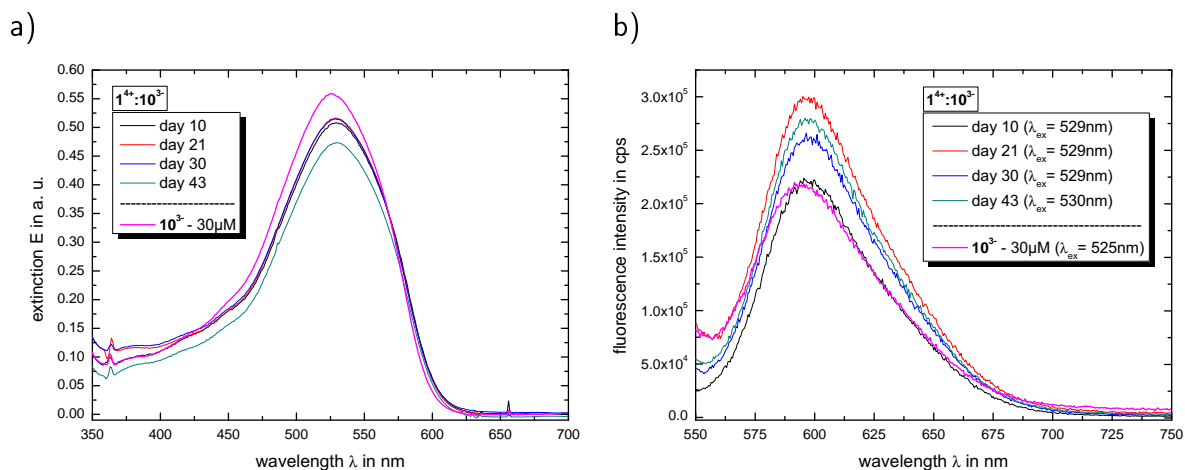


Fig. D.13.: a) UV-vis spectra and b) fluorescence spectra for the cluster system  $1^{4+}:10^{3-}$   $10 \mu\text{M}:30 \mu\text{M}$  in DMSO:glycerol:water 50:43:7 (v/v/v) for all measurement days. Both graphs show a magenta curve highlighting pure Amaranth dye with  $c = 30 \mu\text{M}$ .

## Substitution of $1^{4+}$

As addition to the explanations in Appendix A regarding measuring and analyzing CW EPR spectra, the sets of Euler angles for the studied systems are listed below:

- pure  $3^{2-}$ :  $\alpha = 65^\circ$ ,  $\beta = 90^\circ$ ,  $\gamma = 15^\circ$
- $1^{4+}:3^{2-}$ :  $\alpha = 85^\circ$ ,  $\beta = 90^\circ$ ,  $\gamma = 15^\circ$
- $4^{2+}:3^{2-}$  /  $5^{4+}:3^{2-}$  /  $6^{4+}:3^{2-}$ :  $\alpha = 75^\circ$ ,  $\beta = 90^\circ$ ,  $\gamma = 15^\circ$

## $4^{2+}:2^{2-}$ (phthalcyanine:methanedisulfonate)

Fig. D.14 summarizes all intensity time correlation functions for the system  $4^{2+}:2^{2-}$  with the ratio  $13.3 \mu\text{M}:20 \mu\text{M}$  in DMSO:glycerol:water 50:43:7 (v/v/v). One can clearly state that the decay of the autocorrelation functions is slightly shifted to higher correlation times  $\tau$ , but stays constant throughout all measurement days. This indicates the (partially) formation of anisotropic ionic cluster with rather robust hydrodynamic radii. However, we detect a steady decrease in the y-intercept, which indicates the starting decomposition of the self-assembled entities into more trivial ion pair coordinations.

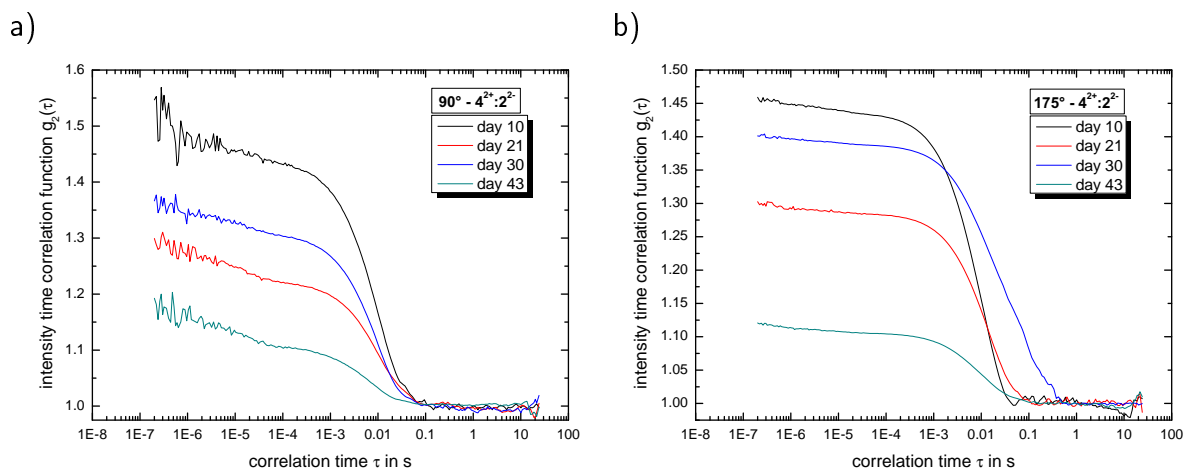


Fig. D.14.: Intensity time correlation function with a) side and b) back scattering for the cluster system  $4^{2+} : 2^{2-}$  13.3  $\mu\text{M} : 20 \mu\text{M}$  in DMSO:glycerol:water 50:43:7 (v/v/v) for all measurement days.

Besides DLS, we tried to apply UV-vis and fluorescence spectroscopy, but even the pure  $4^{2+}$  in the established solvent mixture did not present significant absorption bands, leaving CW EPR as additional method to characterize the adjusted system  $4^{2+} : 3^{2-}$ . The measured and simulated CW EPR spectra with a fixed Fremy's salt concentration of 200  $\mu\text{M}$  at both X- and Q-band frequencies are summarized in Fig. D.15.



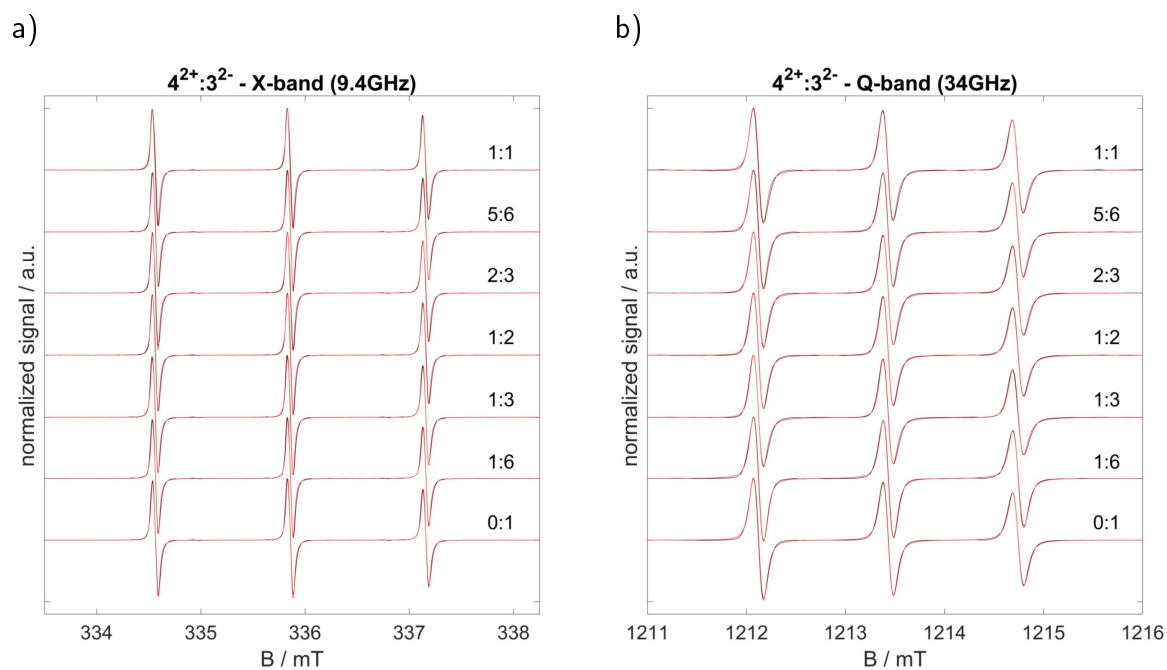


Fig. D.15.: a) X-band and b) Q-band CW EPR spectra of system  $4^{2+}:3^{2-}$  in DMSO:glycerol:water 50:43:7 (v/v/v) depending on the molar ratio. Both graphs show for each mixture the measured spectrum (black line) as well as the simulated spectrum (red line).

At first it seems that increasing the concentration of  $4^{2+}$  has no significant influence on the rotational mobility of Fremy's salt, which is also visible in the FWHM values in Chapter 6. There are no molar ratios initiating a fixed coordination between the cationic and anionic component. Note that one reason for this behavior could be the used concentration region of  $200\ \mu\text{M}$ . However, we can uncover differences between the molar ratios by comparing their rotational correlation times  $\tau_c$  and anisotropy  $T$  (see Fig. D.16).

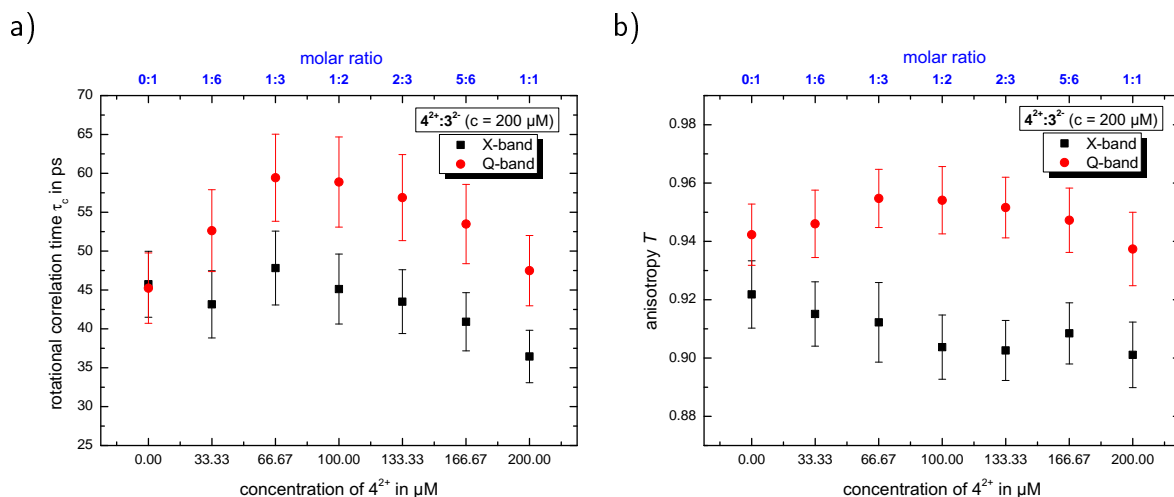


Fig. D.16.: a) Rotational correlation time  $\tau_c$  and b) anisotropy  $T$  of the system  $4^{2+};3^{2-}$  versus the concentration of  $4^{2+}$  in DMSO:glycerol:water 50:43:7 (v/v/v).

At Q-band frequencies, we detect a slight increase in the rotational correlation time  $\tau_c$  for molar ratios 1:3 to 5:6, indicating a slowed-down mobility of Fremy's salt due to local electrostatic interactions. In terms of anisotropy  $T$ , we just see significant changes at the globally averaged interactions and dynamics for the nitroxide based on X-band data. The reduced anisotropy beginning at molar ratio 1:2 (concentration of  $4^{2+}$ :  $100 \mu\text{M}$ ) correlates with a more isotropic environment for Fremy's salt probably due to changes in its solvation shell. Table D.5 summarizes the simulation results for both frequencies.

Table D.5.: Summary of the simulated axial rotational diffusion tensor  $D_{\perp}$  and  $D_{\parallel}$  as well as the calculated rotational correlation time  $\tau_c$  and anisotropy  $T$  of system  $4^{2+};3^{2-}$  in DMSO:glycerol:water 50:43:7 (v/v/v) depending on the molar ratio

ratio	X-band				Q-band			
	$D_{\perp}/s^{-1}$	$D_{\parallel}/s^{-1}$	$\tau_c / \text{ps}$	$T$	$D_{\perp}/s^{-1}$	$D_{\parallel}/s^{-1}$	$\tau_c / \text{ps}$	$T$
0:1	1.1e9	4.0e10	45.73	0.922	1.0e9	5.0e10	45.24	0.942
1:6	1.2e9	4.0e10	43.16	0.915	8.4e8	4.5e10	52.63	0.946
1:3	1.1e9	3.5e10	47.82	0.911	7.0e8	4.5e10	59.44	0.955
1:2	1.2e9	3.5e10	45.12	0.904	7.1e8	4.5e10	58.88	0.954
2:3	1.25e9	3.6e10	43.99	0.903	7.5e8	4.5e10	56.76	0.952
5:6	1.3e9	4.0e10	40.91	0.908	8.2e8	4.5e10	53.49	0.947
1:1	1.5e9	4.25e10	36.45	0.901	9.8e8	4.5e10	47.49	0.937

## $5^{4+}:2^{2-}$ (tetrakis(4-aminophenyl)methane:methanedisulfonate)

Fig. D.17 summarizes all intensity time correlation functions for system  $5^{4+}:2^{2-}$  with 1 mM:3 mM in DMSO:glycerol:water 50:43:7 (v/v/v). We detect a fast decay of the y-intercept for the recorded autocorrelation functions at both scattering angles, indicating the fall apart of initial globular structures. Note that the y-intercept value at day ten for this system is less than for the pure  $5^{4+}$  solution (see Fig. D.3), indicating a decomposition process of the cationic component throughout the initial self-assembly for ionic cluster. Therefore, after the incubation period of ten days, the sample contains (i) homogeneously distributed ions and (ii) ion cloud regions throughout all following measurements.

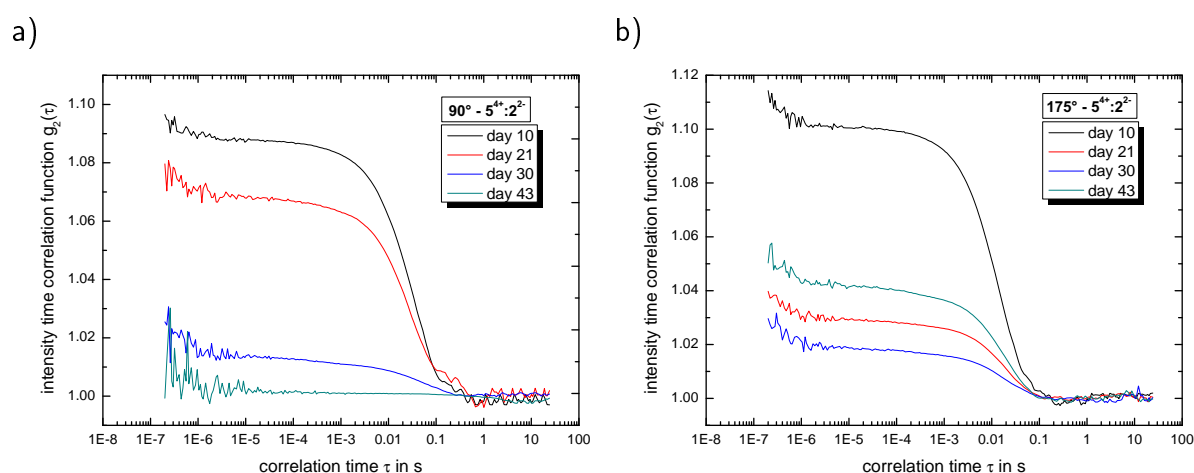


Fig. D.17.: Intensity time correlation function with a) side and b) back scattering of the cluster system  $5^{4+}:2^{2-}$  1 mM:3 mM in DMSO:glycerol:water 50:43:7 (v/v/v) for all measurement days.

To further characterize the beginning of the ionic self-assembly process of compound  $5^{4+}$  with methanedisulfonate, we could also apply CW EPR spectroscopy with the dianion of Frey's salt. The measured and simulated spectra with a fixed nitroxide concentration of 3 mM at both X- and Q-band frequencies are shown in Fig. D.18. Compared to the model system  $1^{4+}:3^{2-}$ , we do not see the same behavior for the rotational mobility of Frey's salt. At X-band frequencies, the rotational correlation time  $\tau_c$  slightly decreases, but the line width stays constant with increasing concentration of the cationic component. The missing increase of the FWHM values indicates the absence of strong electrostatic interactions between  $5^{4+}$  and  $2^{2-}$  for the global environment. For the local surrounding of our spin probe, which can be shown the Q-band spectra, we receive larger FWHM values due to present correlations between both components.

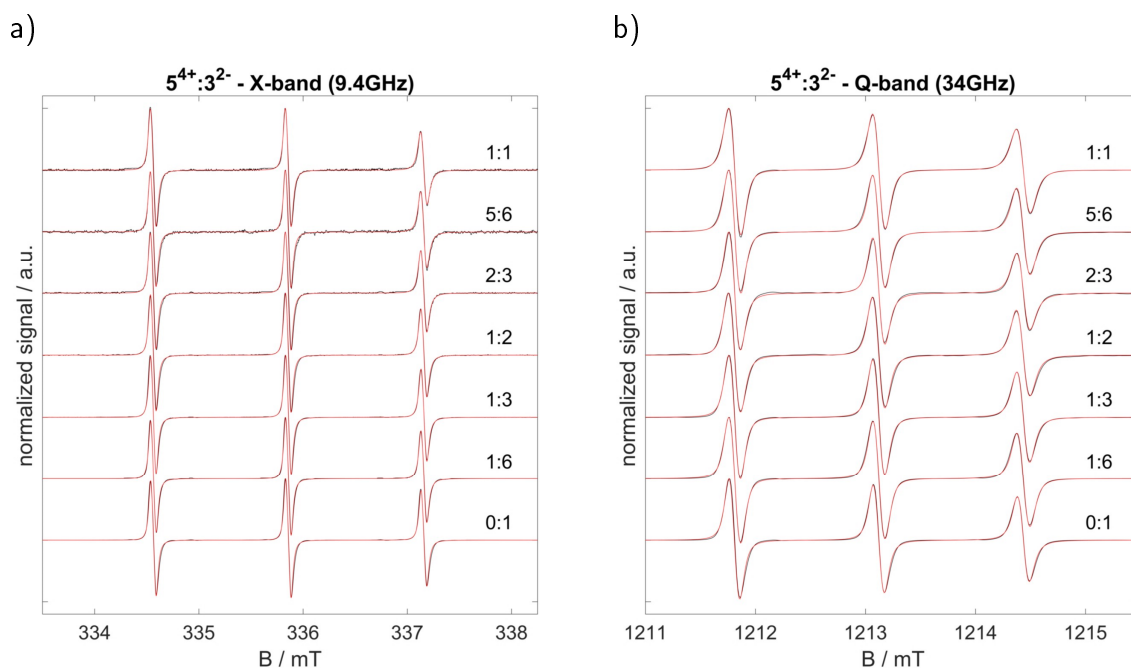


Fig. D.18.: a) X-band and b) Q-band CW EPR spectra of system  $5^{4+}:3^{2-}$  in DMSO:glycerol:water 50:43:7 (v/v/v) depending on the molar ratio. Both graphs show for each mixture the measured spectrum (black line) as well as the simulated spectrum (red line).

Similar to the other CW EPR measurements, we evaluate the rotational correlation time  $\tau_c$  as well as the anisotropy  $T$  of the axial rotational diffusion tensor (see Fig. D.19). One can clearly state that the sudden decrease of  $T$  at X-band frequencies with increasing  $5^{4+}$  is a special feature of the cluster system. The reason for this behavior lies in the steady decrease of  $D_{\parallel}$ , whereas  $D_{\perp}$  shows almost no significant changes. The adjustments of the tensor, which are vice versa compared to our model system with the 'Texas-sized molecular box', provide a possible explanation for the missing long-term stability of the colloid-like ionic structures from the DLS data.

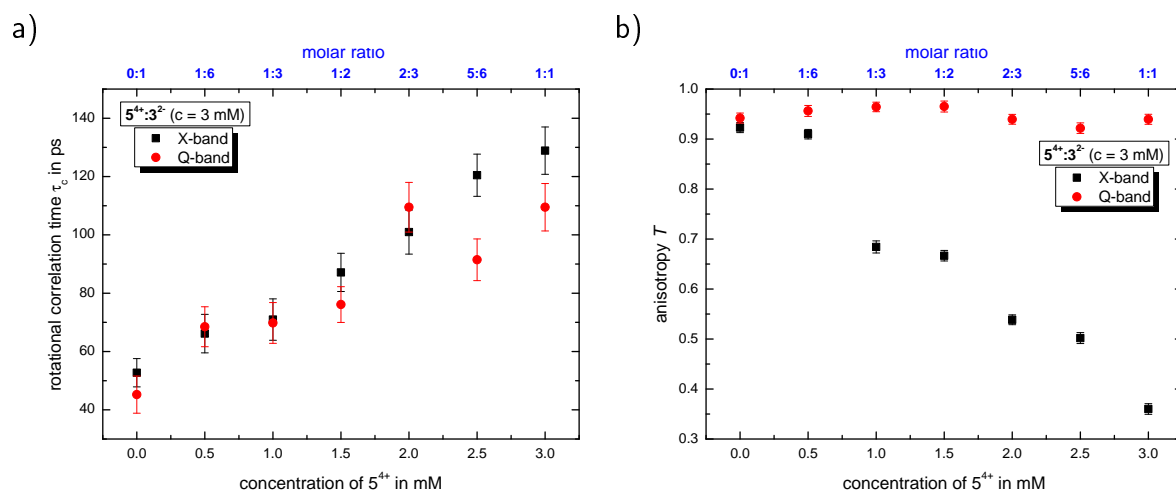


Fig. D.19.: a) Rotational correlation time  $\tau_c$  and b) anisotropy  $T$  of the system  $5^{4+}:3^{2-}$  versus the concentration of  $5^{4+}$  in DMSO:glycerol:water 50:43:7 (v/v/v).

Table D.6 combines all simulation results from X- and Q-band CW EPR spectra.

Table D.6.: Summary of the simulated axial rotational diffusion tensor  $D_{\perp}$  and  $D_{\parallel}$  as well as the calculated rotational correlation time  $\tau_c$  and anisotropy  $T$  of system  $5^{4+}:3^{2-}$  in DMSO:glycerol:water 50:43:7 (v/v/v) depending on the molar ratio

ratio	X-band				Q-band			
	$D_{\perp}/s^{-1}$	$D_{\parallel}/s^{-1}$	$\tau_c / \text{ps}$	$T$	$D_{\perp}/s^{-1}$	$D_{\parallel}/s^{-1}$	$\tau_c / \text{ps}$	$T$
0:1	9.5e8	3.5e10	52.72	0.923	1.0e9	5.0e10	45.24	0.942
1:6	8.0e8	2.5e10	66.14	0.910	6.0e8	4.0e10	68.51	0.956
1:3	1.2e9	9.0e9	70.96	0.684	5.5e8	4.5e10	69.80	0.964
1:2	1.0e9	7.0e9	87.13	0.667	5.0e8	4.2e10	76.11	0.965
2:3	1.0e9	4.5e9	100.95	0.538	4.2e8	2.0e10	109.48	0.940
5:6	8.7e8	3.5e9	120.45	0.502	5.5e8	2.0e10	91.47	0.921
1:1	9.3e8	2.5e9	128.89	0.360	4.2e8	2.0e10	109.48	0.940

## $6^{4+}:2^{2-}$ (spermine:methanedisulfonate)

Fig. D.20 shows all intensity time correlation functions of the system  $6^{4+}:2^{2-}$  with 1.6 mM:1.2 mM in DMSO:glycerol:water 50:43:7 (v/v/v). After the incubation period of ten days we recorded autocorrelation functions with high y-intercept-values for both scattering angles. Note that the decay of the recorded graphs also does not shift to larger correlation times  $\tau$ , indicating the presence of colloid-like ionic structures with constant hydrodynamic radius. The partially formed anisotropic clusters (see Chapter 6) possess a certain durability,

which is visible in the time-dependent development of the y-intercept values of the intensity time correlation functions.

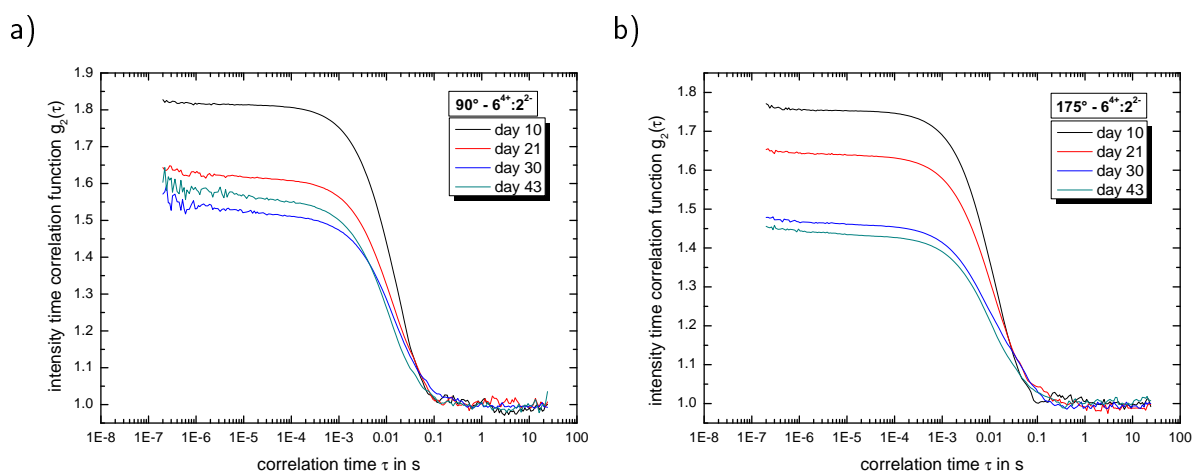


Fig. D.20.: Intensity time correlation function with a) side and b) back scattering for the cluster system  $6^{4+}:2^{2-}$  1.6 mM:1.2 mM in DMSO:glycerol:water 50:43:7 (v/v/v) for all measurement days.

In addition to the information in Chapter 6, Table D.7 combines the important parameter for characterizing the zeta potential for the system  $6^{4+}:2^{2-}$ .

Table D.7.: Summary of the cmPALS results for system made out of spermine and methanesulfonate

compound	$I / \text{mM}$	$F(\kappa a)$	$\mu_e / \frac{\mu\text{mcm}}{\text{Vs}}$	$\zeta / \text{mV}$
$6^{4+}I$	16	1.004	$0.005 \pm 0.008$	$3.6 \pm 5.4$
$6^{4+}:2^{2-}$	19.6	1.183	$0.067 \pm 0.003$	$39.8 \pm 1.8$

$I$  counterion:  $\text{Cl}^-$

The repetitive DLS measurement with back scattering, as shown in Fig. D.21, displays the already mentioned decay in the y-intercept value. The overall shape of the autocorrelation function stays the same, but the particle size distribution just presents one peak, which is located between the two 'original' fractions. In combination with the result from the side scattering (see Chapter 6) we assume that the external electric field mostly affects the shape of the anisotropic ionic cluster, whereas the overall amount of self-assembled entities remains.

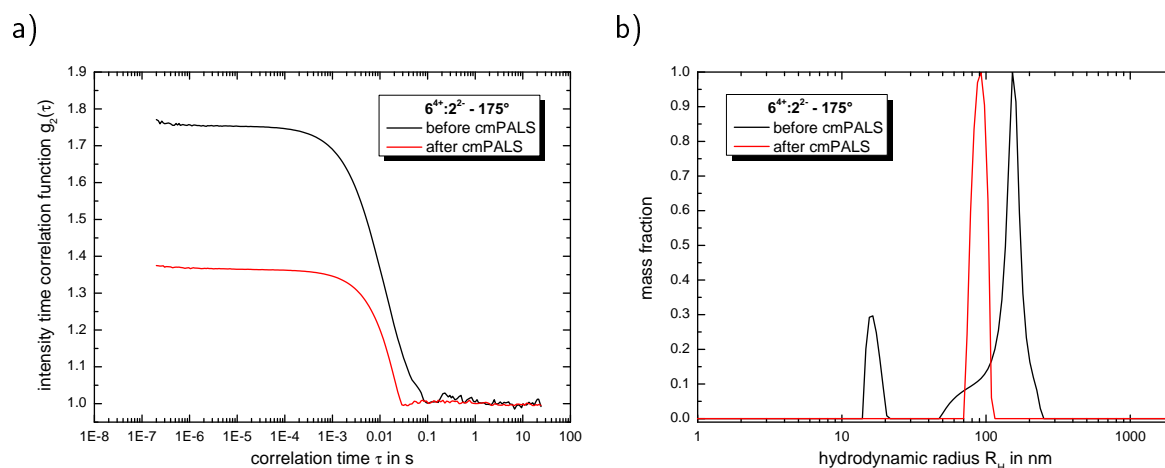


Fig. D.21.: a) Intensity time correlation function and b) particle size distribution with back scattering for the cluster system  $6^{4+}:2^{2-} - 1.6 \text{ mM}:1.2 \text{ mM}$  in DMSO:glycerol:water 50:43:7 (v/v/v) at day 10 before and after cmPALS measurement.

The recorded and simulated CW EPR spectra, which are summed up in Fig. D.22, demonstrate a similar behavior for the rotational mobility of Frey's salt compared to the model system  $1^{4+}:3^{2-}$ . X- and Q-band frequencies show a decreased rotational correlation time  $\tau_c$  and increasing FWHM values with increasing concentration of the cationic component. These effects occur due to electrostatic interactions between  $6^{4+}$  and  $3^{2-}$ , which are important to develop future anisotropic ionic clusters through ionic self-assembly. Note that here the electrostatic interactions with Frey's salt are weaker compared to the 'Texas-sized molecular box'. Reasons can be the slightly lower concentration in the  $6^{4+}:3^{2-}$  system or the size difference of the cationic component, leading to just anisotropic ionic clusters and not globular ionoids.

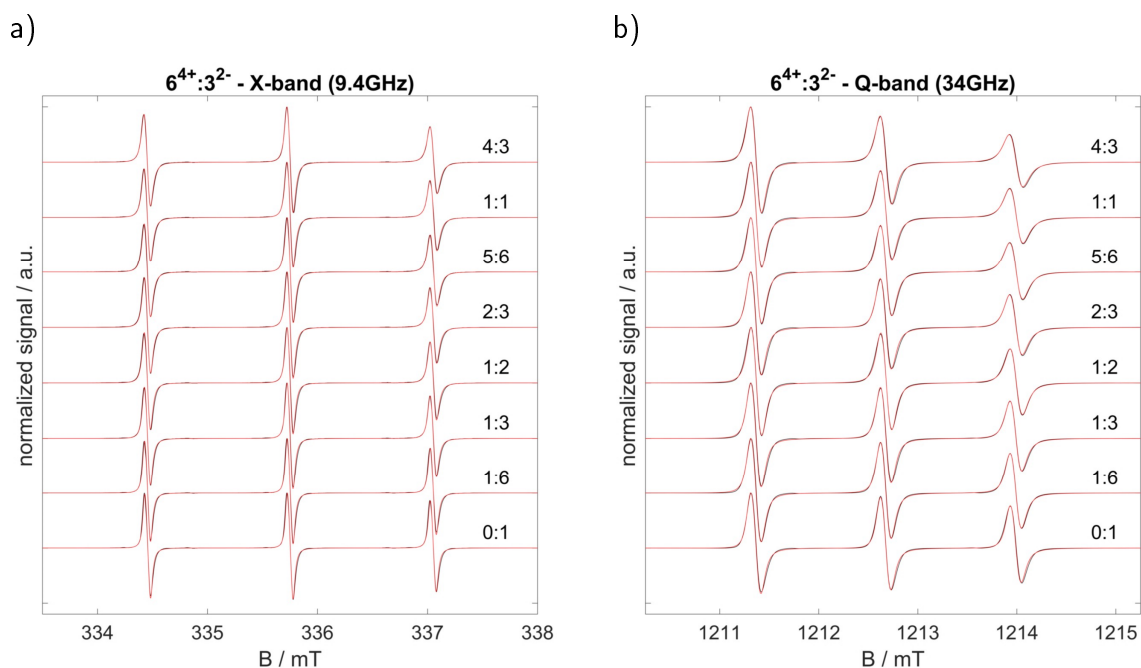


Fig. D.22.: a) X-band and b) Q-band CW EPR spectra of system  $6^{4+}:3^{2-}$  in DMSO:glycerol:water 50:43:7 (v/v/v) depending on the molar ratio. Both graphs show for each mixture the measured spectrum (black line) as well as the simulated spectrum (red line).

Further characterization of the axial rotational diffusion tensor are shown in Fig. D.23, exploiting the rotational correlation time  $\tau_c$  as well as the anisotropy  $T$ . The similar behavior of the  $T$ -values at X- and Q-band frequencies indicates that the global and local environment for Frey's salt are alike. This leads to the following conclusion: The electrostatic interactions between  $6^{4+}$  and  $3^{2-}$  in the ion cloud state dominate the direct coordination behavior of Frey's salt. We do not reach e. g. ion pair formations with higher concentration of  $6^{4+}$ , which happens with compound  $1^{4+}$ . This weakened coordination in the discussed system could be the reason for partially anisotropic ionic clusters based on the DLS data.



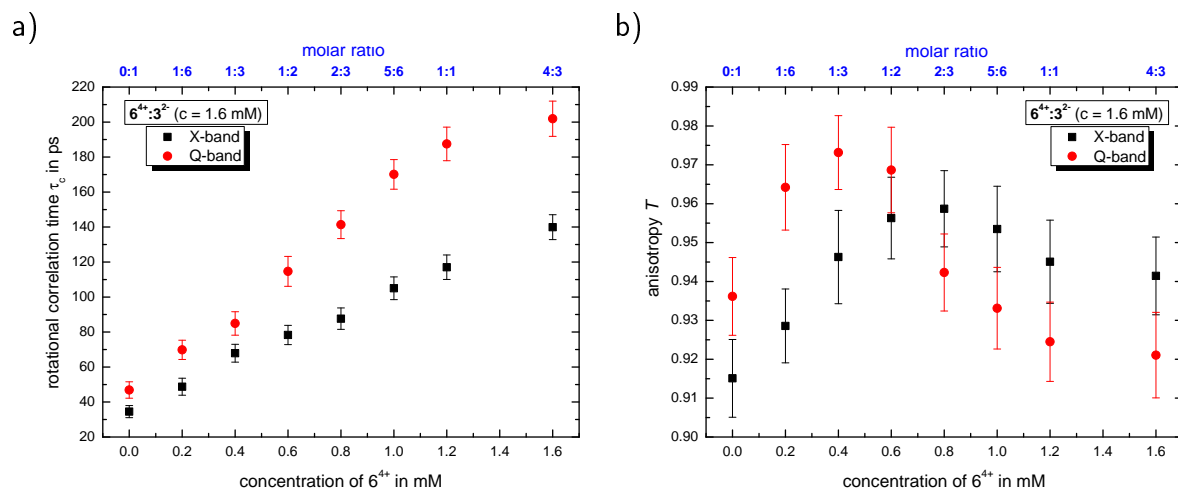


Fig. D.23.: a) Rotational correlation time  $\tau_c$  and b) anisotropy  $T$  of the system  $6^{4+}:3^{2-}$  versus the concentration of  $6^{4+}$  in DMSO:glycerol:water 50:43:7 (v/v/v).

Table D.8 completes the CW EPR data by combining the simulation results from X- and Q-band spectra.

Table D.8.: Summary of the simulated axial rotational diffusion tensor  $D_{\perp}$  and  $D_{\parallel}$  as well as the calculated rotational correlation time  $\tau_c$  and anisotropy  $T$  of system  $6^{4+}:3^{2-}$  in DMSO:glycerol:water 50:43:7 (v/v/v) depending on the molar ratio

ratio	X-band				Q-band			
	$D_{\perp}/s^{-1}$	$D_{\parallel}/s^{-1}$	$\tau_c / \text{ps}$	$T$	$D_{\perp}/s^{-1}$	$D_{\parallel}/s^{-1}$	$\tau_c / \text{ps}$	$T$
0:1	1.5e9	5.0e10	34.52	0.915	1.0e9	4.5e10	46.86	0.936
1:6	1.0e9	4.0e10	48.74	0.929	5.5e8	4.5e10	69.80	0.964
1:3	6.5e8	3.5e10	67.90	0.946	4.1e8	4.5e10	84.90	0.973
1:2	5.25e8	3.5e10	78.29	0.956	3.2e8	3.0e10	114.65	0.969
2:3	4.6e8	3.25e10	87.64	0.959	3.2e8	1.6e10	141.38	0.942
5:6	4.0e8	2.5e10	104.99	0.953	2.8e8	1.2e10	170.09	0.933
1:1	3.8e8	2.0e10	117.04	0.945	2.65e8	1.0e10	187.51	0.925
4:3	3.25e8	1.6e10	139.92	0.941	2.5e8	9.0e9	201.90	0.921

### $6^{4+}:10^{3-}$ (spermine:Amranth dye)

This mixture actually substitutes both model compounds ( $1^{4+}$  and  $2^{2-}$ ) at the same time, creating an inverse system based on the size ratio: small cations together with large anions. Fig. D.24 shows all intensity time correlation functions of the  $6^{4+}:10^{3-}$  system with 10  $\mu\text{M}$ :30  $\mu\text{M}$  in DMSO:glycerol:water 50:43:7 (v/v/v). One can clearly state that the autocorrelation functions

show a large fluctuation in their y-intercept values, indicating the formation of highly dynamic structures. The combination of small cation and large anion shows the potential to build up colloid-like ionic structures, but is not capable of stabilizing them over a longer time period.

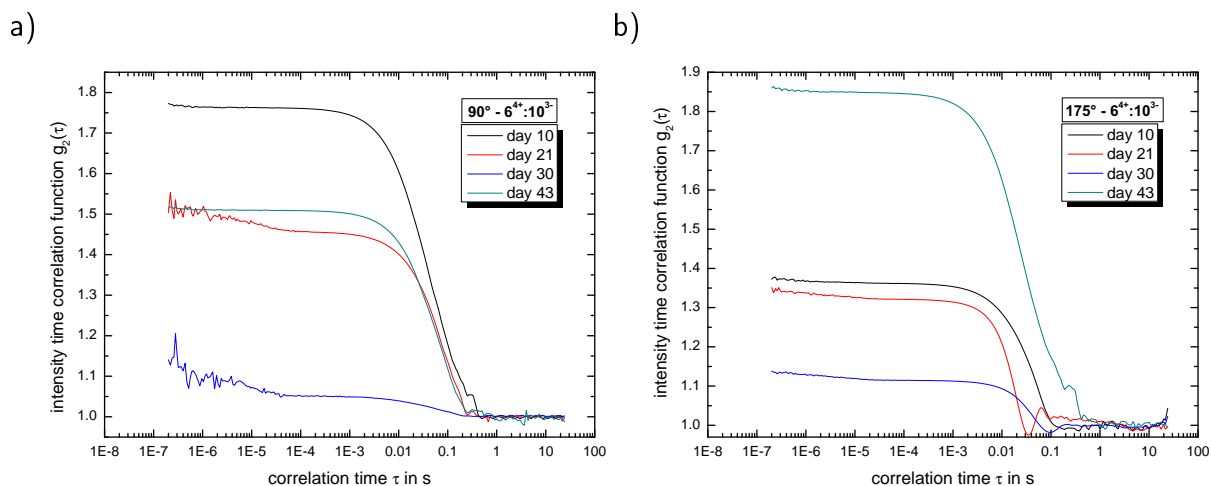


Fig. D.24.: Intensity time correlation function with a) side and b) back scattering of the cluster system  $6^{4+}:10^{3-}$   $10\ \mu\text{M}:30\ \mu\text{M}$  in DMSO:glycerol:water 50:43:7 (v/v/v) for all measurement days.

Possible reasons for the missing durability of anisotropic ionic cluster (or even globular ionoids) are (i) the low concentration ratio  $10\ \mu\text{M}:30\ \mu\text{M}$  and/or (ii) too weak electrostatic interactions between both ionic compounds.

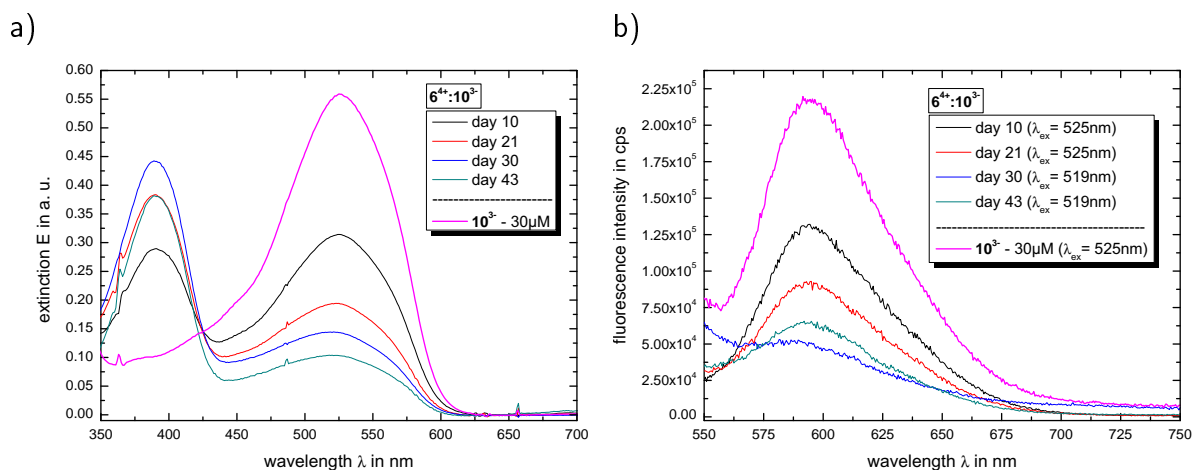


Fig. D.25.: a) UV-vis spectra and b) fluorescence spectra of the cluster system  $6^{4+}:10^{3-}$   $10\ \mu\text{M}:30\ \mu\text{M}$  in DMSO:glycerol:water 50:43:7 (v/v/v) for all measurement days. Both graphs show a gray curve highlighting pure Amaranth dye with  $c = 30\ \mu\text{M}$ .

We further detect through UV-vis and fluorescence spectroscopy a decrease in the absorption as well as emission band correlating to Amaranth dye (see Fig. D.25), indicating a steadily

decomposition of  $\mathbf{10}^{3-}$ . This was not recorded for the system  $\mathbf{1}^{4+}:\mathbf{10}^{3-}$ , leaving the spermine as possible source for this behavior.

# E | Appendix - Chapter 7

## Preparing solvent mixtures

The preparation for the new solvents DMF:glycerol:water, DMSO:ethylene glycol:water and DMSO:glycerol:NMPA are based on the established ternary mixture DMSO:glycerol:water. Here, we combine the solvent compounds DMSO and glycerol 86-88 wt% in a 1:1 volume ratio. For the individual exchange of each solvent compound, we used glycerol with 99.5 wt% to better control its amount in the final mixtures. Therefore, we calculate the volume of all compounds for a total volume of e. g.  $V = 2\text{ ml}$  based on the fixed ratio 50:43:7 (v/v/v):

- DMSO:  $V = 1\text{ ml}$ ,
- glycerol:  $V = 0.85\text{ ml}$  and
- water:  $V = 0.15\text{ ml}$

All new solvent mixtures were prepared with the just calculated volumes, while exchanging (i) DMSO with DMF, (ii) glycerol (gly) with ethylene glycol (eg) and (iii) water with NMPA.

## Preparing molar ratios

Preparing the different molar ratios for the  $\mathbf{1^{4+}:2^{2-}}$  ( $\mathbf{1^{4+}:3^{2-}}$ , respectively) system started with producing following stock solutions in all four solvent mixtures:

- $c(\mathbf{1^{4+}}) = 6\text{ mM}$  and
- $c(\mathbf{2^{2-}}) = c(\mathbf{3^{2-}}) = 6\text{ mM}$ .

The two stock solutions were then combined based on Table E.1 to receive the desired molar ratios.

**Table E.1.:** Summary of all tested molar ratios for the system  $\mathbf{1}^{4+}:\mathbf{2}^{2-}$  ( $\mathbf{1}^{4+}:\mathbf{3}^{2-}$ , respectively) in all four solvent mixtures combined with their calculated ionic ratio

molar ratio	$c(\mathbf{1}^{4+})$ / mM	$c(\mathbf{2}^{2-}/\mathbf{3}^{2-})$ / mM	$V(\mathbf{1}^{4+})$ / $\mu\text{l}$	$V(\mathbf{2}^{2-}/\mathbf{3}^{2-})$ / $\mu\text{l}$	$V(\text{solvent})$ / $\mu\text{l}$	ionic ratio <sup>a</sup>
0:1	0.0	3.0	0	120	120	-
1:6	0.5	3.0	20	120	120	1/3
1:3	1.0	3.0	40	120	80	2/3
1:2	1.5	3.0	60	120	60	1
2:3	2.0	3.0	80	120	40	4/3
5:6	2.5	3.0	100	120	20	5/3
1:1	3.0	3.0	120	120	0	2

<sup>a</sup> calculating ionic ratio using equation (7.1)

Calculating the ionic ratio inside each  $\mathbf{1}^{4+}:\mathbf{2}^{2-}$  ( $\mathbf{1}^{4+}:\mathbf{3}^{2-}$ , respectively) system is based on equation (7.1). Note that we assume a constant charge  $z^\pm$  for the cationic ( $z^+ = +4$ ) and anionic ( $z^- = -2$ ) building block in all tested molar ratios.

## Solvent Properties

The dynamic viscosity  $\eta$  indicates for a laminar flow of a fluid the shear stress to the velocity gradient perpendicular to the plane of shear and was determined by recording flow curves at 20 °C. Our rheometer, the Physica MCR301, uses a cone-plate (CP50-2/TG) measuring system with  $R = 24.929\text{mm}$  and  $\alpha = 2.017^\circ$ . Table E.2 shows the exact procedure of how we recorded the flow curves.

**Table E.2.:** Procedure for recording the flow curves for all solvent mixtures

section	shear rate $\dot{\gamma}$ / $\text{s}^{-1}$	measuring point
1 (pre shearing)	5	1 (discard)
2	-/-	1 (discard)
3	0.1 - 100 (linear)	40

All four solvent mixtures show a Newtonian correlation between the shear rate  $\dot{\gamma}$  and the shear stress  $\tau$ , as described by equation E.1<sup>181</sup>

$$\tau = \eta \cdot \dot{\gamma}, \quad (\text{E.1})$$

whereas the dynamic viscosity  $\eta$  stays constant for all applied shear rates (see Fig. E.1).

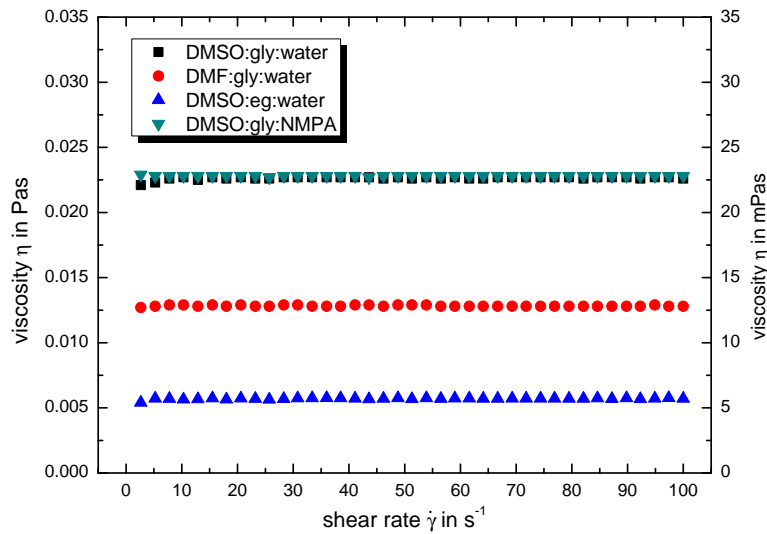


Fig. E.1.: Flow curves for all four solvent mixtures.

The relative permittivity  $\epsilon_r$ , which describes the ratio of the electric field strength in vacuum to that in a given medium, was determined with the Keysight 16452A Liquid Test Fixture in combination with the automatic RLC Meter RLC 300 operating at a frequency of 10 kHz. To determine the  $\epsilon_r$ -values for all four solvent mixtures, we at first measured the capacities  $C$  for several solvents with known relative permittivity and prepared a calibration curve, as shown in Fig. E.2. Note that pure NMPA, which was excluded for the calibration curve, shows a very large measured capacity ( $C = 7253$  pF) due to the parallel alignment of the adjacent molecular dipole moments.

With the recorded calibration curve, which represents a linear correlation ( $R^2 = 0.99989$ ), we are able to transform the measured capacities for all four solvent mixtures into the respective relative permittivities mentioned in Chapter 7 by applying equation (E.2):

$$\epsilon_r = 0.0304 \frac{1}{\text{pF}} \cdot C - 0.0264 . \quad (\text{E.2})$$

The capacities for all four solvent mixture are listed below:

- DMSO:gly:water  $\rightarrow C = 1807.4 \text{ pF} \pm 36.1 \text{ pF}$ ,
- DMF:gly:water  $\rightarrow C = 1576.1 \text{ pF} \pm 31.5 \text{ pF}$ ,
- DMSO:eg:water  $\rightarrow C = 1745.4 \text{ pF} \pm 34.9 \text{ pF}$  and
- DMSO:gly:NMPA  $\rightarrow C = 1750.8 \text{ pF} \pm 35.0 \text{ pF}$ .

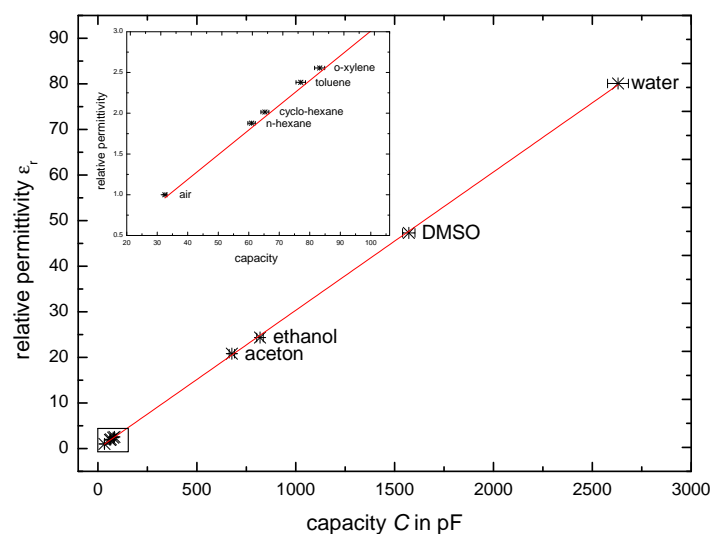


Fig. E.2.: Calibration measurements to determine the relative permittivity  $\epsilon_r$  for all four solvent mixtures. The inset highlights the data points with low capacity values.

## Supplement DLS

Figure E.3 shows the recorded autocorrelation functions for solely the three new solvent mixtures at side and back scattering, whereas these reference samples were similarly prepared compared to the systems containing our ionic building units. The weakly pronounced graphs with y-intercept values not exceeding 1.12 in combination with low scattering intensities demonstrate that the solvent mixtures themselves do not intend to form well-defined structures, just like the established DMSO:gly:water.<sup>94</sup>

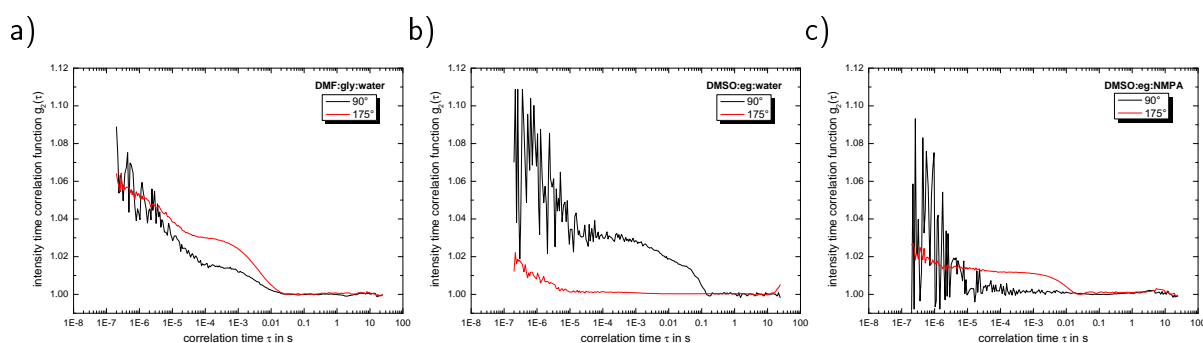


Fig. E.3.: Intensity time correlation functions from the pure solvent mixtures a) DMF:gly:water, b) DMSO:eg:water and c) DMSO:gly:NMPA at both scattering angles.

## Supplement CW EPR

As already mentioned in Appendix A, we started to use the MS5000 benchtop spectrometer for recording CW EPR spectra at X-band frequencies. Due to the reduced modulation ampli-

tude compared to the previous studies with the MS400,<sup>66,92,94</sup> most of the X-band spectra present now line shapes with anisotropic line broadening, which indicate the existence of two components inside the samples. Adding  $\mathbf{1}^{4+}$  to the Fremy's salt leads to a

- 1) 'fast' rotating component, where the unique axis  $D_{\parallel}$  is, similar to pure Fremy's salt (molar ratio 0:1), along the N-S-bond of the nitroxide and
- 2) 'slow' rotating component with the shift of the  $D_{\parallel}$ -axis to the dissection angle of both sulfonate groups.

The respective sets of Euler angles can be summarized as:

- pure  $\mathbf{3}^{2-}$  and  $\mathbf{1}^{4+}:\mathbf{3}^{2-}$  fast rotating component:  $\alpha = 65^\circ$ ,  $\beta = 90^\circ$ ,  $\gamma = 15^\circ$  and
- $\mathbf{1}^{4+}:\mathbf{3}^{2-}$  slow rotating component:  $\alpha = 85^\circ$ ,  $\beta = 90^\circ$ ,  $\gamma = 15^\circ$ .

The respective amount of each component depends on the concentration of cationic building unit as well as present solvent mixture. To compare the results from Q-band spectra with the one at X-band frequencies, we adapted its 'two component approach'. Table E.3 summarizes for all four solvent mixtures the utilized hyperfine coupling values, whereas  $a_{iso}$  describes the isotropic value of the hyperfine coupling tensor with  $a_{iso} = \frac{1}{3} \cdot (A_{xx} + A_{yy} + A_{zz})$ .

**Table E.3.:** Summary for the isotropic values of the hyperfine coupling tensor  $a_{iso}$  at X- and Q-band frequencies, subdivided after fast and slow rotating component

solvent $\nu_{mw}$	DMSO:gly:water		DMF:gly:water		DMSO:eg:water		DMSO:gly:NMPA	
	X-band	Q-band	X-band	Q-band	X-band	Q-band	X-band	Q-band
$a_{iso}/\text{G}$ (fast)	12.91	13.11	12.90	13.11	12.86	13.14	12.90	13.12
$a_{iso}/\text{G}$ (slow)	13.04	13.25	12.99	13.23	12.95	13.16	13.04	13.38



## Analyzing preferential solvation with DLS

At the beginning of this section we present the autocorrelation functions for the molar ratios at measurement day 10, which were not explicitly described in Chapter 7. Fig. E.4 highlights the results for  $1^{4+}:2^{2-}$  1:6 and 1:1 at both scattering angles inside all four solvent mixtures.

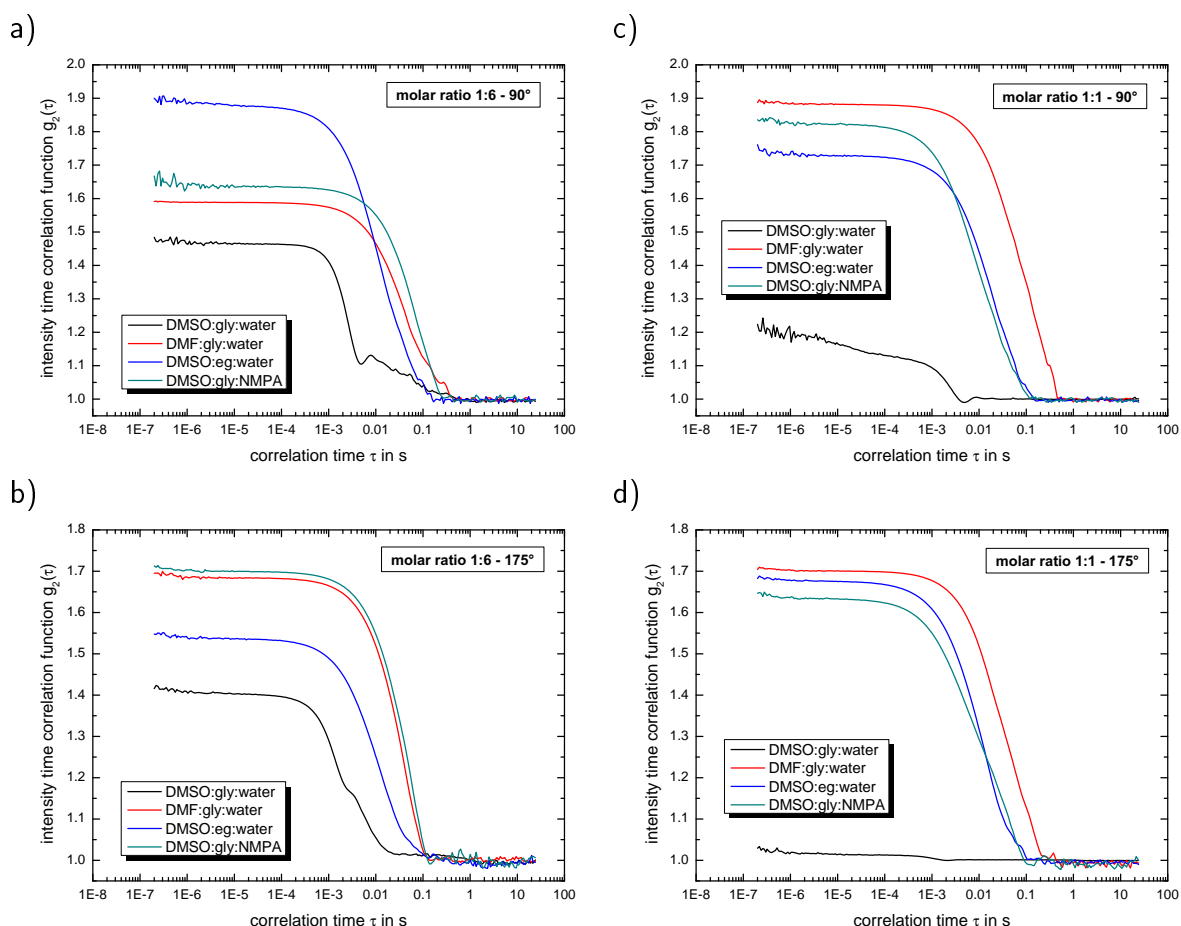


**Fig. E.4.:** Intensity time correlation functions at measurement day ten for all four solvent mixtures at side (a) and c)) and back (b) and d)) scattering. a), b) graphs for  $1^{4+}:2^{2-}$  1:6 and c), d) graphs for  $1^{4+}:2^{2-}$  1:1.

The optimal solvent mixture DMSO:gly:water shows significantly less pronounced intensity time correlation functions with an early decay in both molar ratios compared to the new solvent mixtures. Note that the combinations  $1^{4+}:2^{2-}$  1:6 and 1:1 are not able to build up ionic cluster with long-term stability,<sup>92</sup> which is reflected in their weak scattering intensity. The individual exchange of each solvent compound drastically rises the y-intercept value of the autocorrelation functions, but also shifts their decay to larger correlation times, indicating the formation of enlarged entities besides the build up of well-defined ionic cluster. Further comparison between these solvents demonstrate:

- a late decay in DMF:gly:water and

- a relatively early drop for DMSO:eg:water in both molar ratios, while
- DMSO:gly:NMPA shows 'DMF-behavior' for 1:6 and 'eg-behavior' for 1:1.

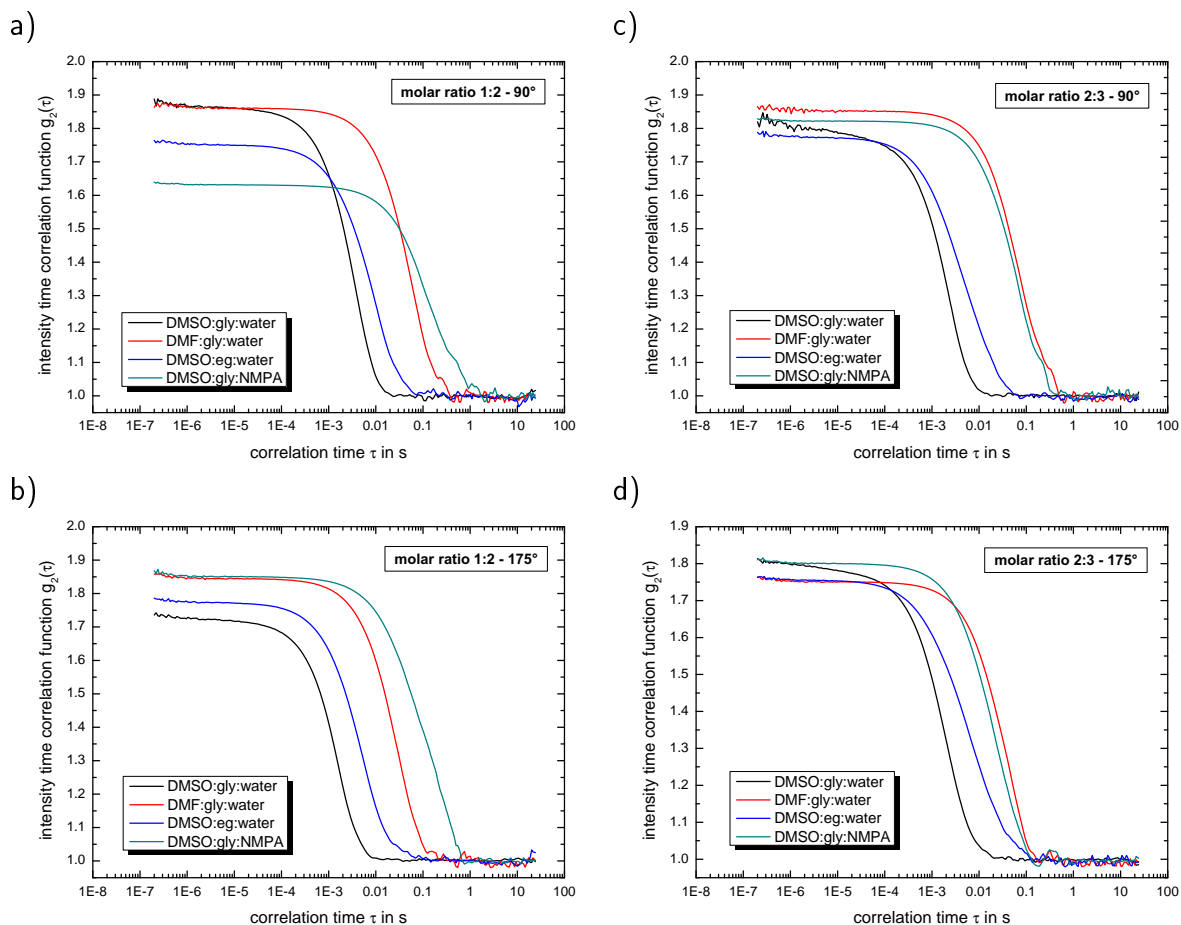


Fig. E.5.: Intensity time correlation functions at measurement day ten for all four solvent mixtures at side (a) and c)) and back (b) and d)) scattering. a), b) graphs for  $1^{4+}:2^{2-}$  1:2 and c), d) graphs for  $1^{4+}:2^{2-}$  2:3.

Fig. E.5 contains the intensity time correlation functions for the remaining molar ratios 1:2 and 2:3. With the increased concentration of cationic component, we record the formation of anisotropic ionic cluster inside the optimal solvent mixture DMSO:gly:water,<sup>92</sup> which is represented by well-pronounced autocorrelation functions with an early decay at both scattering angles. DMF:gly:water does not show significant changes in its scattering profile compared to the already discussed molar ratios.

DMSO:eg:water presents intensity time correlation functions resembling the trend for the optimal solvent mixture, but with a slightly delayed and stretched decay. Both aspects lead to the detection of elongated anisotropic ionic clusters. DMSO:gly:NMPA follows for molar ratio 1:2 the behavior of the 'DMF-solvent', but adjusts its scattering profile beginning at molar ratio 2:3 to the one visible for the 'eg-solvent'. To summarize the self-assembly process for all

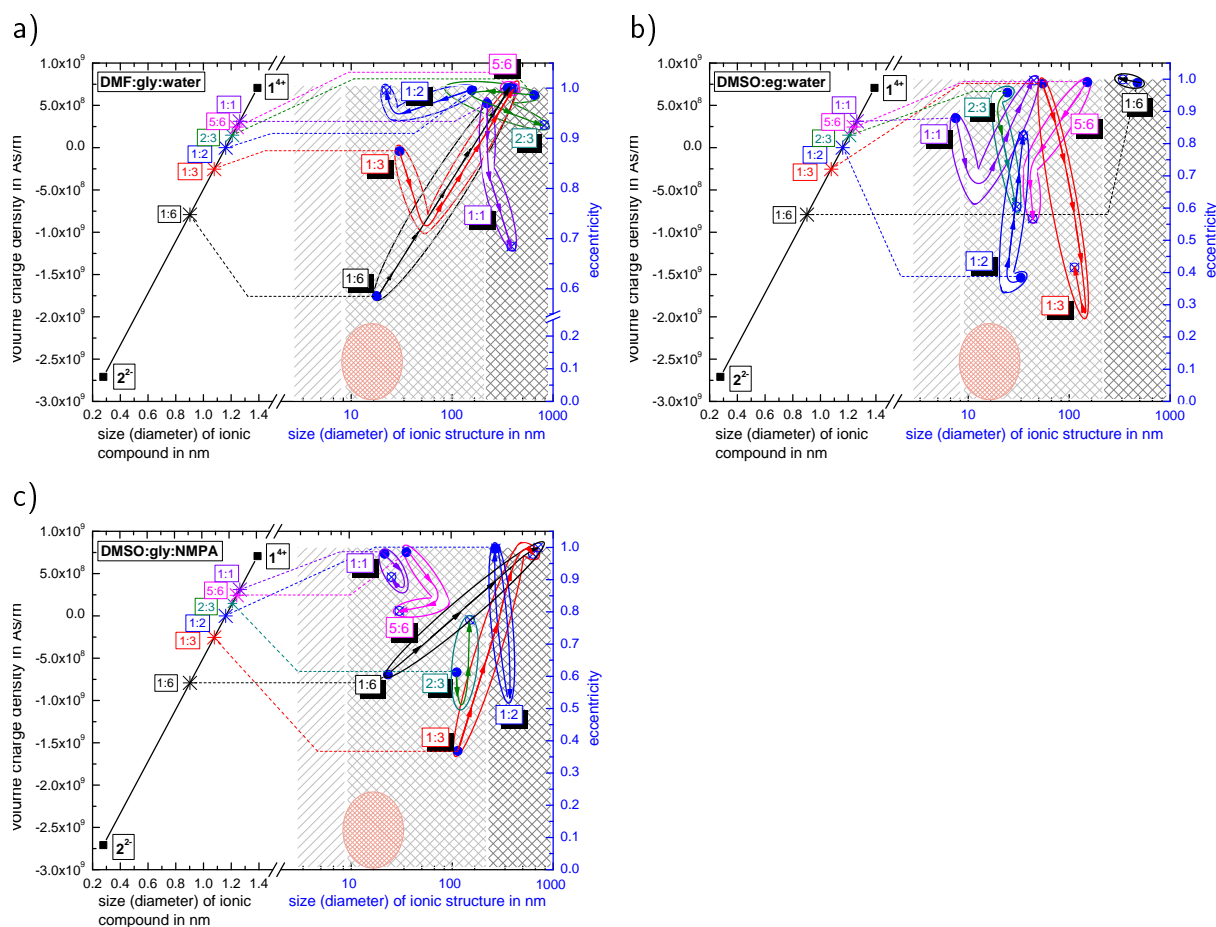


Fig. E.6.: Ionoid evolution diagram (IED) for system  $1^{4+}:2^{2-}$  with all tested molar ratios for the new solvent mixtures a) DMF:gly:water, b) DMSO:eg:water and c) DMSO:gly:NMPA. The IEDs further highlight, similar to the ones in Chapter 7, the three states of the ionic self-assembly process. The total time of observation reflected in the IEDs amounts to 30 days.

molar ratios inside the three new solvents, we include in Fig. E.6 ionoid evolution diagrams (IEDs) divided after these mixtures. After studying the samples over the course of one month, we filtered all solutions and measured them with DLS to validate the stability of the build up ionic cluster under mechanical stress. In Fig. E.7, we focus on the results for the systems  $1^{4+}:2^{2-}$  1:3 and 5:6, which were discussed in Chapter 7.

For the molar ratio 1:3 only the established solvent DMSO:gly:water presents well-pronounced autocorrelation functions at both scattering angles, indicating that in the new mixtures the (i) previous amount of ionic clusters was small or (ii) the self-assembled entities were destroyed due to the mechanical stress of filtering the sample. By increasing the cationic concentration of  $1^{4+}$  (like in molar ratio 5:6), DMSO:eg:water also shows intensity time correlation functions with high y-intercept values. Moreover, we get particles with a fourfold times larger dimension (see Chapter 7) as well as a monodisperse size distribution. Exchanging DMSO with DMF

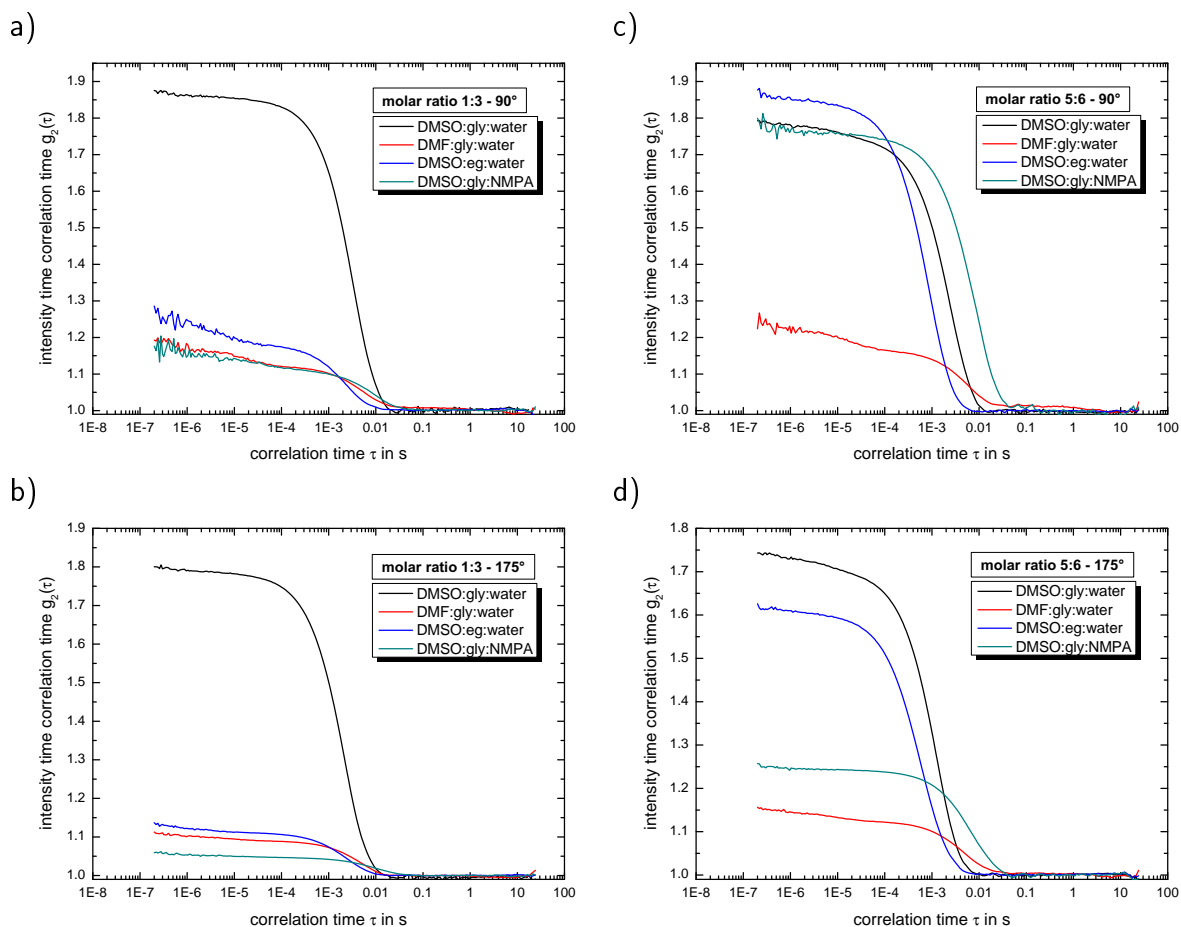


Fig. E.7.: Intensity time correlation functions for all four solvent mixtures at side (a) and c)) and back (b) and d)) scattering after filtering the sample. a), b) graphs for  $1^{4+}:2^{2-}$  1:3 and c), d) graphs for  $1^{4+}:2^{2-}$  5:6.

almost completely wipes out the detected scattering intensity with its connected autocorrelation function. By applying NMPA instead of water, we get a mixed behavior based on the observed scattering angle. This could be due to the build up of more anisotropic ionic cluster, which have larger variations in the scattering intensity compared to spherical structures.

## Analyzing preferential solvation with CW EPR spectroscopy

At first, we show in Fig. E.8 the X- and Q-band spectra of pure Frey's salt (molar ratio  $1^{4+}:3^{2-}$  0:1) in all four tested solvent mixtures, which were already discussed in Chapter 7.

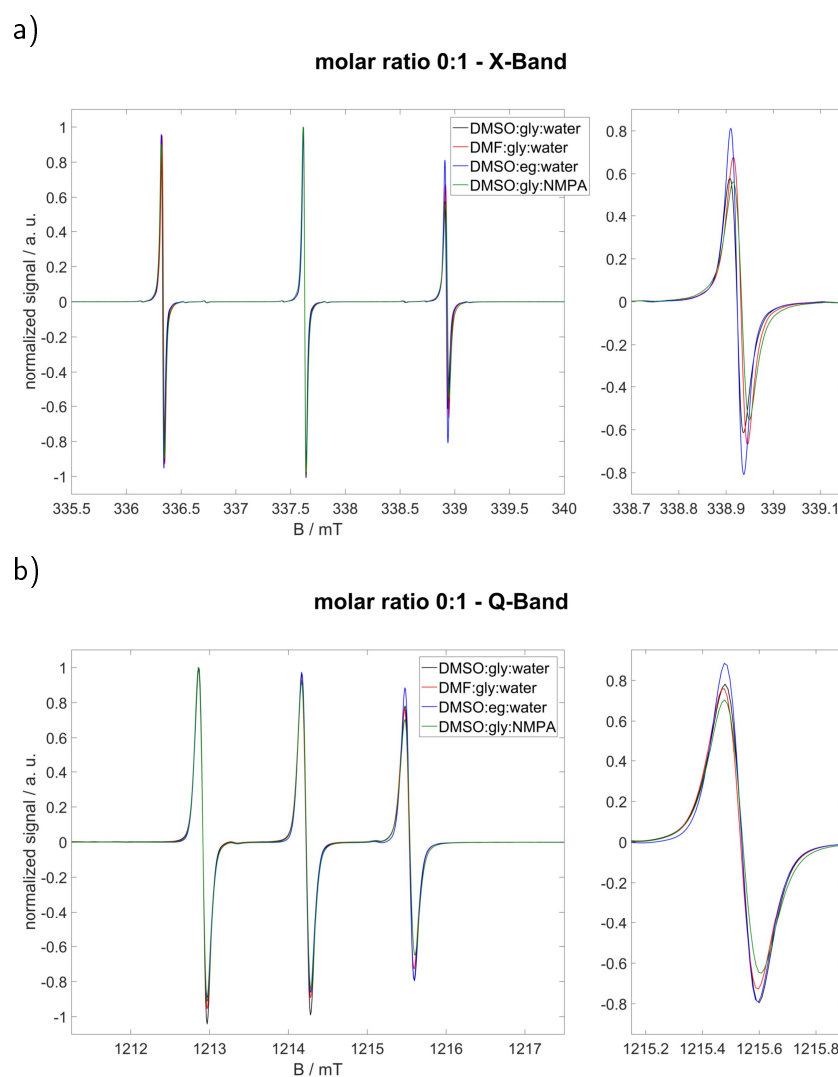


Fig. E.8.: a) X-band and b) Q-band CW EPR spectra of  $1^{4+}:3^{2-}$  with molar ratios 0:1 in all four solvent mixtures. The highfield peak of the spectra is shown separately right next to the full spectra.

In the next step, we highlight the effects of adding  $1^{4+}$  to our Frey's salt at 20 °C, whereas we discuss each solvent separately. Therefore, we present the characteristics for the fast and slow rotating component in each molar ratio as well as their respective share inside the measured sample.

## DMSO:gly:water

Fig. E.9 presents for both frequencies the simulated components of fast and slow rotation, which combined make up the measured spectra. Note that we adjusted the ratio of both components as well as their respective diffusion tensors to minimize the difference between the measured and the simulated spectra.

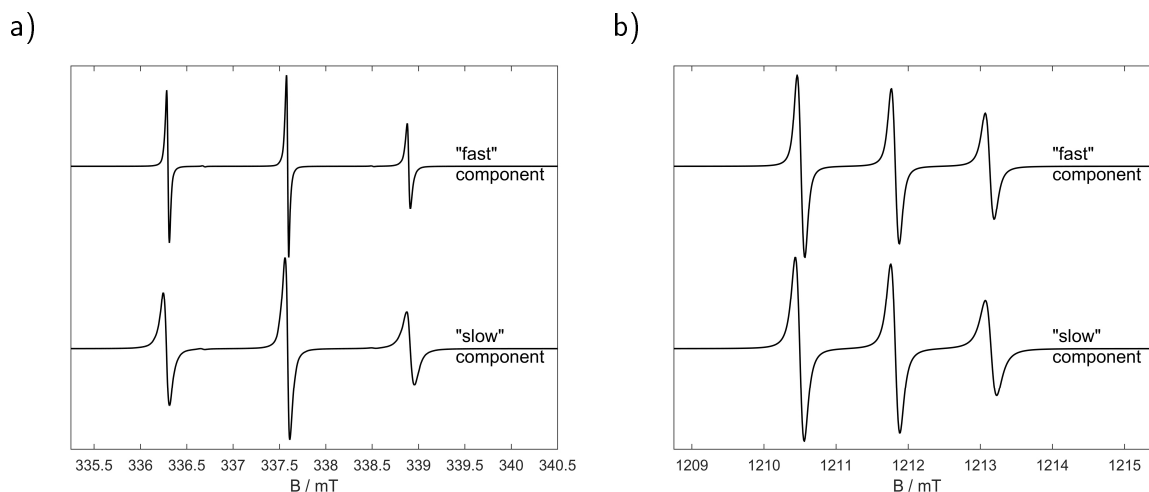


Fig. E.9.: Simulated components of which the CW EPR spectra of a) X-band and b) Q-band spectra in DMSO:gly:water are composed.

Fig. E.10 displays all measured and simulated CW EPR spectra at both X- and Q-band frequencies for the system  $\mathbf{1}^{4+}:\mathbf{3}^{2-}$  in DMSO:gly:water depending on the molar ratio. The transition from a relatively high rotational mobility of Fremy's salt into a more fixed coordination with increasing cationic concentration is connected with the rise of slow component inside the sample due to stronger electrostatic interactions between  $\mathbf{1}^{4+}$  and  $\mathbf{3}^{2-}$ . Note that increasing the cationic concentration also indirectly affects the fast component due to the long-range characteristic of electrostatic interactions. Therefore, Fremy's salt dianions, which are not directly connected to  $\mathbf{1}^{4+}$ , still show a slightly slowed-down rotation.

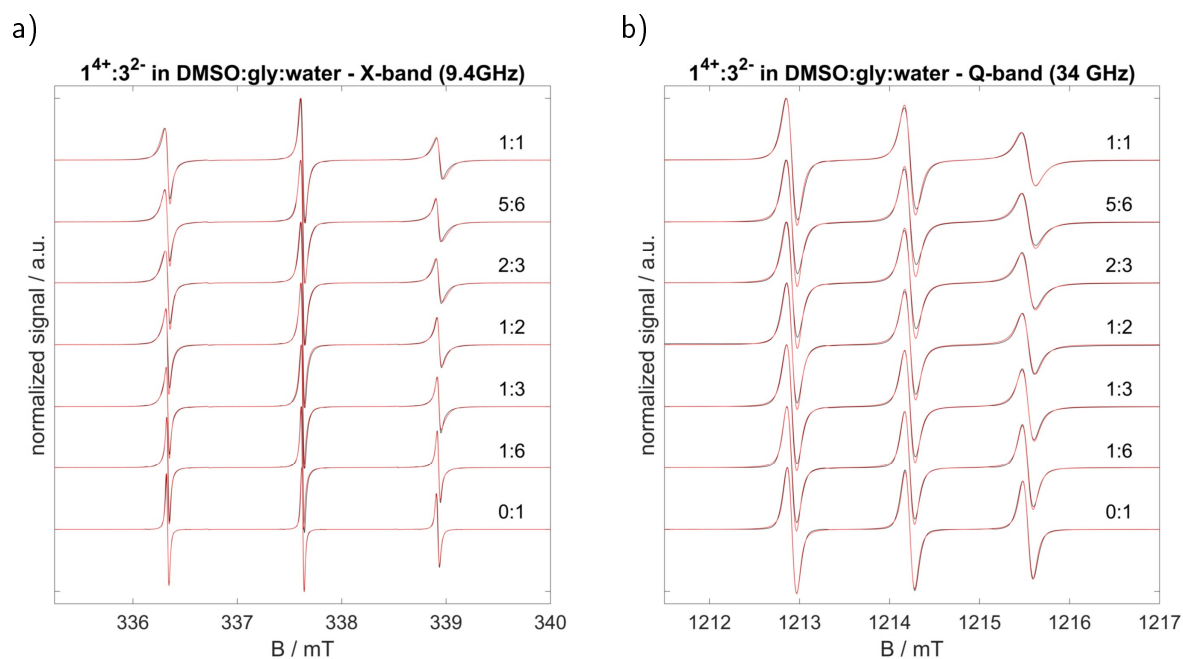


Fig. E.10.: a) X-band and b) Q-band CW EPR spectra for system  $1^{4+}:3^{2-}$  in DMSO:gly:water depending on the molar ratio. Both graphs show for each mixture the measured spectrum (black line) as well as the simulated spectrum (red line).

Table E.4 summarizes the simulation results for both frequencies.

Table E.4.: Summary of the simulated axial rotational diffusion tensor  $D_{\perp}$  and  $D_{\parallel}$  as well as the calculated rotational correlation time  $\tau_c$  and anisotropy  $T$  of system  $1^{4+}:3^{2-}$  in DMSO:gly:water depending on the molar ratio

ratio	compound		X-band			
	fast	fraction	$D_{\perp}/s^{-1}$	$D_{\parallel}/s^{-1}$	$\tau_c / ps$	$T$
0:1	fast	1	6.5e8	4.0e10	64.95	0.953
1:6	fast	0.52	6.3e8	4.0e10	66.31	0.954
	slow	0.48	1.2e8	2.0e10	252.4	0.982
1:3	fast	0.39	3.5e8	4.0e10	98.13	0.974
	slow	0.61	1.1e8	1.9e10	272.1	0.983
1:2	fast	0.31	3.0e8	3.2e10	117.1	0.972
	slow	0.69	1.1e8	1.6e10	288.1	0.980
2:3	fast	0.30	2.1e8	3.0e10	151.8	0.979
	slow	0.70	9.7e7	1.4e10	327.6	0.980
5:6	fast	0.28	2.0e8	3.0e10	156.8	0.980
	slow	0.72	9.5e7	1.3e10	340.4	0.978
1:1	fast	0.27	1.8e8	2.8e10	172.2	0.981

	slow	0.73	9.1e7	1.1e10	370.4	0.976
ratio	compound		Q-band			
		fraction	$D_{\perp}/s^{-1}$	$D_{\parallel}/s^{-1}$	$\tau_c / ps$	$T$
0:1	fast	1	1.0e9	5.0e10	45.24	0.942
1:6	fast	0.79	6.2e8	4.0e10	67.02	0.955
	slow	0.21	2.0e8	2.0e10	179.5	0.971
1:3	fast	0.55	4.0e8	4.0e10	89.77	0.971
	slow	0.45	1.5e8	1.9e10	221.2	0.973
1:2	fast	0.38	3.2e8	3.0e10	114.7	0.969
	slow	0.62	1.2e8	1.4e10	284.2	0.975
2:3	fast	0.35	2.9e8	3.0e10	122.4	0.972
	slow	0.65	1.1e8	1.1e10	326.4	0.971
5:6	fast	0.33	2.7e8	3.0e10	128.4	0.974
	slow	0.67	9.8e7	9.8e9	366.4	0.971
1:1	fast	0.31	2.5e8	3.0e10	135.2	0.975
	slow	0.69	9.5e7	9.5e9	378.0	0.971

At last, we want to highlight the development of the rotational correlation time  $\tau_c$  as well as the anisotropy  $T$  for both CW frequencies. In Fig. E.11, we plot the respective values for fast and slow component based on Table E.4 and a calculated 'mean' value. This score results from the summation of fast and slow component considering their fraction inside each sample, whereas we used the fraction as weighting factor for the calculation. The presented FWHM values in Chapter 7 also show these 'mean' values to demonstrate the line width changes based on the cooperation of both components (fast and slow) with increasing cationic concentration.



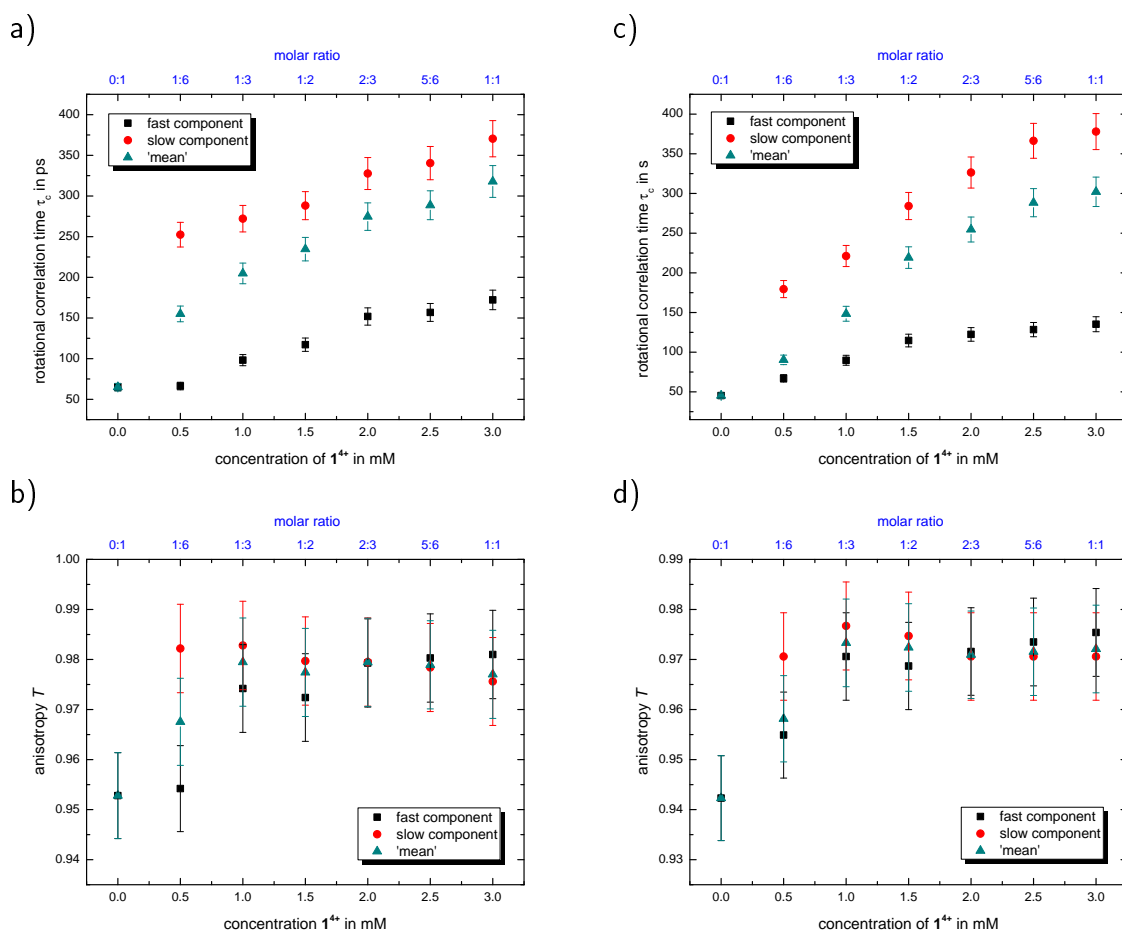


Fig. E.11.: Development of the rotational correlation time  $\tau_c$  (a) and c)) as well as anisotropy  $T$  (b) and d)) for system  $1^{4+}:3^{2-}$  in DMSO:gly:water for all tested molar ratios. a), b) X-band and c), d) Q-band results unraveled for slow and fast component as well as represented with a 'mean' value for the entire samples.

The three new solvent mixtures (i) DMF:gly:water, (ii) DMSO:eg:water as well as (iii) DMSO:gly:NMPA will be summarized in the same manner like the already discussed optimal system DMSO:gly:water.

## DMF:gly:water

Fig. E.12 shows the slow and fast component for simulating the CW EPR spectra at X- and Q-band frequencies.

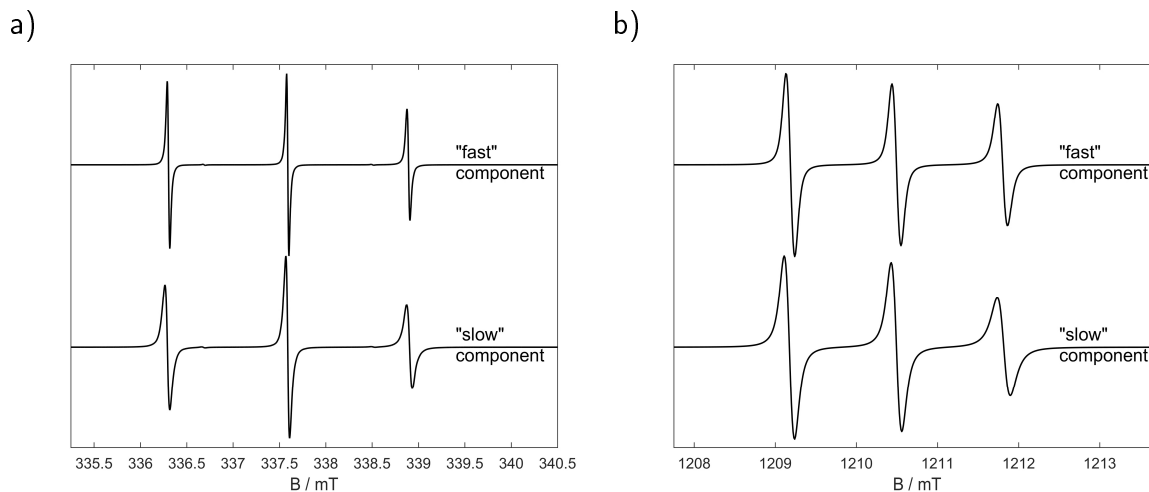


Fig. E.12.: Simulated components of which the CW EPR spectra of a) X-band and b) Q-band spectra in DMF:gly:water are composed.

Increasing the concentration of the 'Texas-sized molecular box' again lead to a more immobilized rotation of Fremy's salt (see Fig. E.13), which results in a higher fraction of the slow component. However, the amount of  $\mathbf{3}^{2-}$  with a more fixed coordination to  $\mathbf{1}^{4+}$  substantial differs between X- and Q-band frequencies. These changes for the rotational mobility at the limit of fast rotation can be more visualized with higher CW frequencies due to their better sensitivity in that region.

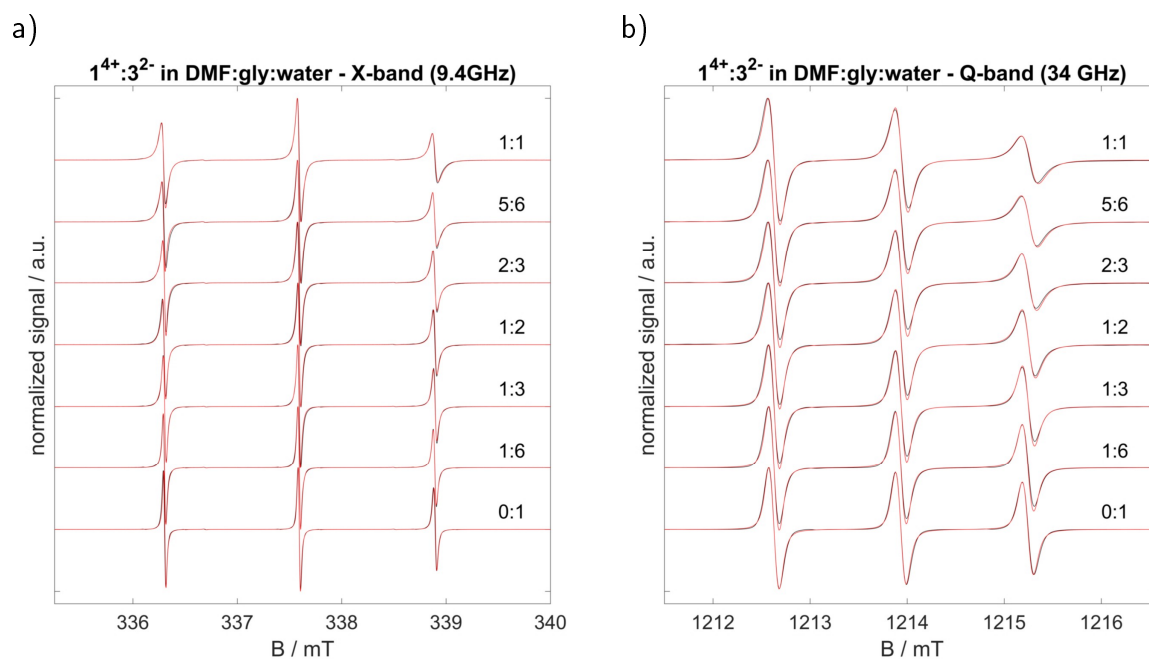


Fig. E.13.: a) X-band and b) Q-band CW EPR spectra for system  $1^{4+}:3^{2-}$  in DMF:gly:water depending on the molar ratio. Both graphs show for each mixture the measured spectrum (black line) as well as the simulated spectrum (red line).

Table E.5 summarizes all simulation results, divided after the two used frequencies.

Table E.5.: Summary of the simulated axial rotational diffusion tensor  $D_{\perp}$  and  $D_{\parallel}$  as well as the calculated rotational correlation time  $\tau_c$  and anisotropy  $T$  of system  $1^{4+}:3^{2-}$  in DMF:gly:water depending on the molar ratio

ratio	compound		X-band			
	fast	fraction	$D_{\perp}/s^{-1}$	$D_{\parallel}/s^{-1}$	$\tau_c / ps$	$T$
0:1	fast	1	9.0e8	4.0e10	52.28	0.935
1:6	fast	0.86	7.2e8	4.0e10	60.67	0.945
	slow	0.14	2.0e8	2.0e10	179.5	0.971
1:3	fast	0.64	6.8e8	4.0e10	63.02	0.951
	slow	0.36	1.8e8	2.0e10	192.6	0.974
1:2	fast	0.48	5.7e8	3.5e10	74.12	0.953
	slow	0.52	1.6e8	2.0e10	208.3	0.976
2:3	fast	0.40	5.0e8	3.0e10	85.15	0.952
	slow	0.60	1.4e8	2.0e10	227.7	0.979
5:6	fast	0.36	3.7e8	2.5e10	110.6	0.957
	slow	0.64	1.2e8	2.0e10	252.4	0.982
1:1	fast	0.33	2.8e8	2.0e10	133.2	0.967

	slow	0.67	1.0e8	2.0e10	285.0	0.985
ratio	compound		Q-band			
		fraction	$D_{\perp}/s^{-1}$	$D_{\parallel}/s^{-1}$	$\tau_c / ps$	$T$
0:1	fast	1	1.0e9	3.5e10	50.95	0.919
1:6	fast	0.92	7.2e8	3.5e10	63.43	0.941
	slow	0.08	2.0e8	2.0e10	179.5	0.971
1:3	fast	0.72	6.0e8	3.0e10	75.40	0.942
	slow	0.28	1.5e8	2.0e10	217.5	0.978
1:2	fast	0.54	4.0e8	2.5e10	105.0	0.954
	slow	0.46	1.2e8	1.7e10	266.4	0.979
2:3	fast	0.47	2.6e8	2.4e10	141.8	0.968
	slow	0.53	1.0e8	1.4e10	321.0	0.979
5:6	fast	0.39	2.0e8	2.0e10	179.5	0.971
	slow	0.61	9.8e7	1.1e10	352.6	0.974
1:1	fast	0.40	1.5e8	1.6e10	234.3	0.972
	slow	0.60	9.2e7	9.8e9	382.2	0.972

The development of the rotational correlation time  $\tau_c$  as well as the anisotropy  $T$  for both CW frequencies can be found in Fig. E.14.

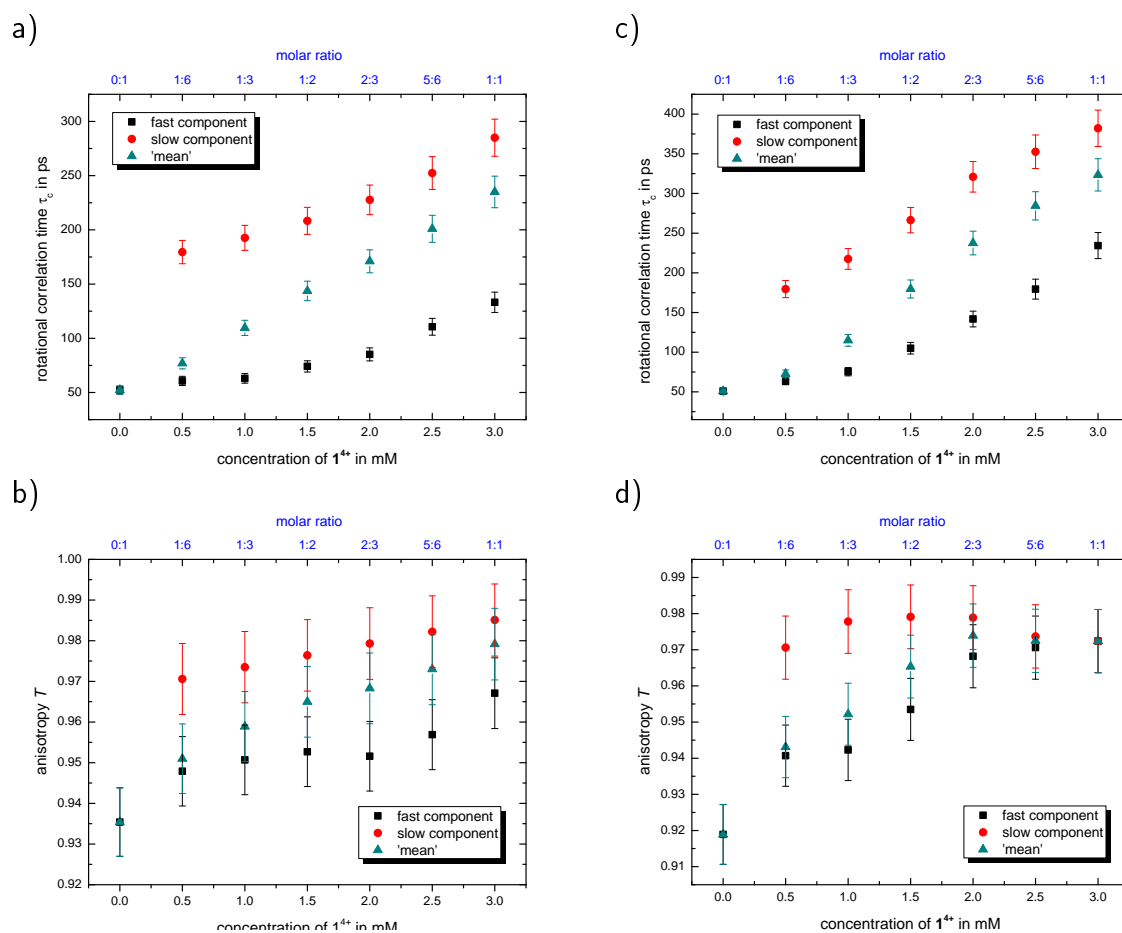


Fig. E.14.: Development of the rotational correlation time  $\tau_c$  (a) and c)) as well as anisotropy  $T$  (b) and d)) for system  $14^+ : 32^-$  in DMF:gly:water for all tested molar ratios. a), b) X-band and c), d) Q-band results unraveled for slow and fast component as well as represented with a 'mean' value for the entire samples.

## DMSO:eg:water

DMSO:eg:water shows a particularity compared to the other three solvent mixtures: We could simulate the recorded CW EPR spectra at X- and Q-band frequencies with just one component (see Fig. E.15). Note that we still recognize a more fixed coordination of Frey's salt with increasing concentration of cationic component due to electrostatic interactions between both building units. However, the line shapes of the spectra do not demonstrate pronounced anisotropic line broadening effects, which indicates the non-essential application of two components for the simulation.

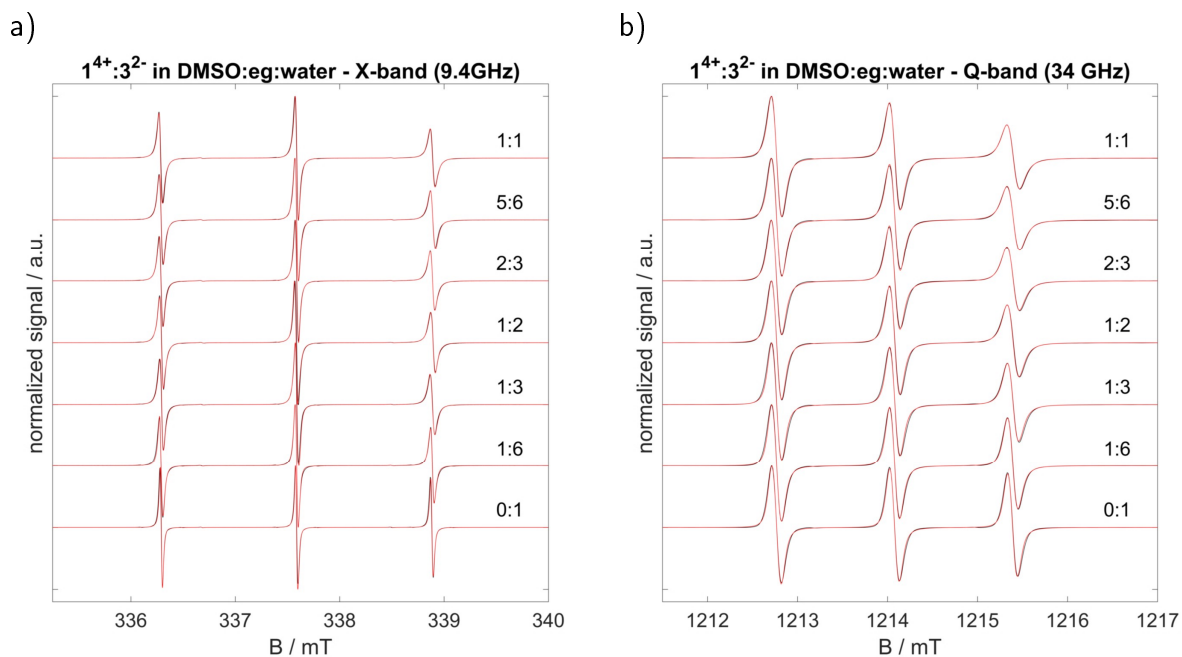


Fig. E.15.: a) X-band and b) Q-band CW EPR spectra for system  $1^{4+}:3^{2-}$  in DMSO:eg:water depending on the molar ratio. Both graphs show for each mixture the measured spectrum (black line) as well as the simulated spectrum (red line).

Table E.6 summarizes the simulation results for both microwave frequencies.

Table E.6.: Summary of the simulated axial rotational diffusion tensor  $D_{\perp}$  and  $D_{\parallel}$  as well as the calculated rotational correlation time  $\tau_c$  and anisotropy  $T$  of system  $1^{4+}:3^{2-}$  in DMSO:eg:water depending on the molar ratio

ratio	X-band				Q-band			
	$D_{\perp}/s^{-1}$	$D_{\parallel}/s^{-1}$	$\tau_c / ps$	$T$	$D_{\perp}/s^{-1}$	$D_{\parallel}/s^{-1}$	$\tau_c / ps$	$T$
0:1	1.8e9	6.0e10	28.77	0.915	2.0e9	5.0e10	28.50	0.889
1:6	4.8e8	4.5e10	76.43	0.969	6.0e8	4.0e10	68.51	0.956
1:3	2.7e8	1.8e10	152.2	0.956	3.5e8	1.8e10	128.0	0.944
1:2	2.7e8	1.7e10	155.2	0.954	2.7e8	1.5e10	161.8	0.948
2:3	2.6e8	1.5e10	165.9	0.950	2.2e8	1.2e10	199.8	0.947
5:6	2.5e8	1.5e10	170.3	0.952	2.1e8	1.1e10	212.1	0.945
1:1	2.5e8	1.4e10	174.3	0.948	2.1e8	1.0e10	219.0	0.940

The development of the rotational correlation time  $\tau_c$  as well as the anisotropy  $T$  for both CW frequencies can be found in Fig. E.16.

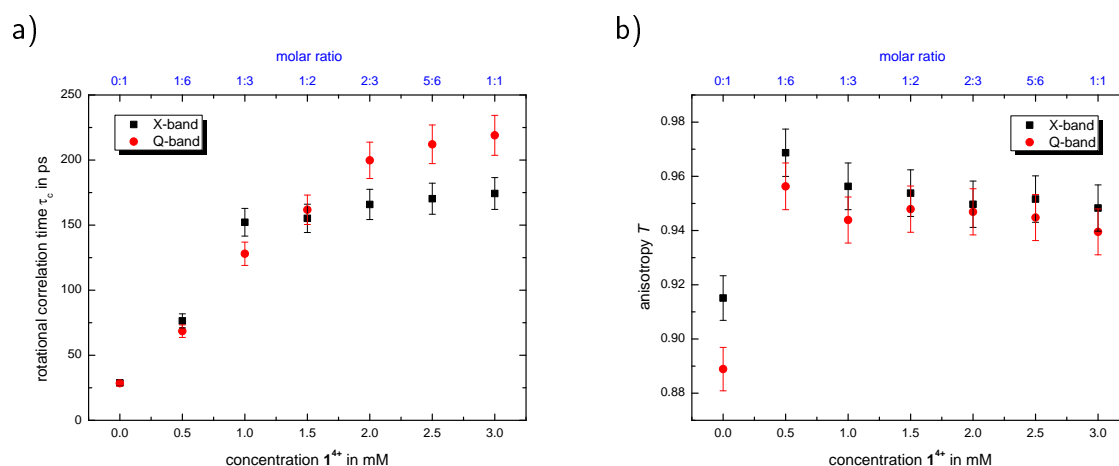


Fig. E.16.: a) Rotational correlation time  $\tau_c$  and b) anisotropy  $T$  of the system  $1^{4+}:3^{2-}$  versus the concentration of  $1^{4+}$  in DMSO:eg:water.

## DMSO:gly:NMPA

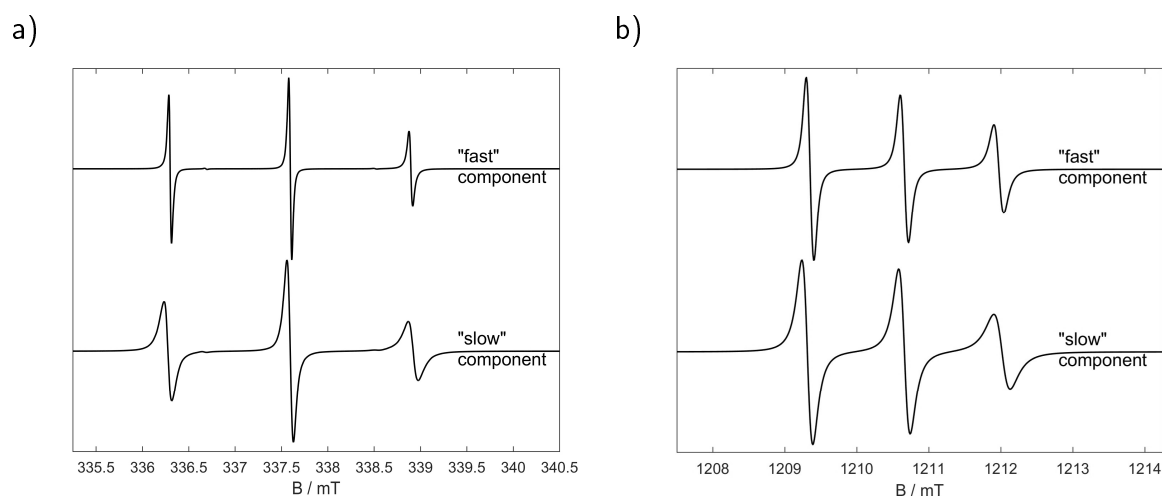


Fig. E.17.: Simulated components of which the CW EPR spectra of a) X-band and b) Q-band spectra in DMSO:gly:NMPA are composed.

Fig. E.17 represents the simulated components of fast and slow rotation, which combined make up the measured spectra. Note that the applied slow component shows an even more immobilized tumbling for Frey's salt than in the optimal solvent mixture with water, indicating a stronger coordination between both building units. In Fig. E.18, we see similar tendencies like in the optimal solvent mixture DMSO:gly:water, but the slow component is even more pronounced, especially for molar ratios 1:2 and higher.

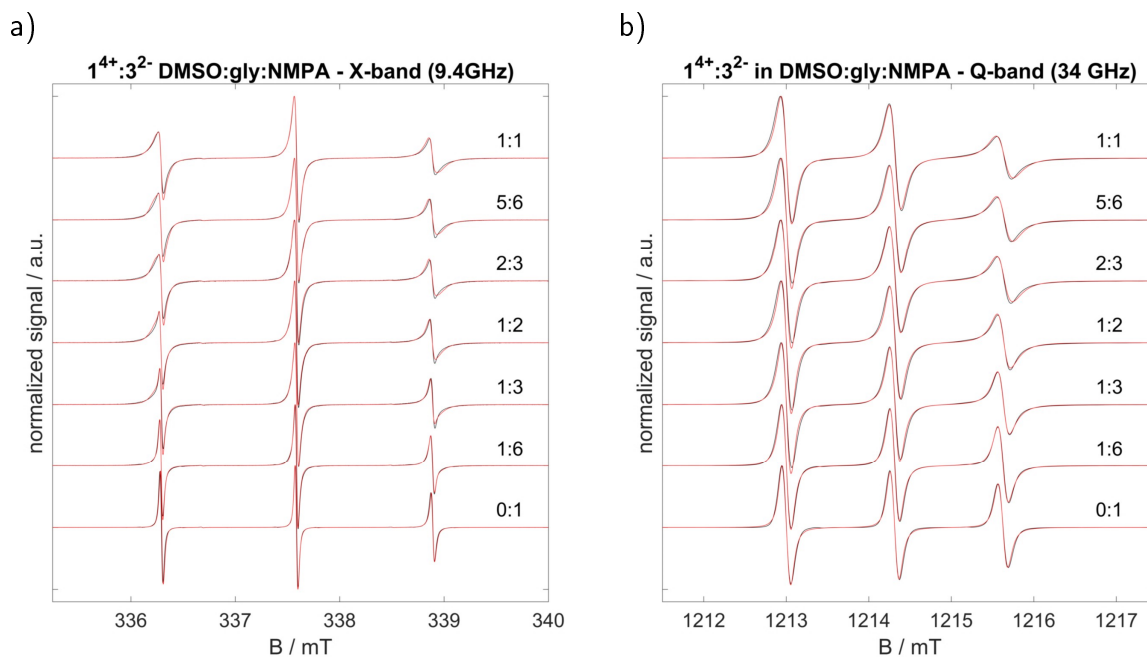


Fig. E.18.: a) X-band and b) Q-band CW EPR spectra for system  $1^{4+}:3^{2-}$  in DMSO:gly:NMPA depending on the molar ratio. Both graphs show for each mixture the measured spectrum (black line) as well as the simulated spectrum (red line).

All simulation results are summarized in Table E.7, separated after X- and Q-band.

Table E.7.: Summary of the simulated axial rotational diffusion tensor  $D_{\perp}$  and  $D_{\parallel}$  as well as the calculated rotational correlation time  $\tau_c$  and anisotropy  $T$  of system  $1^{4+}:3^{2-}$  in DMSO:gly:NMPA depending on the molar ratio

ratio	compound		X-band			
	fast	fraction	$D_{\perp}/s^{-1}$	$D_{\parallel}/s^{-1}$	$\tau_c / ps$	$T$
0:1	fast	1	5.8e8	3.0e10	77.12	0.944
1:6	fast	0.50	4.2e8	2.5e10	101.6	0.951
	slow	0.50	7.8e7	9.5e9	431.1	0.976
1:3	fast	0.32	2.8e8	2.0e10	143.5	0.959
	slow	0.68	7.2e7	9.0e9	454.7	0.978
1:2	fast	0.27	2.2e8	2.0e10	168.5	0.968
	slow	0.73	6.8e7	9.0e9	480.9	0.978
2:3	fast	0.23	2.0e8	1.6e10	193.4	0.963
	slow	0.77	6.5e7	9.0e9	495.6	0.979
5:6	fast	0.24	1.8e8	1.5e10	212.0	0.965
	slow	0.76	6.2e7	9.0e9	511.5	0.980
1:1	fast	0.22	1.7e8	1.5e10	220.2	0.967



	slow	0.78	6.0e7	9.0e9	522.8	0.980
ratio	compound		Q-band			
		fraction	$D_{\perp}/s^{-1}$	$D_{\parallel}/s^{-1}$	$\tau_c / ps$	$T$
0:1	fast	1	6.8e8	3.0e10	69.36	0.935
1:6	fast	0.78	4.5e8	2.5e10	97.06	0.948
	slow	0.22	1.0e8	1.2e10	337.9	0.975
1:3	fast	0.60	2.6e8	2.5e10	139.9	0.970
	slow	0.40	8.0e7	9.2e9	428.4	0.974
1:2	fast	0.52	2.0e8	2.5e10	166.7	0.976
	slow	0.48	7.0e7	8.5e9	480.8	0.976
2:3	fast	0.41	1.5e8	2.0e10	217.5	0.978
	slow	0.59	6.8e7	8.2e9	496.1	0.976
5:6	fast	0.36	1.5e8	1.8e10	225.3	0.975
	slow	0.64	6.8e7	8.0e9	500.2	0.975
1:1	fast	0.31	1.3e8	1.7e10	252.6	0.977
	slow	0.69	6.6e7	7.9e9	512.4	0.975

The development of the rotational correlation time  $\tau_c$  as well as anisotropy  $T$  for both CW frequencies can be found in Fig. E.19.

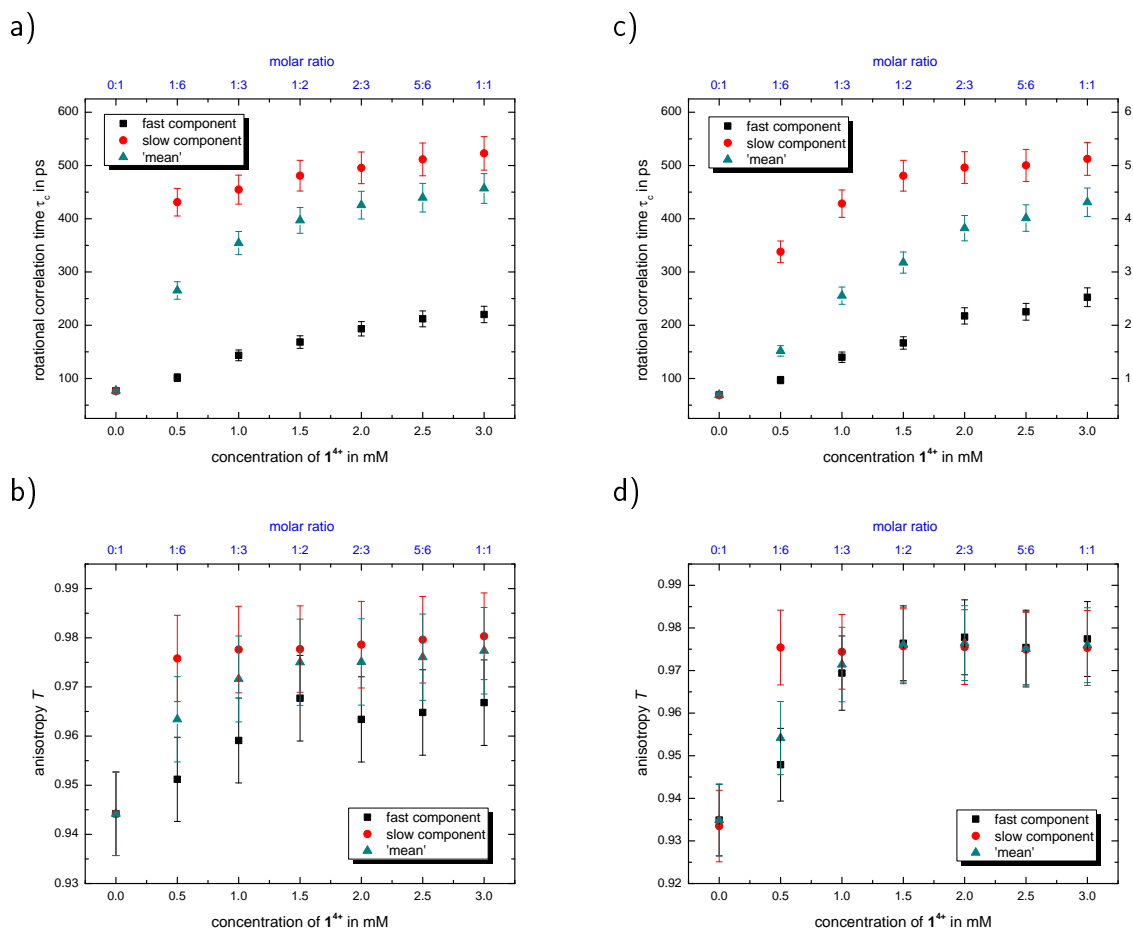


Fig. E.19.: Development of the rotational correlation time  $\tau_c$  (a) and c)) as well as anisotropy  $T$  (b) and d)) for system  $1^{4+}:3^{2-}$  in DMSO:gly:NMPA for all tested molar ratios. a), b) X-band and c), d) Q-band results unraveled for slow and fast component as well as represented with a 'mean' value for the entire samples.

## Q-band low temperature

After analyzing all four solvent mixtures separately at 20 °C, we focus on the low temperature measurements ( $T = 150\text{K}$ ) at Q-band frequencies. The spectra for solely Frey's salt as well as the direct comparison with system  $1^{4+}:3^{2-}$  molar ratio 1:3 in DMSO:gly:water 50:43:7 (v/v/v) can be found in Chapter 7. Fig. E.20 shows for the new solvent mixtures the respective Q-band spectra for the chosen system.

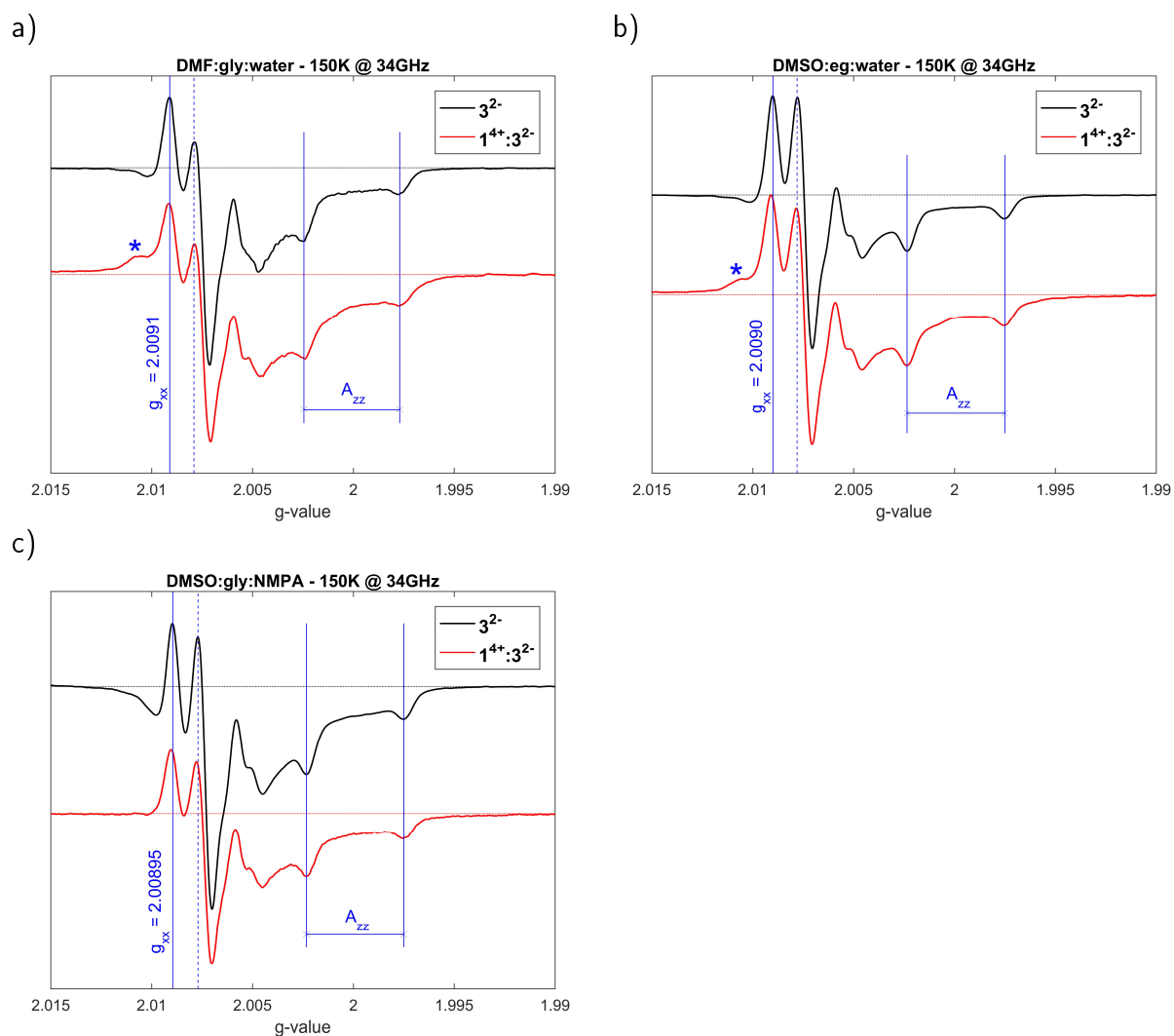


Fig. E.20.: Q-band CW EPR spectra at 150 K of  $1^{4+} : 3^{2-}$  with molar ratios 0:1 and 1:3 for a) DMF:gly:water, b) DMSO:eg:water and c) DMSO:gly:NMPA. The inserted blue lines highlight the position of  $g_{xx}$  as well as  $A_{zz}$  in relation to the  $3^{2-}$  reference.

The spectrum of Fremy's salt in DMSO:gly:NMPA presents a intensity drop before the signal at the  $g_{xx}$  position rises. This could be due to a discrepancy while manually adjusting the signal phase in the respective solvent mixture. Note that this drop occurs at the same position, where the  $1^{4+} : 3^{2-}$  systems normally present their additional 'feature' (see asterisk) due to strong dipolar interactions between the cationic and anionic building unit. Taking the offset of the reference spectrum (solely  $3^{2-}$ ) into account, then we can conclude that these interactions are also present for  $1^{4+} : 3^{2-}$  in DMSO:gly:NMPA.

# F | Appendix - Chapter 8

## Preparing solvent mixtures and molar ratio

The preparation of all solvent mixtures are based on the established mixture containing DMSO, glycerol and water in a volume ratio of 50:43:7. Similar to the description in Appendix E, we calculated the volume per solvent component in respect to a final volume of e. g.  $V = 2\text{ml}$ , which lead to the following values:

- DMSO:  $V = 1\text{ml}$ ,
- glycerol:  $V = 0.85\text{ml}$  and
- water/ $\text{H}_2\text{O}$ :  $V = 0.15\text{ml}$ .

Table F.1 summarizes the analyzed solvent mixtures in this chapter based on the two main aspects: (i) selective substitution of compounds and (ii) incorporation of partially deuterated compounds.

**Table F.1.:** Summary of the applied solvent mixtures in Chapter 8. The bold written solvent compounds are the ones that differ from the established mixture

selective substitution	partially deuterated
<b>DMF</b> :gly:H <sub>2</sub> O	<b>d6-DMSO</b> :gly:H <sub>2</sub> O
DMSO: <b>eg</b> :H <sub>2</sub> O	DMSO:gly: <b>D<sub>2</sub>O</b>
DMSO:gly: <b>NMPA</b>	DMSO: <b>d5-gly</b> :H <sub>2</sub> O
	DMSO: <b>d3-gly</b> :D <sub>2</sub> O

gly - glycerol, eg - ethylene glycol, NMPA - *N*-methylpropionamide, d5-gly - d5-glycerol, d3-gly - glycer-d3-ol

All measurements utilize the  $\mathbf{1^{4+}}:\mathbf{2^{2-}}$  ( $\mathbf{1^{4+}}:\mathbf{3^{2-}}$ , respectively) system with a concentration ratio of 1 mM:3 mM (molar ratio of 1:3). Therefore, we prepared stock solutions of

- $c(\mathbf{1^{4+}}) = 2\text{mM}$  and
- $c(\mathbf{2^{2-}})/c(\mathbf{3^{2-}}) = 6\text{mM}$

in the respective solvent mixtures, which were combined in a 1:1 volume ratio.

## Analyzing the selective substitution of solvent compounds

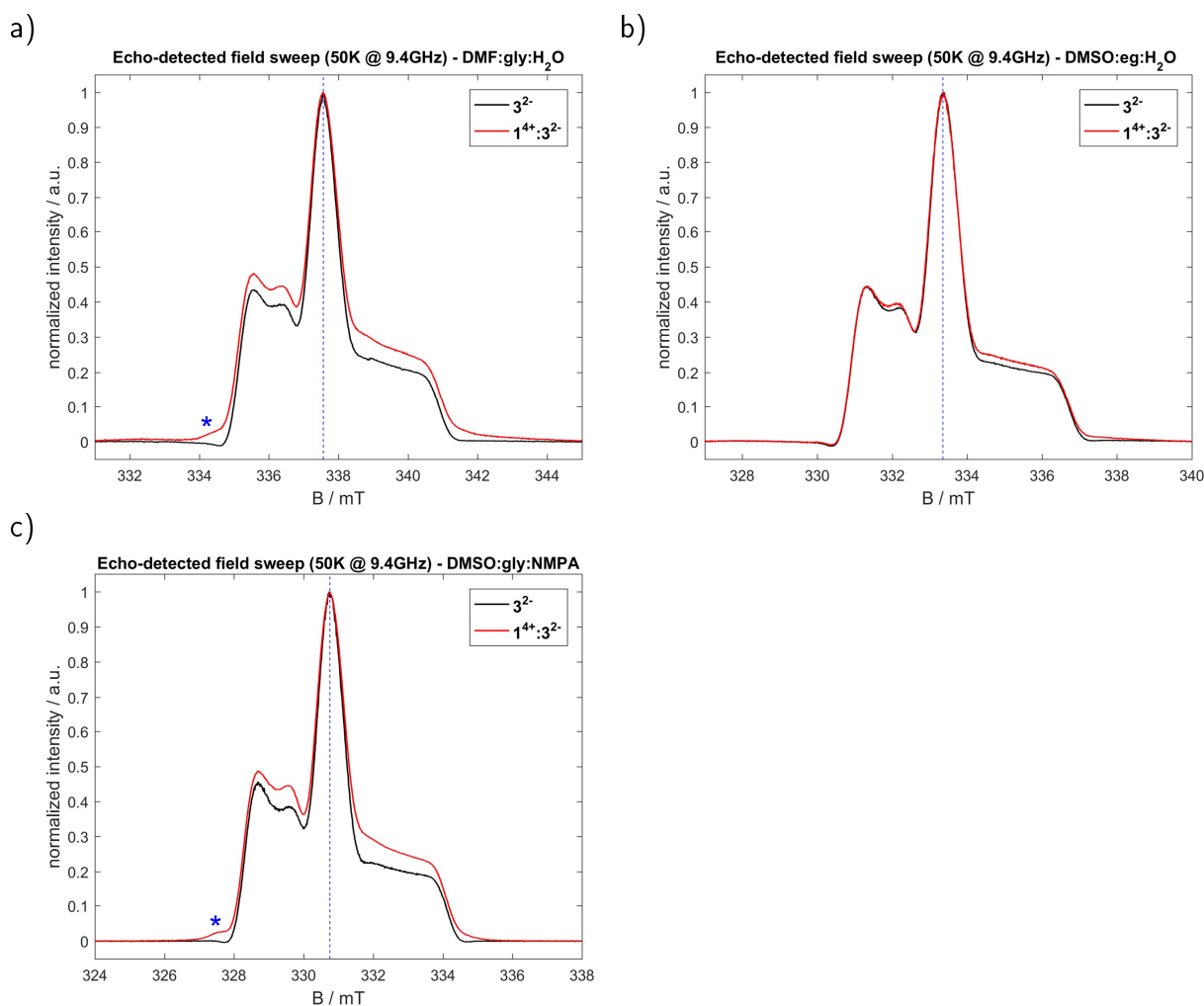


Fig. F.1.: Echo-detected field sweep spectra measured at 50K for solvent mixtures a) DMF:gly:H<sub>2</sub>O, b) DMSO:eg:H<sub>2</sub>O and c) DMSO:gly:NMPA.

Fig. F.1 highlights the echo-detected field sweep spectra from pure Frey's salt as well as from system  $1^{4+}:3^{2-}$  (molar ratio 1:3) in DMF:gly:H<sub>2</sub>O, DMSO:eg:H<sub>2</sub>O and DMSO:gly:NMPA. All spectra incorporating the 'Texas-sized molecular box' show a broadening effect similar to the established solvent mixture (see asterisks in Fig. F.1). Note that this effect is the least pronounced for the solvent containing ethylene glycol, which indicates a weaker coupling between cationic and anionic building unit. We already described similar tendencies for the CW EPR measurements at 20 °C.

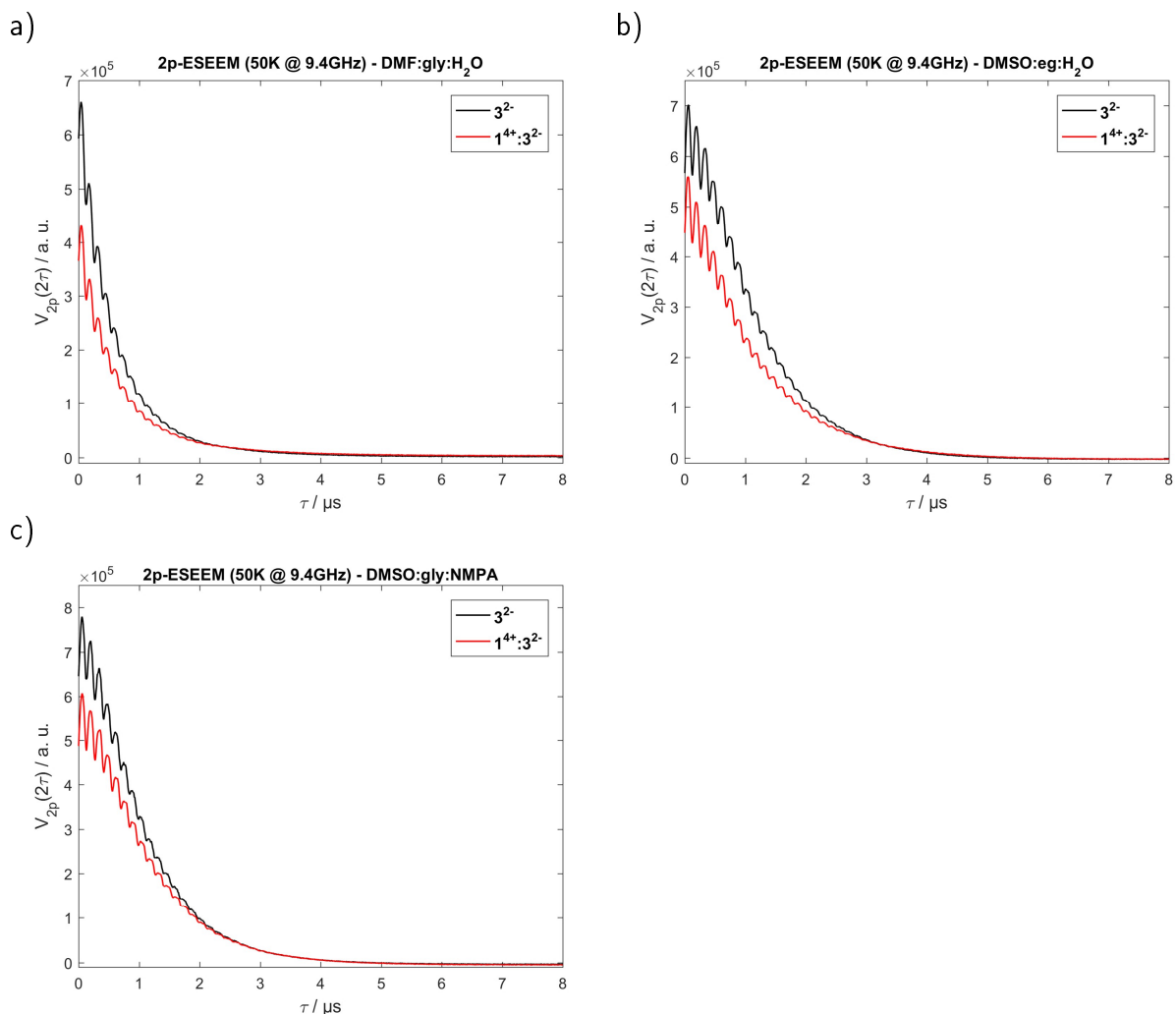


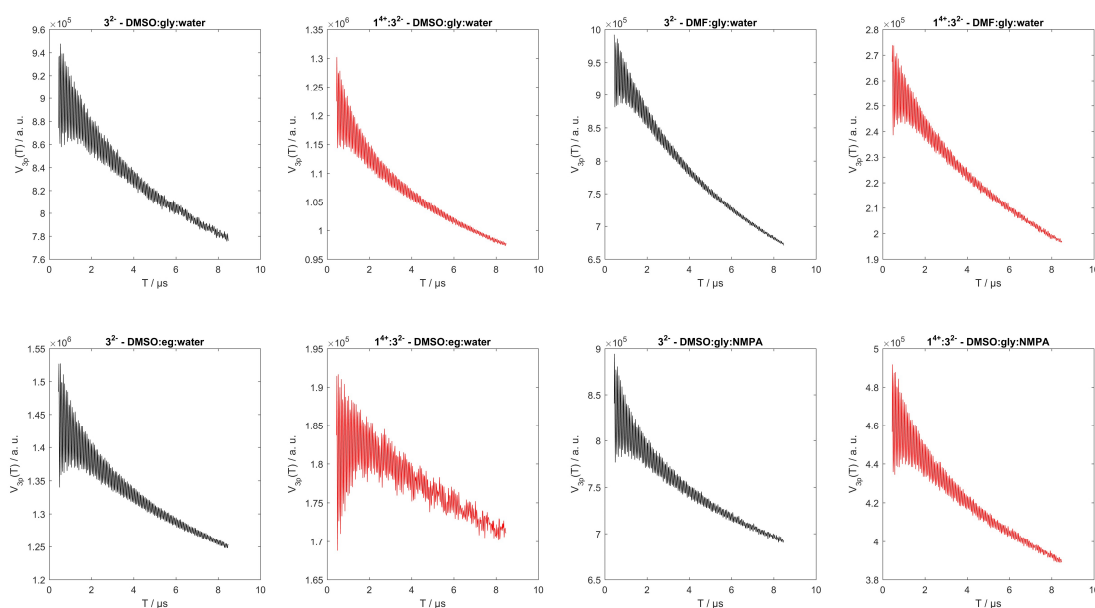
Fig. F.2.: Primary 2p-ESEEM data  $V_{2p}(2\tau)$  at 50 K for solvent mixtures a) DMF:gly:H<sub>2</sub>O:, b) DMSO:eg:H<sub>2</sub>O: and c) DMSO:gly:NMPA.

Fig. F.2 presents the primary 2p-ESEEM data from pure Frey's salt as well as from system  $1^{4+}:3^{2-}$  (molar ratio 1:3) in DMF:gly:H<sub>2</sub>O, DMSO:eg:H<sub>2</sub>O and DMSO:gly:NMPA. As already mentioned in Chapter 8, there are no significant changes in the phase memory time  $T_m$  visible. Analyzing potential changes in the modulation depths  $k$  will not be executed based on the respective 2p-ESEEM data, but later with the recorded 3p-ESEEM data. Table F.2 summarizes the determined phase memory times based on the stretched-exponential fitting routine described in Appendix A.

**Table F.2.:** Summary of the determined phase memory time  $T_m$  for pure Frey's salt and system  $\mathbf{1}^{4+}:\mathbf{3}^{2-}$  (molar ratio 1:3) based on the 2p-ESEEM measurements at 50 K for all tested solvent mixtures

solvent	$T_m(\mathbf{3}^{2-}) / \mu\text{s}$	$T_m(\mathbf{1}^{4+}:\mathbf{3}^{2-}) / \mu\text{s}$
DMSO:gly:H <sub>2</sub> O	1.215	1.295
DMF:gly:H <sub>2</sub> O	0.496	0.503
DMSO:eg:H <sub>2</sub> O	1.323	1.217
DMSO:gly:NMPA	1.177	1.269

To complete the data set for the 3p-ESEEM measurements shown in Chapter 8, we summarized in Fig. F.3 the primary data sets  $V_{3p}(T)$  for pure Frey's salt as well as for system  $\mathbf{1}^{4+}:\mathbf{3}^{2-}$  molar ratio 1:3 in all solvent mixtures.



**Fig. F.3.:** Summary for all recorded 3p-ESEEM time traces  $V_{3p}(T)$  for pure Frey's salt (black curves) and system  $\mathbf{1}^{4+}:\mathbf{3}^{2-}$  molar ratio 1:3 (red curves) with an interpulse delay of  $\tau = 176$  ns.

## Analyzing the incorporation of (partially) deuterated solvent compounds

### DLS data

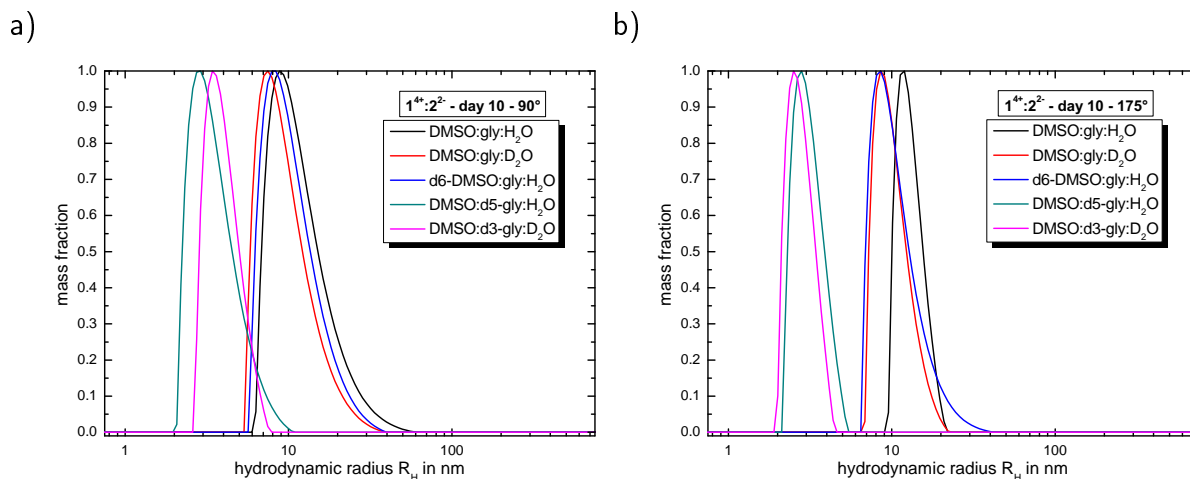


Fig. F.4.: Comparison of particle size distribution functions of system  $1^{4+}:2^{2-}$  molar ratio 1:3 in all tested deuterated solvent mixtures at a) side and b) back scattering.

Fig. F.4 completes the DLS data shown in Chapter 8 with the respective particle size distributions of system  $1^{4+}:2^{2-}$  molar ratio 1:3 in all tested deuterated solvent mixtures. Note that the solvent mixtures DMSO:gly:D<sub>2</sub>O and d6-DMSO:gly:H<sub>2</sub>O form self-assembled entities with similar hydrodynamic radius, which is quite remarkable when comparing the proportion of DMSO (50 vol.%) to water (7 vol.%). The calculated size distributions of solvent mixtures including d5-gly or d3-gly cannot be analyzed with the same certainty due to the weakly pronounced autocorrelation functions.

Table F.3.: Summary of the determined dynamic viscosity  $\eta$  of all applied deuterated solvent mixtures

solvent	$\eta$ / mPas
DMSO:gly:H <sub>2</sub> O	22.64 ± 0.12
DMSO:gly:D <sub>2</sub> O	23.29 ± 0.24
d6-DMSO:gly:H <sub>2</sub> O	23.74 ± 0.24
DMSO:d5-gly:H <sub>2</sub> O	19.58 ± 0.41
DMSO:d3-gly:D <sub>2</sub> O	21.10 ± 0.24

To analyze the recorded DLS data, we determined the dynamic viscosity  $\eta$  of the deuterated



solvent mixtures. Table F.3 summarizes the measured values, which we received similar to the descriptions in Chapter 7.

## CW EPR spectroscopy data

Fig. F.5 contains the remaining CW EPR spectra at X- and Q-band frequencies for pure Frey's salt and system  $\mathbf{1}^{4+}:\mathbf{3}^{2-}$  with molar ratios 1:3 in DMSO:gly:D<sub>2</sub>O and DMSO:d3-gly:D<sub>2</sub>O. Again, we detect a rather drastic difference in the Q-band spectra, where system  $\mathbf{1}^{4+}:\mathbf{3}^{2-}$  shows a pronounced line broadening in the solvent mixture only containing D<sub>2</sub>O, which is missing in the glycer-d3-ol setup.

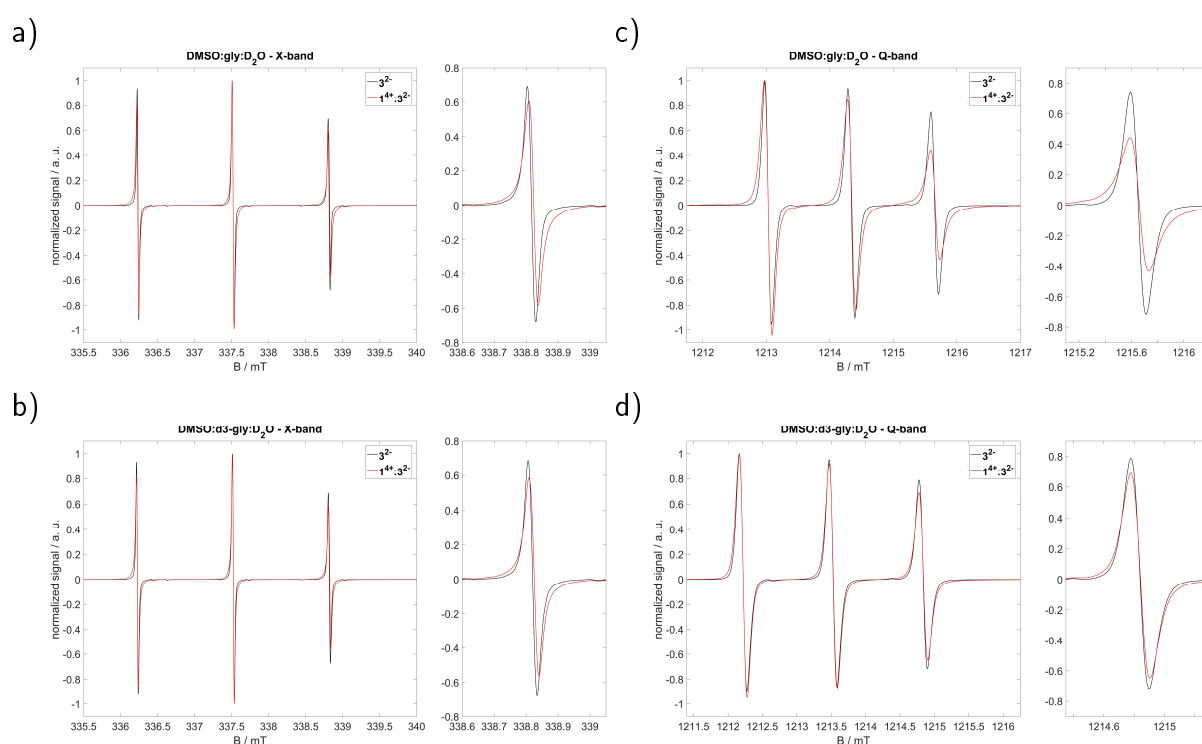


**Fig. F.5.:** a), b) X-band and c), d) Q-band CW EPR spectra of pure Frey's salt and  $\mathbf{1}^{4+}:\mathbf{3}^{2-}$  with molar ratios 1:3 in DMSO:gly:D<sub>2</sub>O (a) and c)) and DMSO:d3-gly:D<sub>2</sub>O (b) and d)). The highfield peak of the spectra is shown separately right next to the full spectra.

Even though we do not discuss the room temperature CW EPR data in detail, Fig. F.6 presents the overlay of measured and simulated spectra. The simulation approach itself was adapted from Chapter 7, where we described the spectra for the  $\mathbf{1}^{4+}:\mathbf{3}^{2-}$  with a fast and a slow rotating component for the nitroxide radical.

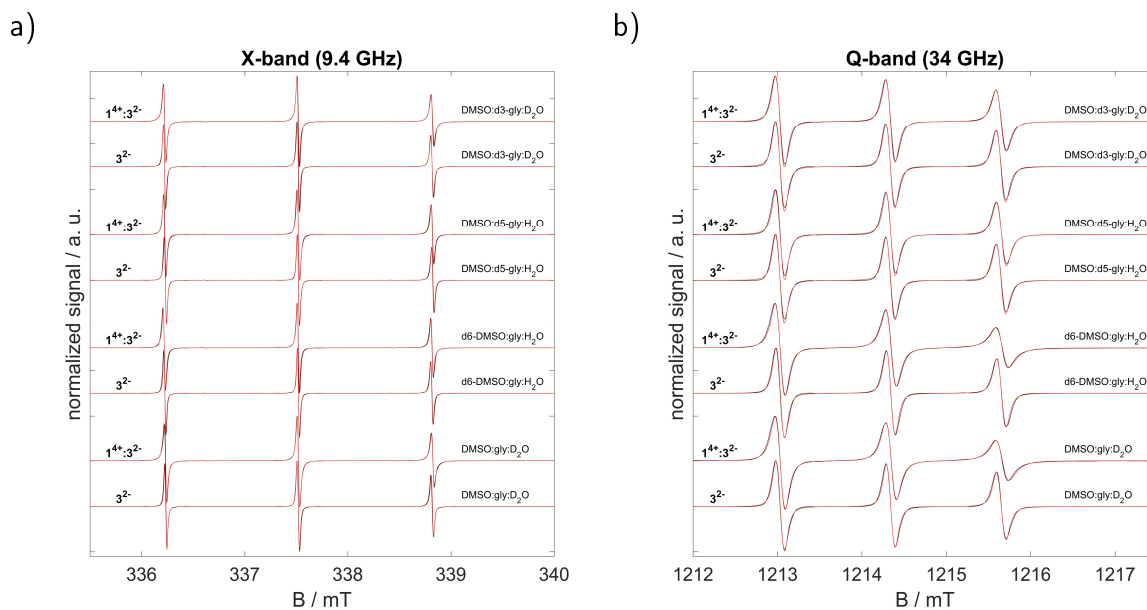


Fig. F.6.: a) X-band and b) Q-band CW EPR spectra for pure Fremy's salt and system  $1^{4+}:3^{2-}$  in all deuterated solvent mixtures. Both graphs show for each measurement the experimental spectrum (black line) as well as the simulated spectrum (red line).

Table F.4 summarizes the simulation results for X-band frequencies.

Table F.4.: Summary of the simulated axial rotational diffusion tensor  $D_{\perp}$  and  $D_{\parallel}$  as well as the calculated rotational correlation time  $\tau_c$ , anisotropy  $T$  and line width (FWHM) of  $3^{2-}$  and system  $1^{4+}:3^{2-}$  at X-band frequencies

ratio	compound		DMSO:gly:D <sub>2</sub> O				
	fast	fraction	$D_{\perp}/s^{-1}$	$D_{\parallel}/s^{-1}$	$\tau_c / ps$	$T$	FWHM/G
0:1	fast	1	1.2e9	5.0e10	40.10	0.931	0.18
1:3	fast	0.51	8.0e8	4.0e10	56.60	0.942	0.20
	slow	0.49	2.0e8	1.5e10	198.0	0.961	0.32
ratio	compound		d6-DMSO:gly:H <sub>2</sub> O				
	fast	fraction	$D_{\perp}/s^{-1}$	$D_{\parallel}/s^{-1}$	$\tau_c / ps$	$T$	FWHM/G
0:1	fast	1	1.3e9	5.0e10	38.00	0.926	0.17
1:3	fast	0.62	1.2e9	4.5e10	41.50	0.924	0.18
	slow	0.38	2.0e8	1.8e10	186.0	0.967	0.30
ratio	compound		DMSO:d5-gly:H <sub>2</sub> O				
	fast	fraction	$D_{\perp}/s^{-1}$	$D_{\parallel}/s^{-1}$	$\tau_c / ps$	$T$	FWHM/G
0:1	fast	1	1.4e9	5.0e10	36.10	0.921	0.19
1:3	fast	0.85	1.0e9	4.0e10	48.70	0.929	0.20
	slow	0.15	2.5e8	1.8e10	160.0	0.960	0.30

ratio	compound		DMSO:d3-gly:D <sub>2</sub> O				
		fraction	$D_{\perp}/s^{-1}$	$D_{\parallel}/s^{-1}$	$\tau_c / ps$	$T$	FWHM/G
0:1	fast	1	1.1e9	5.0e10	42.50	0.937	0.20
1:3	fast	0.56	8.0e8	4.0e10	56.60	0.942	0.20
	slow	0.44	1.8e8	1.5e10	212.0	0.965	0.32

Table F.5 summarizes the simulation results for Q-band frequencies.

**Table F.5.:** Summary of the simulated axial rotational diffusion tensor  $D_{\perp}$  and  $D_{\parallel}$  as well as the calculated rotational correlation time  $\tau_c$ , anisotropy  $T$  and line width (FWHM) of  $3^{2-}$  and system  $1^{4+}:3^{2-}$  at Q-band frequencies

ratio	compound		DMSO:gly:D <sub>2</sub> O				
		fraction	$D_{\perp}/s^{-1}$	$D_{\parallel}/s^{-1}$	$\tau_c / ps$	$T$	FWHM/G
0:1	fast	1	9.5e8	4.0e10	50.40	0.932	1.35
1:3	fast	0.51	2.0e8	3.0e10	157.1	0.980	1.40
	slow	0.49	1.1e8	1.3e10	309.0	0.975	1.65
ratio	compound		d6-DMSO:gly:H <sub>2</sub> O				
		fraction	$D_{\perp}/s^{-1}$	$D_{\parallel}/s^{-1}$	$\tau_c / ps$	$T$	FWHM/G
0:1	fast	1	9.8e8	4.0e10	49.40	0.930	1.32
1:3	fast	0.51	2.0e8	3.0e10	157.1	0.980	1.40
	slow	0.49	1.1e8	1.3e10	309.0	0.975	1.65
ratio	compound		DMSO:d5-gly:H <sub>2</sub> O				
		fraction	$D_{\perp}/s^{-1}$	$D_{\parallel}/s^{-1}$	$\tau_c / ps$	$T$	FWHM/G
0:1	fast	1	1.1e9	4.0e10	45.70	0.922	1.38
1:3	fast	0.79	9.0e8	3.0e10	57.50	0.915	1.40
	slow	0.21	2.0e8	1.8e10	186.0	0.967	1.60
ratio	compound		DMSO:d3-gly:D <sub>2</sub> O				
		fraction	$D_{\perp}/s^{-1}$	$D_{\parallel}/s^{-1}$	$\tau_c / ps$	$T$	FWHM/G
0:1	fast	1	1.2e9	4.0e10	43.20	0.915	1.40
1:3	fast	0.76	8.0e8	3.0e10	62.20	0.924	1.40
	slow	0.24	1.3e8	1.5e10	263.0	0.974	1.55

Fig. F.7 summarizes the CW Q-band low temperature spectra of pure Frey's salt and system  $1^{4+}:3^{2-}$  in all deuterated solvent mixtures. A striking difference compared to the fully protonated solvent is the less pronounced broad peak between  $g$ -values 2.006 and 2.002. It seems that shock freezing the partially deuterated solvent mixtures and analyzing a respective 'snapshot' of the samples prevent the observation of the strong dipolar coupling between cationic and anionic component.

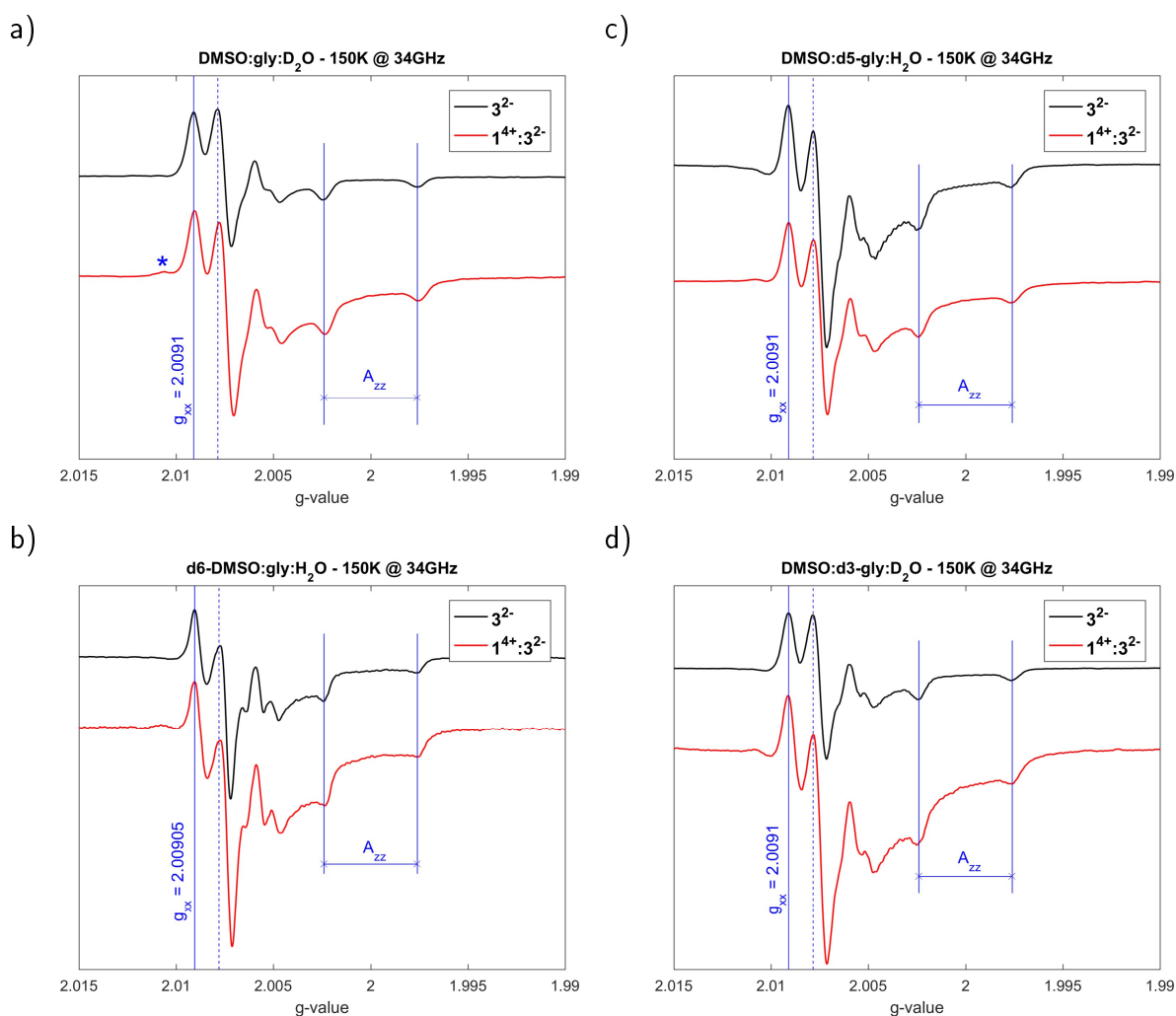


Fig. F.7.: Q-band CW EPR spectra at 150K of  $1^{4+}:3^{2-}$  with molar ratio 0:1 and 1:3 for a) DMSO:gly:D<sub>2</sub>O, b) d6-DMSO:gly:H<sub>2</sub>O, c) DMSO:d5-gly:H<sub>2</sub>O and d) a) DMSO:d3-gly:D<sub>2</sub>O.

## Pulsed EPR spectroscopy data

Similar to the solvent mixture that selectively substitute the solvent compounds DMSO, glycerol and water, we started by recording the echo-detected field sweep spectra for all tested deuterated solvent mixtures (see Fig. F.8).

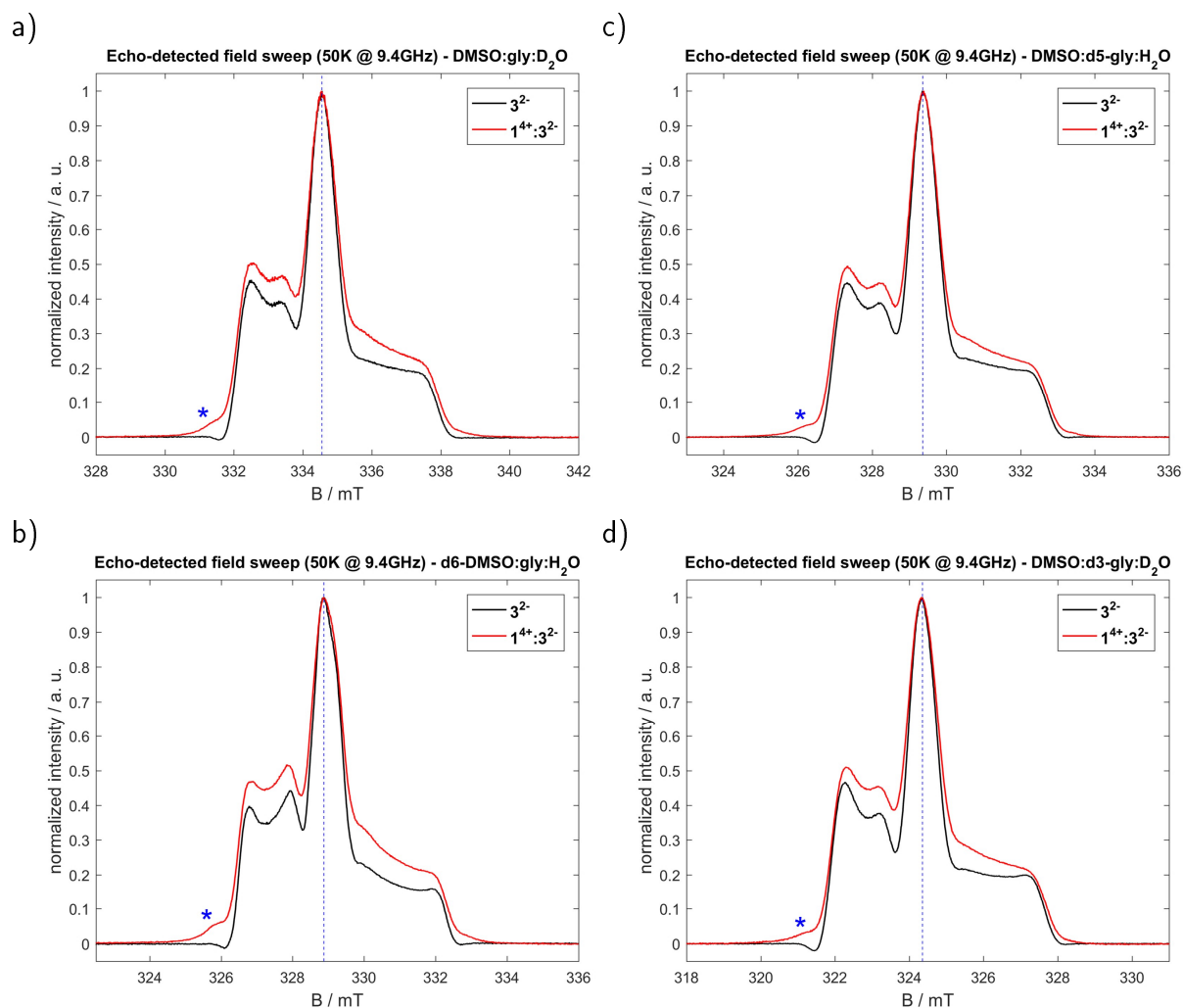


Fig. F.8.: Echo-detected field sweep spectra measured at 50 K for a) DMSO:gly:D<sub>2</sub>O, b) d<sub>6</sub>-DMSO:gly:H<sub>2</sub>O, c) DMSO:d<sub>5</sub>-gly:H<sub>2</sub>O and d) DMSO:d<sub>3</sub>-gly:D<sub>2</sub>O.

The Fremy's salt spectrum in d<sub>6</sub>-DMSO:gly:H<sub>2</sub>O presents a different shape compared to the other samples. Feasible explanations are a better resolution of hyperfine splittings due to a reduced line width (50 vol% of the solvent is deuterated) or an additional coupling between the deuterium nuclei and the unpaired electron from  $3^{2-}$ . Note that adding the 'Texas-sized molecular box' does not disrupt this special feature.

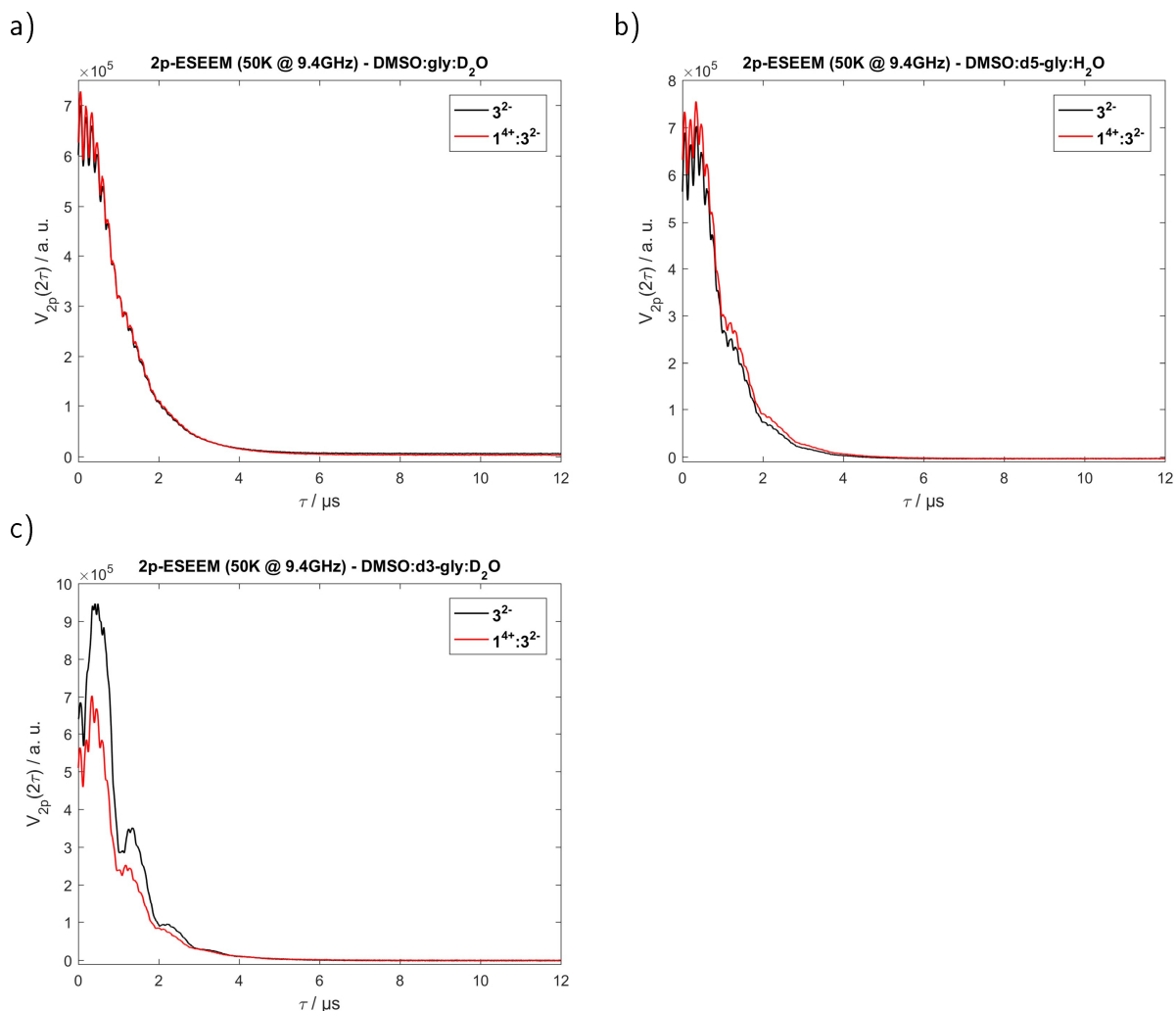


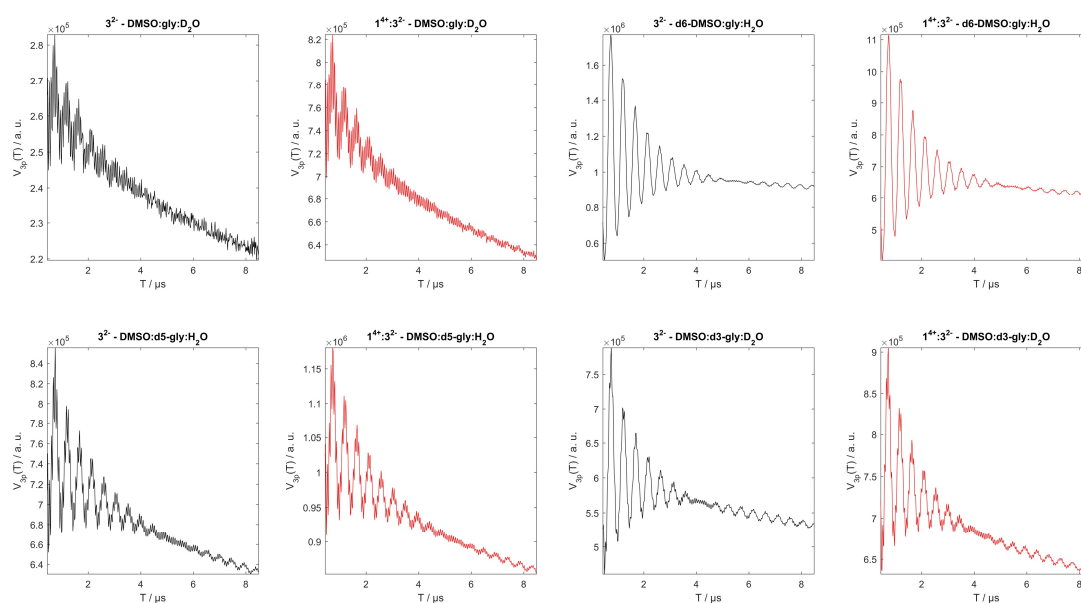
Fig. F.9.: Primary 2p-ESEEM data  $V_{2p}(2\tau)$  at 50 K for solvent mixtures a) DMSO:gly:D<sub>2</sub>O, b) DMSO:d5-gly:H<sub>2</sub>O and c) DMSO:d3-gly:D<sub>2</sub>O.

Fig. F.9 presents the primary 2p-ESEEM data from pure Frey's salt as well as from system  $1^{4+}:3^{2-}$  (molar ratio 1:3) in DMSO:gly:D<sub>2</sub>O, DMSO:d5-gly:H<sub>2</sub>O and DMSO:d3-gly:D<sub>2</sub>O. As already mentioned in Chapter 8, there are no significant changes visible in the phase memory time. Analyzing potential changes in the modulation depths  $k$  will not be executed based on the respective 2p-ESEEM data, but later with the recorded 3p-ESEEM data. Table F.6 summarizes the determined phase memory times based on the stretched-exponential fitting routine described in Appendix A.

**Table F.6.:** Summary of the determined phase memory time  $T_m$  for pure Frey's salt and system  $\mathbf{1}^{4+}:\mathbf{3}^{2-}$  (molar ratio 1:3) based on the 2p-ESEEM measurements at 50 K for all tested solvent mixtures

solvent	$T_m(\mathbf{3}^{2-}) / \mu\text{s}$	$T_m(\mathbf{1}^{4+}:\mathbf{3}^{2-}) / \mu\text{s}$
DMSO:gly:D <sub>2</sub> O	1.277	1.261
d6-DMSO:gly:H <sub>2</sub> O	4.617	4.574
DMSO:d5-gly:H <sub>2</sub> O	1.232	1.260
DMSO:g3-gly:D <sub>2</sub> O	1.369	1.290

To complete the data set for the 3p-ESEEM measurements shown in Chapter 8, one summarized in Fig. F.10 the primary data sets  $V_{3p}(T)$  for pure Frey's salt as well as system  $\mathbf{1}^{4+}:\mathbf{3}^{2-}$  molar ratio 1:3 in all deuterated solvent mixtures.



**Fig. F.10.:** Summary for all recorded 3p-ESEEM time traces  $V_{3p}(T)$  for pure Frey's salt (black curves) and system  $\mathbf{1}^{4+}:\mathbf{3}^{2-}$  molar ratio 1:3 (red curves) with an interpulse delay of  $\tau = 176$  ns.

# G | Appendix - Chapter 9

## Induced Ionoid Formation

For analyzing the count rate traces from DLS measurements at different temperatures and after performing cmPALS measurements, we prepared a reference sample using polystyrene nanospheres to correlate the filter settings of the laser with the mean intensity values, as shown in Fig. G.1.

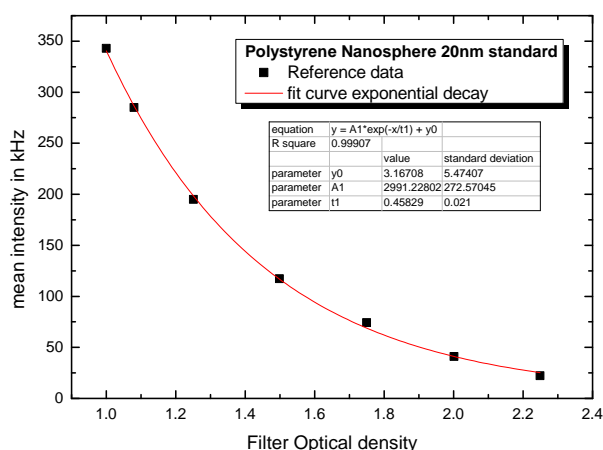


Fig. G.1.: Mean scattering intensity of polystyrene nanospheres (20 nm) in DMSO:gly:H<sub>2</sub>O 50:43:7 (v/v/v) depending on the attenuation of the laser stated as optical density.

## Thermally-induced Ionoid Formation

We executed a specific reference measurement for the discussed CW EPR measurements at X-band frequencies. We studied time dependent changes of the signal intensity of Fremy's salt at 20 °C, 40 °C and 60 °C to determine the stability of the nitroxide radical, as shown in Fig. G.2 a). The signal intensity itself is based on the calculated double integral of the recorded CW EPR spectra, whereas the value at measuring time  $t = 0$  min was used as internal reference. Furthermore, we tested the influence of added multicationic box  $1^{4+}$  to Fremy's salt regarding the stability of  $3^{2-}$  at 20 °C (see Fig. G.2 b)). Here, the promoted decomposition



of the nitroxide radical is based on more impacts between the Fremy's salt dianions due to the electrostatic interactions between both ionic building units.

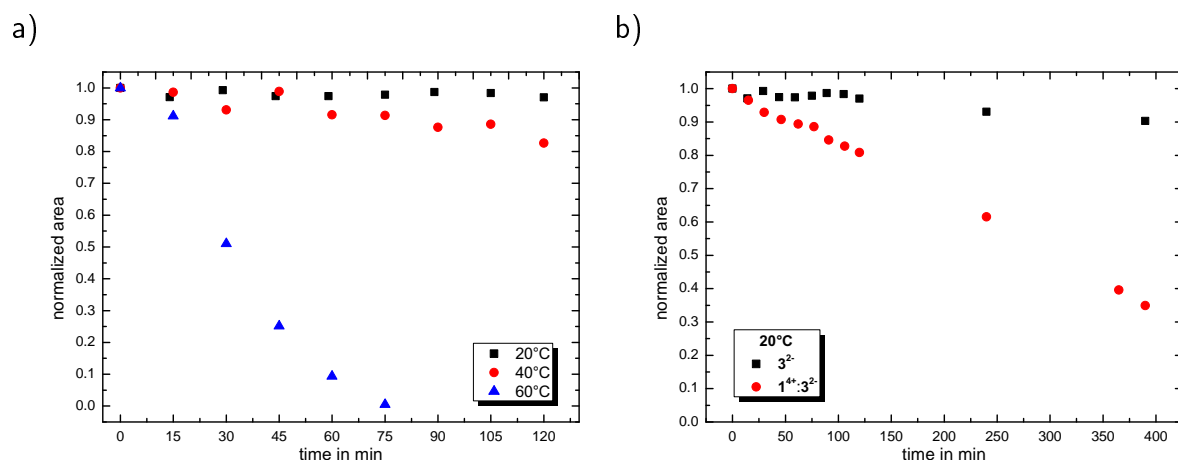


Fig. G.2.: a) Stability of Fremy's salt 3mM in established solvent mixture for 20 °C, 40 °C and 60 °C. b) Comparison of signal intensity (shown as normalized area) of system  $1^{4+}:3^{2-}$  molar ratio 1:3 and pure  $3^{2-}$  over time.

As already mentioned in Chapter 9, we summarized the simulation results for the CW EPR measurements with Fremy's salt and system  $1^{4+}:3^{2-}$  while performing a temperature ramp in the range of 20 °C to 60 °C. Table G.1 contains the simulation results for the respective system.

Table G.1.: Summary of the simulated parameters for Fremy's salt in the established solvent mixture: isotropic hyperfine splitting  $a_{iso}$ , axial rotational diffusion tensor  $D_{\perp}$  and  $D_{\parallel}$ , line width as FWHM value, rotational correlation time  $\tau_c$  and anisotropy  $T$

$T / ^{\circ}\text{C}$	$a_{iso} / \text{G}$	$D_{\perp} / \text{s}^{-1}$	$D_{\parallel} / \text{s}^{-1}$	$\tau_c / \text{ps}$	$T$	lw / G
20	12.92	6.5e8	4.5e10	62.4	0.958	0.22
25	12.94	8.5e8	5.0e10	50.4	0.951	0.21
30	12.95	1.1e9	5.5e10	41.1	0.942	0.21
35	12.96	1.5e9	5.5e10	33.4	0.922	0.22
40	12.98	1.9e9	5.5e10	28.6	0.903	0.22
45	13.00	2.2e9	6.0e10	25.2	0.898	0.22
50	13.01	2.5e9	6.0e10	23.1	0.885	0.22
55	13.02	2.8e9	6.5e10	20.9	0.881	0.21
60	13.05	3.2e9	7.0e10	18.6	0.874	0.21
20	12.92	6.3e8	4.5e10	63.8	0.959	0.20

The solid reduce in the anisotropy  $T$ -value reflects the more isotropic rotational mobility of Fremy's salt with increasing temperature.

Fig. G.3 presents the simulated and measured CW EPR spectra for pure Frey's salt and after adding the multicationic box. Note that for the system  $1^{4+}:3^{2-}$  molar ratio 1:3 we could not record CW EPR spectra at 60 °C and after cooling the sample down to 20 °C (see Chapter 9 for further information).

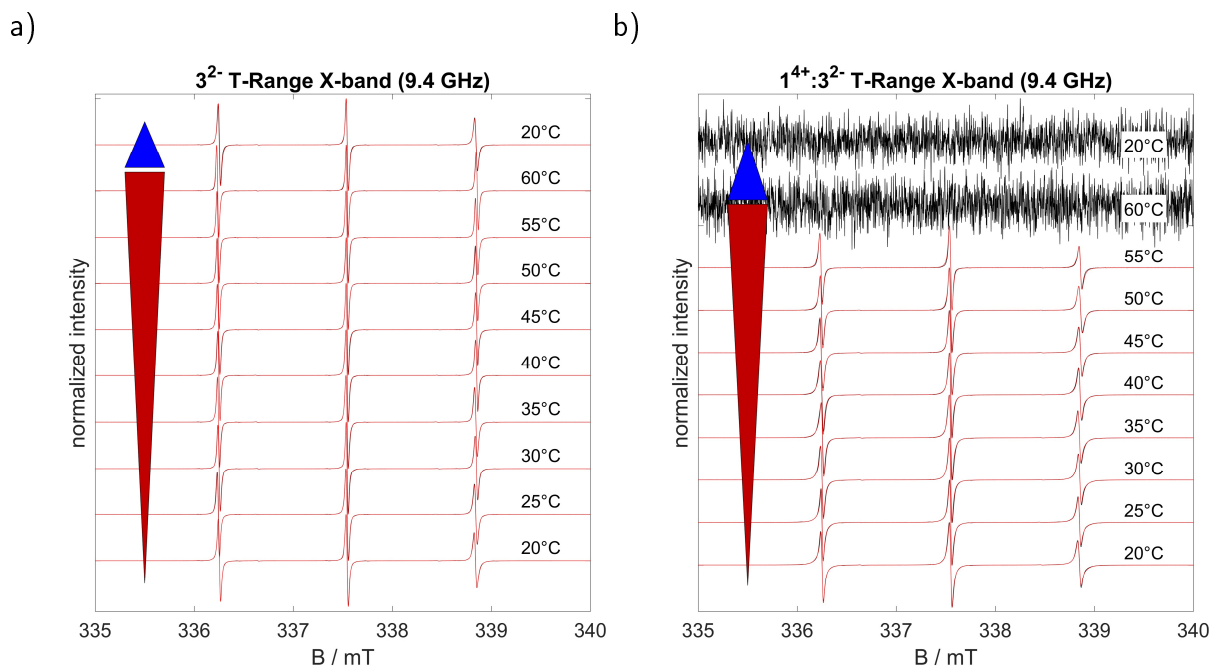


Fig. G.3.: X-band spectra of temperature ramp with a) Frey's salt 3 mM and b)  $1^{4+}:3^{2-}$  in DMSO:gly:H<sub>2</sub>O 50:43:7 (v/v/v). For each temperature the measured (black lines) and simulated (red lines) are overlaid.

Table G.2 summarizes the simulation results for the system  $1^{4+}:3^{2-}$  in the established solvent mixture.

**Table G.2.:** Summary of the simulated parameters for system  $\mathbf{1}^{4+}:\mathbf{3}^{2-}$  in the established solvent mixture: isotropic hyperfine splitting  $a_{iso}$ , axial rotational diffusion tensor  $D_{\perp}$  and  $D_{\parallel}$ , line width as FWHM value, rotational correlation time  $\tau_c$  and anisotropy  $T$

$T / ^{\circ}\text{C}$	compound	fraction	$a_{iso} / \text{G}$	$D_{\perp} / \text{s}^{-1}$	$D_{\parallel} / \text{s}^{-1}$	$\tau_c / \text{ps}$	$T$	lw / G
20	fast	0.38	12.92	6.0e8	4.0e10	68.5	0.956	0.22
	slow	0.62	13.01	1.3e8	1.5e10	263.0	0.974	0.48
25	fast	0.43	12.94	6.5e8	4.0e10	64.9	0.953	0.23
	slow	0.57	13.02	1.3e8	1.5e10	263.0	0.974	0.47
30	fast	0.45	12.95	7.0e8	4.5e10	59.4	0.955	0.24
	slow	0.55	13.02	1.3e8	1.5e10	263.0	0.974	0.47
35	fast	0.47	12.98	7.2e8	4.5e10	58.3	0.953	0.25
	slow	0.53	13.05	1.3e8	1.5e10	263.0	0.974	0.47
40	fast	0.50	13.00	7.3e8	4.5e10	57.8	0.953	0.25
	slow	0.50	13.09	1.3e8	1.5e10	263.0	0.974	0.45
45	fast	0.56	13.02	7.0e8	4.5e10	59.4	0.955	0.25
	slow	0.54	13.09	1.3e8	1.5e10	263.0	0.974	0.40
50	fast	0.62	13.04	6.0e8	4.5e10	65.9	0.961	0.22
	slow	0.38	13.11	1.5e8	2.0e10	217.0	0.978	0.35
55	fast	0.80	13.06	5.0e8	4.0e10	77.4	0.963	0.22
	slow	0.20	13.11	2.0e8	2.0e10	180.0	0.971	0.26

## Electrophoretic-induced Ionoid Formation

As already described in Chapter 9, we performed DLS measurements after using the cmPALS technique with different electric field strengths to induce the formation of globular ionoids in system  $\mathbf{1}^{4+}:\mathbf{2}^{2-}$  with molar ratio 1:3. Fig. G.4 displays the recorded intensity time correlation functions for side and back scattering. All applied voltage values result in strongly pronounced autocorrelation functions, which indicates the formation of at least partially ordered nanostructures in solution. A more refined analyzes based on these graphs alone is difficult due to the similar decay at both scattering angles.

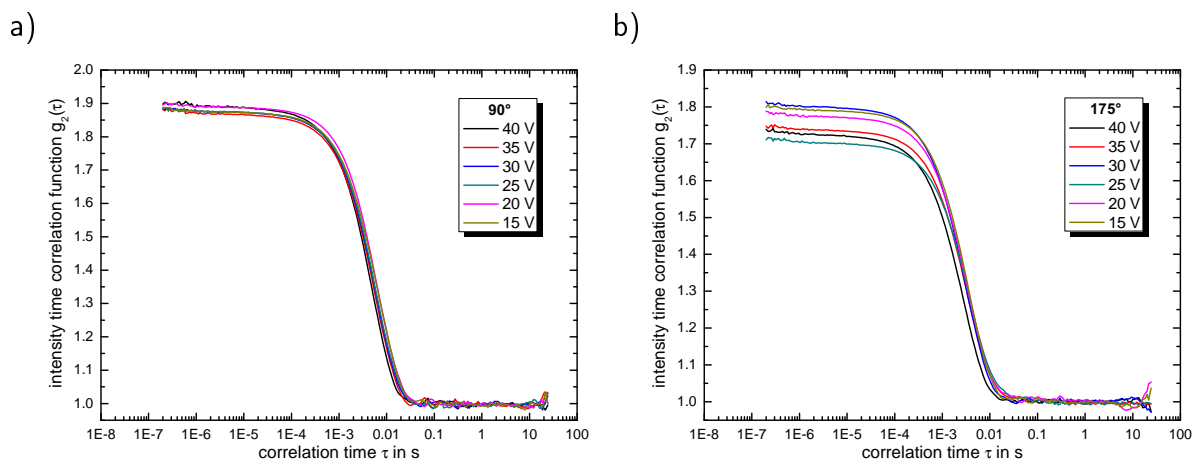


Fig. G.4.: Comparison of the intensity time correlation functions after cmPALS measurements with various voltage values at a) side and b) back scattering for system  $\mathbf{1}^{4+}:\mathbf{2}^{2-}$  with molar ratio 1:3.

Fig. G.5 contains the intensity time correlation functions at both scattering angles over the course of two weeks for system  $\mathbf{1}^{4+}:\mathbf{2}^{2-}$  with molar ratio 1:3 after a cmPALS treatment with 30 V. The shift to larger correlation times as well as the reduced y-intercept value indicate the transition from initially promising self-assembled entities to larger, rather undefined aggregates.

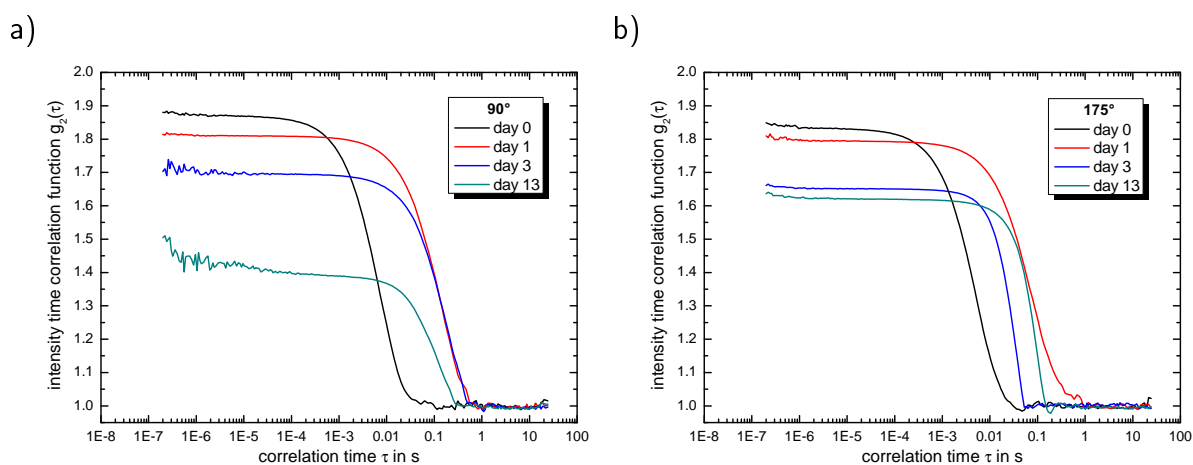


Fig. G.5.: Development of the intensity time correlation functions after cmPALS measurements with 30 V at a) side and b) back scattering for system  $\mathbf{1}^{4+}:\mathbf{2}^{2-}$  with molar ratio 1:3.

Fig. G.6 contains the reference measurement of pure Frey's salt 3 mM after cmPALS treatment with 40 V. Both X- and Q-band spectra do not present drastical changes of the rotational mobility for the nitroxide radical.

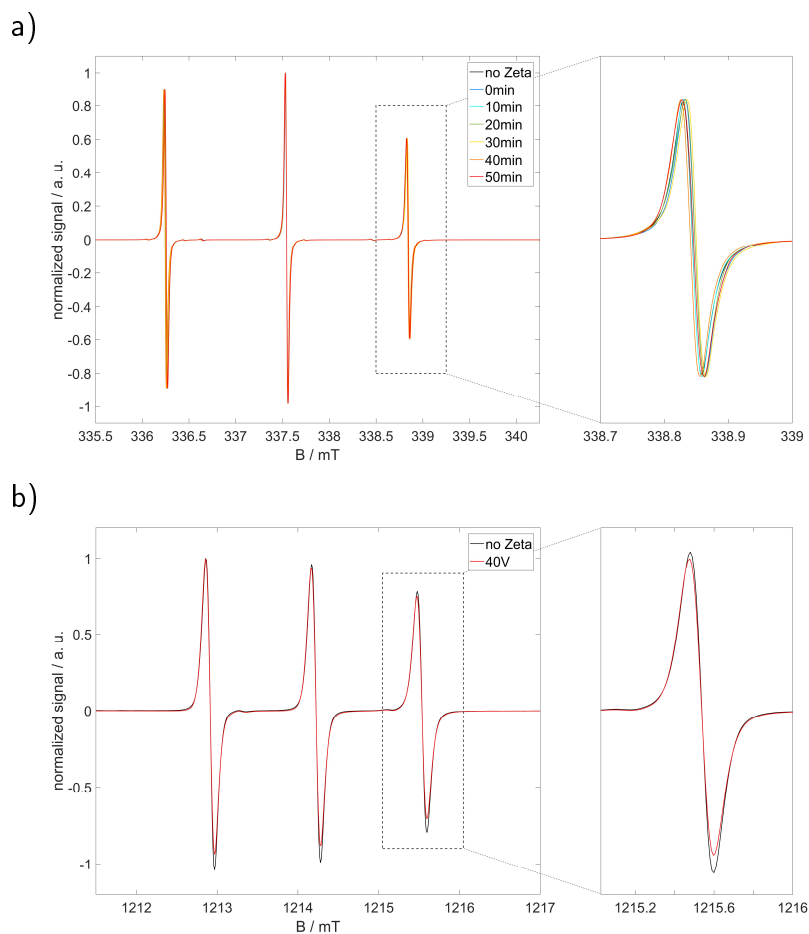


Fig. G.6.: Comparison of a) X-band and b) Q-band CW EPR spectra of pure Fremy's salt with and without cmPALS treatment (see text for further information).

We analyzed the systems  $\mathbf{1}^{4+}:\mathbf{3}^{2-}$  molar ratio 1:3, which were treated with the cmPALS technique at different voltage values, over a course of 50 min at X-band frequencies to estimate changes in the decomposition behavior of the nitroxide radical. Similar to the stability tests for the thermally-induced ionoid formation, we plotted the normalized double integral values of the CW EPR spectra against the measuring time, as shown in Fig. G.7. The alternating electric field induced more collisions between Fremy's salt dianions, which accelerate the decrease in signal intensity.

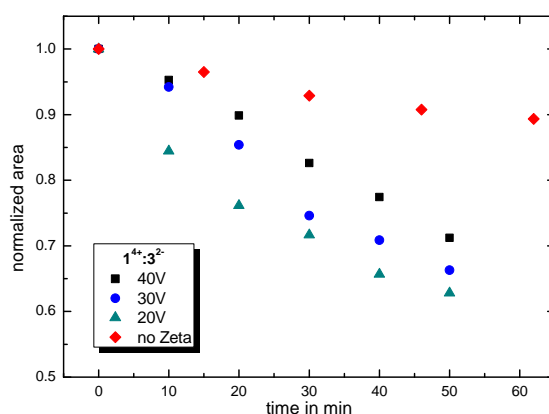


Fig. G.7.: Stability of system  $1^{4+}:3^{2-}$  molar ratio 1:3 with and without cmPALS treatment shown as normalized area values.

To complete the data set for the CW EPR tests with system  $1^{4+}:3^{2-}$  after exposing them in an alternating electric field, Fig. G.8 summarizes the simulated CW EPR spectra for both frequencies.

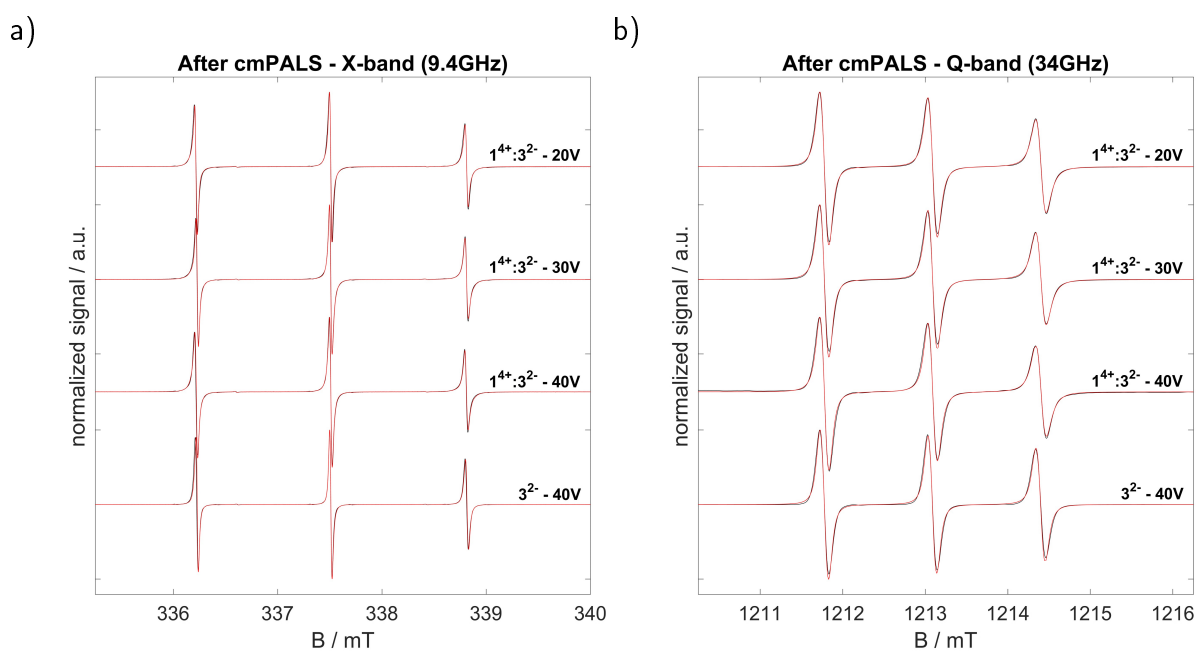


Fig. G.8.: a) X-band and b) Q-band CW EPR spectra of pure Frey's salt and system  $1^{4+}:3^{2-}$  after cmPALS treatment with different electric field strengths. For each sample the measured (black lines) and simulated (red lines) are overlaid.

The respective simulation results are summarized in Table G.3.

**Table G.3.:** Summary of the simulated axial rotational diffusion tensor  $D_{\perp}$  and  $D_{\parallel}$  as well as the calculated rotational correlation time  $\tau_c$  and anisotropy  $T$  of Fremy's salt 3 mM and system  $\mathbf{1}^{4+}:\mathbf{3}^{2-}$  after cmPALS measurements

	compound		X-band			
		fraction	$D_{\perp}/s^{-1}$	$D_{\parallel}/s^{-1}$	$\tau_c / \text{ps}$	$T$
$\mathbf{3}^{2-}$	-	-	6.8e8	4.5e10	62.40	0.958
$\mathbf{1}^{4+}:\mathbf{3}^{2-}$	fast	0.55	5.5e8	4.0e10	72.60	0.960
	40 V slow	0.45	1.2e8	1.5e10	278.0	0.976
$\mathbf{1}^{4+}:\mathbf{3}^{2-}$	fast	0.55	5.8e8	4.0e10	70.10	0.958
	30 V slow	0.45	1.2e8	1.5e10	278.0	0.976
$\mathbf{1}^{4+}:\mathbf{3}^{2-}$	fast	0.59	6.0e8	4.0e10	68.50	0.956
	20 V slow	0.41	1.2e8	1.5e10	278.0	0.976
	compound		Q-band			
		fraction	$D_{\perp}/s^{-1}$	$D_{\parallel}/s^{-1}$	$\tau_c / \text{ps}$	$T$
$\mathbf{3}^{2-}$	-	-	9.0e8	4.5e10	50.30	0.942
$\mathbf{1}^{4+}:\mathbf{3}^{2-}$	fast	0.58	4.5e8	4.0e10	83.00	0.967
	40 V slow	0.42	1.5e8	1.9e10	221.0	0.977
$\mathbf{1}^{4+}:\mathbf{3}^{2-}$	fast	0.60	5.0e8	4.0e10	77.40	0.963
	30 V slow	0.40	1.5e8	1.9e10	221.0	0.977
$\mathbf{1}^{4+}:\mathbf{3}^{2-}$	fast	0.61	5.0e8	4.0e10	77.40	0.963
	20 V slow	0.39	1.5e8	1.9e10	221.0	0.977

## Thermal stability of globular ionoids

Fig. G.9 shows the development of the intensity time correlation functions at both scattering angles for system  $\mathbf{1}^{4+}:\mathbf{2}^{2-}$  exposed to a temperature ramp between 20 °C and 60 °C after the ten-day incubation period. Till a temperature of 40 °C we could record autocorrelation functions with a similar y-intercept value, but a slight shift to smaller correlation times  $\tau$ . The latter point corresponds with the decreased dynamic viscosity  $\eta$  of the solvent mixture DMSO:gly:H<sub>2</sub>O 50:43:7 (v/v/v). At higher temperatures, the shift to smaller  $\tau$  values continues, but additionally the before pronounced autocorrelation functions break down till the y-intercept value reaches a minimum of roughly 1.3. The loss in intensity correlation coheres with the decomposition of the globular ionoids.

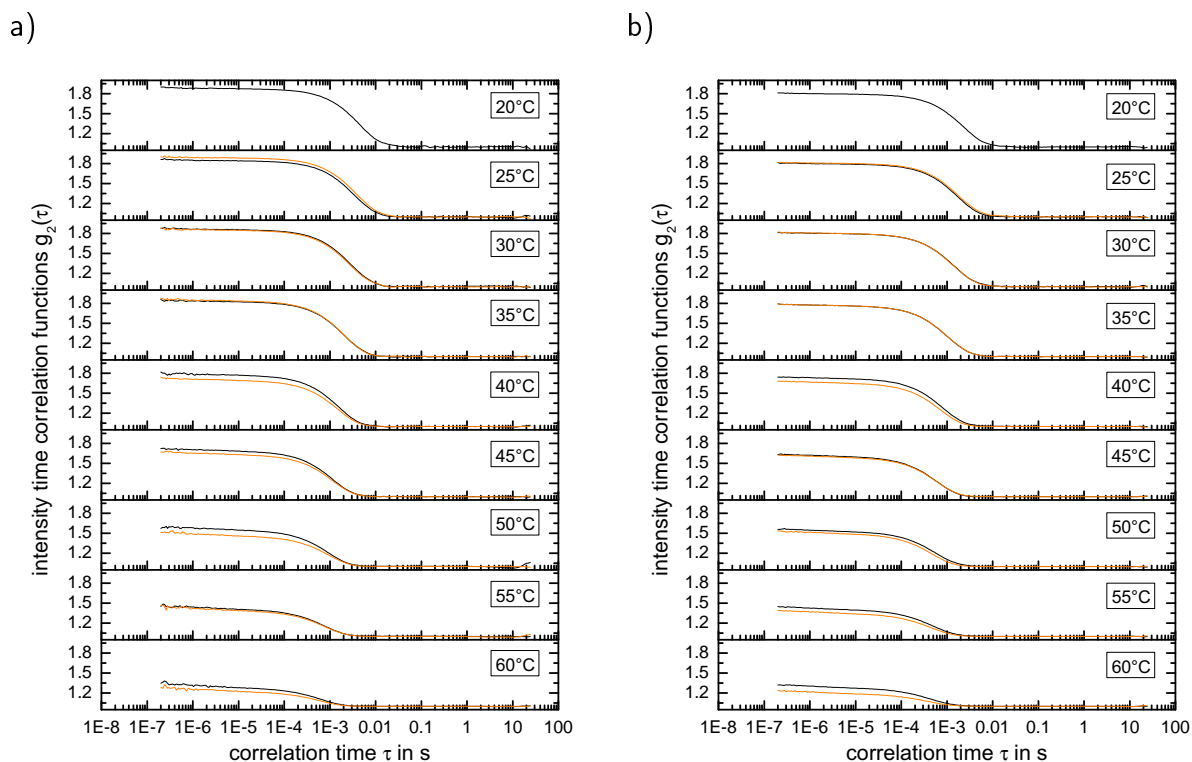


Fig. G.9.: Development of the intensity time correlation functions at a) side and b) back scattering for the model system  $1^{4+};2^{2-}$ . The black lines present the DLS data directly after reaching the desired temperature, whereas the orange lines are recorded after a waiting period of 30 min.

## Analyze globular ionoids with EPR spectroscopy

Fig. G.10 shows the development of the hydrodynamic radius for the 'incomplete' system  $1^{4+};2^{2-}$  after adding Fremy's salt or methanedisulfonate to gain a molar ratio between cationic and anionic building unit of 1:3 (for further descriptions see Chapter 9).



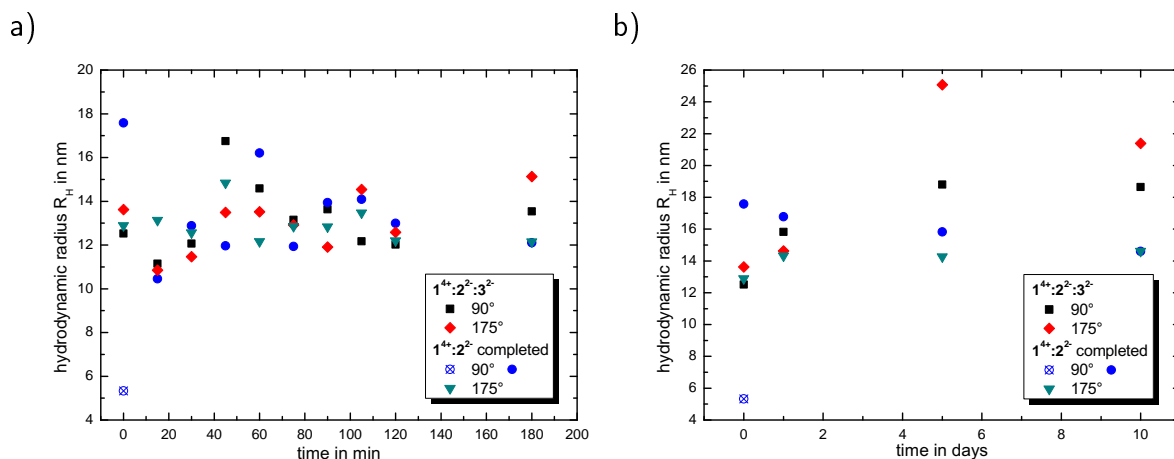


Fig. G.10.: Development of the hydrodynamic radius for systems  $1^{4+}:2^{2-}:3^{2-}$  as well as for  $1^{4+}:2^{2-}$  completed at both scattering angles. a) Focus on the first three hours after inserting the anions, b) Observation over the course of ten days.

X-band CW EPR measurements start with analyzing the development of the signal intensity (see Fig. G.11) for system  $1^{4+}:2^{2-}:3^{2-}$ , where Fremy's salt was added directly after preparing the 'incomplete' setup of 'Texas-sized molecular box' and methanedisulfonate ('day 0') as well as after the ten-day incubation period ('day 10').

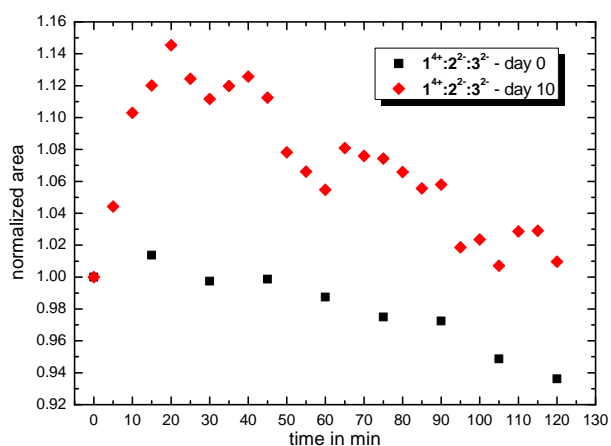


Fig. G.11.: Comparison of signal intensity (shown as normalized area) of  $1^{4+}:2^{2-}:3^{2-}$  systems over the first two hours.

For the highlighted X-band spectra in Chapter 9, Fig. G.12 presents the respective simulated spectra, whereas Table G.4 summarizes the associated results.

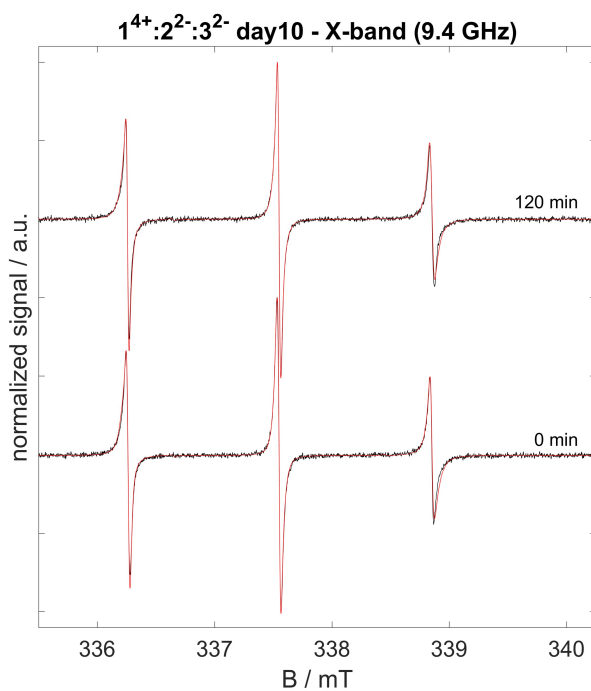


Fig. G.12.: X-band spectra of system  $1^{4+}:2^{2-}:3^{2-}$  'day 10' at the start (0 min) and end (120 min) of the initial two hours observation. For each time step the measured (black lines) and simulated (red lines) are overlaid.

Table G.4.: Summary of simulated parameters for setup  $1^{4+}:2^{2-}:3^{2-}$  'day 10' at X-band frequencies: isotropic hyperfine splitting  $a_{iso}$ , axial rotational diffusion tensor  $D_{\perp}$  and  $D_{\parallel}$ , line width as FWHM value, rotational correlation time  $\tau_c$  and anisotropy  $T$

time/ min	compound	fraction	$a_{iso}/\text{G}$	$D_{\perp}/\text{s}^{-1}$	$D_{\parallel}/\text{s}^{-1}$	$\tau_c/\text{ps}$	$T$	lw/ G
0	fast	0.41	12.92	4.0e8	4.0e10	89.80	0.971	0.215
	slow	0.59	13.04	1.3e8	1.5e10	263.0	0.973	0.39
120	fast	0.41	12.87	3.7e8	4.0e10	94.60	0.973	0.215
	slow	0.59	13.01	1.3e8	1.5e10	263.0	0.974	0.39

In addition to the discussing of the Q-band spectra in Chapter 9, Fig. G.13 presents the simulated spectra for the initial two hours after adding Fremy's salt to the 'incomplete' system of  $1^{4+}:2^{2-}$  after the ten-day incubation period. As internal reference, we have added the simulation result for the 'day 0' setup.

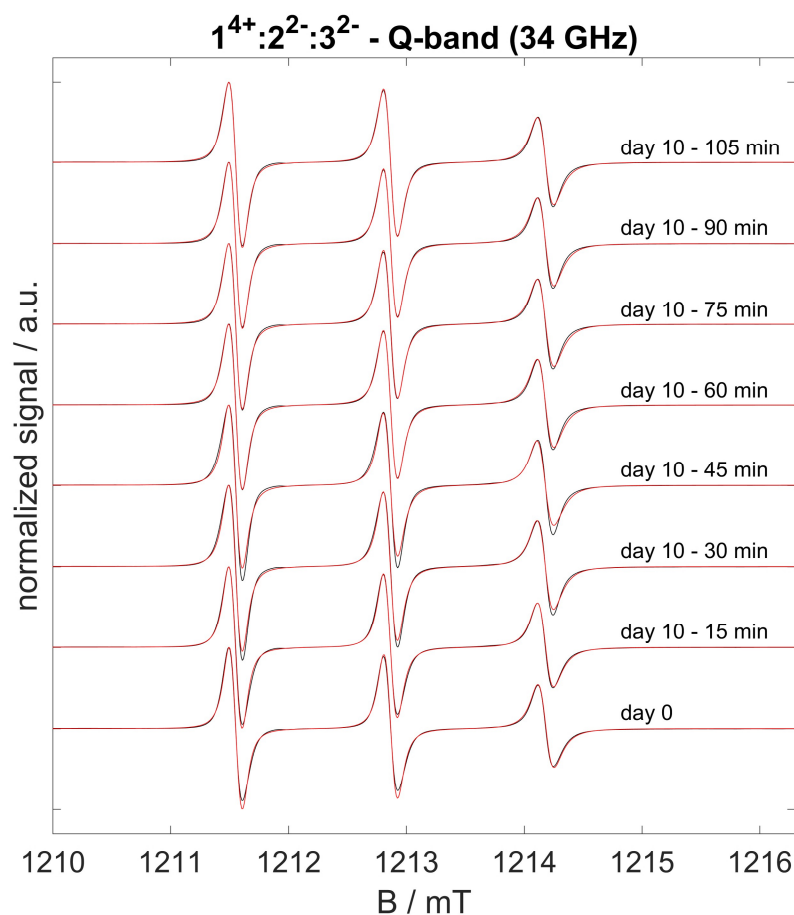


Fig. G.13.: CW Q-band spectra of system  $1^{4+}:2^{2-}:3^{2-}$  'day 10' throughout the initial two hours observation. For each time step the measured (black lines) and simulated (red lines) are overlaid.

The summarized simulation results can be found in Table G.5.

Table G.5.: Summary of the simulated axial rotational diffusion tensor  $D_{\perp}$  and  $D_{\parallel}$  as well as the calculated rotational correlation time  $\tau_c$  and anisotropy  $T$  of system  $1^{4+}:2^{2-}:3^{2-}$  'day 10' at Q-band frequencies

time	compound		Q-band			
	fast	fraction	$D_{\perp}/s^{-1}$	$D_{\parallel}/s^{-1}$	$\tau_c / ps$	$T$
day 0	fast	0.39	4.0e8	3.0e10	98.80	0.961
	slow	0.61	1.2e8	1.5e10	277.8	0.976

---

15 min	fast	0.40	4.4e8	3.0e10	92.70	0.957
	slow	0.60	1.2e8	1.5e10	278.0	0.976
30 min	fast	0.39	4.5e8	3.0e10	91.30	0.956
	slow	0.61	1.2e8	1.5e10	278.0	0.976
45 min	fast	0.38	4.6e8	3.0e10	90.00	0.955
	slow	0.62	1.2e8	1.5e10	278.0	0.976
60 min	fast	0.38	4.5e8	3.0e10	91.30	0.956
	slow	0.62	1.2e8	1.5e10	278.0	0.976
75 min	fast	0.39	4.3e8	3.0e10	94.20	0.958
	slow	0.61	1.2e8	1.5e10	278.0	0.976
90 min	fast	0.39	4.3e8	3.0e10	94.20	0.958
	slow	0.61	1.2e8	1.5e10	278.0	0.976
105 min	fast	0.40	4.4e8	3.0e10	92.70	0.957
	slow	0.60	1.2e8	1.5e10	278.0	0.976

---

# References

- [1] P.-G. de Gennes, *Noble Lecture*, 1991, 8–14.
- [2] *Soft-Matter Characterization*, ed. R. Borsali and R. Pecora, Springer Netherlands, 2008.
- [3] K. J. M. Bishop, C. E. Wilmer, S. Soh and B. A. Grzybowski, *Small*, 2009, **14**, 1600–1630.
- [4] *Nanoscale Assembly - Chemical Techniques*, ed. W. T. S. Huck, Springer Science+Business Media, Inc., 2005.
- [5] I. W. Hamley and V. Castelletto, *Angew. Chem. Int. Ed.*, 2007, **46**, 4442–4455.
- [6] I. W. Hamley, *Introduction to Soft Matter - Synthetic and Biological Self-Assembling Materials*, John Wiley and Sons, Ltd, 2007.
- [7] J.-M. Lehn, *Noble Lecture*, 1987, 444–491.
- [8] J.-M. Lehn, *Science*, 2002, **295**, 2400–2403.
- [9] J.-M. Lehn, *PNAS*, 2002, **8**, 4763–4768.
- [10] J. F. Stoddart, *Angew. Chem. Int. Ed.*, 2017, **56**, 11094–1125.
- [11] P. T. Corbett, J. Leclaire, L. Vial, K. R. West, J.-L. Wietor, J. K. M. Sanders and S. Otto, *Chem. Rev.*, 2006, **106**, 3652–3711.
- [12] M. Mondal and A. K. H. Hirsch, *Chem. Soc. Rev.*, 2015, **44**, 2455–2488.
- [13] C. F. J. Faul and M. Antonietti, *Adv. Mater.*, 2003, **15**, 673–683.
- [14] D. Kurzbach, D. R. Kattnig, N. Pfaffenberger, W. Schärftl and D. Hinderberger, *ChemistryOpen*, 2012, **1**, 211–214.
- [15] H.-Y. Gong, B. M. Rambo, V. M. Lynch, K. Kelly and J. L. Sessler, *J. Am. Chem. Soc.*, 2013, **135**, 6330–6337.
- [16] H.-Y. Gong, B. M. Rambo, E. Karnas, V. M. Lynch, K. M. Keller and J. L. Sessler, *J. Am. Chem. Soc.*, 2011, **133**, 1526–1533.

- [17] B. M. Rambo, H.-Y. Gong, M. Oh and J. L. Sessler, *Accounts of Chemical Research*, 2012, **45**, 1390–1401.
- [18] R. Kimmich, *Principles of Soft-Matter Dynamics - Basic Theories, Non-invasive Methods, Mesoscopic Aspects*, Springer, 2012.
- [19] J. N. Israelachvili, *Intermolecular and Surface Forces*, Elsevier, 2011.
- [20] D. A. Walker, B. Kowalczyk, M. O. de la Cruz and B. A. Grzybowski, *Nanoscale*, 2011, **3**, 1316–1344.
- [21] G. M. Whitesides and M. Boncheva, *PNAS*, 2002, **99**, 4769–4774.
- [22] B. Rybtchinski, *ACS Nano*, 2011, **5**, 6791–6818.
- [23] R. Mezzenga and P. Fischer, *Rep. Prog. Phys.*, 2013, **76**, 1–43.
- [24] L. Verlet, *Physical Review*, 1967, **159**, 98–103.
- [25] W. Demtröder, *Experimentalphysik 2 - Elektrizität und Optik*, Springer Spektrum, 2013.
- [26] J. C. Slater and J. G. Kirkwood, *Physical Review*, 1931, **37**, 682–697.
- [27] C. J. van Oss, M. K. Chaudhury and R. J. Good, *Chem. Rev.*, 1988, **88**, 927–941.
- [28] R. J. Sadus, *Molecular Physics*, 1996, **87**, 979–990.
- [29] J. P. Wagner and P. R. Schreiner, *Angew. Chem. Int. Ed.*, 2015, **54**, 12274–12296.
- [30] J. M. MacLeod and F. Rosei, in *Comprehensive Nanoscience and Technology*, ed. D. L. Andrews, G. D. Scholes and G. P. Wiederrecht, Elsevier, 2011, ch. Volume 3: Nanostructured Surfaces, pp. 13–68.
- [31] Z. S. Derewenda, L. Lee and U. Derewenda, *J. Mol. Biol.*, 1995, **252**, 248–262.
- [32] G. A. Jeffrey, *An Introduction to Hydrogen Bonding*, Oxford University Press, 1997.
- [33] C. Tanford, *Science*, 1978, **200**, 1012–1218.
- [34] B. Götzemann, R. Evans and S. Dietrich, *Physical Review E*, 1998, **57**, 6785–6800.
- [35] H. Löwen, *Physica A*, 1997, **235**, 129–141.
- [36] W. Schärfl, *Light Scattering from Polymer Solution and Nanoparticle Dispersions*, Springer, 2007.

- [37] J. Holoubek, *Journal of Quantitative Spectroscopy & Radiative Transfer*, 2007, **106**, 104–121.
- [38] A. P. Minton, *Analytical Biochemistry*, 2016, **501**, 4–22.
- [39] J. Stetefeld, S. A. McKenna and T. R. Patel, *Biophys. Rev.*, 2016, **8**, 409–427.
- [40] R. Pecora, *Journal of Nanoparticle Research*, 2000, **2**, 123–131.
- [41] S. Bhattacharjee, *Journal of Controlled Release*, 2016, **235**, 337–351.
- [42] B. J. Berne and R. Pecora, *Dynamic Light Scattering. With Applications to Chemistry, Biology and Physics*, Dover Publications, Inc., 2000.
- [43] G. Schmeer, *Dynamische Lichtstreuung an kolloidalen und makromolekularen Systemen*.
- [44] *Principles of Physical Biochemistry*, ed. K. E. van Holde, W. C. Johnson and S. Ho, Pearson Prentice Hall, New Jersey, 2006.
- [45] A. J. F. Siegert, *On the fluctuations in signals returned by many independently moving scatterers*, Radiation Laboratory, Massachusetts Institute of Technology, 1943.
- [46] D. E. Koppel, *J. Chem. Phys.*, 1972, **57**, 4814–4820.
- [47] S. W. Provencher, *Computer Physics Communications*, 1982, **27**, 213–227.
- [48] S. W. Provencher, *Computer Physics Communications*, 1982, **27**, 229–242.
- [49] A. Scotti, W. Liu, J. S. Hyatt, E. S. Herman, H. S. Choi, J. W. Kim, L. A. Lyon, U. Gasser and A. Fernandez-Nieves, *J. Chem. Phys.*, 2015, **142**, 234905.
- [50] G. Jeschke, *Kurze Einführung in die elektronenparamagnetische Resonanzspektroskopie*, 2008.
- [51] N. M. Atherton, *Principles of Electron Spin Resonance*, Ellis Horwood, New York, 1973.
- [52] J. A. Weil, J. R. Bolton and J. E. Wertz, *Electron Paramagnetic Resonance: Elementary Theory and Practical Applications*, Wiley, New York, 1994.
- [53] A. Schweiger and G. Jeschke, *Principles of Pulse Electron Paramagnetic Resonance*, Oxford University Press, 2001.
- [54] O. Stern, *Z. Phys.*, 1921, **8**, 249–253.
- [55] W. Gerlach and O. Stern, *Z. Phys.*, 1922, **9**, 349–352.

- [56] G. E. Uhlenbeck and S. Goudsmit, *Die Naturwissenschaften*, 1925, **13**, 953–954.
- [57] G. E. Uhlenbeck and S. Goudsmit, *NATURE*, 1926, **117**, 264–265.
- [58] M. Junk, *PhD thesis*, Johannes Gutenberg-Universität Mainz, 2010.
- [59] Y. N. Molin, K. M. Salikhov and K. I. Zamaraev, *Spin-Exchange - Principles and Applications in Chemistry and Biology*, Springer Series in Chemical Physics, Vol. 8, Springer-Verlag, Berlin, 1980.
- [60] G. Jeschke, *Macromol. Rapid Commun.*, 2002, **23**, 227–246.
- [61] *Biological Magnetic Resonance, Vol.19: Distance Measurements in Biological Systems by EPR*, ed. L. J. Berliner, S. S. Eaton and G. R. Eaton, Kluwer Academic Publishers, New York, 2000.
- [62] A. H. Beth and B. H. Robinson, in *Biological Magnetic Resonance, Vol. 8, Spin Labeling - Theory and Applications*, ed. L. J. Berliner and J. Reuben, Plenum Press, New York, 1989, ch. Nitrogen-15 and deuterium substituted spin labels for studies of very slow rotational motion, pp. 179–253.
- [63] A. R. Edmonds, *Angular Momentum in Quantum Mechanics*, Princeton University Press, 1960.
- [64] C. Wegener, A. Savitsky, M. Pfeiffer, K. Möbius and H. J. Steinhoff, *Appl. Magn. Reson.*, 2001, **21**, 441–452.
- [65] E. L. Hahn, *Phys. Rev.*, 1950, **80**, 580–594.
- [66] J. Eisermann, L. Prager and D. Hinderberger, *Phys. Chem. Chem. Phys.*, 2018, **20**, 1421–1430.
- [67] T. Zhang, J. Brown, R. J. Oakley and C. F. J. Faul, *Current Opinion in Colloid & Interface Science*, 2007, **14**, 62–70.
- [68] C. F. J. Faul, *Acc. Chem. Res.*, 2014, **47**, 3428–3438.
- [69] Y. Haketa and H. Maeda, *Chem. Commun.*, 2017, **53**, 2894–2909.
- [70] D. Hinderberger, H. W. Spiess and G. Jeschke, *Appl. Magn. Reson.*, 2010, **37**, 657–683.
- [71] Y. Yang, S. Wang, Y. Wang, X. Wang, Q. Wang and M. Chen, *Biotechnology Advances*, 2014, **32**, 1301–1316.



- [72] Z. Liu, Y. Jiao, Y. Wang, C. Zhou and Z. Zhang, *Advanced Drug Delivery Reviews*, 2008, **60**, 1650–1662.
- [73] J. Ge and Y. Yin, *Angew. Chem. Int. Ed.*, 2011, **50**, 1492–1522.
- [74] K. J. M. Bishop and B. A. Grzybowski, *ChemPhysChem*, 2007, **8**, 2171–2176.
- [75] A. Lakshmanan, S. Zhang and C. A. Hauser, *Trends in Biotechnology*, 2012, **30**, 155–165.
- [76] M. Ballauff, *Prog. Polym. Sci.*, 2007, **32**, 1135–1151.
- [77] R. Graf, M. R. Hansen, D. Hinderberger, K. Muennemann and H. W. Spiess, *Phys. Chem. Chem. Phys.*, 2014, **16**, 9700–9712.
- [78] D. Kurzbach, D. R. Kattinig, B. Zhang, A. D. Schlüter and D. Hinderberger, *J. Phys. Chem. Letter*, 2011, **2**, 1583–1587.
- [79] J. K. Klosterman, Y. Yamauchi and M. Fujita, *Chem. Soc. Rev.*, 2009, **38**, 1714–1725.
- [80] A. E. Danks, S. R. Hall and Z. Schnepp, *Mater. Horiz.*, 2016, **3**, 91–112.
- [81] M. E. Leunissen, C. G. Christova, A.-P. Hynninen, C. P. Royall, A. I. Campbell, A. Imhof, M. Dijkstra, R. van Roji and A. von Blaaderen, *NATURE*, 2005, **437**, 235–240.
- [82] T. Kato, T. Yasuda, Y. Kamikawa and M. Yoshio, *Chem. Commun.*, 2009, 729–739.
- [83] T. L. Greaves and C. J. Drummond, *Chem. Soc. Rev.*, 2008, **37**, 1709–1726.
- [84] T. L. Greaves and C. J. Drummond, *Chem. Soc. Rev.*, 2013, **42**, 1096–1120.
- [85] B. Chen, S. Xiang and G. Qian, *Accounts of Chemical Research*, 2010, **43**, 1115–1124.
- [86] H.-Y. Gong, B. M. Rambo, W. Cho, V. M. Lynch, M. Oh and J. L. Sessler, *Chem. Commun.*, 2011, **47**, 5973–5975.
- [87] D. Hinderberger, H. W. Spiess and G. Jeschke, *J. Phys. Chem. B*, 2004, **108**, 3698–3704.
- [88] D. Hinderberger and G. Jeschke, in *Site-specific Characterization of Structure and Dynamics of Complex Materials by EPR Spin Probes*, ed. G. A. Webb, Springer, 2006, ch. Characterization of Structure and Dynamics of Complex Materials, pp. 1529–1537.
- [89] D. Hinderberger, G. Jeschke and H. W. Spiess, *Macromolecules*, 2002, **35**, 9698–9706.
- [90] C. Tschierske, *J. Mater. Chem.*, 1998, **8**, 1485–1508.

- [91] C. Tschierske, *J. Mater. Chem.*, 2001, **11**, 2647–2671.
- [92] J. Eisermann and D. Hinderberger, *Phys. Chem. Chem. Phys.*, 2019, **21**, 1152–1159.
- [93] A. W. A. Pauldrach, *Das dunkle Universum - Der Wettstreit Dunkler Materie und Dunkler Energie: Ist das Universum zum Sterben geboren?*, Springer Spektrum, 2015.
- [94] J. Eisermann, A. Kerth and D. Hinderberger, *RSC Advances*, 2019, **9**, 18627–18640.
- [95] I. Stassen, N. Burtch, A. Talin, P. Falcaro, M. Allendorf and R. Ameloot, *Chem. Soc. Rev.*, 2017, **46**, 3185–3241.
- [96] F. Beuerle and B. Gole, *Angew. Chem. Int. Ed.*, 2018, **57**, 4850–4878.
- [97] S.-Y. Ding and W. Wang, *Chem. Soc. Rev.*, 2013, **42**, 548–568.
- [98] T. Hasell and A. I. Copper, *Nature Reviews Materials*, 2016, **1**, 16053.
- [99] A. J. Howarth, A. W. Peters, N. A. Vermeulen, T. C. Wang, J. T. Hupp and O. K. Farha, *Chem. Matter.*, 2017, **29**, 26–39.
- [100] O. M. Yaghi and H. Li, *J. Am. Chem. Soc.*, 1995, **117**, 10401–10402.
- [101] B. Li, H.-M. Wen, Y. Cui, W. Zhou, G. Qian and B. Chen, *Adv. Mater.*, 2016, **28**, 8819–8860.
- [102] H. Li, M. Eddaoudi, M. O’Keeffe and O. M. Yaghi, *Nature*, 1999, **402**, 276–279.
- [103] P. Z. Moghadam, A. Li, S. B. Wiggin, A. Tao, A. G. P. Maloney, P. A. Wood, S. C. Ward and D. Fairen-Jimenez, *Chem. Matter.*, 2017, **29**, 2618–2625.
- [104] B. Li, M. Chrzanowski, Y. Zhang and S. Ma, *Coordination Chemistry Reviews*, 2016, **307**, 106–129.
- [105] Q. Yang, Q. Xu and H.-L. Jiang, *Chem. Soc. Rev.*, 2017, **46**, 4774–4808.
- [106] S. M. J. Rogge, A. Bavykina, J. Hajek, H. Garcia, A. I. Olivios-Suarez, A. Sepúlveda-Escribano, A. Vimont, G. Clet, P. Bazin, F. Kapteijn, M. Daturi, E. V. Ramos-Fernandez, F. X. Li Xamena, V. V. Speybroeck and J. Gascon, *Chem. Soc. Rev.*, 2017, **46**, 3134–3184.
- [107] Y.-B. Huang, J. Liang, X.-S. Wang and R. Cao, *Chem. Soc. Rev.*, 2017, **46**, 126–157.
- [108] A. Karmakar, A. V. Desai and S. K. Ghosh, *Coordination Chemistry Reviews*, 2016, **307**, 313–341.

- [109] Y. V. Kaneti, J. Tang, R. R. Salunkhe, X. Jiang, A. Yu, K. C.-W. Wu and Y. Yamauchi, *Adv. Mater.*, 2017, **29**, 1604898.
- [110] S. Cao, B. Li, R. Zhu and H. Pang, *Chemical Engineering Journal*, 2019, **355**, 602–623.
- [111] X. Feng, X. Ding and D. Jiang, *Chem. Soc. Rev.*, 2012, **41**, 6010–6022.
- [112] G. Lin, H. Ding, D. Yuan, B. Wang and C. Wang, *J. Am. Chem. Soc.*, 2016, **138**, 3302–3305.
- [113] Y. Du, H. Yang, J. M. Whiteley, S. Wan, Y. Jin, S.-H. Lee and W. Zhang, *Angew. Chem. Int. Ed.*, 2016, **55**, 1737–1741.
- [114] X. Han, Q. Xia, J. Huang, Y. Liu, C. Tan and Y. Cui, *J. Am. Chem. Soc.*, 2017, **139**, 8693–8697.
- [115] Q. Sun, B. Aguila, J. Perman, N. Nguyen and S. Ma, *J. Am. Chem. Soc.*, 2016, **138**, 15790–15796.
- [116] P. J. Waller, F. Gándara and O. M. Yaghi, *Acc. Chem. Res.*, 2015, **48**, 3053–3063.
- [117] Y. He, S. Xiang and B. Chen, *J. Am. Chem. Soc.*, 2011, **133**, 14570–14573.
- [118] X.-Z. Luo, X.-J. Jia, J.-H. Deng, J.-L. Zhong, H.-J. Liu, K.-J. Wang and D.-C. Zhong, *J. Am. Chem. Soc.*, 2013, **135**, 11684–11687.
- [119] P. Li, Y. He, J. Guang, L. Weng, J. C.-G. Zhao, S. Xiang and B. Chen, *J. Am. Chem. Soc.*, 2014, **136**, 547–549.
- [120] H. Wang, B. Li, H. Wu, T.-L. Hu, Z. Yao, W. Zhou, S. Xiang and B. Chen, *J. Am. Chem. Soc.*, 2015, **137**, 9963–9970.
- [121] A. Karmakar, R. Illathvalappil, B. Anothumakkool, A. Sen, P. Samanta, A. V. Desai, S. Kurungot and S. K. Ghosh, *Angew. Chem. Int. Ed.*, 2016, **55**, 10667–10671.
- [122] T. Yu, D. Ou, Z. Yang, Q. Huang, Z. Mao, J. Chen, Y. Zhang, S. Liu, J. Xu, M. R. Bryce and Z. Chi, *Chem. Sci.*, 2017, **8**, 1163–1168.
- [123] P. Li, Y. He, H. D. Arman, R. Krishna, H. Wang, L. Weng and B. Chen, *Chem. Commun.*, 2014, **50**, 13081–13084.
- [124] P. Li, Y. He, Y. Zhao, L. Weng, H. Wang, R. Krishna, H. Wu, W. Zhou, M. O’Keeffe, Y. Han and B. Chen, *Angew. Chem. Int. Ed.*, 2015, **54**, 574–577.
- [125] C. S. Diercks and O. M. Yaghi, *Science*, 2017, **355**, eaal1585.

- [126] M. Denis and S. M. Goldup, *Nature Reviews Chemistry*, 2017, **1**, 0061.
- [127] J. E. M. Lewis, M. Galli and S. M. Goldup, *Chem. Commun.*, 2017, **53**, 298–312.
- [128] C. J. Bruns and J. F. Stoddart, *Acc. Chem. Res.*, 2014, **47**, 2186–2199.
- [129] N. Pairault and J. Niemeyer, *Synlett*, 2018, **29**, 689–698.
- [130] M. A. Olsen, A. B. Braunschweig, T. Ikeda, L. Fang, A. Trabolsi, A. M. Z. Slawin, S. I. Khan and J. F. Stoddart, *Org. Biomol. Chem.*, 2009, **7**, 4391–4405.
- [131] H. Y. Au-Yeung, C.-C. Yee, A. W. H. Ng and K. Hu, *Inorg. Chem.*, 2018, **57**, 3475–3485.
- [132] A. Credi, *J. Phys.: Condens. Matter*, 2006, **18**, S1779–S1795.
- [133] A. de Juan, M. M. Bernal and E. M. Pérez, *ChemPlusChem*, 2015, **80**, 1153–1157.
- [134] S. F. M. van Dongen, S. Cantekin, J. A. A. W. Elemans, A. E. Rowan and R. J. M. Nolte, *Chem. Soc. Rev.*, 2014, **43**, 99–122.
- [135] S.-S. Jester and M. Famulok, *Acc. Chem. Res.*, 2014, **47**, 1700–1709.
- [136] H. Li, A. C. Fahrenbach, S. K. Dey, S. Basu, A. Trabolsi, Z. Zhu, Y. Y. Botros and J. F. Stoddart, *Angew. Chem. Int. Ed.*, 2010, **49**, 8260–8265.
- [137] C. Pezzato, C. Cheng, J. F. Stoddart and R. D. Astumian, *Chem. Soc. Rev.*, 2017, **46**, 5491–5507.
- [138] K. K. Coti, M. E. Belowich, M. Liong, M. W. Ambrogio, Y. A. Lau, H. A. Khatib, J. I. Zink, N. M. Khashab and J. F. Stoddart, *Nanoscale*, 2009, **1**, 16–39.
- [139] F. H. Moser and A. L. Thomas, *Journal of Chemical Education*, 1964, **41**, 245–249.
- [140] F. Ghani, J. Kristen and H. Riegler, *J. Chem. Eng. Data*, 2012, **57**, 439–449.
- [141] J. Liu, W. Zhou, J. Liu, I. Howard, G. Kilibarda, S. Schlabach, D. Coupry, M. Addicoat, S. Yoneda, Y. Tsutsui, T. Sakurai, S. Seki, Z. Wang, P. Lindemann, E. Redel, T. Heine and C. Wöll, *Angew. Chem.*, 2015, **127**, 7549–7593.
- [142] T. Muller and S. Bräse, *RSC. Adv.*, 2014, **4**, 6886–6907.
- [143] G. P. Lorenzi, A. Manassis, N. C. Tirelli and V. Gramlich, *Structural Chemistry*, 1997, **8**, 435–441.
- [144] G. Li and Z. Wang, *Macromolecules*, 2013, **46**, 3058–3066.

- [145] W. Luo, Y. Zhu, J. Zhang, J. He, Z. Chi, P. W. Miller, L. Chen and C.-Y. Su, *Chem. Commun.*, 2014, **50**, 11942–11945.
- [146] D. Kurzbach, C. Velte, P. Arnold, G. Kizilsavas and D. Hinderberger, *Soft Matter*, 2011, **7**, 6695–6704.
- [147] M. C. Staniford, M. M. Lezhnina and U. H. Kynast, *RSC Adv.*, 2015, **5**, 3974–3977.
- [148] M. Snehalatha, C. Ravikumar, N. Sekar, V. S. Jayakumar and I. H. Joe, *J. Raman Spectrosc.*, 2008, **39**, 928–936.
- [149] Y. Ni, Y. Wang and S. Kokot, *Talanta*, 2009, **78**, 432–441.
- [150] N. E. Llamas, M. Garrido, M. S. D. Nezio and B. S. F. Band, *Analytica Chimica Acta*, 2009, **655**, 38–42.
- [151] D. Dey, A. Hussain, R. K. Nath and D. Bhattacharjee, *Spectrochimica Acta Part A*, 2008, **70**, 307–312.
- [152] A. Z. Okkema and S. L. Cooper, *Biomaterials*, 1991, **12**, 668–676.
- [153] N. K. Tierney, S. T. Trzaska and R. A. Register, *Macromolecules*, 2004, **37**, 10205–10207.
- [154] *The Porphyrin Handbook - Volume 19 Applications of Phthalocyanines*, ed. K. M. Kadish, K. M. Smith and R. Guilard, Elsevier, 2000.
- [155] N. Korolev, A. P. Lyubartsev, A. Laaksonen and L. Nordenskiöld, *Biophysical Journal*, 2002, **82**, 2860–2875.
- [156] J. Eisermann, A. F. Roth and D. Hinderberger, *J. Phys. Chem. B*, 2019, **123**, 8154–8165.
- [157] P. Muller, *Pure and Applied Chemistry*, 1994, **66**, 1077–1184.
- [158] O. Tapia, *Journal of Mathematical Chemistry*, 1992, **10**, 139–181.
- [159] Y. Marcus, *Chem. Soc. Rev.*, 1993, **22**, 409–416.
- [160] E. Grunwald and C. Steel, *J. Am. Chem. Soc.*, 1995, **117**, 5687–5692.
- [161] S. J. Rowan, S. J. Cantrill, G. R. L. Cousins, J. K. M. Sanders and J. F. Stoddart, *Angew. Chem. Int. Ed.*, 2002, **41**, 898–952.
- [162] C. Reichardt and T. Welton, *Solvent and Solvent Chemistry in Organic Chemistry*, Wiley-VCH, 2011.

- [163] K. C. Fox, *Science*, 1995, **267**, 1922–1923.
- [164] M. Tarek and D. J. Tobias, *Biophysical Journal*, 2000, **79**, 3244–3257.
- [165] G. Caliskan, D. Mechtani, J. H. Roh, A. Kisliuk, A. P. Sokolov, S. Azzam, M. T. Cicerone, S. Lin-Gibson and I. Peral, *J. Chem. Phys.*, 2004, **121**, 1978–1983.
- [166] J. F. V. Vincent, O. A. Bogatyreva, N. R. Bogatyrev, A. Bowyer and A.-K. Pahl, *J. R. Soc. Interface*, 2006, **3**, 471–482.
- [167] J. F. V. Vincent, *Proc. IMechE Part H: Journal of Engineering in Medicine*, 2009, **223**, 919–939.
- [168] J.-M. Lehn, M. Mascal, A. DeCian and J. Fischer, *J. Chem. Soc., Perkin Trans. 2*, 1992, **0**, 461–467.
- [169] J.-M. Lehn, *Chem. Soc. Rev.*, 2007, **36**, 151–160.
- [170] K. Kanagaraj, M. Alagesan, Y. Inoue and C. Yang, in *Comprehensive Supramolecular Chemistry II*, ed. J. L. Atwood, Oxford, Elsevier, 2017, vol. 1, ch. Solvation Effects in Supramolecular Chemistry, pp. 11–60.
- [171] A. Lattes, E. Perez and I. Rico-Lattes, *C. R. Chimie*, 2009, **12**, 45–53.
- [172] Y. Akdogan, J. Heller, H. Zimmermann and D. Hinderberger, *Phys. Chem. Chem. Phys.*, 2010, **12**, 7874–7882.
- [173] D. R. Kattinig and D. Hinderberger, *Chem. Asian J.*, 2012, **7**, 1000–1008.
- [174] U. Cerajewski, J. Träger, S. Henkel, A. H. Roos, M. Brehm and D. Hinderberger, *Phys. Chem. Chem. Phys.*, 2018, **20**, 29591–29600.
- [175] W.-F. Su, *Principles of Polymer Design and Synthesis*, Springer-Verlag, 2013.
- [176] R. Verduzco, X. Li, S. L. Pesek and G. E. Stein, *Chem. Soc. Rev.*, 2015, **44**, 2405–2420.
- [177] T. Das, D. Bratko, L. B. Bhuiyan and C. W. Outhwaite, *J. Phys. Chem.*, 1995, **99**, 410–418.
- [178] H. J. Limbach and C. Holm, *J. Phys. Chem. B*, 2003, **107**, 8041–8055.
- [179] S. Dragon, L. Ghimici and C. Wandrey, *Macromol. Symp.*, 2004, **211**, 107–119.
- [180] M. Nic, J. Jirat and B. Kosata, *IUPAC. Compendium of Chemical Terminology*, Oxford Blackwell Scientific Publications, 1997.

- [181] T. Mezger, *Das Rheologie-Handbuch: Für Anwender von Rotations- und Oszillations-Rheometern*, Curt R. Vincentz Verlag, 2000.
- [182] M. L. Sheely, *Industrial and Engineering Chemistry*, 1932, **24**, 1060–1064.
- [183] J. B. Segur and H. E. Oberstar, *Industrial and Engineering Chemistry*, 1951, **43**, 2117–2120.
- [184] N. G. Tsierkezos and I. E. Molinou, *J. Chem. Eng. Data*, 1998, **43**, 989–993.
- [185] S. J. Bass, W. I. Nathan, R. M. Meighan and R. H. Cole, *J. Phys. Chem.*, 1964, **68**, 509–515.
- [186] T. B. Hoover, *J. Phys. Chem.*, 1969, **73**, 57–61.
- [187] L. S. Gabrielian and S. A. Markarian, *Journal of Molecular Lipids*, 2004, **112**, 137–140.
- [188] M. Józwiak, M. Tyczynska and A. Bald, *J. Chem. Eng. Data*, 2013, **58**, 217–224.
- [189] C. M. Kinart, A. Bald, W. J. Kinart and A. Kolasinski, *Physics and Chemistry of Liquids*, 1998, **36**, 245–256.
- [190] C. M. Kinart and W. J. Kinart, *Physics and Chemistry of Liquids*, 1996, **33**, 159–170.
- [191] T. A. Litovitz, R. Higgs and R. Meister, *J. Chem. Phys.*, 1954, **22**, 1218–1283.
- [192] F. F. Hanna, B. Gestblom and A. Soliman, *Phys. Chem. Chem. Phys.*, 2000, **2**, 5071–5075.
- [193] A. R. H. Goodwin and K. N. Marsh, *J. Chem. Eng. Data*, 2011, **56**, 167–170.
- [194] C. M. Kinart and W. J. Kinart, *Physics and Chemistry of Liquids*, 1994, **28**, 261–268.
- [195] F. J. Millero, *J. Phys. Chem.*, 1968, **72**, 3209–3214.
- [196] R. Moritz, G. Zardalidis, H.-J. Butt, M. Wagner, K. Müllen and G. Floudas, *Macromolecules*, 2013, **47**, 191–196.
- [197] A. Luzar and D. Chandler, *J. Chem. Phys.*, 1993, **98**, 8160–8173.
- [198] I. A. Borin and M. S. Skaf, *J. Chem. Phys.*, 1999, **110**, 6412–6420.
- [199] R. Chelli, P. Procacci, G. Cardini, R. G. D. Valle and S. Califano, *Phys. Chem. Chem. Phys.*, 1999, **1**, 871–877.
- [200] R. Chelli, P. Procacci, G. Cardini, R. G. D. Valle and S. Califano, *Phys. Chem. Chem. Phys.*, 1999, **1**, 879–885.

- [201] J. L. Dashnau, N. V. Nucci, K. A. Sharp and J. M. Vanderkooi, *J. Phys Chem. B*, 2006, **110**, 13670–13677.
- [202] I. Bako, T. Grosz, G. Palinkas and M. C. Bellissent-Funel, *J. Chem. Phys.*, 2003, **118**, 3215–3221.
- [203] H. Abdelmoulahi, H. Ghalla, S. Nasr, M. Bahri and M.-C. Bellissent-Funel, *Journal of Molecular Liquids*, 2016, **220**, 527–539.
- [204] D. Kurzbach, M. J. N. Junk and D. Hinderberger, *Macromol. Rapid Commun.*, 2013, **34**, 119–134.
- [205] M. Plato, H.-J. Steinhoff, C. Wegner, J. T. Törring, A. Savitsky and K. Möbius, *Molecular Physics*, 2002, **100**, 3711–3721.
- [206] Y. Marcus, *Solvent Mixtures - Properties and Selective Solvation*, CRC Press, Taylor and Francis Group, 2002.
- [207] T. Udagawa, T. Ishimoto, T. Tokiwa, M. Tachikawa and U. Nagashima, *Chemical Physics Letters*, 2004, **389**, 236–240.
- [208] T. Udagawa, T. Ishimoto, H. Tokiwa, M. Tachikawa and U. Nagashima, *J. Phys. Chem. A*, 2006, **110**, 7279–7285.
- [209] D. Attanasio, *J. Phys. Chem.*, 1986, **90**, 4952–4957.
- [210] D. Mustafi and M. W. Makinen, *Inorg. Chem.*, 1988, **27**, 3360–3368.
- [211] H. van Willigen, *Chem. Phys. Lett.*, 1979, **65**, 490–493.
- [212] J. Heller, H. Elgabarty, B. Zhuang, D. Sebastiani and D. Hinderberger, *J. Phys. Chem. B*, 2010, **114**, 7429–7438.
- [213] E. L. H. L. G. Rowan and W. B. Mims, *Phys. Rev.*, 1965, **137**, A61–A71.
- [214] W. B. Mims, *Phys. Rev.*, 1972, **5**, 2409–2419.
- [215] A. Volkov, C. Dockter, T. Bund, H. Paulsen and G. Jeschke, *Biophys. Jour.*, 2009, **96**, 1124–1141.
- [216] M. M. Roessler and E. Salvadori, *Chem. Soc. Rev.*, 2018, **47**, 2534–2553.
- [217] G. Jeschke and Y. Polyhach, *Phys. Chem. Chem. Phys.*, 2007, **9**, 1895–1910.
- [218] T. Ichikawa, L. Kevan, M. K. Bowman, S. A. Dikanov and Y. D. Tsvetkov, *J. Chem. Phys.*, 1979, **71**, 1167–1174.



- [219] J. Harmer, G. Mitrikas and A. Schweiger, in *High Resolution EPR - Applications to Metalloenzymes and Metals in Medicine*, ed. G. Hanson and L. Berliner, Springer Science+Business Media, Inc., 2009, ch. Advanced Pulse EPR Methods for the Characterization of Metalloproteins, pp. 13–61.
- [220] B. L. Bales, E. Wajnberg and O. R. Nascimento, *Jour. Magn. Reson.*, 1996, **118**, 227–233.
- [221] S. K. Brar and M. Verma, *Trends in Analytical Chemistry*, 2011, **30**, 4–17.
- [222] C. Bellman, A. Caspari, C. Moitzi and F. Babick, *Dynamische und elektroforetische Lichtstreuung - Leitfaden zur Partikelgrößenanalyse und Zetapotenzialbestimmung*, Anton Paar GmbH, Austria, 2018.
- [223] Z. Li, Y. Wang, J. Schen and X. Sun, *Optics and Lasers in Engineering*, 2014, **56**, 94–98.
- [224] M. Su, F. Xu, X. Cai, K. Ren and J. Shen, *China Particuology*, 2007, **5**, 295–299.
- [225] H. Noack and C. Moitzi, *U.S. Patent, US 2014/0144780 A1*, May 29, 2014, 1–9.
- [226] C. Moitzi and B. Petrillo, *Faster, more sensitive zeta-potential measurements with cm-PALS and the Litesizer 500*, Anton paar application report d51/a021 technical report, 2016.
- [227] A. V. Delgado, F. González-Caballero, R. J. Hunter, L. K. Koopal and J. Lyklema, *Pure Appl. Chem.*, 2005, **10**, 1753–1805.
- [228] D. Erickson and D. Li, *Journal of Colloid and Interface Science*, 2001, **237**, 283–289.
- [229] H. Keh and J. L. Anderson, *J. Fluid. Mech.*, 1985, **153**, 417–439.
- [230] A. Sze, D. Erickson, L. Ren and D. Li, *Journal of Colloid and Interface Science*, 2003, **261**, 402–410.
- [231] N. Schultz, G. Metrevil, M. Franzreb, F. H. Frimmel and C. Syldatk, *Colloids and Surfaces B: Biointerfaces*, 2008, **66**, 39–44.
- [232] A. Salis, M. Boström, L. Medda, F. Cugia, B. Barse, D. F. Parsons, B. W. Ninham and M. Monduzzi, *Langmuir*, 2011, **27**, 11597–11604.
- [233] B. Derjaguin and L. Landau, *Acta Physicochim. URSS*, 1941, **14**, 633–662.
- [234] E. J. W. Verwey, J. T. G. Overbeek and K. V. Nes, *Theory of the stability of lyophobic colloids : the interaction of sol particles having an electric double layer*, Elsevier Amsterdam, 1948.

- [235] C. Jacobs and R. H. Müller, *Pharmaceutical Research*, 2002, **2**, 189–194.
- [236] J. Reichenwallner, A. Thomas, T. Steinbach, J. Eisermann, C. E. H. Schmelzer, F. Wurm and D. Hinderberger, *Biomacromolecules*, 2019, **20**, 1118–1131.
- [237] J. W. Swan and E. M. Furst, *Journal of Colloid and Interface Science*, 2012, **388**, 92–94.
- [238] A. Morante, R. Forteza and V. Cerdá, *Thermochimica Acta*, 1987, **118**, 215–22.
- [239] S. Stoll and A. Schweiger, *Journal of Magnetic Resonance*, 2006, **178**, 42–55.
- [240] D. J. Schneider and J. H. Freed, in *Biological Magnetic Resonance*, ed. L. J. Berliner and J. Reuben, Plenum Press, New York, 1989, ch. Calculating Slow Motional Magnetic Resonance Spectra, pp. 1–76.
- [241] D. Hinderberger, *PhD thesis*, Johannes-Gutenberg-Universität Mainz, 2004.
- [242] E. Krieger, T. Darden, S. B. Nabuurs, A. Finkelstein and G. Vriend, *Proteins: Struct., Funct., Bioinf.*, 2004, **57**, 678–683.
- [243] B. H. Robinson, C. Mailer and A. W. Reese, *Journal of Magnetic Resonance*, 1999, **138**, 199–209.

# List of Abbreviations and Symbols

## Intermolecular Interaction

$\alpha$	Polarizability
$a$	Extension of orbital in Born repulsive interaction
$a_0$	First Bohr radius
$A_H$	Helmholtz free energy
$C$	(Positive) constant in Born repulsive interaction
$\varepsilon$	Binding energy or depth of the potential well
$\varepsilon_0$	Electric field constant
$\varepsilon_r$	Relative permittivity
$e$	Elementary charge
$E_{q_{1,2}}$	Electric field strength of a point charge
$\vec{E}_{perm}$	Electric field strength of a permanent dipole
$\vec{F}$	Interaction force
$\vec{F}_{Coul,q_{1,2}}$	Coulomb interaction force
$h$	Planck constant
$h'$	Mutual distance of large particles
$\vartheta_{1,2}$	Angles to characterize orientation of dipole moments $\vec{\mu}_{1,2}$ relative to $\vec{r}$
$k_B$	Boltzmann constant
$\vec{l}$	Distance vector for charges in dipole
$l_{perm}$	Length of a permanent dipole
$\vec{\mu}$	Dipole moment
$\vec{\mu}_{perm}$	Permanent dipole moment
$\nu$	Orbiting frequency of an electron
$q$	Net charge
$q_{1,2}$	Point charges
$r$	Separation distance of interaction partners
$\vec{r}$	Unit vector between e. g. point charges
$r_0$	Finite distance where $W$ reaches 0

$r_{min}$	Equilibrium distance where $\vec{F}$ reaches 0
$r_s$	Shell thickness of depletion zones
$T$	Absolute temperature
$\varphi$	Angle between planes spanned by vector pairs $\vec{\mu}_1, \vec{r}$ and $\vec{\mu}_2, \vec{r}$
$V_{avail}$	Available volume
$V_{ex}$	Excluded volume
$w$	Width of the overlap 'lens'
$W$	Interaction potential
$W_{Coul}$	Coulomb interaction potential
$W_{rep}$	Repulsive interaction potential

## Applied Methods and Techniques

2p	Two-pulse
3p	Three-pulse
$\alpha, \beta, \gamma$	Set of Euler angles
$\alpha$	Polarizability
$a$	Particle radius of charged species
$a, b$	Length of semi-major and semi-minor axis
$a_{iso}$	Isotropic hyperfine coupling constant
$\mathbf{A}$	Hyperfine coupling tensor
$\beta$	Coherence factor (autocorrelation function)
$B$	Baseline (autocorrelation function)
$B(t)$	Stretched-exponential function
$B_0$	External magnetic field
$\mathbf{B}_1^T$	Oscillating microwave field
$B_{pp}$	Peak-to-peak width
$c$	Concentration
$C$	Capacity
cmPALS	Continuously monitored phase-analysis light scattering
COF	Covalent organic framework
CW	Continuous wave
$D$	Diffusion coefficient
$D(t)$	Damped harmonic oscillation
$D_{  }$	Rotational diffusion rate parallel to unique axis

---

$D_{\perp}$	Rotational diffusion rate perpendicular to unique axis
DLS	Dynamic light scattering
DMF	<i>N,N</i> -dimethyl formamide
DMSO	Dimethyl sulfoxide
d6-DMSO	d6-Dimethyl sulfoxide
$\epsilon_0$	Electric field constant
$\epsilon_r$	Relative permittivity
$e$	Elementary charge
$e_{IED}$	Eccentricity
eg	Ethylene glycol
$E$	Energy levels
$\Delta E$	Difference of energy levels
$\vec{E}$	Electric field vector
$E_0$	Amplitude of electric field vector
$E_s$	Scattered electric field
ELS	Electrophoretic light scattering
EPR	Electron paramagnetic resonance
ESEEM	Electron-spin-echo envelope modulation
$F(\kappa a)$	Henry's function
FWHM	Full width at half maximum
$\gamma$	Magnetogyric ratio
$\Gamma$	Decay rate
$\mathbf{g}$	$g$ -tensor (with principle elements $g_{xx}, g_{yy}, g_{zz}$ )
$g_1(\tau)$	Normalized electric field autocorrelation function
$g_2(\tau)$	Normalized intensity autocorrelation function
$g_e$	$g$ -factor for free electron
$g_{iso}$	Isotropic $g$ -value
$g_n$	Nuclear $g$ -factor
gly	Glycerol
d3-gly	Glycer-d3-ol
d5-gly	d5-glycerol
$G(\Gamma)$	Distribution function of decay rate
$\eta$	Dynamic viscosity
$\hbar$	Reduced Planck constant
$\vec{H}$	Magnetic field vector
$H_0$	Time-independent Hamiltonian

HOF	Hydrogen bonding organic framework
HRD	Hertzsprung-Russell diagram
$I$	Ionic strength (light scattering)
$I$	Spin operator of coupled nucleus
$\langle I \rangle$	Mean scattering intensity
$I_0$	Intensity of induced light
$I_s$	Intensity of scattered light
$I(\nu)$	Magnitude spectra
IED	Ionoid evolution diagram
ISA	Ionic self-assembly
$\kappa^{-1}$	Thickness of electric double layer
( $k$ )	Length of the wave vector (DLS)
$k$	Modulation depth (EPR spectroscopy)
$k_B$	Boltzmann constant
$k_D$	Deuterium modulation depth
$\lambda$	Wavelength
$\lambda_B$	Bjerrum length
$\lambda_d$	Debye length
$lw$	Line width
$\vec{\mu}$	Dipole moment
$\mu_0$	Vacuum permeability
$\mu_B$	Bohr magneton
$\mu_e$	Electrophoretic mobility
$\mu_n$	Nuclear magneton
$m_I$	Magnetic quantum number for $I$
$m_S$	Magnetic quantum number for $S$
$\mu_{Spin}$	Magnetic moment of electron spin
$M$	Macroscopic magnetization
MIM	Mechanically interlocked molecule
MOF	Metal-organic framework
$\nu$	Frequency
$n$	Refractive index
$N(t)$	Normalized nuclear modulation function
$N_A$	Avogadro's number
NMPA	<i>N</i> -methylpropionamide
NNLS	Non-negative least square

---

$q$	Scattering vector
$\rho$	Volume charge density
$r$	Distance to dipole moment
$R_H$	Hydrodynamic radius
$\vec{S}$	Spin angular momentum
$\theta$	Scattering angle
$\theta, \varphi$	Azimuth and polar angle
$\tau$	Interpulse delay (pulsed EPR spectroscopy)
$\tau$	Correlation time (DLS)
$\tau_c$	Rotational correlation time
$T$	Absolute temperature
$T$	Anisotropy (CW EPR spectroscopy)
$T$	Evolution time (pulsed EPR spectroscopy)
$T_1$	Longitudinal relaxation time
$T_2$	Transverse relaxation time
$\Delta t$	Time intervals
$t_m$	Total measurement time
$T_m$	Phase memory time
$T_m^n$	Nuclear spin-spin relaxation
$v$	Velocity of charged particle
$V$	Volume (for magnetization)
$V$	Volume of ionic building unit (based on molecular surface)
$\Psi_0$	Electron spin density at the nucleus
$\omega_{eff}$	Effective nutation frequency
$\omega_s$	Larmor frequency
$\Omega_s$	Resonance offset frequency
$\zeta$	Zeta potential
$z^\pm$	Constant charge





# Acknowledgements

First of all I would like to thank my supervisor Prof. Dr. Dariush Hinderberger for accepting me into his work group and giving me the opportunity to start working on this very interesting topic back in 2015 as teaching-student for my so called 'Wissenschaftliche Hausarbeit'. His encouragements throughout this initial phase of my academic career constitute a big part for prosecuting this topic in my PhD studies.

My sincere thanks also to Dr. Andreas Kerth for introducing me to Prof. Hinderberger and his work group. Without his lecture 'Physikalische Chemie II' for teaching-students, I would have never started my academic career in this research field. I would also like to thank him for supervising my 'Wissenschaftliche Hausarbeit' and for helping me establishing the DLS technique for this project.

A very special gratitude to my co-workers Dr. Haleh Hashemi Haeri, Katharina Widder and Jörg Reichenwallner for introducing me into the world of EPR spectroscopy and for many helpful discussions regarding the recording and simulation of the respective spectra.

Many thanks to my former school student Lukas Prager, my former bachelor student Anna Franziska Roth and my former master student Andreas Helmut Roos for their successful work on colloid-like ionic clusters. Without their contributions, some of the important results from my thesis would be missing now.

A big thank you to my fellow group members of the Hinderberger group, which I consider as my second family, for many helpful discussions and enjoyable coffee rounds on Friday mornings. I also would like to thank my 'real' family for their continuous support throughout the last years and the upcoming tasks.

At last I thank the 'Fonds der Chemischen Industrie' as well as the 'Graduiertenförderung' of Saxony-Anhalt for supporting my studies with their financial support.



# Scientific Contributions

## List of publications

1. **J. Eisermann**, L. Prager and D. Hinderberger (2018): Solvent and concentration effects on highly-defined, colloid-like ionic clusters in solution. *Phys. Chem. Chem. Phys.*, 20, 1421-1430
2. **J. Eisermann** and D. Hinderberger (2019): Tuning the shape anisotropy of loosely bound colloid-like ionic clusters in solution. *Phys. Chem. Chem. Phys.*, 21, 1152-1159
3. J. Reichenwallner, A. Thomas, T. Steinbach, **J. Eisermann**, C. E. H. Schmelzer, F. Wurm and D. Hinderberger (2019): Ligand-Binding Cooperativity Effects in Polymer-Protein Conjugation. *Biomacromolecules*, 20, 1118-1131
4. **J. Eisermann**, A. Kerth and D. Hinderberger (2019): Dynamic Self-Assembly of Ions with Variable Size and Charge in Solution, *RSC Advances*, 9, 18627-18640
5. **J. Eisermann**, A. F. Roth and D. Hinderberger (2019): Shape, Size and Internal Dynamics of Loosely Bound Colloid-Like Ionic Clusters in Ternary Solvent Systems. *J. Phys. Chem. B*, 123, 8154-8165

## Oral contributions

1. **J. Eisermann** and D. Hinderberger: Multifrequency and pulsed EPR spectroscopy on extremely soft, self-assembled structures in solution. *Asia-Pacific EPR/ESR Society and The International EPR (ESR) Society (IES) Symposium*. Brisbane (Australia), 23.09.2018-27.09.2018
2. **J. Eisermann** and D. Hinderberger: Globular Clusters in the Nanoworld: Formation of ionic clusters in solution based on molecular self-assembly. *Survival of Dense Star Clusters in the Milky Way System*. Heidelberg (Germany), 19.11.2018-23.11.2018

## Poster contributions

1. **J. Eisermann** and D. Hinderberger: From Ion clouds to highly defined, colloid-like ionic clusters. *Bunsentagung 2018 - Kinetics in the Real World*. 10.05.2018-12.05.2018, Hannover (Germany)
2. **J. Eisermann** and D. Hinderberger: Multifrequency and pulsed EPR spectroscopy on extremely soft, self-assembled structures in solution. *40th FGMR Annual Discussion Meeting*. Leipzig (Germany), 10.09.2018-13.09.2018
3. **J. Eisermann** and D. Hinderberger: Dynamic yet Defined: Extremely Soft, Self-Assembled Structures in Solution. *Bunsentagung 2019 - Functional Materials*. Jena (Germany), 30.05.2019-01.06.2019
4. **J. Eisermann** and D. Hinderberger: Dynamic yet Defined: EPR Spectroscopy on Extremely Soft, Self-Assembled Structures in Solution. *EUROISMAR 2019*. Berlin (Germany), 25.08.2019-30.08.2019

# Publishing Permission

The following paragraph contains the e-mail from the 'The Royal Society of Chemistry' with the permission to reuse my already published work for my PhD thesis.

---

**RE: Re-use published context**

---

**Von:** "CONTRACTS-COPYRIGHT (shared)" <Contracts-Copyright@rsc.org>  
**An:** "jana.eisermann@chemie.uni-halle.de" <jana.eisermann@chemie.uni-halle.de>  
**Datum:** Montag, 14. Oktober 2019 10.18 Uhr  
**Betreff:** RE: Re-use published context  
**Anlagen:** TEXT.htm; Mime.822

---

Dear Jana

The Royal Society of Chemistry (RSC) hereby grants permission for the use of your paper(s) specified below in the printed and microfilm version of your thesis. You may also make available the PDF version of your paper(s) that the RSC sent to the corresponding author(s) of your paper(s) upon publication of the paper(s) in the following ways: in your thesis via any website that your university may have for the deposition of theses, via your university's Intranet or via your own personal website. We are however unable to grant you permission to include the PDF version of the paper(s) on its own in your institutional repository. The Royal Society of Chemistry is a signatory to the STM Guidelines on Permissions (available on request).

Please note that if the material specified below or any part of it appears with credit or acknowledgement to a third party then you must also secure permission from that third party before reproducing that material.

Please ensure that the thesis states the following:

Reproduced by permission of The Royal Society of Chemistry

and include a link to the paper on the Royal Society of Chemistry's website.

Please ensure that your co-authors are aware that you are including the paper in your thesis.

Regards

Gill Cockhead  
Contracts & Copyright Executive

Gill Cockhead  
Contracts & Copyright Executive  
Royal Society of Chemistry,  
Thomas Graham House,  
Science Park, Milton Road,  
Cambridge, CB4 0WF, UK  
Tel +44 (0) 1223 432134

The respective permission for the publication in the 'Journal of Physical Chemistry B' is also attached (see below).



RightsLink®

Home

Create Account

Help



ACS Publications  
Most Trusted. Most Cited. Most Read.

**Title:** Shape, Size, and Internal Dynamics of Loosely Bound Colloidlike Ionic Clusters in Ternary Solvent Systems

**Author:** Jana Eisermann, Anna Franziska Roth, Dariush Hinderberger

**Publication:** The Journal of Physical Chemistry B

**Publisher:** American Chemical Society

**Date:** Sep 1, 2019

Copyright © 2019, American Chemical Society

LOGIN

If you're a [copyright.com](#) user, you can login to RightsLink using your [copyright.com](#) credentials. Already a [RightsLink](#) user or want to [learn more?](#)

#### PERMISSION/LICENSE IS GRANTED FOR YOUR ORDER AT NO CHARGE

This type of permission/license, instead of the standard Terms & Conditions, is sent to you because no fee is being charged for your order. Please note the following:

- Permission is granted for your request in both print and electronic formats, and translations.
- If figures and/or tables were requested, they may be adapted or used in part.
- Please print this page for your records and send a copy of it to your publisher/graduate school.
- Appropriate credit for the requested material should be given as follows: "Reprinted (adapted) with permission from (COMPLETE REFERENCE CITATION). Copyright (YEAR) American Chemical Society." Insert appropriate information in place of the capitalized words.
- One-time permission is granted only for the use specified in your request. No additional uses are granted (such as derivative works or other editions). For any other uses, please submit a new request.

BACK

CLOSE WINDOW

Copyright © 2019 [Copyright Clearance Center, Inc.](#) All Rights Reserved. [Privacy statement](#). [Terms and Conditions](#).

Comments? We would like to hear from you. E-mail us at [customercare@copyright.com](mailto:customercare@copyright.com)

# Curriculum Vitae

## Persönliche Daten

---

Name: Jana Eisermann  
Geburtstag: 25. März 1993  
Geburtsort: Plauen

## Akademischer Werdegang

---

seit 04/2016 Promotion  
Martin-Luther-Universität Halle-Wittenberg  
Komplexe Selbstorganisierende Systeme, AG Prof. D. Hinderberger

10/2011-02/2016 Studium Lehramt für Gynasien - Physik und Chemie  
Martin-Luther-Universität Halle-Wittenberg  
Abschluss: Erste Staatsprüfung

09/2002-06/2011 Besuch Lessing-Gymnasium in Plauen  
Allgemeine Hochschulreife

Halle (Saale), den 28.10.2019





# Eigenständigkeitserklärung

Hiermit erkläre ich, dass ich die vorliegende Arbeit selbständig und ohne fremde Hilfe verfasst, andere als die von mir angegebenen Quellen und Hilfsmittel nicht benutzt und die den verwendeten Werken wörtlich oder inhaltlich entnommenen Stellen als solche kenntlich gemacht habe.

.....

Jana Eisermann

Halle (Saale), den 28.10.2019